

Co-funded by the



CEBAMA

➤ (Contract Number: 662147)

Deliverable n°D4.13

Draft of the 3rd Annual Project Workshop Proceeding

Editors: Amphos 21 and KIT

Date of issue of this report: September 2019

Report number of pages: 333

Start date of project: 01/06/2015 Duration: 48 Months

Project co-funded by the European Commission under the Euratom Research and Training Programme on Nuclear Energy within the Horizon 2020 Framework Programme		
Dissemination Level		
PU	Public	x
PP	Restricted to other programme participants (including the Commission Services)	
RE	Restricted to a group specified by the partners of the CEBAMA project	
CO	Confidential, only for partners of the CEBAMA project	

ABSTRACT:

The deliverable presents the draft of the 2nd Annual Workshop Proceedings.

RESPONSIBLE:

Amphos 21

FOREWORD

The present document contains the proceedings of the Second Annual Workshop (AWS) of the EURATOM H2020 Collaborative Project CEBAMA (Cement-based materials, properties, evolution, barrier functions). The electronic version of these proceedings is available on the webpage of the project (<http://www.cebama.eu/>) and at KIT Scientific Publishing (www.ksp.kit.edu). The project started in June 2015 and has a duration of four years. The project is implemented by a consortium with 27 Beneficiaries, from 9 EURATOM Signatory States, Japan and Switzerland. National Waste Management Organizations contribute to the running project by participation in the End-User Group, by co-funding Beneficiaries, and provide for knowledge and information transfer.

These proceedings serve for several purposes. The key purpose is to document and make available the progress of the CEBAMA project to a broad scientific community. For this purpose, a considerable part of the project activity is reported by the proceedings, together with the scientific-technical contributions containing details of the work. The progress shown corresponds to the first three years of life of the activities, and we are very proud to see that all groups are obtaining good results have already been obtained. The project facilitates training mobility measures for students, and the workshop also served to put in place and communicate the procedures for application of these grants. Additional purposes of the proceedings are to ensure on-going documentation of the project outcome, promote systematic scientific-technical development throughout the project and to allow thorough review of the project progress.

All Scientific and Technical papers (S&T) included in the proceedings have been reviewed by the Work Package leaders and the EUG (End-User-Group) of CEBAMA. The EUG is specifically set up within the project representing the interest of the national waste management and/or national regulatory organizations that may use the results of the project for their Safety Cases. For this reason, this EUG had a strong involvement on guiding the priorities of the activities of the project and it is a very useful tool to guarantee that the research is done in a way that allows for future knowledge transfer.

The proceedings give only very brief information about the project structure and the different activities around the project. This type of information is available in detail under <http://www.cebama.eu>.

The editors of the proceedings thank all contributors to the project, especially those submitting Scientific and Technical contributions, and the workpackage leaders who provided the summary of the different workpackages for publication in these proceedings. Special thanks are given to the reviewers, the members of the EUG, whose effort and hard work reflected their commitment and dedication to the project and contribute to a high quality of the research performed within CEBAMA.

Table of Contents

FOREWORD	I
THE PROJECT	1
3RD ANUAL WORKSHOP	3
WP OVERVIEW	7
Overview of Work Package 1	9
Overview of Work Package 2	11
Overview of Work Package 3	13
S + T CONTRIBUTIONS	15
Diffusion of tritiated water and chloride-36 through low pH cements.....	17
Experiments on interface processes at the cement/Callovo-Oxfordian claystone interface and the impact on physical properties; mechanical and flow properties of fresh interfaces.....	29
Effects of porosity evolution on the evaluation of radionuclide diffusion coefficients in mortars and concrete	39
Experimental study of chemical degradation of cementitious materials in boom clay environment	49
Geochemical and thermal impacts on the characteristics of cementitious materials: strength, leachate pH, mineralogy and diffusion.....	59
The physico-chemical evolution of a low-pH cement in contact with groundwater.....	71
Leaching of hardened Portland cement with various C/S-ratios	81
Bonding and hydro-mechanical behavior of Callovo-Oxfordian claystone/concrete interface	89
Time and spatial scales observation of chemical profiles arising from surface interaction of bentonite in different cement environments	101
Degradation processes and alkaline plumes in high and low pH concretes after months and years of interaction with granite water.....	109
Physical and chemical behaviour of Low Hydration Heat/Low pH concretes.....	117
Aged interface between Opalinus Clay and low-pH mortar: sample characterization, X-ray computed tomography and core infiltration experiment	125
Geochemical and microstructural evolution of cementitious materials in contact with a clayey rock at 70°C – In-situ tests in the Tournemire URL and laboratory experiments.....	153
Changes in the anion content of groundwaters following interaction with cement	165
CEBAMA reference mix design for low-pH concrete and paste, intermediate results.....	177

Solubility and hydrolysis of Be(II) in dilute to concentrated NaCl and KCl solutions	191
Uptake mechanisms of radionuclides in cementitious systems: insights from atomistic simulations ..	201
Ra-226 sorption on intact cement pastes based on CEM I and CEM V	211
Uptake and diffusion properties of HTO and inorganic C-14 through hardened cement paste: Influence of water saturation and carbonation	219
Behavior of radium and strontium in contact with cementitious materials relevant for LILW disposal in the Czech Republic.....	231
Effect of redox conditions on sulfur, selenium and iodine binding in AFm phases.....	239
Retention and mobility studies of safety relevant radionuclides in cementitious materials.....	249
Reactive transport modelling of radionuclides migration in the low pH cement/clay interface	261
Influence of internal relative humidity on the hydration of a low-pH cement. A modelling study. ...	271
Pore-scale reactive transport modelling of transport and leaching processes in cementitious materials	281
Coupled THCM models of heating-hydration tests containing OPC concrete and compacted FEBEX bentonite	291
Modelling and interpretation of diffusion experiments of selected radionuclides through cementitious samples.....	301
Nernst-Planck Solver (NPS) applied to diffusion of ions through a constricted pore.....	309

POSTERS	317
----------------------	------------

THE PROJECT

CEBAMA is a Collaborative Project funded by the European Commission under the Horizon 2020 Research and Training Programme of the European Atomic Energy Community (EURATOM) (H2020-NFRP-2014/2015), section B - Contribute to the Development of Solutions for the Management of Ultimate Radioactive Waste, Topic NFRP 6 - 2014: Supporting the implementation of the first-of-the-kind geological repositories).

The Collaborative Project CEBAMA addresses key issues of relevance for long term safety and key scientific questions related to the use of cement-based materials in nuclear waste disposal applications. These materials are key components in the barrier system of repositories, independent on the actual host rocks. They are used as waste forms, liners and structural components as well as sealing materials in a broad variety of applications. Waste forms and their behaviour as well as the technical feasibility and long-term performance of repository components are key topics detailed in the Strategic Research Agenda (SRA) of the Implementing Geological Disposal Technology Platform (IGD-TP) and cover studies related with: (a) the release of radionuclides, (b) long-term behaviour of seals and plugs, (c) evolution of cement-based seals, (d) interaction of cement with clays and (e) optimisation aspects.

The overall objective of CEBAMA is to support the implementation of geological disposal by improving significantly the knowledge base for the Safety Case for European repository concepts. The research planned in CEBAMA is largely independent of specific disposal concepts and addresses different types of host rocks in addition to bentonite. CEBAMA is not focusing on one specific cement material but aims to study a variety of important cement-based materials in order to provide insight on general processes and phenomena.

The ambition of CEBAMA is the development of comprehensive models for predicting the alteration processes and their impact on transport characteristics such as porosity, permeability and diffusion parameters of different cement-based materials in contact with the engineered and natural barriers of repositories in crystalline and argillaceous host rocks. Dedicated studies on radionuclide retention processes on relevant hydrated cement phases, concrete and alteration products are also part of this advanced approach.

The project started on 1st June 2015 and will last 4 years. The project is implemented by a consortium with 27 Beneficiaries, from 9 EURATOM Signatory States, Japan and Switzerland. National Waste Management Organizations (WMO) contribute to the running project by participation in the End-User Group, by co-funding Beneficiaries, and provide for knowledge and information transfer.

Indispensable for CEBAMA is the documentation of the scientific and technical state of knowledge and the dissemination of the generated knowledge not only to the WMO but also to the general scientific community and other interested parties. This dissemination strategy will be implemented by presentations at international conferences and publications in peer-reviewed journals. Interaction with social stakeholders is of relevance for facilitating global understanding for the need of research in nuclear waste management, and CEBAMA aims at helping to bridge this communication process. The aspect of training and education of the next generation of waste management professionals is specifically addressed in CEBAMA.

3rd ANUAL WORKSHOP

The 3rd Annual Workshop of the Collaborative Project CEBAMA was held in Nantes (France), 17th – 18th April 2018. The workshop was hosted by Armines/Subatech at the Westotel. There were 65 attendees, including beneficiaries, End-User-Group members, Associated Group organizations and project external organizations. The workshop was organized in two days and the agenda is shown in Figure 1.

Agenda (17 th - 18 th April 2018)	
Tuesday 17 th April 2018	Wednesday 18 th April 2018
10:30-12:00	1 st ExCom meeting (restricted to ExCom members)
12:00-13:00	LUNCH (restricted to ExCom)
13:00-13:30	Welcome + Presentation by the Coordination Team
13:30-15:00	Individual WP sessions
15:00-15:30	Coffee break (includes brief EUG meeting, restricted to EUG and ExCom)
15:30-17:00	WP2 plenary session
17:00-17:15	Coffee break
17:15-17:30	AG Presentations
17:30-18:00	Poster Session (PhD presentations, 5 min each)
20:00	-- Workshop DINNER --
	09:00-11:00 WP1 plenary session
	11:00-11:30 Coffee break
	11:30-13:30 WP3 plenary session
	13:30-14:30 LUNCH
	14:30-16:00 Topical Session + Stakeholder Panel (Topic: Decommissioning)
	16:00-16:30 Coffee break
	16:30-17:30 EUG feedback + General Assembly
	20:00 Dinner at the Hotel

Figure 1: Agenda of the 3rd Annual Workshop of CEBAMA.

The objectives of the 3rd Annual Workshop are presented below.

- Ensuring that all project partners are aware of the project objectives, work program and reporting obligations.
- Promoting joint research activities within CEBAMA.
- Providing for detailed agreements on the work program, activities and training measures.
- Communicating the status of the different project activities, work and state of progress between all project partners including non-technical stakeholders.
- Discussing the status of the work programme and decide on next steps, including deviations from original work planning, if required.
- Preparing for organization of public Workshop Proceedings for effective documentation and communication of the project achievements.

The 3rd workshop included several sessions/meetings such as the ExCom/EUG meetings, WP sessions and General Assembly. A topical session and Stakeholder Panel were also organized.

☞ ExCom and EUG meetings took place the first and second day of the workshop and were focused on the project management and discussion with EUG on the project progress.

☞ Individual WP sessions were devoted to internal discussions on the progress of each WP and to agree on the data exchange between work-packages in order to achieve the milestones scheduled for the next months.

☞ The 2nd Stakeholder Panel was organized as a Topical Session during the 3rd Annual Workshop of the project. Three scientific experts gave a talk on the role of cementitious materials and recent investigations in the frame of decommissioning and dismantling of radioactive installations. The session was chaired by B. Grambow (Armines/Subatech). The panellists and the corresponding presentations are listed below.

- Overview of CEA decommissioning programs and associated R&D. *Christine Georges (CEA, FR)*
- EDF applications for concrete and cementitious materials. Focus on radioactive waste packages. *Marina Bottoni (EDF, FR)*
- Procedures for measurement of radionuclides in cement-based materials for nuclear decommissioning. *Ben Russell (NPL, UK)*

☞ Plenary sessions of WP1, WP2 and WP3 consisted on a brief overview of the work progress given by the workpackage leader followed by a series of presentations given by partners. These presentations were devoted on showing partners' work and the obtained results. The talks included in each session are provided below.

WP1 Session

- WP1 Overview. *F. Claret (BRGM), E. Holt (VTT), U. Maeder (UniBern)*
- CEBAMA reference mix design for low-pH concrete and paste, intermediate results. *T. Vehmas, M. Leivo, E. Holt, M.C. Alonso, A. Fernandez, J.L. Garcia Calvo, R. Vasicek, R. Cervinka, P. Vecernik, T. Rosendorf, J. Svoboda, N. Fink, V. Montoya, N. Ait Mouheb, K. Dardenne, Jörg Rothe, T. Schäfer, H. Geckeis, S. Gaboreau (VTT, CTU, CSIC, KIT, BRGM, UJV)*
- Experimental study of chemical degradation of cementitious materials in Boom Clay environment. *S. Gaboreau, Q.T. Phung, F. Claret, N. Maes (SCK-CEN, BRGM)*
- A decade of OPC-concrete-compacted FEBEX bentonite interaction under controlled THC conditions. *J. Cuevas, M.J. Turrero, A. Garralón, P. Gomez, J. Pena, L. Sanchez, E. Torres, M.C. Alonso, A. Fernandez, J.L. Garcia Calvo, R. Fernandez, A.I. Ruiz, D.E. Gonzalez-Santamaria, M. Angulo, J. Gonzalez-Yelamos, A. Ortega, E. Rodriguez, J. Cuevas (CSIC, CIEMAT, UAM)*
- Hydro-mechanical behaviours and chemical degradation effects on interface properties. *Z.B. Liu, J.F. Shao, S.Y. Xie, N. Burlion, X. Bourbon, G. Decamps (LML, ANDRA)*
- Geochemical and thermal effects on cementitious materials characteristics: Strength, pH of leachates, mineralogy, diffusion. *R. Vasicek, R. Cervinka, P. Vecernik, T. Rosendorf, J. Svoboda (CTU, UVJ)*
- The physico-chemical evolution of a low-pH cement in contact with ground water. *R. Vasconcelos, C. Corkhill, J. Provis (USFD)*
- Leaching of Hardened Portland Cement with various C/S -ratios. *T. Vehmas, M. Leivo, E. Holt. (VTT)*

WP2 Session

- Status of WP2. *B. Grambow (SUBATECH/ARMINES)*
- Retention and mobility studies of safety relevant radionuclides in cementitious materials. *M. Isaacs, S. Lange, G. Deissman, D. Bosbach, E. Rastrick, M. Felipe-Sotelo, D. Read (SURREY, JUELICH, NPL)*
- Uptake mechanisms of radionuclides in cementitious systems: insights from atomistic simulations. *S. Lange, P.M. Kowalski, M. Psenicka, M. Isaacs, M. Klinkenberg, D. Read, D. Bosbach, G. Deissman (JUELICH, SURREY)*
- Behavior of radium and strontium in contact with cementitious materials relevant for LILW disposal in the Czech Republic. *B. Drtinova (CTU)*
- Ra-226 sorption on intact and degraded HCPs. *C. Bucur, I. Florea, N. Deneanu, R. Dobrin, N. Dulama (RATEN)*
- Uptake and diffusion properties of HTO and inorganic C-14 through hardened cement paste: Influence of carbonation and water saturation. *S. Rasamimanana, C. Landesman, K. Perrigaud, S. Ribet, N. Bessaguet, B. Grambow (SUBATECH/ARMINES)*
- Effect of redox conditions on sulfur, selenium and iodine binding in AFm phases. *L. Nedyalkova, B. Lothenbach, J. Tits, W. Wieland, U. Mäder (EMPA, PSI, UNIBERN)*
- Building blocks on molybdenum retention processes in cement systems. Mo retention onto pure cement phases: Kinetic experiments. *M. Lopez, J. Olmeda, M. Grivé (AMPHOS21)*
- Solubility, hydrolysis and sorption of beryllium in cementitious systems. *X. Gaona, N. Cevirim-Papaioannou, N. Ait Mouheb, V. Montoya, M. Altmaier (KIT)*
- Thermodynamic and crystallographic model for anion uptake by hydrated calcium aluminate (AFm): an example of molybdenum. *(BRGM)*

WP3 Session

- Status of WP3 and Modelling task. *A. Idiart (AMPHOS21)*
- Modelling of radionuclides migration in the low pH cement/clay interface. *V. Montoya, N. Ait Mouheb, T. Schäfer, H. Geckeis (KIT)*
- Influence of water availability on the hydration of the CEBAMA reference mix. *M. Lavina, A. idiart, J. Olmeda (AMPHOS21)*
- An extended membrane polarization model for spectral induced polarization of low-pH cement and concrete. *A. Hördt, M. Bucker, P. Leroy, S. Huisman, E. Zimmermann, S. Gaboreau, F. Claret, H. Stebner (BRGM, JUELICH)*
- Electromigration of Se in Bentonite and Boom Clay: comparing model calculations and experimental results. *H. Meeussen (NRG)*
- Nonisothermal reactive transport model of heating and hydration concrete/bentonite column tests. *J. Samper, A. Mon, L. Montenegro, A. Naves, J. Fernández, J. Cuevas, R. Fernández, M. J. Turrero, E. Torres (UDC)*

- Evaluation of diffusion experiments performed on cementitious samples in Czech laboratories within WP1 and WP2. (*CTU*)

Poster session was held at the end of the second day of the workshop at the same venue. Beneficiaries had the opportunity of presenting their results. The list of posters is provided below and all of them are included in the section *POSTERS*. Three of them were briefly presented at the beginning of that session (highlighted in bold).

- Radionuclide migration at the low pH cement/clay interface: derivation of reactive transport parameters. ***N. Ait Mouheb, V. Montoya, T. Schäfer, H. Geckeis (KIT-INE)***
- Mechanism of molybdenum uptake by hydrated calcium aluminate (AFm). *N.C.M. Marty, S. Grangeon, E. Elkaïm, C. Tournassat, C. Fauchet, F. Claret (BRGM)*
- Experiments on Interface Processes at the Cement/Callovo-Oxfordian claystone interface and the impact on physical properties; Mechanical and flow properties of fresh interfaces. *R. Cuss, A. Wiseall, M. Dobbs, D. Parkes, J. Harrington, J. Talandier, X. Bourbon (BGS, ANDRA)*
- Comparison of mass transfer in concrete-bentonite interface based on HB6 laboratory and full-scale FEBEX in-situ tests. *M.J. Turrero, A. Garraón, P. Gómez, J. Peña, L. Sánchez, E. Torres (CIEMAT)*
- Effects of porosity evolution on the evaluation of radionuclide diffusion coefficients in mortars and concrete. *M. García-Gutiérrez, M. Mingarro, T. Missana (CIEMAT)*
- Pore-scale reactive transport modelling of transport and leaching processes in cementitious materials. *S. Rohmen, A. Idart, G. Deissmann, D. Bosbach (JÜLICH, AMPHOS21)*
- The physico-chemical evolution of UK high-pH backfill material. *R.G.W. Vasconcelos, N.C. Hyatt, J.L. Provis, C.L. Corkhill (USFD)*
- Property of bonded planar interface between COx claystone and low-pH concrete. *Z. Liu, J. Shao, S. Xie, X. Bourbon, G. Decamps (LML, ANDRA)*
- Development of Surface Reactivity Interface Experiments (SERIE) for studying FEBEX bentonite-concrete interaction. *D.E. González-Santamaría, M. Angulo, J. González-Yelamos, R. Fernández, A. Ortega, A.I. Ruiz, E. Rodríguez, J. Cuevas (UAM)*
- Clayey water interaction with high and low-pH concretes. *Á. Fernández, M.C. Alonso, J.L. García Calvo (CSIC)*
- FEniCS-Reaktoro coupling: constricted pores and cement/clay interfaces. ***L. Hax Damiani, Y. Yang, S.V. Churakov, G. Kosakowski (PSI, UNIBERN)***
- Aged interface between Opalinus Clay and low-pH mortar: sample preparation, X-ray computed tomography and core infiltration experiment for hydraulic-chemical properties. *E. Bernard, U. Mäder, A. Jenni (UNIBERN)*
- Changes in groundwater composition following interaction with cement. *E. Rastrick, M. Isaacs, M. Felipe-Sotelo, D. Read (SURREY)*

At the end of the workshop, Seif Ben Hadj Hassine (EUG chairman) gave some statements on behalf of the EUG about the progress of the project. Following, the **general assembly** closed the workshop.

WP OVERVIEW

Overview of Work Package 1

Experiments on interface processes and the impact on physical properties

WP leaders:

Erika Holt (VTT)

Francis Claret (BRGM)

Urs Mäder (UNIBERN)

The 3rd CEBAMA workshop (Nantes, France April 17-18, 2018) provided the fifth occasion for discussing Work Package 1, after the project kick-off meeting (Brussels, July 2015), a meeting in London (November 2015), the 1st Annual Project Workshop in Barcelona (June, 2016) and the 2nd Annual Project Workshop in Finland (May 2017). This 3rd Annual Workshop had participants from 16 of the 19 partner organizations of WP1. Some partners had multiple persons attending, including PhD students.

This Workshop was held near the end of the third year of the project, thus there were many technical presentations on experimental progress and describing integration of results to WP3 modelling. Similar to the previous workshops, a specific discussion meeting for WP1 was scheduled early in the program on the first day, to provide a brief overview from all WP1 partners. Each partner shared a couple slides of information, emphasising progress on the experimental program, data freeze inputs for WP3, impacts to the safety-case, partner/end-user cooperation, and dissemination activities. A poster session provided means for sharing more information about on-going work, with an emphasis on work of PhD students who pitched their posters. On the second day, the two-hour WP1 plenary session had seven detailed presentations of select topics, which are described in more detail below and within the papers of these proceedings.

VTT presented updated mechanical and chemical evolution as well as microstructural results of the benchmark concrete and paste mixtures, which have been investigated by seven partners and are being used for cross-comparison of local recipes and as input to modelling of WP3. Additional technical presentations of WP1 shared about the following topics:

- Chemical degradation of cementitious materials in Boom Clay (SCK·CEN, BRGM)
- OPC-concrete and compacted FEBEX bentonite interaction under controlled THC conditions (CSIC, CIEMAT, UAM)
- Bonding and hydro-mechanical characterization of interface between Callovo-Oxfordian Claystone and a low-pH high performance concrete (LML, Andra)
- Geochemical and thermal effects on cementitious materials characteristic of strength, leachate pH, mineralogy, diffusion (CTU, UJV)
- Physico-chemical evolution of low-PH cement in contact with groundwater (USFD)
- Leaching of hardened Portland cement and varying C/S ratios (VTT)

The topical session on decommissioning had three presentations (by CEA/France, EDF/France, NPL/UK), all of which reflected on the importance of understanding cement chemistry and material interactions when optimizing performance, safety and costs. Discussions within the workshop noted that additional information could be used by WP2 investigations from the WP1 benchmark mixtures and experiments. It was identified that there is a need for having consistent data notations and terminology regarding boundary conditions of WP1 experiments. Dissemination of results continues to increase, with many presentations made at the Clay Conference 2017 (7th International Conference on Clays in Natural and Engineered Barriers for Radioactive Waste Confinement (May 2017, Davos, Switzerland), and planned for other events such as the 3rd International Symposium on Cement-Based Materials for Nuclear Wastes (October 2018, Avignon, France) and the 9th Conference on the Mechanical Behavior of Salt (September 2018, Germany).

Regarding competence development, partners shared about the mobility measures of their PhD student visits, with UAM cooperating with BRGM and VTT with AMPHOS21 within WP1 exchanges. One PhD dissertation has been completed in the project based on WP1 results (of partner TUDelft) and three more are underway (USFD, VTT, KIT). None of the WP1 partners noted significant deviations from the project's research plans. No new deliverables have been produced from WP1 during the past year or presented at the workshop, yet two (D1.06 and D1.07) are planned to be ready during the last year of the project and presented at the 4th Annual Workshop.

Overview of Work Package 2

Radionuclide retention in high pH concrete

WP leader:

Bernd Grambow (ARMINES)

The aim of this WP is to provide insight on general processes and phenomena governing radionuclide retention on high pH cementitious materials and their couplings in overall interaction mechanism, which can then be transferred to different disposal situations and water access scenarios in a high pH repository environment with cementitious materials. It also assesses the impact of chemical alterations (e.g. high pH concrete ageing, carbonation, m/V ratio, temperature, transition from oxidizing to reducing conditions, aging time) on radionuclide retention. The progress of the work of WP2 is as planned. In the reporting period important results on radionuclide retention on well characterized relevant cementitious materials were obtained by conducting leaching and solubility tests, diffusion tests, sorption experiments and co-precipitation studies under well controlled redox conditions and modelling of experimental results. Characterization of the cements and equilibrated waters has been carried out by a large number of techniques.

The incorporation of Se, S and I in AFm phases Se(VI)-, Se(IV)-, S(VI)-, S(IV)- and S(II)-AFm phases was studied. Pure $(\text{HS}^-)_2\text{-AFm}$ and $(\text{HSe}^-)_2\text{-AFm}$ phases were synthesized. Furthermore, the ability of Se and I to form binary solid solutions of the type $(\text{SeO}_3^{2-}\text{-X}^{\text{n-}})\text{-AFm}$ and $(\text{I-X}^{\text{n-}})\text{-AFm}$ (with $\text{X}^{\text{n-}} = \text{SO}_4^{2-}, \text{SO}_3^{2-}, \text{S}_2\text{O}_3^{2-}, \text{CO}_3^{2-}, \text{OH}^-, \text{OH}^-\text{-CO}_3^{2-}$) was examined. For the $(\text{HS}^-)_2\text{-AFm}$ a solubility product, $\log K_s^0 = -28$ at 23°C was determined. Solid solution formation in AFm phases was observed for the pairs $\text{SeO}_3\text{-SO}_4$, I-CO_3 , I-OH-CO_3 and I-OH . A continuous solid solution was found between the rhombohedral $\text{SeO}_3\text{-AFm}$ and $\text{SO}_4\text{-AFm}$ endmembers and between the pairs I-OH-CO_3 and I-OH . The $\text{I}_2\text{-AFm}$ and $\text{CO}_3\text{-AFm}$, on the other hand, form only a limited solid solution. In this case, a miscibility gap with the composition $0.5 \leq \text{CO}_3/(2\text{I} + \text{CO}_3)$ is observed, indicated by the presence of two coexisting phases – an $\text{I}_2\text{-CO}_3\text{-AFm}$ mixed phase and a $\text{CO}_3\text{-AFm}$. The experimental data suggests that $(\text{HS}^-)_2\text{-AFm}$ and $(\text{HSe}^-)_2\text{-AFm}$ phases could be potentially stable under the reducing and alkaline conditions expected in a cement-based L/ILW repository after closure.

The affinity of ^{125}I (in the form I^- , IO_3^-) and ^{75}Se (SeO_3^{2-} , SeO_4^{2-}) for cementitious materials (CEM I, GGBS:OPC, PFA:OPC, NRVB, CEBAMA reference mix) as well as specific mineral phases present in the cements (C-S-H, AFm, AFt) and for carbonated cement pastes has been determined via a series of batch sorption tests. Iodate, in particular, has been shown to have a strong affinity for the AFm- SO_4 phase, with a high R_d (6,800 L/kg) coupled with a distinct morphological change from planar hexagonal to acicular crystals. Through-diffusion experiments showed that the mobility of ^{36}Cl and ^{99}Tc is highly dependent on the type of hardened cement paste (HCP). Mineralisation of chloride within the cement was indicated.

The uptake of radium and Sr-85 from Portlandite water on a hardened cement paste (HCP CEM II) and two types of concrete (Concrete CEM I and Concrete CEM II) has been studied by characterizing the materials and by sorption and diffusion tests at various temperatures and the liquid-to-solid ratio. K_d values for Ra uptake were in the range of 70-650 L/kg, while K_d values for Sr were 10-130 L/kg. In through diffusion experiments K_d values were around 9 L/kg for Sr, independent of the liquid phase used, 100-150 L/kg for Ra. The sorption of ^{226}Ra to various C-S-H phases was investigated in batch-type sorption experiments under anoxic conditions. A strong

retention of ^{226}Ra by C-S-H phases was observed with slight dependency of distribution coefficients on the Ca/Si-ratio of the C-S-H and the alkali content in solution. Ab-initio atomistic simulations based on density functional theory (DFT) were performed to obtain a closer insight into the incorporation mechanism, revealing a significant difference in Gibb's energy between ^{226}Ra incorporation into the stable calcium layer compared to cation exchange in the interlayer, suggesting ^{226}Ra uptake into the interlayer spacing of C-S-H as an additional mechanism to surface sorption.

The sorption of $^{14}\text{CO}_3^{2-}$ on non-degraded and degraded hardened cement pastes (HCP) based on CEM I and CEM V was evaluated. Most of the ^{226}Ra is sorbed on fresh cement pastes with a slow increase of the distribution ratio was observed between 2 and 20 days of contacting. For CEM V the distribution ratio was higher than for CEM I. Using an osmotic technique diffusion parameters for tritiated water and for $^{14}\text{CO}_3^{2-}$ were obtained in partially saturated conditions in carbonated and non-carbonated hardened cement pastes (HCP, CEM V/A Rombas) for different water saturation conditions. Only a slight effect of water saturation and carbonation on the effective diffusion coefficient, $D_e(\text{HTO})$ was observed. C-14 diffusion is very slow and tests are ongoing in order to apply digital β autoradiography for describing C-14 diffusion profiles into HCP samples. Carbonated samples displayed a low and non-reversible uptake of C-14 while in non-carbonated samples uptake was higher and reversible.

The solubility of Be(II) was investigated in dilute to concentrated HCl–NaCl–NaOH, KCl–KOH, NaOH and KOH solutions under Ar atmosphere at $T = (22 \pm 2)^\circ\text{C}$. No transformation of BeO(cr) or Be(OH)₂(am) to Na/K–Be(II)–OH solid phases is observed in alkaline NaCl and KCl solutions within 200 days. Solubility constants $\log *K_{s,0}^\circ\{\text{BeO}(\text{cr})\}$ and $\log *K_{s,0}^\circ\{\text{Be}(\text{OH})_2(\text{am})\}$ were determined considering the hydrolyse scheme for Be in aqueous solution. The hydrolysis constant previously reported for Be(OH)₂(aq) has been shown to be importantly overestimated. Solubility data in alkaline to hyperalkaline conditions are controlled by the predominance of the anionic hydrolysis species Be(OH)₃[–] and Be(OH)₄^{2–} at the pH_m-conditions relevant in cementitious systems. This extensive solubility dataset obtained within CEBAMA will allow deriving chemical, thermodynamic and (SIT) activity models for the system Be²⁺–Na⁺–K⁺(–Ca²⁺)–H⁺–Cl[–]–OH[–]–H₂O(l).

In the following the results of the various partners are summarized. These S+T contributions correspond to the work presented at the third CEBAMA workshop in Nantes/France.

Overview of Work Package 3

Interpretation & modelling

WP leader:

Andrés Idiart (AMPHOS21)

The objective of Work Package 3 (WP3) is to contribute to the interpretation of experimental results generated in CEBAMA. Numerical modelling is used to assess the impact of several physical and chemical processes on transport properties of cementitious systems as well as their interface with clayey materials. In addition, research within WP3 is intended to improve the validity of existing models to predict changes in transport properties of cementitious systems and to contribute to our ability to extrapolate models of system-level to modelling for Safety Case application.

An essential basis for WP3 is the outcome of the experiments and their characterization performed within the CEBAMA project. Every WP3 partner has established collaborations with the experimental Work Packages to model specific sets of experiments. During the 3rd Annual Workshop, several partners presented preliminary results of the modelling and interpretation of experimental data obtained within the project. Participants from 12 out of 13 partner organizations of WP3 attended the workshop, in some cases with multiple persons attending, and including participation of junior staff and PhD students. Training of 4 PhD students continues within WP3 and during the period comprised between the 2nd and 3rd Annual Workshops, 2 mobility measures were completed in WP3. Namely, Stephan Rohmen from JUELICH (Germany) visited PSI (Switzerland), while Aku Itälä from VTT (Finland) visited Amphos 21 (Spain).

In terms of dissemination, several presentations in conferences have been completed and others are planned for the coming months (NUWCEM 2018 in October, Conmod Symposium in August 2018, etc.), while several manuscripts have been submitted for publication and others are being finished or under development.

So far, most of the model implementation work in WP3, including new model features, has been completed, as well as the verification of the modelling tools with existing experiments and benchmarks. During the WP3 Individual Session of the 3rd Annual Workshop in Nantes, each partner provided a brief overview of their status on 3 slides. In addition, important issues were discussed, such as collaborations, modelling task details, and data freezing. All the partners are working in the modelling of laboratory tests from the experimental Work Packages and preliminary results were presented in this workshop. None of the partners claimed significant deviations from their research plan. During the WP3 Plenary Session, six (6) partners presented their progress in more detail, with more focus on modelling results and comparison with experimental data than in previous annual workshops:

- KIT: *Vanessa Montoya*. Reactive transport modelling of radionuclides migration in the low pH cement/clay interface.
- Amphos 21: *Marcelo Laviña*. Influence of water availability on the hydration of the CEBAMA reference mix.
- BRGM: *Philippe Leroy*. An extended membrane polarization model for spectral induced polarization of low-pH cement and concrete.

- NRG. *Hans Meeussen*. Electromigration of Se in Bentonite and Boom Clay: comparing model calculations and experimental results.
- UDC: *Javier Samper*. Sensitivity analysis of a nonisothermal reactive transport model of heating and hydration concrete/bentonite column tests.
- CTU: *Dušan Vopálka*. Evaluation of diffusion experiments performed on cementitious samples in Czech laboratories within WP1 and WP2.

In addition, six (6) scientific and technical contributions from WP3 are included in the 3rd Annual Workshop Proceedings (*this document*).

The main outcomes of the 1st Data Freezing were also presented, based on the template used to collect and compile experimental data about the laboratory tests of WP1. The 2nd Data Freezing will be distributed among WP1 and WP2 partners to gather updated experimental data.

Another important milestone of WP3 was the definition and setup of a common modelling task between some of the WP3 partners. To date, significant progress has been achieved and during the 3rd Annual Workshop, preliminary and promising results were presented and discussed, both in the Individual and Plenary sessions. Specific meetings for the organization of the modelling task were held in Barcelona (13th September 2017, during the Migration Conference) and Davos (27th September 2017, during the 7th International Conference on Clays in Natural and Engineered Barriers for Radioactive Waste Confinement).

Finally, a CEBAMA PhD meeting was held in parallel with the 8th Reactive Transport PhD Workshop at PSI (Villigen, Switzerland) during 22-23 February 2018. A total of 15 PhD students presented their work, including both experimental and modelling work, with very interesting discussions.

S + T CONTRIBUTIONS

Diffusion of tritiated water and chloride-36 through low pH cements

Naila Ait Mouheb^{1*}, Vanessa Montoya^{1*}, Claudia Joseph¹, Thorsten Schäfer¹,
Horst Geckeis¹

¹ KIT-INE, Karlsruhe Institute of Technology -Institute for Nuclear
Waste Disposal (DE)

* Corresponding author: naila.ait-mouheb@kit.edu; vanessa.montoya@kit.edu

Abstract

This work describes the methodology and numerical approximation used to determine the effective diffusion coefficient (D_e) and the rock capacity factor (α) of tritiated water “HTO” and $^{36}\text{Cl}^-$ in three different low pH cement pastes (MIX 3C, MIX 3E and CEBAMA reference paste mix “RPM”). Through-diffusion experiments were performed inside of a glove box under a controlled Ar atmosphere in order to avoid carbonation of the alkaline waters. Transport parameters were obtained for RPM by inverse modelling considering Fickian diffusion as the only transport process and using the finite element code Comsol Multiphysics 5.3 to solve the partial differential equations. The results for the two different RPM disks are similar, demonstrating the reproducibility of the diffusion experiment.

1 Introduction

Deep geological repository concepts are based on the confinement of radioactive waste over up to 1 Ma by a multi-barrier system (ANDRA, 2005; ENRESA, 1995). Concrete and clay materials are normally used as adjacent barriers in most of the concepts developed internationally. During the extended period of the disposal, cementitious materials can undergo alterations leading to changes in their chemical and physical properties. Low-pH cement-based materials were developed for minimizing the alterations on the clay-rock regarding the (i) alkali plume and specially (ii) the temperature generated by the hydration of the binders. The main characteristic of low pH cements is the absence of portlandite as hydrated solid phase and the low alkali content, which reduces the pore water pH to ~ 11 compared to traditional Portland cement materials ($\text{pH} \geq 13$). C-S-H phases are the main solid phases present in the hydrated low-pH cement with a Ca/Si ratio less than 1.0. In order to obtain low pH cements, the clinker content is substituted with supplementary materials like silica fume, blast furnace slag or fly ashes (Coumes et al., 2006; Codina et al., 2008; García Calvo et al., 2010).

Knowledge of the sorption, diffusion, and permeability properties of these new cementitious materials are of high importance for performance and safety assessment of repositories for nuclear waste. In general, there is a lack of data for solute diffusion coefficients in low pH cementitious materials. However, it is well known that the addition of silica fume or fly ash (main additives to obtain low pH cement) in ordinary Portland cement paste considerably reduces the diffusion rate for chloride due to microstructural changes (Byfors, 1987; Ampadu et al., 1999; Bentz et al., 2000; Ogrigbo and Black, 2017) and the increase of the chemical bonding of chloride to cement (Byfors, 1987).

As an example, Table 1 shows the transport parameters of natural Cl^- obtained for different low pH cement materials (Byfors, 1987). By comparing the data, D_e of chloride increases with increasing water binder ratio. The addition of silica fume decreases the D_e in both cases. More C-S-H gels are formed when silica fume is added, which leads to the refinement of the porosity (Cheng-yi and Feldman, 1985) and therefore, to the reduction of the diffusivity (Bentz et al., 2000).

Table 1: Study of natural Cl^- diffusivity in various low pH cement pastes (Byfors, 1987).

Sample type ^a	Water/binder -ratio	$D_e \cdot 10^{-12} \text{ (m}^2/\text{s)}$
OPC + 10% SF	0.4	18
	0.6	99
OPC + 20% SF	0.4	3.2
	0.6	31

^a OPC = Ordinary Portland Cement, and SF = Silica fume

The objective of this work was to provide transport parameters (effective diffusion coefficients D_e and the rock capacity factors α) for two tracers: HTO and $^{36}\text{Cl}^-$ on three different low pH cement pastes by through-diffusion experiments.

2 Materials and methods

2.1 Low pH cement samples

Three different low pH cement pastes have been investigated in this study. Two of the samples (MIX 3C and MIX 3E) have been prepared by mixing different solids (Table 2). After 90 days of hydration, they were characterized, mainly chemically, using various complementary analytical techniques (Ait Mouheb et al., 2017, 2018). The third sample corresponds to the RPM described in Vehmas et al. (2017, 2018) and Vehmas et al. (2018, *this document*). Briefly, the main hydrated phases identified in all the samples are C-S-H and C-A-S-H gels with a Ca:Si ratio between 0.7 - 1.0 and a Al:Si ratio of 0.05. No portlandite or Friedel's salt are present in any of the samples. Unreacted clinker (alite and belite) has also been identified in RPM (see Table 3).

Table 1: Composition (wt.%) of the solid mixtures used to prepare the low pH cement pastes.

(wt.%)	MIX 3C	MIX 3E	RPM
CEM I	39 ^a	50	25 ^b
Silica fume	39	50	27
Limestone filler	19	-	-
Superplasticizer	3 ^c	-	4 ^d
Blast furnace slag	-	-	16
Quartz filler	-	-	28
Water/binder ratio	0.6		0.25

^a CEM I 52.5N SR; ^b CEM I 42.5 MH/SR/LA

^c Inorganic superplasticizer (SioxX®)

^d Superplasticizer naphthalene-based Pantarhit LK (FM)

The porosity of the mixtures MIX 3C and MIX 3E has been measured with mercury intrusion porosimetry (MIP) and are reported in Ait Mouheb et al. (2017). Additionally, the same measurements have been repeated in this work using the same technique to evaluate the reproducibility of the technique and values are reported in Table 3. The porosity for sample RPM was measured by BRGM by MIP and compared with other techniques (Vehmas et al., 2018, *this document*). The density of each sample has been determined from the ratio of the mass of the sample and its geometrical volume and set equal to the bulk density.

Several disks with an average thickness H of $10 \text{ mm} \pm 0.1 \text{ mm}$ have been cut from cylindrical hydrated cement samples of RPM, MIX 3C and MIX 3E (average diameter, $D = 30 \pm 0.1 \text{ mm}$ and average cross-sectional area $A_{\text{(sample)}}$ of $7.07 \pm 0.1 \text{ mm}^2$) using a diamond saw and isopropanol as solvent. An analysis of the samples with the optical microscope “Wild M8” showed that no cracks were generated during the cutting.

Table 3: Hydrates and raw materials identified in the three different low pH cement pastes.

	MIX 3C	MIX 3E	RPM
Hydrated phases	wt. (%)		
C-(A)-S-H	82%	92%	✓
Ettringite	1%	1%	✓
Raw materials	wt. (%)		
Silica fume	✓	✓	✓
Limestone filler	12%	< 2%	< 2%
Alite and Belite	-	-	✓
Blast furnace slag	-	-	✓
Quartz filler	-	-	✓
Bulk density (kg/m^3)	1546	1562	2087
Porosity (%)	24±4	35±5	6.1

2.2 Experimental set-up: Through-diffusion

Through-diffusion experiments of HTO and $^{36}\text{Cl}^-$ on the three low pH cementitious materials (MIX 3C, MIX 3E and RPM) have been conducted inside an Ar glovebox (duplicate experiments were so far only performed for material RPM). A cylindrical diffusion cell has been designed, optimized, and constructed for performing these experiments using transparent polymethyl methacrylate (PMMA) (see Figure 1a). The setup consists of a thin cement sample of 10 mm thickness sealed with PMMA (see Figure 1b) mounted between two compartments, called high and low reservoir in Figure 1a, with total volumes of 50 mL and 3.8 mL, respectively.

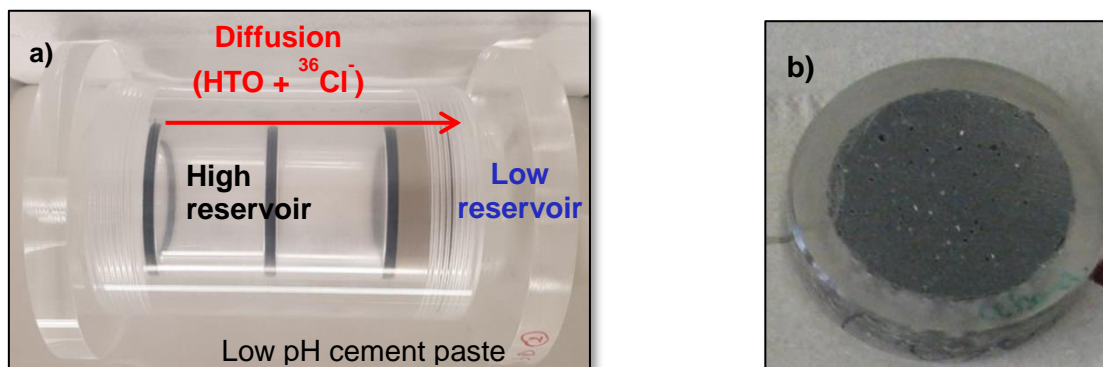


Figure 1: a) Diffusion cell constructed for this study. b) Low pH cement paste sealed with PMMA resin, and thickness = 10 mm.

Before performing the through-diffusion experiments of the selected tracers, the high and low reservoirs were filled with the appropriated tracer-free synthetic low pH cement water (see Table 4). In order to saturate the samples, the synthetic low pH cement waters were left in contact with the selected cement paste inside the diffusion cell for 6 weeks. To initialize the diffusion experiments, the solution inside the high reservoir was replaced with synthetic low pH cement water labelled with HTO and ³⁶Cl⁻ (see Section 1.3). The low reservoir was filled with fresh tracer-free synthetic low pH cement water. Preliminary tests showed that neither HTO nor ³⁶Cl⁻ sorb on the walls of the diffusion equipment (PMMA).

Openings located on both reservoirs allowed a regular sampling of both solutions with a transfer pipette. From the obtained samples the pH value was determined and the HTO and ³⁶Cl⁻ activities were measured by liquid scintillation counting (LSC). After each sampling, the high and low reservoirs were refilled with synthetic low pH cement water labelled with HTO and ³⁶Cl⁻ and tracer-free synthetic low pH cement water, respectively.

2.3 Low pH cement solutions

Three synthetic low pH cement waters were prepared by mixing the artificial low pH cement water (ACW-LpH) described in Ait Mouheb et al. (2018) with powdered material of RPM, MIX 3C and MIX 3E at a solid/liquid ratio of 0.133 kg/L.

After 3 days of pre-equilibration, the different suspensions were decanted. Subsequently, the supernatants were filtrated using polyvinylidene fluoride (PVDF) filters with a pore size of 0.2 µm. Their composition was analyzed by inductively coupled plasma-optical emission spectrometry (ICP-OES) and ion chromatography (IC). Table 4 shows the chemical compositions of the three different equilibrated solutions in comparison with the initial ACW-LpH composition.

Table 4: Chemical compositions of ACW-LpH and the equilibrated solutions of the different low pH cements.

mM	Si	Na	Ca	K	Cl	SO ₄	Al	Mg	Sr	CO ₃ [*]	pH
ACW-LpH	1.46	5.87	3.56	3.76	3.84	5.75	-	-	-	2.76·10 ⁻³	11.00
MIX 3C water	1.30	6.89	3.97	3.49	4.50	8.03	7.72·10 ⁻⁵	1.70·10 ⁻³	5.48·10 ⁻²	6.28·10 ⁻³	10.37

mM	Si	Na	Ca	K	Cl	SO ₄	Al	Mg	Sr	CO ₃ [*]	pH
MIX 3E water	1.02	6.44	4.03	3.74	4.49	8.50	7.21·10 ⁻⁵	1.93·10 ⁻³	5.49·10 ⁻²	3.88·10 ⁻³	10.74
RPM water	0.36	12.32	3.95	4.49	4.90	7.21	1.73·10 ⁻²	3.12·10 ⁻³	1.03·10 ⁻²	3.74·10 ⁻³	11.47

(*) Total carbon concentration

Spiked solutions of the three synthetic low pH cement waters were prepared by adding 23.1 µL of HTO stock solution (1.01·10⁷ Bq/mL) and 26.9 µL of ³⁶Cl⁻ stock solution (7.42·10⁵ Bq/mL) to 100 mL of the respective synthetic low-pH cement water. The concentrations of the radiotracers were measured by LSC giving an initial concentration of [HTO] = 1.86·10⁻⁹ M and [³⁶Cl⁻] = 4.55·10⁻⁶ M for the diffusion experiments.

2.4 Data evaluation and derivation of transport parameters

Transport parameters for HTO and ³⁶Cl⁻ were obtained by inverse modelling of the diffusive flux data [mol/m²·s] determined at the low reservoir by measuring the accumulated activity (in Bq) of both radionuclides (details on flux calculations are given in Tits et al., 2003). Fickian diffusion in a homogeneous isotropic material has been considered as the only transport process. Fick's first law stated that the diffusive flux (J) is proportional to the concentration gradient (see Equation 1).

$$J = -D_e \cdot \frac{\partial c}{\partial x} \quad (1)$$

where $\frac{\partial c}{\partial x}$ is the concentration gradient [mol/m⁴]; and D_e is the effective diffusion coefficient [m²/s]. The change of concentration with time, t [s], is described by Fick's second law (Equation 2):

$$\frac{\partial c}{\partial t} = -D_e \cdot \frac{\partial^2 c}{\partial x^2} \quad (2)$$

The effective diffusion coefficient can be estimated using Archie's law:

$$D_e = \varepsilon_{acc}^m D_w \quad (3)$$

with m [-] as empirical constant, D_w [m²/s] as the diffusion coefficient of the tracer in water, and ε_{acc} as the accessible porosity [-] which is related to the constrictivity (δ) and tortuosity (τ):

$$\varepsilon_{acc}^m = \frac{\delta}{\tau} = \frac{1}{G} \quad (4)$$

Constrictivity (δ) and tortuosity (τ) are assembled together in the geometrical factor (G).

For species which sorb in the solid media, the rock capacity factor α [-] is defined:

$$\alpha = \varepsilon_{acc} + \rho_d K_d \quad (5)$$

where K_d [m^3/kg] is the sorption distribution coefficient, and ρ_d is the density of the solid [kg/m^3]. For non-sorbing tracers, $K_d = 0$. The apparent diffusion coefficient, D_a [m^2/s], is expressed as:

$$D_a = \frac{D_e}{\alpha} \quad (6)$$

Further expressions for effective diffusion coefficients are reviewed by Patel et al. (2016), i.e. as expressions which allow to distinguish contributions of different phases, namely, C-S-H and capillary pores, to diffusion, or use parameters such w/c ratio and volume fraction of different phases in cement paste. For a first approach we used the empirical Archie's law.

The finite element code Comsol Multiphysics 5.3 (COMSOL, 2017) has been used to solve the partial differential equations. Based on the mentioned assumptions, a one-dimensional (1D) single porous medium model have been considered. Appropriated boundary conditions have been also selected according to the experimental methodology:

$$c(x = 0, t > 0) = f_0(t) \text{ and} \quad (7)$$

$$c(x = H, t > 0) = f_1(t) . \quad (8)$$

The initial condition was selected as:

$$c(x, t \leq 0) = 0, \forall x \in \text{transport domain} \quad (9)$$

where x [m] is the spatial coordinate, $f_0(t)$ and $f_1(t)$ the time-dependent change of the radiotracers concentration (HTO and $^{36}\text{Cl}^-$) in the high and low reservoir, respectively.

3 Results and discussion

The accumulated amounts (mol) of HTO and $^{36}\text{Cl}^-$ in the low reservoir and their diffusive fluxes during the diffusion through two RPM samples are shown in Figure 2 and Figure 3, respectively. The upstream concentration of HTO and $^{36}\text{Cl}^-$ are equal to $1.86 \cdot 10^{-9}$ M and $4.55 \cdot 10^{-6}$ M, respectively and keep constant during the studied time (see Figure 4).

Experiments are reproducible and within the first hours the fluxes reached a steady state with a value of $\sim 5 \cdot 10^{-16}$ mol/($\text{m}^2 \cdot \text{s}$) for HTO and $\sim 10^{-13}$ mol/($\text{m}^2 \cdot \text{s}$) for $^{36}\text{Cl}^-$. The transport parameter values obtained by modelling are given in Table 5.

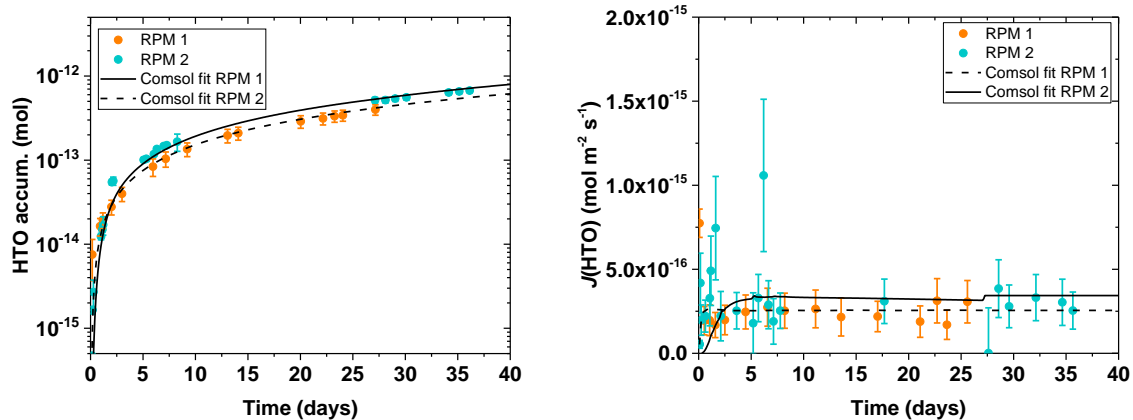


Figure 2: Accumulated amount of HTO in the low reservoir vs. time and its diffusive flux during diffusion experiments through two RPM samples. $[\text{HTO}]_0 = 1.86 \cdot 10^{-9} \text{ M}$. Background electrolyte was RPM water.

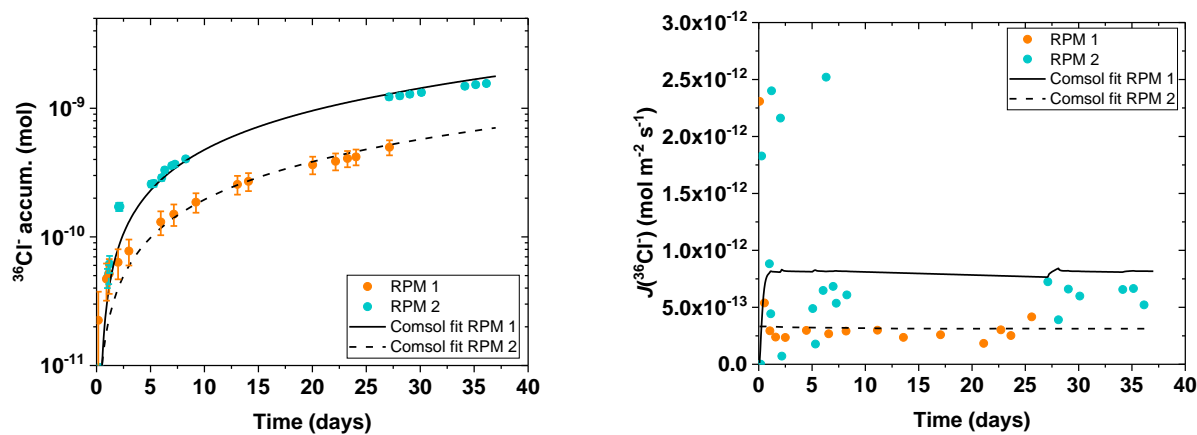


Figure 3: Accumulated amount of $^{36}\text{Cl}^-$ in the low reservoir vs. time and its diffusive flux during diffusion experiments through two RPM samples. $[^{36}\text{Cl}]_0 = 4.55 \cdot 10^{-6} \text{ M} + [\text{Cl}]_0 = 4.90 \cdot 10^{-3} \text{ M}$. Background electrolyte was RPM water.

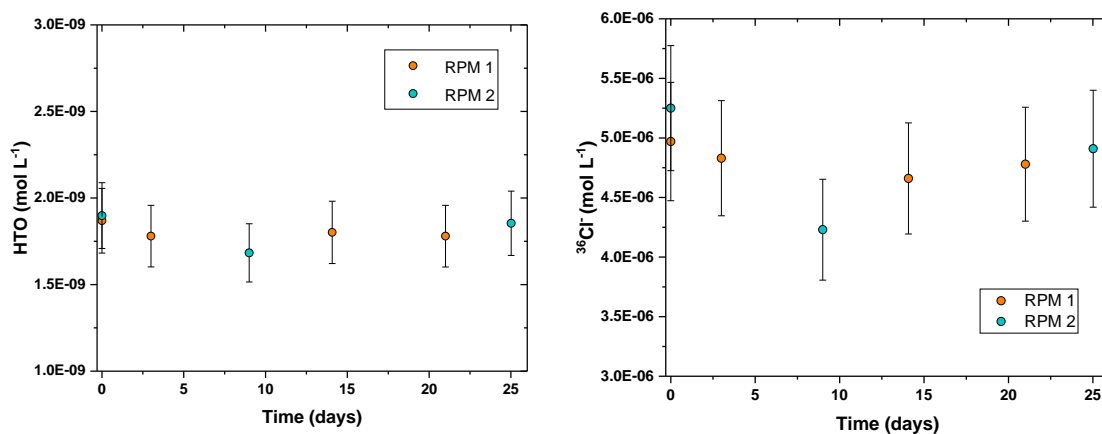


Figure 4: Upstream concentration of HTO and $^{36}\text{Cl}^-$ as a function of time.

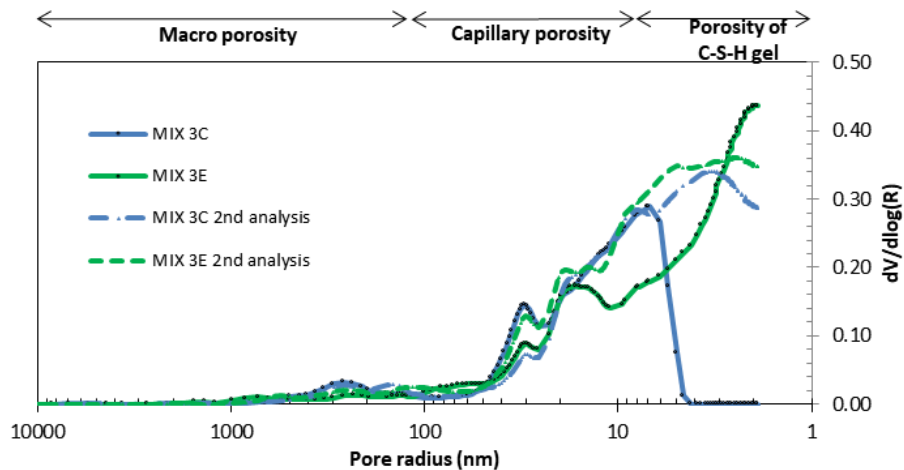
Table 5: Initial transport parameters of HTO and $^{36}\text{Cl}^-$ in different cement-based materials.

Sample type	Water/bin der -ratio	Porosity ^a	ϵ_{acc} [-]	$D_e \cdot 10^{-12}$ [m ² /s]	$R_D \cdot 10^{-3}$ [m ³ /kg] ^b	ρ [kg/m ³]
HTO						
RPM 1	0.25	0.061	0.005	2.25	u.i. ^c	2086
RPM 2			0.003	2.30	u.i. ^c	2086
MIX 3C	0.6	0.24 ± 0.04	u.i. ^c	u.i. ^c	0.40 ± 0.13	1546
MIX 3E		0.35 ± 0.05	u.i. ^c	u.i. ^c	0.40 ± 0.13	1562
³⁶ Cl ⁻						
RPM 1	0.25	0.061	0.003	2.30	u.i. ^c	2086
RPM 2			0.001	0.80	u.i. ^c	2086
MIX 3C	0.6	0.24 ± 0.04	u.i. ^c	u.i. ^c	0.22 ± 0.15	1546
MIX 3E		0.35 ± 0.05	u.i. ^c	u.i. ^c	0.22 ± 0.15	1562

^a Determined by Mercury intrusion porosimetry (MIP)^b Data obtained by kinetic batch sorption experiments (Ait Mouheeb et al., 2018)^c u.i. = under investigation

For MIX 3C and MIX 3E, the steady state in the case of HTO diffusion is reached after 10 days with a flux of $\sim 5 \cdot 10^{-16}$ mol/(m²·s). While the data of $^{36}\text{Cl}^-$ through-diffusion experiments shows that the flux reaches a value of $\sim 5 \cdot 10^{-13}$ mol/(m²·s) after 5 days. The same model approach as for RPM was tested, however, no reasonable good fit was reached. Therefore, no data is shown in this contribution. The current research is focused on finding an appropriate model approach to fit these data sets.

The results of measurements by MIP on MIX 3E and MIX 3C (see Figure 5) did not provide a reproducibility of the pore size distribution of the materials, particularly at the nano-porosity of C-S-H gel in agreement with the conclusions mentioned in the review of Diamond (2000). In this technique, mercury is introduced to surround the specimen by applying pressure to the mercury. The intrusion of mercury at each step is monitored. The set of pressure steps and corresponding volumes intruded provides the basic data for pore size distribution calculations, as it is shown in Figure 5. The calculations are realized with Washburn equation, assuming that pores are cylindrical, and they are entirely and equally accessible to the outer surface of the cement.

**Figure 5:** Pore access at 90 days age of hydrated cement (MIX 3C and MIX 3E) measured by mercury intrusion porosimetry.

Currently, batch sorption experiments are being conducted for HTO and $^{36}\text{Cl}^-$ on crushed RPM samples. However, previous uptake studies of HTO and $^{36}\text{Cl}^-$ by batch sorption experiments indicated very weak sorption ($R_D < 0.40 \pm 0.13 \text{ L/kg}$) on the low pH cement pastes (MIX 3C and MIX 3E) (Ait Mouheb et al., 2018). In the case of the diffusion experiments, it will be interesting if the measured data reflect the observations of the batch sorption experiments. In the current model approach, the sorption is considered in the rock capacity factor α together with the accessible porosity ε_{acc} . The fitted α for RPM is very low (see Table 5), much lower than the total porosity obtained by MIP (when no sorption is assumed, $\alpha = \varepsilon_{\text{acc}}$). HTO or $^{36}\text{Cl}^-$ decay is not considered in the model taking into account the duration of the experiments (35 days) and the half lives of HTO (12 years) and $^{36}\text{Cl}^-$ (301,000 years). Since such low transport porosities are unrealistic, it can be concluded, that the current model approach described in Section 1.4 is not appropriate. Recently, Patel et al. (2016) reviewed different mathematical expressions to model the diffusion data of cement-based materials. It seems that further parameters such as the volume fraction of capillary pores needs to be considered, in order to fit the experimental data of this work. In fact, the diffusivity in cement paste is influenced mainly by capillary pores in the absence of microcracks and in particular, by the nano-porosity present in C-S-H phases. Therefore, among others, the model approach from Bejaoui and Bary (2006) will be tested.

Conclusions and future work

Through-diffusion experiments of HTO and $^{36}\text{Cl}^-$ have been conducted with three different low pH cement pastes (MIX 3C, MIX 3E and RPM). Transport parameters values for HTO and $^{36}\text{Cl}^-$ were obtained for RPM (average of two samples) with $D_e(\text{HTO}) = (2.28 \pm 0.22) \cdot 10^{-12} \text{ m}^2/\text{s}$, $\varepsilon_{\text{acc}}(\text{HTO}) = 0.004 \pm 0.009$ and $D_e(^{36}\text{Cl}^-) = (1.55 \pm 6.74) \cdot 10^{-12} \text{ m}^2/\text{s}$, $\varepsilon_{\text{acc}}(^{36}\text{Cl}^-) = 0.002 \pm 0.009$.

The transport parameters of MIX 3C and MIX 3E are still under investigation, but preliminary experimental results have already shown that due to their heterogeneous small pore scale ($< 10 \text{ nm}$) network, the application of MIP is doubtful to obtain accurate porosity values and that porosity-effective diffusion correlation, which is generally described by empirical law's such Archie's law is not applicable.

Future work focuses on the repetition of the diffusion experiments to validate the results as well as the fitting of the experimental data with a more complex multiporosity approach model. In addition, diffusion experiments with HTO and $^{36}\text{Cl}^-$ through low-pH cementitious materials in contact with MX-80 bentonite pore water are in progress, in order to study the influence of low pH cement degradation on the diffusivity.

Acknowledgement

The research leading to these results has received funding from the European Union's European Atomic Energy Community's (Euratom) Horizon 2020 Programme (NFRP-2014/2015) under grant agreement, 662147 – CEBAMA. Additionally, we would like to acknowledge the colleagues from KIT-INE: Stefanie Kuschel and Sylvia Moisei-Rabung for the IC and ICP-OES analyses, Tanja Kisely for the TIC, Stephanie Kraft, for the lab assistance and advise, and Francis Claret of BRGM for his constructive remarks.

References

ANDRA (2005). Dossier Andra research on the geological disposal of high-level long-lived radioactive waste—results and perspectives, France.

- Ait Mouheb, N., Montoya, V., Borkel, C., Schäfer, T. (2017). Experimental studies on low pH cements / clay interface processes: characterization of low pH cements. *In: M. Altmaier, V. Montoya, L. Duro, A. Valls (Eds.) Proceedings of the 1st Annual Workshop of the CEBAMA Project. KIT Scientific Report, 7734.*
- Ait Mouheb, N., Montoya, V., Schild, D., Soballa, E., Adam, C., Geyer, F., Schäfer, T. (2018). Characterization and sorption properties of low pH cements. *In: M. Altmaier, V. Montoya, L. Duro, A. Valls (Eds.) Proceedings of the 2nd Annual Workshop of the CEBAMA Project. KIT Scientific Report, in press.*
- Ampadu, K.O., Torii, K., Kawamura, M. (1999). Beneficial effect of fly ash on chloride diffusivity of hardened cement paste. *Cement and Concrete Research*, 29, 585-590.
- Bejaoui, S. and Bary, B. (2007). Modeling of the link between microstructure and effective diffusivity of cement pastes using a simplified composite model. *Cement and Concrete Research, Cementitious Materials as model porous media: Nanostructure and Transport processes*, 37, 469-480.
- Bentz, D.P., Jensen, O.M., Coats, A.M., Glasser, F.P. (2000). Influence of silica fume on diffusivity in cement-based materials: I. Experimental and computer modeling studies on cement pastes. *Cement and Concrete Research*, 30, 953-962.
- Byfors, K. (1987). Influence of silica fume and flyash on chloride diffusion and pH values in cement paste. *Cement and Concrete Research*, 17, 115-130.
- Cheng-yi, H. and Feldman, R.F. (1985). Influence of silica fume on the microstructural development in cement mortars. *Cement and Concrete Research*, 15, 285-294.
- Codina, M., Cau-dit-Coumes, C., Le Bescop, P., Verdier, J., Ollivier, J.P. (2008). Design and characterization of low-heat and low-alkalinity cements. *Cement and Concrete Research*, 38, 437-448.
- COMSOL (2017). Multiphysics 5.3. Finite-element software package. COMSOL AB, Stockholm. Available from: <http://www.comsol.com>.
- Coumes, C.C.D., Courtois, S., Nectoux, D., Leclercq, S., Bourbon, X. (2006). Formulating a low-alkalinity, high-resistance and low-heat concrete for radioactive waste repositories. *Cement and Concrete Research*, 36, 2152-2163.
- Diamond, S. (2000). Mercury porosimetry: An inappropriate method for the measurement of pore size distributions in cement-based materials. *Cement and Concrete Research*, 30, 1517-1525.
- Dauzères, A., Le Bescop, P., Cau-Dit-Coumes, C., Brunet, F., Bourbon, X., Timonen, J., Voutilainen, M., Chomat, L., Sardini, P. (2014). On the physico-chemical evolution of low-pH and CEM I cement pastes interacting with Callovo-Oxfordian pore water under its in-situ CO₂ partial pressure. *Cement and Concrete Research*, 58, 76-88.
- ENRESA (1995). Almacenamiento geológico profundo de residuos radiactivos de alta actividad (AGP). Diseños conceptuales genéricos. Publicación Técnica ENRESA, 11/95.
- García Calvo, J.L., Hidalgo, A., Alonso, C., Fernández Luco, L. (2010). Development of low-pH cementitious materials for HLRW repositories: Resistance against ground waters aggression. *Cement and Concrete Research*, 40, 1290-1297.
- Jakob, A. (1999). Diffusion and sorption on hardened cement pastes – Experiments and modelling results. PSI Report 99-05.
- Ogigbo, O.R. and Black, L. (2017). Chloride binding and diffusion in slag blends: Influence of slag composition and temperature. *Construction and Building Materials*, 149, 816-825.
- Patel, R.A., Phung, Q.T., Seetharam, S.C., Perko, J., Jacques, D., Maes, N., De Schutter, G., Ye, G., Van Breugel, K. (2016). Diffusivity of saturated ordinary Portland cement-based materials: A critical review of experimental and analytical modelling approaches. *Cement and Concrete Research*, 90, 52-72.
- Tits, J., Jakob, A., Wieland, E., Spieler, P. (2003). Diffusion of tritiated water and ²²Na⁺ through non-degraded hardened cement pastes. *Journal of Contaminant Hydrology*, 61, 45-62.
- Vehmas, T., Schindler, A., Löjja, M., Leivo, M., Holt, E. (2017). Reference mix design and castings for low-pH concrete for nuclear waste repositories. *In: M. Altmaier, V. Montoya, L. Duro, A. Valls (Eds.) Proceedings of the 1st Annual Workshop of the CEBAMA Project. KIT Scientific Report, 7734.*

Vehmas, T., Leivo, M., Holt, E., Alonso, M.C., García, J.L., Fernández, A., Isaacs, M., Rastrick, E., Read, D., Vašíček, R., Hloušek, J., Hausmannová, L., Večerník, P., Červinka, R., Havlová, V., Lange, S., Klinkenberg, M., Bosbach, D., Deissmann, G., Montoya, V., Ait Mouheb, N., Adam, C., Schild, D., Schäfer, T. (2018). Cebama reference mix design for low-pH concrete and paste, preliminary characterisation. *In*: M. Altmaier, V. Montoya, L. Duro, A. Valls (Eds.) Proceedings of the 2nd Annual Workshop of the CEBAMA Project. KIT Scientific Report, *in press*.

Experiments on interface processes at the cement/Callovo-Oxfordian claystone interface and the impact on physical properties; mechanical and flow properties of fresh interfaces

Robert Cuss^{1*}, Andrew Wiseall¹, Marcus Dobbs¹, Daniel Parkes¹, Jon Harrington¹,
Jean Talandier², Xavier Bourbon²

¹ British Geological Survey (UK)

² Andra (FR)

* Corresponding author: rjcu@bgs.ac.uk

Abstract

The evolution of flow and strength properties of the concrete (T_L)/Callovo-Oxfordian Claystone (COx) interface is of importance to the long-term performance assessment of a repository. Initial testing of fresh samples shows that the COx/T_L interface has little strength, yet is an effective seal. One order of magnitude reduction in flow was seen through the re-hydration of the COx/T_L interface. A second order of magnitude reduction occurred through the shearing of the interface. Shearing was continued up to 10%, with no enhanced flow evident. Further testing will examine the evolution of the mechanical and flow properties of the interface as it ages.

1 Introduction

The weakest part of any gallery or deposition hole seal is likely to be at the interface between the sealing components and the host rock. A single seal completion may comprise a number of elements reflecting different design criteria in order to address specific engineering challenges associated with changes in geochemistry and stress. The interaction of these components with the host rock, their evolution in terms of strength/bonding, cation exchange behaviour and interfacial permeability, and the sensitivity of these properties to an evolving geochemical and physical environment will be key factors in determining the long-term seal performance. The current study aims to examine the temporal evolution of the host-rock/low-alkali cement interface in the French repository concept to changes in geochemistry, mineralogy and stress to assess their impact on the development of hydraulic permeability and strength (shear strength).

Since the previous Workshop Proceedings (Cuss et al., 2016; 2017), experimental emphasis has been on testing the Callovo-Oxfordian claystone/concrete tests in shear, and the uniaxial compression testing of concrete samples.

2 Experimental apparatus

Two Direct Shear Rigs were used, a schematic of which is shown in Figure 1. These comprise 5 main components:

1. Rigid frame that had been designed to deform as little as possible during the experiment;
2. Normal load system comprising a rigid loading frame, a hydraulic ram, and a normal load thrust block;
3. Shear force actuator designed to drive shear as slow as 14 microns a day at a constant rate (equivalent to 1 mm in 69 days);
4. Pore pressure system that can deliver either water or gas through the centre of the top sample directly to the fracture surface; and
5. A state-of-the-art custom designed data acquisition system using National Instruments LabVIEW™ software facilitating the remote monitoring and control of all experimental parameters.

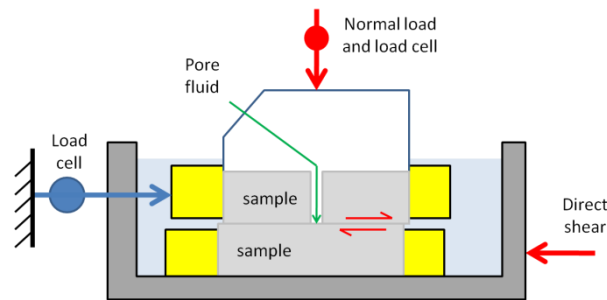


Figure 1: Schematic of the direct shear rig.

The rig was designed to achieve 10 MPa normal stress (36 kN force) on a cubic sample 60 mm × 60 mm. At this normal load, it is expected that shear force will not exceed 25 kN. Normal load is imposed by a hydraulic ram that is pressurised using an ISCO/Teledyne syringe pump. For the CEBAMA study the apparatus has been modified in order to use cylindrical samples of 60 mm diameter. This was deemed necessary as it makes sample preparation more straightforward. This also acts to increase the rig capacity to 12.75 MPa normal load.

3 Test protocol

Well preserved samples of Callovo-Oxfordian Claystone (COx) were provided by Andra from freshly cored boreholes at the Meuse/Haute-Marne URL at Bure, approximately 300 km east of Paris, France. Each core barrel was sub-sampled into 65 mm long sections using a diamond tipped saw, from which a 60 mm diameter and 53 mm height sample was prepared using a lathe. At all times during sample preparation the “exposure” to air time was minimized and the samples stored in vacuum-packed plastic as much as is practicable. The cylindrical samples were prepared perpendicular to bedding. Off-cut material was weighed and basic geotechnical properties determined.

Samples of COx were placed in the experimental apparatus and were initially re-hydrated to bring up to full saturation under a normal stress of 6.5 MPa, representative of the effective stress at repository depths. The samples were hydrated using a synthetic pore fluid under a pore pressure of 0.25 MPa. Following hydration, some samples were sheared for 2.5 days at a rate of 2 mm per day. Data recorded included pore-fluid flow, shear displacement, shear stress, normal stress, and vertical displacement. This gave; initial flow rate, shear yield stress, shear modulus (G), shear peak strength, shear residual strength, dilation/contraction during shear, and change in flow during shear. Each fracture surface was scanned using a NextEngine 3D laser scanner, giving; roughness average, root mean square roughness, peak-to-valley height, kurtosis, skewness, texture direction, texture aspect ratio, and texture direction index. All samples were vacuum packed for medium-term storage.

Casting of concrete

Three bags of material were supplied by ISNA in Toulouse; aggregate (4-12 mm), sand (0-4 mm) and binder. In the T_L ternary binder there was 20% of Portland cement, 32.5% of silica fume and 47.5% of blast furnace slag (Leung Pah Hang et al., 2017). The superplasticizer used was Chryso® Optima 175, which is a highly efficient water reducing agent having good compatibility with silica fume (Leung Pah Hang et al., 2017) and is based on polycarboxylate and modified phosphonate

Ingredients were weighed using scales with capacity of 50 kg to 4 digit precision (i.e. to ± 1 g below 10 kg and ± 10 g above 10 kg). Table 1 lists the weight of ingredients used. The ingredients were added to a cement mixer and thoroughly mixed as per the instructions received. All the aggregate was added to the mixer, then half the sand, the binder, and half the sand. This was mixed for 90 seconds. However, it should be noted that a late decision was taken to cast the concrete in a single session and that the cement mixer was not mixing thoroughly, requiring pausing of the mixer and additional manual mixing using a shovel. This meant that mixing took longer than instructed to create an even mix. Half of the water was added and mixed for one minute, the other half of the water and superplasticizer was added and thoroughly mixed for five minutes. However, it should be noted that additional manual mixing meant this final stage was longer than five minutes.

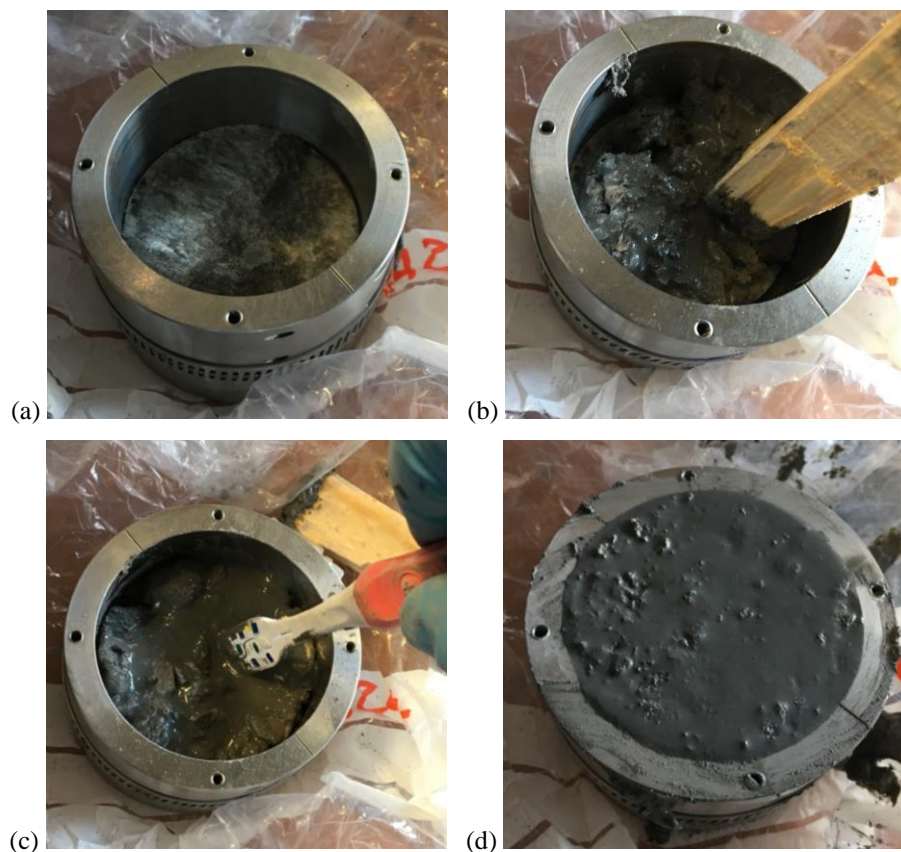


Figure 2: Casting of concrete directly to rock samples. a) an o-ring, collar and jubilee clip were added to all test samples; b) a small amount of concrete was added and tamped at least 25 times using wood; c) additional tamping was conducted using a modified vibrating toothbrush; d) additional layers were added until a flush surface was created using a trowel.

Prior to concrete casting, each test sample was prepared. Sheared and re-hydrated samples that had been stored vacuum-packed were removed from their casing. A 60 mm inner diameter, 3 mm diameter o-ring was placed around the periphery of the protruding rock sample. A sample collar was added and held in position by a jubilee

clip to ensure that the two collars were parallel (Figure 2a). It should be noted that the two-halves of this collar were sealed by means of Hylomar Blue gasket and joining compound. A small amount of concrete was placed directly onto the fracture surface. This was tamped with a piece of wood (Figure 2b) at least 25 times per layer (BS EN 12390-2). As a vibration table was not available, a modified vibrating (ultrasonic) toothbrush was used to aid distribution of concrete and to extract air (Figure 2c). The bristles of the toothbrushes were removed and the brush head trimmed to make a thin vibrating device. A second (\pm third) layer of concrete was added and this was finished flat with the collar using a trowel (Figure 2d). The combination of wood and vibration tamping produced an even mix of concrete with little sign of air bubbles. The samples were vacuum-packed to ensure that the rock samples were not exposed to air for prolonged periods.

Table 1: Weight of ingredients used during concrete casting.

Ingredient	Weight (g)
Super plasticizer	95
Binder	6,331
Sand (0-4 mm)	14,244
Aggregate (4-12 mm)	15,810
Water	2,532
TOTAL	39,012

Large samples for uniaxial, shear, and petrology were prepared in a similar way using wood and vibration tamping described above. Moulds were cut from 2.5 m lengths of 68 mm (outer diameter) PVCu drain pipe manufactured by FloPlast, giving a sample of 64.5 mm diameter. The tube was cut into 180 mm (x 30), 130 mm (x 2) and 100 mm (x 5) lengths. One end of the mould was sealed using duct tape. The 180 mm mould enabled a 150 mm sample to be manufactured once the ends had been trimmed. All sample moulds were stored in a tank filled with lime water until prior to testing (Figure 3).

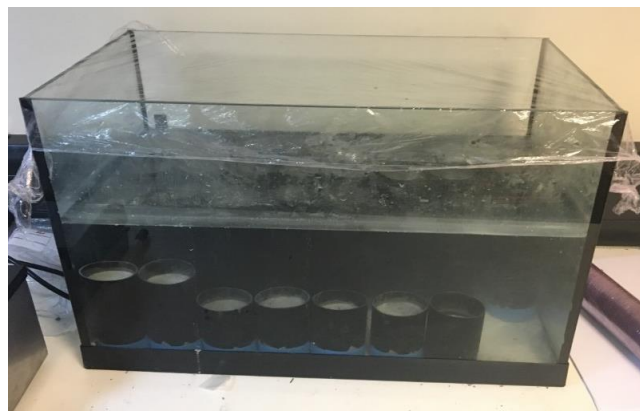


Figure 3: Storage of concrete sample moulds in a lime-water filled tank.

Finishing of the collared shear samples occurred the day after casting. Each sample was removed from its temporary vacuum packing and the surface of the collar on the concrete sample side was cleaned (Figure 4a). A casting collar was added to this end of the sample, as shown in Figure 4b, with a seal achieved between the two collars by means of an o-ring. Within this collar, two squares of cloth saturated with limewater were placed (Figure 4c). This meant that the curing concrete had a supply of water. The sample was then carefully

vacuum-packed (Figure 4d) three times to ensure the arrangement was air-tight. The sample was inverted so that the water-saturated cloth was on the bottom to ensure that excess water did not drain towards the COx. All samples were stored at 20°C within the temperature-controlled laboratory.

It should be noted it was intended to store the samples under realistic in-situ pressures to replicated confining stress. However, testing storage of samples in the polyamide (PA) and polyethylene (PE) composite vacuum-sealed bags at elevated pressures above 1 MPa resulted in a 100% failure rate, resulting in flooding of the contents. The collar arrangements used also meant that a 1-D compression of the sample arrangement would not be possible. Therefore, samples were stored at ambient temperature and pressure.

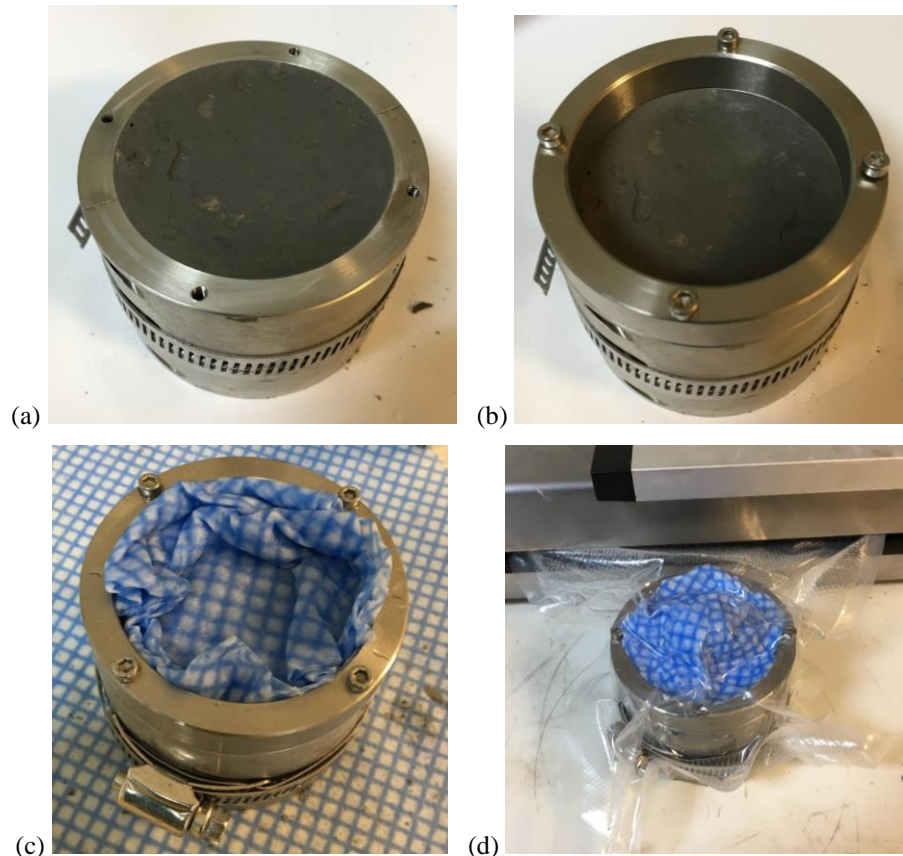


Figure 4: Finishing of samples. a) the top collar surface was cleaned; b) a casting collar was bolted onto the main collar of the sample; c) squares of lime-water saturated cloth were added; d) the sample arrangement was triple vacuum packed.

Example shear/flow test: Test CEBAMA_01

Cuss et al. (2017) described the mechanical shear data for test CEBAMA_01. In this paper, the results are presented on the re-shearing of sample CEBAMA_01 mixture after the casting on concrete onto the fracture surface.

Test sample CEBAMA_01 was retrieved and taken from the vacuum storage bags. Careful examination showed that the sample was in good condition. The casting collar and saturated cloth was removed, the latter still being wet. The centre of the sample was identified on the COx side of the arrangement and a pilot hole of 1 mm diameter was drilled to the depth of the interface between the COx and concrete. It should be noted that injection occurred through the COx to take advantage of the greater self-sealing capacity compared with concrete in response to swelling of the clay content. A 4 mm diameter hole was then drilled, sufficient to accommodate the

injection bore of the apparatus. Drilling occurred slowly a few millimetres at a time to ensure that overheating did not occur, which could potentially damage the rock. The injection bore and bottom of the top thrust block were lightly coated with silicone sealant and the bore was introduced to the sample.

The sample assembly was reconstructed within the DSR apparatus, with a normal stress identical to the load imposed during shearing of the virgin rock. The initial part of the flow test aimed to establish a pore pressure within the interface without causing excessive flow. As shown in Figure 5a, this took approximately 1 day. Initially a pore pressure of 100 kPa was established, creating a relatively high flow. Therefore, the pore pressure pump was stopped and the decay of pore pressure was monitored. Over the course of nearly a day the pore pressure decayed to approximately 50 kPa, suggesting that the sample was sealing. Over the course of a few hours the pore pressure was raised stepwise up to 1 MPa. At the onset of normal load, the sample began to contract (Figure 5b). The rate of contraction increased as the pore pressure was first established. It should be noted that at approximately the age of one day the normal load system was adjusted (normal load was reduced and reinstated) and this led to a second acceleration of contraction. At a pore pressure of 1 MPa the initial flow was approximately 250 $\mu\text{L/h}$ and quickly reduced to a steady flow rate of around 30 $\mu\text{L/h}$ (Figure 5c). This equated to an interface transmissivity of approximately $4 \cdot 10^{-14} \text{ m}^2/\text{s}$ (Figure 5d). Therefore, the rehydration of the interface resulted in a rapid one order of magnitude reduction in flow.

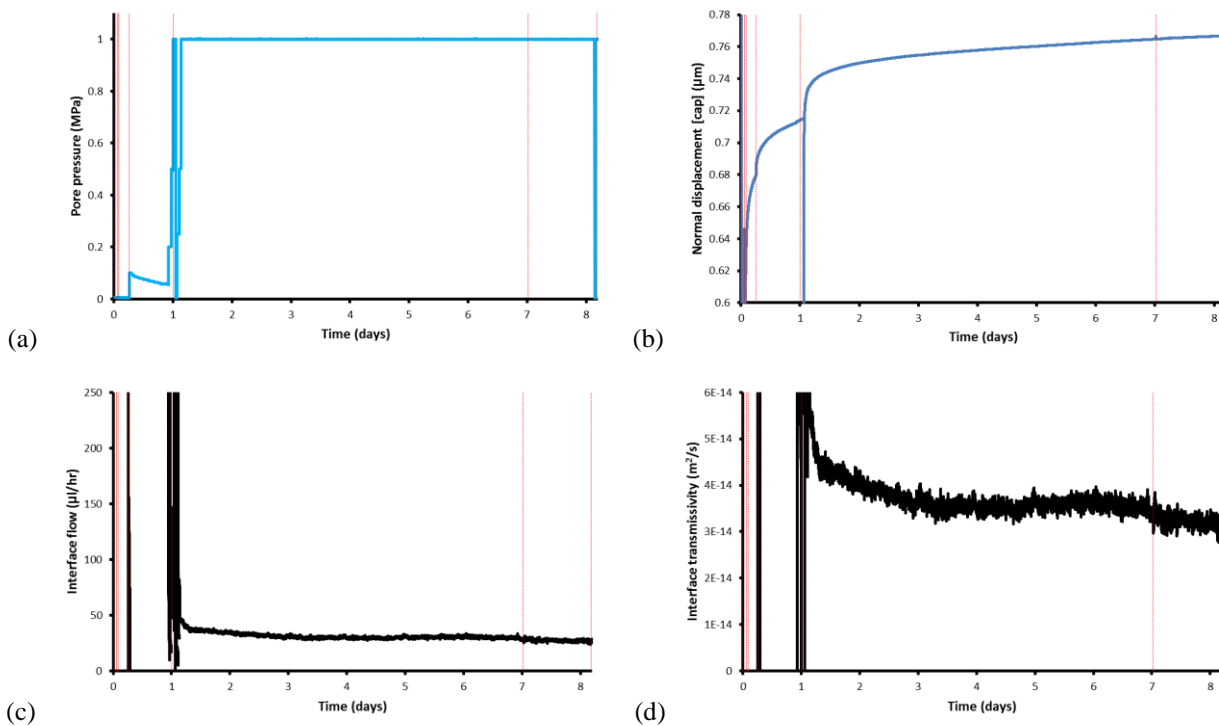


Figure 5: Initial flow of the interface for test CEBAMA_01. a) Pore pressure; b) normal displacement; c) interface flow; d) interface transmissivity.

Shear was initiated around the age of 8 days with the intention to shear for approximately two weeks (Figure 6). As shown in Figure 6a and Figure 6b the interface did not show much strength. Peak shear stress was recorded as approximately 2.68 MPa, considerably less than the 6.19 MPa seen in the intact COx sample. The form of the shear stress is also different with a classic elastoplastic response with a small degree of strain softening post peak, compared with the more classical brittle response seen in the intact rock. Figure 6c shows that flow was generally constant during the initial shearing period and at a time when the slope of the shear stress (Figure 6h) reached a maximum the flow began to decrease, eventually reaching a low flow condition of 3 $\mu\text{L/h}$ or a transmissivity of

$2.8 \cdot 10^{-15} \text{ m}^2/\text{s}$ (Figure 6d). Therefore, the shearing of the interface resulted in a one order of magnitude reduction in flow. Normal displacement of the interface (Figure 6f and Figure 6g) show that throughout the stage the sample tended to contract. Dilation of the interface can be inferred at the age of 9.7 days, but this was soon superseded by further contraction. Figure 6h shows that the slope of the shear stress peaked at approximately 250 MPa, which is considerably lower than the 340 MPa seen in the intact rock.

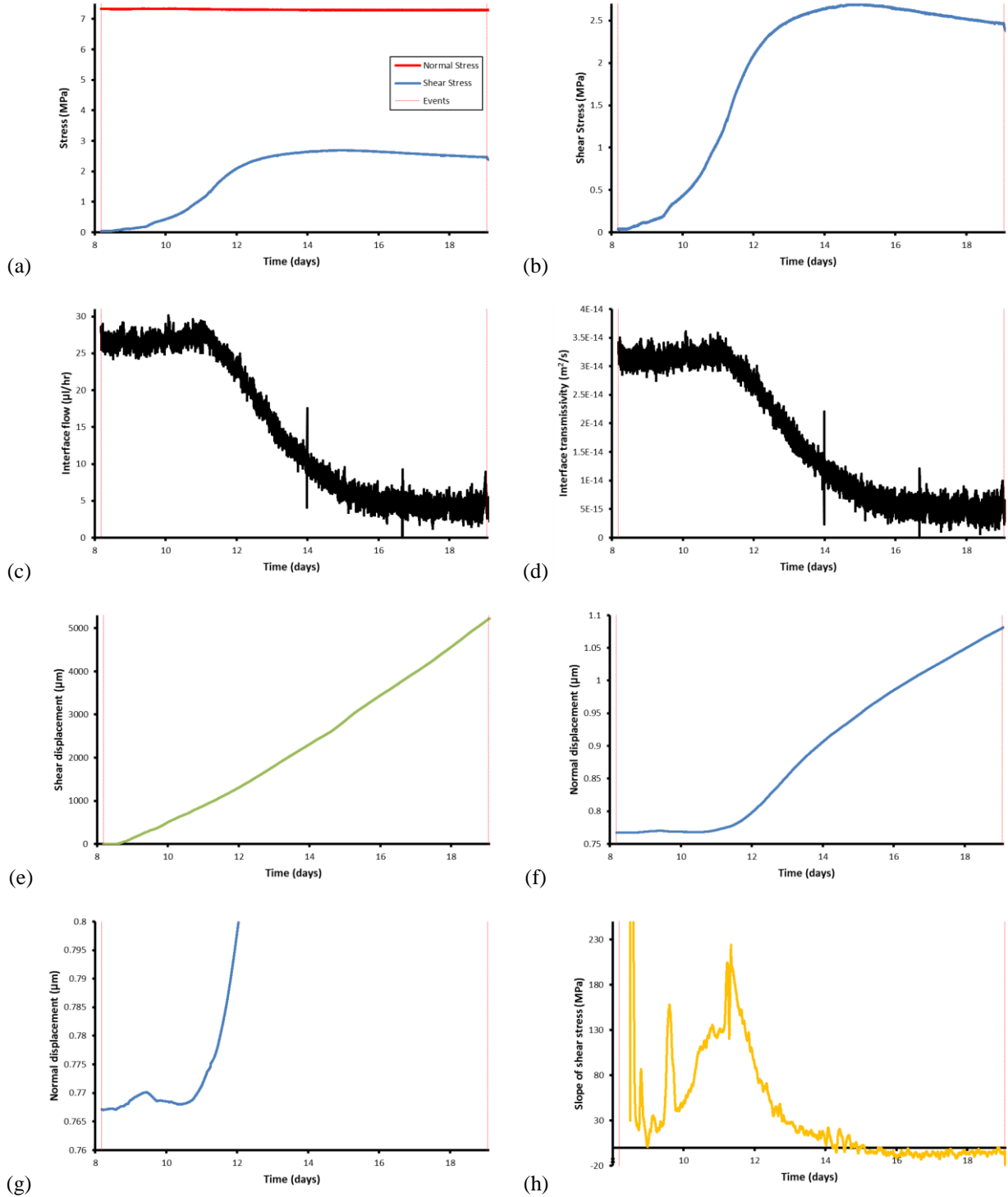


Figure 6: Test results for CEBAMA_01 during shearing of the concrete/Cox interface. a) stress data; b) shear stress; c) interface flow; d) interface transmissivity; e) displacement; f) total normal displacement; g) detail of normal displacement; h) slope of shear stress.

Figure 7 compares the mechanical data recorded for the virgin COx and the COx/concrete interface. This shows that the peak stress of the two tests are considerably different (6.2 MPa COx, 2.7 MPa interface), with the peak stress of the interface test almost identical to the residual shear strength of the COx. This suggests that the interface itself has very little mechanical strength. It cannot be discounted that the interface separated during setting up the experiment and further testing will confirm this. The shear modulus reduced between tests as well, with the virgin COx having a shear modulus of 340 MPa, compared with 250 MPa for the interface. However, despite suggesting that the interface was not bonded well (limited strength), the interface was a good seal.

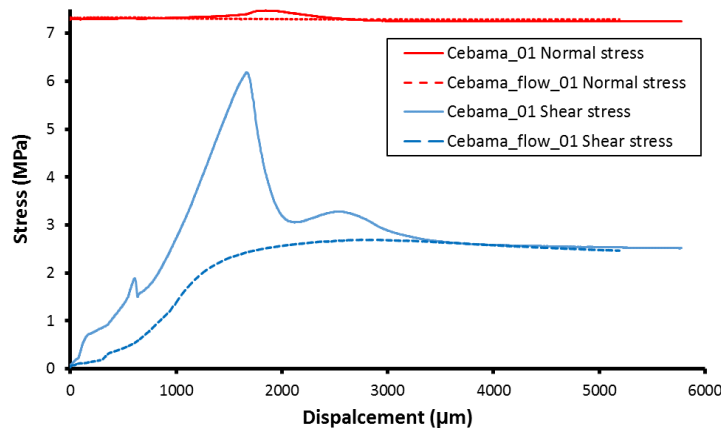


Figure 7: Comparing mechanical data for sample CEBAMA_01 with initial shearing of intact COx (solid line) and shearing of the COx-cement interface (dashed line).

Pore fluid will always flow in the direction that facilitates fluid movement the easiest. It is assumed that the Injection of fluid directly to the Interface between the COx and the concrete is likely to result in fluid movement along the Interface. However, chemical exchange between the COx and concrete may result in a zone that retards flow, resulting in fluid movement into either the COx or the concrete, whichever has the greater permeability. The injection of fluorescein will investigate the direction of fluid movement in detail. The boundary condition of the experimental apparatus means that pore pressure at the edge of the sample is close to zero and fluid migration to the boundary will result in fluid expulsion into the test apparatus bath.

5 Properties of the concrete during curing

Uniaxial tests have been conducted on cylindrical samples of 64.5 mm and 130 mm length (2:1 length ratio). These have occurred at 7, 28 and 85 days following casting with three repeat tests at each time. It was intended to also test at 3 and 56 days, however, the MTS testing apparatus was not available at these times. Figure 8 shows the uniaxial test results. It can be seen that at the first time (7 days, blue lines) there was considerable spread in the data. This has been attributed to two tests prematurely failing due to the small diameter of the test samples (tests 2 and 3). A sample of 65 mm only has 5 maximum aggregate diameters and with aggregate up to of 12 mm samples ideally should have been cast at 120 mm diameter. Therefore, the aggregate size has influenced the results. One test each at 28 and 85 days also has been classified as anomalous (tests 4 and 7).

Figure 9a shows that the strength of the concrete increased. After 7 days the concrete had a strength of 39.3 MPa. This increased to 55.09 and 69.14 after 28 and 85 days. The strength of the TL concrete has been shown to be 69.5 MPa after 28 days (Leung Pah Hang, 2015). Therefore, the strength observed was on the low side after 28 days, but had reached this strength by 85 days. Young's modulus (Figure 9b) and Poisson's ratio (Figure 9c)

also increased during curing. Further tests are needed to get a better understanding of the increase in strength and elastic properties with curing time.

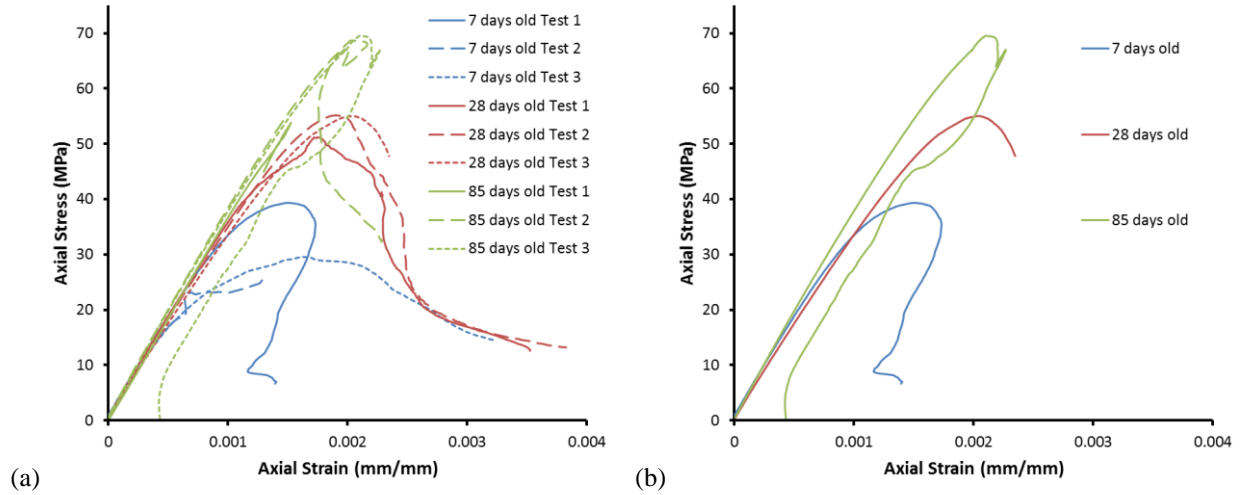


Figure 8: Uniaxial test results for concrete samples. a) all test results showing the three repeat tests at each time interval; b) representative results showing the increase in strength with curing time.

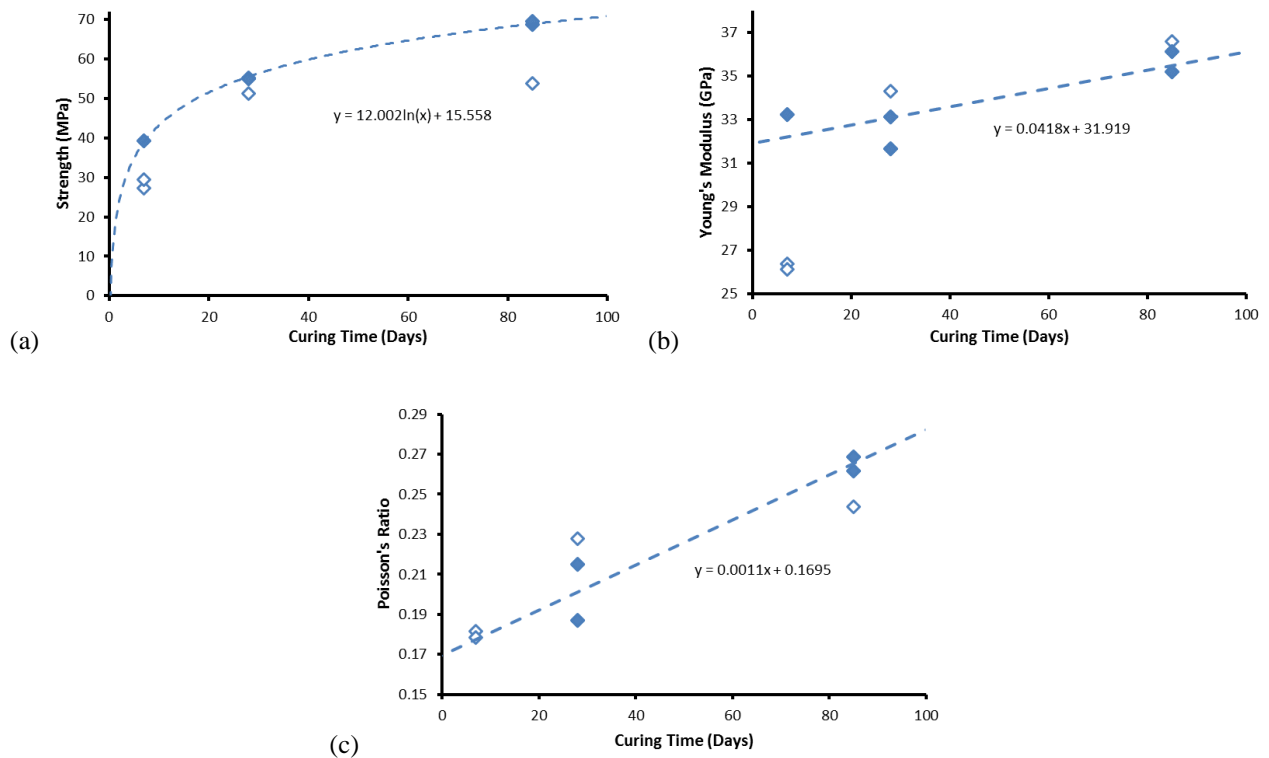


Figure 9: Changes of elastic properties during curing. a) strength; b) Young's modulus; c) Poisson's ratio. Note: open symbols represent tests identified as anomalous or premature failure.

6 Current status and future activities

The test program for fresh interfaces has begun and this paper introduces the first of the tests conducted. Repeat testing will occur at regular intervals as the concrete continues to cure in order to identify changes in mechanical and flow behaviour. All samples that use fluorescein within the injection fluid will undergo fluorescent scanning to identify flow paths of the injection water. SEM analysis will be used to determine chemical aging of the concrete, geochemical reactions between the CO_x and cement, and identify flow paths.

It should be noted that at this point in the experimental programme it is not possible to ascertain the repeatability of the testing methodology. This will be further explored during the subsequent experimentation.

Acknowledgement

The research leading to these results has received funding from the European Union's Horizon 2020 Research and Training Programme of the European Atomic Energy Community (EURATOM) (H2020-NFRP-2014/2015) under grant agreement n° 662147 (CEBAMA). The BGS authors publish with the permission of the Executive Director, British Geological Survey (NERC).

References

- BS EN 12390-2 (2009). Testing hardened concrete. Making and curing specimens for strength tests. British Standards Institution, London.
- Cuss, R.J., Wiseall, A.C., Harrington, J.F., Talandier, J., Bourbon, X. (2016). Experiments on interface processes at the cement/Callovo-Oxfordian Claystone interface and the impact on physical properties; initial findings. *In*: M. Altmaier, V. Montoya, L. Duro, A. Valls (Eds.) Proceedings of the 1st Annual Workshop of the CEBAMA Project. KIT Scientific Report, 7734.
- Cuss, R.J., Wiseall, A.C., Harrington, J.F., Talandier, J., Bourbon, X. (2017). Experiments on interface processes at the cement/Callovo-Oxfordian Claystone interface and the impact on physical properties; initial findings. *In*: M. Altmaier, V. Montoya, L. Duro, A. Valls (Eds.) Proceedings of the 2nd Annual Workshop of the CEBAMA Project. KIT Scientific Report, *in press*.
- Leung Pah Hang, T. (2015). Les bétons bas pH: comportements initial et différé sous contraintes externes. Doctoral dissertation, Université de Toulouse, Université Toulouse III-Paul Sabatier.
- Leung Pah Hang, T., Verdier, J., Vidal, T., Camps, G., Bourbon, X. (2017). Mechanical and transfer properties of low-pH concretes in view of classical HPC substitution in confinement structures. *European Journal of Environmental and Civil Engineering*, 1-18.

Effects of porosity evolution on the evaluation of radionuclide diffusion coefficients in mortars and concrete

Miguel García-Gutiérrez^{1*}, Manuel Mingarro¹, Tiziana Missana¹

¹ CIEMAT, Centro de Investigaciones Energéticas, Medioambientales y Tecnológicas (ES)

* Corresponding author: miguel.garcia@ciemat.es

Abstract

The determination of reliable transport parameters for radionuclides (RN) in cementitious materials is an issue. The physicochemical instability and kinetic processes may produce changes in the system, which are reflected in porosity variations affecting RN diffusivity.

In this work, a few examples will be shown to point out the possible problems related to the determination of RN transport parameters in cementitious materials, due, for example, to the selection of porewater (for tritiated water HTO and ³⁶Cl) or the experimental time (for ¹³⁷Cs).

Through-Diffusion tests of HTO and ³⁶Cl, with concrete samples using CEM I, and mortar samples using CEM IV, were performed saturating the solids with different porewaters. An in-diffusion method was used for determining diffusion coefficients for ¹³⁷Cs, in mortars. The kinetic effects related to the determination of the diffusion coefficient of ¹³⁷Cs were studied by analysing diffusion profiles at different times (from 150 up to approximately 1,500 days).

1 Introduction

Cement-based materials are widely used in repositories for isolating low and medium radioactive waste. Cementitious materials have a good sorption capability for radionuclides (RNs) and generate an alkaline environment which produces a decrease in their solubility (Atkins and Glasser, 1992; Vieno et al., 2003). The main transport process for RN in these materials is diffusion (retarded by sorption), which occurs within the networks of fissures and interconnected pores saturated by the porewater. Thus, the porosity of the system is one of the main important physical parameters for limiting contaminant transport.

The determination of reliable transport parameters in hydrated cement pastes, mortars and concretes is more complicated than in other materials of interest for isolating radioactive waste (compacted or consolidated clays) and conventional experimental methods might not always provide accurate values of effective or apparent diffusion coefficients.

Within the experimental time which, depending on the selected radionuclide, may vary from months to years, appreciable changes associated with chemical and physical perturbations and to non-equilibrium situations may occur. The alteration of matrix, dissolution/precipitation, formation of secondary phases and other interface

processes are likely to occur, affecting the overall porosity of the system; thus, these changes are expected to affect RN diffusivity.

The experimental results can be biased by the physicochemical instability of the system and their interpretation is not always straightforward. Additionally, in these systems, the kinetics may play an important role. The evolution of the porosity in cement-based material, without any interaction with external environments, is usually due to the hydration of cement particles with time. Therefore, to establish a reliable experimental methodology to determine transport parameters in cementitious materials, considering these complications is fundamental.

In this study, conservative elements (HTO and ^{36}Cl) were used to point out the possible problems related to the selection of the porewater. ^{137}Cs , a mildly sorbing element, was used to analyse the kinetic effects related to the determination of the diffusion coefficient in mortars.

2 Materials and Methods

2.1 Solid Samples

Experiments were carried out using CEM I 42.5 R/SR to obtain concrete samples with a water/cement ratio of 0.43, and CEM IV B 32.5 for mortar samples with a water/cement relation of 0.4. The curing time was 28 days. The water/cement ratio is a critical parameter as it influences the final porosity of the samples. Figure 1 shows an example of the concrete (left) and mortar (right) samples used for the experiments.

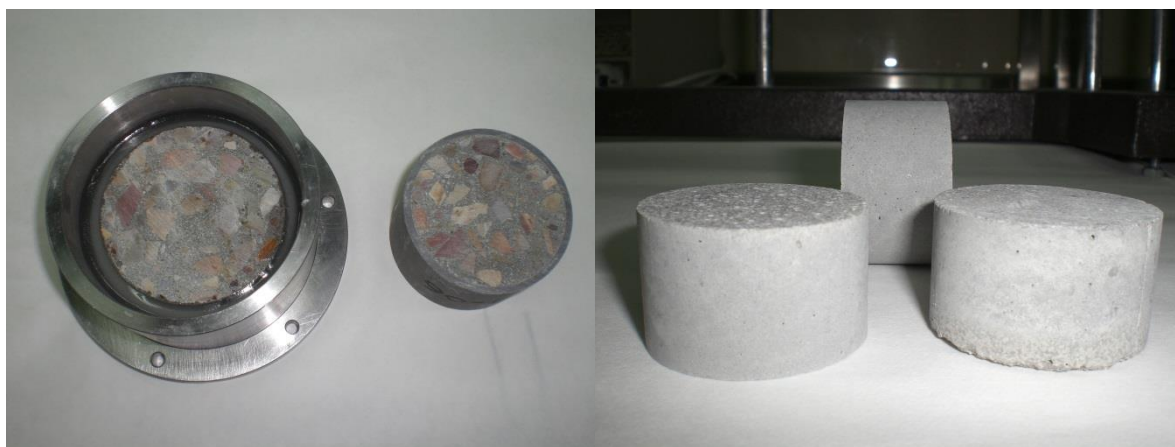


Figure 1: Concrete (left) and mortar (right) samples used for the experimentation.

2.2 Porewaters

Three different porewaters were used to perform diffusion experiments on concrete and mortar. All the waters were prepared under anoxic condition in an anoxic glove box with N_2 atmosphere. The first one was a synthetic water simulating a fresh cement porewater, whereas the other two waters were obtained by contacting the solid (concrete or mortar), at a solid to liquid ratio of 10 g/L, to deionised and decarbonated water, and finally filtered by a Millipore membrane of 0.45 μm .

The main chemical composition of the waters is summarised in Table 1.

Table 1: Cement pore water composition (mol/L).

Element	Synthetic	Equilibrium with Concrete	Equilibrium with Mortar
Na ⁺	4.71·10 ⁻²	1.82·10 ⁻⁴	3.12·10 ⁻⁴
K ⁺	1.79·10 ⁻²	9.26·10 ⁻⁴	1.68·10 ⁻³
Ca ²⁺	8.00·10 ⁻³	1.20·10 ⁻²	7.24·10 ⁻³
Al ³⁺	1.00·10 ⁻⁵	1.22·10 ⁻⁵	1.16·10 ⁻⁴
Cl ⁻	1.97·10 ⁻³	3.86·10 ⁻⁴	3.07·10 ⁻⁴
SO ₄ ²⁻	3.12·10 ⁻⁴	1.46·10 ⁻⁴	8.86·10 ⁻⁵
SiO ₂	5.00·10 ⁻³	2.03·10 ⁻⁵	5.84·10 ⁻⁵
pH	12.8	12.8	12.7

The chemical composition of the solution in the pores of hydrated cement depends on the composition of the concrete/mortar, mainly on the type of cement, but also on the exposure conditions. The water composition is expected to affect the diffusion coefficients, because the speciation and sorption depends on the aqueous chemistry. Furthermore, other changes due to carbonation, precipitations or penetration of salts modify the solid porosity.

2.3 Diffusion tests

2.3.1 Through-Diffusion method (TD)

Effective diffusion coefficient is obtained by the Through-Diffusion (TD) method, fitting the cumulative mass of tracer through the sample vs. the time in the region of constant flux (steady state). A schematic diagram of this experimental setup can be observed in Figure 2. In this method the cement sample is located in between two reservoirs, “in” and “out” reservoirs, where the synthetic water is continuously stirred. After the re-saturation of the sample, for which, approximately four or five weeks are required, the in-reservoir is spiked with the tracer. The concentrations in both reservoirs are kept constant such that steady-state diffusion across the sample is achieved. When steady-state is reached, the diffusive flux across the sample is constant. Different approximations can be used to maintain the concentration gradient constant: by spiking additional tracer in the in-reservoir, if it is necessary, or using large volumes to minimize the concentration decrease; carrying out frequent sampling in the out-reservoir to maintain the concentration near to zero or to use small reservoir and changing them periodically. A configuration with a large (1 L) in-reservoir and a small (20 mL) out-reservoir, which is changed periodically, was used.

The effective diffusion coefficient D_e can be calculated from the slope of the straight line fitting the cumulative mass of tracer that has passed to out-reservoir, through a cross-sectional area S , and thickness L , with a in concentration of C_0 (Crank, 1975; Bourke et al., 1993):

$$D_e = \frac{\text{slope} \cdot L}{S \cdot C_0} \quad (I)$$

This method has been used to determine the effective diffusion coefficients for the conservative (non- sorbing) HTO and ³⁶Cl.

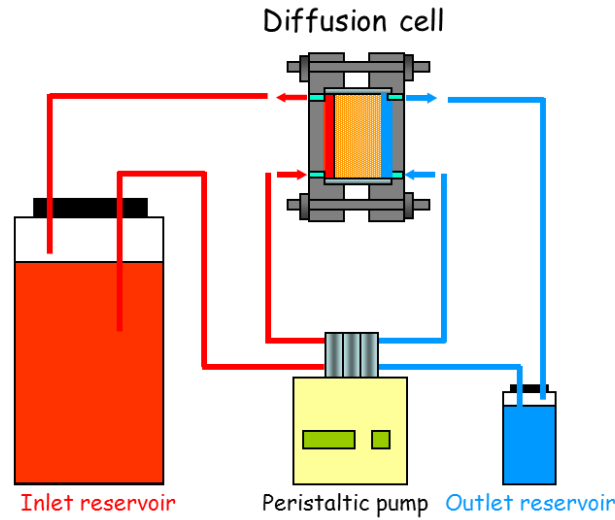


Figure 2: Schematic diagram of the TD experiments.

2.3.2 In-Diffusion method (ID)

In-Diffusion experiments, ID, are typical transient essays. The diffusion cell is immersed in the cement pore water until sample water saturation, and then the tracer is added. From this moment on, the tracer enters through the open side of the plug, and after the estimated diffusion time, we cut the sample using a Profile Grinder in several slices and measured the tracer activity in each slice to obtain a concentration profile into the sample. Experiments are usually designed so that the tracer cannot reach the opposite closed extreme of the sample and the experiment could be treated as a one-dimensional case of diffusion into a semi-infinite medium.

When the In-Diffusion experiments are performed with sorbing tracers, the concentration in the reservoir changes as a function of time, thus small tracer additions avoid significant concentration changes and the constraints are maintained.

In that case, the concentration profile into the clay $C(x,t)$ is given by (Crank, 1975; Grathwohl, 1998):

$$C(x,t) = C_0 \cdot \operatorname{erfc}\left(\frac{x}{2\sqrt{D_a \cdot t}}\right) \quad (2)$$

Where C_0 is the initial concentration, D_a is the apparent diffusion coefficient, x the distance and t the diffusion time.

This method has been used to determine the apparent diffusion coefficient for the mildly sorbing element ^{137}Cs . The total Cs concentration was $1 \cdot 10^{-9}$ M.

3 Experimental results

3.1 Effects of pore water chemistry

Figure 3 shows an example of the experimental results of the flux (left) and cumulative activity (right) of TD experiments for HTO in concrete and mortar in the synthetic porewater.

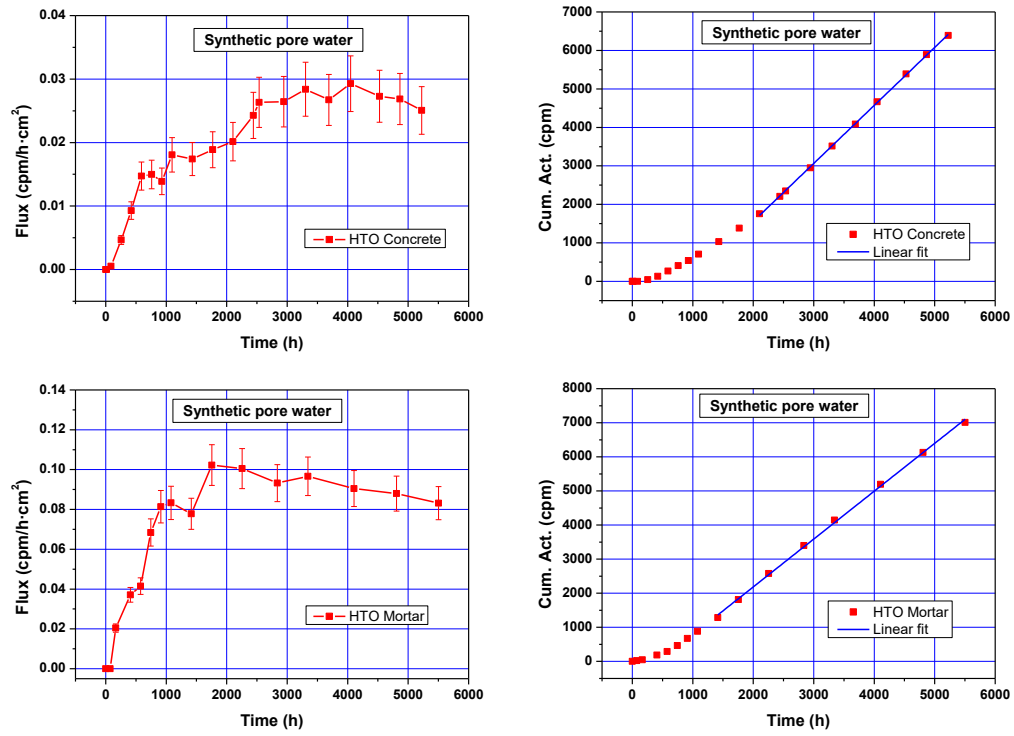


Figure 3: Flux (left) and cumulative mass (right) for HTO in concrete and mortar with synthetic pore water.

Figure 4 y Figure 5 show an example of the experimental results of the flux (left) and cumulative activity (right) of TD experiments for ^{36}Cl in concrete and mortar in the synthetic pore water (Figure 4) and for HTO and ^{36}Cl in concrete with its equilibrium pore water (Figure 5).

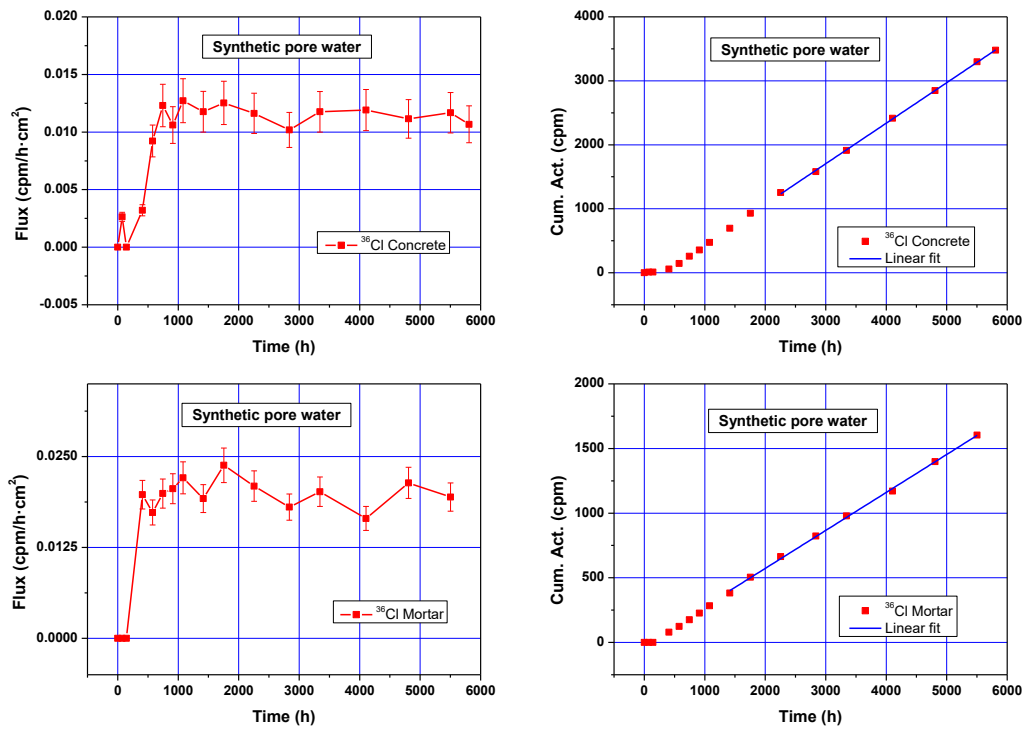


Figure 4: Flux (left) and cumulative mass (right) for ^{36}Cl in concrete and mortar with synthetic pore water.

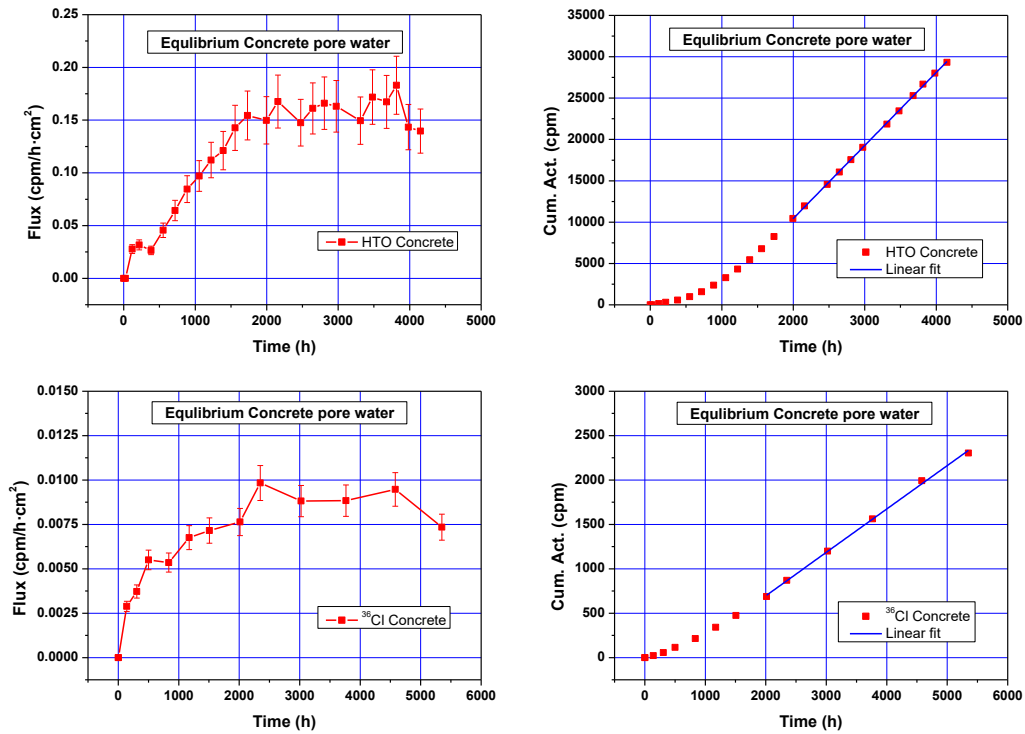


Figure 5: Flux (left) and cumulative mass (right) for HTO and ³⁶Cl in concrete with its equilibrium porewater.

Figure 6 shows an example of the experimental results of the flux (left) and cumulative activity (right) of TD experiments for HTO and ³⁶Cl in mortar with its synthetic pore water.

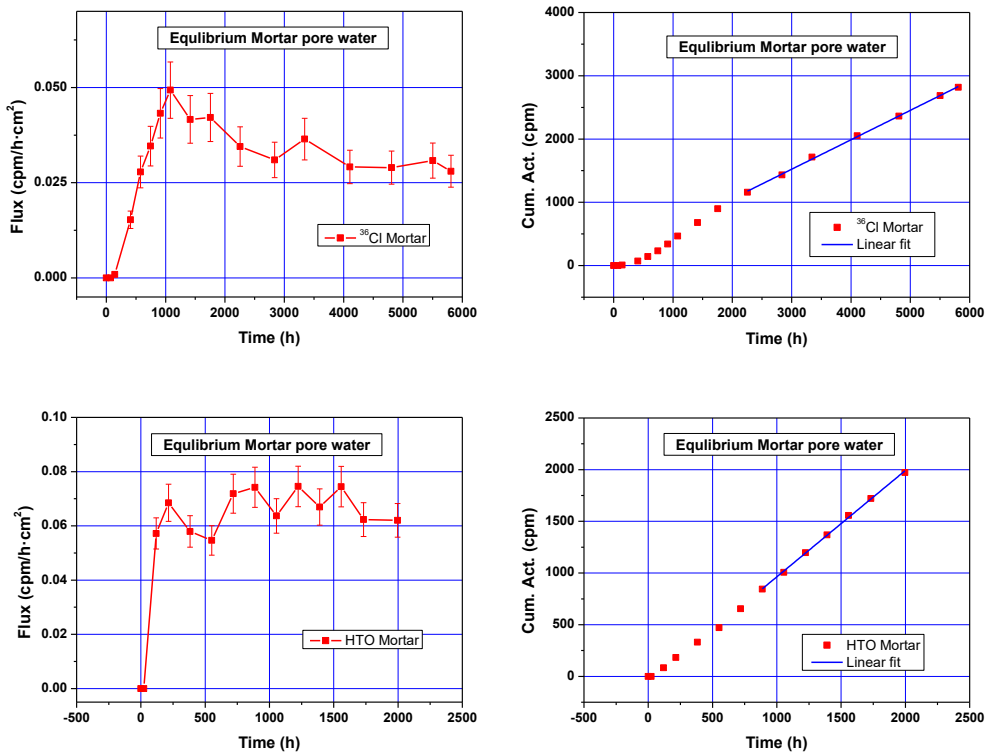


Figure 6: Flux (left) and cumulative mass (right) for HTO and ³⁶Cl in mortar with its equilibrium pore water.

The results of all the tests performed are summarised in Table 2, which shows the range of effective diffusion coefficients obtained for HTO and ^{36}Cl in concrete and mortar using the synthetic water and the water at the equilibrium with the respective solid.

Table 2: Effective diffusion coefficient (m^2/s).

Tracer/Material	Synthetic Porewater	Equilibrium Porewater
HTO Concrete	$(1.1 - 1.9) \cdot 10^{-12}$	$(3.3 - 3.7) \cdot 10^{-12}$
HTO Mortar	$(1.4 - 1.6) \cdot 10^{-12}$	$(1.1 - 1.3) \cdot 10^{-12}$
^{36}Cl Concrete	$(1.6 - 1.9) \cdot 10^{-13}$	$(2.4 - 2.8) \cdot 10^{-13}$
^{36}Cl Mortar	$(2.2 - 2.6) \cdot 10^{-13}$	$(3.4 - 3.9) \cdot 10^{-13}$

Conservative elements as HTO are not adsorbed in the solid and ^{36}Cl is a low sorbing element; therefore, the differences in the diffusion coefficients must be related mainly to changes induced in the solid structure, not to the porewater chemistry itself.

In all the cases, the diffusion coefficients obtained with the respective equilibrium porewaters are slightly higher than those determined with the synthetic porewater (factor 1.5 to 2 approximately). The only exception is the result for HTO in mortar, which cannot be explained so far.

The results indicate that, as the synthetic water is not necessarily in equilibrium with the system, some mineral precipitation may occur (sometimes visible at sight) and bias the results of the tests. For example, some portlandite might have been dissolved and the samples slightly altered. Even the differences are not extremely large in this case, they must be accounted for.

3.2 Effect of experimental time selection

To observe the effects caused by changes in the mortar pore structure In-Diffusion experiments were carried out with ^{137}Cs , using experimental times from 150 up to approximately 1,500 days. Figure 6 shows the concentration profiles measured at three different times and the fit obtained with Eq. 2, to determine the apparent diffusion coefficients.

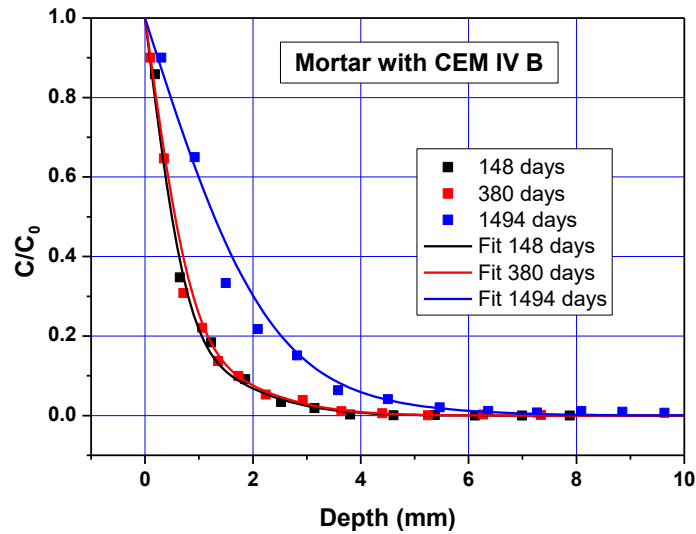


Figure 6: Concentration profiles of ^{137}Cs in mortar at different times.

From the fit of the experimental data, it could be observed that the value of the apparent diffusion coefficients (D_a) varied (decreasing) with the experimental time: after 148 days it was $1.8 \cdot 10^{-14} \text{ m}^2/\text{s}$; after 380 days, $1.2 \cdot 10^{-14} \text{ m}^2/\text{s}$ and after 1,494 days, $0.7 \cdot 10^{-14} \text{ m}^2/\text{s}$.

Apart from this clear variation, it could be pointed out that, in the experiments of less duration, the Cs concentration profiles in mortars could not be adjusted considering a single diffusion coefficient (or a single porosity model). The experimental data were better simulated considering the superposition of two diffusion profiles and assuming that a fraction of Cs (approximately 25%), penetrates more deeply and faster whereas the rest penetrates less. The details of this work can be found in García-Gutierrez et al. (*submitted*).

However, when much longer experimental time is considered, this effect is attenuated and only one diffusion coefficient is enough to explain diffusion data. This seems indicating that a progressive homogenisation of the pore structure is occurring. This effect was even more evident in mortars from other cements (CEM II, for example) as reported in García-Gutierrez et al. (*submitted*).

Furthermore, it has to be taken into account that Cs sorption is not linear, and this can lead to different retention behaviour as a function of its concentration.

As a general conclusion, it can be stated that the appropriate selection of the experimental time is very important to obtain reliable diffusion coefficients in these materials.

4 Conclusions

The experimental constraint for diffusion experiments in cementitious materials must be checked with great accuracy. Cement-based material are not inert materials with a fixed pore distribution, and when water or solute transport through the pore exist, alteration into its pore structure due to cementation process, can change the pore size and distribution. Chemical conditions and their evolution must be accounted for to understand the possible variations of transport parameters.

Additionally, special care must be taken with kinetic processes that might influence the material structure. Diffusion tests with Cs showed that the determination of apparent diffusion coefficients is dependent on the experimental time. Furthermore, if the selected diffusion time is short, the simulation of concentration profiles could be obtained only by the superposition of two diffusion profiles, whereas this was not necessary to fit data obtained upon longer diffusion times (4 years), indicating that the material is evolving with time.

This indicates that more appropriate results are obtained upon large experimental times, which cannot be always attainable for elements more strongly sorbing than Cs, and that the model to interpret the diffusion results is very important.

Acknowledgement

The research leading to these results has received funding from the European Union's Horizon 2020 Research and Training Programme of the European Atomic Energy Community (EURATOM) (H2020-NFRP-2014/2015) under grant agreement n° 662147 (CEBAMA).

References

- Atkins, M. and Glasser, F.P. (1992). Application of Portland cement-based materials to radioactive waste immobilization. *Waste Management*, 12, 105-131.
- Bourke, P.J., Jefferies, N.L., Lever, D.A., Lineham, T.R. (1993). Mass transfer mechanisms in compacted clays. *In*: D.A.C. Manning, P.L. Hall, C.R. Hughes (Eds.) *Geochemistry of Clay-Pore Fluid Interactions*, Chapman & Hall, London.
- Crank, J. (1975). *The mathematics of diffusion*. 2nd edition, Oxford University Press, Clarendon Press.
- García-Gutiérrez, M., Missana, T., Mingarro, M., Morejón, J., Cormenzana, J.L. (2018). Cesium diffusion in mortars from different cements used in radioactive waste repositories. *Applied Geochemistry* (*submitted*).
- Grathwohl, P. (1998). *Diffusion in natural porous media: Contaminant transport, sorption/desorption and dissolution kinetics*. Kluwer Academic Publishers, Boston.
- Vieno, T., Lehtikoinen, J., Löfman, J., Nordman, H., Mészáros, F. (2003). Assessment of disturbances caused by construction and operation of ONKALO. Posiva Report, 2003-6.

Experimental study of chemical degradation of cementitious materials in boom clay environment

Stephane Gaboreau¹, Quoc Tri Phung^{2*}, Francis Claret¹, Norbert Maes²

¹ Bureau de Recherches Géologiques et Minières (BRGM) (FR)

² Belgian Nuclear Research Centre (SCK•CEN) (BE)

* Corresponding author: quoc.tri.phung@sckcen.be

Abstract

This work presents a study of chemical degradation processes occurring at the interface between cementitious materials and Boom Clay with the focus on leaching and carbonation as the most dominant degradation processes. Therefore, an experimental laboratory program was designed to prepare interfaces under carbonation and leaching by putting backfill concrete (high porosity) and Boom Clay in contact in either accelerated percolation or batch-type experiments. Furthermore, 14 years old in-situ interfaces were also investigated. The main goal of this research is evaluate whether clogging occurs in the clay and/or concrete side. To answer this question, the microstructural changes at the interfaces were examined by a number of post-analysis techniques including μ -tomography, ¹⁴C PolyMethylMethAcrylate (PMMA) impregnation combined with autoradiography and Scanning Electron Microscope (SEM). In addition, both diffusivity and permeability were determined before and after alteration for batch experiments, while only the evolution of permeability was measured during percolation experiments.

The results on the alteration of porosity at the interface show an increase in total porosity of the concrete interface due to Ca-leaching. This indicates that clogging at the cementitious materials side might not occur. In contrast, the porosity in the clay side seems to decrease indicating some precipitations which may clog the clay pores in the long-term. The transport properties of cementitious materials are increased as a result of the coarser microstructure.

1 Introduction

Concrete materials have been extensively used for encapsulation of radioactive waste and as engineered barriers for disposal of radioactive waste, both in near-surface repositories for low/intermediate active waste and geological/deep repositories for high level long-lived radioactive waste. Under its service environment, these concrete structures undergo complex chemical interactions with the geological matrices (e.g. clay, granite). The interaction processes are very slow but important for the long-term durability assessment (> 1,000 years). It is well documented that due to the large geochemical contrasts between cement-based materials and clay, chemical reactions are expected to induce modifications in both the chemical and physical properties of both the clayey- and cement-materials which influence the long-term stability of an engineered structure.

The Boom Clay has been considered as a potential host rock for intermediate and high level radioactive waste in Belgium. Concrete and Boom Clay materials have been in contact since 2003 in the underground research laboratory (HADES) located at 225 m in depth at Mol, which are representative for disposal conditions. This work

utilizes a procedure to sample these concrete-clay interfaces (Phung et al., 2017) obtaining 14 years concrete-clay interfaces. Furthermore, an experimental laboratory program was designed to manufacture interfaces under carbonation and leaching by putting backfill concrete (high porosity) and Boom Clay in contact in either accelerated percolation or batch-type experiments. This work is a continuation of previous work (Phung et al., 2017, Phung et al., *in press*) aiming at describing an integrated approach with the goal to quantify and spatialize how the geochemical perturbation surrounding those interfaces will modify the microstructure of both engineered and natural barriers and thereby the effect on the transport properties. Updated experimental results are reported in this paper.

2 Materials and interface sampling

2.1 Examined materials

Materials studied included Boom Clay and high-pH cementitious materials including low porosity, high strength concrete (for in-situ interface) and porous cementitious paste (for lab-made interface) as seen in Figure 1. The material properties and its compositions have been reported in previous work (Phung et al., *in press*).

2.2 Concrete-clay interfaces

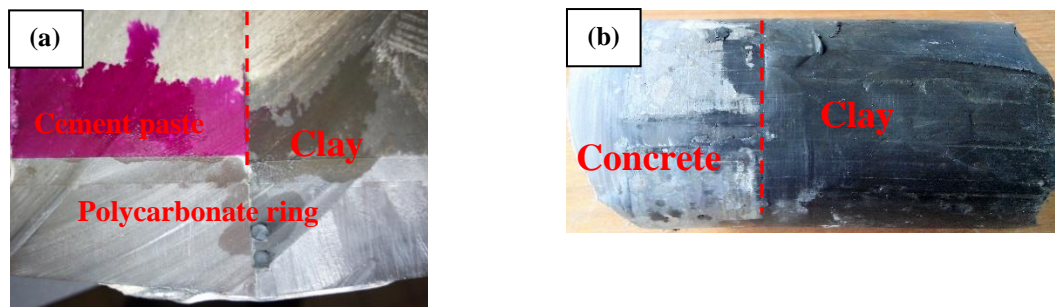


Figure 1: Lab-made interface – Pink color (phenolphthalein spraying) is representative for high pH (> 9) of backfill materials (a) and in-situ interface (b).

14 years-old Boom Clay-concrete interfaces were sampled in the HADES underground research facility (Mol, Belgium). The anchor concept was used to drill the interfaces. Details of the drilling procedure can be found in Phung et al. (2017). In addition, lab-made interfaces were created by either percolation or batch type experiments. Cement pastes were poured and cured in a cylindrical PVC tube with an inner diameter of 97.5 mm. The samples were then continuously rotated for 24 hours to prevent segregation and subsequently cured under sealed conditions in a temperature controlled room ($21 \pm 1^\circ\text{C}$) (Phung et al., 2014a). The cured cement pastes were sawn into 45 mm thick slices. In percolation experiment, the interface was created by putting plugs of Boom Clay and hardened backfill paste in a percolation cell which is a modified design of a permeability cell (Phung et al., 2013). In these experiments, the chemical conditions can be rigorously controlled. The conditions in the HADES underground research facility were mimicked by chemical compositions and advective flow of Boom Clay pore solution.

Batch type experiments were also performed by immersing a backfill concrete disc into a Boom Clay suspension. The experiments were conducted in closed chambers that were modified from leaching tests (Phung et al., 2014b; Phung et al., 2015). CO_2 0.4% was also bubbled in the chambers to mimic in-situ CO_2 concentration. The chemical composition of the suspension was monitored by regular sampling. These experiments are expected to induce more rapid cement degradation due to excess water compared to in-situ experiments. Note that all the

samples need to be saturated following the saturation procedure proposed in Phung et al. (2013). These saturated conditions simulate the real conditions in which concrete is saturated after a few decades in contact with the clay host formation. The readers are referred to the previous work (Phung et al., *in press*) for more details on percolation or batch type experiments.

3 Characterization of the changes in transport properties, microstructure and mineralogy

3.1 Transport properties

The percolation cell was designed in a special way which allows determination of the composite permeability of clay and concrete and also permeability of the separate materials by removal of the concrete or the clay part from the assembly. Prior to the percolation experiments, the permeability of cement paste and clay samples were determined separately using a controlled constant flow method as described in (Phung et al., 2012; Phung et al., 2013). The composite permeability of clay and cement paste samples can be calculated at any specific time during the percolation experiments.

Similar to permeability, the diffusion coefficients of the initial materials were determined before and after a certain time of interaction (only for batch type experiment). A through-diffusion methodology was used, allowing simultaneous determination of diffusivities of two dissolved gases (He and CH₄) in a single experiment as described in (Jacops et al., 2013; Phung et al., 2015a; Phung et al., 2015b).

3.2 Microstructure and mineralogy

A multi-scale investigation methodology, based on clay materials, has been developed during the European FP7 CATCLAY project (Gaboreau and Robinet et al., 2016). The methodology integrates several bulk macroscopic characterization techniques and imaging methods to display quantitative data from macroscopic to nanoscopic scale. The association of several 2D/3D techniques (mineral cartography, autoradiography, X-ray μ -tomography, SEM, FIB-nT and TEM) allows reaching a quantitative and spatial distribution of the mineralogy and the pore network, from nanometer to micrometer represented by several geometric key parameters such as the pore size distribution and the associated mineral distributions. Detailed descriptions of microstructural and mineralogical characterization can be found in previous work (Phung and Gaboreau et al., *in press*).

4 Results and discussion

4.1 Changes in transport properties due to alteration at interfaces

Permeability (reported as hydraulic conductivity) of backfill material and Boom Clay are $5.9 \cdot 10^{-9}$ and $2.4 \cdot 10^{-12}$ m/s, respectively. As the permeability of the backfill sample is about 3 orders of magnitude larger than the clay sample, the flux passing through the percolation cell (containing clay and backfill samples) should be dominated by the permeability of clay. As a result, the composite permeability (for both clay and backfill) can be considered to be very close to the permeability of clay. Figure 2 shows the evolution of the composite permeability in a percolation experiment measured for a period of 4 months. The composite permeability slightly decreased. However, the change compared to the reference permeability of clay can be negligible taken into account the uncertainty of permeability measurement in the percolation experiment. Both precipitation and dissolution might simultaneously occur at the interface. Some precipitation of calcium carbonate could occur in the clay side due to carbonation resulting in a porosity drop. On the other hand, dissolution of some phases in clay due to advective

(and also diffusive) flow could increase the porosity of clay which compensate the porosity decrease due to carbonation. Therefore, a significant change in permeability was not observed. For the backfill side, similar phenomenon could happen. However, these change in microstructure could be too small to interfere with the permeability.

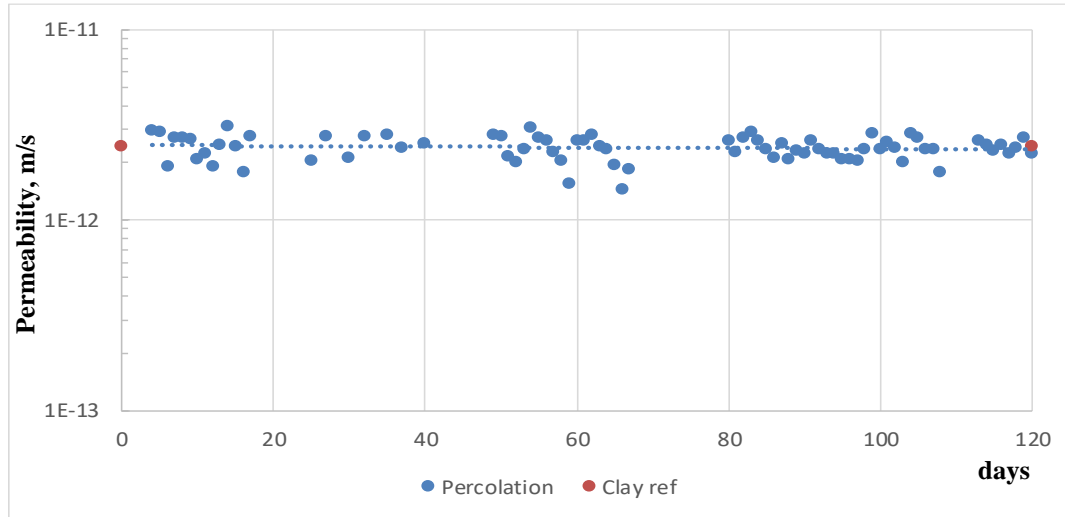


Figure 2: Permeability evolution during percolation experiment.

For batch experiments, both diffusivity and hydraulic conductivity (hereafter referred as permeability) changes were determined. Both the diffusivity (of He and CH₄) and permeability of backfill materials were slightly increased after half year interaction as a consequence of porosity increase due to leaching (Phung et al., 2016a) even in a CO₂ enriched environment (CO₂ equilibrated bicarbonate type pore water).

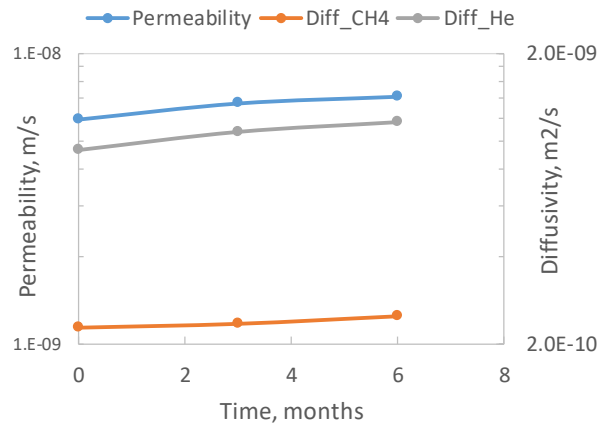


Figure 3: Increase in transport properties of backfill materials during batch experiment.

4.2 Chemical evolution during percolation and batch experiments

Figure 4 shows the concentration of main elements measured in solution collected at the outlet of percolation experiment and clay suspension of batch experiment. The Ca content in batch experiment was much smaller than percolation experiment due to the dilution effect. The volume of clay suspension was much larger than the pore volume of backfill material. The Ca from some hydrated phases of backfill material (mainly portlandite and C-S-H) is believed to be continuously leached out in both batch and percolation experiments. However, for

percolation experiment, the Ca concentration only increased during the first month. It then decreased and stabilized. In the beginning, the leached solution was actually pore solution of the backfill material of which the Ca concentration is very high. After several pore volume replacements by clay water (with low Ca content), the Ca content drops and the incoming water dilutes the Ca content dissolved from hydrated phases. After some time, equilibrium between the dissolving phases and the incoming pore water will be established.

Na concentration was increased as a function of time for both types of experiments indicating the leaching of Na from backfill material. However, Na content in batch experiment was larger because of higher Na concentration in clay water.

The pH was quite stable for batch experiment (buffered by the clay in suspension + CO₂ bubbling) and its value ranged in 8.5 to 8.6 range which was quite close to the pH of Boom Clay pore water. The pH in the percolation experiment slightly increased at the beginning, from 12.4 to 12.8, which was close to the pH of typical OPC cementitious materials. This slight pH increase is attributed to the leaching of Na or/and K that cumulated at the outlet in the beginning. The pH value closes to pH of backfill material also indicates that the pore solution of backfill material controls the pH of leached solution as long as the hydrated phases are not totally dissolved.

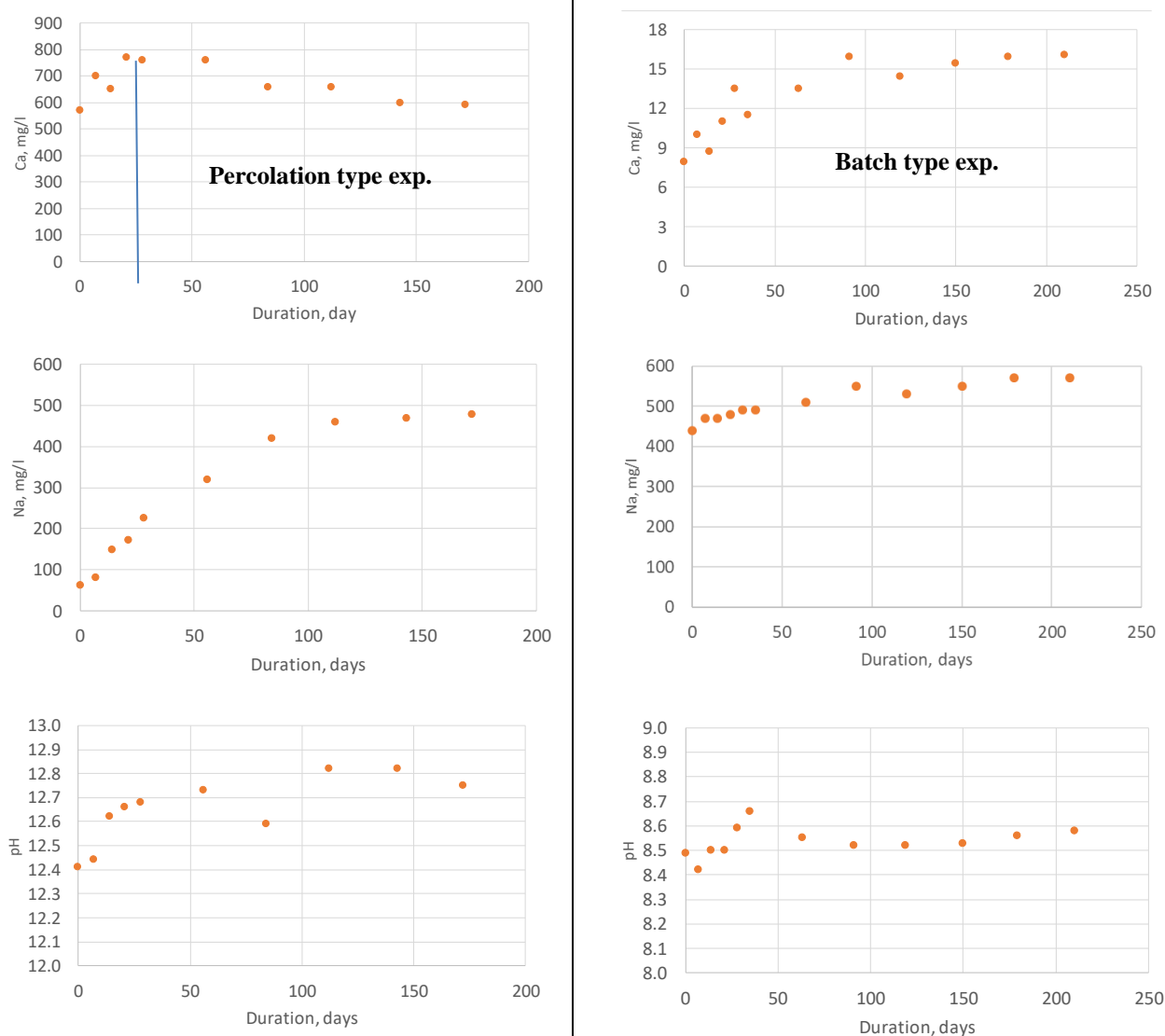


Figure 4: Chemical evolution leached solution collected during percolation (left) and batch (right) type experiments.

4.3 Changes in microstructure at interface

Total porosity of Boom Clay obtained by autoradiography is presented in Figure 5. The total porosities were around 40% (which is close to the typical reported porosity of 37%). However, some area had lower porosities due to the presence of some less porous grains as shown in Figure 6. Furthermore, some cracks were observed at the clay side which is attributed to drilling artefacts (soft clay).

The average porosity of the paste (including sand) of concrete was about 20%. A significant increase in porosity at the concrete interface was observed, up to 35% (black rectangular - Figure 6), indicating a significant dissolution of hydrated phases. As seen in Figure 7, the distribution of porosity in the concrete interface is quite broad, indicating a heterogeneous dissolution of concrete minerals. The degraded thickness was about 2-3 mm.

On the other hand, the clay interface exhibited a decrease in porosity from 40% down to 20%. However, the degradation was only in a thin region (100-200 μm) compared to the degraded depth of concrete. This porosity drop could be due to the leaching of Ca (as seen in batch type experiment) from concrete side, which would then react with dissolved CO_2 in Boom Clay pore water to form calcium carbonate. Other precipitations are also possible such as ettringite formation or mono-sulfate phase due to the presence of sulfate and aluminate, however, this needs to be confirmed by mineralogical analysis on the clay side (on-going work).

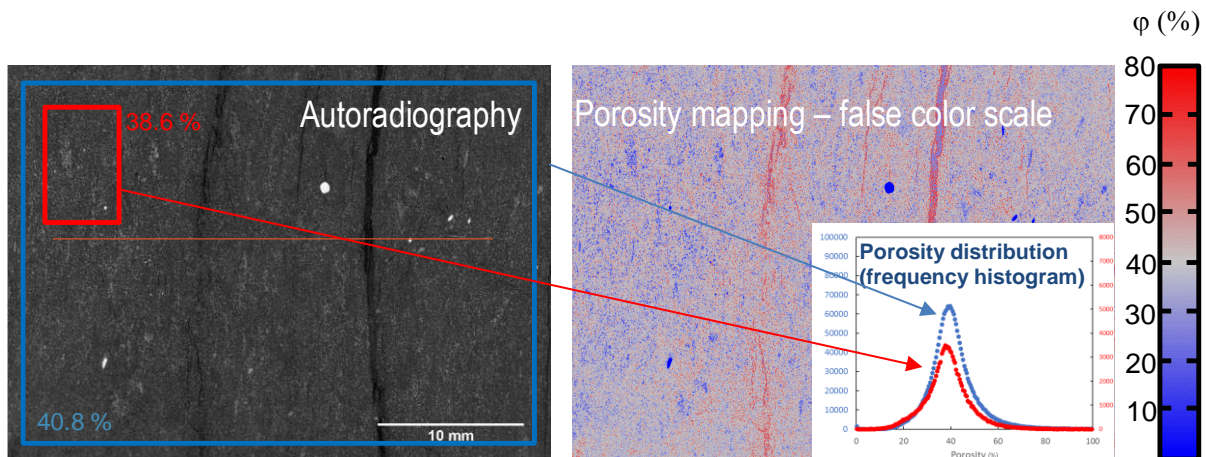


Figure 5: Porosity maps of Boom Clay obtained by autoradiography.

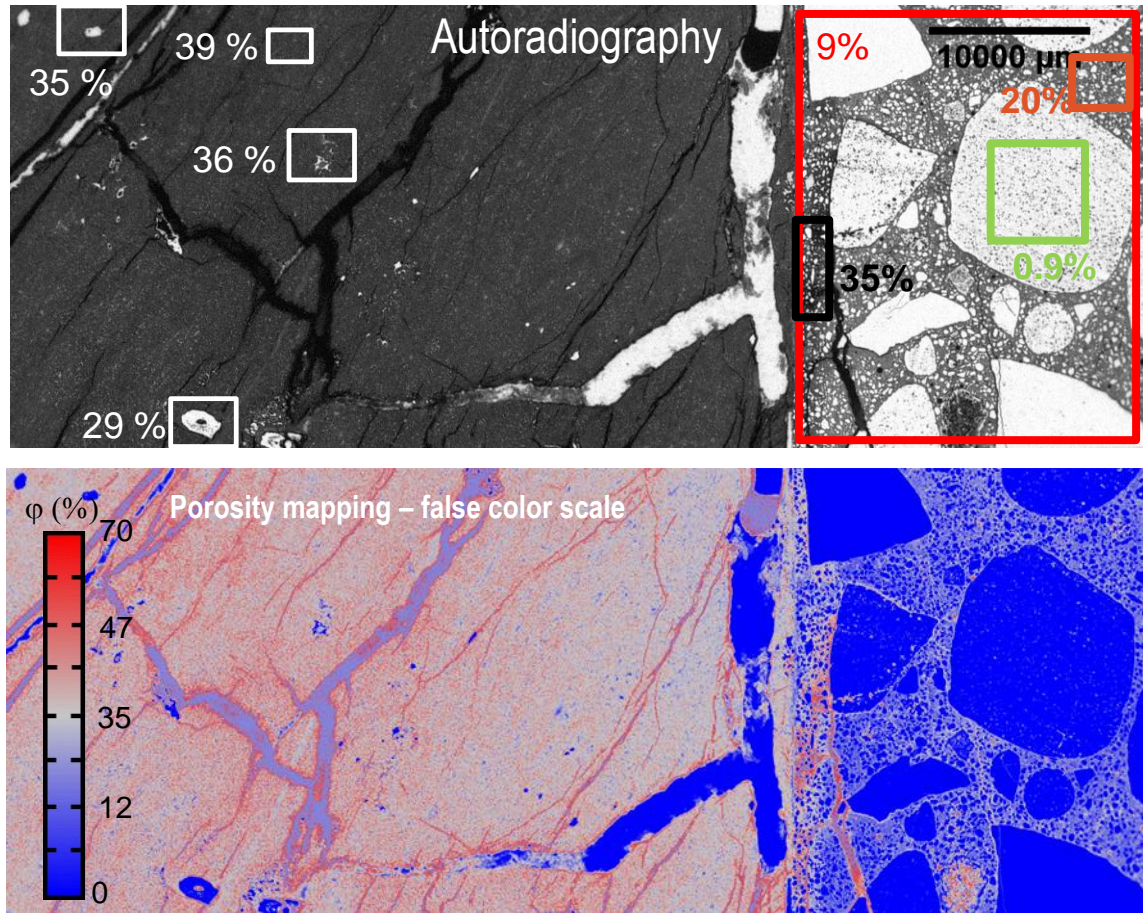


Figure 6: Spatial distribution of porosity at concrete, clay sides and the interface.

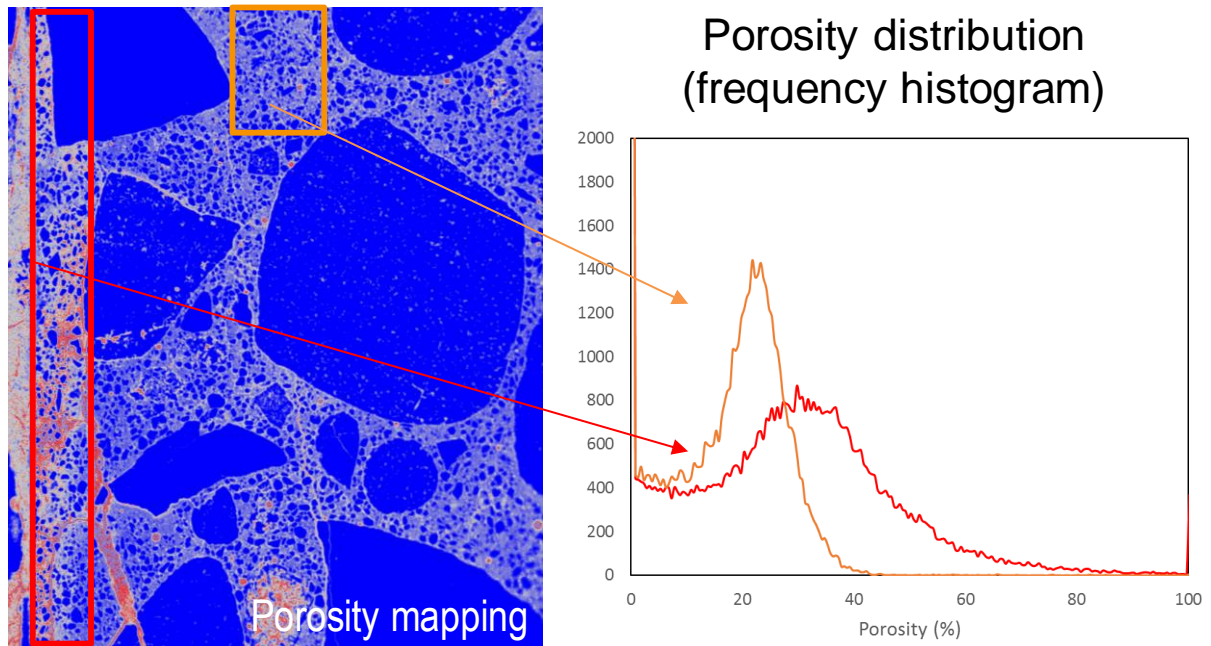


Figure 7: Porosity increase at concrete interface.

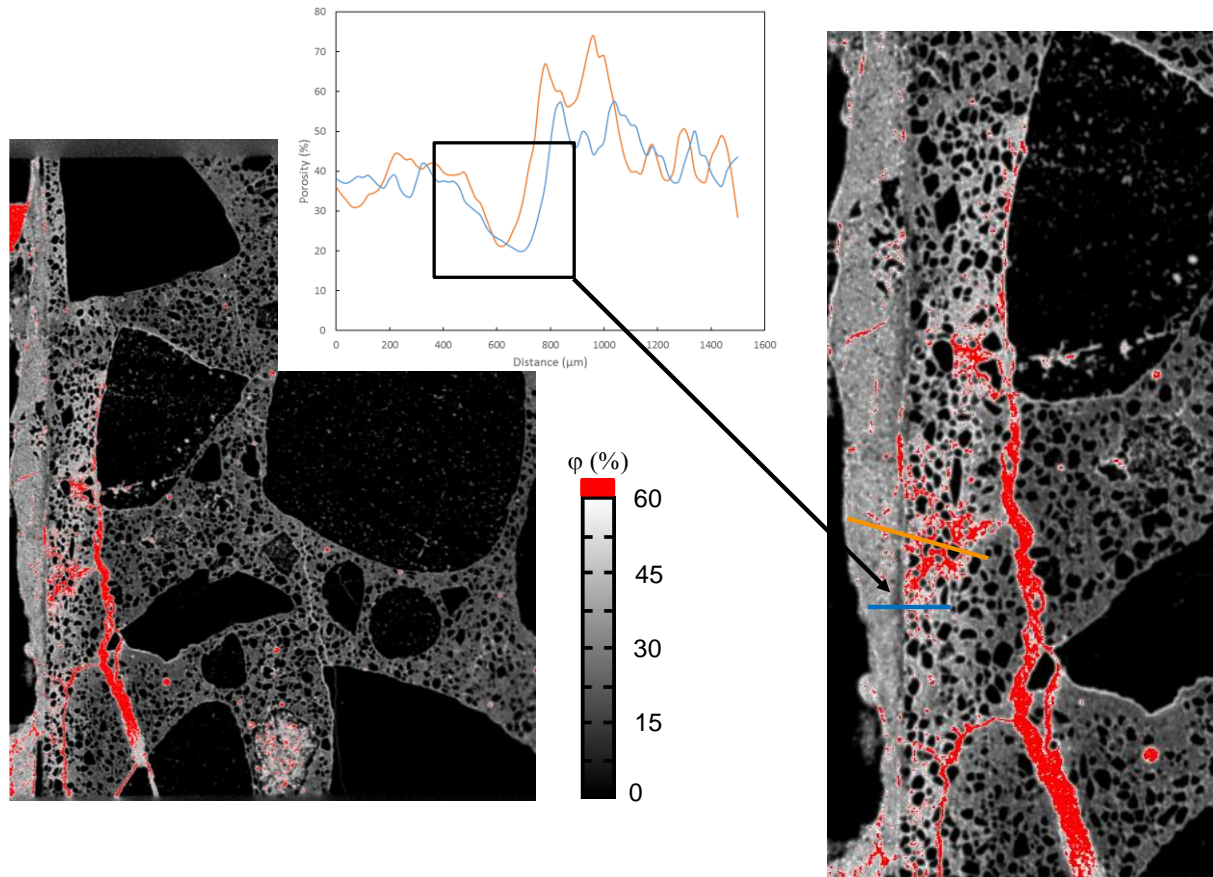


Figure 8: Porosity decrease at clay interface.

4.4 Changes in mineralogy at the interface

Two mineralogical maps were acquired in concrete: both in and outside of the interface region. These mineralogical maps calculated from the quantitative X-ray intensity maps of the major elements constituting the materials are shown in previous work (Phung et al. *in press*). Figure 9 shows the ternary diagram of Si, Ca, and Al-Fe-Mg for concrete interface (orange) and bulk material (red). It is clear that the Ca/Si decreased, while the Al-Fe-Mg increased at the concrete interface. This gives an indication that Ca has been leached from the concrete interface because Si as well as Al, Fe, Mg concentration are quite stable (evidenced from batch and percolation experiments). Further analysis to calculate the mass fraction of each phase, the chemical composition of each mineral and phase by integrating all the pixels constituting a phase are still on-going.

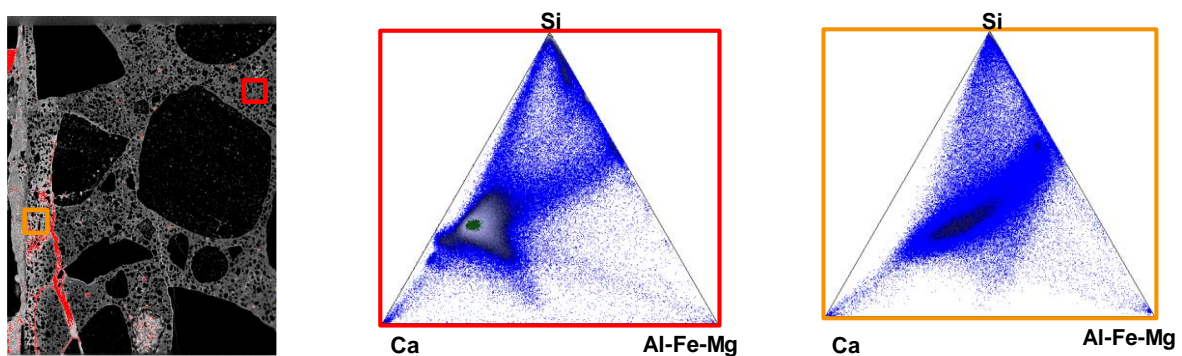


Figure 9: Chemical evolution of the concrete toward the interface – measured in 2 mm thickness from the interface.

5 Conclusions and perspectives

This paper presents preliminary results on examinations of interfaces between concrete and Boom Clay under close to real geochemical conditions as well as under accelerated conditions. The preliminary results on the alteration of the porosity at the interface show an increase in total porosity of the concrete interface and increase in transport properties (batch type experiments). This indicates that clogging at the concrete side might not be the case. The increase in porosity of the concrete interface was due to Ca-leaching (resulting in porosity increase (Phung et al., 2014a; Phung et al., 2015b)) dominating the effect of carbonation (resulting in porosity decrease (Phung et al., 2015d; Phung et al., 2016b; Phung, 2016c)). This porosity increase results in an increase of permeability and diffusivity. Furthermore, the porosity in the clay seems to decrease indicating that precipitation occurred. This is likely attributed to the reaction of leached Ca from the cement reacting with the dissolved CO₂ and bicarbonate in the clay pore waters precipitating CaCO₃ which may clog the clay pores in the long-term. Further study on the changes in microstructure, transport properties and especially identification of phase changes at both concrete and clay sides will help clarifying these issues.

Acknowledgements

The research leading to these results has received funding from the European Union's Horizon 2020 Research and Training Programme of the European Atomic Energy Community (EURATOM) (H2020-NFRP-2014/2015) under grant agreement n° 662147 (CEBAMA). This work is performed in close cooperation with ONDRAF/NIRAS, co-funding this research, as part of the programme on geological disposal of high-level/long-lived radioactive waste.

References

- Gaboreau, S., Robinet, J.-C., Prêt, D. (2016). Optimization of pore-network characterization of a compacted clay material by TEM and FIB/SEM imaging. *Microporous and Mesoporous Materials*, 224, 116-128.
- Jacops, E., Volckaert, G., Maes, N., Weetjens, E., Govaerts, J. (2013). Determination of gas diffusion coefficients in saturated porous media: He and CH₄ diffusion in Boom Clay. *Applied Clay Science*, 83-84(0), 217-223.
- Phung, Q.T. (2015). Effects of carbonation and calcium leaching on microstructure and transport properties of cement pastes. PhD thesis, Ghent University.
- Phung, Q.T., Gaboreau, S., Maes, N., Claret, F. (2018). Preliminary experimental results on the changes in microstructure, mineralogy and transport properties of Boom Clay – concrete interface. *In: M. Altmaier, V. Montoya, L. Duro, A. Valls (Eds.) Proceedings of the 2nd Annual Workshop of the CEBAMA Project. KIT Scientific Report, in press.*
- Phung, Q.T., Maes, N., Claret, F., Gaboreau, S., Leysen, J. (2017). Methodology to study the changes in microstructure and transport properties of the Boom Clay - concrete interface. *In: M. Altmaier, V. Montoya, L. Duro, A. Valls (Eds.) Proceedings of the 1st Annual Workshop of the CEBAMA Project. KIT Scientific Report, 7734.*
- Phung, Q.T., Maes, N., De Schutter, G., Jacques, D., Ye, G. (2013). Determination of water permeability of cementitious materials using a controlled constant flow method. *Construction and Building Materials*, 47(0), 1488-1496.
- Phung, Q.T., Maes, N., Jacques, D., De Schutter, G., Ye, G. (2015a). Investigation of the changes in microstructure and transport properties of leached cement pastes accounting for mix composition. *Cement and Concrete Research*, 79, 217-234.
- Phung, Q.T., Maes, N., Jacques, D., Jacop, E., Grade, A., Schutter, G.D., Ye, G. (2015b). Determination of diffusivities of dissolved gases in saturated cement-based materials. *In: F. Dehn, H.-D. Beushausen, M. G. Alexander and P. Moyo (Eds.) International Conference on Concrete Repair, Rehabilitation and Retrofitting IV. CRC Press, 1019-1027.*

- Phung, Q.T., Maes, N., Jacques, D., Perko, J., De Schutter, G., Ye, G. (2016a). Modelling the evolution of microstructure and transport properties of cement pastes under conditions of accelerated leaching. *Construction and Building Materials*, 115, 179-192.
- Phung, Q.T., Maes, N., Jacques, D., Schutter, G.D., Ye, G. (2014a). Decalcification of cement paste in NH_4NO_3 solution: Microstructural alterations and its influence on the transport properties. 10th fib International PhD Symposium in Civil Engineering, Québec, Canada.
- Phung, Q.T., Maes, N., Jacques, D., Schutter, G.D., Ye, G. (2014b). Microstructural and permeability changes due to accelerated Ca leaching in ammonium nitrate solution. *In*: M. Grantham, P. A. M. Basheer, B. Magee and M. Soutsos (Eds.) *Concrete Solutions - 5th International Conference on Concrete Repair*, CRC Press, 431-438.
- Phung, Q.T., Maes, N., Jacques, D., Schutter, G.D., Ye, G. (2015c). Evolution of microstructure and transport properties of cement pastes due to carbonation under a CO_2 pressure gradient - A modeling approach. *In*: C. Hellmich, B. Pichler, J. Kollegger (Eds.) *CONCREEP 10*. American Society of Civil Engineers, 1032-1041.
- Phung, Q.T., Maes, N., Jacques, D., Schutter, G.D., Ye, G. (2016b). Effect of limestone fillers on Ca-leaching and carbonation of cement pastes. *Key Engineering Materials*, 711, 269-276.
- Phung, Q.T., Schutter, G.D., Maes, N., Jacques, D., Ye, G. (2012). Measuring permeability of cementitious materials. *In*: M. G. Alexander, H.-D. Beushausen, F. Dehn and P. Moyo (Eds.) *Concrete Repair, Rehabilitation and Retrofitting III*, CRC Press, 287-295.
- Phung, Q.T., Norbert, N., Jacques, D., De Schutter, G., Ye, G., Perko, J. (2016c). Modelling the carbonation of cement pastes under a CO_2 pressure gradient considering both diffusive and convective transport. *Construction and Building Materials*, 114, 333-351.

Geochemical and thermal impacts on the characteristics of cementitious materials: strength, leachate pH, mineralogy and diffusion

Radek Vašíček¹, Radek Červinka², Petr Večerník², Tomáš Rosendorf^{2,3}, Jiří Svoboda¹

¹ Centre of Experimental Geotechnics, Faculty of Civil Engineering,
Czech Technical University in Prague (CZ)

² ÚJV Řež, a.s. (CZ)

³ Department of Nuclear Chemistry, Faculty of Nuclear Sciences and
Physical Engineering, Czech Technical University in Prague (CZ)

* Corresponding author: radek.vasicek@fsv.cvut.cz

Abstract

The experimental work of both the Czech partners (ÚJV Řež, a.s. and CTU) conducted as part of the CEBAMA project focused on the alteration and interaction studies of cementitious materials and bentonite. The laboratory work was based on ageing processes with respect to Czech bentonite, cementitious materials (Portland-type, OPC, and a low pH reference mix design designated as LPC = RPM) and groundwater from the Josef Underground Laboratory under in-situ and high temperature (95°C) load conditions. The laboratory study of the ageing processes concerning both types of cementitious materials is ongoing; the first sampling campaign was performed and the initial results analysed after 9 months (OPC and LPC) and, subsequently, after 18 months (OPC). It is expected that the final sampling campaigns for both materials will take place in June 2018.

This contribution summarizes the changes that occurred in the various observed parameters with regard to both of the cementitious materials (OPC and LPC) as a consequence of the influence of thermal load (10°C and 95°C) and the geochemical interactions that took place during the development of the laboratory-induced ageing processes (0-18 months). The results of the evolution of the various parameters - strength on thin plates, deformation at breakpoint, leachate pH, mineralogy, diffusivity for tritium (HTO) and the chemistry of the groundwater following the various interactions - revealed that, in general, thermal load constitutes the dominant factor, while other factors such as the presence of bentonite are less important but not negligible.

1 Introduction

Laboratory work at the CTU and ÚJV is based on ageing processes with respect to Czech Ca-Mg bentonite - Bentonit 75 (B75), CEM II paste (OPC) and a low-pH reference paste (LPC; CEBAMA reference mix design, Vehmas et. al., 2016) and groundwater obtained from the Josef Underground Laboratory (GW Josef) at an elevated temperature of 95°C with 10°C as the reference temperature.

The study of ageing processes with concern to the OPC samples has been underway since March 2016 and that of the low-pH reference paste samples since December 2016. The sampling of OPC and LPC was performed after 18 months and 9 months of ageing respectively and the analysis phase commenced in September 2017. The laboratory analysis of the cementitious materials included principally the determination of the uniaxial strength of thin samples, mineralogical changes, leachate pH and diffusion properties. More details on the ageing processes

and the analysis of the bentonite can be found in the CTU and UJV contributions to the 1st and 2nd CEBAMA Annual Workshops (Večerník et al., 2016; Vašíček et al., 2017).

2 Mechanical behaviour

2.1 Sampling

Carbonate precipitates, consisting principally of calcite, were discovered on some of the samples (Figure 1). With respect to both types of samples (OPC and LPC), the precipitates were most significant following ageing in a bentonite plus GW Josef suspension at approximately 95°C; they were markedly less significant after ageing in the same suspension at 10°C. Oversaturation to calcite was attributed to the large carbonate pool in the bentonite as well as the calcium present in the cement paste. It is known that the solubility of calcite decreases with increasing temperature. Consequently, the brushing of all the affected samples was necessary prior to further testing.



Figure 1: Cement paste samples; left - OPC after 18 months at 95°C in a bentonite B75 and GW Josef suspension; right LPC after 9 months in the same suspension.

2.2 Research methods

The compressive strength test was used as an indicator of changes in the mechanical behaviour of the cement paste samples. Since interaction occurs principally on interfaces (i.e. the surfaces of the samples), the specific shape of the samples was used in order to magnify this effect upon the testing of uniaxial strength. The thin plate (cylinders with a diameter of 50.0 mm and thickness of 8.2 mm) and the corresponding non-standard punch test methods were employed (Figure 2). It provided results in the form of “load at breakpoint [kN]” which were subsequently recalculated to “punch compressive strength [MPa]” and recalculated once more so as to obtain a value corresponding to the testing of ordinary samples (cube/cylinder). Both calculations are based on linear, experimentally determined relationships. More details on this method can be found in Večerník et al. (2016). Ten samples were extracted from each of the ageing processes to be subjected to strength testing.

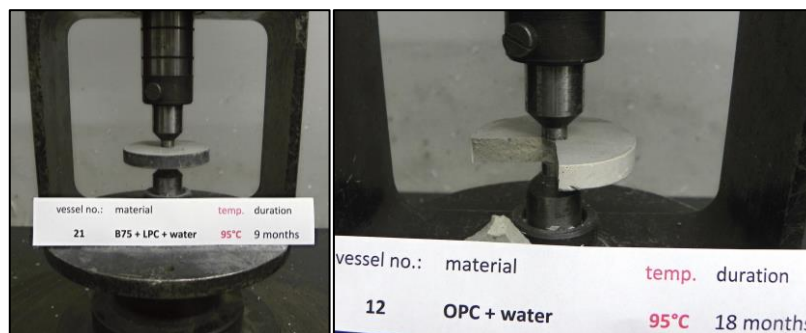


Figure 2: The punch test.

To gain the best benefit from available records, load at breakpoint was evaluated together with “press head displacement”. Press head displacement is related to the deformation of the sample but recorded value includes also a portion related to the deformation of the press machine head itself. The exact proportion of both components of the total deformation cannot be identified during particular tests but it is expected to be very similar for all the test results. Therefore, displacement values cannot be used in a quantitative way for the determination of deformation moduli; nevertheless, they appear to be relatively good indicators of changes in elasticity.

2.3 Results

2.3.1 OPC

The initial uniaxial compressive strength value (non-aged samples) of the OPC was determined, following recalculation, to be around 60 MPa (Večerník et al., 2016). Figure 3 presents the direct outputs of the compressive punch tests (a mean value for each dataset) - press head displacement versus load at breakpoint for the initial (non-aged, full black square) 9- and 18-month aged samples. The ageing periods are distinguished by the size of the datapoints (squares) – the smaller datapoints refer to the 9-month and the larger datapoints to the 18-month samples. An ageing temperature of 10°C is shown in blue and of 95°C in red; the filled squares represent samples aged in a suspension of bentonite and GW Josef. The empty squares represent GW Josef only (blue and red) or humid air (black) as the ageing environments.

The results revealed that temperature exerts a significant effect on both compressive strength and elasticity. Almost all the results related to the same temperature (10°C or 95°C) follow the same trends (see the arrows in Figure 3). Compressive strength decreased in the case of “heated” (95°C) OPC to 60% (approx. 36 MPa) of the initial value while at a temperature of under 10°C compressive strength was seen to slightly increase over time (to around 120%, i.e. to approx. 72 MPa). In addition, elasticity decreased with respect to all the heated samples. While the influence of the presence of bentonite appears to be less important than that of temperature, the results indicate the protective role of bentonite under 95°C (elasticity is less affected). It must, however, be emphasised that the conclusion regarding “elasticity” is indicative only, as mentioned in Section 2.2.

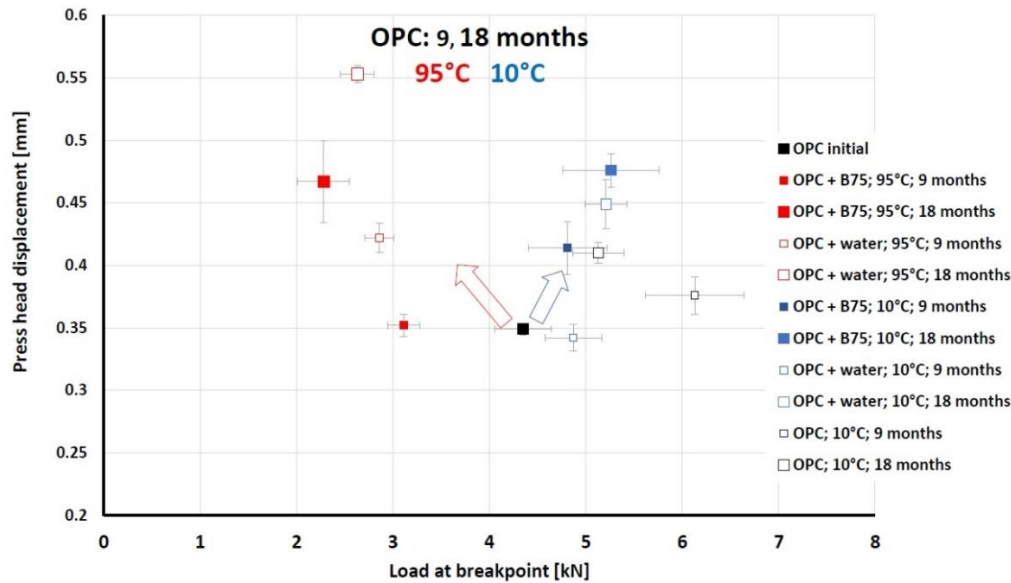


Figure 3: Press head displacement versus load at breakpoint - OPC samples aged for 9 and 18 months under various conditions.

2.3.2 CEBAMA Reference Paste (LPC)

The initial uniaxial compressive strength value (non-aged samples) of the LPC was determined at around 80 MPa (Vašíček et al., 2017). Figure 4 presents the outputs of the compressive punch tests (a mean value for each dataset) - press head displacement versus load at breakpoint for the initial (non-aged, filled black triangle) and 9-month aged samples. An ageing temperature of 10°C is shown in blue and of 95°C in red; the filled triangles represent those samples aged in a suspension of bentonite and GW Josef. The empty triangles represent GW Josef only (blue and red) or humid air (black) as the ageing environments.

Hardening was observed with respect to all the sample types and ageing processes after 9 months. The value pertaining to “humid air at 10°C” (black empty triangle) can be considered to be the result of “hardening under normal conditions”, with an increase of 140% (approx. 112 MPa following recalculation). All the other ageing conditions provided harder samples with a maximum increase of up to 180% (approx. 144 MPa) for the “hot water” (95°C plus GW Josef) environment. The results indicate that temperature exert a certain influence on the evolution of strength, with the “hot” environment producing slightly harder samples.

Since all the results from the “environment without bentonite” (initial value and all the empty triangles) exhibited a linear progression, it can be concluded that elasticity remained unchanged with respect to these samples / ageing environments (i.e. without the presence of bentonite); in contrast, the elasticity of the samples immersed into the “bentonite suspension” decreased.

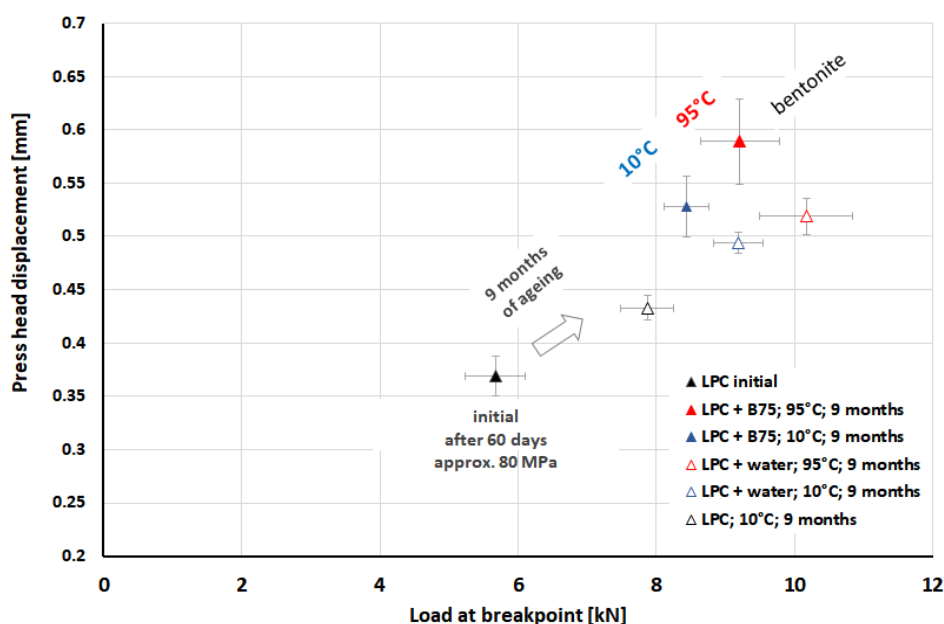


Figure 4: Press head displacement versus load at breakpoint - LPC samples aged for 9 months under various conditions.

3 Geochemical behaviour

3.1 Sampling

Standard sampling and sample pre-treatment techniques were employed. The water samples were filtered using a 0.45 µm membrane filter and acidified in the case of the determination of cations. Precipitated carbonates were removed prior to the conducting of the through-diffusion experiments (TD experiments) on the solid samples. All the TD experiments were performed in filtered solutions from the “OPC/LPC + water; 10°C; 9/18 months” series. The samples were immersed in the solution under low pressure conditions in desiccators for one month; subsequently, the equilibration phase was initiated by means of connecting both reservoirs to the rock sample cells (see Havlová and Vopálka, 2010) for a further two weeks.

3.2 Research methods

3.2.1 Chemistry of GW Josef following OPC and LPC interaction

Standard analytical chemistry methods were employed for the determination of the main chemical composition of GW Josef following interaction with the OPC and LPC samples. The presence of cations was determined using Atomic Absorption Spectroscopy and that of anions by means of Ion Chromatography or Capillary Electrophoresis.

3.2.2 OPC and LPC pH leachates

The pH leachate tests were performed using the procedure described in Alonso et al. (2012). The testing of the pH of the leachate was performed in triplicates with respect to every sampling interval. The standard error of the results obtained was lower than 0.1 pH.

3.2.3 Mineralogy changes determined by X-ray diffraction

Standard X-ray diffraction (XRD) was employed for the determination of the mineralogy composition, and the semi-quantitative determination was based on the Rietveld refinement. The standard addition of ZnO enabled an estimation of the proportion of amorphous phases which were not detectable by means of XRD.

3.2.4 Diffusion experiments

The TD experiments commenced following the pre-treatment of the solid samples. The volume activities of ^3H and ^{36}Cl were measured by means of the liquid scintillation counting method and beta separation spectrum module in both reservoirs, the volume of each of which was 56-59 mL. The sampled liquid phase (0.2 mL) was compensated for the same ^3H and ^{36}Cl initial activity (in the inlet reservoir) or by fresh experimental solution (in the outlet reservoir). The experiments on the LPC samples are ongoing and are discussed in Section 2.3.6. The experiments on the OPC samples lasted from one to four months. Subsequently the OPC samples were gradually abraded in an abrasive bowl filled with artificial corundum ($\text{Al}_2\text{O}_3\text{:B80}$) mixed with cooling water. After two weeks of shaking, the centrifuged abraded suspension (12 g of artificial corundum, 2-4 abraded cementitious samples, 30-40 mL of distilled water) was separated. HTO and ^{36}Cl volume activity were determined in the supernatant so as to determine the concentration profile of HTO and the proportion of the non-sorbed amount of chloride in the OPC sample profile. The abraded samples were then dried at 105°C to a constant weight and subsequently exposed for four weeks to 20 mL of 1 mol/L nitric acid to allow for the desorption of the chloride and the determination of the proportion of the sorbed amount of chloride in the profile.

By means of numerical modelling, it is possible to evaluate the unknown parameters of porosity and geometrical factor (or distribution coefficient) from all three of the known datasets (break-through and depletion curves and concentration profile) as described in Vopálka et al. (2017) and further discussed in the WP3 section of this Annual Workshop report, contribution by Vopálka et al. (2018).

3.3 Results

3.3.1 Chemistry of GW Josef following OPC and LPC interaction

The determination of the chemistry of GW Josef followed the gradual dissolution of the OPC and LPC samples in separate vessels. Differences in the water chemistry are evident from Figure 5 which indicates that the temperature and type of sample (OPC versus LPC) exert the most significant influence. High temperature accelerates the dissolution of the various minerals, especially ettringite (as confirmed via XRD), which results in increasing concentrations of sulphates. GW Josef on interaction with the OPC samples was enriched with potassium and calcium in contrast to the LPC samples, with respect to which sodium dominated. Generally, the pH and total dissolved solids (deduced from conductivity) were found to be significantly higher with concern to GW Josef in contact with OPC than that with LPC. The ranges for OPC were determined at pH 12.3 - 13.1 and conductivity 2.67 - 6.42 mS/cm and for LPC at pH 9.3 - 12.6 and conductivity 0.47 - 0.94 mS/cm.

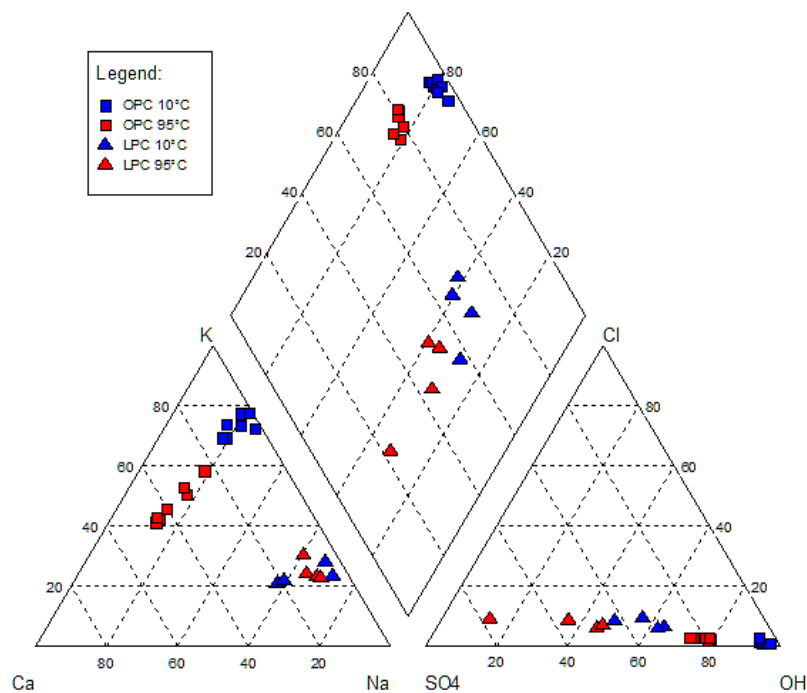


Figure 5: Piper diagram of the chemistry of GW Josef following interaction with OPC and LPC for 10°C and 95°C (months of interactions are not distinguished in the diagram).

3.3.2 LPC Leaching

The results of the pH leachate tests (testing at 40, 175, 322 and 455 days following the casting of the LPC samples) are shown in Figure 6. The leachate pH values obtained 40 days following the casting of the LPC samples can be considered to be initial values for the LPC leachate. pH leaching tests were performed on samples stored under all the ageing conditions and environments (10°C humid air, 10°C groundwater and bentonite suspension, 95°C groundwater and bentonite suspension) after the first sampling period (322 days). Additional sampling campaigns were performed after 175 and 455 days with respect to the 10°C humid air, 10°C groundwater and 95°C groundwater ageing conditions. The trend concerning a significant decrease to pH values of ≤ 11 in the leachate was observed only for those samples heated to 95°C in the groundwater and bentonite suspension. However, the last point of the curve for the samples stored in the 95°C groundwater environment (red triangles in Figure 6) did not correspond to the trend of a continual decrease in the pH values of the heated samples. Following the repetition of the measurement of pH using a different sample, the pH of the leachate was determined at the same level of 11.6 for this sampling point. The next sampling campaign planned for June 2018 will reveal whether the leachate pH values continue the decreasing trend to values lower than 11. With respect to the other ageing conditions (10°C humid air, groundwater and bentonite suspension), no significant decrease in the pH of the leachates towards values of 11 or less was observed (small decreases only of 0.2 - 0.3 pH were determined) following prolonged ageing.

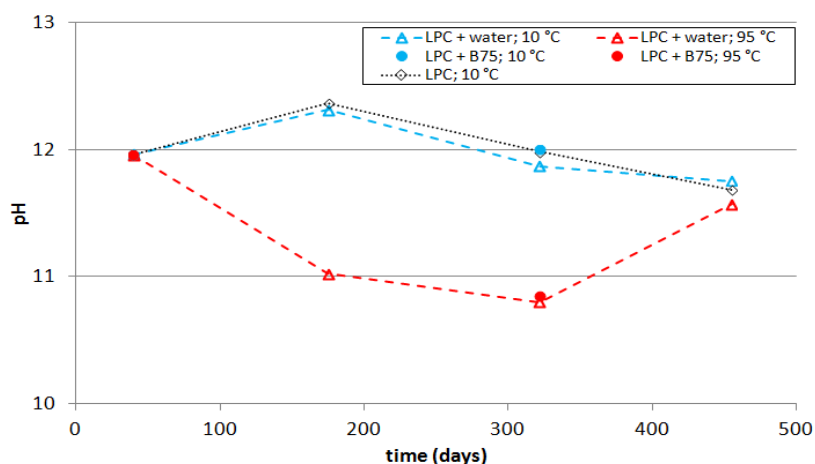


Figure 6: Time evolution of the leachate pH values of the LPC samples, testing at 40, 175, 322 and 455 days following the casting of the LPC samples.

3.3.3 OPC Leaching

The results of the pH leachate tests (testing at 213, 315, 462, 609 and 742 days following the casting of the OPC samples) are shown in Figure 7. The samples were found to maintain their properties with respect to the pH of the leachates regardless of the ageing conditions (water, bentonite suspension, temperature). A small decrease in leachate pH can be observed concerning the samples obtained in the last sampling period following 742 days of ageing - a decrease of 0.2-0.3 pH.

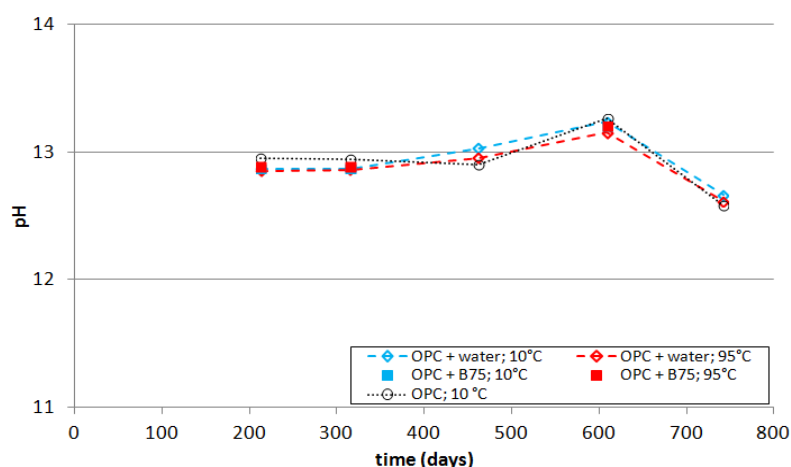


Figure 7: Time evolution of the leachate pH values of the OPC samples, testing at 213, 315, 462, 609 and 742 days following the casting of the OPC samples.

3.3.4 Mineralogy changes determined via X-ray diffraction

In the case of temperature, both the OPC and LPC samples were influenced in terms of mineralogy composition. The heated OPC samples contained the newly-formed hydrothermal mineral katoite ($\text{Ca}_3\text{Al}_2(\text{SiO}_4)(\text{OH})_8$) and lacked those phases which are stable under lower temperatures such as calcium aluminium oxide carbonate hydrate ($\text{Ca}_4\text{Al}_2\text{O}_6\text{CO}_3 \cdot 11\text{H}_2\text{O}$) and hydrocalumite ($\text{Ca}_8\text{Al}_{14}(\text{OH})_{24}(\text{CO}_3)\text{Cl}_2(\text{H}_2\text{O})1.6(\text{H}_2\text{O})_8$). The high-temperature LPC samples were found to contain completely transformed minerals such as ettringite and brownmillerite - C4AF phase ($\text{Ca}_2(\text{Al,Fe})_2\text{O}_5$) and, the extent of the amorphous phase increased by around 8 wt.% as compared to the non-heated LPC sample.

A comparison of the OPC samples stored at 100% relative humidity after 9 and 18 months revealed only minor changes in terms of mineralogy and thus no progress with concern to curing and stable material maturity.

3.3.5 Diffusion experiments: OPC samples

The application of the abrasive technique produced interesting results. The success of obtaining a concentration profile was, in part, related to the mechanical properties of the OPC samples, e.g. hardness, elasticity and brittleness. The heated samples were easily abradable whereas, conversely, the non-heated samples were harder and a number of such samples failed. These subjective observations of mechanical behaviour confirmed the results obtained from the mechanical tests described previously.

The initial results of the HTO TD experiments on the OPC samples from the first sampling campaign (9 months of interaction) revealed that a temperature increase to 95°C negatively influenced the effective diffusion coefficients (D_e), as reported in Rosendorf et al. (2017) and in the WP3 contribution by Vopálka et al. (2018). The mean HTO effective diffusion coefficient values (obtained using GoldSim software) from the three parallel experiments were as follows:

- $D_e = 0.4 \cdot 10^{-11} \text{ m}^2/\text{s}$ in the series: OPC; 10°C; 9 months;
- $D_e = 2.8 \cdot 10^{-11} \text{ m}^2/\text{s}$ in the series: OPC + GW; 95°C; 9 months;
- $D_e = 0.3 \cdot 10^{-11} \text{ m}^2/\text{s}$ in the series: OPC + GW; 10°C; 9 months;
- $D_e = 2.0 \cdot 10^{-11} \text{ m}^2/\text{s}$ in the series: OPC + B75; 95°C; 9 months;
- $D_e = 0.4 \cdot 10^{-11} \text{ m}^2/\text{s}$ in the series: OPC + B75; 10°C; 9 months.

The results of the chloride diffusion testing of the OPC samples from the first sampling campaign were significantly more complicated. In some cases (especially concerning the non-heated samples), despite a large decrease in the volume activity of ^{36}Cl in the inlet reservoir, we registered only background level values; thus, no breakthrough curve could be obtained. The balance of the total activity in both reservoirs and the profile did not correspond to the added initial activity. It was assumed, therefore, that the desorption process of the bounded chloride from the solid to the liquid phase using nitric acid was unsuccessful and, consequently, that the concentration profile dataset was not applicable. The diffusion parameters could only be estimated with great uncertainty from the depletion curve and without the known distribution coefficient (or Langmuir/Freundlich parameters). The conducting of additional batch sorption experiments may assist in estimating the sorption parameters for the evaluation procedure concerning the TD experiments.

A number of TD experiments on OPC samples from the second sampling campaign are being terminated at the time of writing of this contribution.

3.3.6 Diffusion experiments: LPC samples

After more than 2 months of TD experimentation, a maximum of 7% of the initial HTO and 2% of the initial ^{36}Cl volume activity had diffused into the LPC samples; however, no breakthrough curve has yet been obtained which would enable the use of the basic analytical solution method for evaluation purposes or, alternatively, a more sophisticated procedure based on GoldSim software. The only exception consisted of the HTO diffusion series on those LPC samples that interacted with GW Josef under a thermal load of 95°C, with respect to which the first measurable values of ^3H activity in the outlet reservoir have been obtained. The first stage of the application of basic 1D TD analytical solutions to these values revealed that the preliminary results of the effective

diffusion coefficient D_e of HTO on the LPC samples lie in the range $(0.7 - 1.6) \cdot 10^{-12} \text{ m}^2/\text{s}$. All the experiments are still underway.

4 Conclusions and future work

A part of the high level radioactive waste (mainly the waste from nuclear power plant dismantling) is supposed to be emplaced to concrete containers in separate area of deep geological repository and one of the potential backfilling material is bentonite. Assessing the long-term performance of cement material for radionuclide encasement requires knowledge of the radionuclide-cement migration, interaction and mechanisms of retention. This understanding will enable accurate prediction of radionuclides fate when the waste forms come in contact with groundwater. The geotechnical and geochemical stability of cementitious materials in contact with backfilling material and groundwater is important for prediction of its long-term evolution in the safety assessment.

The results of mechanical behaviour test revealed changes in both the strength and elasticity of samples of both types of cement paste. Temperature was found to exert a key effect on OPC. The compressive strength decreased with respect to the “heated” (95°C) OPC to 60% of the initial value while the compressive strength of the OPC treated at a temperature of below 10°C increased slightly over time (up to 120% of the initial value). In addition, a decrease in elasticity was observed with concern to all the heated samples. All the LPC samples exhibited a significant increase in compressive strength with regard to all the ageing processes (up to 180%). There was an indication that the presence of bentonite (in suspension) causes a decrease in elasticity. Temperature appears to make up a less important factor in this case; however, it is important to note that the LPC results available to date refer to just one ageing period (9 months).

The results of the testing of geochemical behaviour confirmed the dominant influence of temperature and the type of material (OPC versus LPC). The chemistry of the GW Josef in contact with the OPC and LPC samples indicated that temperature accelerates mineral dissolution which results in increased concentrations of calcium and sulphates. In case of the OPC samples, these ion concentrations were found to be approximately seven times higher for the heated than for the non-heated samples. Generally, the pH and total dissolved solids (deduced from conductivity) were much higher for that GW Josef exposed to OPC than that exposed to LPC. Temperature was mainly responsible for the variation in the pH of the LPC leachate samples. The pH results of the LPC leachates are gradually approaching those observed for CEBAMA Reference Concrete. In addition, changes in mineralogy were also influenced by temperature. The HTO diffusion coefficients of the OPC samples increased with temperature by approximately one order of magnitude which may have been related to the dissolution of the material under higher temperatures as well as a decrease in elasticity (microcracks). The LPC diffusion experiments are still underway.

A change was observed in the colour of the bentonite in the 2017 sampling campaign. The properties of the bentonite are currently being analysed and the results will be presented at the CEBAMA 2019 Workshop. The experimental work will continue with the sampling of both LPC and OPC in June 2018 (i.e. after 18 and 27 months of ageing) and the related analysis of the cement paste and bentonite samples.

Acknowledgement

The research leading to these results received funding from the European Union Horizon 2020 Research and Training Programme of the European Atomic Energy Community (EURATOM) (H2020-NFRP-2014/2015) according to grant agreement no. 662147 (CEBAMA).

The experimental work conducted at CTU employed the research capacity of the RINGEN (MŠMT LM2015084) large infrastructure.

References

- Alonso, M.C., García Calvo, J.L., Walker, C., Naito, M., Pettersson, S., Puigdomenech, I., Cuñado, M.A., Vuorio, M., Weber, H., Ueda, H., Fujisaki, K. (2012). Development of an accurate pH measurement methodology for the pore fluids of low pH cementitious materials. SKB Report, R-12-02.
- Havlová, V. and Vopálka, D. (2010). HTO as a conservative tracer used for the characterization of contaminant migration in a porous rock environment. *Journal of Radioanalytical and Nuclear Chemistry*, 286, 785-791.
- Rosendorf, T., Vopálka, D., Červinka, R. (2017). Chapter 16 (CTU contribution). Deliverable n° D3.05, CEBAMA: Preliminary results and interpretation of the modelling of the WP1 & WP2 experiments.
- Vašíček, R., Večerník, P., Hloušek, J., Červinka, R., Hausmannová, L., Havlová, V. (2017). Interaction between cement and Czech bentonite under temperature load and in in-situ conditions: Results after the first testing period. *In: M. Altmaier, V. Montoya, L. Duro, A. Valls (Eds.) Proceedings of the 2nd Annual Workshop of the CEBAMA Project. KIT Scientific Report, in press.*
- Večerník, P., Hausmannová, L., Červinka, R., Vašíček, R., Roll, M., Hloušek, J., Havlová, V. (2016). Interaction between cement and Czech bentonite under temperature load and in in-situ conditions: an overview of the experimental program. *In: M. Altmaier, V. Montoya, L. Duro, A. Valls (Eds.) Proceedings of the 1st Annual Workshop of the CEBAMA Project. KIT Scientific Report, 7734.*
- Vopálka, D., Vetešník, A., Hofmanová, E. (2017). Methods of evaluation of through-diffusion experiments on sandwich bentonite cement layers in a simple experimental set-up. *In: M. Altmaier, V. Montoya, L. Duro, A. Valls (Eds.) Proceedings of the 1st Annual Workshop of the CEBAMA Project. KIT Scientific Report, 7734.*
- Vopálka, D., Rosendorf, T., Baborová, L., Kittnerová, J. (2018). Modelling and interpretation of diffusion experiments of selected radionuclides through cementitious samples. *In: M. Altmaier, V. Montoya, L. Duro, A. Valls (Eds.) Proceedings of the 3rd Annual Workshop of the CEBAMA Project. This document.*

The physico-chemical evolution of a low-pH cement in contact with groundwater

Rita Vasconcelos¹, Brant Walkley¹, Neil Hyatt¹, John Provis¹, Claire Corkhill^{1*}

¹ NucleUs Immobilisation Science Laboratory, Department of Materials Science and Engineering, University of Sheffield (UK)

* Corresponding author: c.corkhill@sheffield.ac.uk

Abstract

Low-pH cement materials are being considered for use in several geological disposal facility (GDF) concepts for the disposal of nuclear waste. The advantages of using low-pH cements as an engineered barrier (e.g. in waste forms, as backfill, sealing and structural components) within a GDF are related to the generation of lower pore solution pH (< 11) and a limited heat output during hydration of the cement. These characteristics are designed to limit any detrimental effect of cementitious materials on the other barriers in the GDF (for example, clay based materials). Within a GDF, several hundreds of metres below the ground, cementitious materials will interact with the geological environment, particularly groundwater. During such interactions, alteration of the physico-chemical properties of the cement may occur over time. In this study, we are investigating the long-term phase and structural evolution of a low-pH cement with a composition relevant to the Finnish GDF concept, known as the CEBAMA reference cement. Here, we describe results from the first two months of long-duration leaching experiments using three different types of groundwater (granitic, saline and clay groundwater). Characterisation results show that after 28 days of curing the main hydrate phases present were C-S-H, ettringite, hydrotalcite-group phase, hydrogarnet and monocarboaluminate. However, some unreacted Portland cement, blast furnace slag and silica fume were also observed. An increase in the content of ettringite and differences in the C-S-H structure were observed, which may be due to the partially-hydrated nature of the CEBAMA reference cement.

1 Introduction

Cementitious materials are widely used in the engineered multi-barrier design of a Geological Disposal Facility (GDF), for example as waste forms, for sealing, and as liners and structural components. One advantage of using Portland cement (PC) in a GDF concept includes the high alkalinity of the cement (pH above 12), which reduces the solubility of many radionuclides (Bamforth et al., 2012; Glasser, 1992; Sharp et al., 2003). However, this can be problematic when other barriers are being considered in the GDF (Berner et al., 2013). Bentonite is an example of a material where high pH environment has a negative effect on its properties (Cau-dit-Coumes et al., 2006; Codina et al., 2008). Another consequence of using pure PC is the characteristic high temperature rise from the cement hydration, which may have negative consequences for the long-term durability of the material (e.g. formation of cracks) (Cau-dit-Coumes et al., 2006; Codina et al., 2008). Therefore, a potential solution for these problems is the formulation of a low pH and low heat cement. To achieve these characteristics, the high-percentage replacement of Portland cement (PC) by supplementary cementitious materials (SCM) is an attractive option. Examples of these materials are silica fume (a by-product from producing silicon metal or ferrosilicon), blast-furnace slag (BFS; a by-product of pig iron production) and fly ash (from coal combustion),

which enable the conversion of portlandite into calcium-silica-hydrate (C-S-H) via pozzolanic reaction, reducing in this way the pH (Lothenbach et al., 2011). Other advantages of using these materials are reduction of the heat of hydration due to the use of less PC; and a decrease of the CaO/SiO₂ ratio of the C-S-H, which allows the sorption of more alkalis and, also reducing the pH in equilibrium with this phase (Cau-dit-Coumes et al., 2006; Codina et al., 2008).

The lifetime performance of cementitious materials used in certain applications in the GDF is required to be extremely long, and alterations may occur due to interactions with the geological environment, specifically with groundwater. Understanding how those interactions may affect the physico-chemical properties of these cementitious materials is of crucial importance. As such, a long-duration groundwater-cement contact experiment is being performed on the CEBAMA reference cement (a low pH silica fume, BFS-containing cement) using three different types of groundwater (granitic, clay and saline groundwater), representative of the different geological environments. In this experiment, replacement of the groundwater is being performed to accelerate the process of interaction, and this will give a unique insight to the long-term behaviour of low-pH cement in a geological disposal facility. Results of a characterisation of this material (prior to contact with groundwater) are presented, including X-ray diffraction (XRD), thermogravimetric analysis coupled with mass spectrometry (TG-MS), solid-state nuclear magnetic resonance (NMR) and mercury intrusion porosimetry (MIP). Additionally, preliminary results (TG-MS and XRD) from the first two months of the groundwater-cement contact experiment are also shown.

2 Methods

2.1 Materials

A batch of CEBAMA reference cement was prepared using the following formulation: 1,050 kg/m³ of CEM I 42.5 MH/SR/LA; 1,100 kg/m³ of Silica fume; 650 kg/m³ BFS; 12.6 kg/m³ of plasticizer pantarhit LK (FM); with a water/solid ratio (w/s) of 0.25 (Vehmas et al., 2016). All materials were provided by VTT (Technical Research Centre of Finland). The cement paste was mixed by first adding the silica fume with 15% of the CEM I and BFS to the mixing bowl and slowly adding the water and superplasticizer with hand mixing for 3 minutes. A high shear mixer was used until the paste turned to a liquid and the remainder of the CEM I was added and shear mixed. The cement paste was placed in centrifuge tubes at 40°C and 95% relative humidity, for 28 days. After 28 days of curing, some samples were prepared for characterisation (hydration was stopped by addition of acetone) and some samples were prepared for leaching experiments (where the hydration was not stopped).

The composition of the simulated groundwater solutions used in the contact experiments are shown in Table 1. To obtain these compositions, reagent-grade chemicals were mixed with distilled water.

Table 1: Groundwater composition utilised in this study.

	Granitic groundwater (mmol/L) (Gascoyne et al., 2002)	Saline groundwater (mmol/L) (Gascoyne et al., 2002)	Clay groundwater (mmol/L) (Vinsot et al., 2008)
Na	2.8	140	55
K	0.1	2.1	1.1
Ca	0.5	19.9	7.5
Mg	0.2	0.4	5.7

	Granitic groundwater (mmol/L) (Gascoyne et al., 2002)	Saline groundwater (mmol/L) (Gascoyne et al., 2002)	Clay groundwater (mmol/L) (Vinsot et al., 2008)
Cl	2.1	172.7	52.5
HCO ₃	2.0	2.0	-
SO ₄	0.1	4.0	15
pH	8.2	7.7	7

2.2 Cement – Groundwater Contact Experiment

For the contact experiments, cylindrical monoliths of 15 mm height x 15 mm diameter were prepared. To allow only radial diffusion of the groundwater, the end of the cylinders were sealed with epoxy resin.

Samples were placed in 60 mL vessels (using Teflon baskets) in contact with 50 mL of each of the three groundwaters, to perform a semi-dynamic experiment. The experiment was conducted in an oven at 40°C in a controlled nitrogen environment (i.e. CO_{2(g)} was excluded). Sampling and replacement of the groundwater is being performed every two months for a total time of 1 year. The sampling and replacement of the groundwater is also performed in a controlled environment (CO_{2(g)} and O_{2(g)}-free).

2.3 Analytical Methods

To identify the hydrate phases present in the CEBAMA reference cement before and after contact with groundwater, XRD and TG-MS were performed using powdered samples (< 63 µm). For XRD, a Bruker D2 Phaser instrument with a Cu Kα source was used. Measurements were taken from 5° to 80° 2θ with a step size of 0.02° and 2 s counting time per step. For TG-MS analysis, a PerkinElmer Pyris 1 thermogravimetric analyser was used. The temperature ranged from 20°C to 1,000°C with a heating rate of 10 °C/minute under a N₂ (nitrogen) atmosphere. A Hiden Analytical mass spectrometer (HPR-20 GIC EGA) was used to record the mass spectrometric signals for H₂O and CO₂.

Solid state single pulse ²⁷Al and ²⁹Si magic angle spinning (MAS) NMR spectra were acquired on a Bruker Avance III HD 500 spectrometer at 11.7 T (B₀) using a 4.0 mm dual resonance CP/MAS probe, yielding a Larmor frequency of 130.32 MHz for ²⁷Al and 99.35 MHz for ²⁹Si. ²⁷Al MAS NMR spectra were acquired using a 1.7 µs non-selective (π/2) excitation pulse, a measured 5 s relaxation delay, a total of 512 transients and spinning at 12.5 kHz. ²⁹Si MAS NMR spectra were acquired using a 4 µs non-selective (π/2) excitation pulse, a measured 15 s relaxation delay, a total of 512 transients and spinning at 12.5 kHz. Gaussian peak profiles were used to deconvolute the ²⁹Si MAS NMR spectra (Massiot et al., 2002). The minimum number of peaks possible were fitted.

For total porosity analysis, small pieces of hardened cement paste were prepared and placed into the sample holder of a Micromeritics Autopore V 9600 Mercury Intrusion Porosimeter (MIP). The maximum pressure applied was 208 MPa, the surface tension was 485 mN/m and the contact angle was 130°.

3 Results

3.1 Characterisation of 28 d Cured Material

After 28 days of curing, prior to contact with groundwater, the main hydrated phases in the CEBAMA reference cement were identified using XRD. The broad area of diffuse scattering present in the XRD pattern (Figure 1) highlights the amorphous nature of this cement, arising from the presence of disordered silica fume and BFS, and also the dominant calcium silicate hydrate (C-S-H) binding phase. The main crystalline phases identified were calcite (CaCO_3 ; PDF 01-086-0174), ettringite ($\text{Ca}_6\text{Al}_2(\text{OH})_{12}(\text{SO}_4)_3 \cdot 26\text{H}_2\text{O}$; PDF 00-041-1451), hydrotalcite-like phase ($\text{Mg}_6\text{Al}_2\text{CO}_3(\text{OH})_{16} \cdot 4\text{H}_2\text{O}$; PDF 00-014-0525), hydrogarnet ($\text{Ca}_3\text{Al}_2(\text{OH})_{12}$; PDF 01-084-1354) and the AFm phase monocarboaluminate ($\text{Ca}_4\text{Al}_2(\text{OH})_{12}(\text{CO}_3)_3 \cdot 5\text{H}_2\text{O}$; PDF 01-087-0493). Some unreacted PC was observable as peaks of alite and belite, and it is very likely that unreacted BFS and silica fume are also present, although their glassy nature makes identification by XRD challenging in the presence of C-S-H. The presence of only low quantities of portlandite may be indicative of limitations to the reactivity of the silica fume at early curing time; either kinetic or mass transport limitations mean that the portlandite has not yet been fully consumed by the pozzolanic reaction.

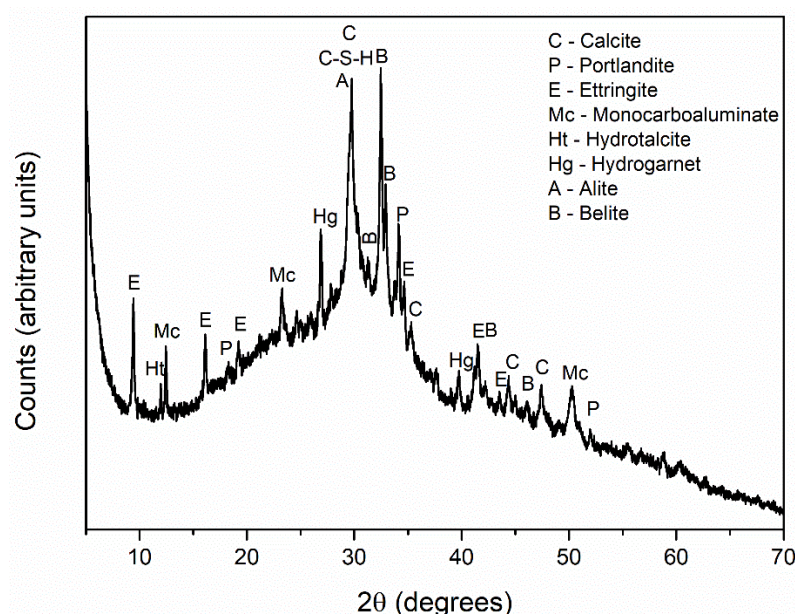


Figure 1: X-ray diffraction pattern for CEBAMA reference cement paste after 28 days of curing. Crystalline phases are labelled.

The results of TG-MS data are shown in Figure 2. It was possible to identify a broad peak corresponding to ettringite and AFm phases between 100°C and 200°C (Taylor, 1997; Scrivener et al., 2016). Some C-S-H was also observed via mass loss between 50°C and 100°C (Taylor, 1997; Scrivener et al., 2016). In agreement with the low quantity observed in XRD, from the TG-MS data the presence of portlandite was not observed.

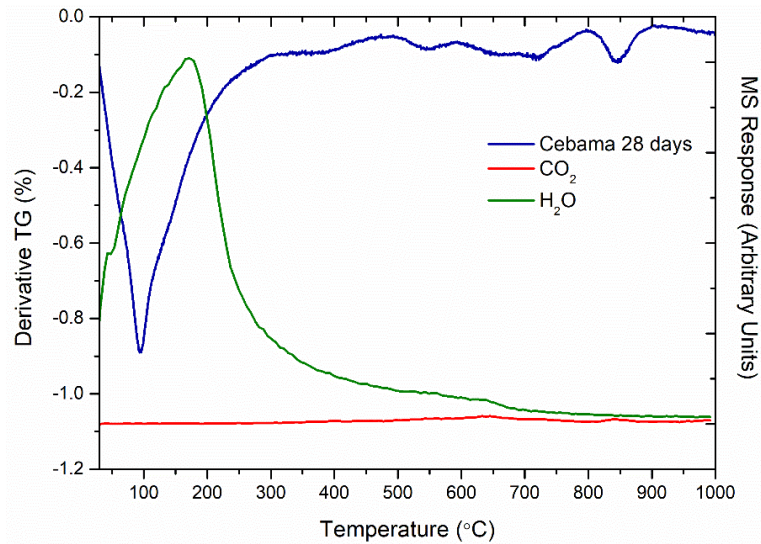


Figure 2: TGA-MS for CEBAMA reference cement paste after 28 days of curing.

The unreacted Portland cement was also visible in the ^{29}Si NMR spectra (Figure 3a), which shows the presence of Q^0 sites in alite (chemical shifts -69 and -73.9 ppm) and belite (-70.8 ppm) (Scrivener et al., 2016). The resonance at -73.9 ppm (marked as Q^0 in Figure 3a) is characteristic of unreacted alite, but will also contain a contribution from Q^0 and/or $\text{Q}^1(1\text{Al})$ sites in BFS. Resonances exhibiting chemical shifts corresponding to the presence of Q^1 (-78.9 ppm), $\text{Q}^2(1\text{Al})$ (-81.6 ppm), Q^2 (-84.5 ppm), Q^3 (-96.1 ppm) and $\text{Q}^3(1\text{Al})$ (-89.8 ppm) silicon environments in C-S-H were also identified (Richardson, 2008; Richardson et al., 2010). The existence of Al within the first coordination sphere of Q^n silicon sites demonstrates the incorporation of this element in an Al-substituted calcium silicate hydrate (C-(A)-S-H) binder phase. This was also visible in the ^{27}Al NMR spectrum (Figure 3b), by the presence of a broad tetrahedral Al peak (between 80 and 50 ppm) that contains contributions from Al^{IV} in C-S-H, and also from unreacted BFS (Anderson et al., 2003; Murgier et al., 2004). In the octahedral Al region of Figure 3b, a peak corresponding to ettringite (14 ppm) and a small shoulder at the chemical shift around 9 ppm, corresponding to the presence of AFm and hydrotalcite-like phases, was also identified. These results are in agreement with previously observed XRD and TG-MS data.

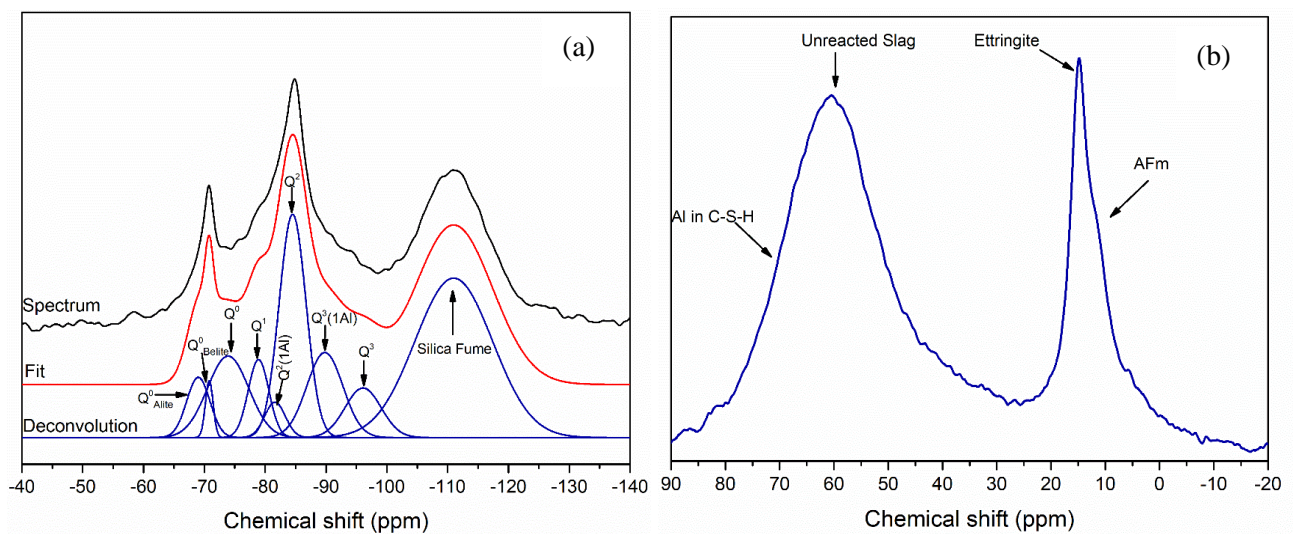


Figure 3: (a) ^{29}Si MAS NMR spectra and deconvolution results and (b) ^{27}Al MAS NMR spectra, of CEBAMA reference cement paste after 28 days of curing.

To study the porosity of the CEBAMA reference cement paste, MIP was used. Figure 4 shows the pore entry size diameter in relation to the cumulative intrusion, and it is possible to observe that the curve allocates the bulk of pores to pore entry sizes below 0.1 μm (smallest pore entry size detected of around 0.003 μm). The total porosity obtained from this measurement was around $19 \pm 1\%$.

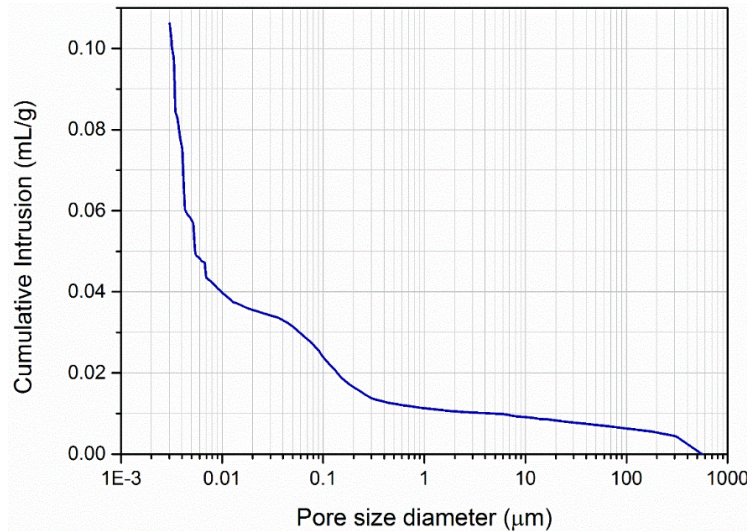


Figure 4: Pore entry size distribution of CEBAMA reference cement paste after 28 days of curing, determined using MIP.

3.2 Cement – Groundwater Contact Experiment

After 2 months of semi-dynamic contact with groundwaters, differences were observed between the CEBAMA reference cement sample not in contact with groundwater and the cement samples that were in contact with granitic, saline and clay groundwater. Figure 5 shows the TGA data for each of the samples. An increase in the intensity of the peak corresponding to ettringite (around 100°C), and the shoulder at $\sim 150^{\circ}\text{C}$ corresponding the AFm phases, was observed in all samples that were in contact with the different groundwaters, particularly for granitic and saline groundwater. A peak situated between 50 and 100°C was also observed in the samples contacted with groundwater (being more intense for the saline solution, and least intense for the clay groundwater solution), which was not present in the corresponding unreacted sample. This peak is consistent with the mass loss due to release of loosely bound water from small pores and/or from within C-S-H. The peaks at 680 , 700 and 840°C correspond to CaCO_3 polymorphs.

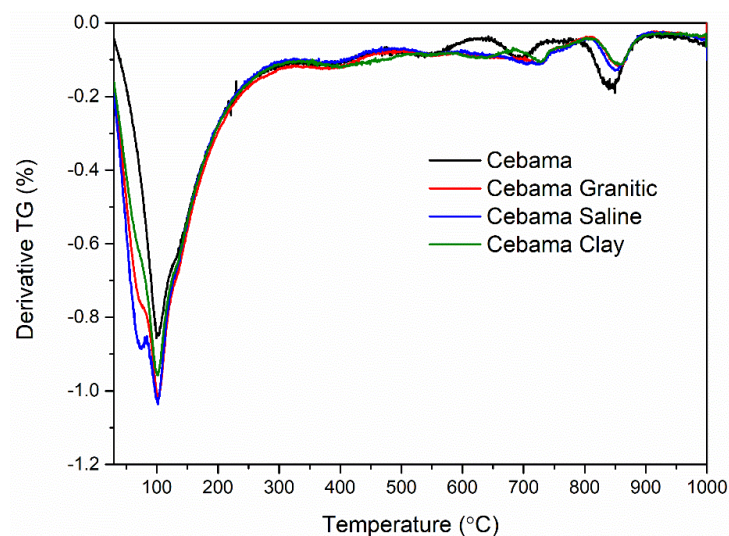


Figure 5: TG analysis of CEBAMA reference cement after 2 months of contact with three different types of groundwater (granitic, saline and clay).

From the XRD data, Figure 6, no major differences were observed between samples after 2 months of contact with groundwater. However, a small decrease in the intensity of the peak corresponding to hydrogarnet is observed for all the samples contacted with groundwater when compared to the control. Further work will include the application of Rietveld refinement to quantify the phases.

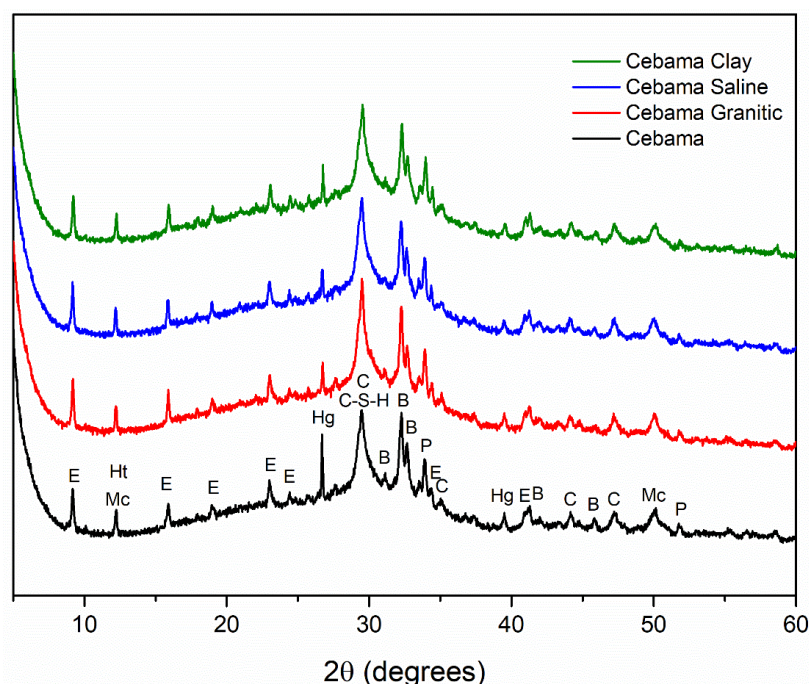


Figure 6: X-ray diffraction pattern of CEBAMA reference cement paste after 2 months of curing and CEBAMA reference cement paste in contact, for 2 months, with granitic, saline and clay groundwater as marked. E – ettringite; Mc – monocarboaluminate; Ht – hydrotalcite; Hg – hydrogarnet; C – calcite; C-S-H – calcium silicate hydrate; B – belite; P – portlandite.

4 Conclusions and Future work

To understand the microstructure and properties of the CEBAMA reference cement, an initial characterisation of this cement paste was presented. Through XRD and TG-MS it was possible to identify the main hydrate phases present after 28 days of curing, being C-S-H, ettringite, a hydrotalcite-group phase, hydrogarnet and monocarboaluminate. We also observed that some of the PC, silica fume and BFS did not fully react at this early age, which was expected. From the NMR experiment, it was shown that some Al from the BFS was incorporated into the C-S-H structure. The total porosity obtained through MIP was around 19%, showing the expected low porosity for this material.

After two months of a long-duration cement-groundwater contact experiment, some differences were observed in the TG analysis for the different samples in contact with granitic, saline and clay groundwater. These differences were related to the increase of ettringite content, and possibly differences in the C-S-H or fine pore structure. Continued sampling and analysis of the long-duration experiment will take place in the next year, with subsequent characterisation of all samples. This characterisation will include all the techniques mentioned in this paper, and also scanning electron microscopy, X-ray computed tomography for porosity measurements, ion chromatography and inductively coupled plasma optical emission spectrometry for the analysis of the solutions.

Acknowledgement

The authors wish to acknowledge funding for this research from Radioactive Waste Management, and funding from the European Union's Horizon 2020 Research and Training Programme of the European Atomic Energy Community (EURATOM) (H2020-NFRP-2014/2015) under grant agreement n° 662147 (CEBAMA). The authors would also like to acknowledge Dr Sandra van Meurs, Department of Chemistry, University of Sheffield, for assistance with NMR experiments. This research was performed in part at the MIDAS Facility, at the University of Sheffield, which was established with support from the Department of Energy and Climate Change

References

- Anderson, M.D., Jakobsen, H.J., Skibsted, J. (2003). Incorporation of aluminum in the calcium silicate hydrate (C-S-H) of hydrated Portland cements: a high-field ²⁷Al and ²⁹Si MAS NMR investigation. *Inorganic Chemistry*, 42, 2280-2287.
- Bamforth, P.B., Baston, G.M.N, Berry, J.A., Glasser, F.P., Heath, T.G., Jackson, C.P., Savage, D., Swanton, S.W. (2012). Cement materials for use as backfill, sealing and structural materials in geological disposal concepts. A review of current status. N° SERCO/005125/001, Issue 3, 1-235.
- Berner, U., Kulik, D.A., Kosakowski, G. (2013). Geochemical impact of a low-pH cement liner on the near field of a repository for spent fuel and high-level radioactive waste. *Physics and Chemistry of the Earth*, 64, 46-56.
- Cau-dit-Coumes, C.C.D., Courtois, S., Nectoux, D., Leclercq, S., Bourbon, X. (2006). Formulating a low-alkalinity, high-resistance and low-heat concrete for radioactive waste repositories. *Cement and Concrete Research*, 36, 2152-2163.
- Codina, M., Coumes, C.C.D., Bescop, P.L., Verdier, J., Ollivier, J.P. (2008). Design and characterization of low-heat and low-alkalinity cements. *Cement and Concrete Research*, 38, 437-448.
- Gascoyne, M. (2002). Influence of grout and cement on groundwater composition. Posiva Working Report, 2002-07.
- Glasser, F.P. (1992). Progress in the immobilization of radioactive wastes in cement. *Cement and Concrete Research*, 22, 201-216.
- Lothenbach, B., Scrivener, K., Hooton, R.D. (2011). Supplementary cementitious materials. *Cement and Concrete Research*, 41, 1244-1256.

- Massiot, D., Fayon, F., Capron, M., King, I., Calve, S.L., Alonso, B., Durand, J.O., Bujoli, B., Gan, X., Hoatson, G. (2002). Modelling one- and two-dimensional solid-state NMR spectra. *Magnetic Resonance in Chemistry*, 40, 70-76.
- Murgier, S., Zanni, H., Gouvenot, D. (2004). Blast furnace slag cement: a ^{29}Si and ^{27}Al NMR study. *Comptes Rendus Chimie*, 7, 389-394.
- Richardson, I.G. (2008). The calcium silicate hydrates. *Cement and Concrete Research*, 38, 137-158.
- Richardson, I.G., Black, L., Skibsted, J., Kirkpatrick, R.J. (2010). Characterisation of cement hydrate phases by TEM, NMR and Raman spectroscopy. *Advance Cement Research*, 22, 233-248.
- Scrivener, K., Snellings, R., Lothenbach, B. (2016). A practical guide to microstructural analysis of cementitious materials. CRC Press, Taylor & Francis Group.
- Sharp, J.H., Milestone, N.B., Hill, J., Miller, E.W. (2003). Cementitious Systems for Encapsulation of Intermediate Level Waste. *In: Proceedings of ICEM '03: The 9th International Conference on Radioactive Waste Management and Environmental Remediation*.
- Taylor, H.F. (1997). *Cement chemistry*. 2nd edition. Thomas Telford Publishing.
- Vehmas, T., Schnidler, A., Löija, M., Leivo, M., Holt, E. (2016). Reference mix design and castings for low-pH concrete for nuclear waste repositories. *In: M. Altmaier, V. Montoya, L. Duro, A. Valls (Eds.) Proceedings of the 1st Annual Workshop of the CEBAMA Project*. KIT Scientific Report, 7734.
- Vinsot, A., Mettler, S., Wechner, S. (2008). In-situ characterization of the Callovo-Oxfordian pore water composition. *Physics and Chemistry of the Earth*, 33, SUPPL. 1.

Leaching of hardened Portland cement with various C/S-ratios

Tapio Vehmas^{1*}, Markku Leivo¹, Erika Holt¹

¹ VTT Technical Research Centre of Finland Ltd. (FI)

* Corresponding author: tapio.vehmas@vtt.fi

Abstract

Leaching of cementitious materials with various calcium/silica -ratios was experimentally studied in ion-exchanged water and saline groundwater. Leaching was performed with a batch-method and the pH of each batch was measured. In saline groundwater, lower pH values compared to ion-exchanged water were observed due the common ion effect. The total dissolved hydroxyl concentrations were calculated from the batches and the accumulated hydroxyl contents with respect to pH limits of 10 and 11 were evaluated. As an example of the data use, the total amount of potentially affected montmorillonite was calculated.

1 Introduction

The use of cementitious materials is difficult to avoid in modern construction. Concrete and other cementitious materials have optimal properties in terms of strength and durability. Behaviour of concrete structures are also well known and predictable. Concrete has naturally good compatibility with other construction materials due to its inorganic nature. In the Finnish deep geological nuclear waste repository, ONKALO, concrete and cementitious materials are used for structural and isolation purposes during the operational phase of the repository.

In KBS3-V (vertical disposal cells) and KBS3-H (horizontal cells) repository concepts, cementitious materials are not a part of the engineered barrier system that ensures the stability of deposited nuclear waste and immobilizes the potentially released radionuclides. The engineered barrier system in KBS3-H and KBS3-V concepts consists of solidified high-level nuclear waste, enclosed in copper canisters with cast iron inserts, compacted bentonite clay that surrounds the copper canisters, and then the surrounding crystalline bedrock. Bentonite clay consists mainly of montmorillonite – a mineral that causes the swelling of bentonite clay. Compacted bentonite clay protects the copper canisters from bedrock movement and absorbs the potentially released radionuclides. Excavated deposition tunnels are further backfilled with bentonite to restore the bedrock close to its natural conditions and prevent the potential changes in groundwater movement.

Although bentonite clay is an optimal solution to protect the copper canisters from bedrock movement and prevent changes in groundwater movement, bentonite is not a stable material in high pH-conditions. Cementitious materials that are used in the operational phase of the repository pose a threat to bentonite stability over the long-term due to groundwater infusion. Groundwater infusion will cause the dissolution of cementitious materials that will induce high-pH leachates that will interact with bentonite clay.

A conservative approach is to assume high-pH leachates to dissolve montmorillonite. Dissolution of montmorillonite induces a precipitation of secondary minerals that does not possess similar swelling capacity. As

a consequence, swelling pressure of bentonite clay decreases and hydraulic conductivity in the repository increases (Koskinen, 2013).

In order to evaluate the effect of cementitious materials on bentonite clay, the composition of the cementitious leachates was determined at various stages of leaching. The composition of the cementitious materials varied from pure low-alkali Ordinary Portland Cement to silica-rich compositions. The pH of cementitious leachates was determined in ion-exchanged water and saline groundwater simulating deep groundwater at ONKALO.

The total released hydroxyl contents were calculated from the pH measurements. As an example, total released hydroxyl contents were used to evaluate the potential damage that cementitious leachates induce to bentonite buffer. The damage which leachates induces to bentonite buffer is a difficult, controversial topic and outside the scope of this article. As an example, a simple evaluation was performed, using total dissolved hydroxyl content and chemical composition of montmorillonite as proposed by Savage and Benbow (2007).

2 Materials and methods

Batch samples of Ordinary Portland Cement (OPC) and colloidal silica were prepared with molar CaO/SiO₂ - ratios: 0.2, 0.4, 0.6, 0.8, 1.0, 1.2, 1.4, 1.6, 1.8, 2.0, 2.6 and 3.14. The water/binder-ratio of the samples was 1. The used OPC was Anlåggningscement from Cementa (elemental oxide composition: CaO 64.70%, SiO₂ 18.10%, Fe₂O₃ 5.17%, SO₃ 4.02%, Al₂O₃ 3.61%, MgO 0.76%, K₂O 0.64%, TiO₂ 0.28%, MnO 0.28%, Na₂O 0.08%). Colloidal silica was Levasil 100/45 from AkzoNobel (Ammonium, sodium stabilized colloidal silica, average particle size 30 nm, pH 10). The samples were stored in sealed vials for over 200 days to reach chemical equilibrium.

Samples were ground to fine powder by using a vibration grinding mill (Herzog HSM 100 A). The pH of the finely ground sample was determined with the method according to Alonso et al. (2012). pH measurements were performed in ion-exchanged water and saline groundwater. Both solutions were decarbonated using a ELE de-airing system. The composition of the saline groundwater is presented in Table 1.

Table 1: Chemical composition of the synthetic Saline Groundwater (SGW) used in the studies.

Element	Concentration
Na ⁺	210 mM
Cl ⁻	410 mM
Ca ²⁺	100 mM
Mg ²⁺	2 mM
Br ⁻	1 mM
K ⁺	0.54 mM
Sr ²⁺	0.4 mM
SO ₄ ²⁻	0.04 mM

Leaching was studied by mixing the finely ground sample with a defined volume of the ion-exchanged water or saline groundwater. After mixing, samples were continuously agitated at least 24 hours. Samples were centrifuged with a Universal 16 - centrifuge for 10 minutes with 2,000 round per minutes. The liquid phase of the centrifuged samples was decanted. pH of the decanted solution was determined with a pH electrode

(Orion9172BNWP, ThermoScientific). The solid part of the sample was mixed again with a known volume of the ion-exchanged water or saline groundwater. The process was repeated to evaluate the pH evolution during leaching.

3 Results

Figure 1 presents the measured pH-values in ion-exchanged water with various leachate volumes. At the beginning of the leaching, a sharp decrease was observed in the pH-values. After the sharp decrease in pH, a more gradual decrease in pH was observed. The gradual decrease was most profound in high C/S-ratio samples ($C/S > 0.6$). In samples with a low C/S-ratio, a gradual increase in pH was observed after the first gradual decrease. With C/S-ratio 0.6 pH remained relatively constant, except for a first sharp decrease in pH.

In saline groundwater, measured pH values were substantially lower than in ion-exchanged water (Figure 3). The trends observed in ion-exchanged water were also present in saline groundwater.

Figure 2 and Figure 4 present the total hydroxyl contents that were released from the samples during leaching. The total amount of released hydroxyls above pH 10 and 11 are presented in Table 2.

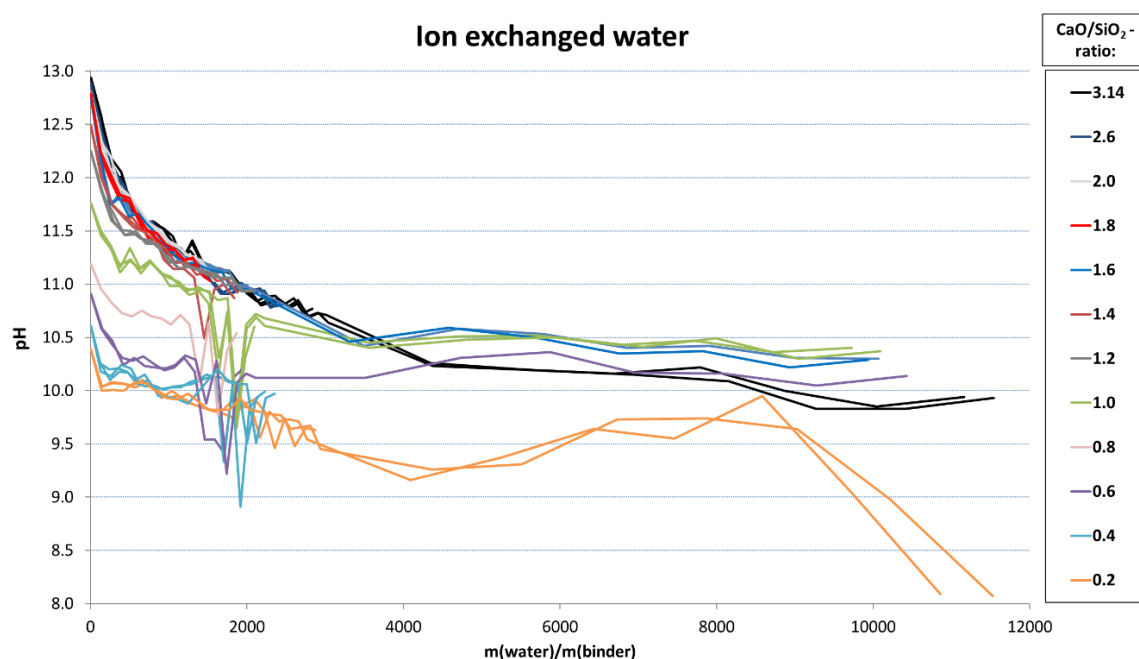


Figure 1: Measured pH values at various leachate volumes in ion-exchanged water. Each line presents a single sample.

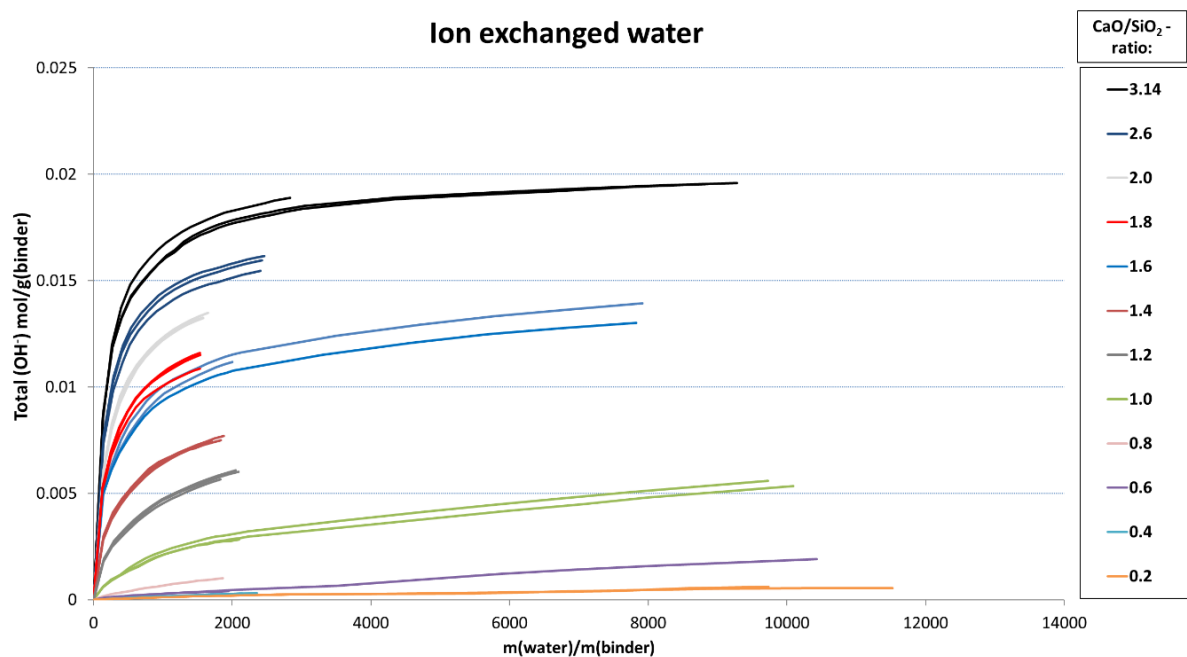


Figure 2: Calculated total OH⁻ content (mol/g(binder)) at various leachate volumes in ion-exchanged water. Each line presents a single sample.

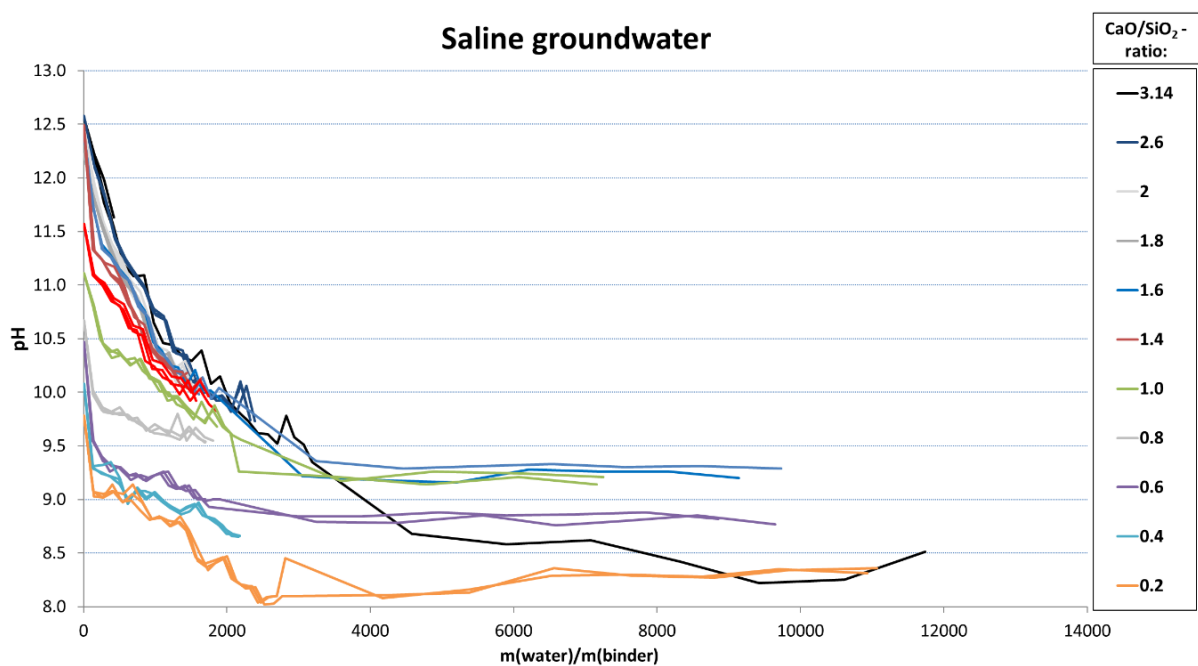


Figure 3: Measured pH values at various leachate volumes in saline groundwater water. Each line presents a single sample.

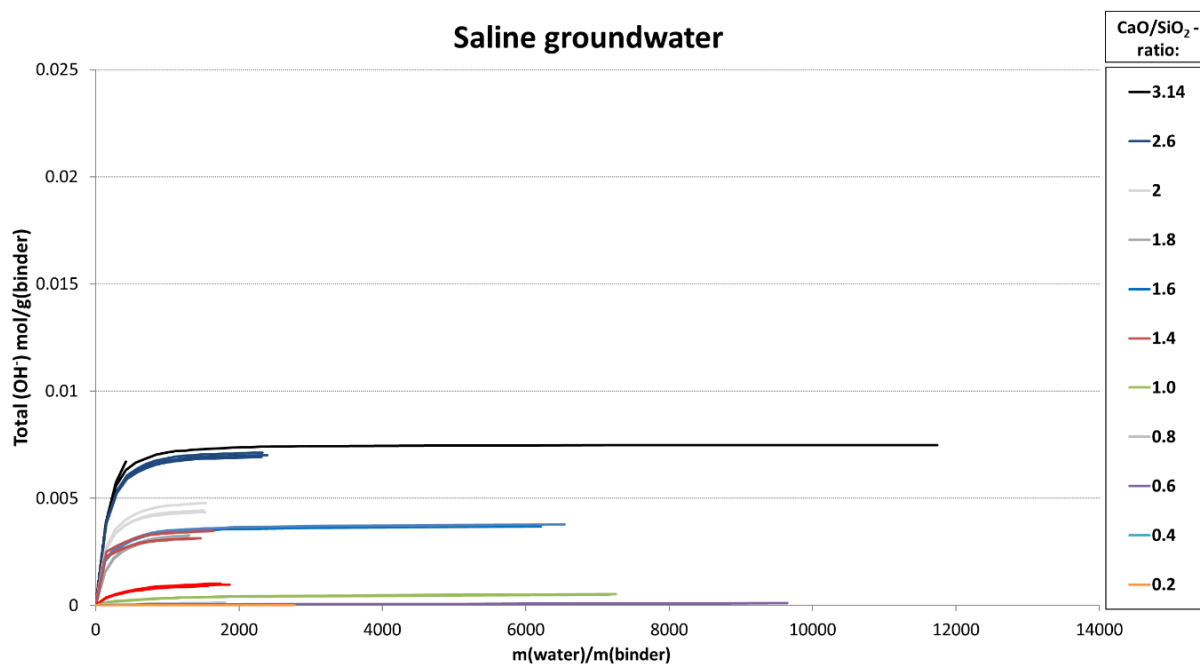


Figure 4: Calculated total OH^- content (mol/g(binder)) at various leachate volumes in saline groundwater. Each line presents a single sample.

Table 2: Total accumulated hydroxyl contents with respect to various pH limits.

Initial C/S-ratio of the binder	Total accumulated hydroxyl content (mol/g(binder))			
	Ion exchanged water		Saline groundwater	
	above pH 10	above pH 11	above pH 10	above pH 11
3.1	$1.96 \cdot 10^{-2}$	$1.80 \cdot 10^{-2}$	$7.38 \cdot 10^{-3}$	$6.18 \cdot 10^{-3}$
2.6	*	$1.47 \cdot 10^{-2}$	$7.08 \cdot 10^{-3}$	$6.75 \cdot 10^{-3}$
2.0	*	$1.22 \cdot 10^{-2}$	$4.35 \cdot 10^{-3}$	$4.09 \cdot 10^{-3}$
1.8	*	$1.05 \cdot 10^{-2}$	$3.15 \cdot 10^{-3}$	$2.86 \cdot 10^{-3}$
1.6	*	$9.75 \cdot 10^{-3}$	$3.55 \cdot 10^{-3}$	$3.17 \cdot 10^{-3}$
1.4	*	$7.09 \cdot 10^{-3}$	$3.14 \cdot 10^{-3}$	$3.00 \cdot 10^{-3}$
1.2	*	$5.34 \cdot 10^{-3}$	$9.17 \cdot 10^{-4}$	$4.70 \cdot 10^{-4}$
1.0	*	$2.13 \cdot 10^{-3}$	$3.65 \cdot 10^{-4}$	$8.64 \cdot 10^{-7}$
0.8	*	$1.67 \cdot 10^{-4}$	$3.79 \cdot 10^{-5}$	0
0.6	*	0	$2.33 \cdot 10^{-5}$	0
0.4	$2.87 \cdot 10^{-4}$	0	$3.61 \cdot 10^{-7}$	0
0.2	$1.04 \cdot 10^{-4}$	0	0	0

* Leachate pH has not yet decreased below pH 10.

4 Discussion

Evolution of pH during leaching followed the general trends described in the literature. Rapid decrease in pH at the beginning of the leaching originated from leaching of alkalis. After the alkali dissolution, incongruent dissolution of calcium-silicate-hydrates (C-S-H) defined the leachate pH. High C/S-ratio leachates mainly consisted of calcium and accompanying hydroxyls (Koskinen, 2013). Due to resolution of the selected dissolution method, solid portlandite induced plateau was not observed in the samples.

At a C/S-ratio 0.2, the dissolving material was likely silicates. At a C/S-ratio 0.2, the excess silicate in the mix designs seemed to stabilize the C-S-H and incongruent dissolution of silicates from C-S-H was not observed until the excess silicates were consumed. Incongruent dissolution of C-S-H at a C/S-ratio 0.2 caused the pH to momentarily increase, until C-S-H was totally dissolved or a congruently dissolving C/S-ratio was reached (leachate volumes 9,000 L/kg).

A clear difference to existing literature was observed at high leachate volumes (Harris et al., 2002). According to current literature, various C/S-ratios should converge to a single congruently dissolving C-S-H at the high leachate volumes. In Figure 1 and Figure 3, C-S-H at C/S-ratios 0.6, 1.0 and 1.6 caused higher pH than pure Ordinary Portland Cement beyond the leachate volumes 4,000 L/kg. According to observed behaviour, the solid composition which dissolves congruently was dependent on the initial composition of the sample. However, at the observed leachate volumes, the pH might not depend on C-S-H but some other sparingly soluble phase. Chemical analysis and modelling is needed to clarify the observation.

Measured pH values were systematically lower in saline groundwater compared to ion-exchanged water. The difference originates from the common ion effect, caused by calcium content of saline groundwater. Dissolved calcium in the groundwater decreased the amount of dissolved C-S-H in saline groundwater, leading to systematic lower observed pH-values.

Total accumulated hydroxyl amounts are presented in Figure 2 and Figure 4. According to literature, bentonite transformation rate is insignificant at pH-values below 10 or 11. Total accumulated hydroxyl amounts above pH 11 and 10 are presented in Table 2. Bentonite transformation is a complex process and outside the scope of this study. However, combining the leaching data with known bentonite transformation models enables the estimation of damage that cementitious leachates may induce to bentonite.

Montmorillonite transformation process has been proposed to occur in line with the aqueous silica speciation dependency (Savage and Benbow, 2007; Koskinen, 2013). Dissolution reaction according to aqueous silica speciation dependency is presented in Eq. 1 (Savage and Benbow, 2007). According to Eq. 1, one mole of hydroxyls dissolves 0.21 moles of montmorillonite which corresponds to a mass of 77 grams. Presented calculation is a very simplified model and does not account the full leachate composition, the effect of secondary precipitates or ionic activities. Calculated affected montmorillonite masses are presented in Table 3.

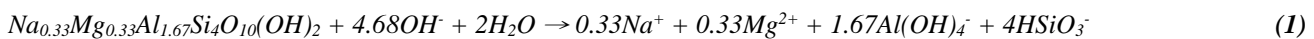


Table 3: Total affected montmorillonite weight with respect to various pH limits.

Initial C/S-ratio of the binder	Total affected montmorillonite (g/g(binder))			
	Ion exchanged water		Saline groundwater	
	above pH 10	above pH 11	above pH 10	above pH 11
3.1	1.48	1.41	0.58	0.48
2.6	*	1.15	0.56	0.53
2.0	*	0.96	0.34	0.32
1.8	*	0.82	0.25	0.22
1.6	*	0.76	0.28	0.25
1.4	*	0.56	0.25	0.24
1.2	*	0.42	0.07	0.04
1.0	*	0.17	0.03	0.00
0.8	*	0.01	0.00	0.00
0.6	*	0.00	0.00	0.00
0.4	0.02	0.00	0.00	0.00
0.2	0.01	0.00	0.00	0.00

* Leachate pH has not yet decreased below pH 10.

According to Table 3, low alkali Ordinary Portland Cement is capable to dissolve 1.5 times the mass of montmorillonite in ion-exchanged water with limiting values of pH 10 and 11. In ion-exchanged water, montmorillonite dissolution is not possible to avoid if a limiting pH 10 is used. Montmorillonite dissolution was observed even in a highly blended mixture ($C/S = 0.2$) in ion exchanged water, using a limiting pH 10. However, the amount of affected montmorillonite is quite low, at 1% of the binder weight. If a limiting pH 11 is used, montmorillonite becomes unaffected at $C/S = 0.6$ in ion exchanged water. At a C/S -ratio 0.8, the amount of affected montmorillonite is 1% of the binder weight.

In Saline groundwater, low alkali Ordinary Portland Cement is capable to dissolve 0.6 and 0.5 times its mass of montmorillonite in ion-exchanged water with limiting values pH 10 and 11, respectively. With limiting pH 10, montmorillonite becomes unaffected at the C/S -ratio 0.8 in binders. With limiting pH 11, montmorillonite becomes unaffected at the C/S -ratio 1.0 in binders, in the studied groundwater.

5 Conclusions and Future work

Leaching of cementitious materials in ion-exchanged water and saline groundwater was studied. The C/S -ratio of the studied materials varied from pristine Ordinary Portland Cement ($C/S = 3.1$) to highly blended ($C/S = 0.2$). The total dissolving hydroxyl concentrations were measured and the accumulated hydroxyl contents relative to pH limits of 10 and 11 were calculated. Dissolution of montmorillonite was calculated according to equation proposed by Savage and Benbow (2007).

The next step is to complete the leaching studies in ion-exchanged water and evaluated the results by thermodynamic modelling to also estimate the longer period evolution and stability.

Acknowledgement

The research leading to these results has received funding from the European Union's Horizon 2020 Research and Training Programme of the European Atomic Energy Community (EURATOM) (H2020-NFRP-2014/2015) under grant agreement n° 662147 (CEBAMA).

References

- Alonso, M.C., García Calvo, J.L., Petterson, S., Puigdomenech, I., Cuñado, M.Á., Vuorio, M., Weber, H., Ueda, H., Naito, M., Walker, C., Takeshi, Y., Cau-dit-Coumes, C. (2012). Round robin test for defining an accurate protocol to measure the pore fluid pH of low-pH cementitious materials. *In*: F. Bart, C. Cau-dit-Coumes, F. Frizon, S. Lorente (Eds.). Cement-Based Materials for Nuclear Waste Storage, Springer, 251-259.
- Harris, A.W., Manning, M.C., Tearle, W.M., Tweed, C.J. (2002). Testing of models of the dissolution of cements - leaching of synthetic C-S-H gels. *Cement and Concrete Research*, 32, 731-746.
- Koskinen, K. (2013). Effects of cementitious leachates on the EBS. Posiva Working Report, 2013-04.
- Savage, D. and Benbow, S. (2007). Low-pH Cements. SKI Report, 2007:32.

Bonding and hydro-mechanical behavior of Callovo-Oxfordian claystone/concrete interface

Zaobao Liu^{1*}, Jianfu Shao^{1*}, Shouyi Xie¹, Xavier Bourbon², Guillaume Decamps²

¹ University of Lille, LaMcube, FRE2016 CNRS (FR)

² French National Agency for Radioactive Waste disposal (FR)

*Corresponding author: zaobao.liu@polytech-lille.fr; jian-fu.shao@polytech-lille.fr

Abstract

It is necessary to characterize the properties of the claystone-concrete interface in the sealing component of the French repository concept. In the framework of the WP1 of European project CEBAMA, this study presents experimental results of the hydro-mechanical properties of the planar interface between the Callovo-Oxfordian (COx) claystone and a low-pH high-performance concrete. Samples were first made in laboratory including planar interfaces between the COx claystone and the low-pH concrete produced according to a special formulation provided by the French National Agency for Radioactive Waste disposal (Andra). Multiscale characterization of the interface was conducted by imaging techniques. Triaxial direct shear experiments were then carried out on the cemented interface samples under three different confining and interstitial pressures in an autonomous device designed at the University of Lille. The effective stress concept was then discussed with the obtained experimental data and previous data from the mechanical tests on the planar interface. Water permeability of the planar COx claystone-concrete interface was also evaluated by water injection tests during triaxial direct shear process of the interface. The results show that the COx claystone can be bonded with the used low-pH concrete at the interface by creating an alteration zone during concrete hardening and curing, although it is vulnerable to cracking with the presence of concrete water. Due to the good bonding of the planar interface, the Biot's effective stress can describe better the direct shear strength of the planar interface than the Terzaghi's effective stress under varying normal and interstitial pressures. The observed cementation at the claystone-concrete interface can induce very low permeability and thus contribute to a good sealing ability in slowing water transport in the repository. The good bonding features of the interface contribute to the mechanical stability of the underground repository. The low water permeability of the interface under high confining pressure suggests the bonded interface under normal conditions do not increase the confining risk of the repository.

Keywords: *Radioactive waste disposal; claystone-concrete interface; hydro-mechanical property; low permeability; triaxial direct shear test*

1 Introduction

The sealing component of the clayey rock hosted underground repositories consists of an assembly of elements composed of different materials, such as the geological barriers, the swelling clay and the massive concrete plug. The inclusion of the multi-materials will inevitably form interfaces at the adjacent contacts of the elements. For example, in the French concept, the low permeable Callovo-Oxfordian (COx) claystone will provide the geological barriers, and the low-pH concretes will be used as the massive plugs and supports. The geological

barriers will work together with the concrete components to guarantee the confining capacity of repositories. Thus, it is necessary to characterize the properties of the interface between the COx claystone and the low pH concretes to assure the confining functionality of the repositories.

The COx claystone has been proven to have favorable properties, such as absence of major cracks and good sealing ability, for the host rock of repositories (Andra, 2012; Liu et al., 2017). The inevitably formed interfaces between the claystone and the concrete (Armand et al., 2017), on the other hand, will induce public concerns and scientific questions on the functionality of the bi-material system for underground disposal of radioactive waste. It has been confirmed that the properties of the COx claystone, substantially different from those of the hard rocks, are strongly water-sensitive (Delage et al., 2015; Liu and Shao, 2016; Liu et al., 2018). Once contacted with water without constraints, the COx claystone will be cracked with fissures generated along the bedding planes and at the locations of chemical-reactive inclusions, which will lead to textural broken and microstructure damage of the COx claystone and thus will eventually degrade its confining property. For this reason, direct contact of the COx claystone with water without confining is not suggested. However, the fabrication and curing of concrete must introduce water (Cau Dit Coumes et al., 2006; García Calvo et al., 2010), which will induce potential influences on the COx claystone.

The contradiction in water presence between the COx claystone and concrete induces technical difficulties in making well-shaped specimens including bonded interfaces for laboratory tests. The claystone are completely different from those of clays or clay soils in mineralogy, texture, structure, and physical and mechanical properties. As a rock, the claystone cannot be remolded as has been widely done for the clay soils in laboratory studies. The method in fabricating samples of the clay soil/concrete interface (Cheng et al., 2013; Hossain and Yin, 2014) is no longer valid for making bonded interface samples between the claystone and concrete. Therefore, there is a need to develop new techniques for evaluating the interface process of the claystone-concrete interface under repository conditions.

Under in-situ conditions of the repository, the concretes have to be poured directly next to the previously present COx claystone barriers. During the concrete pouring, hardening and curing, there will be physical and chemical reactions between the COx claystone and the concrete constituents. The bonding properties and processes at interfaces are fundamental to support a knowledge base of claystone-concrete interface. There are so far some discussions on mechanical properties of the non-bonded interface between clay and concrete (Cheng et al., 2013; Stavropoulou et al., 2018) or bonded interface between non-water-sensitive rock (hard) and concrete (Bost et al., 2015; Buzzi et al., 2008; Dong et al., 2016; Flansbjer and Magnusson, 2014). In those former studies on clay-concrete interfaces, the two materials were previously made and were just put together without cohesion at the interface. There is little discussion on characterization of the interface bonding process during concrete pouring and hardening. The bonded interface between the claystone and concrete have been rarely characterized and very few quantitative laboratory evaluations are available (Kosakowski and Berner, 2013; Mäder et al., 2017; Stavropoulou et al., 2018). Thus, it is necessary to characterize the bonding process of the interface during concrete pouring, hardening and curing, and to evaluate its properties for assuring the safety of repositories.

Therefore, current knowledge on the cement-based material interfaces, such as the interface bonding process, mechanism, strength, and permeability is still inadequate to address the questions in repository conditions. For this reason, the European Union and the French National Agency for Radioactive Waste Management (Andra) have launched new research projects, e.g. the CEBAMA (CEBAMA, 2015-2019), to bridge the gap between current knowledge and technical concerns on bi-material systems for underground radioactive waste disposal. The work here presents experimental results of bonding characteristics and hydro-mechanical properties of the COx claystone-concrete interface.

2 Materials and method

Each of the interface samples consists of two semi-cylinders. One semi-cylinder is made up of the COx claystone and the other is made up of a specially formulated low pH-concrete. The semi-cylinder COx claystone was previously prepared and placed into one side of a cylindrical stainless steel mold. The concrete was then poured into the other side of the cylindrical mold, next to the COx claystone.

2.1 Callovo-Oxfordian claystone

The average distribution of mineral groups in the claystone throughout the whole formation is clay fraction (phyllosilicates) $\sim 42 \pm 11\%$ of the rock, carbonates $\sim 30 \pm 12\%$ of minerals, tectosilicates $\sim 25 \pm 8\%$ of minerals; and ancillary minerals constitute less than 4% (Armand et al., 2016). Mineralogical analyses show the mineral content exhibits low variability in the bedding planes but significant perpendicular to the bedding. The COx clay-rich rock porosity lies between 14% and 20% at the URL site and is close to 18% at the URL main level (Yven et al., 2007), and the natural water content ranges between 5% and 8% (Armand et al., 2013). The average pore size of the COx claystone is about some ten nanometers (Liu et al., 2015; Robinet, 2008) and the majority of pores are in the clay matrix. The rock core used in this paper is labelled EST53549, which was drilled from the argillaceous rich unit of the formation (Armand et al., 2017).

2.1.1 Low-pH high-performance concrete

The formulation of the fabricated concrete is given in Table 1, which is named as TL from the French word “Type Laitier”. Its binder is composed of Portland cement, silica fume and slag. The Portland cement is of the class CEM I 52.5 PM ES CP2 from the Lafarge du Teil company with the standard [NF 197-1, 2012]. This type of cement was selected for its low alkali content and low content in aluminate, and rich in tricalcium silicate (C3S) (Codina, 2007; Engelhardt and Gaida, 1963).

Table 1: Formulation of TL low-pH high performance concrete (kg per m³ concrete).

Superplasticizer (%)	Binder			Sand	Gravels	Effective water
	Portland cement	Silica fume	Slag			
1.5	76	123.5	180.5	855	949	152

The silica fume used is the mechanically densified FS DM 95 from Condensil Company. This type of silica fume is capable of operating in high performance concrete for its granular effect contributed by its spherical smooth and fine-size particles, and the pozzolanic effect contributed by additional hydration of the amorphous silica-rich fume with lime in Portland cement hydration.

The slag used is a type of ground slag supplied by ECOCEM, which complies with the European Standard [NF EN 15167-1, 2006] for granulated blast furnace slag in concrete.

The superplasticizer Chryso® Fluid Optima 175 was chosen for its good compatibility with silica fume in concrete binder. In addition, it does not cause too much occluded fresh air (< 3%) and can guarantee a correct consistency over a practical duration of workability in 2 hours in mixing the concrete. The quantity of the Superplasticizer should be limited to 1.5% since the effects of organic matter in concrete is still unknown in the long term.

The sand and gravels, supplied by Andra, are the limestone aggregates with granular metric class of 0/4 mm and 5/12 mm, respectively. The actual density values were respectively measured 2.65 and 2.69 g/cm³: The gravels were sieved in laboratory excluding the ones larger than 8 mm to comply with the diameter of the cylindrical specimen. The two crushed aggregates were rewashed in laboratory to allow a good adhesion between the binder and the aggregates.

2.2 Sample preparation

Cylindrical samples were made in the laboratory including planar interfaces between the COx claystone and the low pH concrete. Each specimen of 37 mm in diameter was composed of one semi-cylinder of claystone and one semi-cylinder of low pH concrete (Figure 1). The preparation of specimens with a planar interface included the following steps.

- (i) Drill into the rock core EST53549 provided by Andra with a corer to obtain cylindrical COx claystone samples of 37 mm in diameter. The drilled sample axis is perpendicular to bedding planes.
- (ii) Cut each cylindrical COx claystone sample into two half-cylinders along one of its symmetric plan by a diamonded wire saw to assure the precision of sample diameter.
- (iii) Humidify concrete mixer, introduce successively the gravel, the sand, the previously homogenized binder into the mixer to allow anhydrous mixing for 1 minute.
- (iv) Introduce half the water to saturate the aggregate for 1 minute, and then introduce the other half of the water and the superplasticizer to allow mixing for 3 minutes.
- (v) Pour a small amount of concrete into a stainless steel mold to occupy the bottom of the mold with a concrete thickness no less than 1 cm.
- (vi) Put the semi-cylinder of the COx claystone in the mold and pour the concrete to fill the other half and the upper part of the mold.
- (vii) Close the mold and vibrate a little to densify the fresh concrete.
- (viii) Let hardening of the fresh concrete in the mold for three days to gain initial bonding strength and unmold the cylindrical samples carefully.
- (ix) Cover with adhesive tape to prevent direct contact of the claystone from air and water on the side surface of the cylinder samples.
- (x) Store the samples in a relative humidity (RH) controlled container (RH = 98%) for about four months to allow hydration of concrete binder during curing.
- (xi) Cut and polish both end surfaces to keep their perpendicularity to the axis of the cylinder samples as required in laboratory tests (see Figure 1).

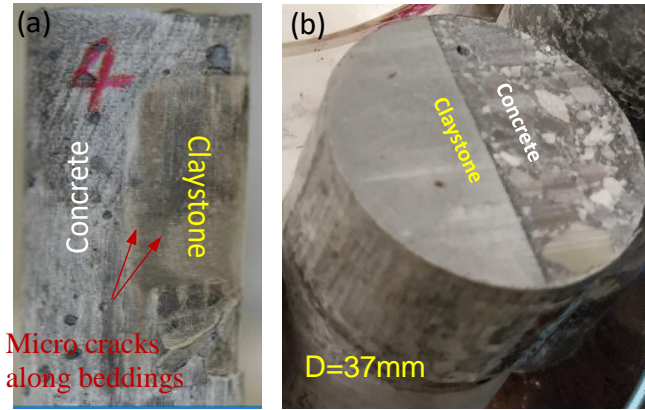


Figure 1: Image of samples including well-bonded planar interface between COx claystone-concrete: (a) sample during concrete curing; (b) sample before test.

2.3 Experimental method and device

The imaging techniques were adopted to characterize the interfaces to investigate firstly the bonding process of the interface between the COx claystone and the concrete. The triaxial direct shear tests with water injection were then carried out to characterize the hydro-mechanical behaviors of the interface samples.

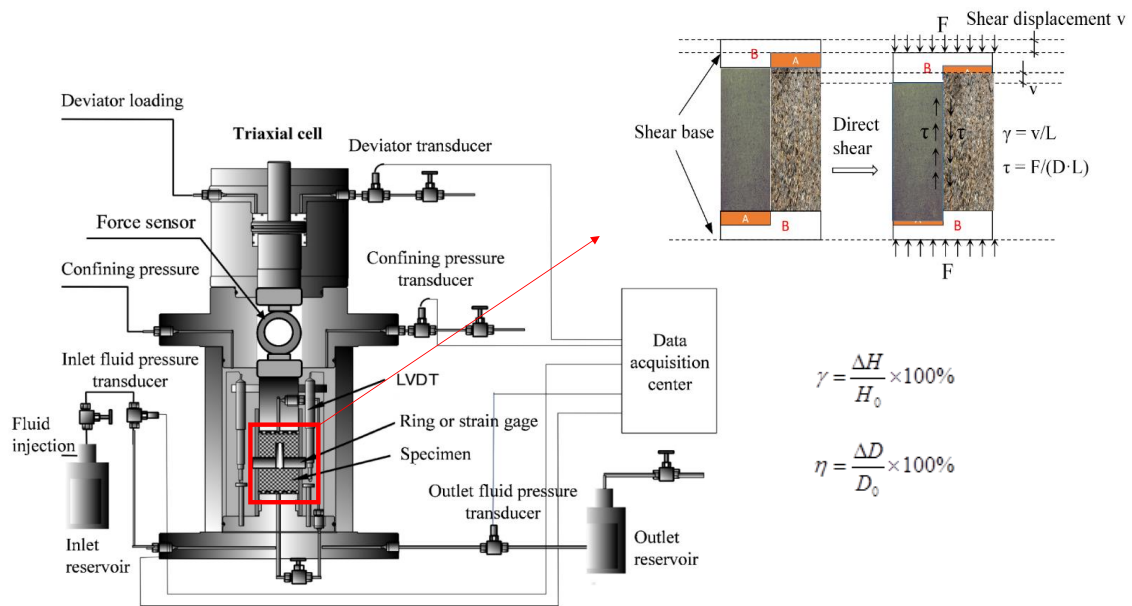


Figure 2: Schematic view of triaxial cell and direct shear device.

The triaxial direct shear tests were conducted in an autonomous triaxial cell with a specific shear component designed at the University of Lille, Laboratory of Mechanics, Multiscale and Multiphysics. A schematic view is given in Figure 2 for the direct shear test of the planar interface included in a cylindrical specimen. The shear force is applied by the compatible shear base A and B. Part B is made of rigid steel and Part A is made of silicone with perfect elasticity and large deformability.

The triaxial system is composed of three independent components, respectively, for axial stress loading leading to the generation of shear stress in the specimen due to the specific device mentioned above, confining pressure that generates the normal stress applied to the specimen, and interstitial pressure generation that creates fluid flow

through the interface specimen. The force, pressure, displacements are continuously monitored by the transducers (e.g. force and pressure sensors, LVDTs and rings) and recorded in a data acquisition system.

In the triaxial direct shear test, we first applied the hydrostatic stress to the representative values of stress in the repositories, i.e. 12 MPa. We then injected the interstitial pressure with the synthetic water formulated from in-situ water chemical constituents to minimize water-swelling effects. We waited a few weeks for the saturation of the samples under constraints in the triaxial cell. The shear test device was then placed in a conventional triaxial compression system (Liu and Shao, 2017) to conduct the triaxial shear of the planar interface. We then loaded the shear stress at a constant shear strain rate about $0.5 \cdot 10^{-6} \text{ s}^{-1}$.

3 Interface bonding features

The overview of an interface sample is shown in Figure 1. One can observe visually that the two materials have an apparent boundary at the interface and have been well cemented together at the interface after concrete hardening and curing.

A detail characterization of the top surface of an interface sample is shown in Figure 3 with the help of Optical Microscopy. As shown in Figure 3a, there are clear boundaries at the interface in this sample. It seems that a boundary of a different color from the two mother materials has been formed as shown in Figure 3b and Figure 3c. In a small scale in Figure 3c, one can observe clearly, there is an alteration zone about $60 \mu\text{m}$ in width, which cements the two materials at the interface. In addition, there are no apparent fissures at the newly-formed buffer zone. However, micro cracks have been observed in the claystone along the structural planes and adjacent to the interface buffer zone (see Figure 1).

These characteristics indicate that the COx claystone and the formulated concrete can be bonded well with properly controlled conditions. The good cementing without fissure at the interface will contribute to the interface low permeability that is favorable to the sealing ability of sealing component of repositories.

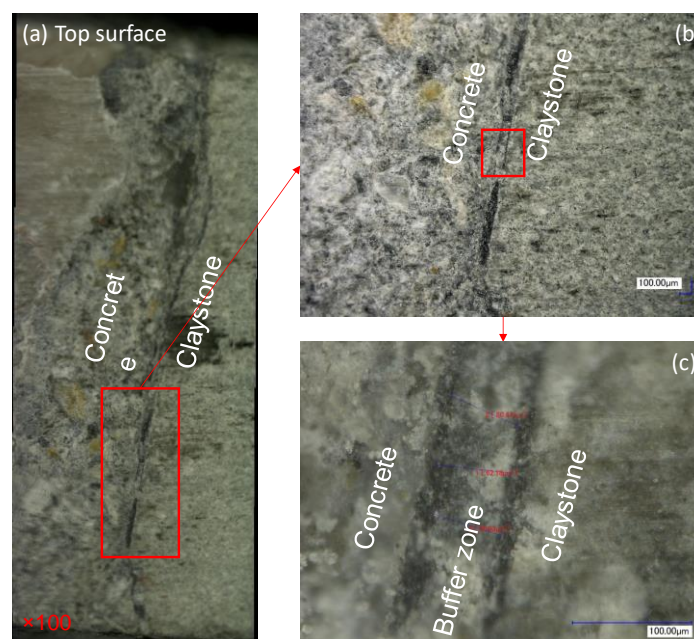


Figure 3: Optical Microscopic characterization of samples including a well-bonded planar interface between COx claystone-concrete.

4 Hydro-mechanical properties

4.1. Mechanical properties during triaxial direct shear

The mechanical curves are shown in Figure 4a for the interface sample during triaxial direct shear under confining pressure of 12 MPa with injection water pressure of 4 MPa and no backpressure. In the mechanical responses curves, positive means compression and negative means dilatation. An overview photo of the sample after tests is shown in Figure 4b and the sheared interface surface is shown in Figure 4c.

It is shown in Figure 4a that the shear stress increases nonlinearly with the shear (axial) strain. However, there is nearly no diameter change (ΔD) at initial loading before the “interface opening” stress (see Figure 4a). After the “interface opening” stress, the interface sample starts to stretch in radius direction. The shear (axial) strain before the “interface opening” stress is contributed by the closure and compression of the micro cracks in the semi-cylinder of the COx claystone generated along the bedding planes during sample preparation. The shear process is progressive due to the constraints of normal stress.

The sample image after test in Figure 4b shows that the two semi-cylinders have been sheared with permanent relative displacement while the two parts can still hold together due to the low bonding force of the saturated COx claystone on the interface surface. Once we open the sheared sample at the interface, we can see from Figure 4c that there are frictional traces of shear at the surface. The phenomena indicate that the triaxial shear process involves frictions between the two semi-cylinders. In addition, the COx claystone can be observed at the shear surface of both semi-cylinders in Figure 4c, which suggests that the COx claystone is much weaker than the concrete in the two-material system. In addition, we can imagine that the COx claystone can be pushed into the pores of the concrete during the saturation process under high compressive stress, which will further lower the permeability of the interface and the two-material system.

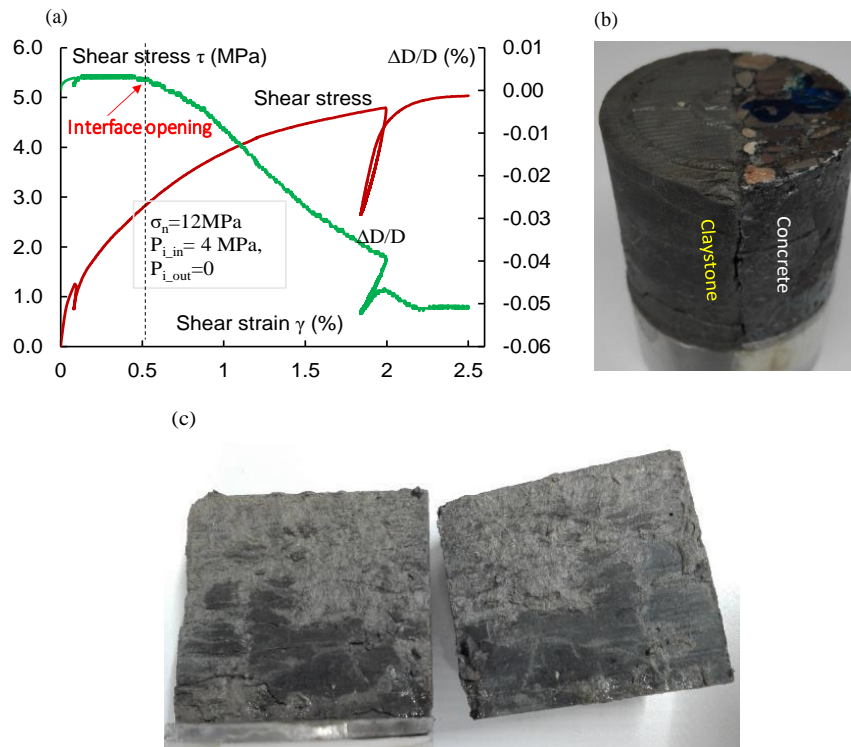


Figure 4: (a) Mechanical responses of an interface sample during direct shear under confining pressure of 12 MPa with water injection pressure of 4 MPa; (b) Sample overview after test; (c) Sheared interface surface.

The mechanical curves are shown in Figure 5a for the interface sample during triaxial direct shear under confining pressure of 10 MPa and water pressure of 2 MPa. An overview of the post-test sample after air drying is shown in Figure 5b and the sheared interface surface of the semi-cylinder of concrete is shown in Figure 5c.

It is shown in Figure 5a that the shear stress increases also with the accumulation of the shear strains and arrives at a saturated value. The diameter change of the sample keeps zero before the “interface opening” and starts to decrease after the “interface opening”. The mechanical responses in Figure 5a are similar to those in Figure 4a except for the difference in values of stress and strains.

As shown in Figure 5a, cracks generate fast in the semi-cylinder of the COx claystone during air-drying of the sample after test. The macro cracks mainly appear along the structural planes. The phenomena indicate that the air-drying at different parts of the water-saturated COx claystone is not homogeneous so that the macro cracks can be generated fast and across the post-test samples. Similar observations as in Figure 4c have been also confirmed in this test as shown in Figure 5c. The COx claystone has been attached to the surface of the semi-cylinder of concrete during the friction-involved shear process of the interface.

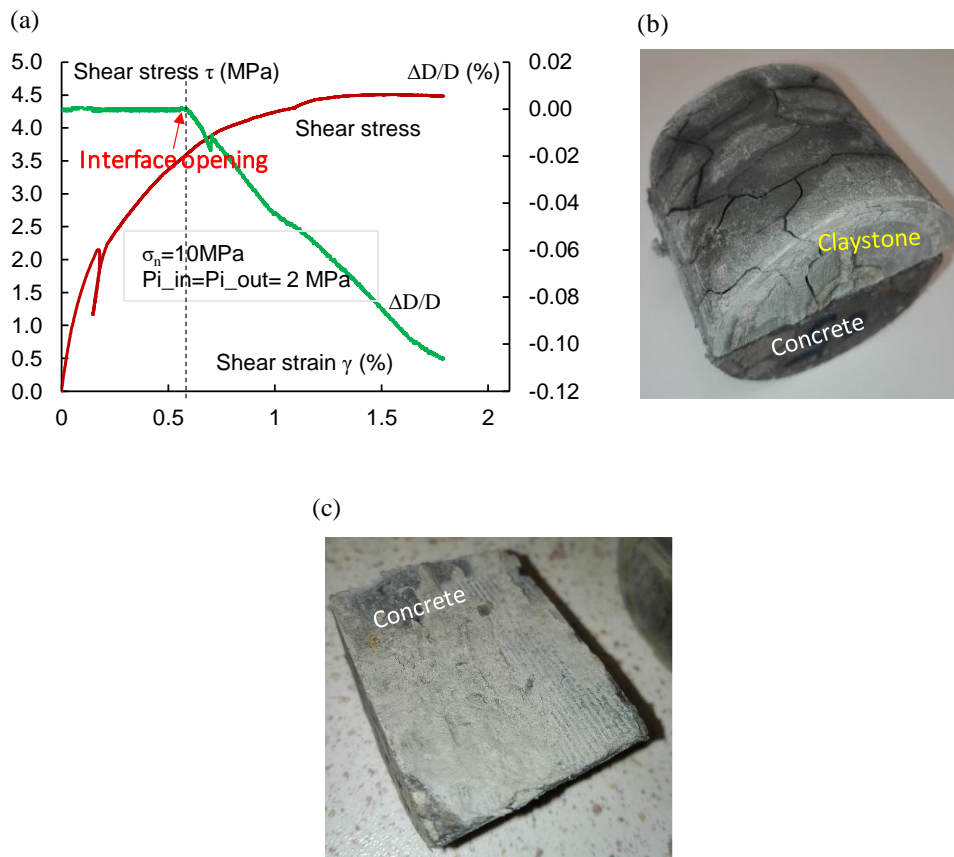


Figure 5: (a) Mechanical responses of an interface sample during direct shear under confining pressure of 10 MPa with water injection pressure of 2 MPa; (b) Claystone cracking during air-drying; (c) Sheared interface surface of concrete.

The mechanical curves are shown in Figure 6a for the triaxial shear test under confining pressure of 9 MPa and water pressure of 1 MPa. The photo of the sample post-test is shown in Figure 6b. The mechanical process in this test is generally similar to those in the previous two tests. The differences lie in the values of the stress and strains. The saturated value of this test is smaller than those former two. The post-test sample photo in Figure 6b shows that there is an important shear displacement between the two semi-cylinders after triaxial shear of the

samples. There are no evident cracks at the sheared interface due to the sealing effect of the COx claystone in water-saturated state.

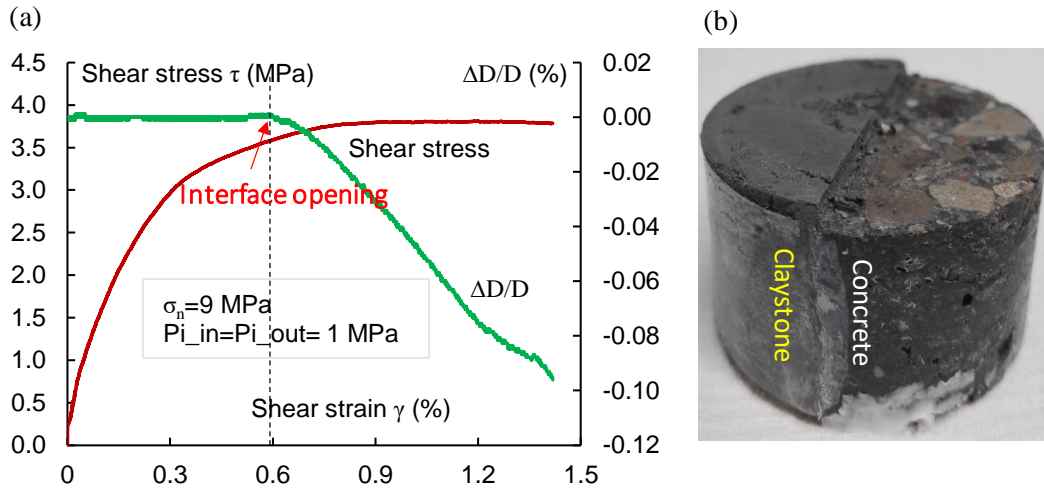


Figure 6: (a) Mechanical responses of an interface sample during direct shear under confining pressure of 9 MPa with water injection pressure of 1 MPa; (b) Sample overview after test.

Therefore, one can summarize from the tests carried out under different conditions that the COx claystone is bonded to the surface of the concrete due to the compression effects of the normal stress under saturated conditions. During the triaxial shear process, friction between the two semi-cylinders is involved and thus the saturated soft granular COx claystone can be pushed into the pores of the concrete at the planar interface surface. This effect will lower importantly the water permeability of the interface under in-situ conditions with high normal stress.

4.2 Validation of effective stress concept

To verify the concept of effective stress, one takes

$$\sigma_n' = \sigma_n - bP_i \quad (1)$$

where σ_n' is the effective normal stress; σ_n is applied normal stress, P_i is average interstitial pressure; b is Biot's coefficient. When $b = 1$, Eq. 1 turns to be the Terzaghi's effective stress.

The obtained saturated shear stress of the interface samples in different tests can be used to verify the validity of Eq. 1 on condition that the shear strength of the interface sample is linearly related to the normal stress. The correlation results of shear strength to effective normal stress are given in Figure 7a, Figure 7b and Figure 7c respectively for the Biot's coefficient of 1.0, 0.9 and 0.75. The evaluation results indicate that the Biot's coefficient $b = 0.75$ can describe better the strength behaviors of the interface samples under different normal and interstitial stresses than the other two values.

Therefore, the Biot's effective stress can describe better the direct shear strength of the interface samples under varying normal and interstitial stresses than the Terzaghi's effective stress. The case with the Biot's coefficient $b = 0.75$ agrees better with the obtained shear strength than the other two values.

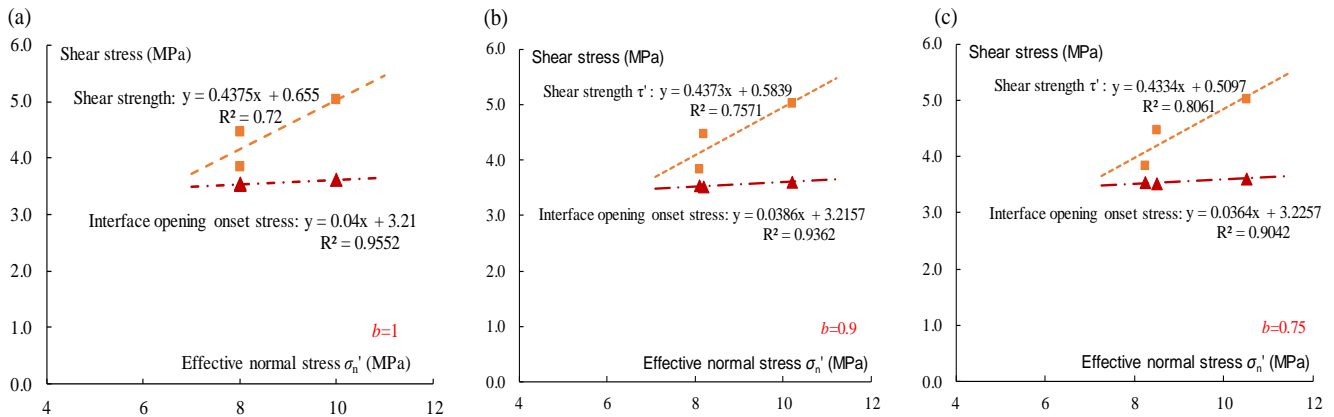


Figure 7: Validation of effective stress concept on shear strength (a) $b = 1.0$ - Terzaghi's effective stress; (b) $b = 0.9$, (c) $b = 0.75$.

5 Conclusions and Future work

The COx claystone can be cemented to the TL-formulated low-pH concrete at the interface by creating an alteration zone during concrete hardening and curing although the COx claystone is vulnerable to cracking in the presence of concrete water at the interface adjacent.

Due to the good bonding of the planar interface, Terzaghi's principle of effective stress can generate great errors in describing the direct shear strength of the planar interface, while Biot's principle stress works well.

The COx claystone under saturated conditions can be compressed into the pores of the concrete at the planar interface surface during the triaxial shear process. The water permeability of the interface is very low, at the same order of the permeability of the concrete and COx claystone, under in-situ conditions with high normal stress due to the presence of the alteration zone at the interface.

The experimental data can be used to calibrate the models describing of the mechanical and hydro-mechanical behavior of the COx claystone-concrete interface. The mechanical strength of the interface suggests that the bonded interface has a relative high strength that is favorable to the stability of the underground repository. The permeability values obtained suggest that the bonded interface under high confining pressure has a low permeability favorable to the confining safety of the repository.

Ongoing and future work will emphasize the permeability evaluation of the interface samples and chemical degradation effects on the interface properties.

Acknowledgement

The research leading to these results has received funding from the European Union's Horizon 2020 Research and Training Programme of the European Atomic Energy Community (EURATOM) (H2020-NFRP-2014/2015) under grant agreement n° 662147 (CEBAMA).

References

- Andra (2012). Recherche et développement à l'Andra pour les projets de stockage. Andra, Paris.
- Armand, G., Bumbieler, F., Conil, N., de la Vaissière, R., Bosgiraud, J.M., Vu, M.N. (2017). Main outcomes from in-situ thermo-hydro-mechanical experiments programme to demonstrate feasibility of radioactive high-level waste disposal in the Callovo-Oxfordian claystone. *Journal of Rock Mechanics and Geotechnical Engineering*, 9(3), 415-427.
- Armand, G., Djizanne, H., Zghondi, J., de La Vaissière, R., Talandier, J., Conil, N. (2016). Inputs from in-situ experiments to the understanding of the unsaturated behaviour of Callovo-Oxfordian claystone. *E3S Web Conferences*, 9, 03004.
- Armand, G., Noiret, A., Zghondi, J., Seyedi, D.M. (2013). Short- and long-term behaviors of drifts in the Callovo-Oxfordian claystone at the Meuse/Haute-Marne Underground Research Laboratory. *Journal of Rock Mechanics and Geotechnical Engineering*, 5, 221-230.
- Bost, M., Rajot, J.-P., Mouzannar, H. (2015). Shear strength of rock-concrete interfaces from direct shear tests: The influence of free spacing between encapsulating material. *In: 13th International Congress on Rock Mechanics, International Society for Rock Mechanics and Rock Engineering, ISRM-13CONGRESS-2015-152*.
- Buzzi, O., Boulon, M., Hervé, M., Su, K. (2008). Leaching of rock-concrete interfaces. *Rock Mechanics and Rock Engineering*, 41, 445-466.
- Cau Dit Coumes, C., Courtois, S., Nectoux, D., Leclercq, S., Bourbon, X. (2006). Formulating a low-alkalinity, high-resistance and low-heat concrete for radioactive waste repositories. *Cement and Concrete Research*, 36, 2152-2163.
- Cheng, Z., Chunfeng, Z., Hui, G. (2013). Elastoplastic analysis of the interface between clay and concrete incorporating the effect of the normal stress history. *Journal of Applied Mathematics*, 2013, 12.
- Codina, M. (2007). Les bétons bas pH: formulation, caractérisation et étude à long terme. INSA de Toulouse.
- Delage, P., Mohajerani, M., Tang, A.M., Conil, N. (2015). On the water sensitivity of claystones. *In: Geotechnical Engineering for Infrastructure and Development*, 2373-2376.
- Dong, W., Wu, Z., Zhou, X. (2016). Fracture mechanisms of rock-concrete interface: experimental and numerical. *Journal of Engineering Mechanics*, 142, 04016040.
- Engelhardt, W.V. and Gaida, K.H. (1963). Concentration changes of pore solutions during the compaction of clay sediments. *Journal of Sedimentary Research*, 33(4), 919-930.
- Flansbjer, M. and Magnusson, J. (2014). System design of Dome plug - Mechanical properties of rock-concrete interface. SKB Report, P-13-38.
- García Calvo, J.L., Hidalgo, A., Alonso, C., Fernández Luco, L. (2010). Development of low-pH cementitious materials for HLRW repositories: Resistance against ground waters aggression. *Cement and Concrete Research*, 40, 1290-1297.
- Hossain, M.A. and Yin, J.-H. (2014). Behavior of a pressure-grouted soil-cement interface in direct shear tests. *International Journal of Geomechanics*, 14, 101-109.
- CEBAMA (2015-2019). Cement-based materials, properties, evolution, barrier functions (CEBAMA). <https://www.cebama.eu/>
- Kosakowski, G. and Berner, U. (2013). The evolution of clay rock/cement interfaces in a cementitious repository for low- and intermediate level radioactive waste. *Physics and Chemistry of the Earth*, 64, 65-86.
- Liu, Z. and Shao, J. (2016). Moisture effects on damage and failure of Bure claystone under compression. *Géotechnique Letters*, 6(3), 1-5.
- Liu, Z. and Shao, J. (2017). Strength behavior, creep failure and gas permeability change in a tight marble under triaxial compression. *Rock Mechanics and Rock Engineering*, 50, 529-541.
- Liu, Z., Shao, J., Xie, S., Conil, N., Zha, W. (2018). Effects of relative humidity and mineral compositions on creep deformation and failure of a claystone under compression. *International Journal of Rock Mechanics and Mining Sciences*, 103, 68-76.

- Liu, Z., Shao, J., Xie, S., Secq, J. (2015). Gas permeability evolution of clayey rocks in process of compressive creep test. *Materials Letters*, 139, 422-425.
- Liu, Z.B., Xie, S.Y., Shao, J.F., Conil, N. (2017). Multi-step triaxial compressive creep behaviour and induced gas permeability change of clay-rich rock. *Géotechnique*, 68(4), 284-289.
- Mäder, U., Jenni, A., Lerouge, C., Gaboreau, S., Miyoshi, S., Kimura, Y., Cloet, V., Fukaya, M., Claret, F., Otake, T., Shibata, M., Lothenbach, B. (2017). 5-year chemico-physical evolution of concrete-claystone interfaces, Mont Terri rock laboratory (Switzerland). *Swiss Journal of Geosciences*, 110(1), 307-327.
- Robinet, J.-C. (2008). Minéralogie, porosité et diffusion des solutés dans l'argilite du Callovo-Oxfordien de Bure (Meuse, Haute-Marne, France) de l'échelle centimétrique à micrométrique. Université de Poitiers.
- Stavropoulou, E., Briffaut, M., Dufour, F., Camps, G. (2018). Experimental characterisation of the mechanical properties of the clay-rock/concrete interfaces and their evolution in time. *Challenges in Mechanics of Time Dependent Materials*, 2, 1-3. Part of the Conference Proceedings of the Society for Experimental Mechanics Series book series (CPSEMS).
- Yven, B., Sammartino, S., Géraud, Y., Homand, F., Villieras, F. (2007). Mineralogy, texture and porosity of Callovo-Oxfordian argillites of the Meuse/Haute-Marne region (eastern Paris Basin). *Mémoires de la Société géologique de France*, 178, 73-90.

Time and spatial scales observation of chemical profiles arising from surface interaction of bentonite in different cement environments

Jaime Cuevas^{1*}, María Angulo¹, Daniel E. González-Santamaría¹, Javier González-Yelamos¹, Raúl Fernández¹, Almudena Ortega¹, Ana Isabel Ruiz¹, Enrique Rodríguez¹

¹ Universidad Autónoma de Madrid (UAM) (ES)

* Corresponding author: Jaime.cuevas@uam.es

Abstract

In the third year of the CEBAMA project, we have completed almost all the programmed characterization and experimental tasks. Actually, mineralogical and chemical profiles taken across different FEBEX-bentonite/concrete interfaces are fully available from millimetre to micrometric spatial scales. Small scale Surface Reactivity Interface Experiments (SERIE) consisted in replicated tests carried out in 4-6 and 18 months including low pH, CEM-I and CEM-II cement mortars in contact with bentonite. Their micrometric chemical profiles reproduced, in 100 μm to 1 mm thickness, the characteristic elemental gradients of Mg-perturbation in the bentonite and carbonation towards the cement materials. These processes of mineralogical alteration are clearly developed in 10 to 13 year time scale experiments within < 5 mm distance from interface. The Mg-perturbation in the bentonite side is less developed in low-pH < CEM-II < CEM-I in parallel with the intensity of carbonation in the cement mortar side. The comparison of chemical profiles is discussed in terms of chemical elements mobility and minerals phases identification. On-going small scale surface interaction experiments are being running using CEBAMA mortar paste in order to compare our results with the cement developed under the project activities. In addition, scientific interactions with other partners have been taken place to explore porosity-mineralogical relationships in our FEBEX bentonite experiments.

1 Introduction

The UAM contribution to CEBAMA project is to be developed by the achievement of two main objectives: (1) to perform the geochemical study of high pH concrete (OPC)-FEBEX-bentonite at in-situ and long-term experiments, and (2) to determine the characteristic surface interface reactivity of compacted FEBEX bentonite induced by OPC based concrete pore water (high and low pH).

The focus of this scientific report is the description and comparison of elemental chemical gradients developed in FEBEX-bentonite/concrete interfaces considering the three experimental testing scenarios reported in Cuevas et al. (2017). The experiments display different spatial and time scales represented by in-situ 13 years CEM-II concrete plug interface in the FEBEX tunnel at the GTS, HB6 10 years cell test with a CEM-I concrete interface implemented in CIEMAT and 0.3 - 1.5 year small cells experiments designed to study the reactivity of the interface at the scale of the surface contact (Surface Reactivity Interface Experiments (SERIE)), González-Santamaría et al. (2018), implemented at UAM. The aspect of preserved interface probes of the materials studied for the three scenarios is shown in Figure 1. All the scenarios reacted at low temperature (< 40°C) and water saturated conditions.

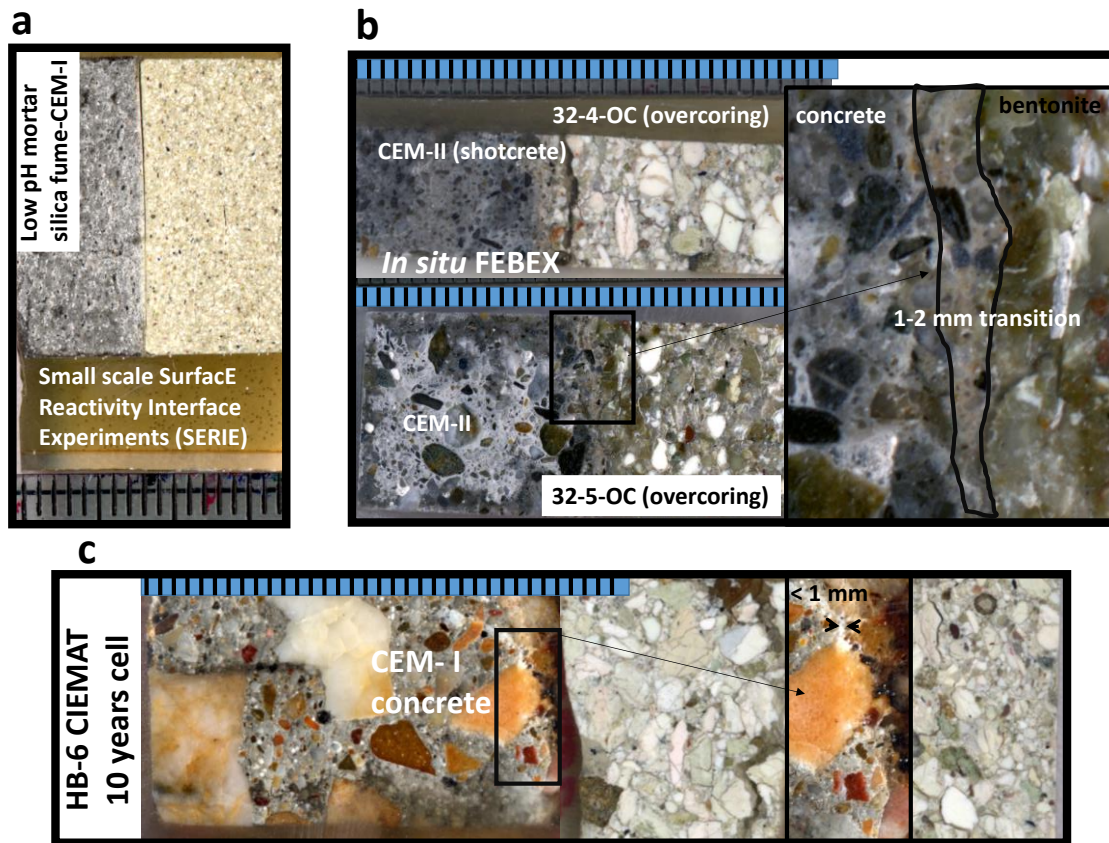


Figure 1: Photographs presented at the same mm scale (blue bar) taken from the three experimental scenarios considered for the study of concrete-bentonite interface interaction: a) low-pH cement mortar in SERIE experiments; b) CEM-II shotcrete at in-situ FEBEX; c): CEM-I concrete in HB6 CIEMAT cell. Black delimited rectangle areas correspond to additional magnified pictures shown in the figures b and c.

2 Methods

2.1 Elemental gradients in concrete-FEBEX bentonite interface

Energy dispersive X-ray analysis (EDX) were acquired in a Scanning Electron Microscope (SEM) equipment in order to obtain chemical elements profiles and measure the spatial extension for chemical perturbation related to interface reactions. The EDX quantification was performed by means of internal standard method for semi-quantitative analyses. Semi-quantitative EDX elemental composition analysis was determined in rectangular or polygonal areas that represent millimetre width slices rather than punctual analysis. To evaluate the quality of these results, EDX spectrum of a 300 x 200 μm area, containing different grains with varied compositions was evaluated. This area is typical of the analysis performed across linear transect sampled in the cement mortar (SERIE) or in the cement paste (CEM-I and CEM-II concretes from in-situ or HB6). The data were acquired using several integration times, from 10 s to 80 s, at 5 s intervals. The % deviation was calculated as 100 times the ratio of the standard deviation to the determined % chemical element value. For major elements in the concrete (Al, Si and Ca), instrumental % deviations, obtained by taking their average value in the 30-50 s interval, were less than 10%, related to their concentration being lower for silicon (< 1%) and higher for Al (9%). The % deviation from Ca measured values, however, was less than 6%. For elements that have contents within 1-5% (K, Fe, Mg), the % deviation from the average of the measured values was typically 10-15 %. Forty seconds was considered enough time to not compromise the analysis quality and to avoid excessively time-consuming data acquisition

(González-Santamaría et al., 2018). As far as no measurements of porosity were measured in this scale, data have to be taken as a relative increase or decrease of a specific element within the examined region. Porosity measurement for in-situ FEBEX are being performed in collaboration with BRGM.

All the analyses have been corrected for a 75% of quartz (SiO_2) amount in the cement mortars in SERIE experiments. In the case of in-situ or HB6 concretes, the analyses have been practised in the concrete matrix, avoiding as possible the presence of small and large aggregates.

3 Results and Discussion

3.1 In-situ and HB-6 experiments

The macroscopic visual aspect of the long-term reacted interfaces for 10 and 13 years is characterized by the presence of whitish 1mm thickness or 1-2 mm pale brown areas (Figure 1b and Figure 1c). These regions correspond approximately with a relative Ca-rich rims in concrete. The bentonite does not show evidence for visual alteration rim at the contacts. In the case of in-situ interface an alternative Ca or Mg relevant concentrations can be observed. Ca, Si, Al and Mg profiles are represented in Figure 2 for the long-term studied interfaces. A transect of 3 cm can be compared for these elements. Besides, a 5 mm transect including the interface is superimposed for each element using an expanded scale. Ca-enrichment is characterized by the precipitation of calcite (Cuevas et al., 2017) and lies within a < 1 mm interface towards the cement or related to the < 1 mm altered rim in the HB6 experiment (Figure 1c). Mg-perturbation is more extended in the in-situ experiments. The global 3 cm scale show a sharp decrease of the perturbation in 1-2 mm in towards the concrete and a more stepped decrease affecting up to 5 mm in the bentonite. Thus, the Mg perturbation is represented by an asymmetric peak with a sharp breakthrough in the concrete and a long tail towards the bentonite. HB6 develop just a < 0.1 mm sharp Mg increase within the interface and a < 1 mm tail towards the bentonite. Si and Al showed very heterogeneous patterns in the concrete as far as they are affected by the concrete aggregates varied composition, combined also with Mg or Ca perturbations. Nevertheless, there is a general trend for Al to decrease from the bentonite interface and to increase within < 1 mm thickness to have penetrated towards the concrete matrix.

3.2 SERIE small scale surface reactivity experiments

Actually, we have obtained the results for the ≈ 0.3 years experiments for these reactive interfaces using the several types of concrete paste to prepare the mortars. The chemical profiles obtained for Ca, Si, Al and Mg (Figure 3), suggest that the main reactions developed in the large (in-situ) to medium scale (HB6) long-term interfaces are reproduced in a short but significant length scale in the SERIE experiments. Calcite rim is developed in a $200\text{ }\mu\text{m}$ band at the concrete; and Mg perturbation within $500\text{ }\mu\text{m}$ in the bentonite side. The Mg-perturbation in the bentonite side is less developed in low-pH $< \text{CEM-II} < \text{CEM-I}$ in parallel with the intensity of carbonation in the cement mortar side. Taking into account that time scale ratio is about 30:1 between the two groups of scenarios (short-term/long-term), we can roughly estimate that the compared progression of the Mg or Ca chemical fronts represent only a 5:1 rate factor. Thus, considering the existence of a mineralogical and chemical heterogeneity produced by the construction of real-like interfaces in the long-term experiments; this slow time advance is a good prospect of the EBS system safety. Presumably, the analysis of the remaining 1.5 years SERIE experiments will give us a more consistent view of the time scaling of the process. Some uncertainties as the evolution of C-S-H (C-A-S-H) Ca/Si ratios in these materials (difficult to estimate in an abundant quartz matrix) and the nature of Mg-silicate phases have to be solved to constrain the modelling exercises to be performed for simulating the evolution of these fronts.

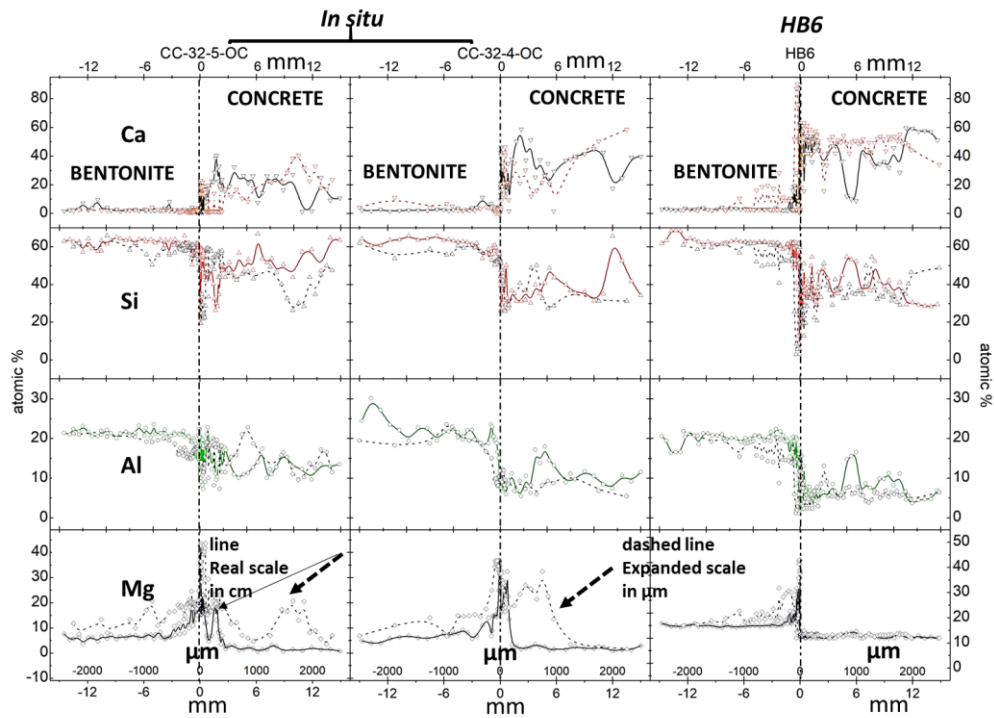


Figure 2: Chemical profiles of elements for FEBEX in-situ (overcoring samples) and HB6 CIEMAT experiment (atom % of element calculated by normalisation to 100% of the analysis excluding C and O). Double scale was used for the distance to the interface “X” axis. Scale outside the frame are mm (negative for the concrete side) referred to the interface position ($X = 0$). The numbers inside the frame, are μm and are used for the dashed lines that plot a detail of -0.25 to 0.25 region within the interface.

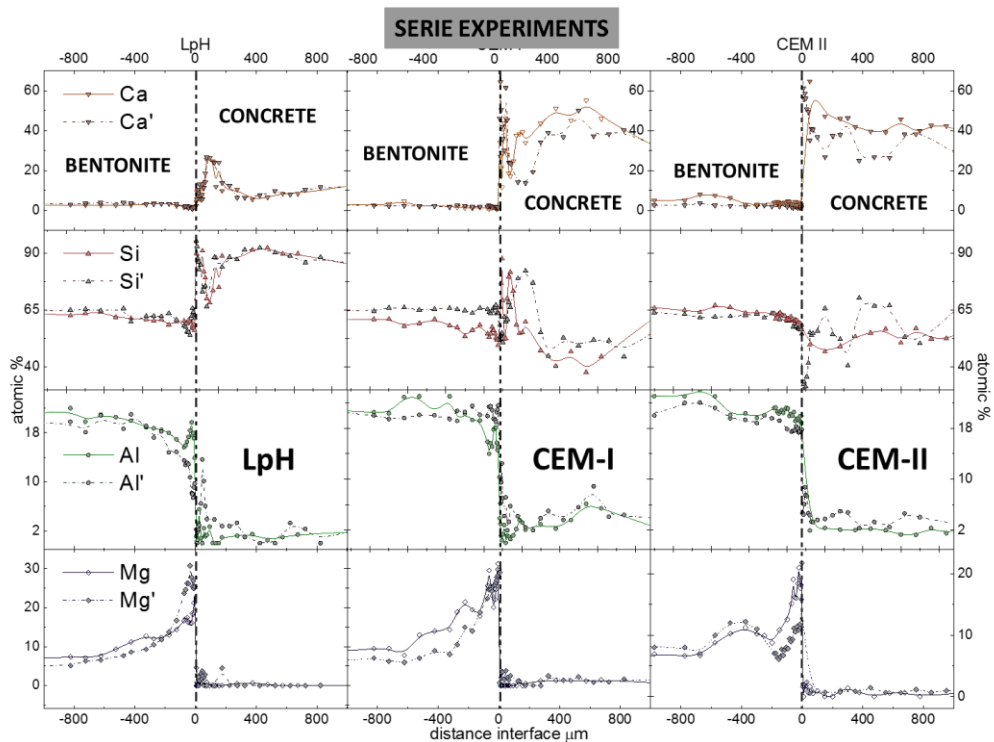


Figure 3: Chemical profiles of elements for SERIE (SurfaceE Reactivity Interface Experiments) (atom % of element calculated by normalisation to 100% of the analysis excluding C and O). The numbers below, outside the frame, are μm . Dashed lines are plots for replicate experiments (').

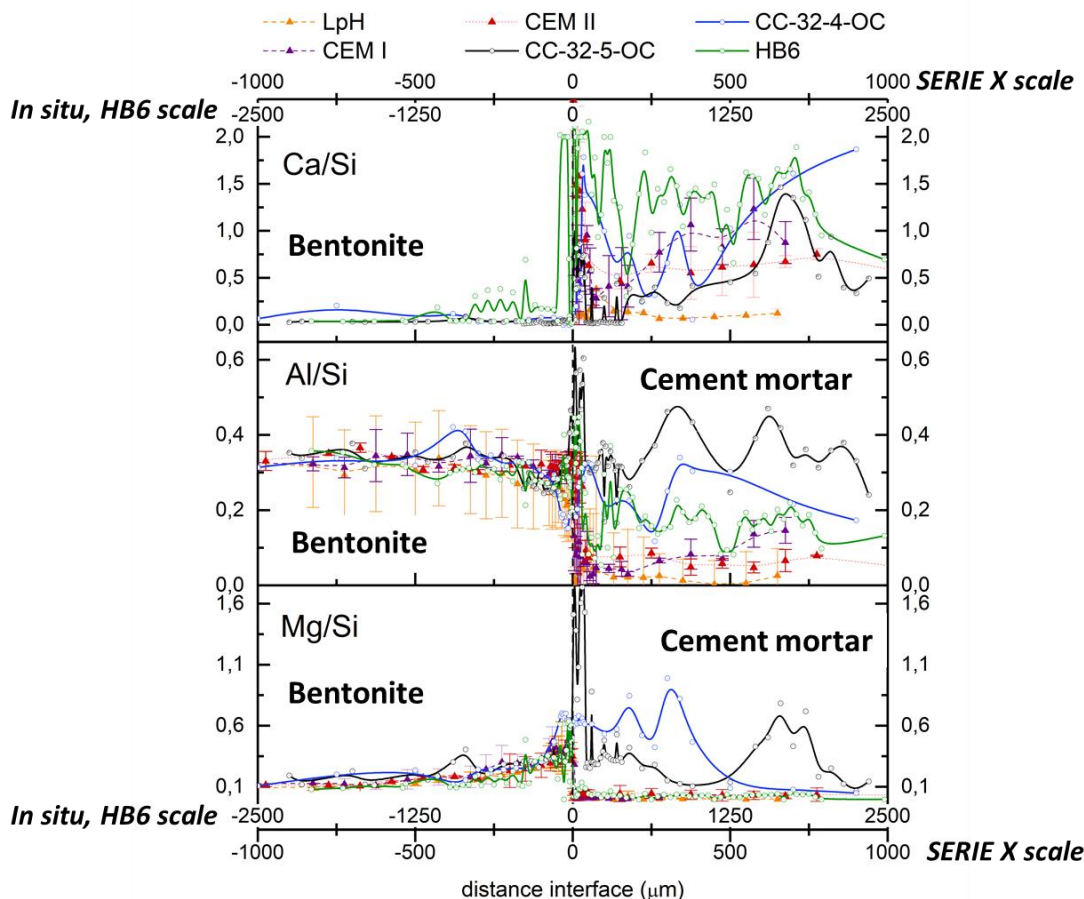


Figure 4: Elemental atomic ratios for major elements in the analysed chemical profiles. Inside frame numbers for the X scale represent the distance for HB6 and in-situ samples. X scale for the outside frame numbers represent the distance for the SERIE experiments (LpH, CEM-I and CEM-II). SERIE experiments data have been averaged using the two independent experiments (error bars).

3.3 Elemental atomic ratios and hypothesis of mineral phase formation

We have scaled the measured chemical profiles of all the experiments dividing by 5 the distance for area analyses of the large scale HB6 and in-situ 3 cm transects regarding the ≈ 1 cm transects for SERIE experiments. This factor allow to compare approximately the long-term experiments with the SERIE short-term experiments, based on the estimated rate factor retardation of 5 between long-term and short-term scenarios. Figure 4 show the peaks and nature for Mg-perturbation (Mg/Si ratio) and the nature of Ca-phases. Calcite presence is presumed to be if $\text{Ca/Si} \approx \gg 1.5$; and the presence of C-A-S-H is determined as a function of Ca/Si (1 - 0.5) and Al/Si ($< 0.2 - 0.4$). Ca/Si ratios are higher in CEM-I and CEM-II in-situ or HB6 concretes matrix and have 0.2 - 0.4 Al/Si ratios consistent with the presence of tobermorite-like C-A-S-H structure (Fernández et al., 2016). In-situ interfaces have high Mg/Si (1 - 1.5) ratios within < 0.5 mm at the interface. However, they evolve to 0.7 - 0.5 in the Mg-perturbation zone (< 2 mm). Figure 5 plots the Mg/Si change produced by mixing different Mg-phases with FEBEX montmorillonite (after Fernández et al., 2018). Mg/Si in the in-situ interface is compatible with the presence of serpentine or discrete brucite, although with a relative high Al content. This can be explained if we consider that the extended Mg perturbation is characterized by mix ratios consistent with the formation of brucite-intercalated montmorillonite and Mg-trioctahedral smectite. The conservation of montmorillonite in the materials mix within this interface is confirmed both by XRD and by the relative constant Al/Si ratio value in the region, close to the one of FEBEX montmorillonite.

FEBEX- mont $\text{Ca}_{0.25}\text{Al}_{1.5}\text{Mg}_{0.50}\text{Si}_4\text{O}_{10}(\text{OH})_2$ **Mg/Si: 0.12; Al/Si: 0.38**
 FEBEX-brucite $\text{Mg}_3(\text{OH})_{5.5}\text{Al}_{1.50}\text{Mg}_{0.50}\text{Si}_4\text{O}_{10}(\text{OH})_2$ **Mg/Si: 0.87; Al/Si: 0.38**
 Tri-Sme: $\text{Ca}_{0.125}\text{Mg}_{2.75}\text{Si}_4\text{O}_{10}(\text{OH})_2$ **Mg/Si: 0.69**
 Serpentine: $\text{Mg}_3\text{Si}_2\text{O}_5(\text{OH})_4$ **Mg/Si: 1.50**

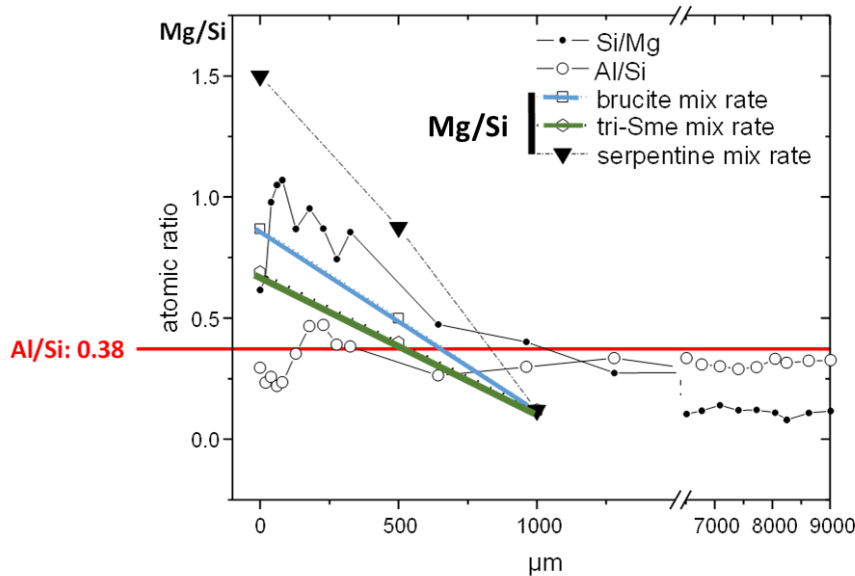


Figure 5: Atomic ratio (Mg/Si and Al/Si) in bentonite interface samples as a function of the distance to the alkaline concrete interface in the in-situ CEM-II 34-10 sample from FEBEX dismantling project (after Fernández et al., 2018). Coloured lines indicate Mg/Si atom ratio = 1.5 characteristic of serpentine / montmorillonite mix; Mg/Si atom ratio = 0.87 characteristic of FEBEX montmorillonite – brucite intercalation phase mix; and Mg/Si atom ratio = 0.69 for a trioctahedral smectite/montmorillonite mix. In red: reference Al/Si atom ratio of FEBEX bentonite. Formulas listed above correspond to the ones used to calculate theoretical atomic ratios.

4 Conclusions and Future work

The visualization of elemental chemical gradients in different time and spatial scales offers a promising prospective to advance in the upscaling of the concrete-bentonite interface perturbation. This perturbation affects < 5 mm thickness in the studied systems and seems to be highly retarded during the first decade of the repository performance. The progress of the perturbation reactions has to be related to the new spatial distribution of minerals and porosity in the interface in order to guide the formulation of realistic reactive transport modelling exercises.

All the experiments and samples under initial consideration in our contribution to CEBAMA are now characterized and we have started with the integration and interpretation task in close collaboration with the CIEMAT and CSIC groups. During the next and final period, we plan to provide the results of integration from local to global (SERIE-HB6-in-SITU) geochemistry scale in order to have outputs for future model validation in the CEBAMA project. Complementary, we are working in collaboration activities with other partners. Basically, (1) we are studying the porosity-mineralogical spatial relationship of in-situ FEBEX bentonite/concrete interface, provided by UniBe, in the BRGM facilities at Orleans (France) taking advantage of a mobility measure budget; (2) on-going small scale surface interaction SERIE experiments are being running using CEBAMA mortar paste in order to compare our results with the cement developed under the project activities; and (3) the mineralogical characterization of clay interfaces other than Febex bentonite are now running with Boom clay once we have solved some technical problems with our XRD equipment during the last 6 months.

Acknowledgement

The research leading to these results has received funding from the European Union's Horizon 2020 Research and Training Programme of the European Atomic Energy Community (EURATOM) (H2020-NFRP-2014/2015) under grant agreement n° 662147 (CEBAMA).

References

- Cuevas, J., María Angulo, M., González-Santamaría, D., González-Yelamos, J., Fernández, R., Ortega, A., Ruiz, A.I. (2017). High pH concrete FebeX-bentonite interface reactions: from months to decades and from cm³ experiments to m³ in-situ scenario. *In*: M. Altmaier, V. Montoya, L. Duro, A. Valls (Eds.) Proceedings of the 2nd Annual Workshop of the CEBAMA Project. KIT Scientific Report, *in press*.
- Fernández, R., Ruiz, A.I., Cuevas, J. (2016). Insight into the formation of C-A-S-H phases as a consequence of the interaction between concrete or cement and bentonite. *Clay Minerals*, 51, 223-235.
- Fernández, R., González-Santamaría, D., Angulo, M., Torres, E., Ruiz, A.I., Turrero, M.J., Cuevas, J. (2018). Geochemical conditions for the formation of Mg silicates phases in bentonite and implications for radioactive waste disposal. *Applied Geochemistry*, 93, 1-9.
- González-Santamaría, D.E., Angulo, M., Ruiz, A.I., Fernández, R., Ortega, A., Cuevas, J. (2018). Low-pH cement mortar-bentonite perturbations in a small-scale pilot laboratory experiment. *Clay Minerals*, *in press*.

Degradation processes and alkaline plumes in high and low pH concretes after months and years of interaction with granite water

María Cruz Alonso^{1*}, Álvaro Fernández¹, José Luis García Calvo¹

¹ CSIC. Institute of Construction Science Eduardo Torroja (ES)

* Corresponding author: mcalonso@ietcc.csic.es

Abstract

The work deals with the impact of low ionic granite water, from the Grimsel site, in the degradation of two concretes types with variable chemical compositions, pH-based, after different time scales of exposure flow. The hydrochemical processes occurring in high and low pH concretes are analysed with respect time of interaction and volume of water in contact. The performance of the high-pH concrete exposed for several months in the laboratory to percolation granite water is compared with the same concrete exposed for 13 years in the real deep geological repository of Grimsel. The low-pH concrete, with 9 years of maturity, is studied during several months of interaction with the granite water using percolation tests. The high-pH concrete (hpH) evaluated at different time scales was made with a CEM II with 20% limestone filler. The low-pH concrete was based on 60% CEM I + 40% silica fume (SF) here identified as lpH-OPC+SF. The aim with this type low-pH concrete was to modify the C-S-H paste to reach a low pH in the bulk of the concrete but without increasing the Al₂O₃ content, so that a silicate based low-pH concrete is the case under study.

The samples studied come from cores taken from real concrete plugs produced by a shotcrete method, the high-pH from Febex Grimsel large scale experiment and low-pH from the plug produced in Äspö during the ESDRED project. The concrete samples tested have heterogeneous pore structure, which affects the volume of water percolated and in consequence the alkaline plume and the alteration of the cement paste.

In the high pH concrete, hpH-CEM II, the alkaline plume was evidenced and its duration (from pH = 12.3 to 9) was independent on the heterogeneity and the amount of water percolated but more related to the water interaction time. It has been confirmed that the alkalis are the ions first released and are the responsible for the alkaline plume decay. The decay in the alkaline plume does not mean the pH of the bulk of the concrete also decreases in the same proportion. The release of Ca has confirmed as a good parameter to identify the alteration of the cement paste. The changes in the microstructure of the cement paste, after the percolation tests in lab (months of interaction), have resulted similar to those detected in the real site after 13 years of interaction: the portlandite progressively has disappeared and new formation of ettringite is detected.

In the low pH concrete, lpH-OPC + SF, the alkaline plume is not detected even at short ages. The release of alkalis is not significant respect that of hpH-CEM II, what confirms the reason for the alkaline plume in hpH concrete. On the contrary the Ca released is similar or more significant that in hpH concrete and the process of leaching maintain longer. Progressive increase of calcite is detected after high volumes of water percolated.

1 Introduction

The CSIC contribution to CEBAMA project on the interaction of cement based materials properties and evolution of barriers is carried out directly in concrete, that allows to classify the work close to the real conditions and the validation of test at lab-scale with real site large scale tests. The work carried out deals with the influence on transport properties due to porosity of concrete alterations observed at two levels: 1) aging of high-pH concretes from in-situ large-scale long-term experiments (granite water/concrete/bentonite and clayey water/concrete interfaces), 2) aging of high and low-pH concretes at interfaces with granite and clayey groundwaters after short-term, from chemical modifications of solid phases to physical alteration properties affecting porosity.

Present results are focused on only those results corresponding to real Grimsel granite water, ionic composition given in Table 1. Typology of concretes under study are those described in Alonso et al. (2017). In the high pH concrete, cores from the shotcreted plug produced for the FEBEX-e experiment at the site of Grimsel (hpH-CEM II) are used. The distances from the host rock considered for identification of the cores taken from Grimsel plug: 1) Core obtained in the middle of the plug, aprox. 1m from host-rock and more that 50 cm from the bentonite so that the maturity of the concrete after 13 years is characterised and identified as initial state (hpH-CEM II-ini) that also allow to obtained samples for percolation tests in lab; 2) core samples taken at a distance of 15 cm from host-rock so that the Grimsel water is expected to have been interacting with granite water (hpH-CEM II-15 cm from host rock). Cylinders of 5 cm x 5 cm were taken for characterisation under percolation tests in lab from cores of 1 m. The time scales effect after the 13 years of water interaction in Grimsel site at 15 cm from the host rock and after several months of water interaction in the laboratory are considered and compared.

In the low-pH concrete (lpH-OPC+SF), as described in Alonso et al. (2016) and Alonso et al. (2017), short term tests are only being considered, although the maturity of the concrete before percolation tests was more than 9 years. The origin of the samples also came from a shotcreted plug produced in Äspö during the ESDRED project.

Table 2 shows the main characteristics of both concretes. The variables characterised with the percolation tests are: periodic analyses of the leachates (volume of eluted water, hydraulic conductivity, ions released and pH). At the end of each percolation test the chemical, mineralogical and microstructural changes in the concretes are analysed (porosimetry, pore water pH, soluble ion content, XRD, TG/DTA, BSEM-EDS) at several distances from the water inlet. Concretes not exposed to water were characterized to identify the initial state of the microstructure.

Table 1: Grimsel granite water chemical composition.

Ion type	Ca	Na	K	Mg	Cl	SO ₄	Fe	SiO ₂	HCO ₃	pH
Content (M)	$1.8 \cdot 10^{-4}$	$3.7 \cdot 10^{-4}$	$2.3 \cdot 10^{-5}$	$1.7 \cdot 10^{-5}$	$2.3 \cdot 10^{-5}$	$6.1 \cdot 10^{-5}$	$2.2 \cdot 10^{-4}$	$1.9 \cdot 10^{-4}$	$4.0 \cdot 10^{-4}$	9.7

Table 2: Concrete samples characterised after granite water interaction.

Sample identification	Binder	Concrete Age (before percolation)	Concrete pH	Time Scale
Febex Shotcrete (hpH-CEM II)	CEM II A-L+ 6.5% nanosilica	13 years	12.8	6-12 m (percolation)/ 13 y Grimsel site
Äspö Shotcrete (lpH-OPC+SF)	60% OPC + 40% SF	9 years	9.2	5-9 m (percolation)

2 Hydrochemical processes of Grimsel granite groundwater on hpH-CEM II concrete: from months to years of interaction

The analyses of the hydrochemical processes occurring in the high pH concrete in contact with Grimsel granite water during percolation tests has been divided in two sections: 1) the alkaline plume evolution and 2) the alteration of the cement paste. Table 3 summarizes the main details of each of the three samples of the hpH-CEM II exposed at the percolation test. The pH and the ionic composition of the percolated waters have been measured periodically.

Table 3: Main data from hpH-CEM II samples exposed to percolation tests.

Sample identification	Plug	Time (months)	K (m/s)	Volume of water percolated (mL)
hpH-CEM II-1	hpH-CEM II-ini	6	$\approx 10^{-10}$	1,706
hpH-CEM II-2	hpH-CEM II-ini	17 (in progress)	$\approx 10^{-13}$	184
hpH-CEM II-3	hpH-CEM II-15 cm from host rock	12	$\approx 10^{-11}$	1,125

2.1 Evolution of the alkaline plume from hpH-CEM II concrete interaction with Grimsel granite water

The hpH-CEM II concrete samples exposed to the percolation test confirm the existence of an alkaline plume, however the length of this alkaline plume is independent of the total volume of percolated water as can be seen in Figure 1-left. Alkalies release faster from the concretes during the first 200 days and they are the responsible for the progressive decay of the pH. When the alkaline plume has decayed (sharp decrease of the pH) the release of alkalies becomes less relevant (Figure 1-right). In the case of the leach of Ca the performance varies with the density of the concrete and the amount of water percolated, included in Figure 4-right, for later comparison with lpH concrete results. A fast percolation of water (in hpH-CEM II-1) the Ca released during 6 m is lower in comparison with that of hpH-CEM II-3 after 12 m, one order of magnitude lower of K in this last sample. The capacity of interaction of the water with the solid phases of the cement paste is higher, as it will be shown later. The release of Si (also in Figure 4-right for later comparison with lpH concrete results) is higher at the start of the test.

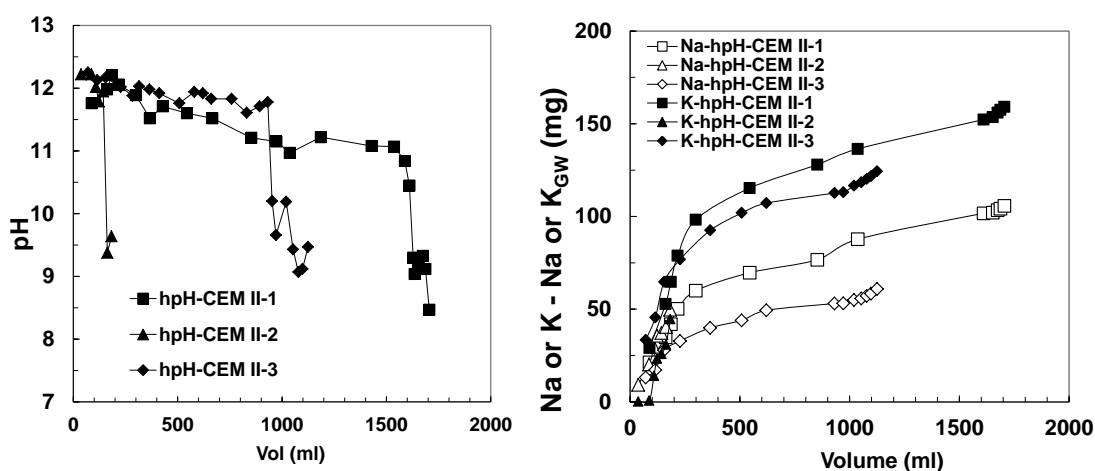


Figure 1: pH (left) and Na and K evolution (discounting the groundwater contents) (right) of the percolated waters in hpH-CEM II.

2.2 Degradation processes in the hpH-CEM II paste in contact with granite water

The changes in the microstructure of the concrete due to the interaction with the Grimsel granite water depends of the volume of liquid percolated, which strongly varies in the concrete samples (Table 2) due to the heterogeneity of the pore structure. The pH in the bulk of the concrete, at different distances from the water inlet, decreases faster as higher is the volume of liquid percolated. The portlandite (CH) is depleted progressively, residual CH remains in the hpH-CEM II-3 sample even after 12 m test while in hpH-CEM II-1 the CH has been completely removed. The two concrete samples after the percolation test show significant differences in the CaO and SiO₂ contents (Figure 2) in the C-S-H composition, although it can be seen that in hpH-CEM II-3, the release of Ca (Figure 4-left) correlates with the loss of CaO content in the cement paste of the concrete, especially in the first mm in contact with the water inlet, in parallel an increase in the relative content of SiO₂ is measured in this sample. On the contrary, the composition of hpH-CEM II-1 is more similar that of the initial concrete, the hydraulic K is higher, the water volume percolated is higher but less effective the leaching interaction.

In the FEBEX hph concrete an increase of ettringite is observed with respect to the initial concrete, a transport of Al and/or SO₄ are expected to occur within the concrete that favor the formation of more ettringite. In the case of the calcite was also higher in the concretes after the percolation test (especially in the sample that has percolated more volume of water, hpH-CEM II-1). In the comparison between the cores after 13 years of exposure from the real Grimsel site close to the host-rock, it is also observed the influence of the proximity to the granitic groundwater, in such a way that the depletion of CH and the increase of the ettringite content is also detected in the sample hpH-CEM II-15 cm from host rock, with respect to the samples from the centre of the plug (hpH-CEM II-ini) and far from the action of the groundwater in the plug. Calcite content is also slightly lower in concrete from the centre the core.

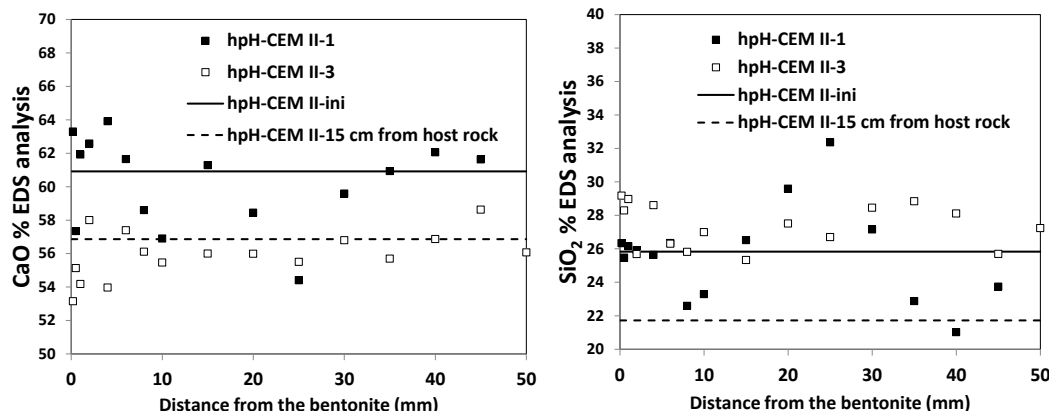


Figure 2: CaO (left) and SiO₂ (right) contents in different hpH-CEM II samples.

3 Hydrochemical processes of Grimsel granite groundwater on lpH-OPC+SF concrete after months of interaction

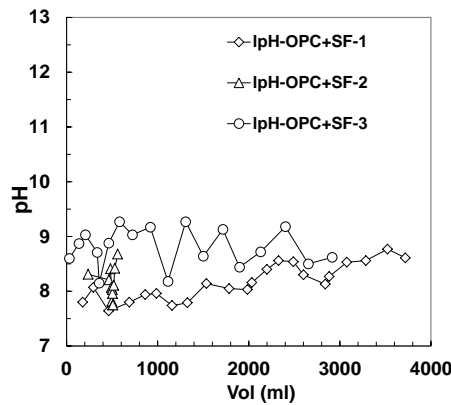
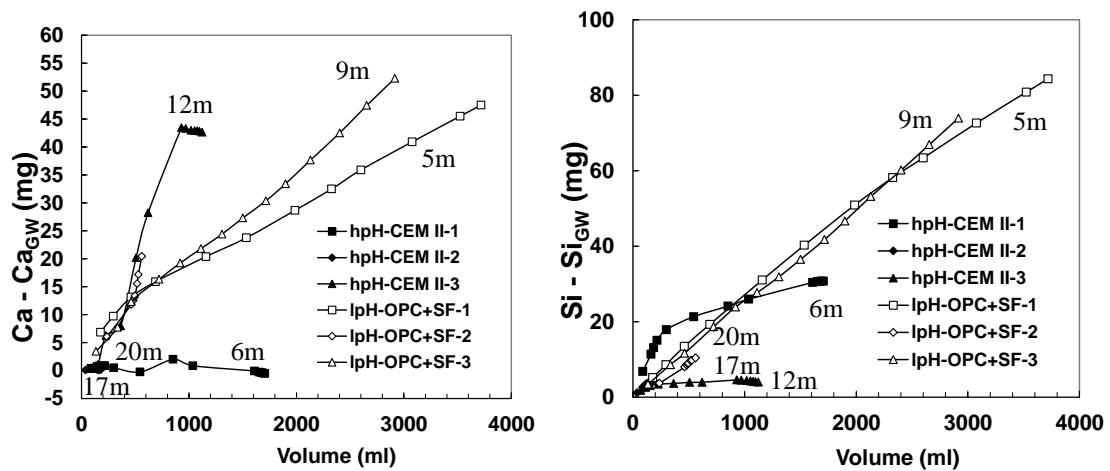
Similarly, to the case of hpH-CEM II, the hydrochemical processes in lpH concrete is divided in two sections: 1) the alkaline plume evolution and 2) the alteration of the cement paste. Table 4 summarizes the details of each sample of lpH-OPC+SF exposed at the percolation test. The pH and the ionic composition of the percolated waters have been followed.

Table 4: Main data from lpH-OPC+SF samples exposed to percolation tests.

Sample identification	Time (months)	K (m/s)	Volume of water percolated (mL)
lpH-OPC+SF-1	5	$\approx 10^{-9}$	3,719
lpH-OPC+SF-2	20 (in progress)	$\approx 10^{-12}$	575
lpH-OPC+SF-3	9	$\approx 10^{-10}$	2,916

3.1 Evolution of the alkaline plume from lpH-OPC+SF concrete interaction with Grimsel granite water

The alkaline plume is not detected even at short ages and low volume of water percolated, as can be seen in Figure 3. The release of alkalis is not significant respect to that of hpH-CEM II, what confirms the reason for the alkaline plume in the OPC and the higher binding capacity of alkalis in the C-S-H of the lpH cement paste as also found in García Calvo et al. (2010). On the contrary, the amount of Ca (Figure 4-left) released is similar or more significant in lpH-OPC+SF concrete and the leaching process is maintained for longer. The Si released is also higher in the lpH concrete for the same volume of water percolated, as can be seen in Figure 4-right.

**Figure 3:** pH of alkaline plume in lpH-OPC+SF samples exposed to percolation test.**Figure 4:** Ca (left) and Si (right) evolution (discounting the ion groundwater contents) of the percolated waters in lpH-OPC+SF and hpH-CEM II concretes removed from percolation tests.

3.2 Degradation processes in the lpH-OPC+SF paste in contact with granite water

The characterization of the samples of lpH-OPC+SF removed from the percolation tests show an increase of calcite content in the concrete with respect to the initial concrete, before the percolation test, except in the first cm in direct contact with the water inlet, especially in the lpH-OPC+SF-3 case. Calcite is not precipitated on the surface, as it was detected in this type of concrete exposed to percolation test but with lower maturity in deionised water percolation tests (García Calvo et al., 2010). XRD and BSEM images confirm the absence of CH and ettringite (as in the initial concretes before the test), in fact, the aspect (Figure 5) and the composition of the cement paste (Figure 6) is quite homogenous in the concrete, being the most significant change with respect to the initial composition the SO₃ enrichment in the zone closer to the water inlet, as can be seen in Figure 6-right. The release of Si in the lpH-OPC+SF samples (Figure 4-right) causes the decrease of SiO₂ content in the cement paste (and the increase of the relative content of CaO), especially in lpH-OPC+SF-3 sample, as can be seen in Figure 6-left.

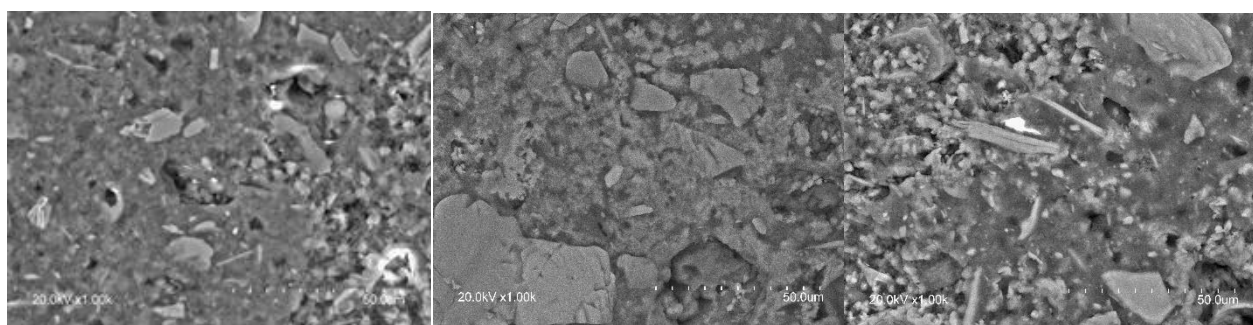


Figure 5: BSEM images (x1000) of the interface of lpH-OPC+SF-1 at 0.1 (left), 1.7 (centre) and 4.9 mm from the water inlet.

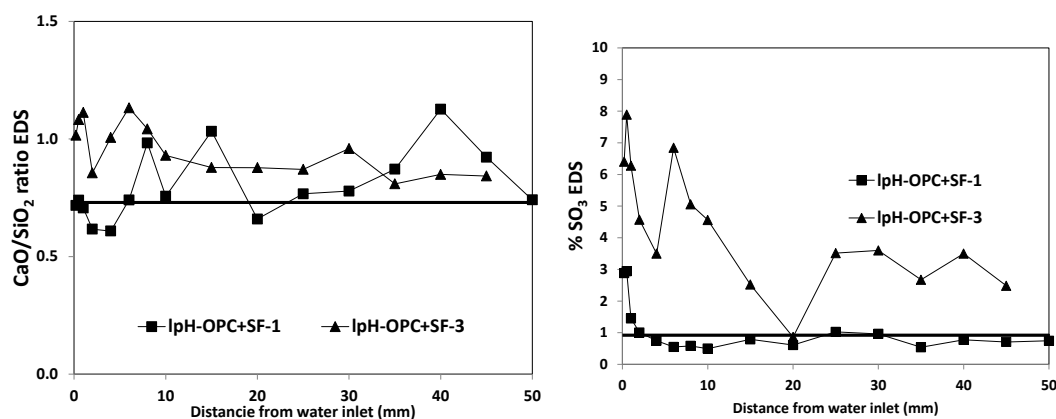


Figure 6: CaO/SiO₂ ratio (left) and SO₃ content (right) in lpH-OPC+SF samples removed from percolation tests at different distances from the water inlet.

4 Conclusions and Future work

- The alkaline plume duration (pH = 12.3 to 9) in Febex hpH-CEM II is independent on heterogeneity and water percolated but more related to the time with water interaction. Alkaline ions release first and are responsible for the alkaline plume decay. The release of Ca is more related to the alteration of cement paste. The alteration processes in cement paste, with percolation tests in lab approach to those

detected in the real site after 13 years of interaction with the portlandite depletion and more ettringite formation.

- In the Äspö lpH-OPC+SF concretes the alkaline plume is not detected. The release of alkalis is not significant respect that of hpH-CEM II, Ca released is more significant in lpH-OPC+SF than in hpH-CEM II concrete and the calcite content increase after long volumes of water percolated.

As future work of CSIC in CEBAMA project will be focused in the completion of the analysis of the short-term tests water interactions through the characterisation of microstructural and transport properties of the concretes after the water infiltration tests with the Grimsel granite water, and with the simulated clayey water, in low and high pH concretes. The reference low-pH concretes high and low density will be also characterised at certain ages of waters interaction. In addition, the data from the characterisation of HB6 cell and the FEBEX overcorings will be added to those from CIEMAT and UAM in order to have an integrated and complete the characterisation of the systems under study by CSIC, described in Alonso et al. (2017).

Acknowledgement

The research leading to these results has received funding from the European Union's Horizon 2020 Research and Training Programme of the European Atomic Energy Community (EURATOM) (H2020-NFRP-2014/2015) under grant agreement n° 662147 (CEBAMA).

References

- Alonso, M.C., García Calvo, J.L., Flor Laguna, V. (2016). Characterisation of concrete aging due to the interaction with groundwaters in contact with different engineering barrier system (EBS). *In*: M. Altmaier, V. Montoya, L. Duro, A. Valls (Eds.) Proceedings of the 1st Annual Workshop of the CEBAMA Project. KIT Scientific Report, 7734.
- Alonso, M.C., García Calvo, J.L., Flor Laguna, V., Fernández, Á. (2017). Ageing of high and low pH concretes after short and long periods in contact with groundwaters. *In*: M. Altmaier, V. Montoya, L. Duro, A. Valls (Eds.) Proceedings of the 2nd Annual Workshop of the CEBAMA Project. KIT Scientific Report, *in press*.
- García Calvo, J.L., Hidalgo, A., Alonso, C., Fernández Luco, L. (2010). Development of low-pH cementitious materials for HLWR repositories resistance against ground waters aggression. *Cement and Concrete Research*, 40, 1290-1297.

Physical and chemical behaviour of Low Hydration Heat/Low pH concretes

Xavier Bourbon^{1*}, Yannick Linard¹, Nicolas Gilardi¹

¹ Andra R&D Division (FR)

* Corresponding author: Xavier.Bourbon@andra.fr

Abstract

The in-situ test proposed by Andra in the CEBAMA project context deal with the chemical and physical behaviour of Low Hydration Heat/Low pH Concretes. Two reference formulations, designed for plugs and seals, will be followed over several years: short term (from day to month scale): preparation, casting, hydration phase; medium term (from month to year scale): evolution in operating conditions.

This experiment is an in-situ test performed in the Andra's underground research laboratory in Bure (Meuse/Haute-Marne laboratory). Two types of concretes are studied. These materials are ternary blends based on CEM I/Silica Fume/fly ash and CEM I/silica fume/blast furnace slag blends.

Cubic meter samples physical evolutions are followed at the different time scale, from setting to operating conditions over few years (temperature and shrinkage evolution with time). The purpose is to correlate these measurements to the physical and chemical evolution (hydration and chemical reaction with the clay host rock) of these concrete with time.

Specific sensors to measure temperature, shrinkage and the water saturation evolutions with time are used. To fulfill our knowledge of the chemical evolution in the same boundary conditions, samples will be analyzed to assess the evolution of sound material compared to those at the interfaces with the atmosphere and with the clay host rock. At present, only physical data are available and assessed.

1 Introduction

The CEBAMA project (CEment BAsed MAterials, properties, evolution and barrier functions) started in June 2015. In this context, Andra proposed an in-situ test to assess the physical and chemical behaviour of Low Hydration Heat/Low pH concretes in operating conditions at the concrete/host rock interface. Data acquisition, in-situ measurements and modelling are planned over a 4 year program.

This test is performed in the French Underground Research Laboratory (URL) in Bure (Meuse/Haute-Marne, France), at 500 m depth in the Callovo-Oxfordian claystone layer, to be representative of the operating conditions of a geological disposal facility and to assess the evolution of the concrete/host rock interface.

Targeted data to be measured on two different formulations are:

- Within a short term time scale: hydration heat, evolution of the physical properties with respect to hydration (mechanical properties, shrinkage),

- Within a long time scale: physical evolution in atmospheric conditions (i.e. impact of drying on shrinkage and cracks, impact of atmospheric carbonation); chemical reactivity at concrete/host rock interface and physical consequences of the chemical reactivity with the geological medium.

A by-product from this experiment is an assessment on sensors behaviour and durability to quantify these physical evolutions.

The cementitious materials to be studied are “Low Hydration Heat/Low pH concretes”, specifically designed for plugs and seals. To assess their physical and chemical behaviour at a representative scale, cubic meter elements have been casted. To follow the evolution of their physical properties with time, the concrete elements are monitored. Temperature and geometrical evolution will be followed with time. To assess the chemical behaviour of such cementitious materials, samples will be taken to analyse both interfaces with the atmosphere and the geological medium.

1.1 In-situ test design

This in-situ test has two main goals:

1. To assess the short timescale physical behaviour of the low hydration heat/low pH concrete formulations at a large scale to validate a physical model including the hydration of such blended cements (El-Bitouri et al., 2016);
2. To assess the physical consequences of the evolution at the interface with the host rock and the interface with the atmosphere in the underground facilities:
 - a. To evaluate the impact of in-situ casting (contact with a clay host rock) on the hydration and the development of the physical properties;
 - b. To quantify the impact of atmospheric carbonation on the concrete based on highly blended cements (kinetic, amplitude).

The specification to formulate those cementitious materials are in connection to the physical and chemical evolution of in-situ casted large concrete elements in contact with the clay host rock. Such concretes must have a low hydration heat to prevent temperature increase during setting and a “low pH” (pH of the hydrated cement pore water) to prevent significant chemical evolution of clay materials with time (the Callovo-Oxfordian claystone, as well as the swelling clay of the seal core). To fulfil these requirements, two types of blended cements have been designed and used.

Within the purpose of the CEBAMA project, this in-situ experiment will provide input data to validate the coupled chemical/physical evolution model used to describe large concrete components at the interface with clay host rocks. In addition, the chemical evolution of low hydration heat/low pH concrete with regards to the atmospheric carbonation could be evaluated in operating conditions.

1.1.1 Formulations

Two formulations are studied. Both recipes fulfil the requirements regarding the physical and the chemical expectations. Both are based on a ternary blend with Clinker, Silica Fume and Fly Ash or Blast Furnace Slag. Compositions of the two concretes, respectively called T_{CV} and T_L are reported in Table 1.

To assess at a representative scale Thermo-Hydro-Mechanical behaviour of such concretes, this test has been designed as walls cast on the clay host-rock in the French-URL, thick and large enough to reach a volume close to 1 m³. As two formulations have been planned to be tested, elements have been duplicated.

Table 1: Compositions of the ternary blends.

Compounds (kg/m ³)	T _{CV}	T _L
CEM I 52.5 PM-ES	140.6	76
Silica Fume	121.9	123.5
Fly Ash	112.5	-
Blast Furnace Slag	-	180.5
superplasticizer (Chryso - Optima 175)	5.63	5.70
Sand (0/2 mm - 0/4 mm)	248.6 - 581.3	253.8 - 593.5
Gravels (5/12 mm)	930.5	940.4
Total water	150	152

Table 2: Mechanical properties of the two low hydration heat/low pH concretes.

Mechanical properties	T _{CV}		T _L	
	28 days	90 days	28 days	90 days
Compressive strength (MPa)	64 ± 4	71 ± 5	70 ± 1	80 ± 2
Tensile strength (MPa)	3.3 ± 0.5	3.7 ± 0.5	3.8 ± 0.5	3.6 ± 0.5
Young's Modulus (GPa)	41 ± 1	42 ± 2	39.5 ± 1.5	40.5 ± 1.5

1.1.2 Concrete walls

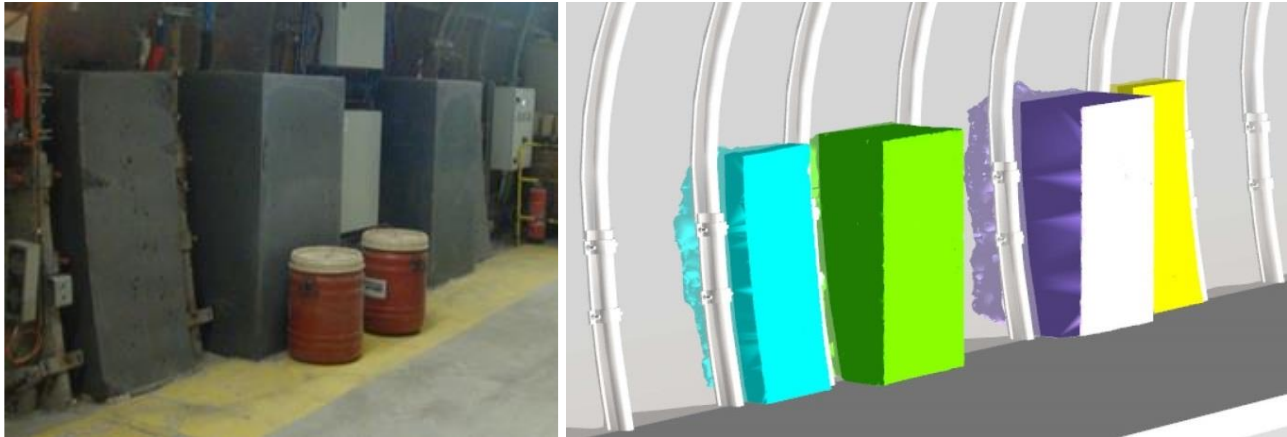
To assess the chemical evolution of the concrete with time, concrete samples will be taken up. To prevent from disturbing the physical measurements, two more thin walls have been dedicated to that purpose. Four specimens were prepared -two concrete elements for each formulation- so that there was the opportunity to measure the physical evolution and the chemical evolution with time of the two tested formulations. Thick walls are instrumented (see below). These four elements are placed between steel sliding arches in the GAN3 gallery of the URL. The theoretical sizes of each element are reported in the following table (Table 3).

Prior to casting the concretes, the shotcrete liner on the gallery walls, has been removed and the host rock surface has been cleaned to have a mechanically stable surface. Anyhow, the experiment is still in contact with the damaged zone in the host rock. The total volume of concrete required was higher than first anticipated. A 3D-scan has been performed to give an estimation of the total volume required for each element (Figure 1).

Thick walls have a total volume between 1.1 and 1.3 m³ and thin walls have a volume between 0.6 and 0.7 m³. This requires a total volume close to 2 m³ for each formulation.

Table 3: Theoretical size of the tested concrete walls.

	Height (m)	Width (m)	Thickness (m)
Thick walls	1.50	0.83	0.83
Thin walls	1.50	0.63	0.20

**Figure 1:** Experimental location in the GAN3 gallery of the concrete elements and 3D modelling.

1.1.3 Sensors

To monitor the physical evolution (especially temperature and shrinkage), number of sensors have been placed in each element to measure the temperature evolution with time, the strain in relation to the endogenous shrinkage and the drying (Figure 2).

Andra drives qualification tests on embedded sensors to be able to provide long term monitoring in its future disposal structures. For combined temperature and strain measurements, the most advanced qualified sensor is the vibrating wire extensometer (abbreviated as VWS for vibrating wire sensor), which benefits from a significant feedback (used for decades for the physical monitoring of several dams in a lot of countries). Temperature measurements are provided by a thermistor, embedded in the VWS casing.

Nineteen VWS with integrated thermometers were embedded into the concretes, to measure temperature and strain in both thick walls. In addition, two other VWS were embedded in two reference samples, cast at the same time as the walls, in semi adiabatic containers. They are used as reference to calibrate the walls' sensors.

For moisture measurements (H), sensing technologies are not as mature as sensors for Thermal and Mechanical (TM) parameters. Four TDR (Time Domain Reflectometry) sensors were selected and placed at different positions (various heights and depths) in the structures, to assess the water saturation gradients in the concretes. Samples were also taken and placed in humidity-controlled chambers. They will provide a calibration: the empirical determination of several concrete saturation levels versus raw measurement, namely the time of flight of an electromagnetic wave that propagates in the TDR sensing line.

More details on sensing technologies and qualification procedure are available from the MODERN project (MODERN, 2013).

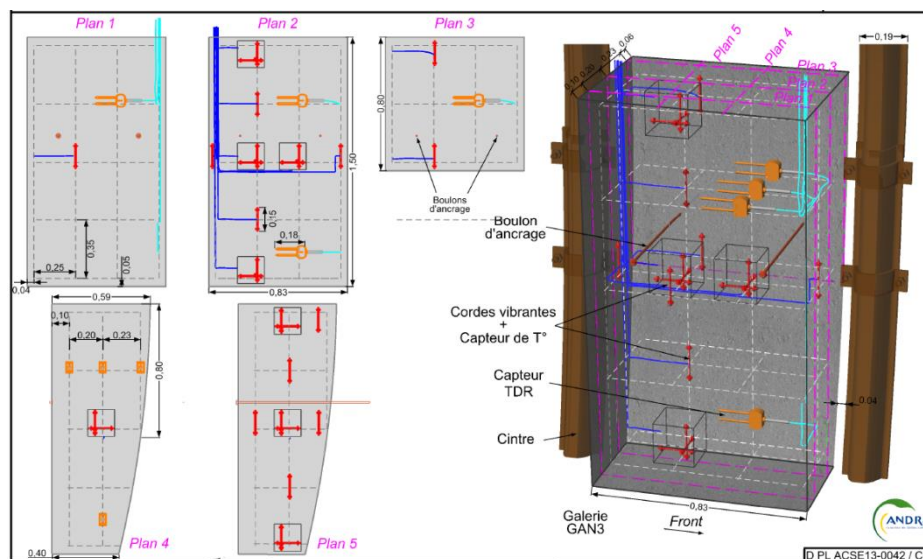


Figure 2: Thick wall geometry and monitoring device display.

2 Observations and acquired data

2.1 Concretes sampling

Samples have been taken from the thin walls to perform chemical and physical analysis. Due to a delay concerning the sampling agenda (in relation to the operations in the URL), no chemical analysis are available yet. However, visual assessments of the concrete samples give no significant evolution/transformation of both concrete at the interface with the Callovo-Oxfordian argillite. This has to be confirmed with microscopic observations. No cracks at a large scale have been detected in both concretes.

At the opposite, the clay host rock appears fractured and impossible to remove with the concrete as a single sample. No particular adherence is noticed. Another sampling technique should be used to remove sound samples with both concrete and clay. The rear of the walls are in contact with the fractured zone surrounding the galleries. Eventhough, prior to casting, the main part of the immediate accessible disturbed host rock has been removed, it remains a significant mechanical disturbed zone. This fractured zone leads to an impossible drilling without any mechanical damages on the clay. The fractured the host rock will be assessed too if possible.

2.2 Concrete monitoring

The mechanical monitoring of the thick walls continue and all sensors are still in operation. Both concrete are then studied, eventhough only results on one formulation are illustrated here.

To assess the physical behaviour of the concrete a significant problem to fix is to calibrate and compensate the sensor to separate what is the consequence of the evolution of the boundary conditions (especially temperature variations) from the concrete evolution. This has been done for the VWS, assessing the reference VWS kept in adiabatic conditions. From the raw data, the physical evolution of the concrete has been corrected from temperature variation in the underground facility to give an overview of the physical evolution.

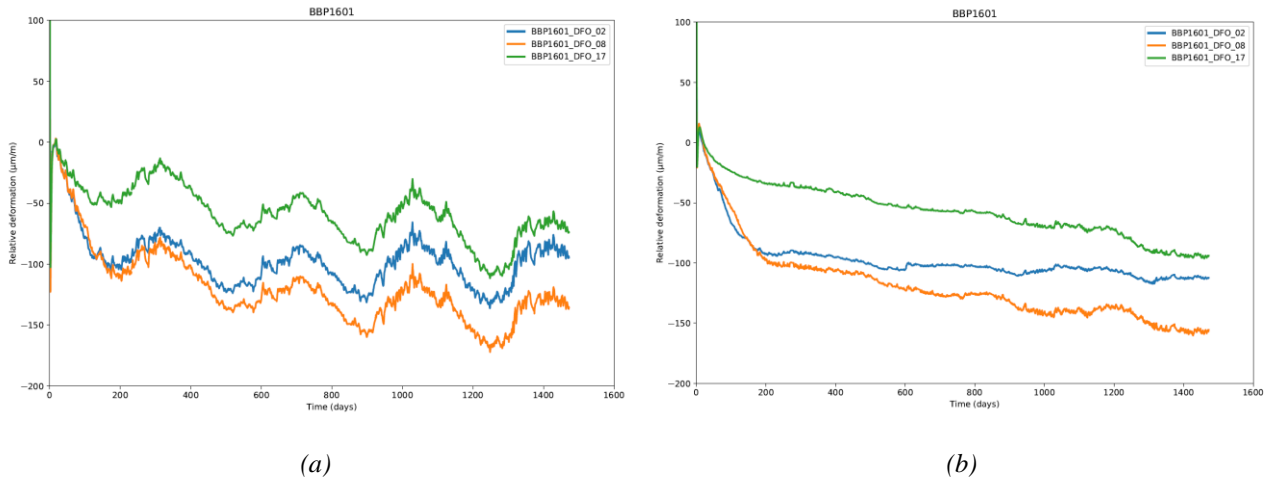


Figure 3: T_{cv} physical evolution (a) raw data; (b) corrected data.

The physical evolution of these “low hydration heat” materials highlight another property regarding the hydration. These materials exhibit a long hydration period (up to few years for a total hydration). What is observed in this case is after a one week thermal transient, few months are still necessary to switch from the hydration period to a “long term” period controlled by the boundary conditions.

Sensors close to adiabatic conditions, as far as possible from any surface, show physical evolutions possible to describe and in accordance with expected behaviour. On the opposite, some of the sensors too close to the surface give unexpected results, impossible to assess.

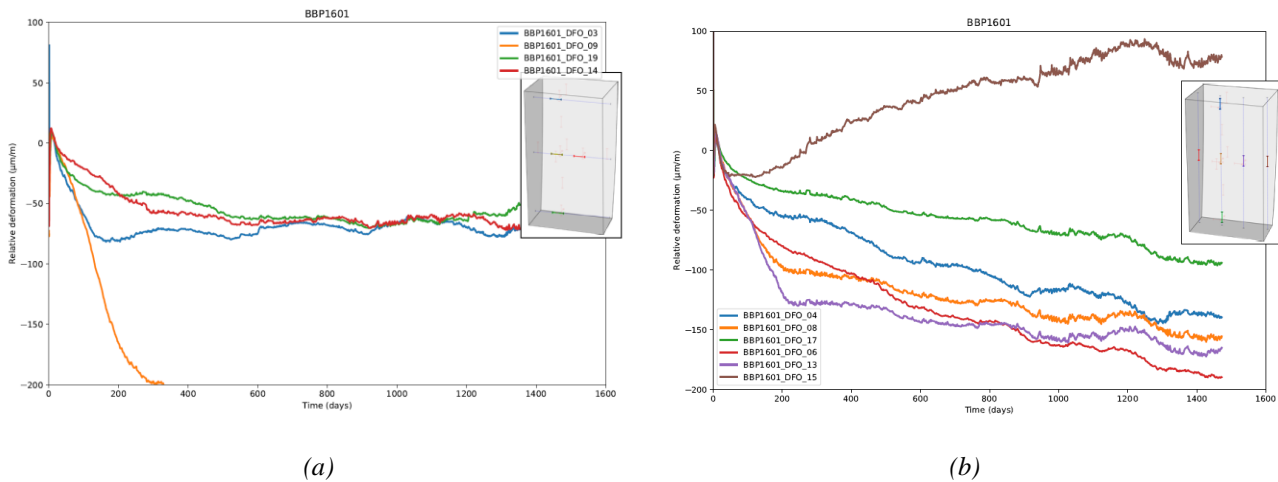


Figure 4: T_{cv} physical evolution (a) horizontal sensors; (b) vertical sensors.

Figure 4 illustrate two different cases:

- Figure 4a: sensor DFO_9 (yellow curve) exhibits a total deformation out of scale compared to the DFO_14 results (red curve). A crack can be at the origin of such an unexpected behaviour. This has to be confirmed;
- Figure 4b: sensor DFO_15 (brown curve) shows an evolution at the opposite of the others. This VWS is close to the surface and close to a steel sliding arch. Probably not placed at the proper depth, this

sensor is too close to the surface and strongly influence by the surrounding materials (steel, atmosphere and clay host rock). It does not represent the behaviour of the concrete.

Precisely taking into account the physical properties of the surrounding materials and their influence remains a key issue to describe properly these evolutions. The “exchange condition” with the atmosphere seems to be easier to quantify than the one for the reinforced (or steel) structures around the tested concrete. Nevertheless, air flow in the galleries could change significantly the boundary condition and then the behaviour of the concrete close to the exposed surfaces. It has to be assessed and taken into account. At present we do not have any information about this parameter. These boundary conditions variations lead to discrepancies between measurements and simulation during setting. Another key issue adding incertitude is the kinetic of hydration of the blast furnace slag in the ternary blend T_L , leading to significant differences between measurements and simulations (close to 20%). The “fly ash” ternary blend kinetic hydration is properly modelled, but measurements to confirm this parameter have to be done for the “slag” ternary blend.

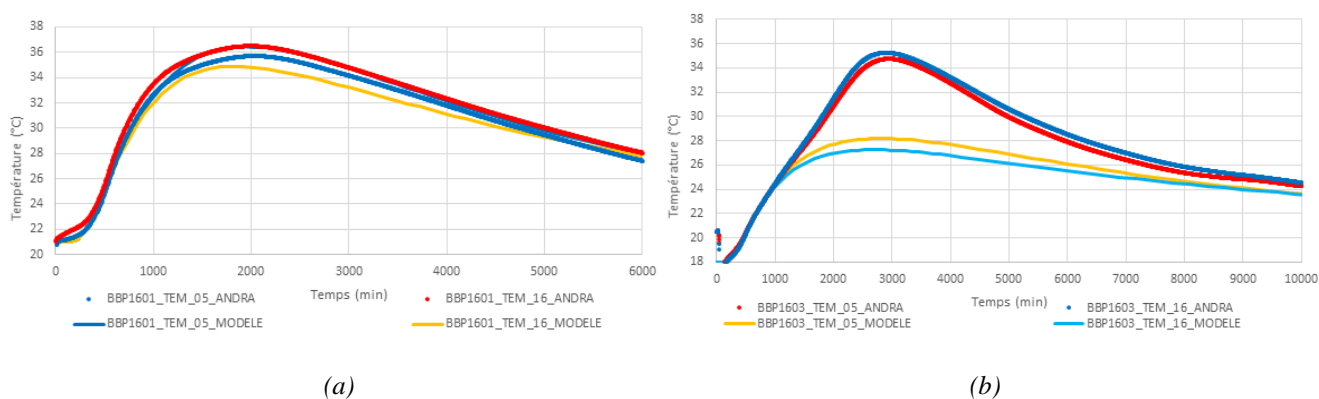


Figure 5: Kinetic of hydration of (a) “fly ash” ternary blend (T_{CV}) and (b) “slag” ternary blend (T_L).

At present, the deformation measured are mainly in relation to the hydric conditions and the water saturation of the concrete, controlled by the geological medium and the atmosphere in the gallery. After few years, the global deformations at large scale exhibit small values in a range of 100-150 $\mu\text{m/m}$. These values are in accordance with the specifications of these materials.

The sensors tested to give the water saturation in the materials remain difficult to use (no validation of the use). Due to a less advanced technology, it is still not possible to assess the water saturation of the concrete with the TDR (Time Domain Reflectometry).

3 Discussion

A first assessment of the physical evolution data gives information about the sensitivity of the sensors and their ability to measure deformations and cracks in these concretes. Even some of them give some “unexpected” results, all the sensors are still operating. The sensitivity of the sensors allows to assess the physical evolution regarding the position of the sensors. This will allow to measure the evolution with the drying of the material with time and to compare the core with the interfaces of these large samples.

Measured temperature are in accordance with lab’scale experiments on these two blended cements. There is a small impact on the temperature evolution at the surface considering the boundary conditions (the maximum temperature reached is not more than 10-12°C higher than the ambient temperature). The temperature elevation

(kinetic and amplitude) is in accordance to what has been measured in other large scale experiments (Bosgiraud et al., 2014). The modelled temperature transient in relation to the hydration of the T_{CV} blended cements is correctly reproduced. Due to the kinetic of hydration of the slag, some discrepancies are still noticed (temperature maximum reached not as high as measured) and need further investigations.

Endogenous shrinkage is in accordance to lab'scale experiments and optimizations realized on the formulation to reach an endogenous shrinkage far bellow 300 µm/m. Considering the main deformation curve in the core of the walls, endogenous shrinkage are close to 150 µm/m. No drying effect of the shrinkage are yet measured, even if the sensors are close to the surface of the walls.

4 Perspectives

The following actions are yet to come:

- Continuing data acquisition and assessment of the THM behaviour;
- Sampling: chemical analysis of the drilled samples to assess the chemical evolution at the interfaces compared to the bulk material.

Acknowledgement

The research leading to these results has received funding from the European Union's European Atomic Energy Community's (Euratom) Horizon 2020 Programme (NFRP-2014/2015) under grant agreement, 662147 – CEBAMA.

J. Olivie and L. Lacarrière, from LMDC (INSA Toulouse), have performed the hydration calculations.

References

- Bosgiraud, J.-M., Foin, R., Bethmont, S. (2014). Full scale demonstration of plugs and seals. DOPAS – WP3. Deliverable 3.11 “Report on FSS cast concrete plug construction”. DOPAS European project 7th european framework, GA#323273.
- El-Bitouri, Y., buffo-Lacarrière, L., Sellier, A., Bourbon, X. (2016). Modelling of chemo-mechanical behaviour of low pH concretes. Cement and Concrete Research, 81, 70-80.
- MODERN (2013). State of Art Report on Monitoring Technology. MODERN European Project n° 232598 D-n° 2.2.2.

Aged interface between Opalinus Clay and low-pH mortar: sample characterization, X-ray computed tomography and core infiltration experiment

Ellina Bernard^{1*}, Andreas Jenni¹, Urs Mäder¹, Simon Reichenwallner¹

¹ University of Bern, Institute of Geological Sciences (CH)

* Corresponding author: ellina.bernard@geo.unibe.ch

Abstract

Transport properties and physico-chemical changes (mineralogy and porosity) at the cement-clay interface are investigated in a laboratory experiment. For comparison, the interfaces between “low-pH” mortar (Portland cement and silica fume binder) and Opalinus Clay (OPA) collected after 3.2 years of interaction in a field experiment are characterised. These samples were recovered during a sampling campaign of the CI Experiment (Cement-Clay Interaction Experiment) at the Mont Terri rock laboratory (St. Ursanne, Switzerland, www.mont-terri.ch).

Experimental devices with a cylindrical sample under confining pressure with independent infiltration under a hydraulic gradient are an excellent way to investigate the reactive transport properties of the system. The analysis of the exfiltrating aliquots that percolated across the aged interface gives the advection-dominated transport properties of a water tracer (D₂O) and anions (mainly Cl), and the bulk hydraulic conductivity according to Darcy’s law. In case of a compound sample including a mortar/claystone interface, a back analysis can be made knowing the individual properties of the undisturbed materials involved.

The porosity of interface samples is usually measured post-mortem and therefore very sensitive to sample preparation (cutting and desaturation which can lead to dislocation of the sample; drying effects; artefacts from epoxy impregnation for stabilisation, etc.). Therefore, computed X-ray tomography (X-ray CT), a non-destructive technology, is a good tool to detect and minimize the artefacts of sample preparation. The macro-porosity and pore geometry may be quantified, but the smaller-scale porosity remains obscured. A sample size of 50 mm diameter and 40 mm height has been chosen to compromise between spatial resolution (for X-ray CT) and ensuring that the representative elementary volume (REV) for reactive transport is much smaller and thus is representative of the overall interface properties.

Physico-chemical properties of the original materials and those recovered after 3.2 years are summarized, as well as the available details of the reaction zone at the interface. The data set is released for WP3 partners for the purpose of reactive transport modelling. New data for the presently on-going core infiltration experiment will be supplemented in an update.

1 Introduction

The safe disposal of radioactive wastes in underground engineered repositories is a critical issue addressed by European countries. The various options to store radioactive wastes in deep geological strata considered in France or Switzerland include the use of large volumes of cementitious materials for infrastructure in contact with

argillaceous rocks, and also cementitious volumes for waste matrix and buffer, depending on waste type and repository design. Clay-based geological barriers have a low permeability which limits the ingress of groundwater and are thus favorable to contain radionuclides (NAGRA, 2002; ANDRA, 2005).

The long-term safety of such a geological repository is ensured by a multi-barrier system where the wastes are embedded in suitable packages (“inert” matrix as glass, concrete, etc.), enclosed by engineered barriers of the underground facility enclosed in the geological environment (host rock). Together they should ensure a very long-term containment of long-lived radionuclides and prevent its release (above safe limits) to the biosphere at any time in the future.

Any chemical interactions that involve materials at the cement-claystone and cement-bentonite interfaces may alter any of the safety-relevant properties of cement/concrete and clay-based materials. Studies conducted on the interaction zone between clayey and cementitious materials systematically highlighted progressive chemical/mineralogical alterations due to the transport and exchange of solutes of both materials (Claret et al., 2002; Cuevas et al., 2006; Gaucher and Blanc, 2006; Fernandez et al., 2009; Garcia Calvo et al., 2010; Gaboreau et al., 2012; Jenni et al., 2014; Dauzères et al., 2016; Lerouge et al., 2017; Mäder et al., 2017).

For a repository in Switzerland, Bradbury et al. (2014) showed that the interfaces between the concrete liner and both the Opalinus Clay and bentonite have a strong tendency to clog after a few thousand years. However, it remains difficult to predict long-term behavior and material properties from short-term experimental data or modeling predictions. The primary objective of the work of this project within CEBAMA is to assess the chemical-physical evolution of the Opalinus Clay adjacent to cementitious materials and to understand the impact of this evolution on safety-relevant properties of rock, including its radionuclide transport and retention properties. Over the last ten years, experimental and modeling work (e.g. within the CI experiment at Mont Terri URL, Mäder et al., 2017) has shown that interactions at cement-clay interfaces start almost immediately upon contact, but progress very slowly. For example, experiments involving 5-year old samples show only up to few mm of reacted materials (Jenni et al., 2014).

The physical, chemical and hydraulic properties of Opalinus Clay have been studied during the last decades (NAGRA, 2002; Pearson et al., 2003). The properties of the cementitious materials as Portland concrete or specific low-pH binders developed for the geological repositories were also studied (e.g. Lothenbach et al., 2012; Lothenbach et al., 2014). However, little is known about the behavior of the interaction zone and its hydraulic properties. Good physical, chemical, and hydraulic data are required to model the experimental observations that are now available for up to 10 years of cement-claystone interaction. Understanding the coupled physico-chemical processes may allow for a more reliable forward modeling prediction.

Experimental devices under confining pressure with independent control of the hydraulic gradient are an excellent way to look at the reactive transport properties of the system. The analysis of the sample aliquots collected in syringes that percolated across the aged interface gives the advective properties of water transport (D_2O) and anion transport (Cl).

The computed X-ray tomography repeated over the experimental duration combined with the core infiltration data allows the follow-up of the chemical modifications (mineralogy and porosity) both spatially and temporally in laboratory experiments.

Usually, a compromise has to be made between specimen size (spatial resolution), acceleration of transport (chemical resolution, experimental duration, and large hydraulic gradients), a focus on solid phase characterization (e.g. X-ray computed tomography) or on recording the mobile phase (e.g. neutron scattering, positron emission tomography, PET). Most detailed characterizations of the solid phase rely on post-mortem

analysis, while the internal evolution of the pore fluid largely remains unresolved. Recent developments in synchrotron techniques also allow highly resolved bulk chemical (μ XRF, X-ray fluorescence) or mineralogical information (μ XRD, X-ray diffraction) to be acquired in tomographic mode, but with limits on sample size and experimental duration (beam time).

It is in this context that intermediate-scale laboratory experiments play an important role in bridging scales, by providing relatively highly-resolved information but in a set-up of sufficient complexity and at relevant boundary conditions. The challenges are manifold with respect to equipment design and analytical techniques, and this is detailed and illustrated below. The upscaling of results from small-scale and short-term experiments is a major issue in transferring system understanding and quantitative modeling of system evolution to the scale of barrier components or an entire repository, and to long time scales of 1,000's to 100,000's of years.

This project plans to use aged interface samples to more directly assess the physical and hydraulic properties via experiments using the core infiltration technique for hydraulic-chemical properties coupled with X-ray computed tomography for pre and post characterisation. Additionally, complementary samples are under preparation for classical scanning electron microscopy and ^{14}C -MMA autoradiography analysis of porosity. Further, an experiment in combinations with positron emission tomography (PET) is planned that allows imaging of the mobile phase.

2 Materials and methods

The interface samples between cementitious materials and Opalinus Clay were obtained from the Mont Terri CI Project, an on-going 20-year project. These samples will be used for core infiltration experiments combined with computed X-ray tomography whereby the hydraulic and chemical effects, both spatially and temporally of the interface can be probed.

2.1 CI field experiment

2.1.1 Description of the field experiment

The CI Experiment (Cement-Clay Interaction Experiment) was installed in 2007 at the Mont Terri rock laboratory (St. Ursanne, Switzerland, www.mont-terri.ch) to study the chemical evolution of different interfaces between clayey and cementitious materials over time. This experiment was planned for at least 20 years and is located in the HE-D niche adjacent to Gallery-98 (excavated in 1998, Mäder et al., 2017). The floor of the gallery and niche is a thick concrete plate (30-60 cm), and shotcrete protects the walls.

One focus of this project was on the behavior of the Opalinus Clay placed in contact with Portland concrete and two “low-pH” binder concretes (ESDRED composition is detailed below) and therefore elucidates a potentially different behavior of the two different concretes at the interfaces. The second focus of the CI experiment was the following of chemical changes at the interfaces between bentonite and the concretes (not addressed within CEBAMA).

After the first sampling campaign to recover concrete/Opalinus Clay interface samples, the boreholes of the second sampling campaign conducted in 2012 were backfilled with Portland and ESDRED pastes and mortars to make available materials not obscured by large amounts of aggregates at the interface that were emplaced originally in 2007.

Existing samples from interfaces between ESDRED mortar and Opalinus Clay drilled 3.2 years after emplacement (third sampling campaign, drilled in 2015) have been selected for this core infiltration experiment carried out under the CEBAMA work plan.

2.1.2 Description of the materials used in the CI project

Opalinus Clay (OPA)

The Opalinus Clay (OPA) had previously been studied in detail (Pearson et al., 2003). The OPA, where the CI experiment is located, consists of approximately 62 wt% clay minerals (24 wt% kaolinite, 20 wt% illite, 10 wt% illite/smectite mixed layers, 8 wt% chlorite). Additionally, 20 wt% calcite, 10 wt% quartz, 3 wt% feldspars, 2 wt% siderite, 1 wt% dolomite/ankerite, 1 wt% pyrite, and < 1 wt% organic carbon were quantified (Mäder et al., 2017). The total porosity was averaged to 16% with a water content of ~6 wt%. The porosity is known to be largely connected and therefore the water content also reflects the total (and connected) porosity.

Table 1: Surface area, density, porosity, and hydraulic properties of the Opalinus Clay studied from (Thury and Bossart, 1999; Pearson et al., 2003; Bossart et al., 2017).

Opalinus Clay (Mont Terri, shaly facies)				
Parameters			Range^a	best estimated
Sample	BWS-A5 (8 m)	BPC-A1 (10 m)		
Grain density (kg/dm ³)	2.743 ± 0.004		2.40 - 2.53	2.45
Bulk dry density (kg/dm ³)	2.30 ± 0.01			
Specific surface area (m ² /g)	24 ± 1			
Porosity (vol%)	16	16.5	13-21	16
Water content (wt%)		6.8	5.0 - 8.9	6.6
Effective diffusivity (m ² /s)				
Tritium (HTO)	1 · 10 ⁻¹¹	(normal to bedding)	7.1 · 10 ⁻¹² - 1.1 · 10 ⁻¹¹	1 · 10 ⁻¹¹
	3 · 10 ⁻¹¹	(parallel to bedding)	5 · 10 ⁻¹¹ - 6.8 · 10 ⁻¹¹	5.4 · 10 ⁻¹¹
I ⁻	3 · 10 ⁻¹²	(normal to bedding)	2.3 · 10 ⁻¹² - 4.2 · 10 ⁻¹²	3 · 10 ⁻¹²
	8 · 10 ⁻¹²	(parallel to bedding)	1 · 10 ⁻¹¹ - 3 · 10 ⁻¹¹	2 · 10 ⁻¹¹
Hydraulic conductivity (m/s)	3.2 · 10 ⁻¹⁵ to 5 · 10 ⁻¹³ ^b	2.1 · 10 ⁻¹³	2 · 10 ⁻¹⁴ - 1 · 10 ⁻¹²	2 · 10 ⁻¹³

^a latest summary in (Bossart et al., 2017)

^b values measured between 1996 and 1997

ESDRED mortar

The ESDRED cement is a binary blend of 40% silica fume with 60% CEM I 42.N with a w/b equal to 0.5. Note that adding a significant amount of silica fume leads to poor workability and thus, to a heterogeneous mix during sample preparation (agglomerated silica fume particles and a macro-porosity). Therefore, superplasticizer and accelerator have been added to this mix to reach correct workability; details are given in Table 2.

Table 2: Composition of the ESDRED mortar placed in the field in 2012 (Jacobs, 2012); the water permeability tests after 3.4 years have been performed on the core collected during the 3rd campaign in 2015, the tests were performed on 3 samples and a mean value is given (Jacobs, 2015).

material/property	unit	ESDRED Mortar
Cement CEM I 42,5 N Holcim	kg/m ³	495
SikaFume HR7 TU	kg/m ³	332
Superplasticizer ACE 331 BASF	kg/m ³	9.7
Accelerator Sigunit - L53 AF, Sika	kg/m ³	40
water	kg/m ³	411
w/c-ratio	kg/m ³	0.8
w/b-ratio	kg/m ³	0.5
sand 0.1/0.3 mm Bernasconi	kg/m ³	573
Backfill density	kg/m ³	1,860
<i>Test after 3 years</i>		
water permeability	10 ⁻¹⁷ m ²	23
standard deviation		36
wet density	kg/m ³	1,970
Porosity	%	31

2.1.3 Location of the sample

The ESDRED mortar and Opalinus Clay interface chosen had been recovered in a physically and chemically undisturbed state and corresponded to the bottom interface of the ESDRED mortar installed in 2012 and collected during the 3rd campaign in 2015 at approximately 2.7 m depth as schematically shown in Figure 1 (Borehole BCI-12).

The sample of current interest was 3.2 years old when put under vacuum in a plastic bag to be stored at 7°C. The storage of this interface should have kept the water content and relative humidity constant inside both materials. Reaction progress at the interface may have proceeded during storage and may correspond actually to a longer stage of interaction than 3.2 years.

Similar interfaces from an earlier campaign including ESDRED concrete had previously been chemically characterized (e.g. Jenni et al., 2014; Mäder et al., 2017).

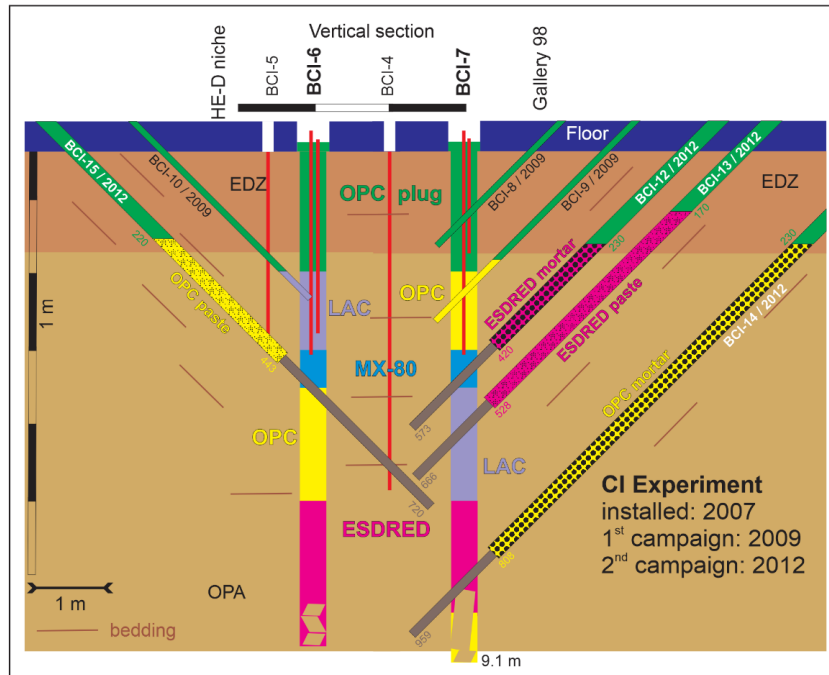


Figure 1: Setup of the CI Experiment drawn to scale with the distribution of concrete sections and bentonite in two vertical piles, and monitoring boreholes (red). Sampling boreholes inclined at 45° are shown for the 2009 1st sampling campaign (BCI-8 to BCI-10) and the 2012 2nd campaign (BCI-12 to BCI-15, telescoped) with boreholes back-filled with paste and mortar. EDZ: approximate excavation-disturbed zone below the gallery; OPA: Opalinus Clay; OPC: ordinary Portland cement concrete; LAC, ESDRED: low-pH concrete; MX-80: bentonite section. The sampling boreholes are not all in the same plane of view but are projected.

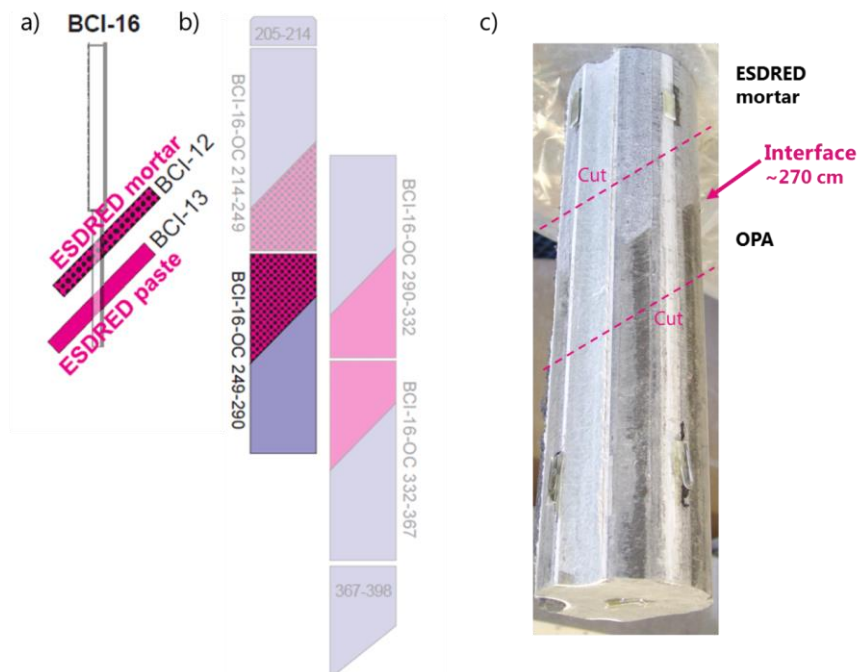


Figure 2: a) Schematic of the geometry of the ESDRED material/OPA interface recovered from the 3rd sampling campaign (BCI-16, in 2015), b) bottom ESDRED mortar/OPA core chosen (BCI-16 OC 249-290), and c) location of the interface for the CEBAMA project on the specific core chosen (BCI-16-OC 249-290). Numbers refer to depth in cm along the borehole axis.

2.2 Sample preparation

First, we have cut the BCI-16-OC 249-290 core, as detailed in Figure 2c, to isolate the interface with 5 cm of OPA and ESDRED mortar on each side. Then, a fast-setting epoxy resin was directly put on the mortar face (few millimeters) while the OPA side was encased with 1 - 1.5 cm of epoxy Sikadur 52™ as shown in Figure 3 to protect the sample from carbonation or change of relative humidity and to provide physical strength for further cutting and drilling.

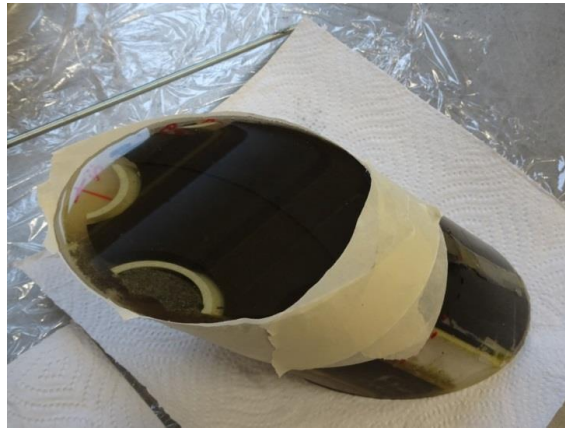


Figure 3: Partial BCI-16 core containing the bottom interface (~270 cm) in still liquid Sikadur-52™ epoxy resin.

To get a well-preserved interface in a core of 50 mm in diameter without dislocations, we adopted a similar technique than the one adopted during the field core recovery. This consisted of emplacing six parallel fiberglass reinforcements into boreholes arranged circularly. The geometry in the laboratory, much smaller, corresponded to 8 mm boreholes filled with 5 mm carbon fiber tubes embedded in Sikadur 52™ epoxy resin. The selected position to get the best of the interface (large amount of OPA and ESDRED mortar on each side) without the fiberglass reinforcements is shown in Figure 4. The coordinates of the future 6 fiberglass holes were initiated (few millimeters) on epoxy resin on a milling machine; then, the 8 mm holes were drilled manually with a core drill stand as shown in Figure 5, operated with air cooling. The different steps and the final stage of stabilization are detailed in Figure 6.

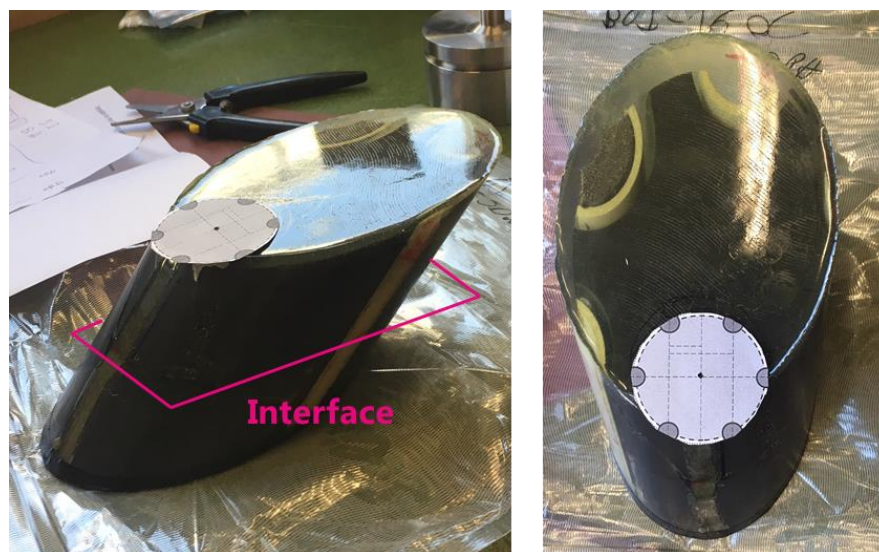


Figure 4: 52 mm diameter core location and positions of the 8 mm stabilization cores.

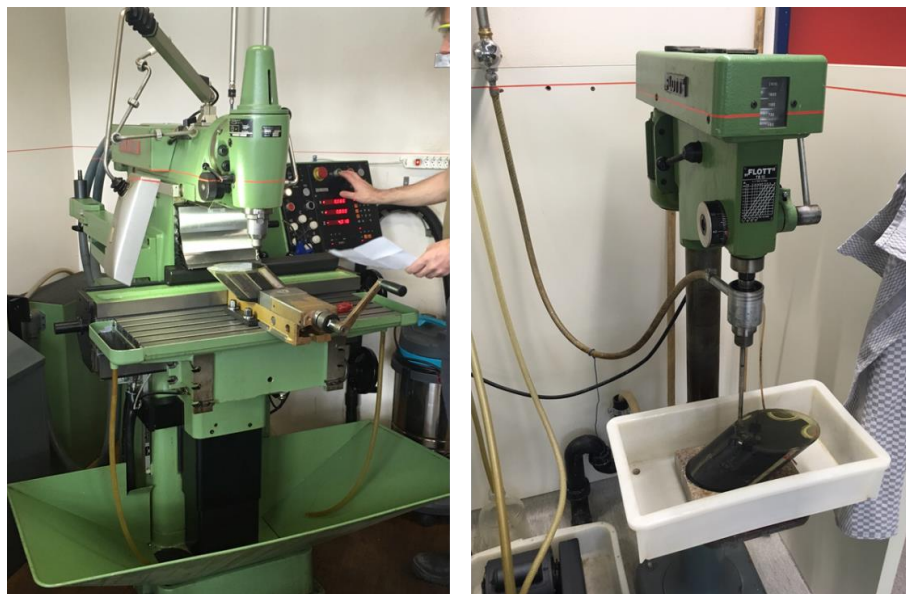


Figure 5: Left: milling machine to place the coordinates on the epoxy; right: core drilling machine operated in dry mode to drill 8 mm cores.



Figure 6: Top, at left: coring of the 8 mm holes for stabilization; at right: injection of Sikadur 52TM epoxy in the fiberglass reinforcements placed in the boreholes. Bottom: after stabilization.

Finally, after 3 days, the stabilization of the 52 mm core was slowly dry drilled as described in Figure 7. The interface is nicely located in the middle of the core as shown in Figure 8. The bedding of the OPA is parallel to the interface, some defects can be observed by eye related to brittle fractures. However, the interface seems well conserved without dismemberment or fractures in the interaction area. The sample was wrapped with masking tape shortly after cutting to avoid any change in the relative humidity of the material or any chemical changes.



Figure 7: Core drilling machine in dry mode for drilling 52 mm cores.

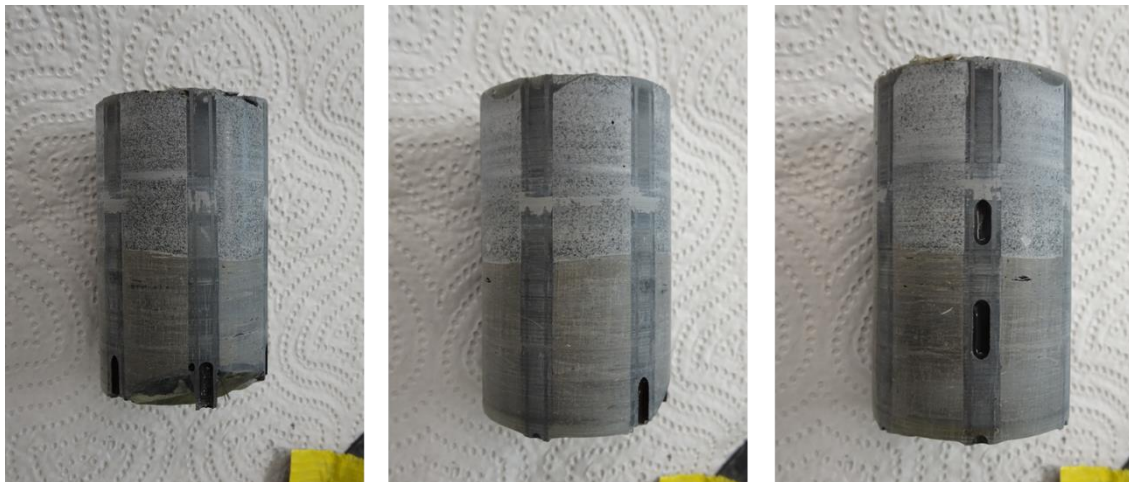


Figure 8: Three sides of the core sample (ESDm_OPA_3_IF3) just after dry cutting. Gas voids are located in the carbon fiber tubes that were not completely filled with resin.

2.3 Core infiltration experiment

To look at the reactive transport properties of the system, the method of advective displacement through a triaxial-type cell (Mäder, 2018) under confining pressure with independent control of the hydraulic gradient is a good option and has been adopted in this study. Triaxial testing equipment is widely used in rock and soil deformation studies whereby a hydrostatic confining pressure (total stress) is imposed on a cylindrical sample, and axial/radial displacement and load are controlled; see (Mäder, 2018) for more details of the setup. Here, we operate the test at constant and a fixed sample length, e.g. without deformation.

2.3.1 Description of the setup

A rigid steel cylinder as pressure vessel used for example in Mäder (2018) is opaque to X-rays and cannot be used for monitoring by CT during the progress of an experiment. A compromise for our experiment is that we examine the sample only before and after the core infiltration experiment by CT, but obtain a continuous record of the hydraulic behavior, and information on chemical evolution by sampling aliquots. Postmortem analysis (mineralogy, porosimetry) may be performed for a more detailed analysis, if desired.

The characteristics of the cylindrical sample are detailed in Table 3. After measurement of the characteristics, the sample was mounted between two POM adapters and separated by a PEEK filter fabric with an additional small filter of CFK placed at the inlet and outlet of the PEEK capillary connections as shown in Figure 9. The adapters and filters were required to distribute and collect the in-flow and outflow to and from a sample.

Table 3: Initial characteristics of the OPA/ESDRED mortar interface sample (ESDm_OPA_3_IF3) for the infiltration experiment.

height (mm)				average
43.7	43.8	43.6	43.7	43.7
OPA diameter (mm)		ESDm diameter (mm)		average
51.9	51.9	51.9	51.9	51.9
OPA height (mm)				average
max	16.3	min	12.7	14.5
masse of the sample (g)			188.24	

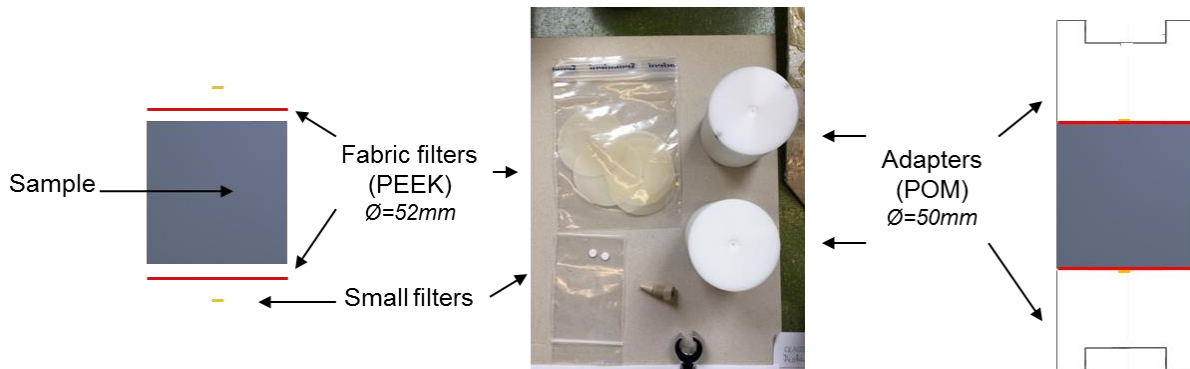


Figure 9: Schematic of the core sample assembly (sample + filters + adapters).

The sample core is isolated from the confining medium (water) by a Teflon membrane (chemical isolation) and an outer latex rubber sleeve (hydraulic barrier). The column reactor allows the application of a hydraulic confining pressure on the sample without transferring confining water to it. The Teflon layer covers the transition to filter and adapter, and the rubber sleeve is additionally sealed with silicone to the adapter to provide a good initial seal.

The core assembly (sample + adapters described in Figure 9) is coupled to inserts and mounted in a pressure vessel (depicted in Mäder, 2018). A spindle is used to adjust to the length of the core assembly and provides the axial confinement (fixed length). The system is self-sealing once the confining pressure is stepped up. Pressure is

quasi-isostatic, with the axial load exerted by the adapters somewhat reduced compared to total stress by a small area where the adapters connect to the inserts. The confining pressure is best generated in a water/argon separation cylinder that also provides effective compensation for changes in laboratory temperature. Such systems can maintain stable pressures for years without control.

PEEK capillary tubes of 1/16" OD (outer diameter) are fed to the surface of the filter and are sealed and held in place by compression fittings. A fluid of the desired composition is injected on one side for driving advective flow, and the outflow is collected on the other side. It is best to use helium for pressurizing a supply tank and drive fluid flow in this manner at constant pressure during long-term experiments with low-permeability media. Helium is the gas of choice because of its low solubility and low pressure-dependence of solubility to avoid de-gassing phenomena. The mass flow rate is determined at each sampling time, and an accurate hydraulic conductivity can be calculated for the sampling period according to Darcy's law.

Sample collection at ambient pressure is easiest done by syringes, and this also provides good sample protection from atmosphere and evaporation, a requirement when using water isotopes as tracers, for example. A small back pressure is exerted by the friction of the plunger seal, and this friction is approximately known.

2.3.2 Artificial Opalinus Clay pore water used

A recent internal report from the Mont Terri CI experiment with the analysis of the Opalinus Clay pore water (Mäder, 2017) gives a composition for relatively undisturbed OPA pore water from exactly this location where also the interface samples were recovered. This report complemented earlier long-term experiments on the OPA pore water at Mont Terri. Several small aliquots were collected between January and July 2016 from a closed-in sampling interval after 10 years of equilibration time.

The measured pH (at 24°C), alkalinity and ion concentrations are summarized in Table 4. The alkalinity corresponds to the CO₂ partial pressure of the OPA in-situ. The calculated speciation (phreeqc, default TDB) and saturation indices indicate supersaturation of the carbonate minerals due to outgassing of CO₂ and coupled increase in pH during sampling and sample storage. The aliquots are at celestite saturation and somewhat supersaturated with respect to quartz for reasons not known.

Table 4: Measured pH (at 24°C), alkalinity and ion concentrations measured in the samples CI-4-A, CI-4-B and CI-4-C.

number	pH	Alkalinity meq/L	Na mmol/L	K	Ca	Mg	Sr	Cl	S(6) as SO ₄	description
1	7.85	2.33	231.3	1.3	14.6	15.6	0.5	256.8	13.1	CI-4-A
2	7.88	2.30	238.9	1.4	15.2	16.2	0.5	271.9	13.9	CI-4-B
3	7.16	2.33	240.2	1.4	15.1	16.0	0.5	271.0	14.0	CI-4-C

To keep it simple, the artificial pore water (APW) was back-calculated to calcite-dolomite saturation in equilibrium with the atmospheric CO₂ pressure and was only composed of salts (Na⁺, K⁺, Sr⁺, Ca²⁺, Mg²⁺, Cl⁻, HCO₃⁻, SO₄²⁻). The additions of starting materials are listed in Table 5 (nominal composition). The composition was modelled with phreeqc in similar fashion as used for modelling the reference pore water compositions for the safety case (Mäder, 2009). Finally, deuterium (D₂O) was added to the APW as a tracer. The actual artificial pore water will be soon analyzed.

Table 5: Salts used in the artificial pore water.

	NaCl	NaHCO ₃	CaCl ₂ ·2H ₂ O	KCl	MgCl ₂ ·6H ₂ O	Na ₂ SO ₄	SrCl ₂ ·6H ₂ O	D ₂ O
g/L	12.393	0.044	2.134	0.108	3.337	2.018	0.131	~ 0.035

2.3.3 Pressure/temperature measurements and liquid analysis

The temperature of the confined cell, the confining pressure, and the injection pressure are monitored every minute. The collected outflowing fluid is sampled in normal O-ring fitted syringes. The temperature was not regulated but the laboratory ambient temperature (20-23°C) is stable, with less than +/- 0.5 K diurnal fluctuations, and not more than +/- 2 K of seasonal variation over an extended time period.

The Electric Conductivity (EC) is measured in-line with a very small-volume flow-through cell such as used in ion chromatography equipment. The pH, stable water isotopes, and the ion concentrations of the collected fluid are measured after sampling 1.5 to 2 mL. The pH is measured with a Ross semi-micro pH electrode with an Orion meter and the ion concentrations will be measured with equipment as detailed in Table 6.

Table 6: Parameters and equipment used for analysis, from (Mäder, 2017).

Parameter	Method	Equipment
Anions: F, Cl, Br, SO ₄ , NO ₃	Ion chromatography	Metrohm ProfIC AnCat MCS Column: ASupp7-250
Anions: I, S ₂ O ₃	Ion chromatography	Metrohm ProfIC AnCat MCS Column: ASupp5-150
Cations: Na, K, Ca, Mg, NH ₄	Ion chromatography	Metrohm ProfIC AnCat MCS Column: C4-150
Minors: Sr, Ba, Si, Al	ICP-OES	Varian 710 ES
Minors, centrifuge-filtered: Sr, Si	ICP-OES	Varian 710 ES
LMWOA: formate, acetate, lactate, propionate	Ion chromatography	Metrohm ProfIC AnCat MCS Column: ASupp7-250
Total alkalinity	Titration	Metrohm Titrino DMP 785
TOC (NPOC)/TIC	Combustion NDIR	Analytic Jena NC2100S
Stable isotopes: $\delta^{18}\text{O}$, $\delta^2\text{H}$ (VSMOW)	CRDS (*)	PICARRO

(*) CRDS: cavity ring-down spectroscopy

The recording of the (partial) breakthrough of the D₂O and Cl in the collected syringes will be used to derive water transport and anion transport parameters.

2.4 SEM/EDS analysis

A sample of the ESDRED mortar / OPA interface was studied in collaboration with a study directed at applying synchrotron X-ray micro-diffraction to alteration assemblages in 2017 (Fisch et al., 2017). The sample was vacuum-impregnated for stabilization and prepared by an elaborate technique on a very thin optical glass slide. The method of X-ray micro-diffraction and the data evaluation are not part of this project, and only some key findings are adopted here at face value.

The uncoated sample surface was examined in a scanning electron microscope (SEM, Zeiss EVO-50 XVP) equipped with an EDAX Sapphire light element detector in low vacuum mode (10 Pa) with a beam acceleration of 20 kV and a working distance of 8.6 mm. The beam current was adjusted to yield a dead time of 10-20%. Element dispersive spectroscopy (EDS) maps with 512 x 400 pixels were acquired using a dwell time of 200 μ s, and frames were averaged for 8-12 h. Higher resolution maps (1,024 x 800 pixels), but lower dwell time were used to acquire backscatter electron (BE) images, which depict the average proton number at beam location. Brightness and contrast of the maps were adjusted to reveal gradients within cement or clay matrix, often resulting in over- or under-saturation (in grey-scale) of phases of no interest. Exploring precision of the SEM stage movement, electron beam stability, and image distortion, smaller maps and BE images were also acquired and assembled. The best quality micrographs are shown in this report, but they are consistent with micrographs acquired with alternative settings, at different locations, or on different samples.

2.5 X-ray diffraction

Conventional XRD patterns were measured on sample surfaces parallel to the interface at different distances from it, in both OPA and mortar. An approximately 4 cm cube containing the interface was ground to expose the surfaces to be analysed. Diffraction data were collected with a PANalytical X'Pert Pro MPD diffractometer, equipped with a Cu X-ray source and an X'Celerator detector, from 4 to 70° 2 θ with a total integration time of 80 s per step. Automatic divergence slits (9 mm irradiated length) and 0.02 radian Soller slits were used. Prior to qualitative data evaluation, all diffraction patterns were converted to "fixed slit" data with PANalytical HighScore Plus v.4.6.1. After each exposure, the sample surface was ground and an appropriate amount of sample thickness was removed to produce an XRD data stack with a relatively good spatial resolution for a bulk method.

More detailed spatially resolved μ XRD measurements were performed on two synchrotron facilities. An ultrathin section perpendicular to the interface containing up to 3 mm of OPA and mortar was measured in transmission mode with a beam of 15 to 100 μ m in diameter. The resulting 2D diffraction patterns of each point of the μ XRD map were integrated to 1D. Rietveld quantifications of these patterns or main peak intensities were used to generate phase distribution maps. More details can be found in Fisch et al. (2017).

2.6 Computed Tomography

2.6.1 Nanotomograph X-ray CT and software

The computed X-ray tomography (CT) was performed at the University of Fribourg, Department of Geosciences, with a latest-generation Bruker Skyscan 2211 Multi-Scale nano-CT instrument. Imaging was performed with a flat panel detector (6 Mp). Data were reconstructed with Bruker InstaRecon software optimized for GPU support. Data analysis and visualization were performed with Dragonfly 3.1 software (academic license).

2.6.2 X-ray CT characteristics of OPA and mortar

The identification of the OPA by X-ray CT is relatively easy, marked by bedding and especially abundant pyrite. The micro-porosity of the clayey materials (associated with illite/smectite) is not visible by X-ray CT. The pyrite (high X-ray absorbance) results in light grey (white) voxels while the larger-scale porosity, usually cracks (filled by air, epoxy or water) are darker than the OPA matrix. The ESDRED mortar contains multiple large former gas pores homogeneously distributed, and the fabric differs greatly from the OPA.

3 Results

3.1 Microscopical, chemical, XRD, and Micro-XRD characterisation

The aim of this preliminary evaluation of the SEM/EDS data is to provide the scale of interaction and its major characteristics. Data presentation is in form of element distribution maps for an identical sample area. Some select micro-diffraction maps are also included as smaller overlays on the element maps.

3.1.1 Optical microscopy

The optical micrograph (Figure 10) displays the quartz grains in the mortar as well as the presence of some large agglomerates of silica fume that did not fully disperse during mortar mixing and that also not fully reacted to form hydrate phases. Cracks in the OPA are enhanced or newly formed due to sample drying and are subparallel to bedding. The interface is well preserved and lacks mechanical disturbances.

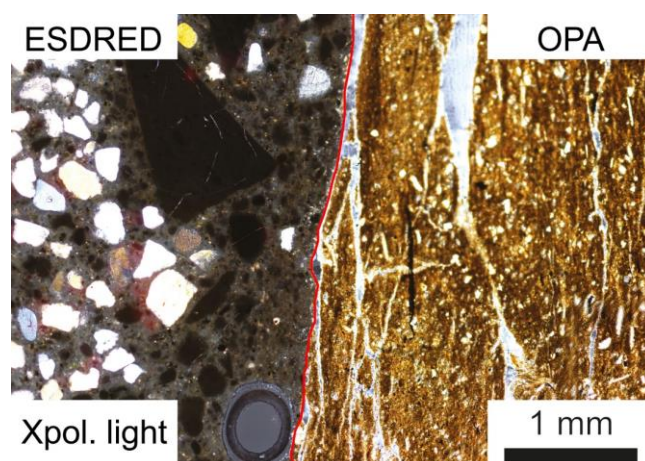


Figure 10: Optical microscopy (crossed polarized light) of the ESDRED mortar (left) - OPA (right) thin section. The interface is indicated with the red line. Large triangular aggregate in the mortar is unreacted silica fume.

3.1.2 SEM/EDS analysis elemental distribution maps

Element distribution maps are included for calcium (Figure 11), magnesium (Figure 12), sulfur (Figure 13) and silicon (Figure 14). Each image is a composite of a BSE image (back-scattered electrons) covering the entire area and a narrower insert of the respective element map. Each element map is a composite of smaller images, merged automatically by software, with sometimes changes in the intensity level evident along the sub-map boundaries.

A reaction zone is most prominently seen in the magnesium map (Figure 12) where an enrichment is seen on both sides of the interface. It is approximately 200-250 μm wide on the mortar side and 100-150 μm on the OPA side. A moderate sulfur enrichment is seen (Figure 13) between about 200-900 μm from the interface in the cement paste of the mortar. Calcium is relatively depleted in the cement paste towards the interface (Figure 11) for a zone of approximately 800 μm width compared to the mortar matrix at depth. The silicon map is fairly uniform (Figure 14) but does show somewhat brighter grey values near the interface (1.5 mm) compared to the matrix away from it. Additionally, the silicon map highlights the absence of sand (quartz grain) or amorphous silica aggregate in the 0.2 mm close to the interface.

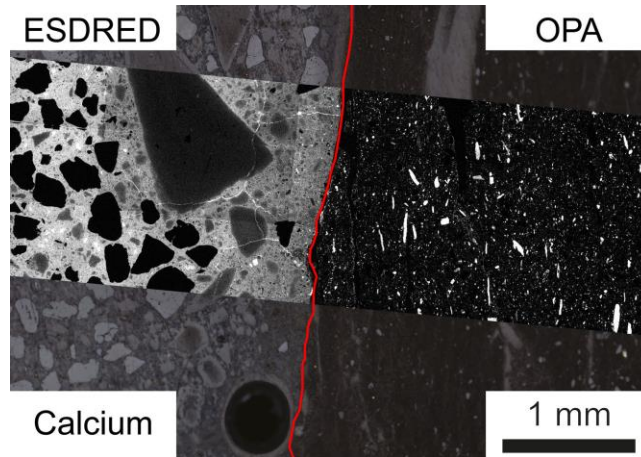


Figure 11: SEM/EDS analysis, elemental distribution of calcium on the ESDRED mortar (left) - OPA (right) thin section. Brighter areas represent higher elemental abundance. The interface is indicated with a red line.

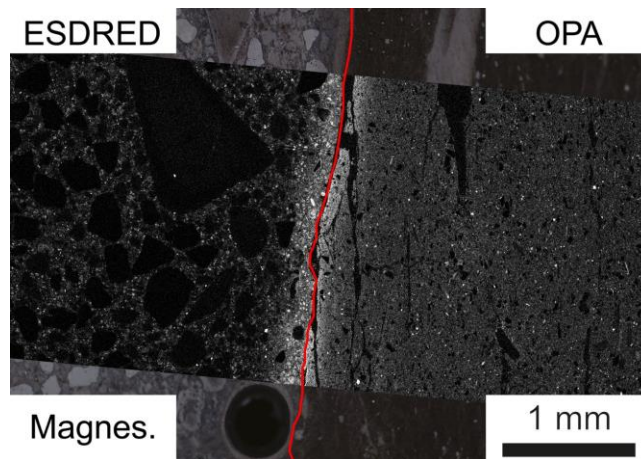


Figure 12: SEM/EDS analysis, elemental distribution of magnesium on the ESDRED mortar (left) - OPA (right) thin section. Brighter areas represent higher elemental abundance. The interface is indicated with a red line.

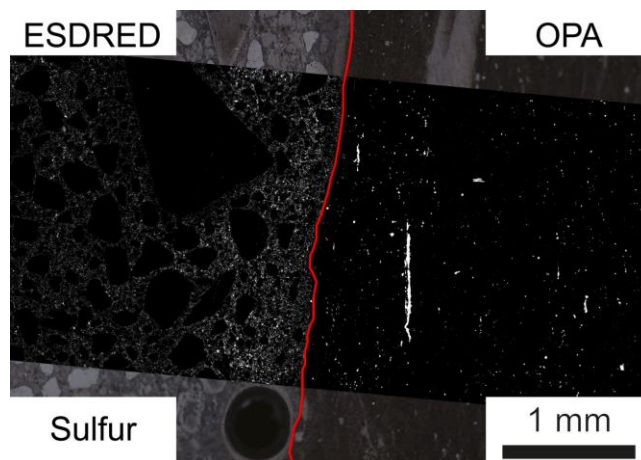


Figure 13: SEM/EDS analysis, elemental distribution of sulfur on the ESDRED mortar (left) - OPA (right) thin section. Brighter areas represent higher elemental abundance. The interface is indicated with a red line.

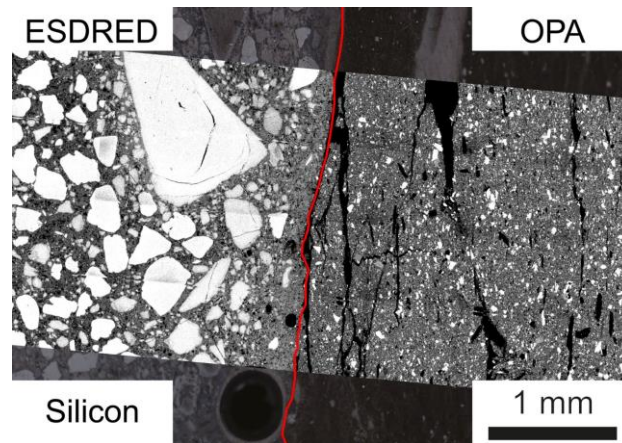


Figure 14: SEM/EDS analysis, elemental distribution of silicon on the ESDRED mortar (left) - OPA (right) thin section. Brighter areas represent higher elemental abundance. The interface is indicated with a red line.

3.1.3 Conventional X-ray diffraction patterns

The XRD patterns measured at different distances from the interface in each material are shown in Figure 15. Far from the interface (19 mm), the OPA pattern exhibited the characteristic reflection of the major minerals as illite (and illite/smectite), kaolinite, calcite, and quartz. The observation of the other minor minerals was difficult. The patterns recorded at 5 and 7 mm from the interface and directly adjacent to the interface were very comparable to the undisturbed OPA observed at 19 mm except for the pattern at 7 mm which showed an asymmetric broad hump located at $\sim 19^\circ 2\theta$. The patterns of the ESDRED directly adjacent to the interface and close to it (0.15 mm) contained illite and kaolinite. This indicates that some OPA was also exposed by grinding the ESDRED side and approaching the uneven interface with OPA. However, at 1.1 mm away from the interface, none of the minerals characteristic of the OPA were observed. Far from the interface (9 mm), C-S-H with broad reflections related to their nano-size (Allen et al., 2007; Skinner et al., 2010; Haas, 2012; Roosz et al., 2015) at 29.2 and $32.0^\circ 2\theta$ (Lothenbach et al., 2015) were observed. Additionally, ettringite and maybe monosulfate were potentially detected. Only C-S-H was seen closer to the interface until 0.15 mm. Nevertheless, C-S-H could not be detected at the interface due to its absence, but possibly due to the overlapping with a main peak characteristic of calcite. Calcite was observed at the interface and further away with the main reflections at 29.5 and $39.4^\circ 2\theta$. Some of the calcite at the interface and at 0.15 mm is coming from the OPA, as are traces of illite or kaolinite. However, the depth of calcite formation in the ESDRED is larger than the perturbation of the analysis by the OPA. In this case, the calcite would be formed in-situ, from the decalcification of the C-S-H phase as already established in literature (Jenni et al., 2014; Dauzères et al., 2016; Lerouge et al., 2017; Mäder et al., 2017).

Nevertheless, the calcite is absent further away from the interface. The intensity of the reflection peaks associated to the quartz was largely increasing from the interface to the sound ESDRED mortar confirming the low content of sand close to the interface observed by SEM/EDS (Figure 14).

At the so-called ESDRED interface side, no C-S-H or cement phases were detected. Major minerals from OPA, and a large amount of the same nano-crystallite type were detected with an asymmetric broad hump located at $\sim 19^\circ 2\theta$ similar to the one observed in the OPA at 7 mm. Described in literature (Jenni et al., 2014; Dauzères et al., 2016; Lerouge et al., 2017; Mäder et al., 2017), one characteristic of ESDRED mortar deterioration in contact with OPA is the magnesium enrichment at the interface observed by SEM in this study (Figure 12). This enrichment of magnesium at the interface in cement paste was attributed to the precipitation of magnesium silicate hydrate (M-S-H). This phase recently studied has a variable Mg/Si ratio and a layered structure like a phyllosilicate. M-S-H was compared to deweylite by Bish and Brindley (1978), a naturally occurring hydrous

amorphous magnesium silicate with a composition between $\text{Mg}_3\text{Si}_4\text{O}_{10}(\text{OH})_2 \cdot 0.3\text{--}0.7\text{H}_2\text{O}$ and $\text{Mg}_3\text{Si}_2\text{O}_5(\text{OH})_4 \cdot 0.3\text{--}0.7\text{H}_2\text{O}$ (Bernard et al., *submitted*). This is an extremely fine-grained or disordered talc-like or stevensite-like mineral, possibly mixed with minerals from the serpentine group such as lizardite or antigorite. Anyhow, the characteristic pattern of this synthetic nano crystallite neo-formed magnesium silicate hydrate has his highest reflection peak at $\sim 19.5^\circ 2\theta$ (002 and 020 reflection) (Bernard et al., *submitted*).

Surprisingly, no hump characteristic of the neo formation of a hydrated magnesium silicate phase in the OPA at the interface could be observed at the place where a magnesium enrichment was observed by SEM (Figure 12). One may say that the sample “ESDRED interface” was actually exposed to the magnesium rich OPA and the “OPA interface” is located a bit further away of the interface. This magnesium enrichment could be caused by the precipitation of nano-crystalline hydrated magnesium silicate.

Finally, a smaller hump located at $\sim 19^\circ 2\theta$ was also observed at the 7 mm from the interface in the OPA. But no magnesium enrichment was confirmed by SEM/EDS as it was for the OPC/OPA interface (Mäder et al., 2017).

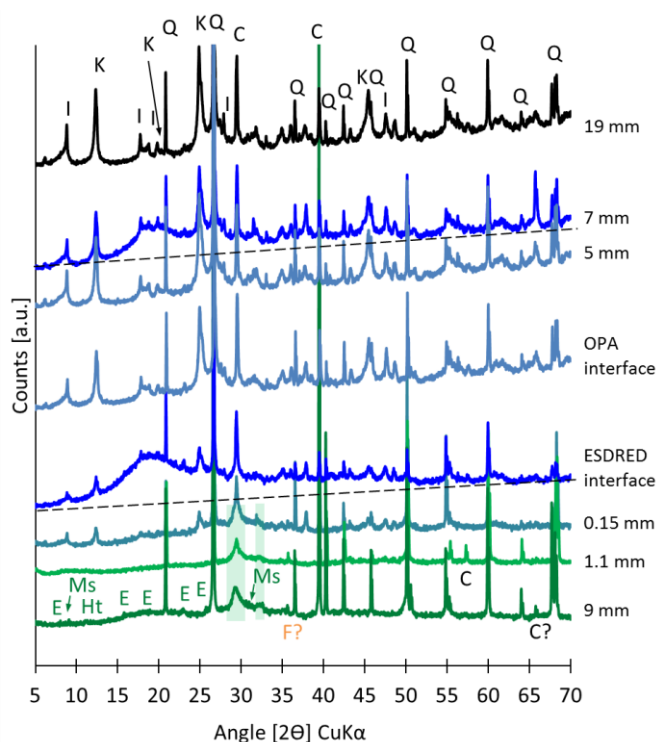


Figure 15: XRD patterns of the slices in OPA at the interface, at 5, 7 and 19 mm away of it, and in the ESDRED mortar at the interface, at 0.15, 1.1 and 9 mm away from of it. C = calcite, Q = quartz, I = illite, K = kaolinite, E = ettringite, Ms = monosulfate, F = Fe_2O_3 .

3.1.4 μ -XRD maps of phases

The X-ray diffraction maps for calcite (Figure 15), calcium-silicate-hydrate (C-S-H) (Figure 16) and hydrocalumite (Figure 17) are included below. These patterns were evaluated with a Rietveld-like method and the approximate mineral abundance is color-coded.

Calcite is shown to be enriched near the interface on the mortar side (Figure 15). C-S-H is relatively evenly distributed, just depleted right at the interface (Figure 16). Hydrocalumite is an AFm-type layered double hydroxide phase (part of hydrotalcite super-group of phases), essentially a Ca-aluminate hydrate with extensive

substitutions for cations and especially also for anions. This phase usually present in the cement phase is confirmed further away from the interface in the unaltered cement (Figure 17). However, its distribution is seen to be largely absent within 1 mm from the interface due to a lower pH.

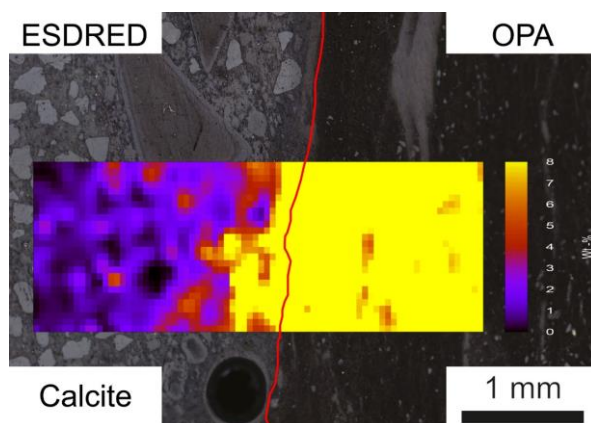


Figure 16: Semi-quantitative μ -XRD distribution map (SNBL data) of calcite on the ESDRED mortar (left) - OPA (right) thin section. Brighter areas represent higher abundance. The interface is indicated with the red line.

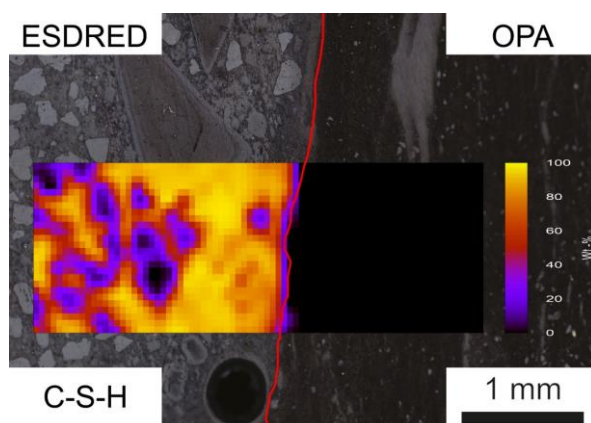


Figure 17: Semi-quantitative μ -XRD distribution map (SNBL data) of C-S-H on the ESDRED mortar (left) - OPA (right) thin section. Brighter areas represent higher abundance. The interface is indicated with the red line.

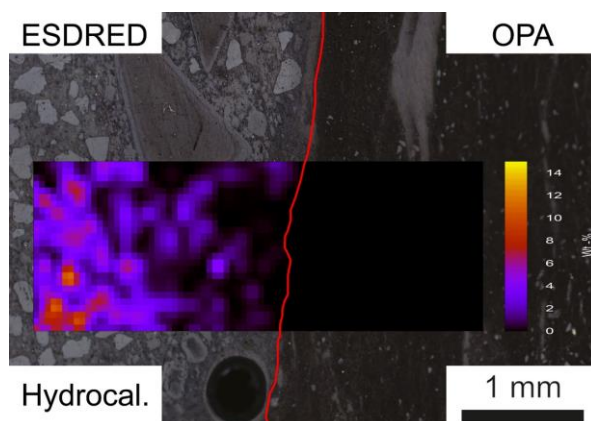


Figure 18: Semi-quantitative μ -XRD distribution map (SNBL data) of hydrocalumite on the ESDRED mortar (left) - OPA (right) thin section. Brighter areas represent higher abundance. The interface is indicated with the red line.

The overall chemical and mineralogical characteristics of the interface region may be summarized as follows:

- Deterioration of cement paste with approximately 1 mm in width, as seen in Ca, Si and S maps, and likewise the distribution of AFm (here named hydrocalumite).
- Mg-enrichment at the interface, much better developed in mortar, and essentially absent in OPA except for a narrow band (0.1 - 0.2 mm).
- The mineralogical details are not yet fully characterized, specifically the identity of a possible Mg-rich phase has not been detected (such as for example Mg-Si-hydrate).
- We cannot derive information on changes in porosity across the interface from these methods.

3.2 *Computed Tomography before the core infiltration*

3.2.1 Representative elementary volume (REV) sample for the core infiltration

A preliminary evaluation of the data recorded within the last few weeks is presented. The primary data consists of a data stack with a pixel/voxel size of 30 μm , 1,920 x 1,536 pixels in TIF format for each section, each 5.62 MB in file size. Thus, the entire stack (parallel to the core axis) is ca. 10 GB. The sample was scanned before cutting the core to its final length (43.7 mm) for the infiltration, and it was 55 mm long.

After the reconstruction of the data with Bruker InstaRecon software, the image size was about 1,920 x 1,920 pixels (sections perpendicular to the core axis) and the images were stacked along the core axis (vertical direction in the CT scanner).

Figure 21 shows different sections of the reconstruction corresponding to two characteristic cross sections of OPA and ESDRED mortar. Bright specks represent small inclusions of phases with very high X-ray attenuation, such as pyrite. A trace of a fracture subparallel to bedding (more or less horizontal) is seen in the OPA image as a sinusoidal trace containing some macro-porosity. The pyrite network in the OPA is shown in 3D in Figure 22.

The ring artifacts can be observed with a denser and heavier composition at the edge of the ring and an apparent higher porosity in the center. However, the beam hardening artifact was strongly decreased by the set-up chosen.

The cross-section of the interface is shown in Figure 23. The overall fabric of the ESDRED mortar is homogeneous at this scale. The distribution of the biggest pores and supposedly that of the hydrates are uniform. OPA is clearly fractured subparallel to bedding. This fracturing is a primary feature at certain locations, usually only a few cms thick but laterally more persistent. The sample preparation for the sampling in the field and that in the laboratory for the experiment did not result in further disturbances but preserved this fractured aspect well. Because the fractures have no significant apertures and are oriented perpendicular to the future transport direction in the core infiltration experiment, the hydraulic effect may be small compared to intact OPA.

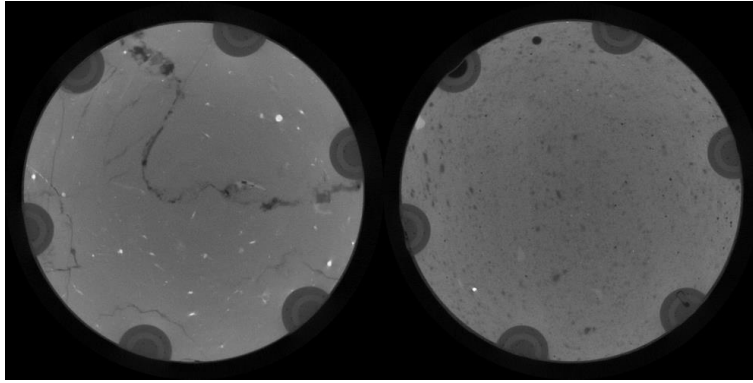


Figure 19: CT sections across OPA (left) and ESDRED mortar (right) parallel to the interface after reconstruction.

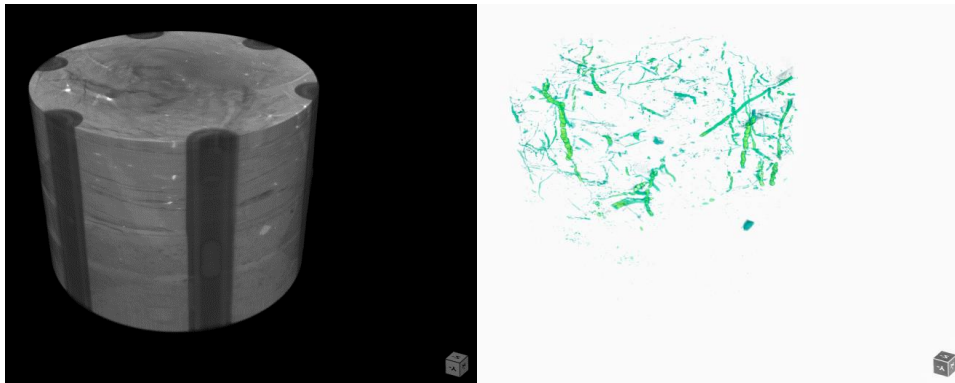


Figure 20: 3D reconstruction from X-ray CT image data of the sample with dragonfly software. Left: entire volume and right: pyrite network in green (mainly in the OPA).

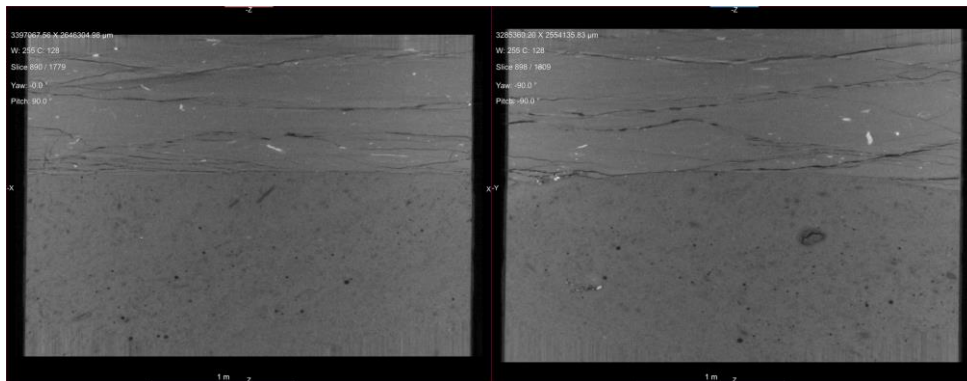


Figure 21: CT sections across the interface visualized with dragonfly software.

3.2.2 Smaller samples

To reach a higher resolution, smaller samples were required. A cylindrical volume of interest was cut from the same sample (just next to the 52 mm core) for easier handling in the X-ray CT. However, the sample preparation was difficult and a second square sample, bigger, was prepared to keep the sample and the interface safe. The two embedded samples are shown in Figure 24. The diameter of the OPA/ESDRED was approximately 10 mm and 10/19 mm in these two samples.

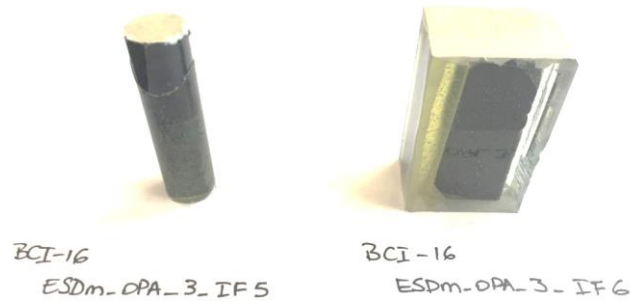


Figure 22: Embedded interface samples (ESDm_OPA_3_IF5 and ESDm_OPA_3_IF6) for X-ray CT at higher resolution.

Similarly to the former X-ray CT scans, the OPA and ESDRED sections of the two smaller samples are shown in Figure 23. The sections of the OPA are comparable to the first scan. However, the details in the fabric of the ESDRED are enhanced, the empty pores from air bubbles trapped during the mixing of the mortar are observed as previously. Additionally, mineral grains can be detected. These might include the quartz sand used for the mortar, and unhydrated and hydrated phases constituting the paste. A porosity network is also observed in between the grains. Some light grey grains indicate the presence of a material with high X-ray absorbance as ferrite or Fe-hydrate phases.

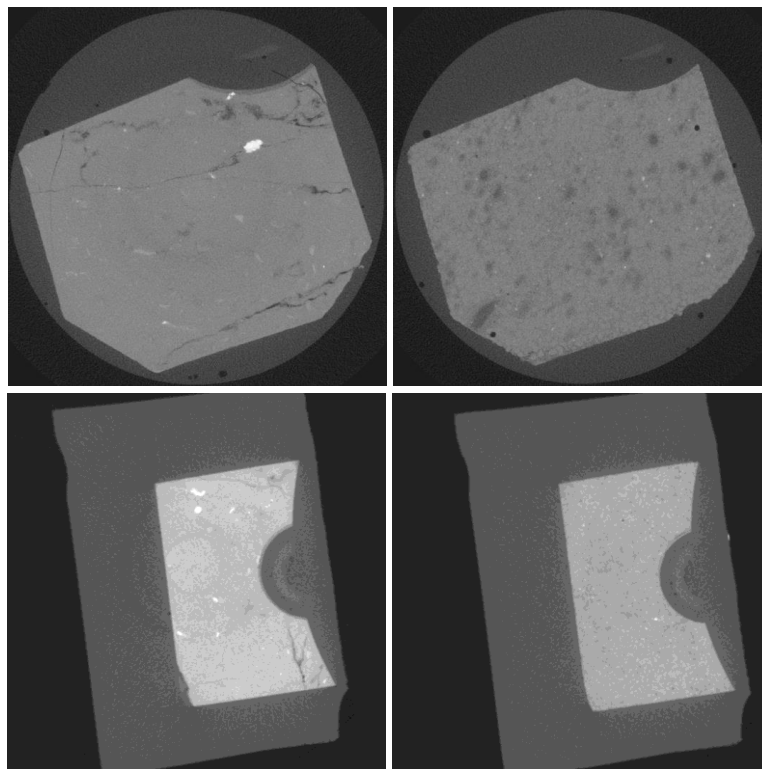


Figure 23: CT sections across OPA (left) and ESDRED mortar (right) of the samples ESDm_OPA_3_IF5 (top, sample size, epoxy included: $\varnothing = 12$ mm) and ESDm_OPA_3_IF6 (bottom, sample size epoxy included: 22 x 30 mm) after reconstruction.

Looking closer to the interfaces in Figure 24, Figure 25, and Figure 26, we can observe an increase in the porosity of the mortar close to the interface with a clear network of porosity starting at the interface. Additionally, a distinct and regular reaction zone in the mortar at the interface is observed. The physicochemical studies of this transitional zone are detailed in Fisch et al. (2017).

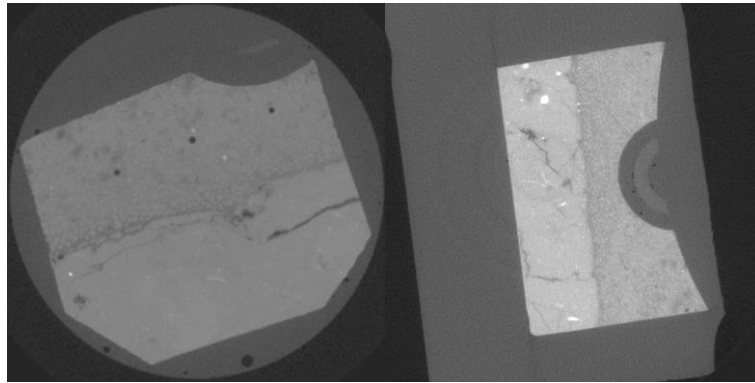


Figure 24: CT sections across the interface in the samples ESDm_OPA_3_IF5 (left) and ESDm_OPA_3_IF6 (right) after reconstruction.

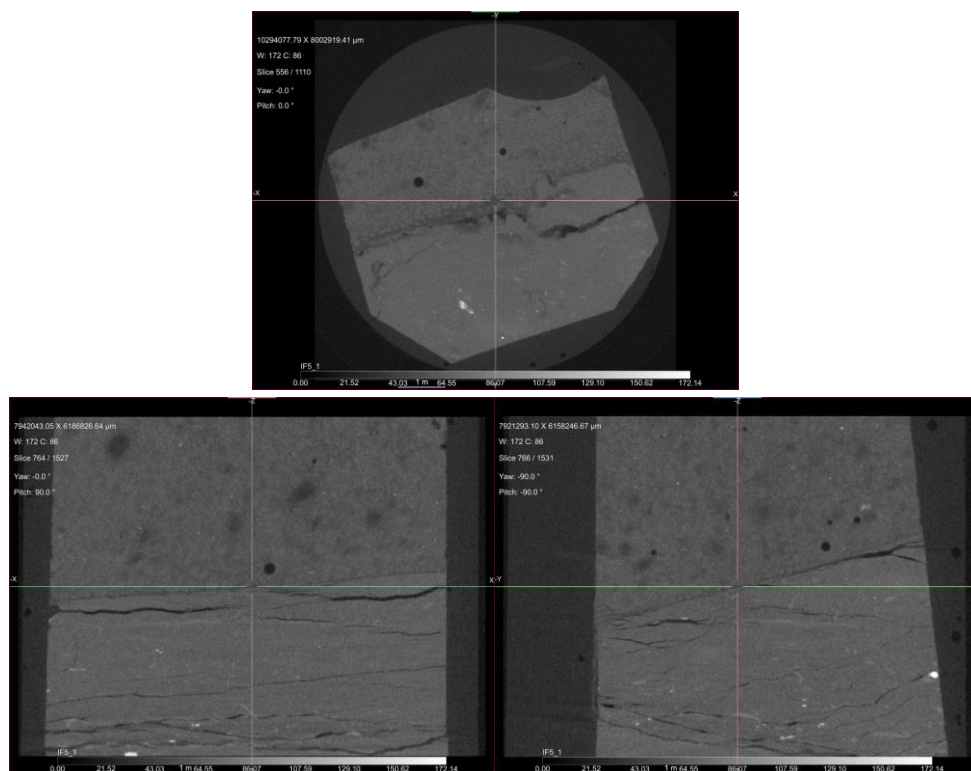


Figure 25: CT sections visualized with dragonfly across the sample ESDm_OPA_3_IF5 after reconstruction.

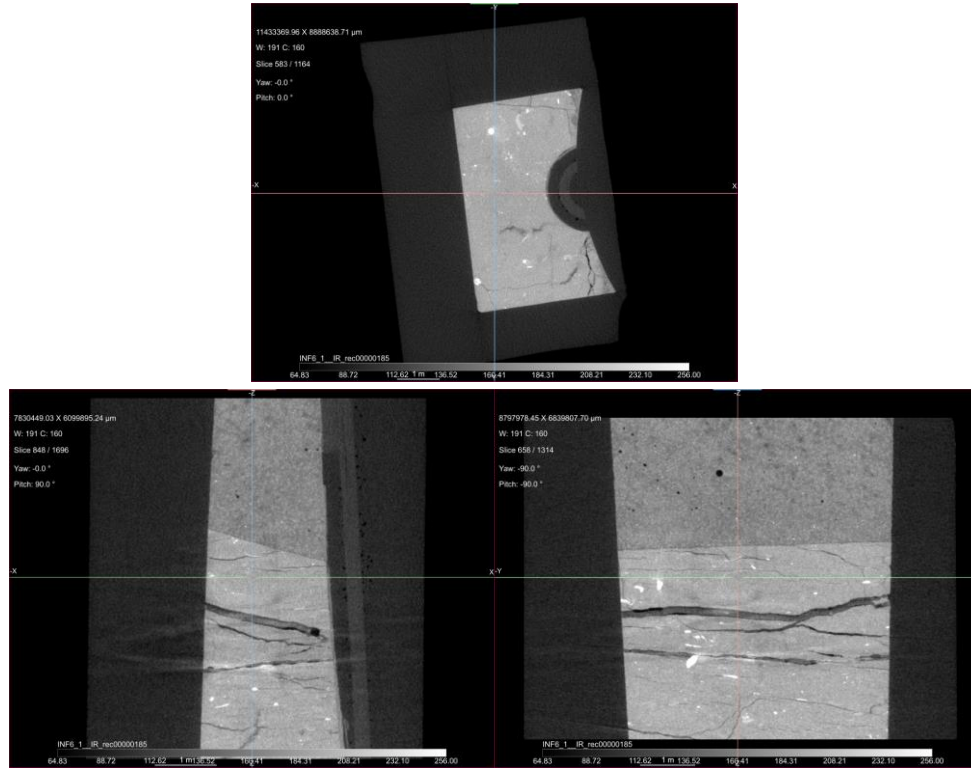


Figure 26: CT sections visualized with dragonfly across the sample ESDm_OPA_3_IF6 after reconstruction.

3.3 Preliminary results of the core infiltration experiment

The confining pressure has been set to 4.6 - 4.7 MPa. After few hours to verify the absence of leaks, the injection pressure has been set to 2.0 MPa during 2 hours to accelerate the outgassing/saturation of the sample. Then the injection pressure has been set to approximately 0.5 MPa (5 bar). Successfully, no leaking has been observed until now, and the experiment performs in a stable manner.

3.3.1 Darcy's law

The bulk hydraulic conductivity of the sample is calculated according to Darcy's law. A back-analysis of the hydraulic conductivity of the perturbed interface will be made knowing the individual properties of the undisturbed sound OPA and sound ESDRED mortar materials involved.

Darcy's law is simplified following the geometry of the system in Eq. 1:

$$q = \frac{Q}{A} = K \frac{\Delta h}{l} \quad (I)$$

$$q = \frac{Q}{A} = K \frac{\Delta h}{l} \quad (I)$$

With:

- q = specific discharge (m/s) or specific flux (m³/m²/s)
- K = hydraulic conductivity (m/s)

- Q = average volumetric flow rate (m³/s)
 l = length of sample (m)
 A = cross sectional area of sample (m²)
 Δh = average hydraulic head difference (m water column);

Darcy's law can be generalized for a layered medium (perpendicular to the flow direction), using the hydraulic resistivities of the individual layers of thickness l_i , $R_i = l_i/K_i$ in Eq. 2.

$$q = \frac{\Delta h}{\sum_i R_i} \quad (2)$$

For a three-layer medium, such as the core used in this experiment, consisting of OPA, ESDRED mortar and an alteration zone (skin), one may write as Eq. 3:

$$q = \frac{\Delta h}{\frac{l_{ESDRED}}{K_{ESDRED}} + \frac{l_{skin}}{K_{skin}} + \frac{l_{OPA}}{K_{OPA}}} \quad (3)$$

It is evident in the above equation that layers of low hydraulic conductivity and a relatively large thickness are dominant in controlling the flux. ESDRED mortar with a hydraulic conductivity much larger than OPA (see below) bears little weight in the equation. A skin can only be hydraulically effective (detectable) if its hydraulic resistance is similar or larger than that of the OPA layer. Given the small thickness of the skin (mm), its hydraulic conductivity needs to be correspondingly much smaller to be detectable in such an experiment, by a factor of 10-20 at least.

At this stage of the experiment, only a few drops of liquid and mainly gas have been collected from the advection experiment over the past 28 days. The sample, even stored in sealed condition at 7°C seems dryer than expected and so far, 12 mL have already been outgassed (representing a significant portion of total porosity). The hydraulic conductivity of the system will be calculated when it will be possible to measure a volumetric flow rate, and it can be evaluated if a strong skin effect is present or absent.

3.3.2 Water permeability of the ESDRED mortar

A water permeability test performed in July 2015 on 3 samples detailed in Table 2 showed a large standard deviation. The associated water permeability from Darcy's law has been calculated equal to $2.2 \cdot 10^{-9}$ m/s (with a large standard deviation: $3.5 \cdot 10^{-9}$ m/s). Additionally, the properties may have somewhat changed due to possible chemical interactions between 2015 and now. Two new samples have been prepared in February 2018 from the same sample (BCI-16) and send to TFB to proceed to new measurements. This time, the water permeability from Darcy's law has been calculated equal to $9.0 \cdot 10^{-11}$ m/s with a lower standard deviation ($6.1 \cdot 10^{-11}$ m/s). The large difference between the two results measured with 3-year difference might be due to the clogging of some porosity by calcite precipitation. However, the previous results have to be taken into account and a trade-weighted average of $1.5 \cdot 10^{-10}$ m/s will be used.

3.3.3 Water permeability of OPA (Mont Terri)

Hydraulic conductivity of the OPA from Mont Terri has been widely studied; however, the value depends on sample lithology and possibly also on sample preparation and the experimental approach. A range of $3 \cdot 10^{-15}$ to $5 \cdot 10^{-13}$ m/s (see Table 1) is reported by (Pearson et al., 2003). More appropriate is a well constrained value of

$1.3 \cdot 10^{-13}$ m/s experimentally measured perpendicular to bedding in Mäder (2018) over a period of 15 years on a sample from the same facies from very near the location of the CI experiment, or a recommended average values for the shaley facies from the latest summary: $2.0 \cdot 10^{-13}$ m/s (Bossart et al., 2017).

4 Conclusions and Future work

Any chemical interactions that involve materials at the cement-claystone/bentonite interfaces, and which may affect the chemical environment and thus may alter any of the safety-relevant properties of cement/concrete and clay-based materials must be assessed in the context of performance assessment. Advective displacement and its extension as a core infiltration experiment can yield a large amount of data to constrain the composition of the pore water preserved in a sample and transport properties derived from the breakthrough of tracers. The experiment is started; when it will be possible, the volumetric flow rate will be measured and the chemical composition of the liquid recovered will be analyzed.

The analysis obtained by X-ray CT on the 3.2 years' interface before the infiltration showed a homogeneous overall fabric of the ESDRED mortar at this scale. The distribution of the biggest pores in the cement mortar is uniform and OPA is clearly fractured subparallel to bedding. Looking closer at smaller samples, the mortar's porosity close to the interface seems to increase.

The SEM/EDX and μ -XRD data confirmed the deterioration of the cement paste within ~ 1 mm in width (for more details on the evolution of cement/mortar/concrete-OPA interfaces see Jenni et al., 2014; Dauzères et al., 2016; Lerouge et al., 2017; Mäder et al., 2017) and Mg-enrichment at the interface, much better developed in mortar, and essentially absent in OPA except for a narrow band (0.1 - 0.2 mm). However, the mineralogical details are not yet fully characterized, specifically the identity of a possible Mg-rich phase has not been detected (such as for example Mg-Si-hydrate).

The further work will be to collect all the data and give proper water transport properties of the ESDRED mortar and of the perturbed interface and to do the link with the chemical changes. Classical chemical analysis by autoradiography (performed at the University of Helsinki) will be added to the accessible porosity observed by X-ray CT to interpret the water transport properties obtained by the core infiltration.

All this work will be applied in parallel to the Portland concrete - OPA interface aged now for 10 years and collected during the last CI drilling campaign (2017). In addition, positron emission tomography (PET) will be conducted on a similar sample at the University of Dresden.

Combination of the core infiltration method with PET is a means to also image the transport of the mobile phase that normally cannot be observed with X-ray CT and normal pore water compositions. Recent improvements in imaging and data processing offer essential complementary information to methods that focus more on the stationary phase.

Acknowledgment

The research leading to these results has received funding from the European Union's Horizon 2020 Research and Training Programme of the European Atomic Energy Community (EURATOM) (H2020-NFRP-2014/2015) under grant agreement n° 662147 (CEBAMA). Christoph Neururer, Anneleen Foubert and Eva De Boever (all at the University of Fribourg, Switzerland) supported the X-ray CT work on the Bruker Skyscan 2211 instrument at the University of Fribourg (Swiss National Science Foundation R'EQUIP Grant n° 150731). The CI Mont Terri

Project rock laboratory (Veerle Cloet, Nagra, Principal Investigator) kindly shared data and funded the sampling campaign.

References

- Allen, A.J., Thomas, J.J., Jennings, H.M. (2007). Composition and density of nanoscale calcium–silicate–hydrate in cement. *Nature materials*, 6, 311-316.
- ANDRA (2005). Evaluation of the feasibility of a geological repository in an argillaceous formation. Collection Les Rapports 2005. ANDRA, France.
- Bernard, E., Lothenbach, B., Chlique, C., Wyrzykowski, M., Dauzères, A., Pochard, I., Cau-Dit-Coumes, C. (*submitted*). Characterization of magnesium silicate hydrate (M-S-H), *submitted*.
- Bish, D.L. and Brindley, G. (1978). Deweylites, mixtures of poorly crystalline hydrous serpentine and talc-like minerals. *Mineralogical Magazine*, 42, 75-79.
- Bossart, P., Bernier, F., Birkholzer, J., Bruggeman, C., Connolly, P., Dewonck, S., Fukaya, M., Herfort, M., Jensen, M., Matray, J.-M. (2017). Mont Terri rock laboratory, 20 years of research: introduction, site characteristics and overview of experiments. *Swiss Journal of Geosciences*, 110, 3-22.
- Bradbury, M.H., Berner, U., Curti, E., Hummel, W., Kosakowski, G., Thoenen, T. (2014). The long term geochemical evolution of the nearfield of the HLW repository. Nagra Technical Report, 12-01.
- Brindley, G., Bist, D.L., Wan, H.-M. (1977). The nature of kerolite, its relation to talc and stevensite. *Mineralogical Magazine*, 41, 443-452.
- Claret, F., Bauer, A., Schäfer, T., Griffault, L., Lanson, B. (2002). Experimental investigation of the interaction of clays with high-pH solutions: A case study from the Callovo-Oxfordian formation, Meuse-Haute Marne underground laboratory (France). *Clays and Clay Minerals*, 50, 633-646.
- Cuevas, J., Vigil De La Villa, R., Ramirez, S., Sanchez, L., Fernandez, R., Leguey, S. (2006). The alkaline reaction of FEBEX bentonite: a contribution to the study of the performance of bentonite/concrete engineered barrier systems. *Journal of Iberian Geology*, 32, 151-174.
- Dauzères, A., Achiedo, G., Nied, D., Bernard, E., Alahrache, S., Lothenbach, B. (2016). Magnesium perturbation in low-pH concretes placed in clayey environment - solid characterizations and modeling. *Cement and Concrete Research*, 79, 137-150.
- Fernandez, R., Maeder, U.K., Rodriguez, M., Vigil de la Villa, R., Cuevas, J. (2009). Alteration of compacted bentonite by diffusion of highly alkaline solutions. *European Journal of Mineralogy*, 21, 725-735.
- Fisch, M., Jenni, A., Mäder, U.K., Grolimund, D., Cloet, V. (2017). CI Experiment: Micro-XRD studies on interfaces between Opalinus Clay and 2.5-year-old OPC and ESDRED mortar samples (3rd sampling campaign 2015). Internal report, Mont Terri Project.
- Gaboreau, S., Lerouge, C., Dewonck, S., Linard, Y., Bourbon, X., Fialips, C., Mazurier, A., Prêt, D., Borschneck, D., Montouillout, V. (2012). In-situ interaction of cement paste and shotcrete with claystones in a deep disposal context. *American Journal of Science*, 312, 314-356.
- Garcia Calvo, J.L., Hidalgo, A., Alonso, C., Fernández Luco, L. (2010). Development of low-pH cementitious materials for HLRW repositories: Resistance against ground waters aggression. *Cement and Concrete Research*, 40, 1290-1297.
- Gaucher, E.C. and Blanc, P. (2006). Cement/clay interactions—a review: experiments, natural analogues and modeling. *Waste Management*, 26, 776-788.
- Haas, J. (2012). Etude expérimentale et modélisation thermodynamique du système CaO-SiO₂-(Al₂O₃)-H₂O. PhD Thesis, Université de Bourgogne.
- Jacobs, F. (2012). CI Experiment: Manufacturing of 5 different concrete and their emplacement (Phase 17). Internal report, Mont Terri Project.

- Jacobs, F. (2015). CI-Experiment: Water permeability analysis of 2 year old samples. Internal report, Mont Terri Project.
- Jenni, A., Mäder, U., Lerouge, C., Gaboreau, S., Schwyn, B. (2014). In-situ interaction between different concretes and Opalinus clay. *Physics and Chemistry of the Earth, Parts A/B/C*, 70, 71-83.
- Lerouge, C., Gaboreau, S., Grangeon, S., Claret, F., Warmont, F., Jenni, A., Cloet, V., Mäder, U. (2017). In-situ interactions between Opalinus Clay and low alkali concrete. *Physics and Chemistry of the Earth, Parts A/B/C*, 99, 3-21.
- Lothenbach, B., Le Saout, G., Ben Haha, M., Figi, R., Wieland, E. (2012). Hydration of a low-alkali CEM III/B–SiO₂ cement (LAC). *Cement and Concrete Research*, 42, 410-423.
- Lothenbach, B., Nied, D., L'Hôpital, E., Achiedo, G., Dauzères, A. (2015). Magnesium and calcium silicate hydrates. *Cement and Concrete Research*, 77, 60-68.
- Lothenbach, B., Rentsch, D., Wieland, E. (2014). Hydration of a silica fume blended low-alkali shotcrete cement. *Physics and Chemistry of the Earth, Parts A/B/C*, 70, 3-16.
- Mäder, U. (2018). Advective displacement method for the characterisation of pore water chemistry and transport properties in claystone. *Geofluids*, 2018.
- Mäder, U., Jenni, A., Lerouge, C., Gaboreau, S., Miyoshi, S., Kimura, Y., Cloet, V., Fukaya, M., Claret, F., Otake, T., Shibata, M., Lothenbach, B. (2017). 5-year chemico-physical evolution of concrete-claystone interfaces. *Swiss Journal of Geosciences*, 110, 307-327.
- Mäder, U.K. (2009). Reference pore water for the Opalinus Clay and "Brown Dogger" for the provisional safety-analysis in the framework of the sectoral plan - interim results (SGT-ZE). *Nagra Arbeitsbericht, NAB 09-14*, Nagra, Switzerland.
- Mäder, U.K. (2017). CI (Cement Clay Interaction) experiment: sampling and analysis of Opalinus Clay pore water from test interval BCI-4 (2015/2016). Internal report, Mont Terri Project.
- NAGRA (2002). Project Opalinus Caly, Safety Report. Demonstration of feasibility of disposal for spent fuel, vitrified high-level waste and long-lived intermediate-level waste ("Entsorgungsnachweis"). *Nagra Technical Report*, 02-05.
- Pearson, F.J., Arcos, D., Bath, A., Boisson, J.-Y., Fernandez, A.M., Gäbler, H.-E., Gaucher, E., Gautschi, A., Griffault, L., Hernan, P., Waber, H.N. (2003). Mont-Terri Project – Geochemistry of Water in the Opalinus Clay Formation at the Mont Terri Rock Laboratory. *Reports of the FOWG, Geology Series*, 5, 319.
- Roosz, C., Grangeon, S., Blanc, P., Montouillout, V., Lothenbach, B., Henocq, P., Giffaut, E., Vieillard, P., Gaboreau, S. (2015). Crystal structure of magnesium silicate hydrates (MSH): The relation with 2: 1 Mg–Si phyllosilicates. *Cement and Concrete Research*, 73, 228-237.
- Skinner, L., Chae, S., Benmore, C., Wenk, H., Monteiro, P. (2010). Nanostructure of calcium silicate hydrates in cements. *Physical Review Letters*, 104, 195502.
- Thury, M.F. and Bossart, P.J. (1999). Mont Terri Rock Laboratory: Results of the hydrogeological, geochemical and geotechnical experiments performed in 1996 and 1997. *Geologische Berichte*, 23, Landeshydrologie und -geologie.

Geochemical and microstructural evolution of cementitious materials in contact with a clayey rock at 70°C – In-situ tests in the Tournemire URL and laboratory experiments

Alexandre Dauzères^{1*}, Philippines Lalan^{1,2}, Adèle Grellier¹, Laurent De Windt²

¹ Institute for Radiation Protection and Nuclear Safety (FR)

² Mines Paris Tech (FR)

* Corresponding author: alexandre.dauzeres@irsn.fr

Abstract

Radioactive wastes in future clayey underground disposal sites will potentially induce, in function of the architecture chosen, a temperature increase at the interface between the cementitious materials and the host rock. To understand the evolution of cementitious materials (Portland and low-pH cements) in this environment, laboratory experiments and in-situ specific device named CEMTEX (CEMent Temperature EXperiment) were respectively developed in the IRSN Underground Research Laboratory in Tournemire (France). CEM I and two types of low-pH cement pastes were put in contact with the clayey rock under water-saturated conditions at 70°C for 9 experiments in the in-situ conditions. Only the CEM I/clayey rock interface was tested in classical laboratory.

The first six in-situ experiments, three for CEM I and three for the first low-pH cement paste (Mix of CEM I, silica fume and fly ashes) were started in 2012 for a duration of 1, 2 and 5 years. In April 2016, three other in-situ experiments were started with a second type of low-pH cement paste (Mix of CEM III, silica fume and filler), based on a self-consolidating concrete (SCC) (Poyet et al., 2014). Three timescales were tested in the lab. experiments during 2, 6 and 12 months.

This publication is dedicated to the characterization of the lab. and in-situ experiments related to the interactions between CEM I (OPC) and the clayey rock by XRD and SEM-EDS for the three durations and by TGA, X-Ray microtomography and autoradiography on a sample impregnated with ¹⁴C-PMMA.

After one, two and five years of interaction in in-situ conditions, partial decalcification and diffuse carbonation (calcite precipitation) was observed in the cement paste, globally resulting in a total porosity decrease. Close to the interface, in the heterogeneity linked to the initial bedding of the rock, a layer rich in potassium, silicon and aluminium is systematically formed, constituted of zeolites as phillipsite, well-crystallized C-S-H as tobermorite (only after one year), and C-(A)-S-H. The lab. experiments exhibit the same results, except the zeolite precipitation due to kinetic reasons.

To summarize, at 70°C, the CEM I cement past is protected against the alteration of the clayey rock due to carbonates precipitation. As at 1 and 2 years, after 5 years of interaction, the degradation is limited to 1 mm in the depth.

1 Introduction

In France, the decision has been taken to design a radioactive waste disposal facility in a natural clayey environment with favourable radionuclide containment properties. However, for stability reasons during the excavation work and for facilitating the installation of radwastes, galleries excavated in clayey rocks must generally be mechanically supported by concrete components. The contact between the clayey rock and the concrete inevitably leads to an alkaline plume spreading from the concrete toward the host rock, while a multi ionic attack occurs from the clayey pore water against the cementitious material side.

Several types of cementitious binders are selected as references today for the design of deep disposal facilities: an ordinary Portland cement and two low-pH binders. The low-pH binders were formulated to induce a less aggressive alkaline plume mainly due to a lower pore water pH. Over the last decades, interest has grown about the geochemical behaviour of cementitious materials in a clayey environment. Studies have focused mainly on the physico-chemical evolution of clay under alkaline conditions and not on the material interface. Only a handful of studies have discussed the interactions at the interface between cement binder and claystone. Such interfaces have been created at ambient temperature by pouring cement mixes into boreholes (Gaboreau et al., 2011; Jenni et al., 2014; Bartier et al., 2013; Dauzères et al., 2016) or by putting disks of material into contact in transport cells (Dauzères, 2010). In the current design of the French radioactive waste deep disposal facility (Andra, 2005), the thermal transient, due to the presence of heat-emitting waste, is expected to entail a temperature increase of up to 70°C in the concrete plugs located in the high-level waste cells and potentially also in the intermediate long-lived waste cells. Based on the existing literature, only a few laboratory studies have focused on the impact of such a temperature level on the evolution of the interface between natural rock and anthropic material, and even fewer in-situ studies have been carried out.

The CEMTEX experiment (CEMent Temperature EXperiment) (Lalan et al., 2016) aims to fill the lack of knowledge about the geochemical and micro-structural evolutions of these interfaces under representative thermo-hydraulic conditions (i.e. 70°C and full water saturation), which should provide input for future studies on the durability of cementitious materials. Within this framework, six in-situ experiments (three with CEM I and three with a low-pH cement) have been set up in IRSN's underground research laboratory in Tournemire (France) in 2012, before the starting of the CEBAMA project and three other with a second low-pH cement paste were started inside the CEBAMA project in 2016. In parallel, laboratory experiments were started to test the interaction between CEM I and clayey rock in well controlled conditions. This paper presents quickly the experimental devices already describe in previous papers (Lalan, 2016a; Lalan et al., 2016b, and focus on results obtained on both the first in-situ experiments putting in contact CEM I and clayey rock after 1, 2 and 5 years of interaction and the laboratory experiments after 2, 6 and 12 months of interaction.

2 Experimental device

2.1 In-situ experimental device

Nine downward vertical boreholes of 1 m depth and 25 cm of diameter were drilled into the argillite in the Tournemire tunnel (6 in 2012 and 3 in 2016). This depth was chosen to ensure that the devices were located out of the excavation disturbed zone (EDZ) created while the gallery was dug. The bottom of each borehole was polished with a specific tool and all the dust was carefully vacuum cleaned to obtain an as perfect as possible contact surface between the rock and the cementitious material. Three cups filled with water and humidity probes were placed into the borehole, which was then tightly closed to resaturate the rock by vapour phase. The rock was considered saturated when the measured relative humidity within the borehole reached a value of 99.5%. In each

borehole, the relative humidity reached 97.5% and 99.5% after 7 and 45 days, respectively. To force a one-dimensional mass transport (vertical) across the interface and to protect the borehole sides from hyperalkaline solution, a PVC tube (25 cm outer diameter, 0.5 cm thick, 125 cm height) was placed within the borehole. A rubber seal was placed at the bottom of the PVC tubing to seal the bottom of the tube from the borehole wall.

At the same time, heater devices were built outside the boreholes (Dauzères et al., 2016b). Four temperature sensors (PT 100) were attached to a single support in order to monitor the temperature during the experiment. Two sensors were close to the centre of the coil, one at 1 cm height from the future interface (M1) and the other at 20 cm (M0). The two other sensors were placed just inside the coil, again at 1 cm (M2) and 20 cm (M3). The coil top and the temperature sensor support were fixed to a PVC shell of 20 cm diameter. A rubber seal provided sealing between the argillite borehole bottom and this latter PVC shell. After the argillite saturation, the entire device was placed into the borehole and then connected to a boiler via 12 mm diameter PFA pipes (perfluoroalkoxy) and to the temperature acquisition system (ALMEMO). Once all these steps had been achieved, the cement paste was poured onto the heater device and the temperature sensors to fill the full inner PVC volume constituting a 30 cm height OPC and low-pH paste plug. A small amount of cement paste was also poured between the two PVC shells over a few centimetres.

One month after the beginning of the cement hydration, heating was started while the device was being maintained under the equilibrium solution at the good pH value with the considered cementitious material in order to ensure water saturation throughout the test. The water reservoir is trapped between the cement paste and a layer of Resin to limit the evaporation of water. The system is closed and protected.

2.2 Laboratory experimental device

The argillite disks were resaturated by vapour phase in airtight container at 100% relative humidity. To set up the diffusion cell, first stage of the process was to place the material in the sample holder while ensuring water tightness around the material. For this end, on the porous plate located at the bottom of the sample holder a thin rubber seal was placed. An argillite disk whose edge was before coated with mastic (Resoltech 3030), embedded in a thick rubber seal (1 cm thick, 52 mm inner diameter), the latter also coated with mastic and then the whole, was put into the sample holder. A second thick rubber seal was stuck in the sample holder on the top of the first one. After mastic hardening, 24 hours later, cement paste was poured onto the argillite disk, in the central room of the second thick rubber seal. In this way, after hardening, the cement paste was a 52 mm diameter and 1 cm thick disk. After 24 hours the diffusion cell parts were put together and the reservoirs filled with the water corresponding to the material on contact. Three diffusion cells were prepared simultaneously with the same cement mix and stored at 70°C and 80% of relative humidity in a climatic chamber. Figure 1 details the geometry of the diffusion cells.

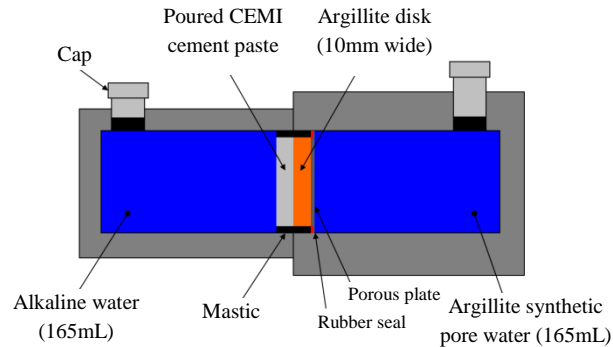


Figure 1: Diffusion cell scheme showing the cement and argillite disks in contact with reservoirs filled with alkaline water and argillite pore water.

Solution was sampled every 3 days the first two weeks, then once a week the following 20 weeks and then once every two weeks. 2 mL were sampled from the alkaline reservoir and 4 from the argillite synthetic water reservoir. After each sampling, each reservoir was refilled with the corresponding initial solution at 70°C. The experiments were stopped after 76 (cell C), 202 (cell D) and 415 (cell T) days by dismantling the diffusion cells.

3 The materials

The present paper describes the evolution of the Ordinary Portland Cement (in-situ and lab exp.), Sulphate Resisting Portland Cement (OPC-SRPC) from Val d’Azergues (France, Lafarge®). The cement paste had a water/cement ratio of 0.42 (Lalan et al., 2016; Dauzères et al., 2016b). It was put in place in 2012 in 3 tests.

The clayey rock is the Toarcian argillite in the Tournemire URL. The different properties of this rock are detailed in Lalan et al. (2016) and Tremosa et al. (2012).

4 The results

At the interface for the two last diffusion cells (202 and 415 days), a more or less width layer mixed of C-S-H, tobermorite and calcite was observed by SEM-EDS and confirmed by XRD (Figure 2). The Ca/Si and Al/Si ratios measured in the C-S-H structure by EDS were 0.83 and 0.18, respectively. This is coherent with decalcified C-S-H (C/S ratio in the C-S-H matrix equal to 1.6/1.7 in the non-disturbed area), tobermorite and presence of C-A-S-H. The average width of this layer was determined relying on the XRD measurement and on SEM-SE pictures (Figure 3). This brittle layer was about 100 µm thick after 415 days.

As shown in Figure 2, XRD intensity profile of portlandite decreased from the interface over 250 µm for cell C and D, and over 400 µm for cell T. Dissolution of portlandite is a rapid phenomenon, already occurring at the time of the installation of the diffusion cells.. Indeed, portlandite clusters visible in the sound cement paste on the elementary maps of Ca was smaller and less abundant at the interface on the same depth. Absent at 76 days, carbonation of the cement paste by calcite precipitation occurred on 150 µm after 202 days and on the same distance at 415 days. At the interface, calcite crystals are unequally distributed for the two latter samples. Progressive carbonation of the C-S-H and tobermorite layer at the interface was also noticed.

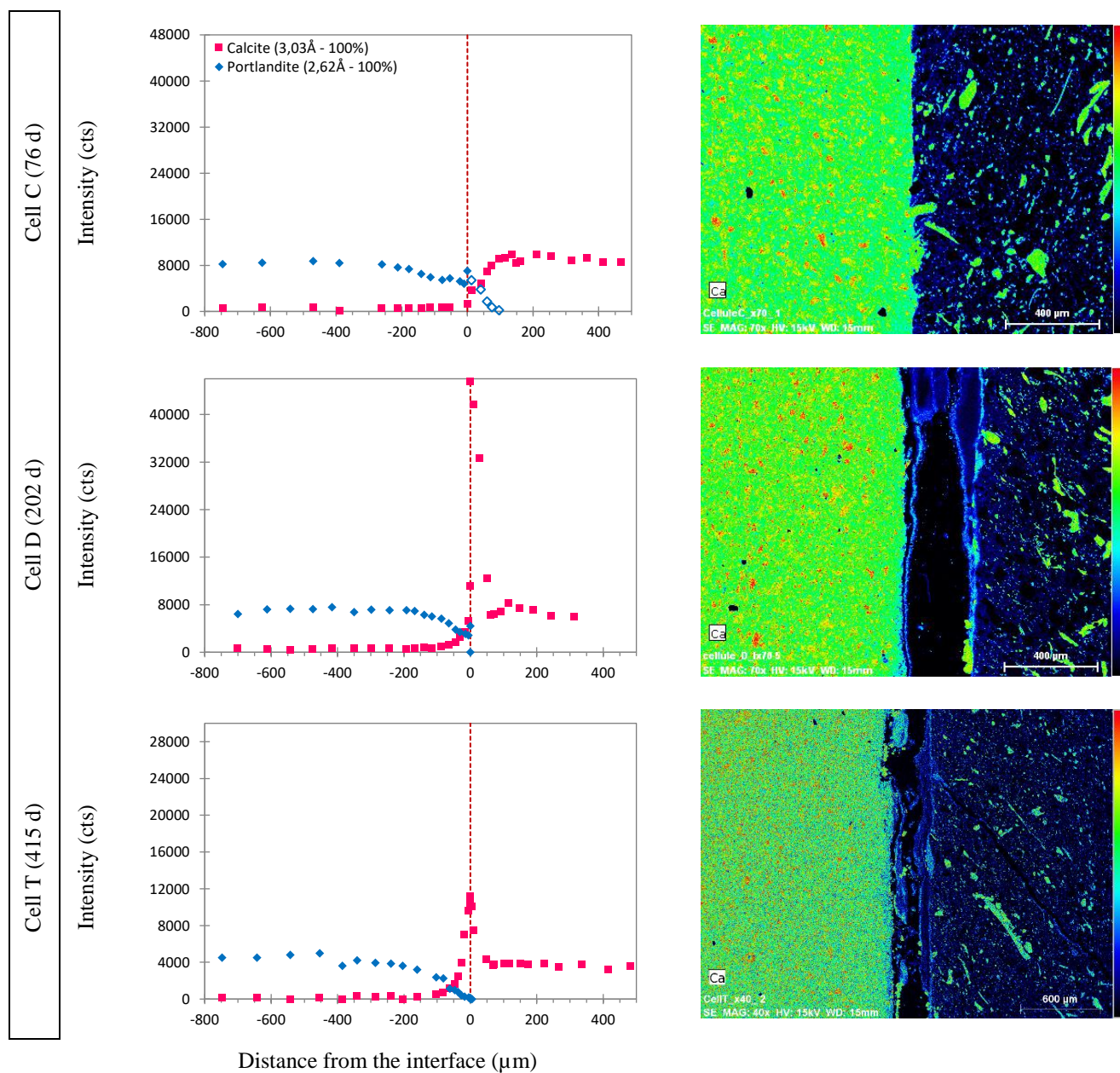


Figure 2: XRD intensity profiles of portlandite (2.62 Å) and calcite (3.03 Å) over distance from the interface (left), and EDS elementary map of Ca (right); i stands for interface. As the interface of cell C was cohesive, XRD analyses were performed from the argillite through the sound cement paste. Elementary map scales are from 0 (blue) to 100% (red), percentage of the element in each pixel; minimum meaning absence, maximum meaning pixel with the highest content of the element on the map.

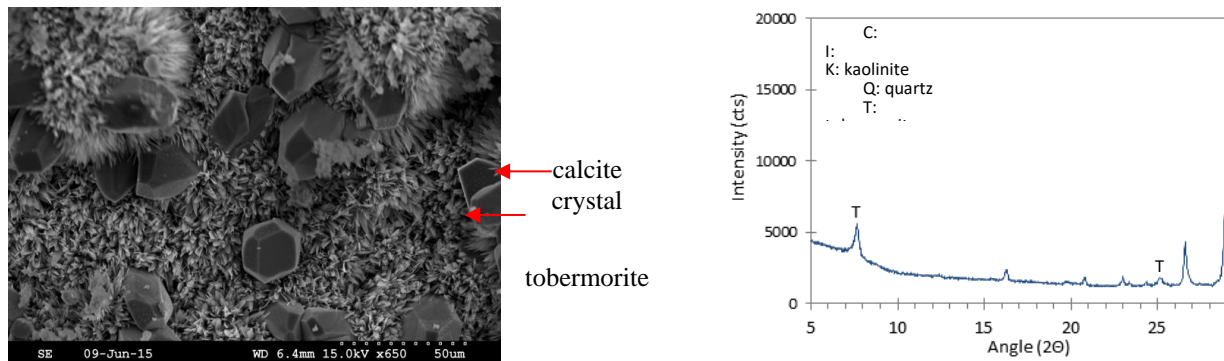


Figure 3: SEM-SE picture and XRD diffractogram of the cement/argillite interface, argillite side (cell D, 202 days).

Always in the laboratory experiments, the evolution of the argillite phases was followed by XRD analysis of the total rock (without clayey phase extraction). A slight carbonation of the argillite occurred within the argillite as calcite precipitation. Overall, signals of the argillite phases decreased at the interface. This general and concomitant decrease could be due to a matrix effect. Indeed, dissolution and precipitation probably occurred in this area and could lead to an evolution of the material structure itself. No conclusion could then be made to explain this global decline. Nevertheless, few other information could be extracted from the XRD analysis. First, about chlorite, signal of this mineral after 76 days was measured from the interface till the sound material whereas after 415 days its presence was observed in the argillite not before 50 μm away from the interface. Dissolution of the chlorite was then likely (Lalan, 2016b). In the cell D (202 days), signal of the chlorite was not identified from the background noise of the diffractograms even in the sound argillite and could not confirm this conclusion. Second, about kaolinite and illite, kaolinite main peak intensity to illite main peak intensity ratio was always higher than one in the sound argillite, but the ratio dropped below one close to the interface (Figure 4). This could correspond to a disturbance within the clay phases corresponding to kaolinite dissolution (and maybe illite formation). This perturbation was of the order of 100 μm within the argillite. It remains difficult to conclude on an argillite disturbance only from the XRD analysis, but it seems reasonable to conclude that argillite was altered on 100 μm from the argillite and that this alteration mainly affected the clay phases.

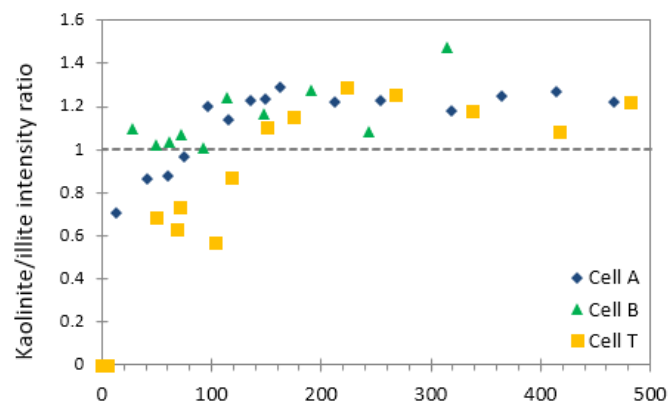


Figure 4: Evolution of the ratio between the kaolinite main peak intensity to illite main peak intensity using the XRD data.

Macroporosity was characterized using microtomography at a resolution of 1 μm . Only a portion of the greatest pores was characterized, i.e. the pores bigger than one micrometre. This is why the term macroporosity is used here, instead of porosity. Microtomography analyses were performed on the cement paste side of the separation

surface between the materials. The argillite side of the separation surface was not analysed. Indeed, the majority of the argillite pore has an average diameter smaller than 200 nm, and thus porosity could not be measured by this tool. Nevertheless, for the cell C (76 days), as both materials stayed stuck to each other, some argillite was analysed. It confirmed that the interface was really contiguous (Figure 5). Porosity containing air, less dense than materials, appears with the darker pixels on the microtomography pictures of Figure 8. This porosity could be considered as a threshold according to morphological considerations. Then the surface occupied by pores on each slice parallel to the interface was quantified in order to build macroporosity profiles (Figure 5).

At 76 days, macroporosity at the interface opened up links to portlandite dissolution. Indeed, on the microtomography slides (Figure 5), the large and light clusters are smaller in size and in amount at the interface in comparison with the sound material. These denser clusters were mainly composed by portlandite. According to the XRD analysis, portlandite dissolution occurred on 200 μm whereas according to tomography macroporosity opening occurred on about 60 μm (Figure 5). However, in this diffusion cell carbonation of the cement paste was weak (Figure 2). Therefore, this mechanism could not explain a macroporosity decrease. Thus, portlandite dissolution generated a macroporosity opening close to the interface where the process was the most intense. Same evolution applied to the two other cells. The interface evolved clearly with time in parallel to the formation of the layer. A physical separation between cement and clay was observed after 6 months. At 202 and 415 days, macroporosity opening spread about 100 μm whereas portlandite dissolution was respectively about 200 and 400 μm in each cell. Nevertheless, even though the macroporosity opening was not deeper for these two cells, the opening was higher with time. The macroporosity opening is then more intense with time at the interface. On Figure 5, the layer of C-(A)-S-H, tobermorite and calcite is also clearly visible at the interface.

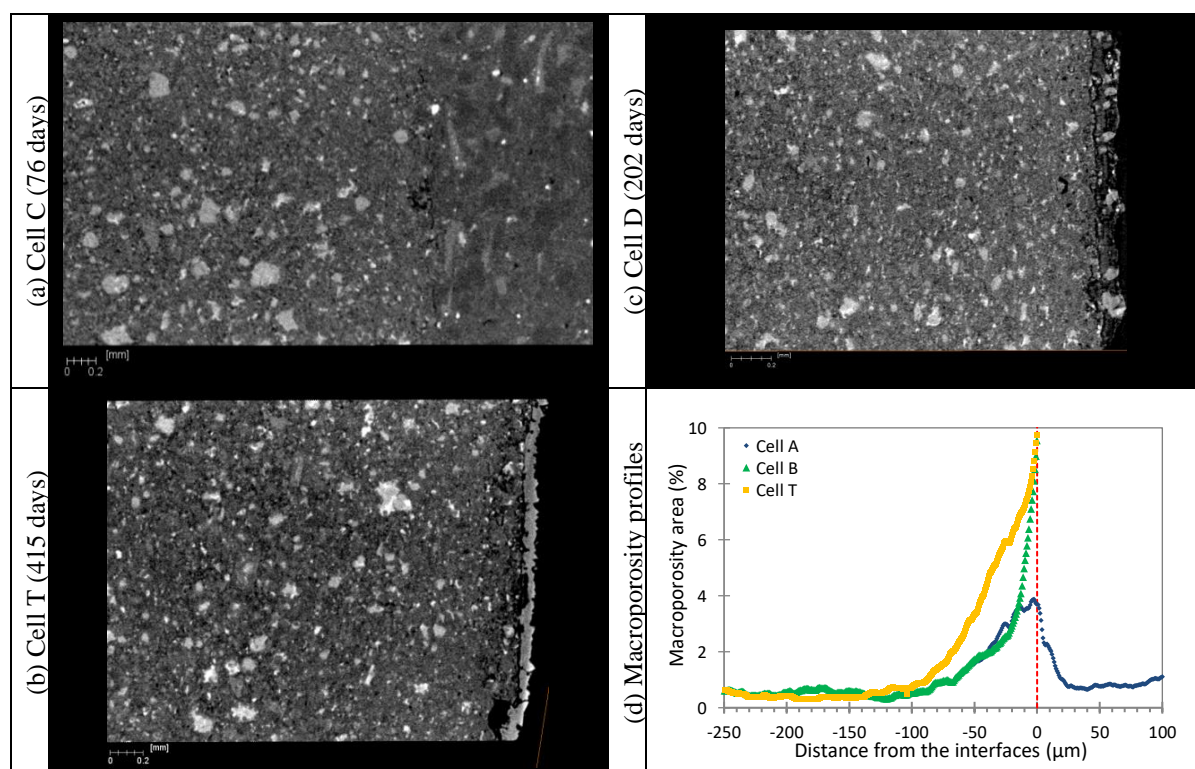


Figure 5: Microtomography slides perpendicular to the interface of each diffusion cell. The bottom right graph stands gives the macroporosity profiles built from the microtomography data (cell C corresponds to 76 days, cell D to 202 days and cell T to 415 days).

The same kind of homogeneous layer was observed at the interface between clays and CEM I cement pastes after 1, 2 and 5 years in the in-situ experiments. The unique difference is the presence of Phillipsite crystals in addition to the tobermorite in this layer (Figure 6). Kinetics reasons may explain this difference.

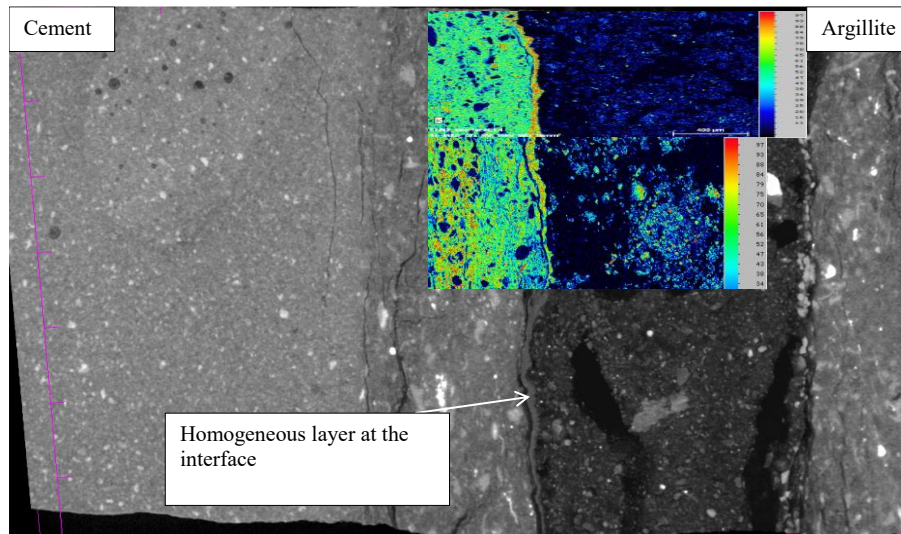


Figure 6: CT scan of the CEM I cement paste/argillite interface after 2 years of interaction in in-situ conditions and EDS-SEM mappings of K (top) and Al (bottom).

The textural analyses of the surface of the homogenous layer illustrates a progressive growing of the phillipsite crystals. After 5 years, the phillipsite layer (confirmed by XRD analyses) is really dense (on the base of SEM pictures) (Figure 7), given kinetic information about its development.

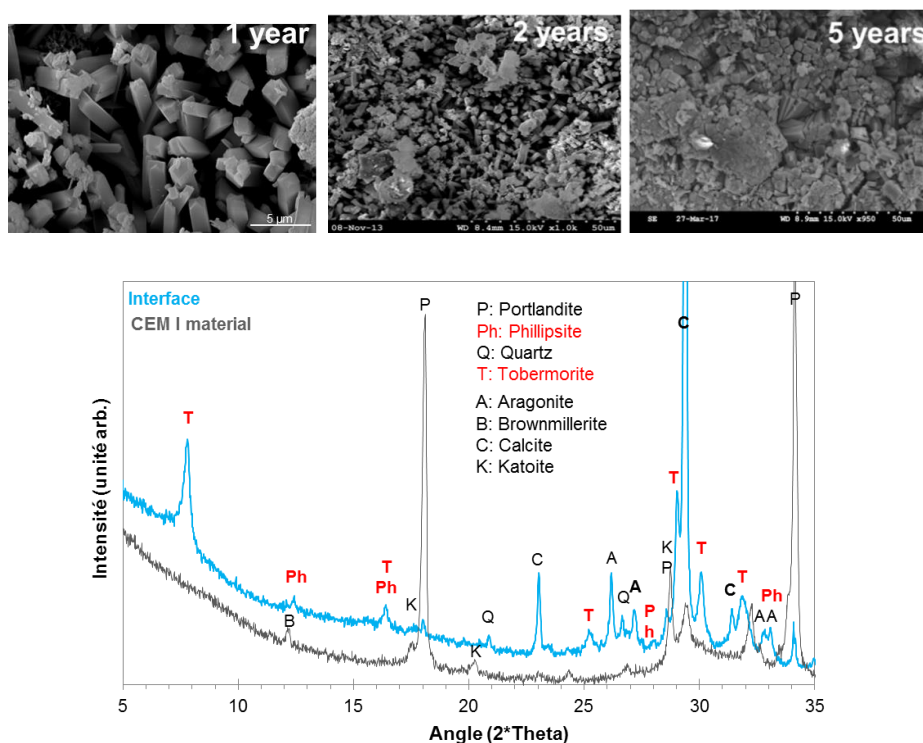


Figure 7: SEM pictures after one, two and five years of interaction and XRD diagram after 2 years of the homogeneous layer at the CEM I / argillite interface.

Autoradiographs of the diffusion cells are shown in Figure 8. These results indicate that the C14-MMA intruded fully into the samples' pore space. In cell C (76 days), materials are still partially in direct contact with each other. A crack was present within the argillite. At the end point of this crack a lower porosity spot was present in cement paste (green profile on the right graph). Thus the alteration did not propagate towards the bottom of the porosity map where the interface appeared not contiguous. Therefore, the opening of the interface occurred after the alteration processes. It confirmed again that the interface was cohesive during the experimental time. In cell D (202 days), a crack was also present, a spot was observed in the cement paste, but also circumscribed around the crack end point, without propagation along the interface. Then for each cell the interface was cohesive during the whole experiment. Manipulation of the samples during the diffusion cell dismantling and during their preparation for the analysis caused the separation of the materials. The amount of these cracks however might be related to the initial structure of the argillite phase. Similar cracks can also be present in sound argillite.

In cement paste in the area not affected by a crack in the argillite, porosity decreased from 33 to 29% over 3-mm depth after 76 days. This porosity decrease extended deeper than the macroporosity opening and the mineralogical perturbations revealed by DRX. At 202 days, the same porosity decrease as at 76 days was observed. But at 415 days, the cement paste tended towards an opening with an average porosity value of 34% at the interface and punctually a value of 37%. Two tendencies were then opposed in the cement paste, initially, from 0 to 6 months, the cement paste porosity reduced, then after 6 months it enlarged. This reversible trend was not observed on the situ sample, where porosity decrease was still present after one year. Near an argillite crack in the cementitious material of the cells, the porosity decreased sharply to 25%. A crack is a preferential path for fluids and the elements are more available there than in a material matrix. Crack proximity led to the reduction of the porosity in the cementitious material, probably by the precipitation of phases such as calcite. On each sample, in the cement phase there is a trend on higher porosity area emerging on the outer edge. This is probably an artefact due to the technic used.

In the argillite, at the interface of cell C (72 days), there was a thick band of lower porosity that reaches a value of 10%. By difference with the plateau value away from the interface, the difference is 5%. This band was not observed at other times but something similar was present on in-situ samples aged of one year. Further away, the argillite porosity is significantly higher than the sound value. Table 3 indicates that the total porosity constantly increased with the experiment time (from 13 to 19%). This may be due to a uniform dissolution of the minerals induced by the highly alkaline plume that crossed the full sample (e.g. kaolinite dissolution, although not detected by XRD). A progressive release of dissolved organic matter from the clayey material with time concomitant to the propagation of the alkaline plume was measured et may also be an indicator of a strong perturbation of the argillite texture. The in-situ sample also showed an increase of the argillite total porosity after one year, although less intensely than in the cells.

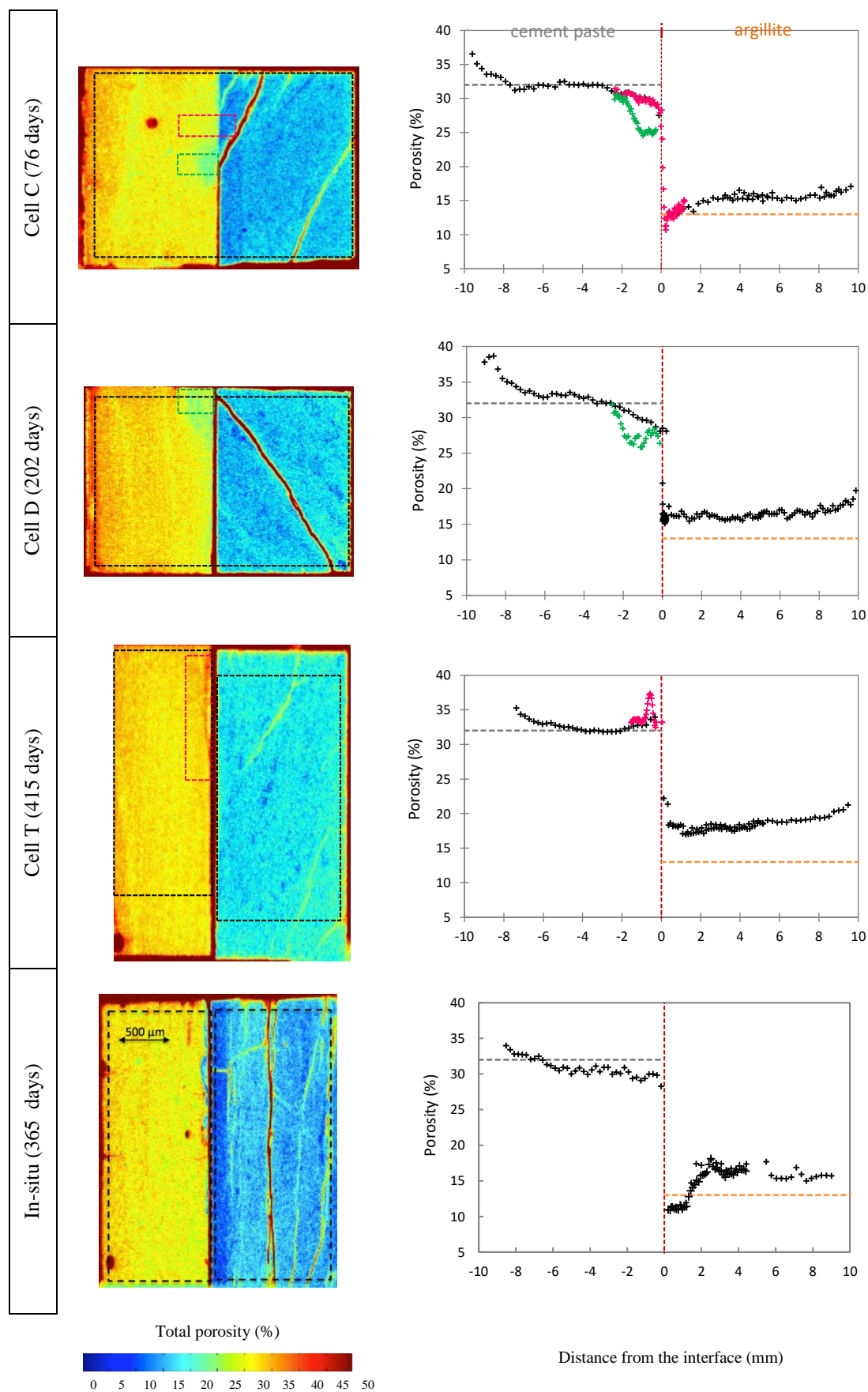


Figure 8: Total porosity profile around the CEM I / clayey rock interface after 1 year of interaction, measured by autoradiography on doped sample with ^{14}C -PMMA.

5 Conclusions and Future work

The CEMTEX project is always in progress and the first step of the work concerning the characterization of CEM I cement paste/clayey rock interface is almost finished. The important results in terms of exchange of soluble species, mineralogy changes causing microstructure modifications were acquired. The first new important result in term of reactive mechanism is the systematic precipitation of zeolite and tobermorite at 70°C after 1, 2 and 5 years of interaction in the in-situ conditions. Before one year, in the lab. experiments, only the tobermorite is observed at the interface. That is an important validation data for modelling. This kind of precipitation was never observed in the previous study putting in contact CEM I cementitious material and clayey rock in representative conditions of geological disposal (especially the zeolite), but was already observed in batch experiments superior to 60°C. The second important result is the very low degradation of the CEM I material. The temperature seems favoured the carbonation causing a small decreasing of the total porosity contrary to the results in previous study at 20°C. The impact on the microstructure of the cementitious material is a low decrease of the porosity in contact with the clayey rock. The CEMTEX project provides clearly new structural and mineralogical data for modelling. The next and last year of the CEBAMA project would allow obtaining the same level of knowledge about the low-pH cementitious materials in contact with the argillite at 70°C.

Acknowledgement

The research leading to these results has received funding from the European Union's Horizon 2020 Research and Training Programme of the European Atomic Energy Community (EURATOM) (H2020-NFRP-2014/2015) under grant agreement n° 662147 (CEBAMA).

References

- Andra (2005). Dossier 2005 Argile - Evaluation de la faisabilité du stockage radioactif en formation argileuse. Site de Meuse/Haute-Marne, Andra.
- Bartier, D., Techer, I., Dauzères, A., Boulvais, P., Blanc-Valleron, M.-M., Cabrera, J. (2013). In-situ investigations and reactive transport modelling of cement paste/argillite interactions in a saturated context and outside an excavated disturbed zone. *Applied Geochemistry*, 31, 94-108.
- Codina, M., Cau-Dit-Coumes, C., Le Bescop, P., Verdier, J., Ollivier, J.P. (2008). Design and characterization of low-heat and low-alkalinity cements. *Cement and Concrete Research*, 38(4), 437-448.
- Dauzères, A., Le Bescop, P., Sardini, P., Cau Dit Coumes, C. (2010). Physico-chemical investigation of clayey/cement-based materials interaction in the context of geological waste disposal: Experimental approach and results. *Cement and Concrete Research*, 40, 1327-1340.
- Dauzères, A., Achiedo, G., Nied, D., Bernard, E., Alahrache, S., Lothenbach, B. (2016). Magnesium perturbation in low-pH concretes placed in clayey environment-solid characterizations and modeling. *Cement and Concrete Research*, 97, 61-72.
- Dauzères, A., Lalan, P., De Windt, L., Detilleux, V., Bartier, D., Techer, I. (2016b). Geochemical evolution of cementitious materials in contact with a clayey rock at 70°C. *In*: M. Altmaier, V. Montoya, L. Duro, A. Valls (Eds.) *Proceedings of the 1st Annual Workshop of the CEBAMA Project*. KIT Scientific Report, 7734.
- Gaboreau, S., Prêt, D., Tinseau, E., Claret, F., Pellegrini, D., Stammose, D. (2011). 15 years of in-situ cement–argillite interaction from Tournemire URL: Characterisation of the multi-scale spatial heterogeneities of pore space evolution. *Applied Geochemistry*, 26, 2159-2171.
- Jenni, A., Mäder, U., Lerouge, C., Gaboreau, S., Schwyn, B. (2014). In-situ interaction between different concretes and Opalinus Clay. *Physics and Chemistry of the Earth, Parts A/B/C*, 70- 71, 71-83.

- Lalan, P., Dauzères, A., De Windt, L., Bartier, D., Sammaljärvi, J., Barnichon, J.-D., Techer, I., Detilleux, V. (2016a). Impact of a 70°C temperature on an Ordinary Portland Cement paste / claystone interface: an in-situ experiment. *Cement and Concrete Research*, 83, 164-178.
- Lalan, P. (2016b). PhD thesis.
- Poyet, S., Le Bescop, P., Touze, G., Moth, J. (2014). Formulating a low-alkalinity and self-consolidating concrete for the DOPASS-FSS experiment. NUWCEM 2014, Avignon.
- Tremosa, J., Arcos, D., Matray, J.M., Bensenouci, F., Gaucher, E.C., Tournassat, C., Hadi, J. (2012). Geochemical characterization and modelling of the Toarcian/Domerian porewater at the Tournemire underground research laboratory. *Applied Geochemistry*, 27(7), 1417-1431.

Changes in the anion content of groundwaters following interaction with cement

Emily Rastrick^{1*}, Matthew Isaacs^{1,2}, Mónica Felipe-Sotelo¹, David Read^{1,3}

¹ University of Surrey (UK)

² Institute of Energy and Climate Research: Nuclear Waste Management and Reactor Safety (IEK-6) (DE)

³ National Physical Laboratory (UK)

* Corresponding author: e.rastrick@surrey.ac.uk

Abstract

This paper summarises the results to date from the University of Surrey's contribution to the CEBAMA project under Work Package 1. Two experimental protocols are being used to investigate the interaction of various groundwaters with cements. The cementitious materials were chosen to cover those being considered as part of different European repository concepts: a Portland cement (CEM I), a ground granulated blast furnace slag: ordinary Portland cement blend (GGBS:OPC), Nirex Reference Vault Backfill (NRVB) and a CEBAMA reference blend, chosen to allow cross-comparison between the various research groups working on the project. The synthetic groundwaters under investigation are intended to represent granitic, clay and saline host rock environments. Groundwater conditioning cement experiments involve a large excess of groundwater compared to the cement blocks (solid/solution ratio = 0.075), in order to maximise the extent of cement-groundwater interaction. Conversely, cement conditioning groundwater experiments use equal volumes of cement and groundwater, whereby changes in groundwater composition should be more evident. Data have been obtained over a period of six months for the former experiments and one month for the latter. As expected, the pH of the solutions showed an increase due to interaction with cementitious materials; however, changes in groundwater anion concentrations appear to be independent of the cement to groundwater ratio. In all experiments, the chloride concentration of the groundwaters decreased following interaction with the cement blends. A greater decrease in groundwater sulphate concentrations was observed when the groundwaters were in contact with CEM I and NRVB cement blends.

1 Introduction

Disposal concepts for low and intermediate level waste in higher-strength rocks and lower-strength sedimentary rocks in the UK envisages the use of cementitious materials for structural purposes, waste grout and as backfill material. The high pH of the cement is intended to reduce the solubility and limit the migration of radionuclides, such as selenium (Felipe-Sotelo et al., 2016a), nickel (Felipe-Sotelo et al., 2016b) and the actinides (Young et al., 2013; Felipe-Sotelo et al., 2017). In contrast, Finland and Sweden are opting for less alkaline matrices owing to concerns surrounding the effect of high pH solutions generated by cement on other barrier materials (Read et al., 2001; Gaucher and Blanc, 2006; Dauzeres et al., 2010). Upon closure of the repository, the influx of groundwater will cause the cement to alter and evolve with time. Alteration processes include changes in pH, leaching of alkali hydroxides and decalcification (NDA, 2010a; Jacques et al., 2014). The extent of

degradation will depend on the type of cement and the composition of the groundwater with which it is in contact. This project studies four cement blends to cover those considered for European repository concepts; namely a Portland cement (CEM I), a ground granulated blast furnace slag: ordinary Portland cement (GGBS:OPC) blend, Nirex Reference Vault Backfill (NRVB) and a CEBAMA reference blend chosen as an inter-laboratory benchmark. The addition of supplementary cementitious materials within the blends modifies their properties; for example, silica fume is used to lower the pH and limit disturbance to host rocks (Gaucher and Blanc, 2006; Dauzères et al., 2010; Read et al., 2001). Three synthetic groundwaters under investigation emulate generic granitic, clay and saline host rock environments, respectively. The composition of the groundwater upon interaction will also change due to leaching of components from the cement (NDA, 2010a,b; Crossland and Vines, 2010) and uptake of groundwater ions by adsorption and mineralisation. This may lead to the formation of chloride- and sulphate-containing phases such as Friedel's Salt and ettringite, respectively. The aim of this work is to better understand the evolution of cement materials and groundwater in order to further constrain uncertainties in the safety case for geological disposal.

The cement powders described above have been characterised using X-ray fluorescence (XRF). This report focuses on analysis of the groundwater solutions following interaction with each cement.

2 Methodology

2.1 Experimental programme

Most of the published literature on cement-water interaction is based on batch experiments using disaggregated material where the solution is in substantial excess, typically $\geq 20:1$ (e.g. Jacques et al., 2014). This setup accentuates alteration of cement surfaces but is not a realistic representation of conditions in-situ. Recent advection and diffusion experiments conducted on intact monoliths (e.g. Felipe-Sotelo et al., 2017) give very different estimates of retardation and have revealed the importance of secondary cement phase development rather than surface adsorption in radionuclide retention. Both experimental protocols have been used in the present work in order to evaluate the effect of solid to solution ratios and to best observe the evolving cement mineralogy and groundwater (GW) chemistry, respectively.

2.2 Changes to groundwater composition with solution in excess

Diffusion experiments involved submersion of the hardened cement paste blocks, made from the four cement blends described previously, into the different synthetic groundwaters (Figure 1). Chemical and mineralogical changes in the groundwater and cementitious materials were studied; including changes to groundwater ion concentrations and the dissolution of cement phases. Samples were taken every two months. The large volume of synthetic groundwater (400 cm³) ensured maximum opportunity for diffusion into the hardened cement paste blocks. Ten cement blocks of 3 cm³ were submerged in the groundwater giving a solid to liquid ratio of 0.075 (400 cm³ GW to 30 cm³ cement). One cement block and one groundwater sample were removed at each time of sampling. The baseline samples for the groundwater and cement block were the groundwater as prepared and the cement block without submersion in synthetic groundwater. The groundwater was not replaced during the experiment as there is a large excess even after removal of samples.

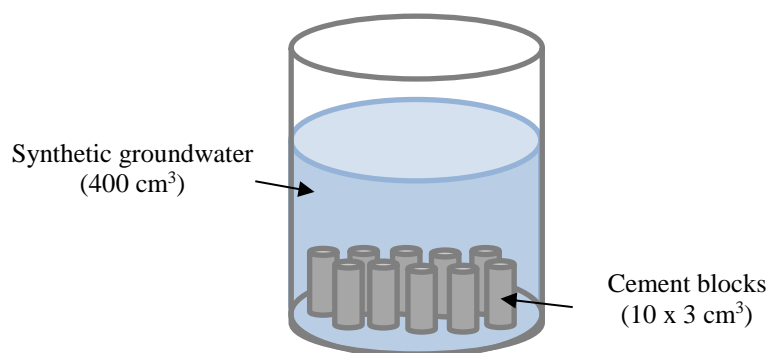


Figure 1: Set-up for changes to groundwater composition experiments.

2.3 Changes to groundwater chemistry following interaction with cement at solid/solution ratio = 1

The second set of experiments represent a more realistic situation for when the repository is sealed and the cement remains in contact with groundwater over a long period of time. A 200 cm³ cement block, made from the four cement blends described previously, was submerged in 200 cm³ of synthetic groundwater (Figure 2), with each cement blend in contact with each respective groundwater solution. The sampling times were once a week for four weeks with subsequent samples taken monthly. Groundwater samples of 1.0 cm³ volume were removed at each stage; the groundwater was not replaced after sampling. The baseline for the experiment was the synthetic groundwater as produced and the cement block without submersion in groundwater, allowing any chemical changes to the groundwater and mineralogical changes to the cement to be observed.

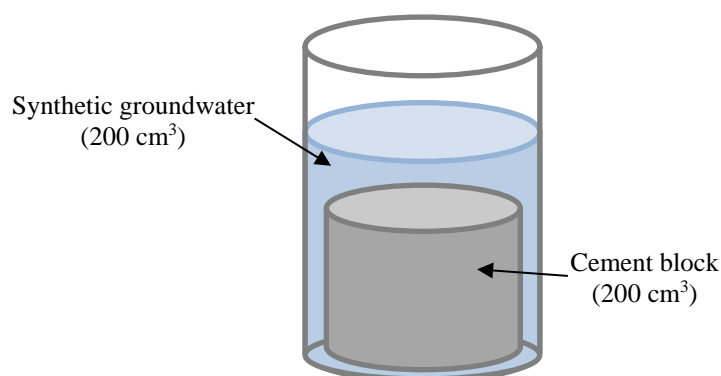


Figure 2: Set-up for changes to groundwater chemistry following interaction with cement at solid/solution ratio = 1.

2.4 Materials and Methods

The cements are used in the form of hardened pastes. The compositions of the cement powders are shown in Table 1 with the mixing proportions for the cement blends shown in Table 2. After hydration, the resultant cement paste was placed into moulds and cured in tap water for 28 days. After 28 days, the cured cement blocks were removed and placed into the relevant synthetic groundwater.

Table 1: Composition of cement powders as determined by XRF spectroscopy. Percentage composition data normalised to 100%, LOI data in addition to XRF data.

	Units	OPC	GGBS	Hydrated Lime	Lime Flour	Silica Fume	CEMI - Finnish	GGBS - Finnish
CaO	%	66.27	42.93	97.75	96.57	1.46	67.72	43.13
SiO ₂	%	17.86	31.92	1.37	1.70	93.10	17.60	32.30
Al ₂ O ₃	%	4.78	11.40	0.35	0.71	1.44	3.42	9.85
SO ₃	%	3.98	4.10	0.08	0.18	0.47	3.81	3.68
MgO	%	2.75	6.76	0.20	0.29	0.88	0.60	7.40
Fe ₂ O ₃	%	2.65	0.53	0.03	0.16	0.91	5.17	0.74
K ₂ O	%	1.52	1.19	0.33	0.69	1.73	1.30	1.20
TiO ₂	mg/kg	2,000	4,800	61	232	50	1,700	13,600
P ₂ O ₅	mg/kg	< LOD	< LOD	102	< LOD	< LOD	< LOD	< LOD
Mn	mg/kg	363	6,900	132	412	221	2,100	3,400
Sr	mg/kg	858	591	252	215	45	310	412
Zn	mg/kg	459	20	14	44	44	129	2
U	mg/kg	19	27	3	4	16	12	25
Th	mg/kg	10	28	2	3	2	9	48
LOI	%	2.15	0.00	30.98	43.22	3.36	2.13	0.00

XRF = X-ray fluorescence spectroscopy, OPC = ordinary Portland cement, GGBS = ground granulated blast furnace slag, NRVB = Nirex Reference Vault Backfill, LOD = limit of detection and LOI = loss on ignition

Table 2: Powder ratios of cement blends studied within this project.

Cement blend	OPC	GGBS	Hydrated Lime	Lime Flour	Quartz	Silica Fume	Water to cement ratio
CEM I	1.00	-	-	-	-	-	0.45
GGBS:OPC	1.00	9.00	-	-	-	-	0.45
NRVB	1.00	-	0.38	1.10	-	-	0.55
CEBAMA Reference mix	1.00	0.62	-	-	1.10	1.05	0.45

The phases present within the hardened cement paste, after 28 days curing, were determined by X-ray diffraction (XRD) using a Philips 1830 X-ray diffractometer with a Cu source at 8 keV. The voltage and current applied was 40 kV and 30 mA, respectively (1,200 W). Data were collected over 5-80° 2θ with a step size of 0.02° and a count time of 2 s. Figure 3 shows the phases identified; Rietveld refinement will be used in future in order to quantify the phases present. Other solid state characterisation techniques such as nuclear magnetic resonance (NMR), will be used for amorphous calcium silicate hydrate (C-S-H).

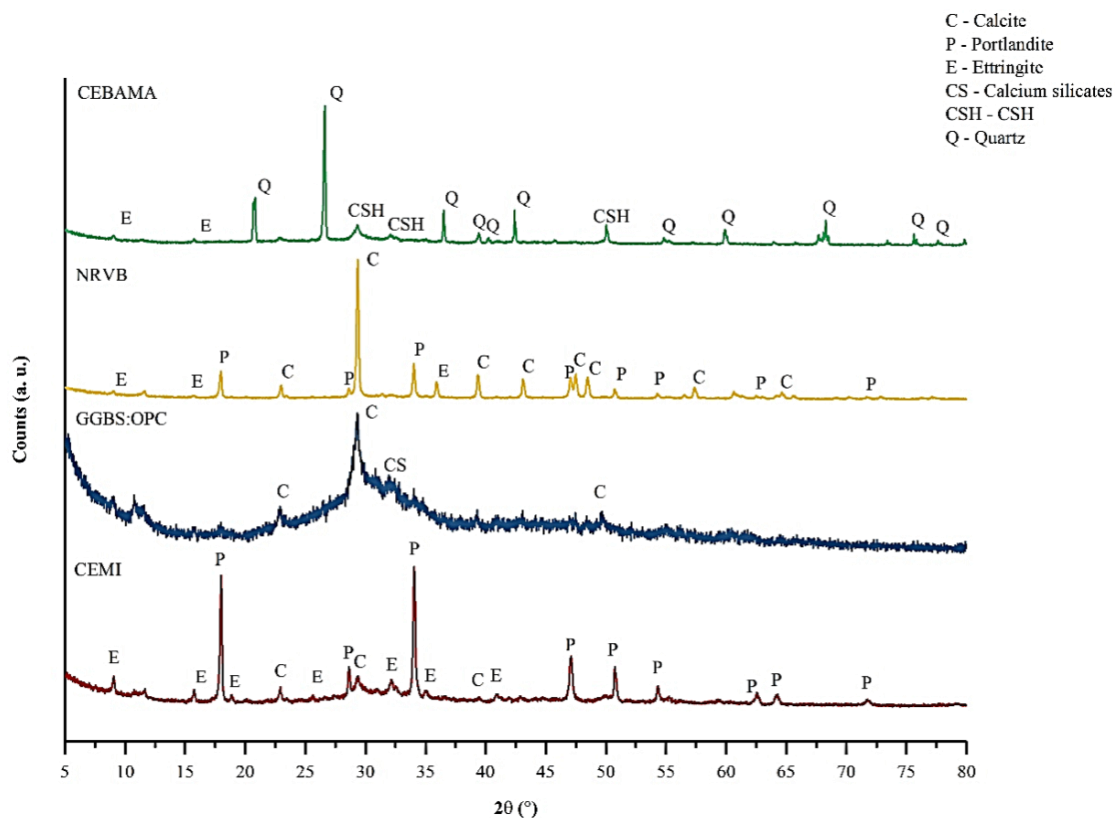


Figure 3: X-ray diffraction patterns for the four hardened cement pastes.

The synthetic groundwaters were prepared by dissolution of inorganic salts (Table 3) in deionised water and left to equilibrate for 14 days. The anion content of the solutions was characterised by ion chromatography. Alkali and alkaline earth metals were determined by flame atomic spectroscopy. The concentrations determined are shown in Table 4.

Table 3: Reagents used in 12 L of deionised water to produce synthetic groundwaters.

Chemicals	Chemical details
KCl	Fisher Scientific – Analytical grade
Na ₂ SO ₄	Anhydrous, Fisher Scientific – laboratory reagent grade
MgCl ₂ ·6H ₂ O	BDH AnalaR
CaCl ₂	Fisher Scientific
NaCl	Fisher Scientific
NaHCO ₃	ACS Reagent – Sigma Aldrich

Table 4: Reference and measured composition of three synthetic groundwaters determined by ion chromatography. All concentrations are reported as mg/L. Reference values are quoted for granitic and saline groundwaters (Gascoyne, 2002) and for clay groundwater (Vinsot et al., 2008).

Element	Granitic GW (R)	Granitic GW (M)	Clay GW (R)	Clay GW (M)	Saline GW (R)	Saline GW (M)
Na	64.4	63.2	1,264.5	1,118.1	3,218.6	3,035.9
K	3.9	4.1	43.0	52.6	82.1	104.7
Ca	20.0	16.2	300.6	241.4	797.6	682.3
Mg	4.9	4.7	138.5	153.7	9.7	8.2
Cl ⁻	70.9	75.0	1,772.5	1,941.0	6,381.0	6,389.0
SO ₄ ²⁻	9.6	10.3	1,440.8	1,626.0	384.2	507.5
HCO ₃ ^{-a}	122.0	ND	-	-	122.0	ND
pH	8.2	8.7	7.4	7.6	7.7	7.4

GW = Groundwater, R = Reference, M = Measured, ND = Not Determined

^a The groundwaters were prepared under ambient atmospheric conditions.

3 Results and Discussion

3.1 Changes in pH due interaction between cement and groundwater

The solution pH was monitored for changes to groundwater chemistry following interaction with cement (solid to solution ratio = 1, Figure 4 to Figure 6). It can be seen that after 9 days the pH increased to values greater than pH 11.5. The pH change for CEM I and NRVB is similar; however, the GGBS:OPC blend leads to consistently lower groundwater pH compared to the other two cement blends. It is important to understand pH evolution as higher pH will tend to produce more intense alteration in host rocks (Gaucher and Blanc, 2006; Dauzeres et al., 2010; Read et al., 2001). Hence, the use of supplementary cementitious materials, such as pulverised fuel ash and silica fume, in order to produce lower pH cements (pH < 11) for some applications.

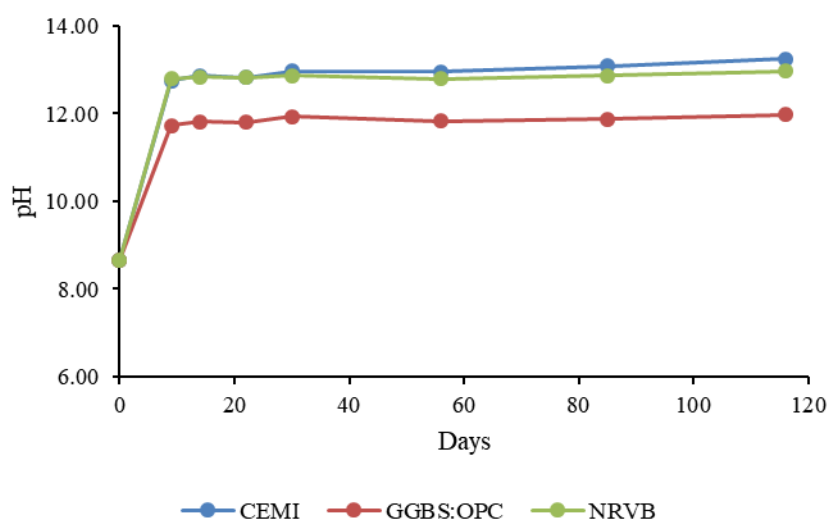


Figure 4: Changes in granitic groundwater pH as a result of interaction with cementitious materials.

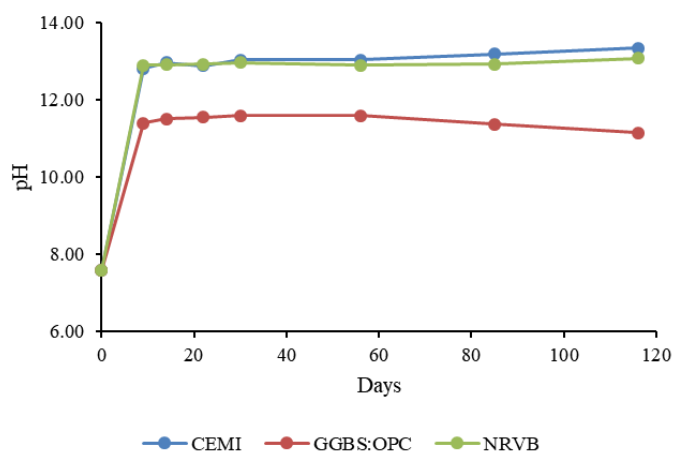


Figure 5: Changes in clay groundwater pH as a result of interaction with cementitious materials.

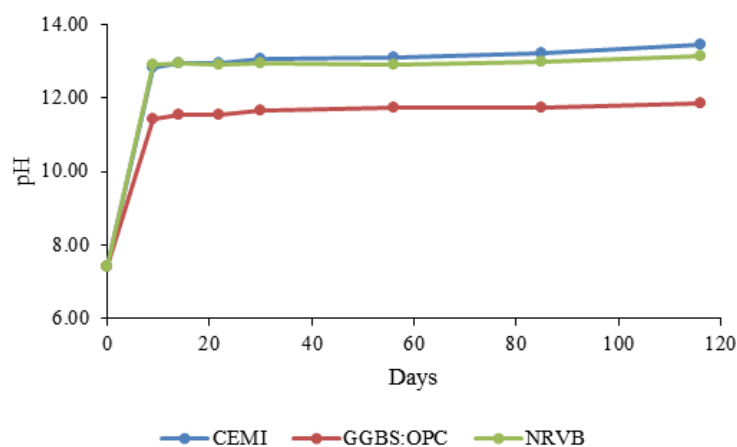


Figure 6: Changes in saline groundwater pH as a result of interaction with cementitious materials.

The CEBAMA reference blend was studied under the same ambient conditions. Results for the first 30 days are shown in Figure 7. It can be seen that the pH initially increased over the first three days yet steadily decreased from this point. The high pH at the beginning of the experiment is due to the dissolution of alkali hydroxides in the cement (NDA, 2010a); further analysis to determine sodium and potassium concentrations will provide confirmation.

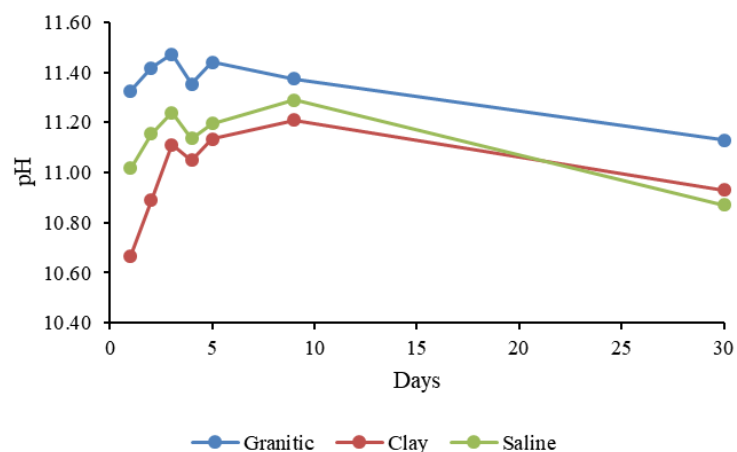


Figure 7: Change in groundwater pH as a result of interaction with CEBAMA reference blend.

3.2 Changes in major anion composition

Data for the groundwater chemistry experiments have been gained over a period of six months. All of the cement blends show the same trend of a decrease in solution chloride concentration after six months following interaction with cement, reflecting chloride uptake. Solid phase characterisation will confirm whether this is due to phases such as Friedel's Salt. Interaction with CEM I caused the greatest decrease in chloride content for all of the groundwaters.

There is a clear difference between groups of the cement blends in terms of sulphate (Figure 8 to Figure 10). The groundwaters in contact with the CEM I and NRVB cement blends have much lower sulphate concentrations due to uptake of sulphate ions by CEM I and NRVB and sulphate leaching from GGBS:OPC and the CEBAMA reference material.

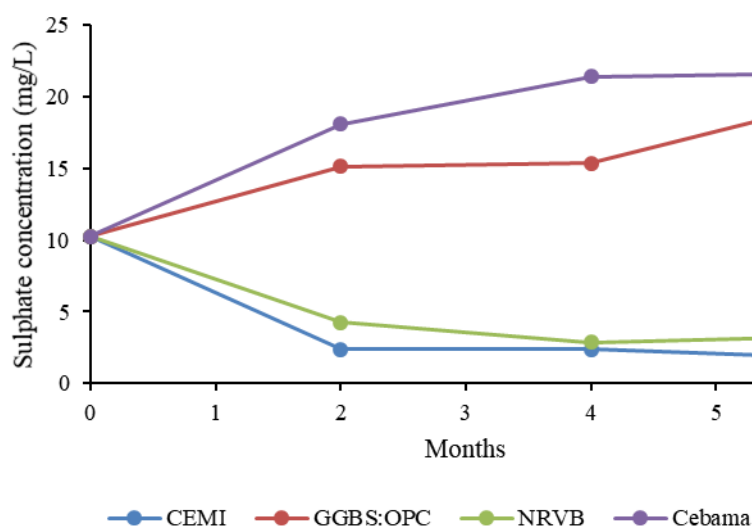


Figure 8: Change in sulphate concentration of granitic groundwater.

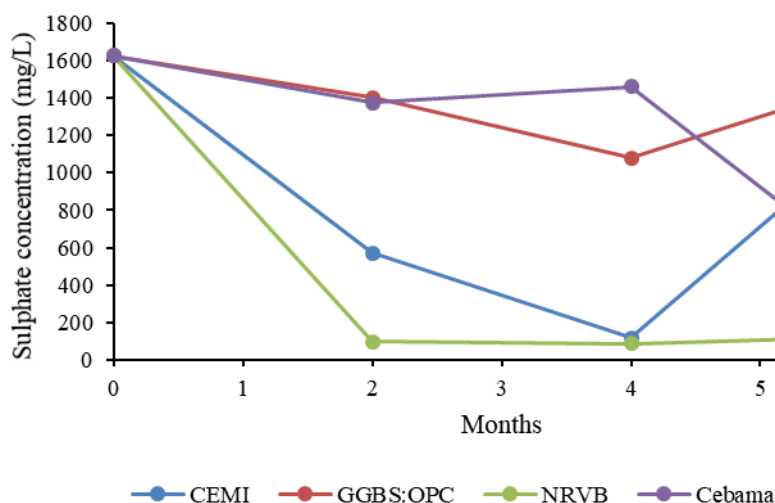


Figure 9: Change in sulphate concentration of clay groundwater.

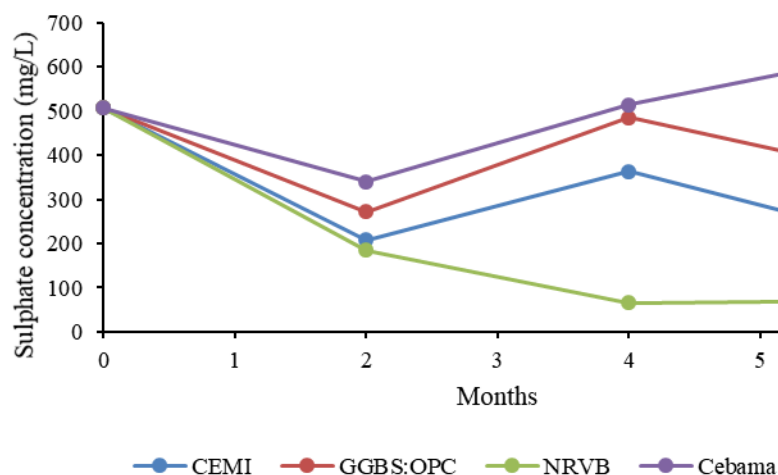


Figure 10: Change in sulphate concentration of saline groundwater.

3.3 Changes to groundwater chemistry following interaction with cement at solid/solution ratio = 1

Data have been gained for cement-groundwater interaction after a period of 116 days. Figure 11 to Figure 13 show changes in chloride and sulphate concentrations of granitic, clay and saline groundwaters, respectively following interaction with cement. For all of the groundwaters, the same trend can be observed for each of the cement blends. The cement blends can be split into two groups; CEM I and NRVB in comparison to GGBS:OPC. CEM I and NRVB behave similarly with the chloride and sulphate concentrations of the groundwaters decreasing over time. Conversely, for the GGBS:OPC blend, the anion concentrations remain around the initial composition of the groundwater. It is important to note the different initial concentrations of chloride and sulphate in the synthetic groundwaters; for example the granitic groundwater has lower concentrations than the clay and saline groundwaters. As the migration of the ions is due to diffusion, this would lead to a lower diffusion gradient for the granitic groundwaters in contact with cements. All of the data in Figure 11 to Figure 13 are based on single measurements. Multiple measurements will be completed on future samples in order to determine the error associated with the data and whether the variation is statistically significant. This is especially important for the GGBS:OPC cement blend as there is inconsistency in the early data (Figure 11 to Figure 13).

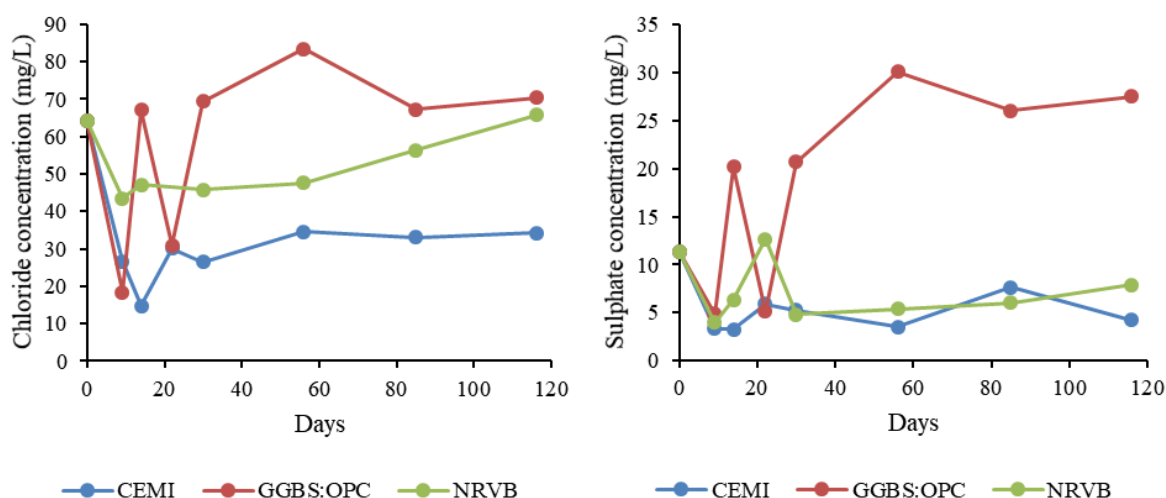


Figure 11: Changes in chloride and sulphate concentrations of granitic groundwater after interaction with cement for 116 days.

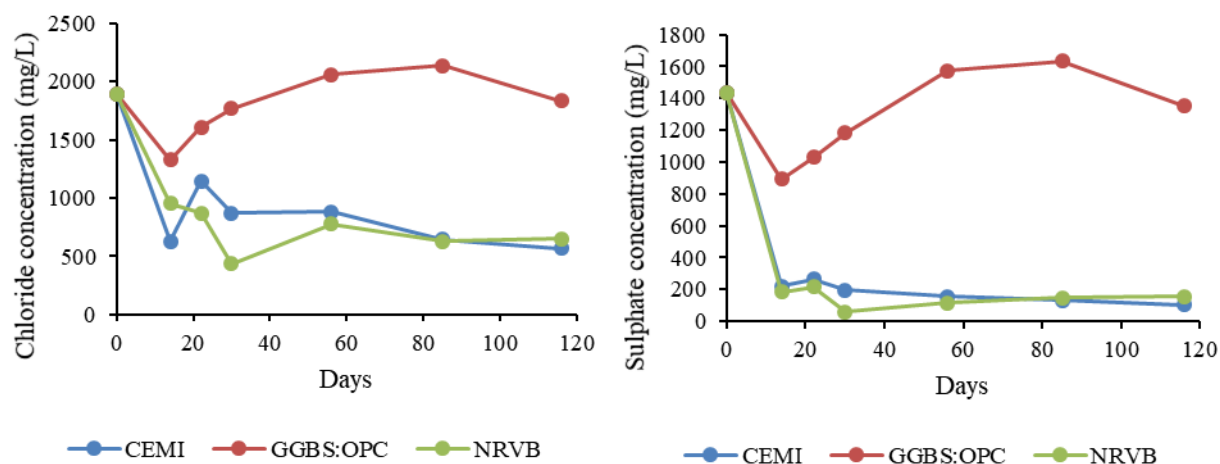


Figure 12: Changes in chloride and sulphate concentrations of clay groundwater after interaction with cement for 116 days.

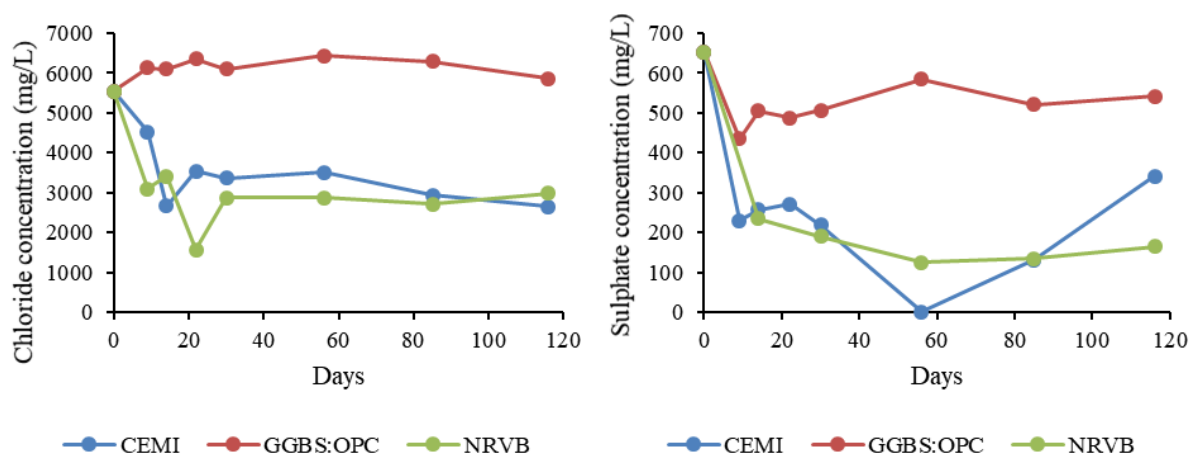


Figure 13: Changes in chloride and sulphate concentrations of saline groundwater after interaction with cement for 116 days.

4 Conclusions

For both sets of experiments, the data gained to date show that the changes in chloride and sulphate concentrations are similar despite the differences in volume of cement and groundwater used. Groundwaters in contact with GGBS:OPC show little change in solution chloride and sulphate concentrations. With a solid/solution ratio of 1 the pH of the surrounding groundwater increased to pH > 11.5 after only 9 days and then remained at this level for the duration of the experiment. For the CEBAMA reference material, the pH increased for 3 days before showing a steady decrease. The high alkaline pH of the system is important with respect to radioactive waste disposal in order to limit the migration of several safety relevant radionuclides into the environment.

Future Work

Future work will include analysis of the hardened cement paste in order to determine mineralogical changes that occur at the interface between the cements and groundwater and to observe whether discrete chloride- and sulphate-containing phases can be identified within the cement samples. X-ray computed tomography, scanning

electron microscopy-energy dispersive X-ray spectroscopy and XRD will be carried out in order to observe the zonation that is caused due to groundwater attack. Analysis of cations in the groundwaters will also be completed to determine if alkali and alkaline earth metals are leaching out of the cement. The experiments are long-term so will continue for up to two years, with sampling and analysis taking place at set intervals.

Acknowledgements

The research leading to these results has received funding from the European Union's Horizon 2020 Research and Training Programme of the European Atomic Energy Community (EURATOM) (H2020-NFRP-2014/2015) under grant agreement n° 662147 (CEBAMA) and from Radioactive Waste Management (RWM), to whom the authors are extremely grateful.

References

- Crossland, I. and Vines, S. (2001). Why a cementitious repository? Nirex Report N/034, 1-18.
- Dauzeres, A., Le Bescop, P., Sardini, P., Cau Dit Coumes, C. (2010). Physico-chemical investigation of clayey/cement-based materials interaction in the context of geological waste disposal: Experimental approach and results. *Cement and Concrete Research*, 40, 1327-1340.
- Felipe-Sotelo, M., Hinchliff, J., Evans, N.D.M., Read, D. (2016a). Solubility constraints affecting the migration of selenium through the cementitious backfill of a geological disposal facility. *Journal of Hazardous Materials*, 305, 21-29.
- Felipe-Sotelo, M., Hinchliff, J., Field, L.P., Milodowski, A.E., Holt, J.D., Taylor, S.E., Read, D. (2016b). The solubility of nickel and its migration through the cementitious backfill of a geological disposal facility for nuclear waste. *Journal of Hazardous Materials*, 314, 211-219.
- Felipe-Sotelo, M., Hinchliff, J., Field, L.P., Milodowski, A.E., Preedy, O., Read, D. (2017). Retardation of uranium and thorium by a cementitious backfill developed for radioactive waste disposal. *Chemosphere*, 179, 127-138.
- Gascoyne, M. (2002). Influence of grout and cement on groundwater composition. Posiva Working Report, 2002-07.
- Gaucher, E.C. and Blanc, P. (2006). Cement/clay interactions – A review: Experiments, natural analogues, and modelling. *Waste Management*, 26, 776-788.
- Jacques, D., Perko, J., Seetharam, S.C., Mallants, D. (2014). A cement degradation model for evaluating the evolution of retardation factors in radionuclide leaching models. *Applied Geochemistry*, 49, 143-158.
- NDA (2010a). Geological Disposal: Near-field evolution status report. NDA Report, NDA/RWMD/033.
- NDA (2010b). Geological Disposal: Radionuclide behaviour status report. NDA Report, NDA/RWMD/034.
- Read, D., Glasser, F.P., Ayora, C., Guardiola, M.T., Sneyers, A. (2001). Mineralogical and microstructural changes accompanying the interaction of Boom Clay with ordinary Portland cement. *Advances in Cement Research*, 13, 175-183.
- Vinsot, A., Mettler, S., Wechner, S. (2008). In-situ characterization of the Callovo-Oxfordian pore water composition. *Physics and Chemistry of the Earth*, 33, S75-S86.
- Young, A.J., Warwick, P., Milodowski, A.E., Read, D. (2013). Behaviour of radionuclides in the presence of superplasticiser. *Advances in Cement Research*, 25, 32-43.

CEBAMA reference mix design for low-pH concrete and paste, intermediate results

Tapio Vehmas^{1*}, Markku Leivo¹, Erika Holt¹, María Cruz Alonso², Álvaro Fernández²,
José Luis García Calvo², Radek Vašíček³, Radek Červinka⁴, Petr Večerník⁴, Tomáš
Rosendorf^{4,5}, Jiří Svoboda³, Nicolas Finck⁶, Vanessa Montoya⁶, Naila Ait Mouheb⁶,
Kathy Dardenne⁶, Jörg Rothe⁶, Thorsten Schäfer⁷, Horst Geckeis⁶, Stéphane Gaboreau⁸

¹ VTT Technical Research Centre of Finland Ltd. (FI)

² CSIC Institute of Construction Science Eduardo Torroja (ES)

³ Centre of Experimental Geotechnics, Faculty of Civil Engineering,
Czech Technical University in Prague (CZ)

⁴ ÚJV Řež, a.s. (CZ)

⁵ Department of Nuclear Chemistry, Faculty of Nuclear Sciences and
Physical Engineering, Czech Technical University in Prague (CZ)

⁶ Institute for Nuclear Waste Disposal (INE), Karlsruhe Institute of
Technology (KIT) (DE)

⁷ Applied Geology, Institute of Geosciences, Friedrich-Schiller-
Universität Jena (DE)

⁸ The French Geological Survey (BRGM) (FR)

* Corresponding author: tapio.vehmas@vtt.fi

Abstract

Reference low-pH concrete and paste mixes were manufactured within the CEBAMA project. The reference mixtures were cast at VTT in March 2016 and samples were distributed among some of the CEBAMA partners. Reference mix designs were used as common materials to study their behaviour in contact with waters of different composition and interaction with radionuclides. This article provides intermediate results of the reference low-pH concrete and paste studies, including mechanical properties measurements, chemical composition analysis, microstructure evaluation and transport property measurements.

1 Introduction

Reference low-pH concrete and paste mixtures for the CEBAMA project were manufactured in March 2016 by VTT and distributed to some of the partners. Reference mix designs and samples enable comparison of various research methods applied in the CEBAMA project. Reference mix designs consisted of both a reference concrete (RCM) and reference paste (RPM). The composition and detailed information of the RCM and RPM are described in 1st - and 2nd Annual Workshop Proceedings of CEBAMA (Vehmas et al., 2016; Vehmas et al., 2017). Additional reference concrete with lower density (RCM-LD) was manufactured for CSIC. Lower density was obtained by increasing the water content and adding air entrainment admixture. Water/binder ratio of RCM-LD was 0.6 and air entraining agent dosage was 0.12% from binder weight (Air Mix admixture from Finnsementti). Air content of RCM-LD was 2.7% (according to SFS-EN 12350-7) and the density was 2,320 kg/m³.

Some of the experiments are still ongoing and will be reported in the 4th Annual Workshop Proceedings of CEBAMA in 2019.

This article provides intermediate results of the reference low-pH concrete and paste studies, including mechanical properties measurements, chemical composition analysis, microstructure evaluation and transport property measurements.

Czech Technical University (CTU) and ÚJV Řež (UJV) studied mechanical properties by performing uniaxial strength tests on thin samples, which have been stored in an environment that corresponds to the Czech waste repository. The Technical Research Centre of Finland (VTT) has measured the compression strength development of RCM and RPM, which have been stored submerged in water.

The chemical compositions of RPM and RCM were studied by the Institute of Construction Science Eduardo Torroja (CSIC), Karlsruhe Institute of Technology, Institute for Nuclear Waste Disposal (KIT-INE) and VTT. CSIC's main characterization methods were X-ray diffraction (XRD), differential thermal analysis (DTA), thermogravimetry (TG), backscattering scanning electron microscopy with energy dispersive spectroscopy (BSEM-EDS), measurements of pore solution pH and ion composition. KIT-INE has studied RCM and RPM composition with X-ray absorption spectroscopy (XAS). VTT has measured the pH of RCM and RPM in ion-exchanged water and in saline groundwater which corresponds to the deep groundwater of Finland's nuclear waste repository in Olkiluoto.

CSIC, UJV and the French Geological Survey (BRGM) have studied the microstructure of the reference samples. CSIC has imaged the RCM samples with scanning electron microscopy (SEM) and measured the porosity with Mercury Intrusion Porosimetry (MIP). UJV has measured the porosity with water immersion test and calculated the porosity from the diffusion measurements. BRGM has conducted an extensive porosity study on RCM and RPM by applying MIP, helium pycnometer and kerosene porosity method and deriving the total porosity of the samples from the measurements.

CSIC has studied the transport properties with two different testing methods: chloride transport and water leaching resistance from percolation tests.

2 Research methods

2.1 Mechanical properties

Laboratory works at CTU & UJV are based on ageing procedures with Czech Ca-Mg bentonite (Bentonit 75, B75), low-pH binder (RPM) and groundwater from the underground laboratory Josef (GW Josef) under high temperature of 95°C and 10°C as a reference. The ageing procedures on low-pH reference paste samples are ongoing since December 2016. Sampling after 9 months of ageing was performed and analyses commenced in September 2017. Laboratory analyses mainly include uniaxial strength tests on thin samples, mineralogy, pH of leachates and diffusion properties. More details can be found in CTU & UJV's contribution to the 2nd CEBAMA Annual Workshop (Vašíček et al., 2017).

Because the interaction occurs mainly on interfaces (i.e. the sample surface), a specific shape of the samples is used to magnify this effect when uniaxial strength in compression is tested. Thin plates (cylinders with diameter of 50.0 mm and height of 8.2 mm) and a corresponding non-standard punch test method are being used (Figure 1). Such tests provide output as "Load at breakpoint (kN)" which can be recalculated into "punch compressive strength (MPa)" and then recalculated again to a value relevant to tests on ordinary samples (cube/cylinder). Both

calculations are based on linear, experimentally determined, relationships. More on this method can be found in Večerník et. al. (2016). Each of the ageing procedures provided 10 samples for strength tests, which created datasets for further evaluation.

As extra work to take advantage of available records of the press test machine, records of the “press head displacement” were evaluated together with load at breakpoint. Press head displacement is related to deformation of the sample but the total displacement includes also a portion related to deformation of the head itself. This portion cannot be precisely identified but is believed that it is introduced in a systematic manner over all the datasets. Therefore, the displacement values cannot be used in quantitative way to determine deformation moduli however they still seem to be quite a good indication of changes of the elasticity.

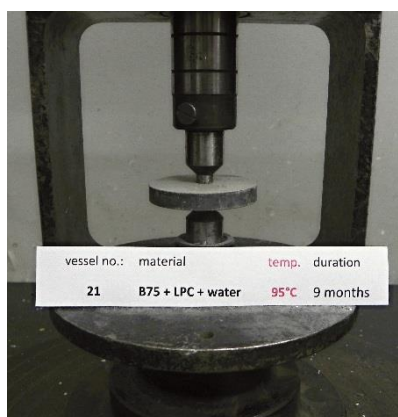


Figure 1: Punch test on RPM sample aged for 9 months at 95°C in suspension of bentonite B75 and groundwater, from CTU-UJV.

VTT has measured compression strength of the CEBAMA reference concrete (RCM) and reference Paste (RPM) up to 728 days. Samples (150 x 150 x 150 mm) were stored submerged in water up to testing age. The compression strength of the concrete samples was determined according EN 12390-3.

2.2 Chemical composition

The chemical composition of RCM and RCM-LD (Low Density) after 15 and 2 months of maturity, respectively, was analysed to complete the characterization initiated in Vehmas et al. (2017) by CSIC. The characterization methods were: XRD, DTA/TG, BSEM-EDS, pore pH and soluble ions measured according to Alonso et al. (2012).

The CEBAMA low-pH paste and concrete contain low amounts of iron and chlorine in their chemical composition (Vehmas et al., 2017). Despite their low concentration, their presence and specially their speciation could be relevant to study radionuclide migration in these environments. Information on the speciation of these two elements was provided by KIT-INE by application of X-ray absorption spectroscopy (XAS), which is an element specific and non-destructive technique, at the Fe *K*-edge and at the Cl *K*-edge. XAS spectra can be divided into two energy regions. The X-ray absorption near-edge structure (XANES) around the absorption edge is particularly sensitive to e.g. oxidation station and coordination geometry and can be used as “fingerprint” of the binding environment. Comparison with reference compounds allows identifying the nature of the chemical environment. At higher energies, the extended X-ray absorption fine structure (EXAFS) contains information on the nature, coordination number and interatomic distance of neighbouring shells.

For both samples Fe *K*-edge XAS data were collected at the European Synchrotron Radiation Facility (ESRF, Grenoble, France) at the BM26A beamline (Nikitenko et al., 2008) and Cl *K*-edge XAS data were collected at the KIT synchrotron light source Karlsruhe Research Centre, (Karlsruhe, Germany) at the INE-Beamline (Rothe et al., 2012). Data were collected either in transmission or in fluorescence detection mode for the powdered samples and for relevant reference compounds. Some reference compounds were synthesized and provided by BRGM (Friedel's and Kuzel's salt, C-S-H phases with Ca:Si = 0.8, 1.0 and 1.6) and EMPA (ferrites C₂F and C₄AF). Data were treated following standard procedures using the Athena interface to the Ifeffit software (Ravel and Newville, 2005).

VTT has measured pore solution pH according to a method described in the literature (Alonso et al., 2012). pH was also determined for samples where the ion exchanged water was replaced with saline groundwater. Saline groundwater (SGW) composition is a reference deep groundwater representative of 450 metres depth in ONKALO, with a composition as presented in Table 1. Saline groundwater presents the cementitious materials pH in close vicinity of the concrete surface at the repository environment.

Table 1: Chemical composition of the Saline Groundwater (SGW) used in the pH measurements of VTT.

Element	Concentration
Na ⁺	210 mM
Cl ⁻	410 mM
Ca ²⁺	100 mM
Mg ²⁺	2 mM
Br ⁻	1 mM
K ⁺	0.54 mM
Sr ²⁺	0.4 mM
SO ₄ ²⁻	0.04 mM

2.3 Microstructure

The microstructure of the RCM and RCM-LD concretes was studied in the same systems through SEM (in the case of RCM) and MIP by CSIC. Also, the microstructure of concretes after percolation tests was analysed.

Porosity measurements were performed by ÚJV. Two different approaches were used: water immersion method based according to Melnyk and Skeet (1986) and evaluation from performed diffusion experiments. Both types of porosity testing require fully saturated samples. In the water immersion method, weights of saturated and dried samples are compared and a porosity is calculated from these values. For this type of test, samples after diffusion experiments will be used. In the second approach of porosity evaluation, the porosity values are calculated from experimental diffusion data.

BRGM conducted Mercury Intrusion Porosimetry (MIP) measurements. Intrusion and extrusion curves were obtained using a Micromeritics Autopore IV 9500 volumetric set up on blocks of 2 cm³ from atmospheric pressure up to 200·10⁶ Pa. All the samples were heated under vacuum conditions at 100°C for at least 36 hours and cooled under vacuum. Cumulative pore throat size distribution, up to the critical pore diameter, is calculated from the intrusion curve based on Washburn's law and a contact angle of 141.3° (Washburn, 1921), assuming a cylindrical pore shape. The bulk density (ρ) of each sample was also obtained before the first pressure step (3·10³ Pa). The

total intrusion porosity ϕ MIP is also estimated from the maximum intruded volume of mercury V (intr.max) (m^3/kg) and ρ , (kg/m^3) using the following Eq. 1:

$$\phi_{\text{MIP}} = V (\text{intr.max}) \times \rho \quad (1)$$

Grain density was measured by helium pycnometry using a Micromeritics Accupyc 2020. Prior to measurement, the sample were dried at 100°C under vacuum for at least 36 hours. Total bulk porosity and grain density were measured with the kerosene porosity method (Gaboreau et al., 2011) and calculated from measured grain density (ρ_{gr}) (helium pycnometry) and apparent dry density (ρ) (mercury intrusion porosimetry) according to the following Eq. 2:

$$\phi = 1 - (\rho/\rho_{\text{gr}}) \quad (2)$$

2.4 Transport properties

The transport properties of RCM and RCM-LD were characterised by CSIC by two different testing methods: 1) Chloride transport and 2) water leaching resistance with percolation tests. The resistance to Cl transport is analysed with both natural and accelerated tests. The natural diffusion is measured according to prCEN/TS 12390-11 standard (1st results after 12 months exposure). The accelerated Cl transport (migration) is measured according to NT Build 492 standard. The percolation tests were started on RMC at 6-9 months age and RCM-LD after 2 months of maturity. Two groundwaters are used: 1) low ion content (Grimsel granite representative of the Grimsel test Site URL) and 2) high ion content (simulated clayey water). One sample for each reference concrete type has been removed from the percolation tests after 13 (RCM) and 7 (RCM-LD) months and concrete modifications have been analysed.

The pH leachate tests (up to 455 days since RPM mixing) were performed by ÚJV. The procedure is described in Alonso et al. (2012) and is similar to the method used by VTT and CSIC. In every sampling interval the testing of the leachate pH was performed in triplicates. The standard error of the obtained results is lower than 0.1 pH unit.

The determination of changes in tritium (as HTO) and chloride (^{36}Cl) diffusivities on samples of hardened RPM CEBAMA reference mix that interacted with underground water (GW Josef representative of the Czech Republic repository) or bentonite B75 suspension, belongs to the goals of Czech laboratory programme. The interaction experiments were designed for 9 and 18 months under two different temperatures (10°C and 95°C) in the pressure vessels. Through-diffusion experiments were launched on the specimens (thickness 8-9 mm, diameter 50-51 mm) sampled in the first period of the CEBAMA project. All through-diffusion experiments are performed in the filtered solutions from vessels where the LPC samples interacted with GW Josef at 10°C . Volumetric activities of ^3H and ^{36}Cl (using liquid scintillation counting method) are measured in both reservoirs having a volume 56-59 mL. The sampled liquid phase (0.2 mL) is compensated by the same initial activity of ^3H and ^{36}Cl (in the inlet reservoir) or by the fresh experimental solution (in the outlet reservoir).

3 Results

3.1 Mechanical properties

CTU performed compressive strength measurements on the RPM. Uniaxial compressive strength of reference samples was about 80 MPa (Vašíček et. al., 2017). Figure 2 presents outputs of compressive punch tests (a mean value of each dataset) - the press head displacement vs. load at breakpoint for initial (not aged, full black triangle) and 9 months aged samples. Ageing temperature of 10°C is in blue and 95°C in red; full triangles represent samples aged in suspension of bentonite and GW Josef. Empty triangles represent only GW Josef (blue and red) or humid air (black) as ageing environment.

Hardening is observed for all types of samples/ageing procedures after 9 months. Value from “humid air at 10°C” (black empty triangle) can be taken as a result of “hardening under normal condition”, with increase to 140% (approx. 112 MPa after recalculation). In such cases it could be concluded that all other ageing conditions provided harder samples with an increase up to about 180% (approx. 144 MPa) for “hot water” (95°C + GW Josef). Figure shows that temperature (10 or 95°C) have also certain influence on strength evolution, in that the “hot” environment produced harder samples after 9 months.

As all results from “environment without bentonite” (initial and all empty triangles) created linear trends, it can be estimated that elasticity remained unchanged for such samples / ageing environments (i.e. without bentonite). Contrary to this, samples from “bentonite suspension” have lost part of their elasticity.

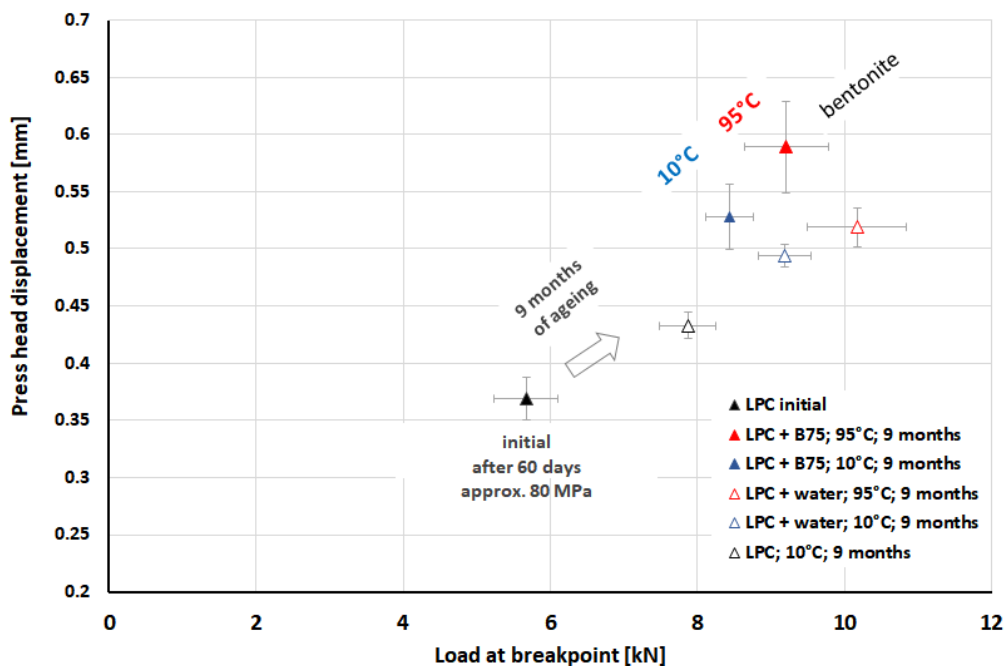


Figure 2: Press head displacement vs. load at breakpoint - RPM (LPC) samples aged for 9 months under various conditions, from CTU.

Compression strength development of the CEBAMA reference concrete (RCM) and paste (RPM) measured by VTT is presented in Figure 3. For comparison purposes binary and ternary mix designs are also presented (Vehmas et al., 2017). According to the results, CEBAMA reference concrete has an increased compression strength during 420-720 days, whereas binary and ternary mix designs strength development had ceased.

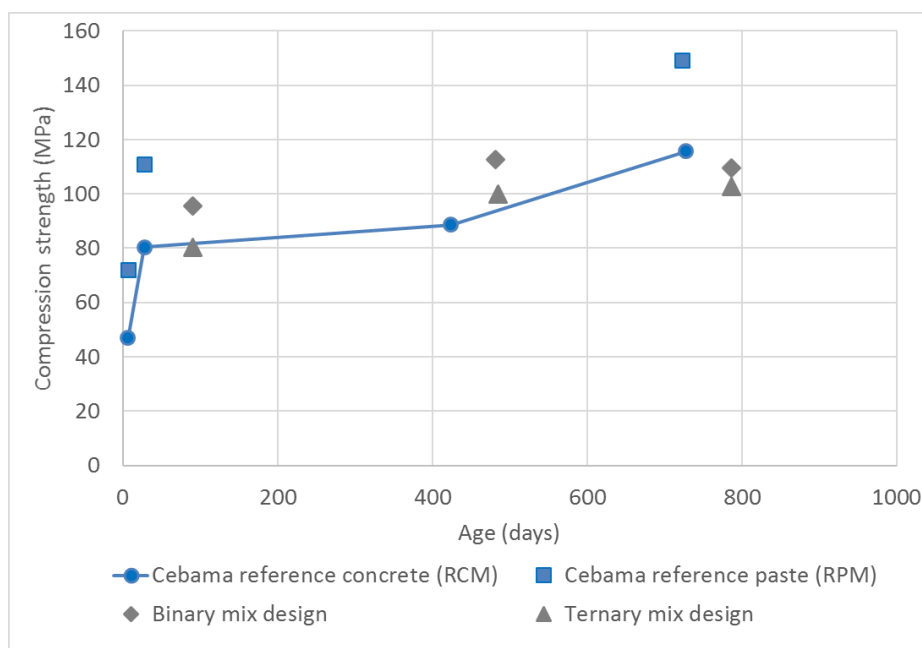


Figure 3: Compression strength development of CEBAMA reference concrete and paste, from VTT.

3.2 Chemical composition

CSIC did not observe significant differences in chemical composition of RCM and RCM-LD at 15 and 2 months of maturity compared to that at 5 months for RCM included in Vehmas et al. (2017). The pH in RCM is 11.40 after 15 months. Portlandite is not detected in any of the concretes. Sulphoaluminate phases and C-S-H gel are not detected by XRD, probably due to the interference of aggregates. The bound water, measured by DTA/TG, vary from 1.6% in RCM to 1.2 in RCM-LD at 15 and 2 months, respectively. The EDS reveal mean CaO/SiO₂ -ratio around 0.60 in RCM and 0.46 in RCM-LD and CaO/Al₂O₃-ratio around 7.8 and 4.8 respectively.

In KIT studies, Cl *K*-edge XANES were recorded for the samples and reference compounds (Figure 4 left). The main absorption edge is located at a similar position in all samples and reference compounds, implying that Cl is present only in –I oxidation state. Some reference compounds exhibit a shoulder after the edge crest or white line (WL) at around 2,826.6 eV that may arise from multiple scattering effects at medium-range distance around Cl. Some compounds have as well a feature at around 2,832.7 eV. In the 0.5 mol/L NaCl reference solution the height of the shoulder at 2,826.6 eV is comparable to that of the main edge, in agreement with reported data (Huggins and Huffman, 1995). The XANES of the low pH artificial cement pore water (ACW), prepared as described in Ait Mouheb et al. (2018), differs from that of the 0.5 mol/L NaCl solution by the absence of a shoulder and a different width of the WL. This result suggests differences in the aqueous speciation that may arise from the nature of the counter-ions and the Cl concentration in solution (Huggins and Huffman, 1995). The XANES of Friedel's and Kuzel's salts are very similar and differ from all other compounds. The speciation of Cl in the C-S-H phases seems to depend on the Ca:Si ratio (Ca:Si = 0.8 and 1.6 were measured), and the XANES also differ from that of all other compounds.

The Cl *K*-edge XANES of the paste and the concrete are very similar, pointing to comparable chemical environment, but completely differ from that of ACW and the NaCl solution. Data further suggest that no NaCl or KCl salt precipitated in these samples. The Cl environment in the paste and in the concrete differs from that of the Friedel's and Kuzel's salts and from that of the C-S-H phases because of the absence of a shoulder at 2,826.6 eV and the lower WL height. Interestingly, the XANES of the paste and concrete seem to have similarities

with that of the $\text{CaCl}_2 \cdot 2\text{H}_2\text{O}$ salt, in terms of WL height and absence of additional features or a shoulder. This result indicates that the Cl chemical environment in both samples may be close to that of Cl in this salt.

Additionally, Fe *K*-edge XAS data were recorded by KIT for the paste and concrete and compared to data recorded for several reference compounds containing Fe in octahedral (^{56}Fe) or tetrahedral (^{57}Fe) coordination (Figure 4 middle and right). These environments can be discriminated from the intensity of the pre-edge features at ~ 10 eV before the main edge: only very weak features are observed for ^{56}Fe (e.g. goethite, ferrihydrite) whereas the pre-edge is of higher intensity for ^{57}Fe (FePO_4) (Figure 4 middle) (Westre et al., 1997).

The CEM I clinker and both ferrites (C_2F ($\text{Ca}_2\text{Fe}_2\text{O}_5$) and C_4AF ($\text{Ca}_2(\text{Al},\text{Fe})_2\text{O}_5$)) have comparable XANES: the pre-edge features are of comparable intensity and the XANES exhibit two shoulders on the high-energy side of the edge crest at $\sim 7,137$ and $\sim 7,144$ eV. These results are similar to EXAFS spectra and hint at comparable chemical environments in these compounds. The XAS data of both C-S-H phases are very similar to each other suggesting comparable Fe speciation.

The XANES of the CEBAMA paste has features similar to that of the C-S-H phases, especially the sample having $\text{Ca}:\text{Si} = 1.0$ because of the intensity of the shoulder at 7,137 eV. However, small differences observed in the XANES, such as the WL height, may suggest that Fe is not located in a single phase in the paste but in more than one. This result is qualitatively corroborated by the comparison of the EXAFS spectra.

The XANES of the CEBAMA concrete does not contain the feature at 7,137 eV, which suggests differences in the Fe chemical speciation between the CEBAMA paste and the concrete. This finding is supported by the comparison of EXAFS spectra. The WL of the concrete has similarities with that of the ferrihydrite, but differences in the first oscillation after the edge centred at 7,190 eV corroborate differences in chemical environments, which is also suggested from the respective EXAFS spectra. Finally, the Fe chemical environment in the paste and in the concrete differ from that of the magnetite, hematite, goethite, silica fume, Fe sulfate and FePO_4 reference compounds, meaning that these phases are absent in both samples or present in very low amounts.

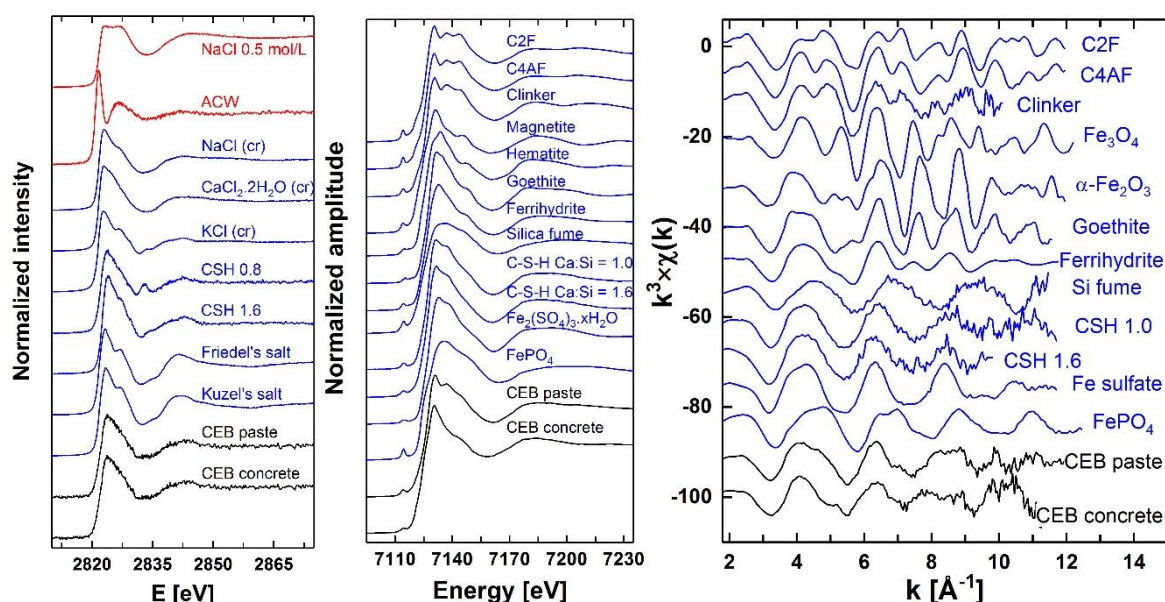


Figure 4: Experimental Cl *K*-edge XANES (left) and Fe *K*-edge XANES (middle) and EXAFS spectra (right) of the paste and concrete with reference compounds from measurements performed by KIT.

VTT has measured pore solution pH development of CEBAMA reference-concrete (RCM) and -paste (RPM). Results are presented in Figure 5. Pore solution pH of RCM has decreased and is not equal to reference mix designs. In saline groundwater, the pH is substantially lower than in ion exchanged water. Pore solution pH of the RPM is still higher than RCM and the RPM pH has not decreased during 420-720 days. This might originate from significantly lower water/binder -ratio of the RPM compared to RCM.

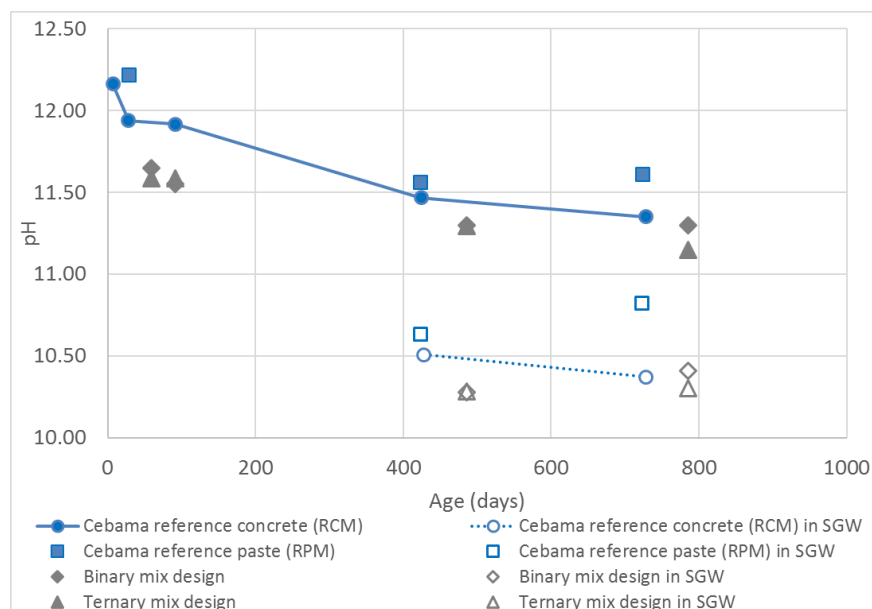


Figure 5: pH development in ion exchanged water and saline groundwater of CEBAMA reference concrete and paste, from VTT.

3.3 Microstructure

CSIC studied the RCM microstructure with scanning electron microscope (SEM). SEM images in RCM after 15 months confirm the dense microstructure, shown in Figure 6, and dense aggregate-cement paste at the interfacial transition zone (ITZ), similar to that found at 5 months (Vehmas et al., 2017). The pore structure and the total porosity hardly changes from 5 to 15 months in RCM (2.3 - 2.5%), while in RCM-LD the total porosity is 12.2% after 2 months.

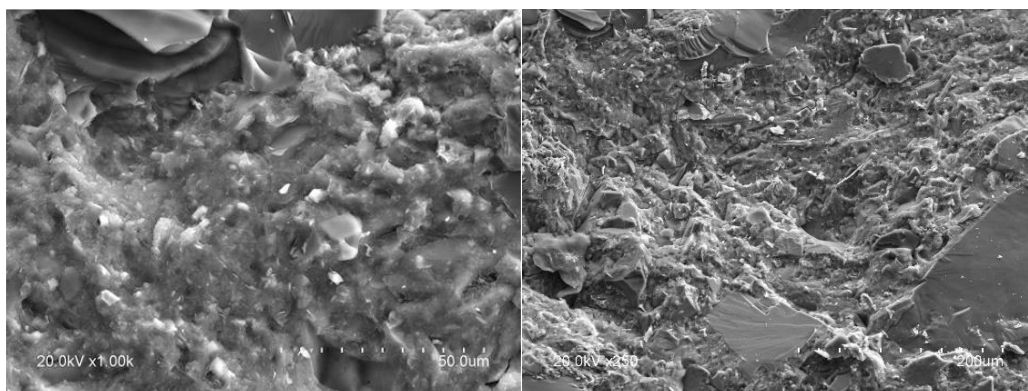


Figure 6: SEM images of RCM after 15 months of curing x1000 (left) and x250 (right), from CSIC.

UJV performed the evaluation of porosity by the water immersion method and from the diffusion experiments that are closely connected to performing the diffusion tests with the same LPC samples. The diffusion experiments are still running, so the evaluation of the porosity can be performed after the finishing of diffusion tests.

BRGM porosity measurement data is summarized in Table 2. The total porosity includes the capillary and gel porosity. The bulk density obtained from MIP and kerosene are coherent for both materials. The grain density at 2.48 and 2.61 for RPM and RCM, respectively are consistent with the mineralogy and the grain density of the main phase constituting the material, i.e. C-S-H (Roosz et al., 2016) for RPM and silicate aggregate for concrete.

The measured porosities with MIP are 6.07 and 3.8% for RPM and RCM, respectively; while with kerosene the porosities are at 26 and 12% in agreement with the calculated porosity. This discrepancy between MIP and the others method is due to the limited intrusion of mercury in the pore network of the cement materials.

Table 2: Summary of the density and porosity measured and calculated from the different acquired data from BRGM.

Material	MIP		He pycnometer	Kerosene porosity		Calculated porosity
	Bulk density (ρ)	ϕ MIP	Grain density(ρ_{gr})	Bulk density (ρ)	Total porosity	$\phi = 1-(\rho/\rho_{gr})$
RPM	1.878 g/cm ³	6.07%	2.48 g/cm ³	1.830 g/cm ³	26.21%	24.3%
RCM	2.275 g/cm ³	3.8%	2.61 g/cm ³	2.284 g/cm ³	12.47%	12.8%

The mercury intrusion curves obtained on RPM and RCM are displayed on Figure 7. The curves are given in mL/mL in order to compare directly with the porosity value. The curves are also normalized to the total calculated porosity value (Table 2) in order to illustrate the porosity probe by mercury for both materials. With MIP, only 30% of the pore volume is probed. For both materials, the main pore throat size is centred on 13 nm. Two different throat size domains are detected around 1 and 100 μ m, the last one is mainly due to heterogeneity at the surface of the samples.

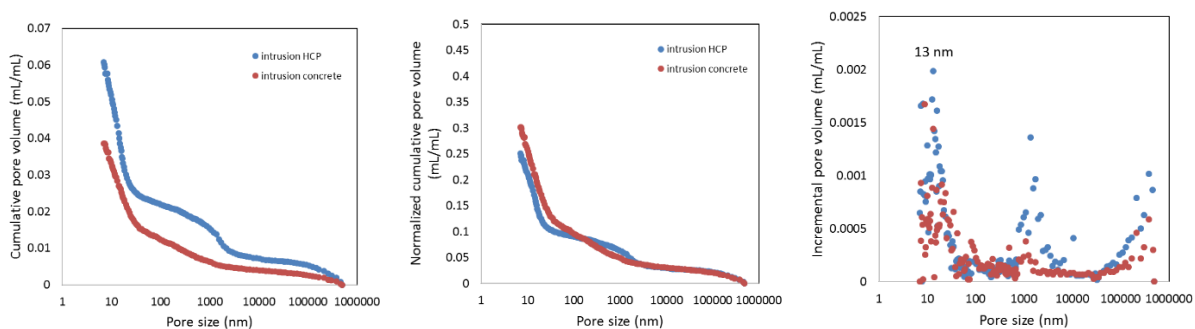


Figure 7: Intrusion MIP curve for RPM (in figures: HCP) and RCM (in figures: concrete), from BRGM.

3.4 Transport properties

CSIC results of the non-steady chloride migration coefficient show a high resistance of the concretes to the penetration of chlorides, especially, in the RCM ($D_{nssm} = 2.6 \pm 1.1 \cdot 10^{-15} \text{ m}^2/\text{s}$ vs. $3.0 \pm 1.0 \cdot 10^{-13} \text{ m}^2/\text{s}$ in RCM-LD).

The hydraulic conductivity (K) of RCM is extremely low ($\approx 10^{-13} - 10^{-14} \text{ m/s}$), although slightly higher with the clayey water. This low hydraulic conductivity in RCM does not allow inducing significant changes in the

chemical composition and microstructure of the concretes during the percolation test. RCM-LD shows higher K ($\approx 10^{-12}$ - 10^{-13} m/s) due to its lower density and higher porosity than RCM. An alkaline plume is not detected in either of the cases due to the low pH of both concretes. In the RCM-LD, higher ion (as alkalis, Ca or S) contents and lower pH in the soluble water of the concrete was measured up to 1 cm depth from the contact with the water inlet. After 13 months for RCM and 7 months for RCM-LD percolation test RCM exposed to granite groundwater shows a slight worsening of the pore refinement compared to the initial reference, while RCM-LD show a strong reduction of the porosity and a better refinement of the porous structure, especially in the upper part of the concrete with both groundwaters. Figure 8 shows the pH (left) and Ca and S pore ion concentrations (right) were analysed in RCM-3 and RCM-LD3 after percolation tests with granite water at different distances from the water inlet. BSEM-EDS analyses are being carried out to complete the characterization from percolation.

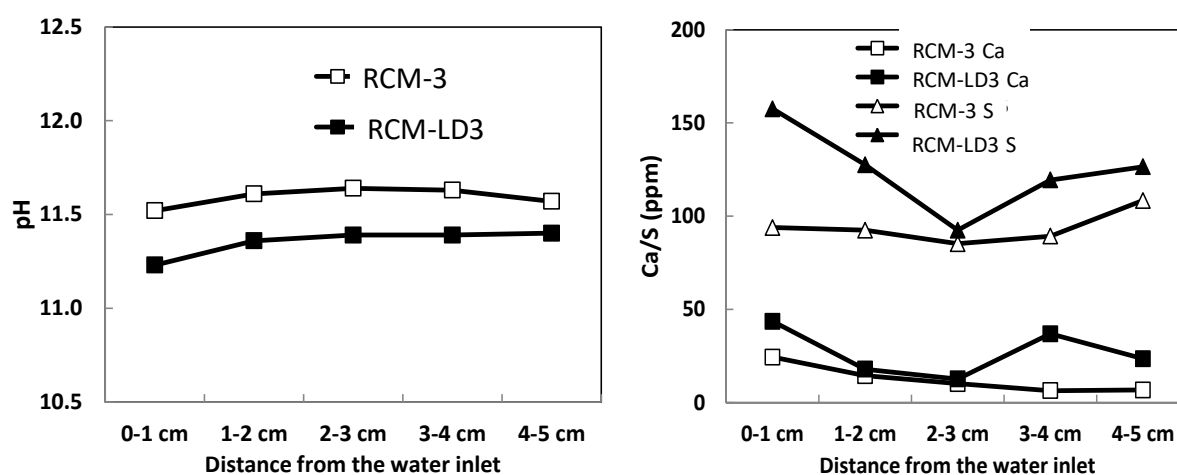


Figure 8: pH (left) and Ca and S soluble content (right) in different zones in RCM-3 and RCM-LD 3 samples from CSIC.

Results of UJV pH leachate tests are shown in Figure 9 (testing at 40, 175, 322 and 455 days after the casting of the RPM samples). The leachate pH values obtained after 40 days after casting the RPM specimens can be considered as initial values of RPM leachate. In the first sampling period (after 322 days) pH leaching tests were performed on samples stored in all ageing conditions and environment (10°C humid air, 10°C groundwater and bentonite suspension, 95°C groundwater and bentonite suspension). Additional sampling campaigns were performed after 175 and 455 days for ageing conditions 10°C humid air, 10°C groundwater and 95°C groundwater. The trend of significant decrease to the values ≤ 11 of pH in the leachate was observed only for samples heated up to 95°C in groundwater and bentonite suspension. The last point of curve for samples stored in 95°C groundwater environment (red triangles in Figure 9) do not fit into the trend of continuous decreasing of pH values of heated samples. Even though the pH measurement was performed again on another sample, the pH of the leachate was repeatedly evaluated as 11.6 for this sampling point. After the next sampling campaign it should be possible to see if the values of pH leachate continue with the decreasing trend with values lower than 11. For other ageing conditions (10°C humid air, groundwater and bentonite suspension), no significant decrease of pH in the leachates to the pH values of 11 or less was observed.

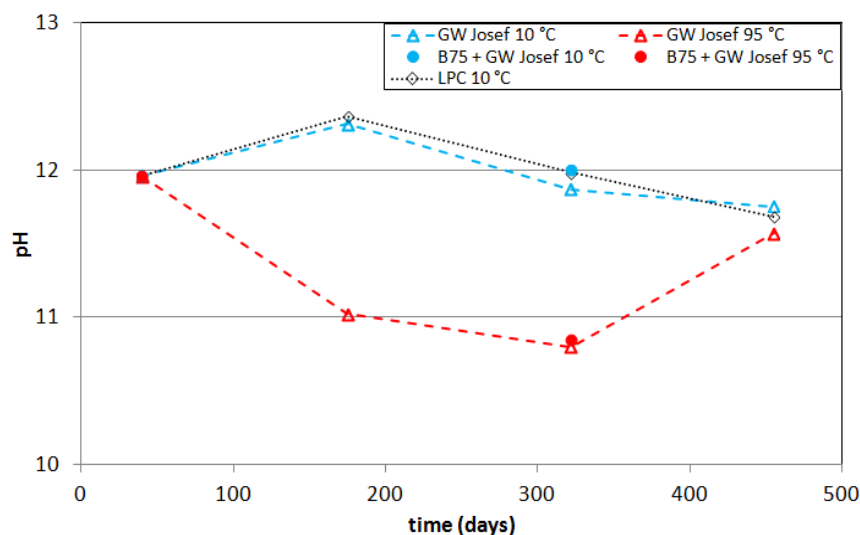


Figure 9: Time evolution of leachate pH values of RPM samples, testing in 40, 175, 322 and 455 days after the casting of the RPM samples, from UJV.

After 50 days of through-diffusion experiments in UJV, a maximum 6% of the initial HTO and 2% of the initial ^{36}Cl volume activity had diffused into LPC samples, but a breakthrough curve was not obtained yet to use a simple analytical solution method for evaluation, or alternatively, a more sophisticated procedure with the GoldSim software. The only exception is the diffusion series of HTO on RPM samples that interacted with GW Josef under thermal load of 95°C, where the first measurable values of ^3H activity in the outlet reservoir were obtained. In the first step, the basic analytical solutions of 1D-through diffusion on these values was applied, with the preliminary results of effective diffusion coefficient D_e of HTO on RPM samples are in the range $(0.7 - 1.60) \cdot 10^{-12} \text{ m}^2/\text{s}$. All experiments are still on-going and will be reported in the future.

Conclusions

According to CSIC, the chemical composition of RCM and RCM-LD is stable with time. The microstructure of RCM is also stable with age of maturity. The extremely low K-value of RCM limits the percolation of waters in a certain level to interact with cement paste components. The absence of an alkaline plume is confirmed from the percolation tests. After several months of interaction in RCM-LD, the concrete chemical composition shows higher pore ion concentrations and lower pH in the first cm closest to the water inlet.

According to KIT, XANES allowed comparing the Fe and Cl environments in the CEBAMA paste and concrete with the ones of the selected reference compounds and provided information on the nature of the chemical environment. At the Fe K-edge these findings were corroborated by EXAFS spectra. The data suggest that both elements may not be located in a single phase, but may rather be distributed among several phases in various amounts. For chloride, it seems clear that the speciation in the concrete and in the paste is similar and close to the environment of Cl in the $\text{CaCl}_2 \cdot 2\text{H}_2\text{O}$ salt. The speciation of Fe in the CEBAMA paste differs from that in the concrete. For the CEBAMA paste, it seems that Fe could be located in C-S-H phases, whereas in the concrete a portion of Fe may be present as ferrihydrite.

BRGM measured the total porosity of RCM and RPM. The total porosity for RPM and RCM, considering the given water to binder ratio, is around 24 and 12%, respectively. With MIP, only 30% of the pore volume was probed. The main pore throat size was 13 nm for both RPM and RCM. 70% of the non-probed volume is connected by throat size lower than the percolation threshold of MIP (7 nm).

According to VTT's compression strength and pH measurements, CEBAMA reference concrete binder has further reacted within the 420-720 day period. Reaction of pozzolanic materials in binary and ternary references has ceased compared to RCM. Pore solution pH of RPM was higher than RCM although the binder composition is identical. pH of the RPM has not decreased during the 420-720 day period.

Future work

CSIC will complete the characterization of the transport properties through the percolation tests (two samples per type and water still in progress) and the natural chloride diffusion in both concretes RCM and RCM-LD.

All CTU and UJV work will continue with sampling of RPM in June 2018 (i.e. after 18 months of ageing) and related analyses.

KIT Experimental Fe *K*-edge EXAFS spectra will be modeled to obtain information on the nature and type of neighbouring atoms as well as their distances from the absorber. These results will allow better identify the nature of the chemical environment and thus the nature of the phase(s) containing Fe.

VTT is going to perform the leaching test for RCM to complete the reference mix design studies.

Acknowledgements

The research leading to these results has received funding from the European Union's Horizon 2020 Research and Training Programme of the European Atomic Energy Community (EURATOM) (H2020-NFRP-2014/2015) under grant agreement n° 662147 (CEBAMA).

KIT acknowledge KARA and ESRF for provision of synchrotron radiation beam time and D. Banerjee for assistance during measurements at the BM26A beamline. We thank B. Lothenbach (EMPA, Switzerland) for providing the C₂F and C₄AF compounds, S. Grangeon (BRGM, France) for providing the Friedel's and Kuzel's salt and S. Gaboreau (BRGM, France) for providing the C-S-H phases.

References

- Ait Mouheb, N., Montoya, V., Schild, D., Soballa, E., Adam, C., Geyer, F., Schäfer, T. (2018). Characterization and sorption properties of low-pH cements. *In*: M. Altmaier, V. Montoya, L. Duro, A. Valls (Eds.) Proceedings of the 2nd Annual Workshop of the CEBAMA Project. KIT Scientific Report, *in press*.
- Alonso, M.C., García Calvo, J.L., Petterson, S., Puigdomenech, I., Cuñado, M.Á., Vuorio, M., Weber, H., Ueda, H., Naito, M., Walker, C., Takeshi, Y., Cau-dit-Coumes, C. (2012). Round robin test for defining an accurate protocol to measure the pore fluid pH of low-pH cementitious materials. *In*: F. Bart, C. Cau-dit-Coumes, F. Frizon, S. Lorente (Eds.) Cement-Based Materials for Nuclear Waste Storage, Springer, 251-259.
- Gaboreau, S., Pret, D., Tinseau, E., Claret, F., Pellegrini, D., Stammose, D. (2011). 15 years of in-situ cement-argillite interaction from Tournemire URL: Characterisation of the multi-scale spatial heterogeneities of pore space evolution. *Applied Geochemistry*, 26, 2159-2171.
- Huggins, F.E. and Huffman, G.P. (1995). Chlorine in coal: an XAFS spectroscopic investigation. *Fuel*, 74, 556-569.
- Melnyk, T.W. and Skeet, A. (1986). An improved technique for determination of rock porosity. *Canadian Journal of Earth Sciences*, 23, 1068-1074.

- Niukitenko, S., Beale, A.M., van der Eerden, A.M.J., Jacques, S.D.M., Leynaud, O., O'Brien, M.G., Detollenaere, D., Kapein, R., Weckhuysen, B.M., Bras, W. (2008). Implementation of a combined SAXS/WAXS/QEXAFS set-up for time-resolved in-situ experiments. *Journal of Synchrotron Radiation*, 15, 632-640.
- Ravel, B. and Newville, M. (2005). ATHENA, ARTEMIS, HEPHAESTUS: data analysis for X-ray absorption spectroscopy using IFEFFIT. *Journal of Synchrotron Radiation*, 12, 537-541.
- Roosz, C., Gaboreau, S., Grangeon, S., Prêt, D., Montouillout, V., Maubec, N., Ory, S., Blanc, P., Vieillard, P., Henocq, P., (2016). Distribution of water in synthetic calcium silicate hydrates. *Langmuir*, 32, 6794-6805.
- Rothe, J., Butorin, S., Dardenne, K., Denecke, M.A., Kienzler B., Löble, M., Metz, V., Seibert, A., Steppert, M., Vitova, T., Walther, C., Geckeis, H. (2012). The INE-Beamline for actinide science at ANKA. *Review of Scientific Instruments*, 83, 043105.
- Vašíček, R., Večerník, P., Hloušek, J., Červinka, R., Hausmannová, L., Havlová, V. (2017). Interaction between Cement and Czech Bentonite under Temperature Load and In In-Situ Conditions: Results after First Testing Period. *In: M. Altmaier, V. Montoya, L. Duro, A. Valls (Eds.) Proceedings of the 2nd Annual Workshop of the CEBAMA Project. KIT Scientific Report, in press.*
- Večerník, P., Hausmannová, L., Červinka, R., Vašíček, R., Roll, M., Hloušek, J., Havlová, V. (2016). Interaction between cement and Czech bentonite under temperature load and in in-situ conditions: an overview of experimental program. *In: M. Altmaier, V. Montoya, L. Duro, A. Valls (Eds.) Proceedings of the 1st Annual Workshop of the CEBAMA Project. KIT Scientific Report, 7734.*
- Vehmas, T., Leivo, M., Holt, E., Alonso, M.C., García, J.L., Fernández, Á., Isaacs, M., Rastrick, E., Read, D., Vasíček, R., Hlousek, J., Hausmannova, L., Vecerník, P., Cervinka, R., Havlova, V., Lange, S., Klinkenberg, M., Bosbach, D., Deissmann, G., Montoya, V., Mouheb, N.A., Adam, C., Schild, D., Schäfer, T. (2017). CEBAMA reference mix design for low-ph concrete and paste, preliminary investigations. *In: M. Altmaier, V. Montoya, L. Duro, A. Valls (Eds.) Proceedings of the 2nd Annual Workshop of the CEBAMA Project. KIT Scientific Report, in press.*
- Vehmas, T., Schindler, A., Löija, M., Leivo, M., Holt, E. (2016). Reference mix design and castings for low-pH concrete for nuclear waste repositories. *In: M. Altmaier, V. Montoya, L. Duro, A. Valls (Eds.) Proceedings of the 1st Annual Workshop of the CEBAMA Project. KIT Scientific Report, 7734.*
- Westre, T., Kennepohl, P., DeWitt, J.G., Hedman, B., Hodgson K.O., Solomon, E.I. (1997). A multiplet analysis of Fe *K*-edge 1s → 3d pre-edge features of iron complexes. *Journal of the American Chemical Society*, 119, 6297-6314.

Solubility and hydrolysis of Be(II) in dilute to concentrated NaCl and KCl solutions

Xavier Gaona^{1*}, Nese Cevirim-Papaioannou¹, Melanie Böttle¹, Marcus Altmaier¹

¹ Institute for Nuclear Waste Disposal, Karlsruhe Institute of Technology (DE)

* Corresponding author: xavier.gaona@kit.edu

Abstract

The solubility of Be(II) was investigated in dilute to concentrated HCl–NaCl–NaOH, KCl–KOH, NaOH and KOH solutions under Ar atmosphere at $T = (22 \pm 2)^\circ\text{C}$. Experiments were performed from undersaturation conditions using commercial BeO(cr) or synthetic Be(OH)₂(am) solid phases. No transformation of BeO(cr) or Be(OH)₂(am) to Na/K–Be(II)–OH solid phases is observed in alkaline NaCl and KCl solutions within $t \leq 200$ days. Solubility data obtained with both solid phases confirm the amphoteric character of Be(II) with a solubility minimum at $\text{pH}_m \approx 9$. At this pH_m value, [Be(II)] in equilibrium with BeO(cr) and Be(OH)₂(am) is $\approx 10^{-7.6}$ and $\approx 10^{-7.2}$ M, respectively. No relevant differences are observed between [Be(II)] quantified in the clear supernatant and after 10 kD ultrafiltration, thus excluding any significant contribution of dissolved colloidal beryllium species to the total solubility. The combination of solubility data determined in acidic pH_m conditions and the hydrolysis scheme reported in the literature for cationic hydrolysis species of Be(II) allows the determination of $\log *K_{s,0}^{\circ}\{\text{BeO}(\text{cr})\}$ and $\log *K_{s,0}^{\circ}\{\text{Be}(\text{OH})_2(\text{am})\}$ for the solid phases used in the present study. Solubility data obtained in weakly alkaline conditions clearly show that the hydrolysis constant previously reported for Be(OH)₂(aq) in potentiometric studies is importantly overestimated. Slope analysis of the solubility data in alkaline to hyperalkaline conditions supports the predominance of the anionic hydrolysis species Be(OH)₃[−] and Be(OH)₄^{2−} at the pH_m -conditions relevant in cementitious systems. This extensive solubility dataset obtained within CEBAMA will allow deriving chemical, thermodynamic and (SIT) activity models for the system $\text{Be}^{2+}\text{--Na}^+\text{--K}^+\text{--}(\text{Ca}^{2+})\text{--H}^+\text{--Cl}^-\text{--OH}^-\text{--H}_2\text{O}(\text{l})$. These models provide an accurate and robust tool for the evaluation of Be(II) solubility and speciation in a diversity of geochemical conditions, including the calculation of source term concentrations or the mechanistic modelling of the surface retention of dissolved Be species in the context of safety assessments for nuclear waste repositories.

1 Introduction

Beryllium is a chemotoxic element expected in specific waste forms to be disposed of in repositories for radioactive waste. The amphoteric behaviour of Be(II) is widely accepted in the literature (Baes and Mesmer, 1976; Wood, 1992; Brown and Ekberg, 2016), although the number of experimental studies reporting the formation of anionic hydrolysis species (Be(OH)₃[−] and Be(OH)₄^{2−}) under alkaline to hyperalkaline pH conditions is very scarce (Gilbert and Garrett, 1956; Soboleva et al. 1977). The formation of ternary Na–Be(II)–OH and Ca–Be(II)–OH solid phases under hyperalkaline pH conditions has been described in the literature (Everest et al., 1962; Schmidbaur et al., 1998; Schmidt et al., 1998). These solid phases may eventually control Be(II) solubility

in the different phases of cement degradation, but no thermodynamic data are available so far for these systems. This work focuses on the aquatic chemistry of Be(II) under alkaline to hyperalkaline pH conditions, with the aim of developing comprehensive thermodynamic and activity models for the system $\text{Be}^{2+}\text{--Na}^+\text{--K}^+\text{--Ca}^{2+}\text{--H}^+\text{--Cl}^-\text{--OH}^-\text{--H}_2\text{O(l)}$. These models can be implemented in thermodynamic databases (TDB) and further used in geochemical calculations of relevance in the context of nuclear waste disposal.

2 Thermodynamic data available in the literature

As discussed in our previous S&T contribution (Gaona et al. 2016), thermodynamic data available for Be(II) solubility and hydrolysis is very sparse for alkaline systems, but rather complete for acidic conditions. Table 1 summarizes thermodynamic data used in the present work for solubility calculations. The reader is referred to Gaona et al. (2016) for a detailed discussion of individual references. Note that two, very discrepant values are considered for $\log {}^*\beta_{(1,2)}^\circ$ arising from potentiometric and solvent extraction studies.

Table 1: Summary of thermodynamic data available on the solubility and hydrolysis of Be(II). Data marked in bold are used in the present work for solubility calculations.

Reference	Method	Medium	T (°C)	log ₁₀ *K	log ₁₀ *K°
α-Be(OH) ₂ (cr) + 2 H ⁺ ⇌ Be ²⁺ + 2 H ₂ O(l)					
Gilbert and Garrett (1956)	solubility	HCl / HClO ₄	25		(6.86 ± 0.05)
					(6.69 ± 0.02) ^a
					(6.87 ± 0.05) ^b
β-Be(OH) ₂ (cr) + 2 H ⁺ ⇌ Be ²⁺ + 2 H ₂ O(l)					
Bruno et al. (1987)	solubility	3.0 M NaClO ₄	25	(6.18 ± 0.03)	(5.9 ± 0.1)
2 Be ²⁺ + H ₂ O(l) ⇌ Be ₂ (OH) ³⁺ + H ⁺					
Bruno (1987)	e.m.f.	3.0 M NaClO ₄	25	− (3.23 ± 0.05)	− (3.47 ± 0.05)
3 Be ²⁺ + 3 H ₂ O(l) ⇌ Be ₃ (OH) ₃ ³⁺ + 3 H ⁺					
Bruno (1987)	e.m.f.	3.0 M NaClO ₄	25	− (8.656 ± 0.002)	− (8.86 ± 0.05)
5 Be ²⁺ + 6 H ₂ O(l) ⇌ Be ₅ (OH) ₆ ⁴⁺ + 6 H ⁺					
Bruno (1987)	e.m.f.	3.0 M NaClO ₄	25	− (18.81 ± 0.03)	− (19.5 ± 0.1)
6 Be ²⁺ + 8 H ₂ O(l) ⇌ Be ₆ (OH) ₈ ⁴⁺ + 8 H ⁺					
Bruno (1987)	e.m.f.	3.0 M NaClO ₄	25	− (26.70 ± 0.05)	− (26.3 ± 0.1)
Be ²⁺ + 2 H ₂ O(l) ⇌ Be(OH) ₂ (aq)					
Green and Alexander (1965)	sol. ext.	”self medium”	25	− (13.65 ± 0.04)	− (13.65 ± 0.05) ^a
Bruno (1987)	e.m.f.	3.0 M NaClO ₄	25	− 11.07	− (11.00 ± 0.05)
Be ²⁺ + 3 H ₂ O(l) ⇌ Be(OH) ₃ [−] + 3 H ⁺					
Gilbert and Garrett (1956)	solubility	NaOH	25		− (23.26 ± 0.04) ^a
					− (23.46 ± 0.05) ^b
Be ²⁺ + 4 H ₂ O(l) ⇌ Be(OH) ₄ ^{2−} + 4 H ⁺					
Gilbert and Garrett (1956)	solubility	NaOH	25		− (37.4 ± 0.2) ^a
					− (37.59 ± 0.05) ^b

a. recalculated in Baes and Mesmer (1976); b. recalculated in Bruno (1987).

3 Experimental

All sample preparation and handling was performed under protective atmosphere in an Ar-glove box at $T = (22 \pm 2)^\circ\text{C}$. Solubility experiments were performed from undersaturation conditions using commercial BeO(cr) and synthetic Be(OH)₂(am). The latter phase was prepared within this study at room temperature by precipitating a ≈ 0.35 M BeSO₄ stock solution at $\text{pH}_m \approx 10.5$, and washed three times with the corresponding background electrolyte solution before use. A total of 120 independent batch samples were prepared by contacting 0.5 - 5 mg of solid phase (per sample) with the following systems: (i) 0.1 - 5.0 M NaCl–NaOH (5 series, with $5 \leq \text{pH}_m \leq 14.5$); (ii) 0.1 - 4.0 M KCl–KOH (5 series, with $9 \leq \text{pH}_m \leq 14.3$); (iii) 0.01 - 4.0 M NaOH; (iv) 0.01 - 4.0 M KOH ((iii) and (iv) in the absence of MCl salts). The hydrogen ion concentration ($\text{pH}_m = -\log [\text{H}^+]$, in molal units) was measured using combination pH electrodes (ROSS, Orion) calibrated with standard pH buffers (pH 1-12, Merck). Experimentally measured pH_{exp} values were corrected with empirical “ A_m ” factors to obtain pH_m ($\text{pH}_m = -\log [\text{H}^+] = \text{pH}_{\text{exp}} + A_m$, with $[\text{H}^+]$ in molal units). Such corrections are required in solutions of ionic strength $I \geq 0.1$ mol/kg, where pH_{exp} is an operational value significantly deviating from pH. A_m -factors entail both the liquid junction potential of the electrode and the activity coefficient of H^+ at a given background electrolyte concentration. A_m -factors reported in literature were used for the determination of pH_m in NaCl and KCl systems (Altmaier et al., 2003; Baumann et al., 2017). In the systems with $[\text{OH}^-] > 0.03$ m, $[\text{H}^+]$ was calculated from the known hydroxide concentration and the conditional ion product of water (K'_w) for the given NaCl or KCl concentration. Total concentration of Be(II) in the aqueous phase was quantified by ICP-MS after ultrafiltration with 10 kD filters, with a detection limit $\approx 10^{-9}$ M (depending upon dilution factor required). The [Be(II)] in the clear supernatant (without phase separation) of selected solubility samples was also determined with the aim of assessing the possible presence of colloidal Be species. Concentration values obtained in molar units (M, mol/L) were converted to molal units (m, mol/kg_w) using the conversion factors reported in the NEA–TDB (Guillaumont et al., 2003).

Solid Be phases in selected solubility experiments were characterized by XRD. For this purpose, an aliquot of the selected solid (≈ 1 mg) was washed 3-4 times with 1 mL of ethanol under Ar-atmosphere to remove the matrix solution (containing NaCl or KCl) which would interfere with XRD analysis. After the final cleaning step, the solid was re-suspended in ethanol, deposited on a XRD sample plate, dried under Ar atmosphere for a few minutes and after mounting of a protective dome to the sample plate transferred outside the glovebox for the collection of the XRD diffractogram. XRD measurements were performed on a Bruker AXS D8 Advance X-Ray powder diffractometer at measurement angle $2\theta = 10\text{--}90^\circ$ with incremental steps of 0.02° and a measurement time of 1.5 seconds per step. The diffractograms obtained were compared to the Joint Committee on Powder Diffraction Standards database (JCPDS, 2001).

4 Results and discussion

4.1 Solid phase characterization

Figure 1 shows the XRD patterns of the BeO(cr) and Be(OH)₂(am) solid phases investigated in this study. The diffractogram of the amorphous phase was taken after 14 days of equilibration, and it is expected to evolve with time towards the formation of a more crystalline phase, likely β -Be(OH)₂(cr).

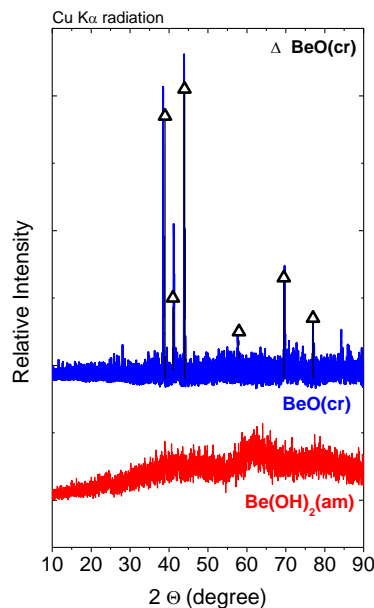


Figure 1: XRD patterns of $\text{BeO}(\text{cr})$ and $\text{Be}(\text{OH})_2(\text{am})$ (after $t = 14$ days) solid phases used in this study. $\text{BeO}(\text{cr})$ reference patterns as reported in JCPDS database.

4.2 Solubility experiments

Figure 2 to Figure 5 show $\text{Be}(\text{II})$ experimental solubility data determined in the present work in dilute to concentrated NaCl – NaOH and KCl – KOH solutions, respectively. The figures also show the solubility of $\alpha\text{-Be}(\text{OH})_2(\text{cr})$ and $\beta\text{-Be}(\text{OH})_2(\text{cr})$ calculated at $I = 0$ using thermodynamic data summarized in Table 1.

The shape of all solubility curves obtained in dilute to concentrated NaCl and KCl systems confirm the amphoteric character of $\text{Be}(\text{II})$ (see Figure 2 and Figure 3), with the formation of cationic and anionic hydrolysis species below and above $\text{pH}_m \approx 9$, respectively. Solubility experiments with $\text{BeO}(\text{cr})$ attain a fast equilibrium (constant $[\text{Be}(\text{II})]$ measured after ≈ 14 days), whereas slow kinetics are observed for solubility experiments using $\text{Be}(\text{OH})_2(\text{am})$. Hence, at $\text{pH}_m \approx 9$, $[\text{Be}(\text{II})]$ in equilibrium with $\text{Be}(\text{OH})_2(\text{am})$ decreases from $10^{-5.7}$ M to $10^{-7.2}$ M within 200 days. Although solid phase characterization of this solid phase after attaining equilibrium conditions is not yet undertaken, this observation likely relates with the transformation of $\text{Be}(\text{OH})_2(\text{am})$ into $\beta\text{-Be}(\text{OH})_2(\text{cr})$.

No relevant differences are observed between $[\text{Be}(\text{II})]$ quantified in the clear supernatant and after 10 kD (≈ 2 nm) ultrafiltration, thus excluding any significant contribution of dissolved colloidal beryllium species to the total solubility. The combination of solubility data determined in acidic pH_m conditions and the hydrolysis scheme reported by Bruno (1987) for cationic hydrolysis species of $\text{Be}(\text{II})$ will allow the determination of $\log {}^*K_{s,0}\{\text{BeO}(\text{cr})\}$ and $\log {}^*K_{s,0}\{\beta\text{-Be}(\text{OH})_2(\text{cr})\}$ for the solid phases used in the present study. Solubility data obtained in weakly alkaline conditions clearly show that the hydrolysis constant previously reported for $\text{Be}(\text{OH})_2(\text{aq})$ in potentiometric studies is importantly overestimated. Instead, our data is consistent with the solvent extraction study by Green and Alexander (1965). Although a final modelling of the solubility data is missing, a preliminary slope analysis (slope 0, +1 and +2 within $\text{pH}_m \approx 8$ and ≈ 14 , see Figure 4 and Figure 5) of the available data indicates that the value of $\log {}^*\beta_{(1,3)}^\circ$ available from a single solubility study (Gilbert and Garrett, 1956) might be slightly overestimated, accordingly underestimating $\log {}^*K_4^\circ$ for the step-wise reaction (1). Note that the solubility experiment by Gilbert and Garrett (1956) was conducted at rather high concentrations of NaOH (0.02 - 0.71 M), which likely prevented a more accurate characterization of $\log {}^*\beta_{(1,3)}^\circ$.



If confirmed, Be(OH)_4^{2-} instead of Be(OH)_3^- would be the aqueous species of Be(II) prevailing at pH_m above ≈ 12 , which would have important implications for the interpretation and modeling of the sorption of Be(II) in the stages I ($\text{pH} \approx 13.3$) and II ($\text{pH} \approx 12.5$) of cement degradation. Note that Tits et al. (2014) have shown a much stronger sorption of $\text{UO}_2(\text{OH})_3^-$ than $\text{UO}_2(\text{OH})_4^{2-}$ by C-S-H phases.

Note that the discussion above might be (slightly) affected by dissolution kinetics. A final evaluation of solubility data after attaining equilibrium conditions (e.g. constant pH_m and $\log [\text{Be(II)}]$) will be used to derive comprehensive thermodynamic and SIT activity models for the system $\text{Be}^{2+}\text{--Na}^+\text{--K}^+(\text{--Ca}^{2+})\text{--H}^+\text{--Cl}^-\text{--OH}^-\text{--H}_2\text{O(l)}$.

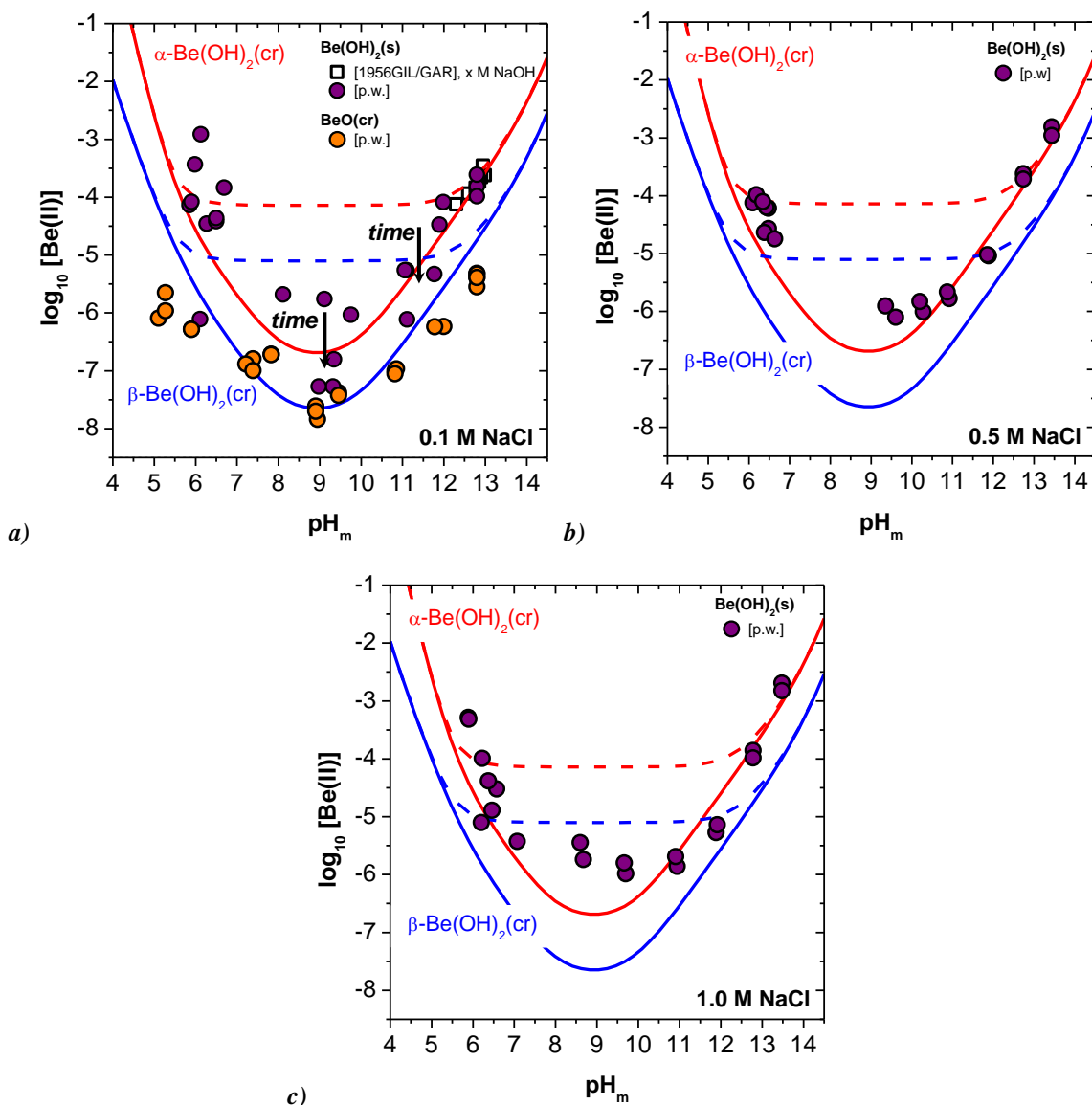


Figure 2: Experimental solubility data determined in the present work for $\text{BeO}(\text{cr})$ and $\text{Be(OH)}_2(\text{s})$ in (a) 0.1 M NaCl, (b) 0.5 M NaCl and (c) 1.0 M NaCl solutions. Red and blue lines correspond to the solubility of $\alpha\text{-Be(OH)}_2(\text{cr})$ and $\beta\text{-Be(OH)}_2(\text{cr})$, respectively, calculated at $I = 0$ using thermodynamic data summarized in Table 1. Solid and dashed solubility lines calculated using $\log * \beta^{(1,2)}$ reported from solvent extraction and potentiometric studies, respectively (see Table 1). The term p.w. stands for “present work”.

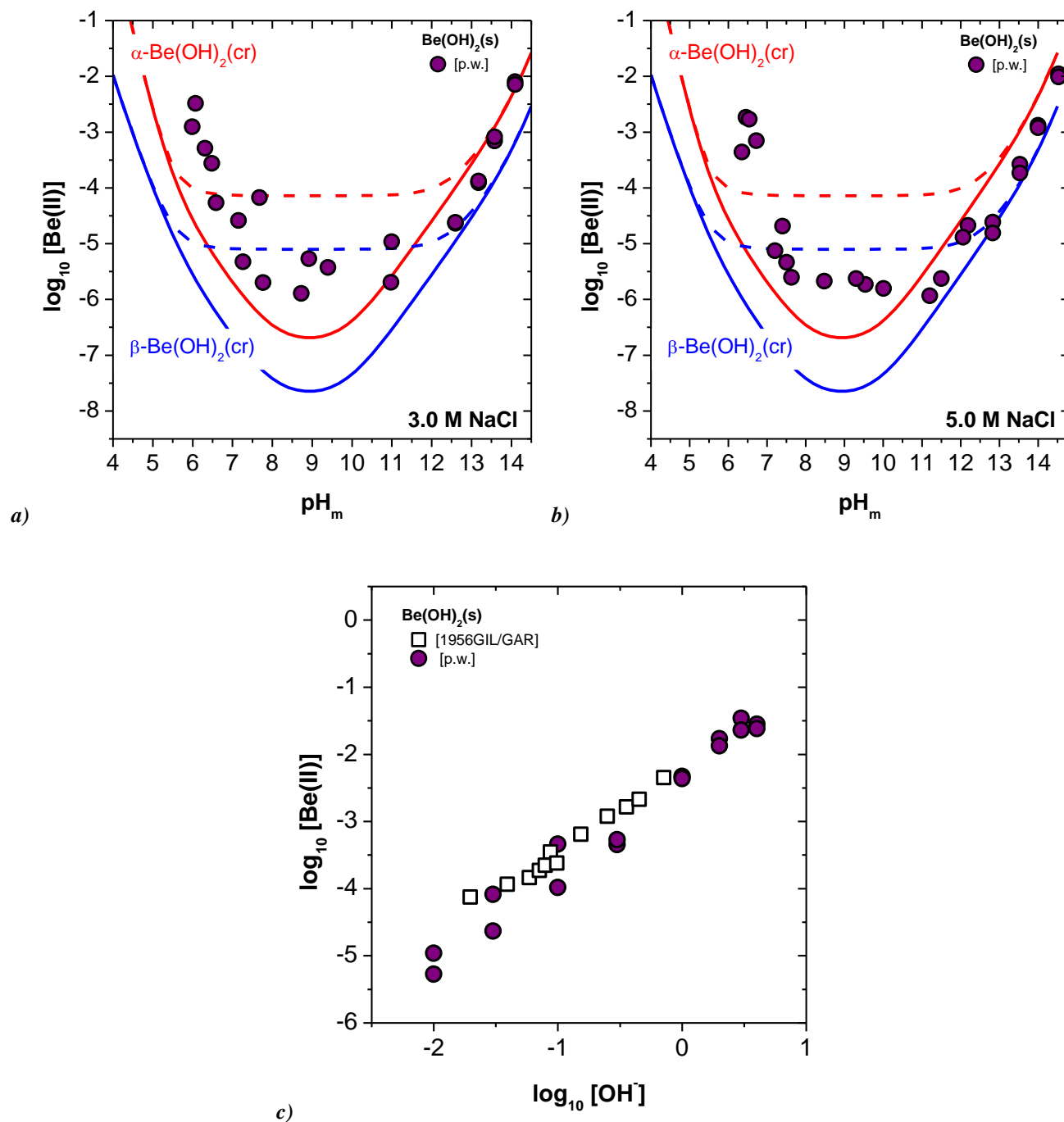


Figure 3: Experimental solubility data determined in the present work for $\text{Be(OH)}_2(\text{s})$ in (a) 3.0 M NaCl, (b) 5.0 M NaCl and (c) 0.01 – 4.0 M NaOH solutions. Red and blue lines correspond to the solubility of $\alpha\text{-Be(OH)}_2(\text{cr})$ and $\beta\text{-Be(OH)}_2(\text{cr})$, respectively, calculated at $I = 0$ using thermodynamic data summarized in Table 1. Solid and dashed solubility lines calculated using $\log^* \beta^{\circ}_{(1,2)}$ reported from solvent extraction and potentiometric studies, respectively (see Table 1). The term p.w. stands for “present work”.

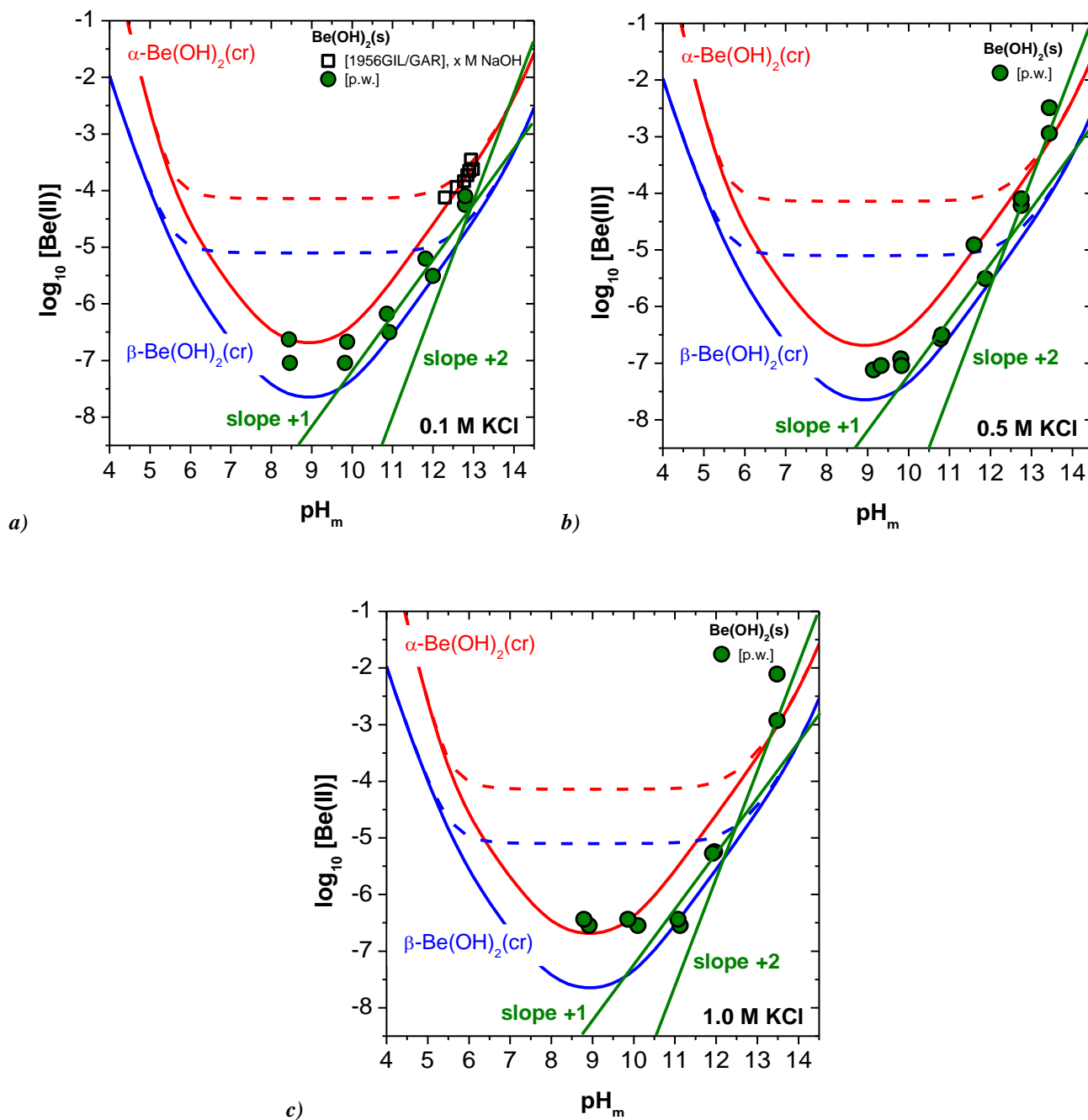


Figure 4: Experimental solubility data determined in the present work for $\text{Be(OH)}_2(\text{s})$ in (a) 0.1 M KCl, (b) 0.5 M KCl and (c) 1.0 M KCl solutions. Red and blue lines correspond to the solubility of $\alpha\text{-Be(OH)}_2(\text{cr})$ and $\beta\text{-Be(OH)}_2(\text{cr})$, respectively, calculated at $I = 0$ using thermodynamic data summarized in Table 1. Solid and dashed solubility lines calculated using $\log^* \beta_{(1,2)}^{\circ}$ reported from solvent extraction and potentiometric studies, respectively (see Table 1). Green lines provide a preliminary slope analysis of the available solubility data. The term p.w. stands for “present work”.

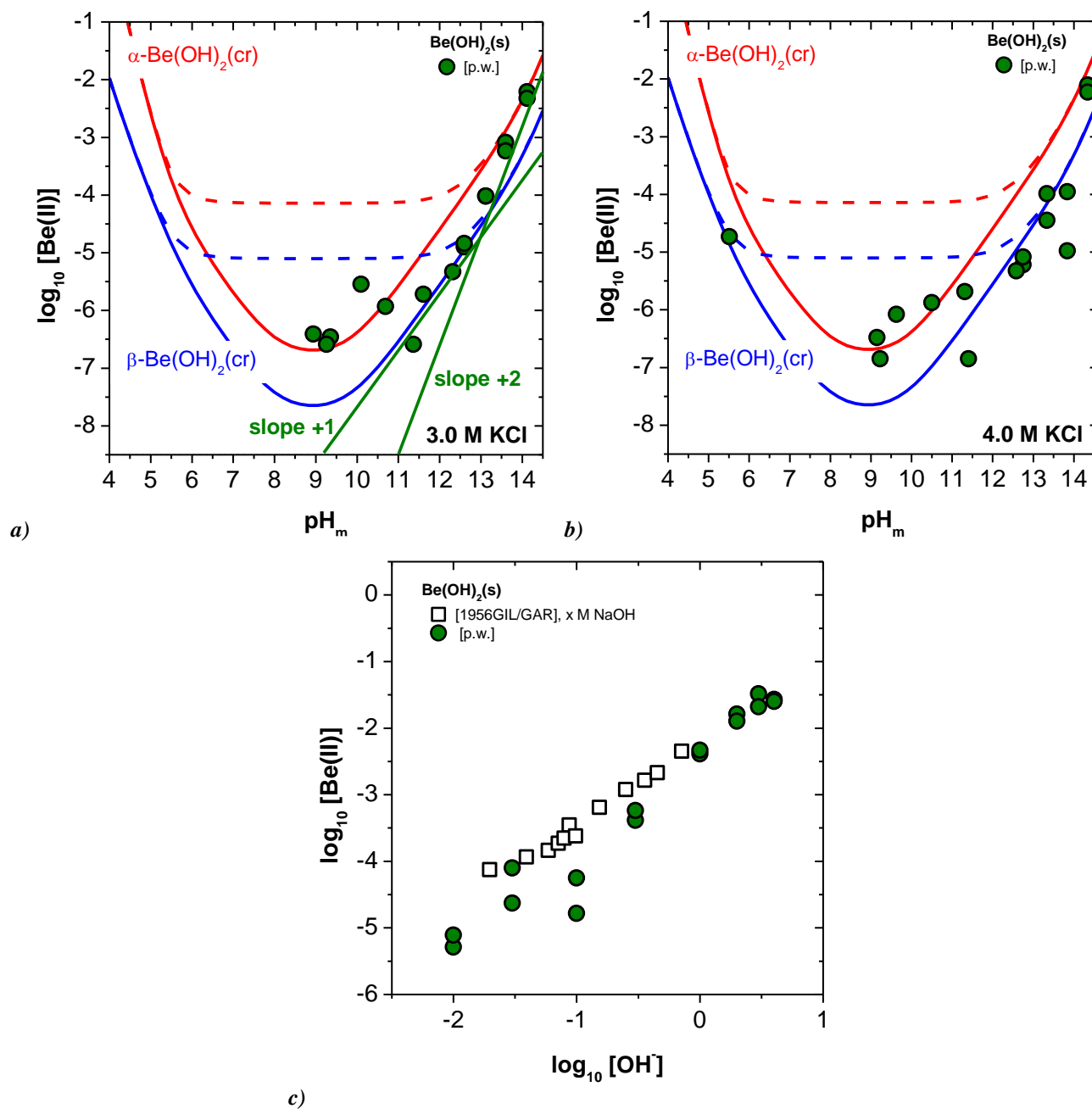


Figure 5: Experimental solubility data determined in the present work for $\text{Be(OH)}_2(\text{s})$ in (a) 3.0 M KCl, (b) 4.0 M KCl and (c) 0.01 - 4.0 M KOH solutions. Red and blue lines correspond to the solubility of $\alpha\text{-Be(OH)}_2(\text{cr})$ and $\beta\text{-Be(OH)}_2(\text{cr})$, respectively, calculated at $I = 0$ using thermodynamic data summarized in Table 1. Solid and dashed solubility lines calculated using $\log^* \beta^\circ_{(1,2)}$ reported from solvent extraction and potentiometric studies, respectively (see Table 1). Green lines provide a preliminary slope analysis of the available solubility data. The term p.w. stands for “present work”.

5 Conclusions and Future work

Comprehensive solubility experiments were performed with $\text{BeO}(\text{cr})$ and $\text{Be(OH)}_2(\text{s})$ in dilute to concentrated NaCl and KCl solutions. In the absence of complexing ligands other than water, $\beta\text{-Be(OH)}_2(\text{cr})$ expectedly controls the solubility of Be(II) in acidic to hyperalkaline pH_m conditions. No transformation to Na/K- Be(II) -OH solid phases was observed in alkaline NaCl and KCl solutions within $t \leq 200$ days. Preliminary slope analysis of

the solubility data supports the predominance of $\text{Be}(\text{OH})_3^-$ and $\text{Be}(\text{OH})_4^{2-}$ under the alkaline to hyperalkaline pH conditions defined by cementitious systems. Solubility data in combination with solid phase characterization and ^9Be -NMR will allow deriving comprehensive chemical, thermodynamic and SIT activity models for the system $\text{Be}^{2+}\text{--Na}^+\text{--K}^+\text{--H}^+\text{--Cl}^-\text{--OH}^-\text{--H}_2\text{O(l)}$. Beyond this solubility study, three additional topics related with Be(II) chemistry are targeted at KIT-INE within WP2 of the CEBAMA project: (i) Be(II) solubility and hydrolysis in alkaline, dilute to concentrated CaCl_2 solutions (on-going); (ii) Be(II) solubility and complex formation in dilute to concentrated $\text{NaCl--NaHCO}_3\text{--Na}_2\text{CO}_3$ systems (planned for the second half of 2018); and (iii) uptake of Be(II) by ordinary Portland cement (OPC, fresh) and C–S–H phases with different Ca:Si ratio (on-going as part of PhD thesis of Naila Ait-Mouheb).

Acknowledgements

The technical support provided by Frank Geyer (KIT-INE) and Ezgi Yalcintas (LANL) is kindly acknowledged. The research leading to these results has received funding from the European Union's Horizon 2020 Research and Training Programme of the European Atomic Energy Community (EURATOM) (H2020-NFRP-2014/2015) under grant agreement n° 662147 (CEBAMA).

References

- Altmaier, M., Metz, V., Neck, V., Müller, R., Fanghänel, Th. (2003). Solid-liquid equilibria of $\text{Mg}(\text{OH})_2(\text{cr})$ and $\text{Mg}_2(\text{OH})_3\text{Cl}\cdot 4\text{H}_2\text{O}(\text{cr})$ in the system $\text{Mg--Na--H--OH--Cl--H}_2\text{O}$ at 25°C. *Geochimica et Cosmochimica Acta*, 67, 3595.
- Baes, C.F. and Mesmer, R.E. (1976). *The Hydrolysis of Cations*. Wiley.
- Baumann, A., Yalcintas, E., Gaona, X., Altmaier, M., Geckeis, H. (2017). Solubility and hydrolysis of Tc(IV) in dilute to concentrated KCl solutions: an extended thermodynamic model for $\text{Tc}^{4+}\text{--H}^+\text{--K}^+\text{--Na}^+\text{--Mg}^{2+}\text{--Ca}^{2+}\text{--OH}^-\text{--Cl}^-\text{--H}_2\text{O(l)}$ mixed systems. *New Journal of Chemistry*, 41, 9077-9086.
- Brown, P.L. and Ekberg, C. (2016). *Hydrolysis of Metal Ions*. Wiley-VCH.
- Bruno, J. (1987). Beryllium(II) hydrolysis in 3.0 mol dm^{-3} perchlorate. *Journal of the Chemical Society, Dalton Transactions*, 2431-2437.
- Bruno, J., Grenthe, I., Sandström, M., Ferri, D. (1987a). Studies of metal carbonate equilibria. Part 15. The beryllium(II)–water–carbon dioxide(g) system in acidic 3.0 mol dm^{-3} perchlorate media. *Journal of the Chemical Society, Dalton Transactions*, 2439-2444.
- Everest, D.A., Mercer, R.A., Miller, R.P., Milward, G.L. (1962). The chemical nature of sodium beryllate solutions. *Journal of Inorganic and Nuclear Chemistry*, 24, 525-534.
- Gaona, X., Böttle, M., Rabung, Th., Altmaier, M. (2016). Solubility, hydrolysis and sorption of beryllium in cementitious systems. *In*: M. Altmaier, V. Montoya, L. Duro, A. Valls (Eds.) *Proceedings of the 1st Annual Workshop of the CEBAMA Project*. KIT Scientific Report, 7734.
- Gilbert, R.A. and Garrett, A.B. (1956). The equilibria of the metastable crystalline form of beryllium hydroxide. $\text{Be}(\text{OH})_2$ in hydrochloric acid, perchloric acid and sodium hydroxide solutions at 25°. *Journal of the American Chemical Society*, 78, 5501-5505.
- Guillaumont, R., Fanghänel, J., Neck, V., Fuger, J., Palmer, D. A., Grenthe, I., Rand, M.H. (2003). *Chemical Thermodynamics Vol. 5. Update on the Chemical Thermodynamics of Uranium, Neptunium, Plutonium, Americium and Technetium*. (OECD, NEA-TDB) Elsevier, North Holland, Amsterdam.
- JCPDS (2001). Powder diffraction files. Joint Committee on Powder Diffraction Standards, Swarthmore, USA.

- Schmidbaur, H., Schmidt, M., Schier, A., Riede, J., Tamm, T., Pykkö, P. (1998). Identification and structural characterization of the predominant species present in alkaline hydroxyberyllate solutions. *Journal of the American Chemical Society*, 120, 2967-2968.
- Schmidt, M., Schier, A., Riede, J., Schmidbaur, H. (1998). The novel binuclear hydroxyberyllate species $[\text{Be}_2(\text{OH})_7]^{3-}$ and the hydroxide hydrate anion $[\text{H}_3\text{O}_2]^-$ as components of beryllate equilibria. *Inorganic Chemistry*, 37, 3452-3453.
- Soboleva, G.I., Tugarinov, I.A., Kalinina, V.F., Khodakovskiy, I.L. (1977). Investigation of equilibria in the system $\text{BeO}-\text{NaOH}-\text{HNO}_3-\text{H}_2\text{O}$ in the temperature interval 25-250°C. *Geokhimiya*, 7, 1013-1024 (*in Russian*).
- Tits, J., Gaona, X., Laube, A., Wieland, E. (2014). Influence of the redox state on the neptunium sorption under alkaline conditions: Batch sorption studies on titanium dioxide and calcium silicate hydrates. *Radiochimica Acta*, 102(5), 385-400.
- Wood, S.A. (1992). Theoretical prediction of speciation and solubility of beryllium in hydrothermal solution to 300°C at saturated vapor pressure: Application to bertrandite/phenakite deposits. *Ore Geology Reviews*, 7, 249-278.

Uptake mechanisms of radionuclides in cementitious systems: insights from atomistic simulations

Steve Lange^{1*}, Piotr M. Kowalski¹, Milan Pšenička², Matthew Isaacs^{1, 3}, Martina Klinkenberg¹, David Read^{3,4}, Dirk Bosbach¹, Guido Deissmann¹

¹ Forschungszentrum Jülich GmbH, Institute of Energy and Climate Research (IEK-6): Nuclear Waste Management and Reactor Safety (DE)

² Charles University (CZ)

³ University of Surrey (UK)

⁴ National Physical Laboratory (UK)

* Corresponding author: s.lange@fz-juelich.de

Abstract

Cementitious materials are used in various applications in nuclear waste management, in particular due to their capability for radionuclide retention and immobilization. Above all, the calcium-silicate-hydrates (C-S-H) and calcium aluminates are considered to be the most important phases in ordinary Portland cement based formulations, governing the radionuclide retention processes in cementitious materials, due to their abundance and their appropriate structures allowing for cation and anion binding. In the present study, the binding of ²²⁶Ra to various C-S-H phases was investigated in batch-type sorption experiments under anoxic conditions. A strong retention of ²²⁶Ra by C-S-H phases was observed with slight dependency of distribution coefficients on the Ca/Si-ratio of the C-S-H and the alkali content in solution. Ab-initio atomistic simulations based on density functional theory (DFT) were performed to obtain a closer insight into the incorporation mechanism, revealing a significant difference in Gibb's energy between ²²⁶Ra incorporation into the stable calcium layer compared to cation exchange in the interlayer, suggesting ²²⁶Ra uptake into the interlayer spacing of C-S-H as an additional mechanism to surface sorption. Another set of DFT calculations was launched to gain structural insights into the mechanisms of molybdate uptake by AFm-SO₄.

1 Introduction

Cement-based materials are widely used in the barrier systems of nuclear waste repositories, for example in solidification of low and intermediate level wastes, as barrier materials, or in certain waste containers, such as the Belgian Supercontainer (e.g. Atkins and Glasser, 1992; Glasser, 1997, 2001; Bel et al., 2006; Jantzen et al., 2010; Glasser, 2011; Drace and Ojovan, 2013). Radionuclide migration in cementitious materials is controlled by radionuclide solubility phenomena at high pH conditions, diffusion, surface complexation, or incorporation of radionuclides into solid phases, including the formation of solid solutions. Within the framework of CEBAMA, we study the uptake of selected safety relevant long-lived fission and decay products such as ¹²⁹I, ⁷⁹Se and ²²⁶Ra in cementitious systems. The aim of these investigations is to enhance the mechanistic understanding of the radionuclide uptake and retention in cementitious materials, and to evaluate the relevance of cement alteration processes, such as carbonation, on the solid speciation of radionuclides in aged concrete. A bottom up approach is used to unravel contributions of individual hydrated cement phases on the radionuclide retention behavior,

studying radionuclide interaction with synthesized cement hydration phases, such as various calcium silicate hydrates (C-S-H), monosulphate (AF_m) and ettringite (AF_t), in addition to hardened cement pastes. Here, we report on detailed experimental investigations of the ²²⁶Ra uptake by C-S-H. Complementary to solution chemical studies, atomistic modelling was applied to provide a more detailed view on the ion exchange mechanism for ²²⁶Ra on C-S-H.

2 Materials and Methods

2.1 Synthesis of model phases

The model phases representative for hydration products in hardened cement pastes were synthesized using well established procedures. Synthesis and sample preparation was carried out in an argon glove box (< 10 ppm CO₂); details on the chemicals used are compiled in Table 1. C-S-H were prepared according to the procedure of Atkins et al. (1992) by mixing freshly produced CaO obtained from the ignition of CaCO₃ with SiO₂. To achieve C-S-H with different Ca/Si-ratios (C/S), different amounts of CaO, typically 1.8 g up to 3.4 g (weighted after 2 hours of calcination at 1,000°C), were mixed with SiO₂ in the desired ratio and suspended in water to achieve a water/solid ratio of 20. Products were cured for 1 to 5 months at room temperature followed by centrifugation (30 min at 4,500 rpm) and resuspension in water three to five times. The washed solids were separated by filtering using a Büchner funnel and a paper filter (Whatman); drying was carried out over CaCl₂ using a desiccator under continuous evacuation.

Table 1: Details of chemical substances used in the synthesis of the C-S-H phases.

Compound	Description	Provider
CaO	puriss., 96 - 100.5% ex ignited substance	Sigma Aldrich
SiO ₂	fumed silica 395 m ² /g	Sigma Aldrich

2.2 Phase characterization

Structure and purity of synthesized cement model phases were confirmed by XRD using either a D8 Advance spectrometer with θ - θ geometry or a D4 Endeavour spectrometer with θ -2 θ geometry (Bruker AXS GmbH), employing CuK α -radiation ($\lambda = 0.15406$ nm). XRD patterns were obtained in the 2 θ range from 5 to 80° at ambient conditions, using a step size of 0.02°/2 θ and a counting time of 2 s per step. XRF-analyses were conducted by an external service company (Terrachem GmbH). Phase morphology and sample microstructure was studied by SEM using a Quanta 200F instrument from FEI equipped with a field emission cathode. Energy dispersive X-ray spectroscopy (EDS) was performed with an Apollo X Silicon Drift Detector (SDD) from EDAX.

2.3 Sorption experiments

Batch sorption experiments were carried out in 20 mL LDPE bottles, using liquid/solid ratios (L/S) ranging between 20 and 200 L/kg, depending on the aim of the respective experiments. Weighted amounts of dried model phases were equilibrated with deionized water prior to use. The suspensions were stored at room temperature for 14 days under anoxic conditions to achieve equilibrium between aqueous and solid phases. After equilibrium was reached, the liquid was separated from the solids by filtration. Fresh solids were added to this solution and additionally stored for 14 days before the tracer (here: RaBr₂; $c(^{226}\text{Ra}^{2+}) = 10^{-8}$ mol/L) was added for sorption

studies. Tracer sorption to the reaction vessels and filters was tested prior to the experiments and found to be negligible. Experiments to determine uptake kinetics were performed at $L/S = 200 \text{ L/kg}$ until solution concentrations reached steady state, using individual test batches for each timestep. The timeframe for experiments to determine equilibrium R_d -values were defined based on the results of the kinetic experiments; here a L/S of 25 L/kg was employed. In addition to the sorption experiments using solutions equilibrated with the respective solids (equilibrium solution, ES), selected systems were studied using alkali-rich artificial young cement water (ACW) to address effects of pH and alkali-content on the R_a -uptake. The ACW representative for young cementitious materials (i.e. $\text{pH} \sim 13.5$; Wieland et al., 1998) was prepared by filtration and dilution of highly concentrated alkali hydroxide solutions (NaOH and KOH), stored over $\text{Ca}(\text{OH})_2$, following the procedure of Sipos et al. (2000). The obtained solution containing 0.114 mol/L NaOH and 0.18 mol/L KOH was saturated with $\text{Ca}(\text{OH})_2$ and filtered prior to use.

2.4 Solution analyses

Concentrations of ^{226}Ra in the aqueous phase were determined by γ -spectroscopy (186 keV γ -line) using $500 \mu\text{L}$ sample aliquots in a 2 mL borosilicate glass, placed in a high-purity germanium coaxial N type detector system (type: EGC 35-195-R) from Eurisys Mesures, equipped with a spectrometer system from EG & G Ortec. Analysis of the spectra was performed with the GammaVision® Modell A66-B32 software (version 5.20).

2.5 Evaluation of experimental data

The radionuclide uptake by the respective solids is described in terms of a distribution ratio R_d between solid and liquid phase according to:

$$R_d = \frac{A_{\text{ini}} - A_t}{A_t} \cdot \frac{V}{m} \quad (1)$$

with

- A_t : concentration at time t in liquid phase (Bq or M)
- A_{ini} : initial concentration in liquid phase (Bq or M)
- V : volume of liquid phase (L)
- m : mass of solid phase (kg).

Uncertainties of the R_d values were estimated based on propagated uncertainties associated with the experimental set-up and those related to the determination of ^{226}Ra activities in solution.

A quantitative evaluation of the experimental data on the ^{226}Ra uptake by C-S-H was performed assuming cation exchange with Ca (cf. Tits et al., 2006a) according to:



with C-S-H(Ca) referring to the exchangeable Ca in the C-S-H structure. The selectivity coefficient, K_c , for this reaction can then be defined as follows:

$$K_c = \frac{N_{\text{Ra}} \cdot a(\text{Ca}^{2+})}{N_{\text{Ca}} \cdot a(\text{Ra}^{2+})} \quad (3)$$

where $a(\text{Ca}^{2+})$ and $a(\text{Ra}^{2+})$ are the activities of the cations in the aqueous phase and N_{Ra} and N_{Ca} represent the equivalent fractional occupancies defined as:

$$N_M = \frac{2 \cdot \{M_s^{2+}\}}{\text{CEC}} \quad (4)$$

where $\{M_s^{2+}\}$ is the amount of the divalent cations sorbed (mol/kg), and CEC the cation exchange capacity of the C-S-H phase in eq/kg. Activity coefficients for both cations are equal and activities can be substituted by concentrations for homovalent cation exchange:

$$K_c = \frac{N_{\text{Ra}} \cdot [\text{Ca}^{2+}]}{N_{\text{Ca}} \cdot [\text{Ra}^{2+}]} \quad (5)$$

If sorption is attributed only to cation exchange, the relation between the distribution coefficient R_d (Eq. 1) for Ra and the selectivity coefficient for the Ra-Ca exchange can be formulated as:

$$R_d = \frac{0.5 \cdot \text{CEC} \cdot K_c}{[\text{Ca}^{2+}]} \quad (6)$$

3 Results

C-S-H with C/S of 0.96 (C-S-H 0.96) and 1.4 (C-S-H 1.4) were synthesized and used in the uptake experiments. Phase purity and composition were confirmed by XRD and XRF. The XRD patterns revealed diffuse reflexes at 29.1, 31.8, 49.8, 55.1 and 66.4°/2 θ (cf. Figure 1), respectively, typical for C-S-H (cf. Baur et al., 2004; Chen et al., 2004; Nonat et al., 2004). No portlandite was detected by XRD indicating that potential impurities due to this phase were below 1 wt.%.

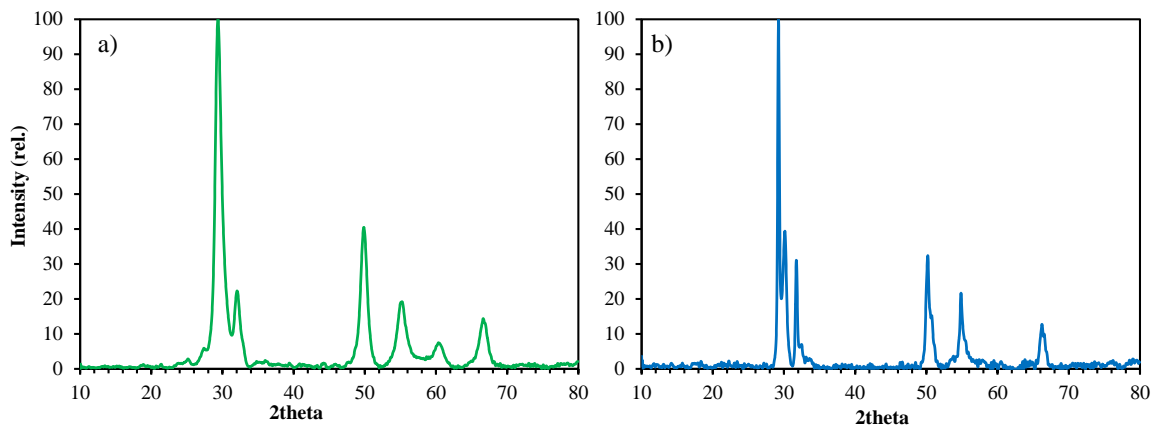


Figure 1: XRD patterns of C-S-H0.96 (a) and C-S-H1.4 (b).

The kinetics of the Ra(II) uptake by the C-S-H phases were determined in the absence ($\text{pH}(\text{C-S-H } 0.96) = 11.9$; $\text{pH}(\text{C-S-H } 1.4) = 12.1$) and in the presence of alkalis ($\text{pH} = 13.3$) for up to 100 days. The pH in the respective solutions was found to be constant over the time of the experiments. The uptake of Ra(II) was fast and sorption equilibrium was attained within 28 days (cf. Figure 2). The equilibrium R_d values for the ^{226}Ra uptake by C-S-H in the different systems are detailed in Table 2. A distinct dependence of the ^{226}Ra uptake on C/S and solution composition was observed (cf. Tits et al., 2006a). The uptake of ^{226}Ra by C-S-H was found to decrease

significantly with increasing C/S, from about 22,000 L/kg (C-S-H 0.96) to 13,000 L/kg (C-S-H 1.4) in alkali-free systems. This effect is probably due to the negative surface charge at $C/S < 1.2$, facilitating cation uptake, as well as the higher competition with Ca ions in solution for sorption sites at high C/S (cf. Atkins et al., 1992; Tits et al., 2006a). The lower R_d values (about a factor of 2) in systems with ACW are probably due to competition with alkalis for sorption sites (cf. Tits et al., 2006a), as well as changes in C-S-H surface charge and speciation at higher pH.

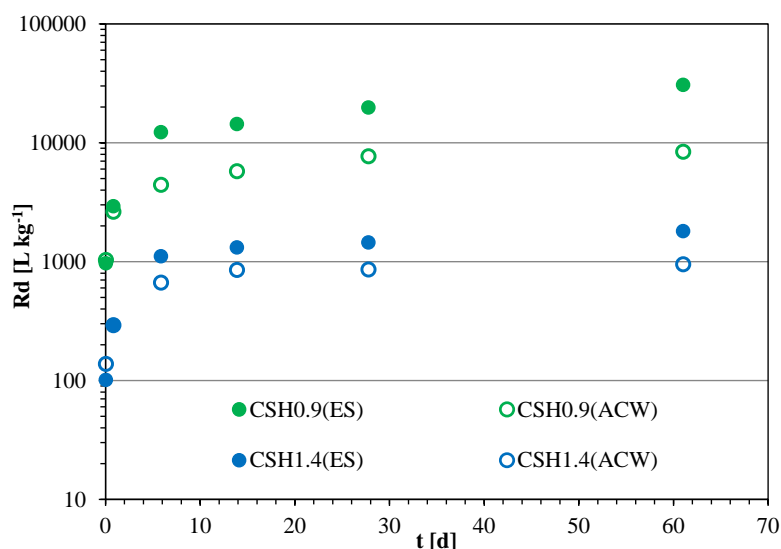


Figure 2: Uptake of ^{226}Ra by C-S-H phases in different solutions as function of time (ES: equilibrium solution; ACW: artificial young cement water (pH 13.3)).

Table 2: Distribution coefficients R_d for the ^{226}Ra uptake by C-S-H in different solutions (ES: equilibrium solution; ACW: artificial young cement water (pH 13.3)).

Phase	R_d (L/kg)	
	ES	ACW
C-S-H 0.96	$22,529 \pm 3,980$	$13,328 \pm 2,356$
C-S-H 1.4	$1,805 \pm 722$	951 ± 380

The uptake of ^{226}Ra by C-S-H is generally explained in terms of cation exchange with Ca and sorption to two silanol-like sites at the C-S-H surface (Tits et al., 2006a; Missana et al., 2017). The selectivity coefficient for Ra uptake on C-S-H can be calculated from the R_d -values and Ca-concentrations obtained from the sorption experiments using equation 6. For the CEC of C-S-H, the value of 1.2 eq./kg derived by Tits et al. (2006b) was used. Based on this, we obtained selectivity coefficients for the Ra/Ca exchange in the alkali free systems of $\log K_c = 2.2$ for C-S-H 0.96 and $\log K_c = 1.8$ for C-S-H 1.4. These values are distinctively higher than the value of $\log K_c = 0.78 \pm 0.6$ determined by Tits et al. (2006a) for the Ra/Ca exchange on C-S-H under similar conditions. A comparison to selectivity coefficients for the uptake of other alkaline-earth elements by C-S-H (Ba: $\log K_c = 1.05$, Missana et al., 2017; Sr: $\log K_c = 0.08$, Tits et al., 2006b) reveals a decreasing affinity for uptake by C-S-H in the order $\text{Ra} > \text{Ba} > \text{Sr}$. Hence, Sr seems to be no meaningful analogue for the uptake of ^{226}Ra in cementitious systems due to the significantly lower selectivity coefficient.

3.1 Atomistic simulations

As an additional uptake mechanism to surface sorption, the incorporation of bivalent cations into the C-S-H interlayer has been discussed by various authors (e.g. Komarneni et al., 1986; Shrivastava and Glasser, 1986; Komarneni and Tsuji, 1989; Shrivastava and Komarneni, 1994; Tits et al., 2006a,b; Missana et al., 2017). It was concluded that cations like Ni, Co or Sr can replace Ca in the C-S-H interlayer, whereas the uptake of cations larger than Ca is limited to sorption at surface sites. Hence, the uptake of Ra and Ba is attributed mainly to cation exchange with Ca and potentially also to sorption by silanol-like sites at the C-S-H surface (e.g. Tits et al., 2006a; Missana et al., 2017). However, recent investigations on the uptake of Np(VI/V) and U(VI) by C-S-H suggested that also large cations can be incorporated into the C-S-H interlayer spacing (Gaona et al., 2011, 2012; Tits et al., 2011, 2014).

Therefore, we performed ab-initio atomistic simulations to investigate the potential of Ra incorporation into the C-S-H structure, in addition to surface sorption. In a first step, a substitution of Ca coordinated to silanol groups in the interlayer spacing by Ra (A) was compared to a structural Ra uptake into C-S-H due to exchange with Ca in the stable octahedral CaO_2 layers (B) (cf. Figure 3), using simplified C-S-H structure models based on the 11 Å tobermorite structure (Hamid, 1981). The differences in the enthalpies (reaction enthalpies) for the two configurations computed with the density functional theory (DFT)-based plane-wave Quantum-ESPRESSO simulation code were found to be rather large (184 kJ/mol for C-S-H 0.75), with the lower enthalpy related to the Ra uptake into the interlayer. The enthalpy differences were even more pronounced for C-S-H 0.9 (260 kJ/mol) and C-S-H1.0 (202 kJ/mol). This strongly indicates that Ra substitution for interlayer Ca would be highly preferred over incorporation into the octahedral layer.

In order to assess the potential of an exchange reaction of Ra from solution with interlayer Ca in the C-S-H, the ΔG of the exchange reaction was estimated from the DFT-reaction-enthalpy (ΔH), using an estimate of the reaction entropy ΔS . For the solid C-S-H phase it was assumed here that the change in entropy is given by the differences in Latimer entropies of elements in solids (Latimer, 1921). For the entropies of the aqueous Ca^{2+} and Ra^{2+} ions, values from Shock et al. (1997) were used. As a result from uncertainties in the thermodynamic data, the error on the ΔG derived in this way was estimated to be ~ 20 kJ/mol. Despite these uncertainties and the simplified C-S-H model, the computed data clearly show that the reaction enthalpy and the free energy of the exchange reaction with Ca in the interlayer increase significantly with increase of C/S, consistent with the observed decrease of the Ra uptake with increasing C/S. The distinctively negative free energy computed of the exchange reaction for C-S-H 0.75 (about -76 kJ/mol) suggests that the uptake of Ra in the C-S-H interlayer is a plausible mechanism, in particular for low C/S.

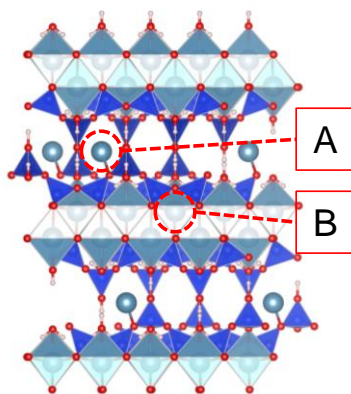


Figure 3: Schematic representation of the C-S-H0.75 structure with substitution positions in the interlayer (A) and octahedral CaO_2 layer (B).

Thus, atomistic simulations performed complementary to solution chemical studies and advanced microscopic/spectroscopic investigations (e.g. by TEM, EXAFS) can provide additional insights into the structural uptake of radionuclides by cementitious materials. In addition to the ab-initio simulations of the Ra uptake by C-S-H described above, further ongoing simulation activities concern the structural uptake of molybdenum by AFm phases. Here, the atomistic simulations address the uptake of MoO_4^{2-} in terms of interlayer exchange for sulfate anions, surface sorption and edge sorption, based on observations obtained from our respective sorption experiments and literature data (e.g. Ma et al., 2017). The supercell designed for these simulations is based on the structural model of kuzelite ($[\text{Ca}_4\text{Al}_2(\text{OH})_{12}][(\text{SO}_4) \cdot 6\text{H}_2\text{O}]$) from Pöllmann et al. (1997).

4 Conclusions and Future work

In this study the uptake of ^{226}Ra by C-S-H phases with different C/S was addressed. The uptake of ^{226}Ra by C-S-H phases was found to be generally fast, leading to sorption equilibrium in less than 30 days. A strong retention of ^{226}Ra by C-S-H phases was observed (R_d up to 22,000 L/kg); the distribution coefficients (R_d) were found to decrease with increasing C/S and depend on the content of alkalis in solution and solution pH. The lower R_d values in systems with artificial young cement water (pH 13.3) suggest a higher Ra retention and lower mobility in alkali free, aged cementitious systems in the portlandite stage (pH \sim 12.5) compared to young cementitious materials. Ab-initio atomistic simulations performed on the uptake of Ra in the C-S-H interlayer reveal negative free energies for the cation exchange reaction, suggesting that Ra uptake in the interlayer, in addition to surface sorption, is a plausible Ra uptake mechanism in particular at low C/S. It could be shown that atomistic simulations performed complementary to solution chemical studies and microscopic/spectroscopic investigations can provide valuable insights into the mechanisms controlling the uptake and sorption of radionuclides in cementitious materials. Work intended in the near future comprises DFT calculations to gain insights into the mechanisms governing the structural uptake of molybdate ions by AFm- SO_4 phases.

Acknowledgement

The research leading to these results has received funding from the European Union's Horizon 2020 Research and Training Programme of the European Atomic Energy Community (EURATOM) (H2020-NFRP-2014/2015) under grant agreement n° 662147 (CEBAMA). The authors gratefully acknowledge the JARA-HPC awarding body for computing time on the computing resources at RWTH Aachen University and Forschungszentrum Jülich provided on the JARA-HPC Partition.

References

- Atkins, M. and Glasser, F.P. (1992). Application of portland cement-based materials to radioactive waste immobilization. *Waste Management*, 12, 105-131.
- Atkins, M., Glasser, F.P., Kindness, A. (1992). Cement hydrate phases: solubility at 25°C. *Cement and Concrete Research*, 22, 241-246.
- Baur, I., Keller, P., Mavrocordatos, D., Wehrli, B., Johnson, C.A. (2004). Dissolution-precipitation behaviour of ettringite, monosulfate, and calcium silicate hydrate. *Cement and Concrete Research*, 34, 341-348.
- Bel, J.P., Wickham, S.M., Gens, R.M.F. (2006). Development of the supercontainer design for deep geological disposal of high-level heat emitting radioactive waste in Belgium. *Materials Research Society Symposia Proceedings*, 932.

- Chen, J.J., Thomas, J.J., Taylor, H.F.W., Jennings, H.M. (2004). Solubility and structure of calcium silicate hydrate. *Cement and Concrete Research*, 34, 1499-1519.
- Drace, Z. and Ojovan, M.I. (2013). A summary of IAEA coordinated research project on cementitious materials for radioactive waste management. *In: Bart, F., Cau-dit-Coumes, C., Frizon, F., Lorente, S. (Eds.) Cement-based materials for nuclear waste storage*, Springer, 3-11.
- Gaona, X., Dähn, R., Tits, J., Scheinost, A.C., Wieland, E. (2011). Uptake of Np(IV) by C-S-H phases and cement paste: An EXAFS Study. *Environmental Science & Technology*, 45, 8765-8771.
- Gaona, X., Kulik, D.A., Mace, N., Wieland, E. (2012). Aqueous-solid solution thermodynamic model of U(VI) uptake in C-S-H phases. *Applied Geochemistry*, 27, 81-95.
- Glasser, F.P. (1997). Fundamental aspects of cement solidification and stabilization. *Journal of Hazardous Materials*, 52, 151-170.
- Glasser, F.P. (2001). Mineralogical aspects of cement in radioactive waste disposal. *Mineralogical Magazine*, 65, 621-633.
- Glasser, F.P. (2011). Application of inorganic cements to the conditioning and immobilisation of radioactive wastes. *In: Ojovan, M.I. (Ed.) Handbook of advanced radioactive waste conditioning technologies*, Woodhead, 67-135.
- Hamid, S.A., 1981. The crystal structure of the 11 Å natural tobermorite $\text{Ca}_{2.25}[\text{Si}_3\text{O}_{7.5}(\text{OH})_{1.5}] \cdot 1 \text{ H}_2\text{O}$. *Zeitschrift für Kristallographie*, 154, 189-198.
- Jantzen, C., Johnson, A., Read, D., Stegemann, J. (2010). Cements in waste management. *Advances in Cement Research*, 22, 225-231.
- Komarneni, S., Roy, R., Roy, D.M. (1986). Pseudomorphism in xonotlite and tobermorite with Co^{2+} and Ni^{2+} exchange for Ca^{2+} at 25°C. *Cement and Concrete Research*, 16, 47-58.
- Komarneni, S. and Tsuji, M. (1989). Selective cation exchange in substituted tobermorites. *Journal of the American Ceramic Society*, 72, 1668-1674.
- Ma, B., Fernandez-Martinez, A., Grangeon, S., Tournassat, C., Findling, N., Claret, F., Koishi, A., Marty, N.C.M., Tisserand, D., Bureau, S., Salas-Colera, E., Elkaïm, E., Marini, C., Charlet, L. (2017). Evidence of multiple sorption modes in layered double hydroxides using Mo as structural probe. *Environmental Science & Technology*, 51, 5531-5540.
- Missana, T., García-Gutiérrez, M., Mingarro, M., Alonso, U. (2017). Analysis of barium retention mechanisms on calcium silicate hydrate phases. *Cement and Concrete Research*, 93, 8-16.
- Nonat, A. (2004). The structure and stoichiometry of C-S-H. *Cement and Concrete Research*, 34, 1521-1528.
- Pollmann, H., Witzke, T., Kohler, H. (1997). Kuzelite, $[\text{Ca}_4\text{Al}_2(\text{OH})_{12}][(\text{SO}_4) \cdot 6\text{H}_2\text{O}]$, a new mineral from Maroldsweisach/Bavaria, Germany. *Neues Jahrbuch Mineralogie Monatsheft*, 423-432.
- Shock, E.L., Sassani, D.C., Willis, M., Sverjensky, D.A. (1997). Inorganic species in geologic fluids: Correlations among standard molal thermodynamic properties of aqueous ions and hydroxide complexes. *Geochimica et Cosmochimica Acta*, 61, 907-950.
- Shrivastava, O.P. and Glasser, F.P. (1986). Ion-exchange properties of 11-Å tobermorite. *Reactivity of Solids*, 2, 261-268.
- Shrivastava, O.P. and Komarneni, S. (1994). Cesium selectivity of (Al+Na)-substituted tobermorite. *Cement and Concrete Research*, 24, 573-579.
- Sipos, P., May, P.M., Hefter, G.T. (2000). Carbonate removal from concentrated hydroxide solutions. *Analyst*, 125, 955-958.
- Smith, D.W. (1977). Ionic hydration enthalpies. *Journal of Chemical Education*, 54, 540.
- Tits, J., Gaona, X., Laube, A., Wieland, E. (2014). Influence of the redox state on the neptunium sorption under alkaline conditions: Batch sorption studies on titanium dioxide and calcium silicate hydrates. *Radiochimica Acta*, 102, 385-400.
- Tits, J., Geipel, G., Mace, N., Eilzer, M., Wieland, E. (2011). Determination of uranium(VI) sorbed species in calcium silicate hydrate phases: A laser-induced luminescence spectroscopy and batch sorption study. *Journal of Colloid and Interface Science*, 359, 248-256.

- Tits, J., Iijima, K., Wieland, E., Kamei, G. (2006a). The uptake of radium by calcium silicate hydrates and hardened cement paste. *Radiochimica Acta*, 94, 637-643.
- Tits, J., Wieland, E., Mueller, C.J., Landesman, C., Bradbury, M.H. (2006b). Strontium binding by calcium silicate hydrates. *Journal of Colloid and Interface Science*, 300, 78-87.
- Wieland, E., Tits, J., Spieler, P., Dobler, J.P. (1998). Interaction of Eu(III) and Th(IV) with sulfate-resisting portland cement. *Materials Research Society Symposia Proceedings*, 506, 573-578.

Ra-226 sorption on intact cement pastes based on CEM I and CEM V

Crina Bucur¹*, Ionut Florea¹, Relu Dobrin¹, Nicolae Dulama¹, Nicoleta Deneanu¹

¹ Institute for Nuclear Research Pitesti (RO)

* Corresponding author: crina.bucur@nuclear.ro

Abstract

Cement based materials are used as engineered barriers in geologic disposal facilities for spent fuel and long lived radioactive waste as well as the main engineered barrier in a near surface repository for short lived radioactive waste. These materials exhibit a moderate uptake for the ²²⁶Ra contained in the radioactive waste.

In this study the ²²⁶Ra sorption on non-degraded hardened cement pastes (HCP), based on CEM I and CEM V, was evaluated. Kinetic tests to evaluate the time needed to reach the sorption equilibrium and tests to derive the sorption isotherms were carried out.

The measurements of ²²⁶Ra in solutions were based on ²²²Rn accumulation in a biphasic mixture and measurement of ²²²Rn by liquid scintillation counting technique (LSC) using a LSC counter with alpha/beta discrimination.

The results from the kinetic sorption tests indicate that most of the ²²⁶Ra in solution is sorbed on fresh cement pastes in the first day of contacting and a slow increase of the distribution ratio was observed between 2 and 20 days of contacting. Similar behaviour was observed for both type of cements, but for CEM V the distribution ratio seems to be a little bit higher than for CEM I. From linear sorption isotherms, ²²⁶Ra distribution coefficient was evaluated to be 282.8 L/kg for CEM I and 381.5 L/kg for CEM V.

1 Introduction

²²⁶Ra is one of the major daughter nuclides of the most abundant uranium isotope (²³⁸U) and it is an important isotope in the radioactive waste, mainly generated from nuclear fuel fabrication, but also from nuclear research and power plants.

Cementitious materials constitute in many disposal concepts an important engineered barrier aimed to reduce radionuclide solubility and enhance sorption. Available data on radium sorption on cementitious materials indicate that Ra(II) sorption is significant, with distribution coefficient (K_d) values ranging from 50 to 500 L/kg. The Ra(II) sorption kinetics and reversibility, as well as the effect of the solid to liquid ratio and the CaO/SiO₂ ratio on Ra(II) uptake on fresh and degraded hardened cement pastes (HCP) were investigated by Tits (Tits et al., 2006a). Their results show that the uptake of Ra(II) by the degraded Hardened Cement Paste is fast (sorption equilibrium was attained within one day) with a K_d value at equilibrium of 140 L/kg. A clear dependence on the CaO/SiO₂ ratio was observed.

For fresh HCP, a two-step process was used to explain the Ra(II) uptake: fast sorption occurring within one day, giving rise to a distribution ratio (R_d) value of 260 L/kg. In a second step, over a period of 60 days, the Ra(II) uptake appears to increase slowly reaching a R_d value of 400 L/kg. Nevertheless, the authors noted that the

significance of the slow increase in the R_d value can be questioned due to the high uncertainties on the data. Their experiments were carried out at low ^{226}Ra concentration ($\sim 1.5 \cdot 10^{-8} \text{ M}$) and consequently, the relative uncertainties on the measured sorption data are quite large ($\sim 50\%$) (Tits et al., 2006a).

It is assumed that Ra(II) only sorbs on the C-S-H fraction in HCP and that the aqueous Ra(II) speciation is dominated by the Ra^{2+} species. In these conditions, the cation-exchange model developed by Tits et al. (Tits et al., 2006a) for the Ra(II) sorption on C-S-H phases in the absence of alkalis can be used to estimate the K_d value for the Ra(II) sorption on degraded HCP.

Even chemical analogues of Ra(II) , such as Sr(II) and Ba(II) , are often recommended to be used in sorption databases for the cementitious near-field (Wieland and Van Loon, 2002), the experiments performed by Tits et al. (Tits et al., 2006a, Tits et al., 2006b) show that sorption values for radium are almost 5 times greater than those obtained for strontium. Consequently, specific radium sorption experiments have to be conducted to get accurate sorption data for radium sorption on cementitious materials.

According to the existing experimental data, competition with alkalis leads to weaker uptake of radium in Stage I compared to Stage II of the cement degradation, while decreasing Ca concentrations gives rise to the opposite effect, meaning an increasing radium uptake in Stage I compared to Stage II of the cement degradation (Wieland, 2014). The consequence of the later effect is that the Ra uptake is higher in Stages I and III compared to Stage II of cement degradation (Wieland, 2014).

Experimental data regarding the effect of the cement degradation (under disposal conditions) on radium sorption are limited and the on-going experiments in RATEN ICN, carried out in the frame of CEBAMA WP2, are specifically oriented to assess the influence of HCP degradation on ^{226}Ra sorption and this paper presents the preliminary results obtained from this experimental programme.

2 Materials and methods

2.1. Preparation of fresh HCP and ^{226}Ra spiked solutions

Two hardened cement pastes (HCP), one based on CEM I (Ordinary Portland Cement) and the other one on CEM V, were used in this study. These cement pastes were received in 2016 from ARMINES, where they were kept for almost 7 years in saturated portlandite water ($\text{pH} = 12.4$) at 20°C . Both cement pastes were prepared with a water to cement ratio of 0.4, using CEM I 52.5 (LAFARGE, Val d'Aizergues factory), and CEM V/A 32.5 (HOLCIM, Heming factory), respectively. To avoid their carbonation, both cement pastes were also kept in saturated portlandite water and room temperature ($20 \pm 3^\circ\text{C}$) between receiving time and using them in sorption experiments.

To be used in experimental tests to evaluate the ^{226}Ra sorption on non-degraded HCP, the hydrated cement pastes were crushed and sieved under nitrogen atmosphere (using nitrogen of 99.99 grade purity) and the 125-250 μm fraction was used in sorption experiments. Also, this fraction will be used to prepare the degraded states of the cement pastes.

^{226}Ra spiked solutions used in sorption tests were prepared using a standard solution (water solution of barium and radium chlorides in hydrochloric acid), with ^{226}Ra activity of $3.34 \cdot 10^4 \text{ Bq/g}$ (EUROSTANDARD CZ) and an artificial cement pore water (ACW) that is in equilibrium with ordinary Portland cement, with a pH of 13.5 (Tits et al., 2003), and chemical composition given in Table 1.

Table 1: Chemical composition of ACW (Tits et al., 2003) used to prepare ^{226}Ra spiked solutions.

Chemicals	Concentration (g/L)
KOH	11.9
NaOH	4.6
CaCO_3	1.0
CaO	0.76
Na_2SO_4	0.426
$\text{Al}_2(\text{SO}_4)_3$	$7.82 \cdot 10^{-3}$

Doubly demineralised water, conditioned by ultrafiltration with a Simplicity Millipore system for ultrapure water (Simplicity, Merk, USA) and reagent grade chemicals were used to prepare the ACW.

2.2. Batch sorption experiments

The ^{226}Ra uptake on non-degraded HCPs were studied by batch sorption experiments carried out for a solid to liquid ratio of 2.5 g/L (0.03 g of crushed and sieved cement paste in contact with 12 mL of ^{226}Ra spiked ACW solution), at room temperature ($23 \pm 3^\circ\text{C}$), in polypropylene (PP) centrifuge tubes. Before use, the PP tubes were prewashed in diluted nitric acid (0.1 M HNO_3) and thoroughly rinsed with deionised water. Blank batches were prepared for measuring the ^{226}Ra background in the cement pastes and the ^{226}Ra sorption on the PP tube walls was checked. All experiments were carried out in duplicate and all operations, excepting the solution sampling for ^{226}Ra measurement, were carried out under nitrogen atmosphere.

Before adding the ^{226}Ra spiked solution, all HCP samples were pre-equilibrated with ACW for 24 hours, by adding 4 mL of ACW and gently shake the tubes placed horizontally on an orbital shaker.

Since the distribution coefficient is defined at equilibrium, assuming that the system is reversible and, at low tracer concentration, it is independent of the contaminant concentration in the aqueous phase, three sets of sorption experiments were performed for each cement paste:

- kinetic tests to assess the time needed to reach the phases equilibrium – carried out for ^{226}Ra activity in contacting solutions of around 45 Bq/mL;
- tests to derive the sorption isotherms for three different initial concentrations of ^{226}Ra in contacting solution (46, 91 and 136 Bq/mL);
- tests to assess the experimental uncertainties (8 batch tests carried out for CEM I cement paste with the same S/L ration and ^{226}Ra concentration).

Furthermore, to assess the reversibility of ^{226}Ra uptake on non-degraded HCPs, desorption tests are going to be performed.

After equilibration, the test tubes were centrifuged at 11,000 rpm for 20 min, followed by the supernatant filtration through 0.45 μm Millipore filters. Ten millilitres from each filtered supernatant were mixed with an organic immiscible scintillator (UltimaGold F) for ^{226}Ra measurement.

2.3. Method for ^{226}Ra measurement

^{226}Ra measurement in contacting solutions as well as in all solutions resulted from the batch sorption tests were achieved by alpha-LSC method. This method is based on the absorption of the ^{222}Rn resulted by ^{226}Ra decay into an immiscible organic scintillator and counting of the alpha-particles emission of ^{222}Rn and its short-lived daughters (^{218}Po and ^{214}Po).

Due to the radon's affinity for organic solvents with long carbon chain, the radon generated as gas from ^{226}Ra decay was absorbed into UltimaGold F scintillator. After around 3 hours, needed to establish the equilibrium between ^{222}Rn and its daughters, the mixtures were counted at different time interval for a period of 25 days necessary to reach the equilibrium between ^{226}Ra and ^{222}Rn .

Liquid Scintillator Counter (LSC) with alpha-beta discrimination, model 4910 TRICARB Perkin Elmer, was used for ^{222}Rn measurements. A standard ^{226}Ra solution was used for LSC counter calibration, according to ISO standard no. 13164-4:20136. A mixture of ^{226}Ra standard solution and organic scintillator is placed in a glass scintillation vial and is left for about 25 days to achieve equilibrium with the progenies. Afterwards, the alpha count rate is measured and the counting efficiency is determined by dividing the count rate (in cps) to the known activity of the ^{226}Ra solution. In literature, a generic value of 2.7 cps/Bq is commonly indicated. This unusual, higher than 1, value of the counting efficiency is due to the counting of ^{222}Rn and its alpha-emitting daughters (^{218}Po and ^{214}Po), which, after 25 days, are completely extracted in the organic phase and are in secular equilibrium with ^{226}Ra , giving three alpha particles emitted in the scintillator for every ^{226}Ra decay (Dulama et al., 2017).

3 Results

3.1 Sorption kinetics on hardened cement pastes (CEM I and CEM V)

The kinetic tests were carried out for ^{226}Ra initial activity in contacting solution of 44.75 Bq/mL and the activity ^{226}Ra in liquid phase was measured after 2, 4, 6, 8, 17 hours, 1, 2, 10, 20, 30 and 40 days of contacting.

The uptake of ^{226}Ra on HCPs during kinetic tests was quantified in terms of distribution ratio, R_d , describing the partitioning of radium between the solid phase and the liquid phase in a batch sorption experiment, and defined as:

$$R_d = \frac{A_{\text{aq}}(t_i)}{C_{\text{aq}}(t_i)} = \frac{C_0 - C_{\text{aq}}(t_i)}{C_{\text{aq}}(t_i)} \times \frac{V}{m} \quad (1)$$

where:

- $A_{\text{aq}}(t_i)$ ^{226}Ra activity on solid phase, at time t_i (Bq/g);
- $C_{\text{aq}}(t_i)$ ^{226}Ra activity in the aqueous phase, at time t_i (Bq/mL)
- C_0 initial ^{226}Ra activity in the contacting solution (Bq/mL)
- V volume of liquid phase (mL)
- m mass of solid phase (g)

The mass of crushed HCP samples used in sorption tests is expressed as dry mass determined by ignition of HCP at 1,100°C.

The results obtained for the kinetic of ^{226}Ra uptake on CEM I and CEM V show that for both types of HCPs, a fast uptake takes place in the first two days of contacting, followed by a slower increase in the distribution ratio till 20 days of contacting (Figure 1).

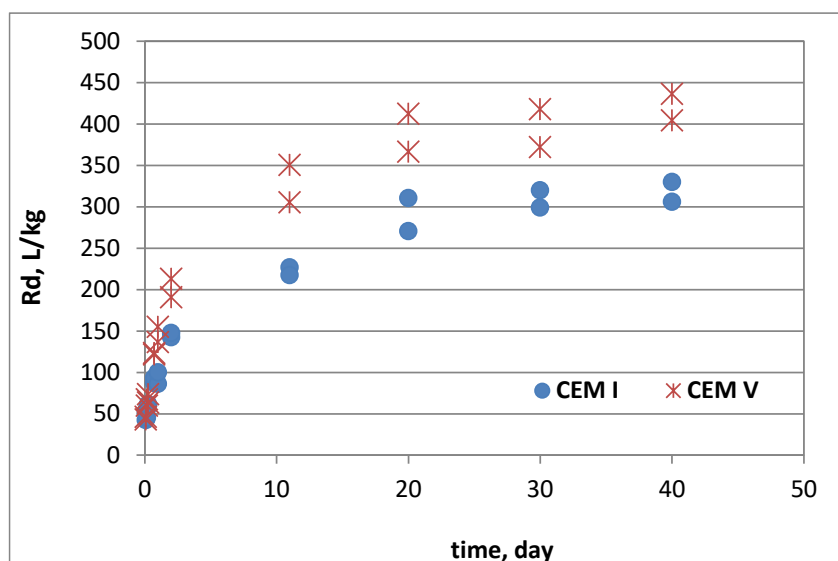


Figure 1: The evolution of the ^{226}Ra distribution ratio on the two non-degraded cement pastes.

The experimental data from sorption kinetic tests show that ^{226}Ra uptake is higher on CEM V than on CEM I, with a distribution ratio at equilibrium of around 290 L/kg for CEM I and 389 L/kg for CEM V. Nevertheless, it should be noted that the ACW used both in kinetic tests and in sorption isotherm is in equilibrium with ordinary Portland cement. Since both HCPs used in these sorption tests were kept in saturated portlandite water for more than 9 years, the C:S ratio of the C-S-H phases in both cements are the same because the C:S ratio is defined by the Ca concentration in portlandite saturated solution. The Ra uptake in cement is most probably controlled by the C-S-H fraction in both cements (Tits et al., 2006a) and since the C-S-H composition in both cements did not change during the sorption experiments (the ACW is saturated with regard to portlandite), radium uptake should be similar on both pastes. However, the ACW used in these experiments is not in equilibrium with regards the minor elements such as Al, Mg and S and some cement components such as ettringite, AFm phases etc., may recrystallize, dissolve or precipitate in contact with the ACW used in these experiments. To be sure that any change of these cement components have no influence on the Ra sorption, sorption tests will be repeated with ACW in equilibrium with regards to Al, Mg and S with both HCPs.

3.2 Sorption isotherms on hardened cement pastes (CEM I and CEM V)

The experiments to derive ^{226}Ra sorption isotherms were performed for ^{226}Ra initial activities in contacting solution of 45.5, 90.7 and 135.6 Bq/mL. As well as for the kinetic tests, all samples used in the experiments for deriving sorption isotherms were pre-equilibrated for 24 hours with ACW before adding the ^{226}Ra spiked solutions.

After 20 days of equilibration, ^{226}Ra activity in the liquid phase was measured and the results were plotted as ^{226}Ra activity in liquid phase versus ^{226}Ra activity on solid phase (Figure 2 and Figure 3).

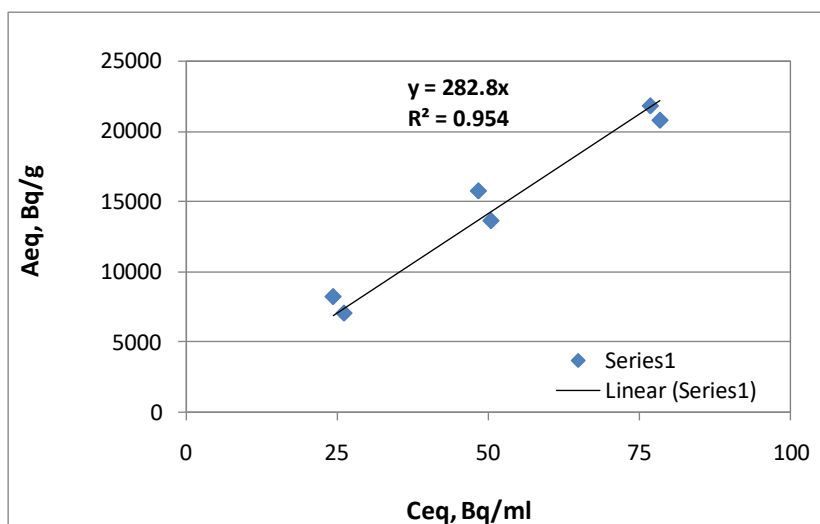


Figure 2: ^{226}Ra linear sorption isotherm on CEM I HCP.

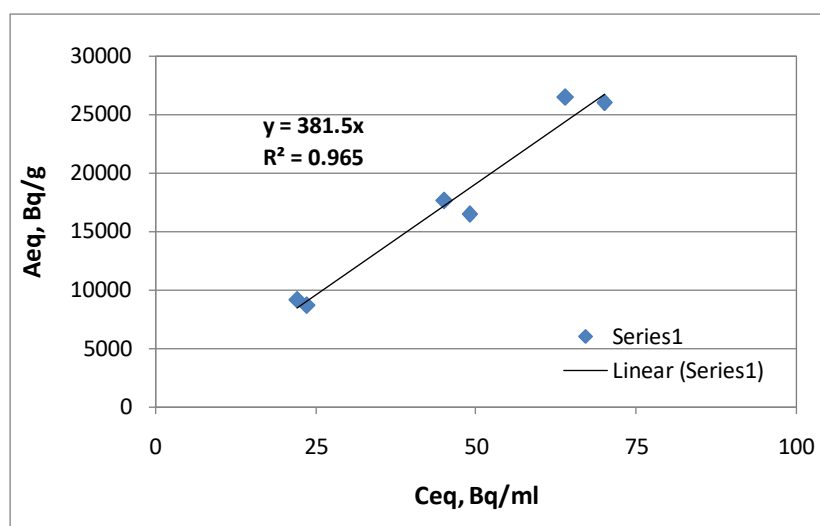


Figure 3: ^{226}Ra linear sorption isotherm on CEM V HCP.

For both type of cements, linear sorption isotherms fit well the experimental data. The values for the distribution coefficient estimated as the slope of the linear isotherms are 282.8 ± 31.1 L/kg for CEM I and 381.5 ± 41.9 L/kg for CEM V. These results obtained for the ^{226}Ra distribution coefficient on the two cement pastes are closed to the distribution ratio values obtained from the kinetic tests.

4 Conclusions and future work

The data presented in this paper are preliminary experimental data of the on-going sorption tests carried out to assess the influence of the cement paste degradation on ^{226}Ra uptake on hardened cement pastes based on CEM I and CEM V.

The kinetic tests show the equilibrium between solid and liquid phases was attained after 20 day of contacting. ^{226}Ra uptake is fast in first two days of contacting, with a distribution ratio of 92.99 ± 8.74 L/kg and 145.69 ± 14.13 L/kg for CEM I and CEM V, respectively. The distribution ratio increases up to 20 days of contacting to 290.75 ± 28.21 L/kg for CEM I and 389.52 ± 37.78 L/kg for CEM V.

The experimental data obtained from the experiments carried out to derive the sorption isotherms are well fitted by linear approximation, indicating that the ^{226}Ra sorption on non-degraded HCPs could be described by the linear sorption model. The values for distribution coefficient estimated from the linear sorption isotherms are 282.8 ± 31.1 L/kg for CEM I and 381.5 ± 41.9 L/kg for CEM V, very closed to the values obtained from the kinetic tests.

Since all sorption tests were carried out with ACW that is in equilibrium with ordinary Portland cement, the sorption tests for CEM V will be repeated with cement pore water with a chemical composition that will not generate any cement components changes during sorption tests. Also, further characterisation of C-S-H phases in both HCPs will give an explanation of different radium retention on CEM I and CEM V HCP used in these experiments.

The experimental programme will continue with desorption tests for non-degraded cement pastes to evaluate the reversibility of ^{226}Ra uptake.

To assess the influence of cement degradation on ^{226}Ra uptake, two degraded states for each HCPs will be obtained by hydrolysis leaching in degassed deionised water (DDW) and one degradation state by chemical degradation (using NH_4NO_3) followed by hydrolysis leaching in DDW. Tests to evaluate the kinetic of ^{226}Ra uptake on these degraded states, both for CEM I and CEM V HCPs, will be performed, as well as sorption and desorption tests to derive de sorption isotherm and assess the reversibility of ^{226}Ra uptake on degraded HCPs. The batch tests will be complemented by different investigations (SEM-EDS, TGA, XRD, ICP-OES) aimed to characterize the cement pastes and the artificial pore waters used to prepare the ^{226}Ra spiked solutions for each set of experiments.

Acknowledgement

The research leading to these results has received funding from the European Union's Horizon 2020 Research and Training Programme of the European Atomic Energy Community (EURATOM) (H2020-NFRP-2014/2015) under grant agreement n° 662147 (CEBAMA).

References

- Dulama, N., Dobrin, R., Toma, Al., Hirićă, O. (2017). Development of improved LSC methods for measurement of radon concentration in groundwater. *Journal of Nuclear Research and Development*, 14, 53-56.
- ISO 13164-4:2015. Water quality — Radon-222 — Part 4: Test method using two-phase liquid scintillation counting.
- Tits, J., Jakob, A., Wieland, E., Spieler, P. (2003). Diffusion of tritiated water and $^{22}\text{Na}^+$ through non-degraded hardened cement pastes. *Journal of Contaminant Hydrology*, 61(1), 45-62.
- Tits, J., Iijima, K., Wieland, E., Kamei, G. (2006a). The uptake of radium by calcium silicate hydrates and hardened cement paste. *Radiochimica Acta*, 94, 637-643.
- Tits, J., Wieland, E., Müller, C.J., Landesman, C., Bradbury, M.H. (2006b). Strontium binding by calcium silicate hydrates. *Journal of Colloid and Interface Science*, 300, 78-87.
- Wieland, E. and Van Loon, L. (2002). Cementitious near-field sorption database for performance assessment of an ILW repository in Opalinus Clay. PSI Report Nr., 03-06 and Nagra Technical Report, NTB 02-20.
- Wieland, E. (2014). Sorption data base for the cementitious near field of L/ILW and ILW repositories for provisional safety analyses for SGT-E2. Nagra Technical Report, NTB 14-08.

Uptake and diffusion properties of HTO and inorganic C-14 through hardened cement paste: Influence of water saturation and carbonation

Sabrina Rasamimanana^{1*}, Catherine Landesman¹, Solange Ribet¹, Katy Perrigaud¹,
Nicolas Bessaguet¹, Bernd Grambow¹

¹ SUBATECH/ARMINES (Institut Mines Télécom Atlantique,
Université de Nantes, CNRS) (FR)

* Corresponding author: rasamima@subatech.in2p3.fr

Abstract

Diffusion parameters of HTO were investigated through non-carbonated and carbonated hardened cement paste (HCP, CEM V/A Rombas) for different water saturation conditions. The results showed only a slight effect of water saturation and carbonation on the effective diffusion coefficient, $D_e(\text{HTO})$. The observed increase of $D_e(\text{HTO})$ was interpreted as being due to a change in the HCP microstructure, which have resulted from the drying and carbonation processes. The characterization of the microstructure of the samples is ongoing to support these results (RMN ^{29}Si , X-ray tomography).

The diffusive behaviour of inorganic C-14 ($^{14}\text{CO}_3^{2-}$) was studied after reaching the stationary diffusion of HTO. As we expected, upstream C-14 concentrations remained constant over time and no C-14 was observed in the downstream reservoirs. Tests are ongoing in order to apply digital β autoradiography for describing C-14 diffusion profiles into HCP samples.

Uptake and reversibility of C-14 were investigated on dispersed HCP samples (batch experiments). The results showed that carbonated samples displayed a low uptake (isotopic exchange) while non-carbonated samples displayed a medium uptake (sorption to C-S-H or portlandite surfaces). Uptake seemed to be reversible for both carbonated and non-carbonated samples. Sorption isotherms experiments will be conducted to better understand these mechanisms.

1 Introduction

The pore spaces of cemented wastes may remain partially unsaturated with water for a long time in their disposal locations and C-14 species when released from waste may react with unsaturated cement materials. C-14 sources in nuclear waste are numerous and thus its speciation in solution may be complex (release of aqueous/volatile and/or inorganic/organic species). In cementitious environments, which exhibit a strong affinity for CO_2 due to carbonation process (also in unsaturated conditions), it is thus likely that inorganic C-14 becomes trapped by the crystalline structure of formed calcite. The objective of the present work is to investigate the different uptake mechanisms (sorption, dissolution/precipitation, isotopic exchange) and transport properties of inorganic C-14 ($^{14}\text{CO}_3^{2-}$) and tritiated water (HTO) through non-carbonated and carbonated hardened cement pastes (HCP) for different water saturation (S_w) conditions.

The previous CEBAMA report (Rasamimanana et al., 2017) aimed at i) describing the preparation of the materials used (non-carbonated or carbonated HCP), ii) characterizing the carbonated samples, iii) developing a specific diffusion set-up using osmosis for imposing water suction (and thus water saturation S_w) in order to determine the diffusion parameters in partially saturated conditions. This technique has been validated with tritiated water (HTO) on both non-carbonated and carbonated samples.

The current report focusses on i) the determination of the effective diffusion coefficients of HTO at different degrees of water saturation, ii) the study of the diffusive behavior of C-14 on the same samples (after reaching the permanent state for HTO), iii) the investigation of the uptake and reversibility of C-14 on dispersed carbonated and non-carbonated HCP samples (batch experiments).

2 Materials and methods

2.1 Preparation of carbonated and non-carbonated samples

The experiments were carried out on a CEM V/A Rombas (Ciment Calcia, France) HCP prepared with a water/cement ratio of 0.43, cured for at least 6 months in wet conditions and stored in an artificial cement porewater (ACW) solution (pH = 13.5) (Macé et al., 2015). Carbonated samples were prepared in experimental conditions chosen to represent atmospheric carbonation condition (Auroy et al., 2015). An accelerated carbonation process was performed in an in-house specific device at $P_{CO_2} = 3\%$ vol. Relative humidity (RH) was kept at $55 \pm 1\%$ ($T = 20 \pm 1^\circ C$) by an oversaturated $Mg(NO_3)_2 \cdot 6H_2O$ solution in order to work at the maximal carbonation rate. In parallel, non-carbonated samples were dried until constant weight at $RH = 55 \pm 1\%$ and also at $RH = 81 \pm 2\%$ (KBr oversaturated solution) in order to check the effect of the drying conditions on samples.

2.2 Diffusion experiments in partially saturated conditions

2.2.1 Osmotic technique

The diffusion parameters of HTO and C-14 in partially saturated conditions have been investigated using a specific diffusion set-up in which the water suction is generated by an osmosis process between the water in the cement pore space and a highly concentrated solution of polyethylene glycol PEG (Savoye et al., 2010). The sample is separated from the PEG solution (PEG 6000 Sigma-Aldrich) by a semi-permeable membrane (Spectra-Por 3,500 Da, Spectrum laboratory) which is permeable to water molecules and all dissolved species but PEG. The exclusion of PEG from the sample pore water produces a chemical potential imbalance between the pore water and the external solution. This osmotic suction has the effect of keeping the sample partially saturated. A mass concentration of 0.95 kg of PEG/kg_{solution} has been chosen in order to reach a maximal suction potential of 9 MPa. Water saturation (S_w) of the HCP sample is determined by petrophysical measurements (see Rasamimanana et al., 2017 for details). Four experiments have been performed with non-carbonated and carbonated samples, in the following experimental conditions:

- Saturated ($S_w = 1$), [PEG] = 0
- Partially saturated ($S_w = 0.8$), [PEG] = 0.95 kg/kg_{solution}

2.2.2 HTO Through-Diffusion experiments

HCP disks inside diffusion cells were equilibrated for one week with a weighed volume of ACW (with or without PEG depending on experimental conditions). Then, tritiated water (HTO, Eckert & Ziegler) was added into the upstream reservoir (2.0 ± 0.1 kBq/g_{sol}). An aliquot of solution (1 mL) was periodically taken from the downstream reservoir and replaced by an equivalent volume of solution in order to maintain the total volume at its initial value. Radioassay are performed using a TriCarb 3170 TR-SL (Perking Elmer) liquid scintillation analyzer. Samples for radioassay are prepared by mixing 1 mL of aliquot to 4 mL of Ionic FluorTM (Perking Elmer) scintillation cocktail dedicated for alkaline sample.

The experimental data were modelled by applying the analytical solution of the second Fick's law (Crank, 1975; equation 4.24a):

$$\frac{\partial C}{\partial t} = \frac{D_e}{\alpha} \frac{\partial^2 C}{\partial x^2} = \frac{D_e}{\varepsilon_a + \rho R_d} \frac{\partial^2 C}{\partial x^2} \quad (I)$$

where C is the HTO volumetric activity (Bq/m³); t , the time (s); D_e , the effective diffusion coefficient (m²/s); ε_a , the diffusion accessible porosity; ρ , the bulk dry density (kg/m³); R_d , the sorption distribution ratio (m³/kg); and α , the apparent porosity. The initial and boundary conditions are: $C(x,t) = 0$, $t=0$; $C(x,t) = C_0$, $x = 0$, $t > 0$; $C(x,t) = 0$, $x = L$, $t > 0$ with L is the sample thickness.

The temporal evolution of the results is expressed in terms of i) the HTO normalized cumulative activity, which is the ratio of the total diffused HTO activity (Bq) to the volume activity in the upstream reservoir (Bq/m³) and ii) the normalized flux which is the ratio of the instantaneous flux (Bq/m²/s) to the volume activity of the upstream compartment (Bq/m³). The analysis of those data allowed the extraction of values for the effective diffusion coefficient, D_e (HTO) and the apparent porosity, α . The diffusion accessible porosity values, ε_a , are assumed to be equal to the water porosity measured from water porosimetry (data originated from the previous report, Rasamimanana et al., 2017).

Six through-diffusion experiments were performed with HTO in order to study:

- i. The effect of drying: samples were dried at different relative humidity values (RH = 100%, 81% and 55%) and fully resaturated ($S_w = 1$)
- ii. The effect of water saturation: samples were dried at RH 55% and partially ($S_w = 0.8$) or fully ($S_w = 1$) resaturated
- iii. The effect of carbonation: samples were dried at RH 55%, carbonated (P_{CO_2} 3%) and resaturated ($S_w = 1$ or 0.8)

These six experiments are summarized in Table 1 and Table 2. All experiments are carried out in duplicate at room temperature (20 ± 1 °C) in a glove box under Argon atmosphere to minimize any atmospheric carbonation.

Table 1: HTO through-diffusion experiments at $S_w = 1$: effect of drying stage.

	Drying	RH 100%	RH 81%	RH 55%
Water Saturation				
$S_w = 1$		Exp. #1	Exp. #2	Exp. #3

Table 2: HTO through-diffusion experiments: effect of water saturation and carbonation.

Carbonation Water Saturation	Non-carbonated	Carbonated
$S_w = 1$	Exp. #3	Exp. #5
$S_w = 0.8$	Exp. #4	Exp. #6

2.2.3 $^{14}\text{CO}_3^{2-}$ Diffusion experiments

After reaching the permanent state for HTO diffusion, C-14 diffusion was investigated on the same samples (experiments #1, #4, #5 and #6). An activity of C-14 ($\text{NaH}^{14}\text{CO}_3$, $2.0 \pm 0.1 \text{ kBq/g}_{\text{sol}}$) was added into the upstream reservoir. Up and downstream C-14 concentrations were monitored by following the same procedure as for HTO. Upstream C-14 concentration was kept constant and the total volume was maintained as its initial value for the downstream reservoir.

The temporal evolution of the results is expressed in term of i) C-14 upstream concentration (mol/L) and ii) the normalized diffusive concentration of C-14 in downstream reservoir which is the ratio of the diffused to the initial C-14 upstream concentration.

2.3 Uptake and reversibility experiments

C-14 batch experiments were performed either with carbonated and non-carbonated dispersed HCP samples. They were carried out at ambient temperature ($20 \pm 1^\circ\text{C}$) in polypropylene tubes with a solid to liquid ratio of 25 g/L (0.5 g of cement to 0.02 L of solution). Batch preparation and supernatant sampling were performed in an inert glove box under Argon in order to avoid atmospheric carbonation. Samples were pre-equilibrated in ACW pore water for one week. Then a spike of radiolabeled compound C-14 ($\text{NaH}^{14}\text{CO}_3$, Perkin Elmer) was added. Experiments were performed at trace level of C-14 (about $6 \cdot 10^{-8} \text{ M}$) which is lower than calcium carbonate solubility in ACW solution calculated with PhreeqC (around $1.6 \cdot 10^{-4} \text{ M}$). In consequence, precipitation of calcium carbonate is not expected. All experiments were carried out in duplicate samples. Blank batches were prepared for checking C-14 sorption on tubes walls. The kinetics of the reaction was investigated over 110 days by successive samplings. Before sampling, tubes were centrifuged at 4,000 rpm for 30 min. An aliquot of 100 μL was taken, weighted and analyzed by beta liquid scintillation counting. Samples for radioassay were prepared by mixing 1 mL of aliquot to 4 mL of Ionic Fluor scintillation cocktail.

After reaching a steady state, the supernatant was replaced by the same volume of ACW (free of C-14) to assess the reversibility of the reaction.

Experimental results are expressed with solid/solution distribution ratio (R_d , L/kg) and defined by Eq. 2 (sorption step) and Eq. 3 (desorption step):

$$R_d = \frac{C_{\text{sorbed}}}{C_{\text{aq}}} = \frac{C_0 - C_{\text{aq}}}{C_{\text{aq}}} \times \frac{V}{m} = \frac{A_0 - A_{\text{aq}}}{A_{\text{aq}}} \times \frac{V}{m} \quad (2)$$

$$R_{dd} = \frac{A_0 - A_{\text{aq}} - A_{\text{des}}}{A_{\text{des}}} \times \frac{V}{m} \quad (3)$$

where C_{sorbed} is the concentration of C-14 on solid (mol/kg), C_{aq} is the concentration of C-14 in the aqueous phase (mol/L), C_0 is the C-14 initial concentration (mol/L), V is the volume of the solution (L) and m is the mass of the cement paste (g).

3 Results and discussion

3.1 Through-Diffusion experiments with HTO

3.1.1 Effect of drying stage

Experiments #1 (RH 100%), #2 (RH 81%) and #3 (RH 55%) were performed to study the effect of the drying stage on through-diffusion of HTO in full saturated conditions ($S_w = 1$). The results are presented in Figure 1.

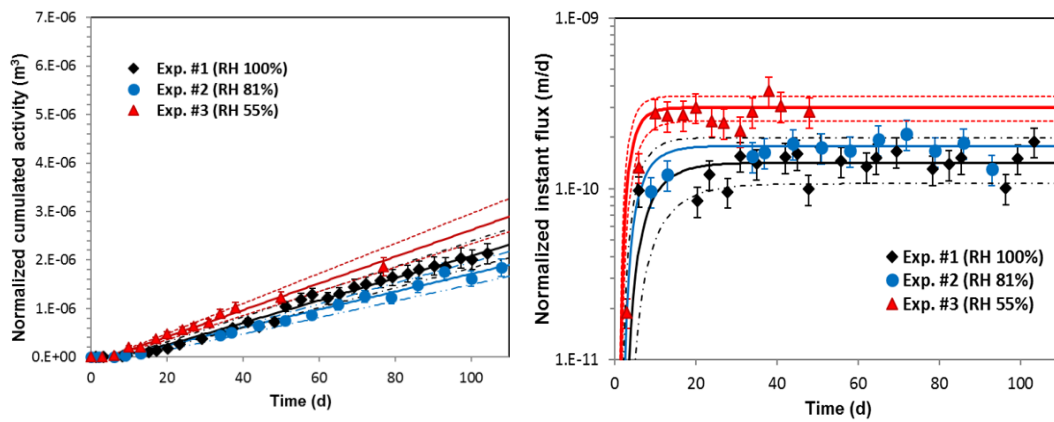


Figure 1: Normalized cumulative activity (left) and instant fluxes (right) for HTO through-diffusion in fully saturated conditions: Effect of drying stage (RH 100%, 81% and 55%). Solid curves represent the best fit of the experimental data.

The values of the effective diffusion coefficients, $D_e(\text{HTO})$, obtained from the best fit of the experimental points with the corresponding α values are presented in Table 3.

Table 3: α and $D_e(\text{HTO})$ values obtained for fully saturated samples dried at different relative humidity (RH).

$S_w = 1$	Experiment #1 (RH 100%)	Experiment #2 (RH 81%)	Experiment #3 (RH 55%)	Savoye et al. (2017) (RH 70%)
Porosity ϵ_a	0.33 ± 0.01	0.31 ± 0.01	0.33 ± 0.01	-
α	0.33 ± 0.01	0.36 ± 0.03	0.37 ± 0.03	-
$D_e(\text{HTO})$ (m^2/s)	$(3 \pm 1) \cdot 10^{-13}$	$(3.7 \pm 0.4) \cdot 10^{-13}$	$(6 \pm 1) \cdot 10^{-13}$	$(7.5 \pm 1.5) \cdot 10^{-13}$

Given the experimental uncertainties, the α value is similar to the water accessible porosity ϵ_a . This indicates that there is no significant retardation of HTO for all the conditions. No difference on $D_e(\text{HTO})$ is evidenced between the sample without drying (RH 100%) and those dried at RH 81%. On the other hand, at RH 55%, $D_e(\text{HTO})$ value increases by a factor of 2. This result is in agreement with Savoye et al.'s result obtained on the same cement (HCP CEM V Rombas) dried at RH 70% (Savoye et al., 2017). D_e is affected by the microstructure of the sample, which can be expressed in terms of tortuosity (τ) and constrictivity (δ) according to the Eq. 4.

$$D_e = \frac{\delta}{\tau^2} D_0 \varepsilon_a \quad (4)$$

With constant molecular diffusion coefficient in free water (D_0) and constant accessible porosity (ε_a), the increase of $D_e(\text{HTO})$ is assumed due to a probable modification of pore distribution which may occurred during the drying stage. X-ray tomography analyses are on-going to check the integrity of the microstructure and thermoporometry will be investigated to study the pore distribution of the HCP samples after drying/resaturation.

3.1.2 Effect of water saturation

The results of the HTO through-diffusion experiments for non-carbonated samples in partially saturated conditions ($S_w = 0.8$, Exp. #4) are presented in Figure 2. Exp. #4 have been carried out in triplicate. A statistical study (Fischer test of the equality of variances) has been performed to ensure that the data obtained can be averaged. Statistically, there is no significant difference between the triplicate samples (critical values $F = 0.4$ and $p\text{-value} = 0.5$ with significance level = 0.05). So, the average values of α and $D_e(\text{HTO})$ are presented in Table 4 and compared to the results of the Exp. #3 to discuss the effect of water saturation conditions.

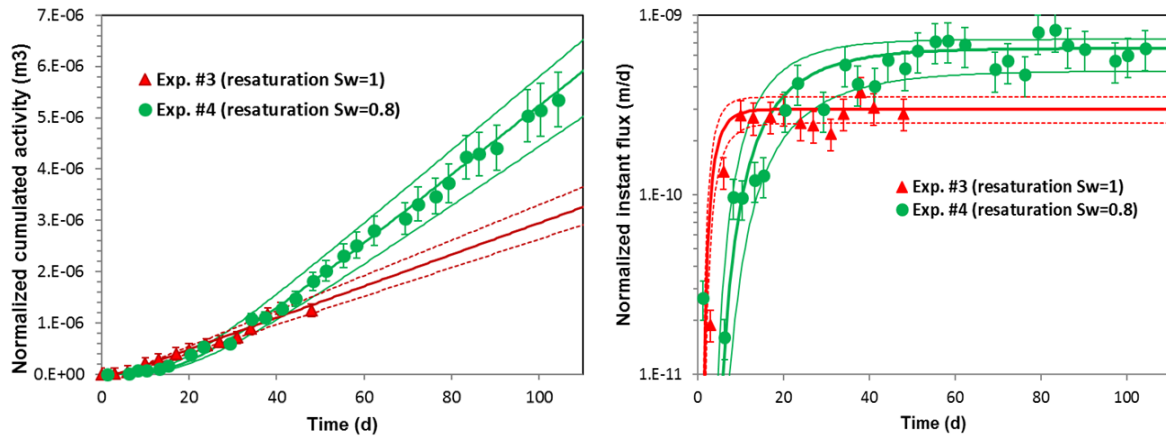


Figure 2: Normalized cumulated activity (left) and instant fluxes (right) for HTO through-diffusion in fully (Exp. #3) and partially (Exp. #4) saturated non-carbonated HCP samples. Solid curves represent the best fit of the experimental data.

Table 4: α and $D_e(\text{HTO})$ values obtained for non-carbonated samples at $S_w = 1$ and $S_w = 0.8$.

Non-carbonated samples	Experiment #3 $S_w = 1$	Experiment #4 $S_w = 0.8$
Porosity ε_a	0.33 ± 0.01	0.31 ± 0.01
α	0.37 ± 0.03	2 ± 1
$D_e(\text{HTO})$ (m^2/s)	$(6 \pm 1) \cdot 10^{-13}$	$(11 \pm 2) \cdot 10^{-13}$

At partially saturated conditions, a decrease of ε_a and D_e values is expected due to the draining of the largest pores. Results show a slight reduction of ε_a by about 6% but an increase of $D_e(\text{HTO})$ by a factor of 2, that characterizes the mobility of HTO in the HCP samples. The effect of partially resaturation of the samples by the osmotic process may be considered to explain our results. This step, like the drying stage, may affects the HCP microstructure leading to the increase of $D_e(\text{HTO})$ (Eq. 4). An increase of α by a factor of 5 is noted despite the increase of D_e value, HTO seems have an interaction with the HCP samples. This interaction is assumed due to

the creation of dead ends zone leading to a slight retardation of HTO ($R_d = 0.9 \pm 0.4$ L/kg). Interpretations are still on going for understanding these results. Characterization of the HCP microstructure will be investigated (tomography X, thermoporometry).

3.1.3 Effect of carbonation

The evolutions of the HTO through-diffusion experiments for carbonated samples in fully saturated conditions ($S_w = 1$, Exp. #5) are presented in Figure 3. The average values of α and $D_e(\text{HTO})$ are presented in Table 5 and compared to the results of the Exp. #3 to discuss the effect of carbonation at $S_w = 1$.

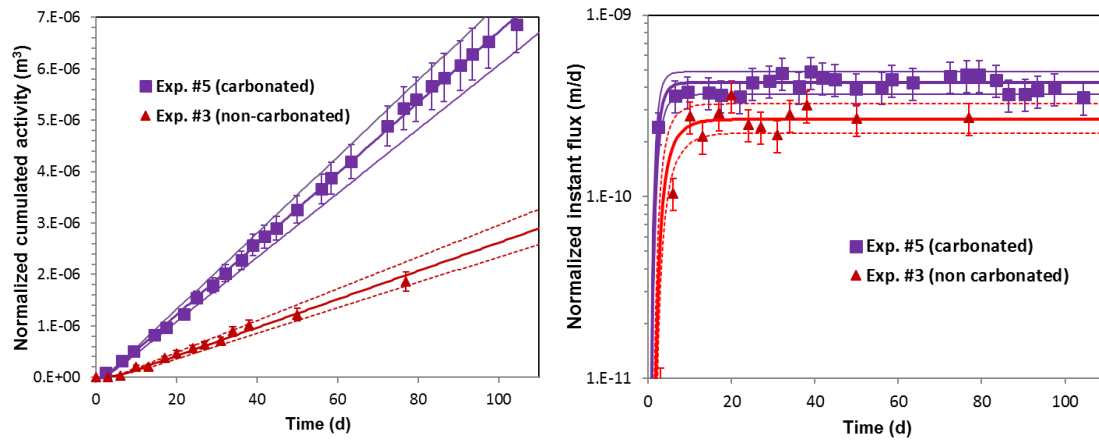


Figure 3: Normalized cumulative activity (left) and instant fluxes (right) for HTO through-diffusion in fully saturated non-carbonated (Exp. #3) and carbonated (Exp. #5) HCP samples. Solid curves represent the best fit of the experimental data.

Table 5: α and $D_e(\text{HTO})$ values obtained with non-carbonated and carbonated samples at $S_w = 1$.

$S_w = 1$	Experiment #3 Non-carbonated samples	Experiment #5 Carbonated samples
Porosity ϵ_a	0.33 ± 0.01	0.21 ± 0.01
α	0.37 ± 0.03	0.23 ± 0.03
$D_e(\text{HTO})$ (m²/s)	$(6 \pm 1) \cdot 10^{-13}$	$(12 \pm 2) \cdot 10^{-13}$

For carbonated samples, ϵ_a and α values decrease due to the precipitation of calcium carbonate (porosity clogging). An increase of $D_e(\text{HTO})$ by a factor of 2 after carbonation is observed despite the decrease of porosity. The same trend is reported by Auroy et al. (2015) on the study of the water permeability of carbonated CEM V paste. The authors highlighted a competition between the porosity clogging and microcracking due to decalcification of C-S-H during the carbonation process. It seems that the existence of microcracks creates preferential paths to HTO diffusion without changing the porosity leading to the increase of $D_e(\text{HTO})$. Characterization of the microstructure of the HCP samples (RMN ^{29}Si , X-ray tomography) will be done to verify this hypothesis.

The evolutions of the HTO through-diffusion experiments in carbonated samples at partially saturated conditions ($S_w = 0.8$, Exp. #6) are presented in Figure 4.

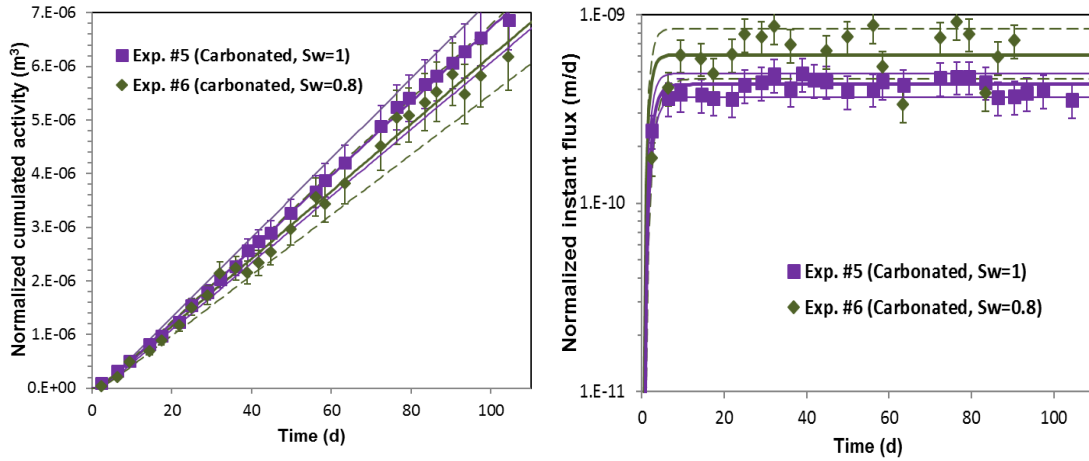


Figure 4: Normalized cumulative activity (left) and instant fluxes (right) for HTO through-diffusion in partially ($S_w = 0.8$) and fully ($S_w = 1$) saturated carbonated samples. Solid curves represent the best fit of the experimental data.

For carbonated partially saturated sample, the best fit of the experimental points give $\alpha = 0.20 \pm 0.02$ and $D_e(\text{HTO}) = (16 \pm 3) \cdot 10^{-13} \text{ m}^2/\text{s}$. $D_e(\text{HTO})$ are in the same range for the two conditions of saturation even if a tendency of high D_e value at high suction potential ($S_w = 0.8$) is indicated.

3.2 Diffusion experiments with $^{14}\text{CO}_3^{2-}$

After reaching the permanent state of HTO diffusion, the diffusive behaviour of C-14 is studied on the same samples (Exp. #1, #4, #5, #6). The results of the monitoring of the up and downstream C-14 concentrations are presented in Figure 5 and Figure 6 for non-carbonated and carbonated samples respectively.

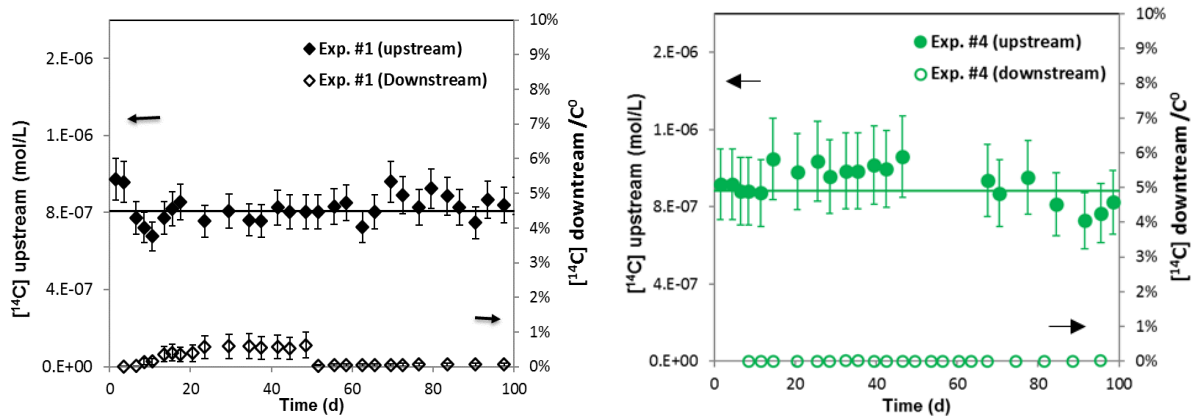


Figure 5: Up and downstream C-14 concentrations for non-carbonated samples in full (left) and partially (right) saturated conditions.

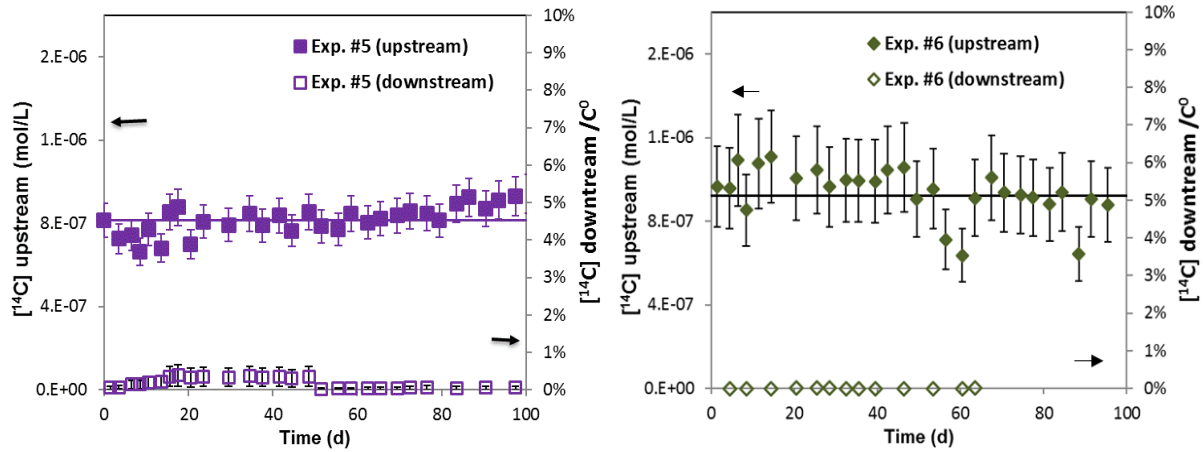


Figure 6: Up and downstream C-14 concentrations for carbonated samples in full (left) and partially (right) saturated conditions.

For all the conditions, upstream C-14 concentrations remain constant over time. The homogeneity of the experimental data has been checked with the Fisher test of the equality of variances. In parallel, no C-14 diffusive concentration is observed in the downstream reservoirs. These preliminary results will be supplemented by a solid analysis using quantitative autoradiography of β particle emission (Sardini et al., 2016) to describe the C-14 diffusion profiles into these HCP samples. Samples preparation are now ongoing (cutting, polishing).

3.3 Kinetics and irreversibility of C-14 on carbonated and non-carbonated samples

The data describing the sorption kinetics has been fitted by a first-order rate kinetic model (Lempinen and Lehto, 2016).

$$R_d(t) = \left[\frac{A_0}{(A_0 - A_{aq}) \exp(-kt) + A_{aq}} - 1 \right] \times \frac{V}{m} \quad (5)$$

In this equation k (d^{-1}) is the equilibrium rate constant of the uptake of C-14.

Results for carbonated and non-carbonated samples are presented in the Figure 7 and Figure 8.

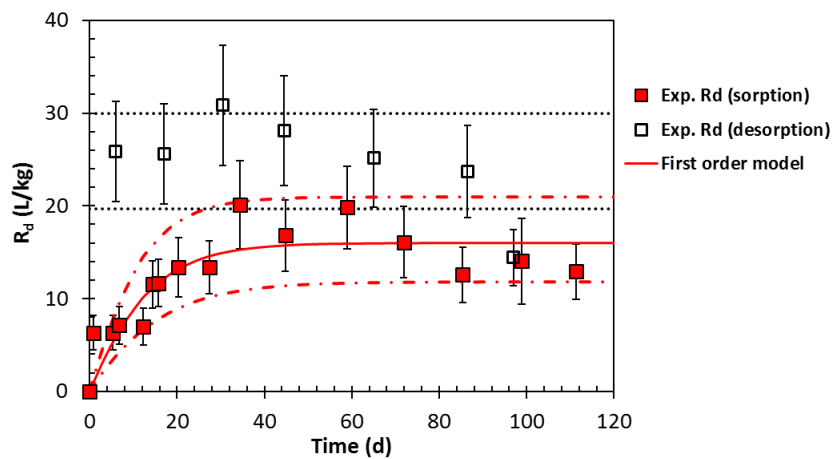


Figure 7: The evolution of the distribution ratio (R_d) for C-14 on carbonated HCP samples.

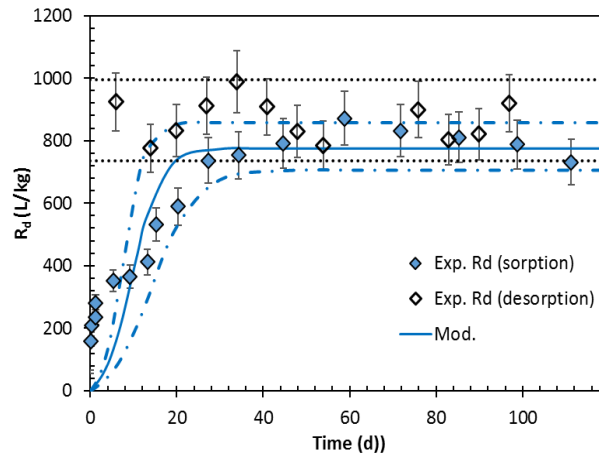


Figure 8: The evolution of the distribution ratio (R_d) C-14 for non-carbonated HCP samples.

The corresponding sorption and desorption parameters are listed in Table 6.

Table 6: Sorption/desorption parameters of C-14 for non-carbonated and carbonated HCP samples. [1] Wieland et al. (2014), [2] Pointeau et al. (2008).

	A_0 (Bq/g)	A_{aq} (Bq/g)	k (d ⁻¹) $T = 20 \pm 1^\circ\text{C}$	$R_{d \text{ mod.}}$ (L/kg)	$R_{d \text{ desorption}}$ (L/kg)	$R_{d \text{ literature}}$ (L/kg)
Carbonated	140 ± 15	110 ± 9	0.1 ± 0.02	16 ± 4	25 ± 5	$80 \pm 60^{[1]}$
Non-carbonated		7.6 ± 0.7	0.3 ± 0.1	775 ± 80	866 ± 130	$600 \pm 300^{[2]}$

The distribution ratio (R_d) increases during about 30 days and reaches a plateau thereafter. These results indicate that the uptake of C-14 on cement pastes is probably related to a complex mechanism rather than a simple surface sorption, which is known to be a more rapid process. Many studies demonstrated that sorption begins with a rapid initial step (few hours) and then proceeds with a slower step which is the isotope exchange (Tertre et al., 2010; Avramahov et al., 2013). This isotope exchange mechanism is expected to be operative in the case of carbonated samples which initially contains about 7.7% w/w of calcite (Rasamimanana et al., 2017). The fit of the experimental points give a rate constant of the isotope exchange, $k = 0.1 \pm 0.02 \text{ d}^{-1}$ ($T = 20 \pm 1^\circ\text{C}$). For non-carbonated samples which sorption to C-S-H or portlandite phases is expected, it is difficult to fit the experimental points by the single-constant kinetic model even if an uncertainty of 30% was imposed.

The R_d values at plateau are 40 times higher for non-carbonated samples ($775 \pm 80 \text{ L/kg}$) than for carbonated ones ($16 \pm 4 \text{ L/kg}$). This indicates that fewer surface sites available for the uptake of C-14 since all sites are likely to be saturated by carbonation. The R_d values are in the expected range compared to the literature (Pointeau et al., 2008, $R_d(\text{CEM I HCP, pH 13.2}) = 600 \pm 300 \text{ L/kg}$ and Wieland et al., 2014, $R_d(\text{carbonated CEM II HCP, pH 13.1}) = 80 \pm 60 \text{ L/kg}$). Given the experimental uncertainties, uptake on carbonated and non-carbonated samples seems to be reversible ($R_d \text{ sorption} = R_d \text{ desorption}$). Further experiments (isotherms with variation of concentrations and solid/liquid ratio) will be investigated to better understand the C-14 uptake mechanisms.

4 Conclusions and Future work

HTO diffusion parameters were investigated through non-carbonated and carbonated HCP samples for different water saturation conditions. Results showed that i) for a non-carbonated fully saturated sample (reference), $D_e(\text{HTO})$ value of $(3 \pm 1) \cdot 10^{-13} \text{ m}^2/\text{s}$ was obtained; ii) for the other conditions, $D_e(\text{HTO})$ increased by a factor of 2 for dried samples, by a factor of 4 for partially saturated non-carbonated samples and also for fully saturated carbonated samples and by a factor of 5 for partially saturated carbonated sample. This increase of $D_e(\text{HTO})$ is assumed due to a change in HCP microstructure which occurred during the drying stage (modification of pore distribution) or carbonation process (potential competition between porosity clogging and microcracking). It seems that the probable modification of pore distribution or the existence of microcracks create preferential paths to HTO diffusion without changing the total water accessible porosity. Results in partially saturated conditions are not yet completely understood as a decrease of $D_e(\text{HTO})$ is expected due to the draining of the largest pores.

C-14 diffusive behaviour was studied after reaching the permanent state of HTO through-diffusion. As we expected, upstream C-14 concentrations remain constant over time and no C-14 was observed in the downstream reservoirs. This indicates that the diffusion of C-14 is very low.

Uptake and reversibility of C-14 were investigated on dispersed HCP samples. For both carbonated and non-carbonated samples, results from kinetics experiments showed that a stationary state was reached after 30 days and uptake seemed to be reversible. Carbonated samples displayed a low uptake by isotopic exchange while non-carbonated samples displayed a medium uptake (sorption to C-S-H or portlandite surfaces).

The schedule for the next months will focus on:

- The characterization of the pore distribution of HCP samples after the drying/resaturation step by thermoporometry analyses.
- The study of the integrity of the microstructure of HCP samples by X-ray tomography analyses.
- The description of the C-14 diffusion profiles into HCP samples by quantitative β autoradiography analyses.
- The investigation of the C-14 sorption isotherms in order to model the C-14 uptake mechanisms.

Acknowledgement

The research leading to these results has received funding from the European Union's Horizon 2020 Research and Training Programme of the European Atomic Energy Community (EURATOM) (H2020-NFRP-2014/2015) under grant agreement n° 662147 (CEBAMA).

References

- Avrahamov, N., Sivan, O., Yechieli, Y., Lazar, B. (2015). Carbon isotope exchange during calcite interaction with brine: implications for ^{14}C dating of hypersaline groundwater. *Radiocarbon*, 55, 81-101.
- Auroy, M., Poyet, S., Le Bescop, P., Torrenti, J-M., Charpentier, T., Moskura, M., Bourbon, X. (2015). Impact of carbonation on unsaturated water transport properties of cement-based materials. *Cement and Concrete Research*, 74, 44-58.
- Bourbon, X. (2013). Référentiel des matériaux d'un stockage de déchets de haute activité et de moyenne activité à vie longue-tome 2 : les matériaux cimentaires. Rapport Andra, CG.RP. ASCM.12.0014, février 2013.

- Crank, J. (1975). The Mathematics of Diffusion. University, Second Editions, Clarendon press: London.
- Lempinen, J. and Lehto, J. (2016). Rate of radiocarbon retention onto calcite by isotope exchange. *Radiochimica Acta*, 104(9), 663-671.
- Macé, N., Nerfie, P., Coreau, N., Thory, E., Le Bescop, P., Touze, G. (2015). Préparation et caractérisations des PCH CEM V/A ROMBAS dans le cadre du GL CTEC. Report CEA, DPC/SECR/ST/2015/057 indice A.
- Pointeau, I., Coreau, N., Reiller, P.E. (2018). Uptake of anionic radionuclides onto degraded cement pastes and competing effect of organic ligands. *Radiochimica Acta*, 96(6), 367-374.
- Rasamimanana, S., Perrigaud, K., Ribet, S., Bessaguet, N., Grambow, G., Landesman, C. (2017). Radionuclide through-diffusion experiments in partially saturated carbonated and non-carbonated hardened cement paste using the osmotic technique (SUBATECH). *In*: M. Altmaier, V. Montoya, L. Duro, A. Valls (Eds.) Proceedings of the 2nd Annual Workshop of the CEBAMA Project. KIT Scientific Report, *in press*.
- Sardini, P., Angileri, A., Descostes, M., Duval, S., Oger, T., Patrier, P., Rividi, N., Siitari-Kauppi, M., Toubon, H., Donnard, J. (2016). Quantitative autoradiography of alpha particle emission in geo-materials using the BeaverTM system. *Nuclear Instruments and Methods in Physics Research A*, 833, 15-22.
- Savoye, S., Page, J., Puente, C., Imbert, C., Coelho, D. (2010). New experimental approach for studying diffusion through an intact and unsaturated medium: a case study with Callovo-Oxfordian argillite. *Environmental Sciences of Technology*, 44, 3608-3704.
- Savoye, S., Macé, N., Lefèvre, S., Rajyaguru, A., Spir, G., Robinet, J.-Ch. (2017). How mobile is tritiated water through unsaturated cement-based materials? Poster, Migration conference, September 10-15 2017, Barcelona Spain.
- Tertre, E. (2010). Methodology to obtain exchange properties of the calcite surface-application to major and trace elements: Ca(II), HCO₃⁻, and Zn(II). *Journal of Colloid and Interface Science*, 347(1), 120.
- Tits, J., Jakob, A., Wieland, E., Spieler, P. (2003). Diffusion of tritiated water and ²²Na⁺ through non-degraded hardened cement pastes. *Journal of contaminant Hydrology*, 61, 45-62.
- Wieland, E. (2014). Sorption data base for the cementitious near field of L/ILW and ILW repositories for provisional safety analyses for SGT-E2. PSI and Nagra Report, 14-08.

Behavior of radium and strontium in contact with cementitious materials relevant for LILW disposal in the Czech Republic

Barbora Drtinová^{1*}, Jana Kittnerová¹, Dušan Vopálka¹, Lucie Baborová¹

¹ Department of Nuclear Chemistry, Czech Technical University in Prague (CZ)

* Corresponding author: barbora.drtinova@fjfi.cvut.cz

Abstract

The uptake of the ^{223}Ra (used as an analogue of ^{226}Ra) and Sr with radiotracer ^{85}Sr by three cementitious materials, a hardened cement paste (HCP CEM II) and two types of concrete (Concrete CEM I and Concrete CEM III, both actually used in the storages of radioactive waste in the Czech Republic), was studied. The diffusion experiments were done also.

Sorption experiments with ^{223}Ra were carried out strictly in a carrier-free arrangement with the concentration of Ra approx. 10^{-12} mol/L, while those with Sr were done with the initial concentration of Sr $c_0 = 3.5 \cdot 10^{-4}$ mol/L labelled by ^{85}Sr or carrier-free. All cementitious materials used contain Sr, which had to be taken into account in evaluation of experiments. The experiments were conducted at temperatures of 22, 50, 65, and 80°C and the liquid-to-solid ratio V/m from 10 to 1,000 L/kg. The starting solution was Portlandite water (saturated $\text{Ca}(\text{OH})_2$). Sorption isotherms revealed that K_d values for Ra uptake were in the range of 70-580 L/kg, while K_d values for Sr were 10-130 L/kg. Through diffusion experiments over a 0.5 cm wide layer formed by pressing of crushed HCP CEM II were performed with Portlandite water and also with synthetic cement pore water CPW. Concentrations and forms of both elements studied on the input side of diffusion cells were same as those applied in batch studies. K_d values determined by evaluation of diffusion experiments were close to values obtained by evaluation of batch equilibrium experiments performed for lower values of liquid-to-solid ratios.

1 Introduction

The uptake and diffusion of radium and strontium were studied in presence of cementitious materials. These materials can occur in a deep underground repository of spent fuel planned in the Czech Republic. Ra and Sr behavior was characterized by the distribution coefficient between liquid and solid phases, K_d .

The isotope ^{223}Ra was obtained from an $^{227}\text{Ac}/^{223}\text{Ra}$ generator (Kozempel et al., 2015). It has a half-life of 11.43 days, decaying to ^{219}Rn with a half-life of 4 s, which does not interfere with the measurement of ^{223}Ra . The short half-life of generated radon enables to work more safely in comparison to the use of ^{226}Ra and ^{222}Rn .

In the case of strontium, the isotope ^{85}Sr was utilized either with ($c_0 = 3.5 \cdot 10^{-4}$ mol/L) or without a carrier.

Three blocks of highly humid hydrated raw cement were crushed and sieved for fraction ≤ 0.4 mm and then used for the experiments:

- **Hardened Cement Paste (HCP)** – cement CEM II/ A-S 42.5 R, hydrated for six months;
- **Concrete A** – cement CEM I 42.5 with fine and rough aggregates and fly ash, hydrated for one month, utilized in ÚJV Řež a.s. to stabilize the solidified waste container;
- **Concrete B** – cement CEM III B/32.5 with fine and rough aggregates, hydrated for one month, concrete used to fill chambers in intermediate radioactive waste repository Richard.

All these materials contain Sr. In the case of HCP the exchangeable amount of Sr was determined to be equal to 4.04 mmol/kg (Drtinová et al., 2016). The content of strontium in the leachates of cementitious materials in distilled water at the phase ratio 1:3 was determined as 0.24 mmol/kg for HCP. For concrete A, the Sr content is about 60% (0.14 mmol/kg) in comparison to HCP, and in concrete B about 30% (0.08 mmol/kg). If it is assumed that concentration ratios in the leachates are same as ratios of exchangeable amounts, an estimation of exchangeable amounts of Sr in concretes it can be obtained: Concrete A – 2.36 mmol/kg, Concrete B – 1.35 mmol/kg.

2 Sorption experiments with ²²³Ra and Sr

A comparison of the sorption properties of strontium and radium was performed. The ratios V/m ranged from 10 to 1,000 L/kg, the temperature was varied from 22 to 50 and 80°C. As liquid phase Portlandite water was used (saturated Ca(OH)₂). The moisture in cementitious materials studied was determined after 3 days drying at 105°C. The uptake of both isotopes reached equilibrium (for Sr also isotopic exchange) after less than 96 hours (Drtinová et al., 2016, 2017). Therefore, this time period was chosen for the duration of sorption experiments, by which the equilibrium value of distribution coefficient (K_d) was determined.

For the determination of K_d , based on the activity change corresponding to spikes used (⁸⁵Sr and ²²³Ra), the formula (1) was used:

$$K_d = \frac{A_{init} - A_{term}}{A_{term}} \frac{V}{m} \quad (1)$$

where A_{init} [Bq] is the initial activity of radiotracer in solution, A_{term} [Bq] the activity after the termination of the experiment, V [L] is the volume of the liquid phase, and m [kg] the mass of solid phase used in the experiment - corrected for the moisture content.

The results of K_d determination are collected in Table 1 to Table 3; the results for radium were presented formerly (Drtinová et al. 2016, 2017). The concentration of ²²³Ra was not controlled due to the carrier-free arrangement. Activities in the range of 400-1,500 Bq in 2 mL of solution were used, which is equivalent to initial concentration of ²²³Ra between $4.7 \cdot 10^{-13}$ and $1.8 \cdot 10^{-12}$ mol/L. Sr was added in form of SrCl₂ with an initial concentration of Sr $c_0 = 3.5 \cdot 10^{-4}$ mol/L. This is close to the strontium concentration determined in HCP CEM II leachate after one month of the leaching (V/m = 5 L/kg). The solutions were labelled by ⁸⁵Sr. Some experiments were carried out also carrier-free to approach the conditions of the sorption with the Ra.

The sorption on the walls of the experimental vial was also determined. For Ra, sorption on ampoule walls was equal to 7.8%, and for Sr it was 5.8% (in average, determined for each experimental arrangement).

Table 1: Distribution coefficients K_d (L/kg) for Ra and Sr in contact with cementitious materials in $\text{Ca}(\text{OH})_2$ saturated solution.

$\text{Ca}(\text{OH})_2, 22^\circ\text{C}$					
V/m (L/kg)	Material	Ra		Sr with carrier ($c_0 = 3.5 \cdot 10^{-4}$ mol/L)	
		Concrete A	Concrete B	Concrete A	Concrete B
10	K_d	131.0	95.9	9.0	46.2
	s	0.2	5.2	0.2	7.6
60	K_d	181.1	179.0	8.9	14.8
	s	0.9	7.6	0.2	0.5
100	K_d	225.8	224.0	11.0	14.5
	s	9.4	7.6	0.3	0.2
600	K_d	377.2	495.6	21.0	19.9
	s	11.1	51.1	3.0	1.0
1000	K_d	403.2	573.6	128.9	39.5
	s	25.1	24.1	12.5	0.2

The obtained distribution coefficients, K_d , were compared for three cementitious materials studied and different temperatures in dependence on the phase ratio. Average values of K_d (calculated from two parallel measurements) with estimated standard deviations s are given in Table 1 to Table 3.

A comparison of sorption behavior of Sr and Ra on both concretes is shown in Table 1. The K_d for Ra are higher than in the case of Sr by factor, mean value of which is 14 ± 2 with no difference between concretes A and B. For both spikes an increase of K_d was observed with increasing phase ratio V/m that can be explained by the decrease of concentration of competing cations in the working solution (Table 4). This effect we observed also for bentonite (e.g. Klika et al., 2007).

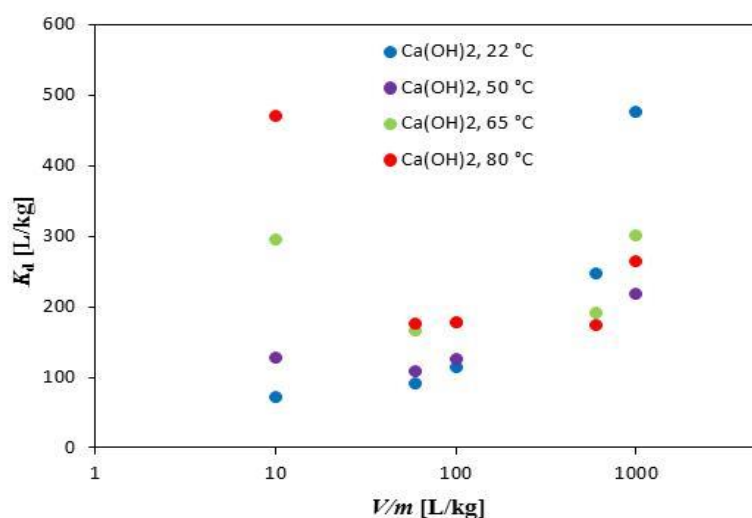
**Figure 1:** Dependence of determined K_d values describing Ra uptake on HCP on the phase ratio V/m in $\text{Ca}(\text{OH})_2$ at various temperatures.

Table 2: Distribution coefficients K_d (L/kg) for Ra in contact with HCP in solutions saturated with $\text{Ca}(\text{OH})_2$ for different temperatures.

		HCP, Ca(OH) ₂			
Temperature		22°C	50°C	65°C	80°C
V/m (L/kg)					
10	K _d	72.5	128.8	296.1	470.6
	s	4.5	8.1	9.0	3.0
60	K _d	91.0	108.2	165.7	176.0
	s	1.6	0.2	3.7	8.0
100	K _d	114.8	126.2	177.8	178.2
	s	6.4	0.6	9.6	0.4
600	K _d	246.8	×	190.6	174.0
	s	1.8	×	11.9	16.3
1000	K _d	477.6	218.6	301.7	265.7
	s	3.7	10.8	15.0	4.0

The influence of increasing temperature was convincingly recorded only for radium (Table 2). For the temperatures 22, 50, and 80°C it was already shown in our previous contribution (Drtinová et al., 2017). The presented values are corrected with respect to sorption on ampoule walls. To determine the interesting trend for the phase ratio $V/m = 10$ L/kg, dependence for a temperature of 65°C was also done (Figure 1). On the other hand, the effect of temperature on the strontium sorption is so small that it is not possible to distinguish it from the statistical fluctuation of experimental results (Table 3). The effect of temperature on Ra uptake is evident for smaller phase ratios. The high phase ratio (1,000 L/kg) shows no clear temperature effect for both elements. This effect can be caused by a very small mass of the solid phase.

Table 3: Distribution coefficients K_d (L/kg) for Sr in contact with HCP in $\text{Ca}(\text{OH})_2$ saturated solutions for different temperatures.

		HCP, Ca(OH) ₂					
		Sr with carrier (<i>c</i> ₀ = 3.5·10 ⁻⁴ mol/L)			Sr without carrier		
		Temperature	22°C	50°C	80°C	22°C	80°C
V/m (L/kg)							
10	K _d	12.9	16.1	18.1	14.0	19.3	
	s	0.3	0.2	0.4	0.2	0.4	
60	K _d	11.4	13.3	12.3	12.4	13.6	
	s	0.2	0.2	0.2	0.9	0.2	
100	K _d	11.4	14.6	13.0	12.8	13.9	
	s	0.4	0.5	0.5	0.3	0.2	
600	K _d	18.2	×	24.7	14.2	15.1	
	s	1.5	×	0.2	0.9	3.2	
1000	K _d	48.4	111.5	72.8	20.7	31.6	
	s	4.9	3.7	0.2	1.3	1.3	

The resulting distribution coefficients of strontium in contact with HCP are approaching the K_d values corresponding to Sr in contact with Concrete A and Concrete B, even with increasing temperature (Table 3, Figure 2). The resulting K_d values were not significantly affected by the presence or absence of the carrier. This observation can be pointed out as evidence that isotopic equilibrium (^{85}Sr – stable isotopes ^{87}Sr and ^{88}Sr) was maintained in experiments performed and that the uptake of Sr was not concentration dependent.

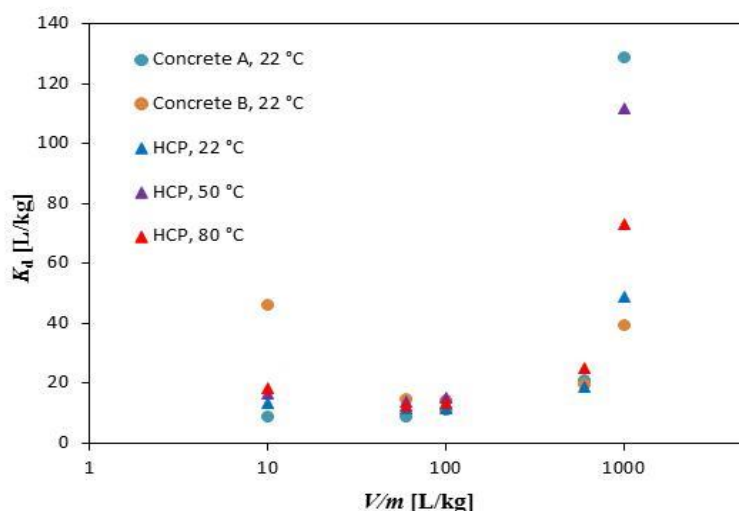


Figure 2: Dependence of determined K_d values describing Sr uptake on cementitious materials on the phase ratio V/m in $\text{Ca}(\text{OH})_2$ at various temperatures.

The distribution coefficients of Ra on cementitious materials in Portlandite water are considerably higher than that of Sr under conditions that differ only in concentrations of both elements. Obtained K_d values for Ra uptake ranged from 70 to 580 L/kg, whereas that for Sr were determined equal to 10-130 L/kg. In the range of V/m from 10 to 600 L/kg distribution coefficients for Sr slightly increase from 10 to 20 L/kg. The K_d for Ra are rising more steeply.

For both studied elements the effect of V/m values can be explained by the dependence of composition of equilibrated working solutions for different phase ratios: the greater portion of cementitious materials in the system produced higher ionic strength, which depressed the uptake of studied elements. From the comparison of the K, Na and Sr content in Portlandite water or RPCW and in the leachate from HCP at $V/m = 3$ L/kg, for example, a 10-fold increase in Na concentration and an increase in Sr and K concentration up to 3 orders were found in cement leachate. This increase was not observed in case of Ca, indicating that Ca is precipitated during leaching (Table 4).

Table 4: Concentration changes of selected cations in working solutions during leaching: solid phase - HCP, $V/m = 3$ L/kg, for 2 months in Portlandite water, and for 21 days in CPW.

	Concentration (mol/L)			
	Ca^{2+}	Sr^{2+}	Na^+	K^+
Portlandite water	$1.99 \cdot 10^{-2}$	$1.08 \cdot 10^{-6}$	$4.30 \cdot 10^{-4}$	$3.47 \cdot 10^{-5}$
Portlandite water with HCP	$8.08 \cdot 10^{-3}$	$2.58 \cdot 10^{-4}$	$8.73 \cdot 10^{-3}$	$3.78 \cdot 10^{-2}$
CPW	$1.04 \cdot 10^{-2}$	$8.42 \cdot 10^{-7}$	$6.85 \cdot 10^{-4}$	$5.20 \cdot 10^{-4}$
CPW with HCP	$6.12 \cdot 10^{-3}$	$1.81 \cdot 10^{-4}$	$7.71 \cdot 10^{-3}$	$2.89 \cdot 10^{-2}$

Orderly similar results of sorption experiments were achieved in several works. In a study of Tits et al. (2006), the distribution coefficients of ^{226}Ra (with initial concentration about 10^{-8} mol/L) reached values about 140-400 L/kg on HCP (type CEM I). This type of cement is contained in our Concrete A sample. The results of study made by Bayliss et al. (1989) with sulphate resisting Portland cement (SRPC) and ordinary Portland cement blended with blast furnace slag (OPC:BFC) are K_d of Ra (concentration about 10^{-8} - 10^{-11} mol/L) in the range of 50-500 L/kg for SRPC and 850-1,800 L/kg for OPC:BFS.

In the comparison, K_d for strontium on HCP of type CEM II (slightly different material than HCP used in this work) was determined within the range 12-22 L/kg in our previous research (Drtinová et al., 2016). In the study of Li and Pang (2014), which compares various Sr sorption studies with cementitious materials, K_d achieved maximum values of 100 L/kg. In our case these values are slightly exceeded only for the phase ratio V/m 1,000 L/kg.

3 Diffusion experiments with ^{223}Ra and Sr

In order to compare the behavior of Sr and Ra, a set of diffusion experiments was carried out in Portlandite water or synthetic cement water CPW through the HCP layer, which was obtained by pressing a crushed hydrated cement paste. This approach allows simple cutting of the compacted cement layer after the experiment has terminated. Acquired activity was then measured in the obtained material slices. The method was also used for other materials, e.g. bentonite (Baborová et al., 2016). The composition of CPW represents a deeper groundwater circulating in the fissures of the crystalline rocks of the Bohemian Massif, in equilibrium with $\text{Ca}(\text{OH})_2$ (Drtinová et al., 2017).

The plug of compacted crushed HCP had a diffusion length of 0.5 cm and was saturated with the selected solution prior to the addition of the migrating element. The volume of the inlet and outlet reservoirs was 50 mL. The initial concentrations of both radionuclides were the same as for sorption experiments. Strontium was used only with a carrier ($c_0 = 3.5 \cdot 10^{-4}$ mol/L). The duration of the experiment was 3 weeks.

The behavior of both elements confirmed the assumption that the diffusion of radium throughout the cell will be slower than that of Sr. The decrease in Ra concentration in the inlet reservoir was steeper (on average 44% for both solutions used after 21 days) in comparison with Sr (31% reduction in concentration). In the outlet reservoir, Sr was after 20 days at 5% of the initial concentration. Breakthrough of Ra did not occur during the experimental time and the experiment could not be continued longer due to the short half-life of the ^{223}Ra isotope.

On the basis of the previously determined distribution coefficients, which are much higher for the radium, the observed capture in the first layer of cement material was more than 5 times higher for radium than for strontium (Figure 3).

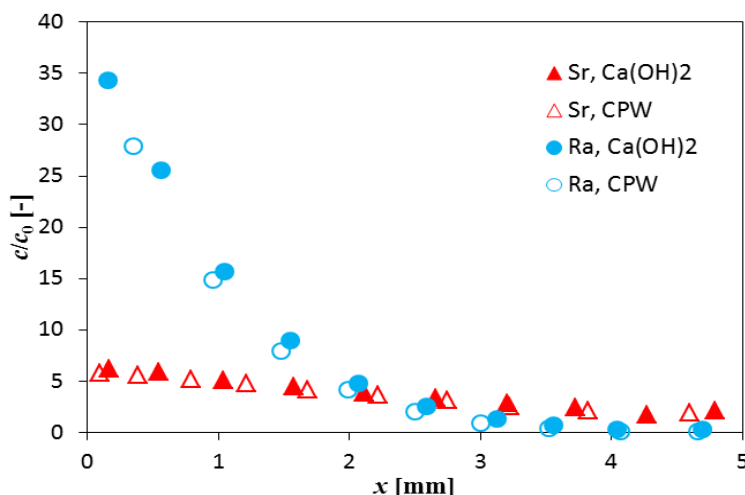


Figure 3: Concentration profile of the sorbed element in HCP in the environment of Portlandite water ($\text{Ca}(\text{OH})_2$) or synthetic cement water (CPW).

The evaluation of diffusion experiments is discussed in detail in Vopálka et al. (2018). The determined K_d values were about 9 L/kg for Sr, independently of the liquid phase used, 150 L/kg for Ra in the Portlandite water, and 100 L/kg for Ra in CPW.

4 Conclusions and Future work

Sorption experiments under various conditions showed significantly higher sorption of Ra on cementitious material than in the case of Sr. Diffusion experiments confirmed values obtained in sorption experiments. Acquired results are in good agreement with literature. However, the concentrations of the two monitored elements were significantly different in this study.

The influence of increasing temperature in the systems containing cementitious materials in contact with Portlandite water for the phase ratio V/m from 10 to 1,000 L/kg was convincingly recorded only for radium, where higher temperature provides higher K_d values in general. In the experiments using strontium, no apparent effect of the use of a carrier on distribution coefficients was observed, that can be explained by the linearity of the sorption isotherm. As for strontium, there is almost no difference between sorption on HCP, Concrete A, and Concrete B, with the exception of the phase ratio $V/m = 1,000$ L/kg. In general, this phase ratio shows ambiguous values in several experiments; this effect can be caused by large errors due to the use of a very small amount of the solid phase.

Behavior of radium and strontium in contact with cementitious materials will be further studied. A more detailed study of changes in the concentrations of the most important components in working solutions during the interaction experiments will be included, with the aim of creating a formal sorption model of Ra, eventually also Sr, on cementitious materials.

Acknowledgement

The research leading to these results has received funding from the European Union's Horizon 2020 Research and Training Programme of the European Atomic Energy Community (EURATOM) (H2020-NFRP-2014/2015)

under grant agreement n° 662147 (CEBAMA). This contribution is a partially result of Radioactive Waste Repository Authority project “Research support for Safety Evaluation of Deep Geological Repository”.

References

- Baborová, L., Vopálka, D., Vetešník, A., Hofmanová, E. (2016). Migration behaviour of strontium in Czech bentonite clay. *Journal of Sustainable Development of Energy, Water and Environment Systems*, 4(3), 293-306.
- Bayliss, S., Ewart, F.T., Howse, R.M., Lane, S.A., Pilkington, N.J., Smith-Briggs, J.L., Williams, S.J. (1989). The solubility and sorption of radium and tin in a cementitious near-field environment. *Materials Research Society Symposia Proceedings*, 127, 879-885.
- Drtinová, B., Kittnerová, J., Vopálka, D. (2016). Characterization of hydrated cement paste (CEM II) by selected instrumental methods and a study of ⁸⁵Sr uptake. *In: M. Altmaier, V. Montoya, L. Duro, A. Valls (Eds.) Proceedings of the 1st Annual Workshop of the CEBAMA Project. KIT Scientific Report, 7734.*
- Drtinová, B., Kittnerová, J., Vopálka, D. (2017). Study of radium uptake by cementitious materials relevant for LILW disposal in the Czech Republic. *In: M. Altmaier, V. Montoya, L. Duro, A. Valls (Eds.) Proceedings of the 2nd Annual Workshop of the CEBAMA Project. KIT Scientific Report, in press.*
- Kozempel, J., Vlk, M., Málková, E., Bajžíková, A., Bárta, J., Santos-Oliveira, R., Malta Rossi, A. (2015). Prospective carriers of ²²³Ra for targeted alpha particle therapy. *Journal of Radioanalytical and Nuclear Chemistry*, 304, 443-447.
- Klika, Z., Kraus, L., Vopalka, D. (2007). Cesium uptake from aqueous solutions by bentonite: A comparison of multicomponent sorption with ion-exchange models. *Langmuir*, 23, 1227-1233.
- Li, K. and Pang, X. (2014). Sorption of radionuclides by cement-based barrier materials. *Cement and Concrete Research*, 65, 52-57.
- Tits, J., Iijima, K., Wieland, E., Kamei, G. (2006). The uptake of radium by calcium silicate hydrates and hardened cement paste. *Radiochimica Acta*, 94, 637-643.
- Vopálka, D., Rosendorf, T., Baborová, L., Kittnerová, J. (2018). Modelling and interpretation of diffusion experiments of selected radionuclides through cementitious samples. *In: M. Altmaier, V. Montoya, L. Duro, A. Valls (Eds.) Proceedings of the 3rd Annual Workshop of the CEBAMA Project. This document.*

Effect of redox conditions on sulfur, selenium and iodine binding in AFm phases

Latina Nedyalkova^{1,2*}, Barbara Lothenbach¹, Jan Tits², Erich Wieland², Urs Mäder³

¹ Empa (CH)

² PSI (CH)

³ University of Bern (CH)

* Corresponding author: latina.nedyalkova@psi.ch

Abstract

Selenium-79 and iodine-129 emanating from low and intermediate level radioactive waste (L/ILW) repositories are important dose-determining radionuclides. Under the alkaline ($10 < \text{pH} < 13.5$) and reducing conditions expected in cement-based L/ILW repositories the thermodynamically predominant aqueous species are SeO_3^{2-} , HSe^- , Se_x^{2-} (with $x = 2, 3, 4$) and I^- , respectively. All these anions could potentially exchange for the common interlayer anions in the structure of the AFm phases. Additionally, sulfur anionic species (SO_4^{2-} , SO_3^{2-} , $\text{S}_2\text{O}_3^{2-}$, HS^-) may be present as competitive anions for the available ion exchange sites. To study the Se uptake mechanism in AFm phases as well as the effect of the competition with S, an attempt was made to synthesize pure $(\text{HS}^-)_2\text{-AFm}$ and $(\text{HSe}^-)_2\text{-AFm}$ phases. Furthermore, the ability of Se and I to form binary solid solutions of the type $(\text{SeO}_3^{2-}\text{-X}^n)\text{-AFm}$ and $(\text{I-X}^n)\text{-AFm}$ (with $\text{X}^n = \text{SO}_4^{2-}$, SO_3^{2-} , $\text{S}_2\text{O}_3^{2-}$, CO_3^{2-} , OH^- , OH-CO_3^{2-}) was examined.

XRD analyses of the synthesized $(\text{HS}^-)_2\text{-AFm}$ and $(\text{HSe}^-)_2\text{-AFm}$ phases revealed an AFm-like (rhombohedral) structure with d-spacing of 8.46 Å and 8.27 Å, respectively. For the $(\text{HS}^-)_2\text{-AFm}$ a solubility product, $\log K_s^0 = -28$ at 23°C was determined. Partial oxidation of HSe^- in the liquid phase hindered the accurate determination of the $(\text{HSe}^-)_2\text{-AFm}$ solubility. Solid solution formation in AFm phases was observed for the pairs $\text{SeO}_3\text{-SO}_4$, $\text{I}_2\text{-CO}_3$, $\text{I}_2\text{-OH_CO}_3$ and $\text{I}_2\text{-OH}$. A continuous solid solution was found between the rhombohedral $\text{SeO}_3\text{-AFm}$ and $\text{SO}_4\text{-AFm}$ end members where a progressing exchange of the smaller SeO_3^{2-} anion by the larger SO_4^{2-} anion results in a gradual peak shift of the basal reflexion towards higher d-values. Continuous solid solutions were also found between the pairs $\text{I}_2\text{-OH_CO}_3$ and $\text{I}_2\text{-OH}$ visible by a continuous peak shift from one end member to the other. The $\text{I}_2\text{-AFm}$ and $\text{CO}_3\text{-AFm}$, on the other hand, form only a limited solid solution. In this case, a miscibility gap with the composition $0.5 \leq \text{CO}_3/(2\text{I}+\text{CO}_3)$ is observed, indicated by the presence of two coexisting phases – an $\text{I}_2\text{-CO}_3\text{-AFm}$ mixed phase and a $\text{CO}_3\text{-AFm}$.

The experimental data suggests that $(\text{HS}^-)_2\text{-AFm}$ and $(\text{HSe}^-)_2\text{-AFm}$ phases could be potentially stable under the reducing and alkaline conditions expected in a cement-based L/ILW repository after closure. The formation of AFm solid solutions with Se and I anionic species seems to be controlled by the crystal symmetry, the size of the interlayer anion and the hydration state of the phase.

1 Introduction

A potential retardation mechanism for dose-relevant selenium-79 and iodine-129 emanating from low and intermediate level radioactive waste (L/ILW) repositories is their uptake by AFm phases. AFm phases are layered

double hydroxides (LHD) which form during the hydration of cement. Their lamellar structure consists of a positively charged main layer, $[\text{Ca}_4(\text{Al,Fe})_2(\text{OH})_{12}]^+$, and a negatively charged interlayer, $[\text{X} \cdot n\text{H}_2\text{O}]^{2-}$, where X stands either for two monovalent anions or for a bivalent anion. Common anions found in the interlayer are OH^- , SO_4^{2-} , Cl^- and CO_3^{2-} (Taylor, 1997).

Under the alkaline ($10 < \text{pH} < 13.5$) and reducing ($-700 \text{ mV} < E_h < -230 \text{ mV}$ (SHE); Wersin et al., 2003) conditions expected in cement-based L/ILW repositories, the aqueous speciation of Se is dominated by SeO_3^{2-} , HSe^- and Se_x^{2-} (with $x = 2, 3, 4$) (Olin et al., 2005). The thermodynamically stable aqueous species of I is iodide (I^-). The Se and I anions have the potential to exchange for the common interlayer anions (OH^- , SO_4^{2-} , Cl^- , CO_3^{2-}) in the structure of the AFm phases. At the same time, they may face the competition of reduced S anionic species (SO_3^{2-} , $\text{S}_2\text{O}_3^{2-}$, HS^-) also present in the cementitious matrix for the available ion exchange sites.

The potential of the AFm phases to incorporate the various Se, S and I anions in their structure has been the subject of several studies before (e.g. Baur and Johnson, 2003; Bonhoure et al., 2006; Mace et al., 2007 for Se; Motzet and Pöllmann, 1999 for S; Aimoz et al., 2012a for I) but only few are dealing with the strongly reduced HSe^- (Rojo et al., 2018) and HS^- (Le Cornec et al., 2017) anions. This is mainly due to the experimental difficulties related to the stabilization of the S(-II) and Se(-II) oxidation state. Apart from the precipitation of stable mono-Se and mono-I AFm phases, the formation of AFm solid solutions has also been reported (e.g. $(\text{I}_2\text{-SO}_4)\text{-AFm}$ solid solution, Aimoz et al., 2012b). Solid solutions can thermodynamically stabilize mixed compositions with respect to other mineral phase assemblages and may play an important role in the immobilization of Se and I.

The aim of this study is to further investigate the incorporation of selenium, sulfur and iodine in AFm phases and to work towards the construction of a thermodynamic model able to predict their uptake. In a first phase of this project pure AFm end members with the more oxidized Se and S anionic species ($\text{SeO}_3\text{-AFm}$, $\text{SeO}_4\text{-AFm}$, $\text{SO}_4\text{-AFm}$, $\text{SO}_3\text{-AFm}$, $\text{S}_2\text{O}_3\text{-AFm}$) were synthesized and characterized. Crystal structure analysis of the samples revealed AFm phases with rhombohedral ($\text{SeO}_3\text{-}$, $\text{SO}_4\text{-}$, $\text{SO}_3\text{-AFm}$) or monoclinic ($\text{SeO}_4\text{-}$, $\text{S}_2\text{O}_3\text{-AFm}$) symmetry. The phases with rhombohedral structure share an identical position of the main layer reflection (hkl 110) but show differences in the interlayer distances (hkl 003 and 006) as a function of the size of the interlayer anions and/or the number of water molecules present in the interlayer.

Building on these results, in a second phase, several types of solid solution series with $\text{SeO}_3^{2-}\text{-X}^{n-}$ and I-X^{n-} (with $\text{X}^{n-} = \text{SO}_4^{2-}$, SO_3^{2-} , $\text{S}_2\text{O}_3^{2-}$, CO_3^{2-} , OH^- , OH-CO_3^{2-}) as the intercalating anions were examined. A further goal was to develop an experimental procedure for the synthesis and the characterization of AFm phases containing reduced Se and S. Pure $(\text{HS}^-)_2\text{-AFm}$ and $(\text{HSe}^-)_2\text{-AFm}$ phases were synthesized and characterized by XRD and aqueous phase analyses.

2 Materials and methods

2.1 Synthesis and characterization of solid solution series

The solid solution series were synthesized by mixing stoichiometric amounts of C_3A , CaO and an appropriate amount of $\text{Na}_2\text{-X}$ ($\text{pH} \sim 13$) or Ca-X ($\text{pH} < 13$) salt to obtain different total selenite/iodide mole fractions ($x_{\text{SeO}_3} = \text{SeO}_3^{2-}/(\text{SeO}_3^{2-} + \text{X}^{n-}) = 0, 0.1, 0.3, 0.5, 0.7, 0.9, 1$). The samples were aged for 3 months in closed PE-bottles at 20°C on a rotary shaker. After the equilibration time, the solids were separated from the liquid phase by vacuum filtration through a 0.45μ nylon filter and dried over a saturated NaOH solution ($\text{RH} \sim 8\%$) for several weeks. Sample preparation and filtration were performed in a N_2 filled glove box to minimize atmospheric CO_2 contamination.

X-ray powder diffraction patterns were obtained on a PANalytical X'Pert Pro MPD diffractometer using CuK α radiation; the diffraction patterns were recorded between 5-70° (2 θ) with a step size of 0.017° (2 θ) and a counting time of 0.6 s per step. Attenuated total reflectance infrared spectra were recorded in the 4,000 to 600 cm⁻¹ range on a Bruker Tensor 27 FTIR spectrometer.

2.2 Synthesis and characterization of the (HS⁻)₂- and the (HSe⁻)₂-AFm phases

The (HS⁻)₂-AFm phase was synthesized by mixing stoichiometric amounts of C₃A, CaO and Na₂S·9H₂O in 0.1 M NaOH (pH = 13). The sample was aged for 1 month in a glovebox under N₂ atmosphere (O₂ partial pressure < 0.1 ppm). To confirm that no sulphide oxidation occurs in these conditions, in a parallel experiment, a sulphide solution was monitored with a Mettler Toledo ion-selective perfectION Ag/S₂ Combination Electrode over a period of 3 months. The AFm-suspension was centrifuged and the obtained solid was dried over a saturated NaOH solution (RH ~8%) for several weeks.

The (HSe⁻)₂-AFm phase was synthesized by mixing stoichiometric amounts of C₃A, CaO and Na₂Se·9H₂O in 0.1 M NaOH (pH = 13). The Na₂Se·9H₂O salt was obtained by electrochemical reduction of Se(IV) solution (0.4 M Na₂SeO₃ in 4 M NaOH), following the procedure of Landesman et al. (2012). The precipitate was filtered, washed with ethanol and dried under N₂ atmosphere over a saturated NaOH solution (RH ~8%) in a glovebox. UV-Vis spectra recorded during the preparation showed the complete reduction of Se(IV) to Se(-II) and XRD analyses of the precipitated salt confirmed the formation of Na₂Se·9H₂O. To avoid re-oxidation of Se(-II) during the synthesis of the (HSe⁻)₂-AFm, the experiment was carried out in the electrochemical cell with a constant redox potential of -0.7 V (SHE) for the whole period of equilibration (1 month).

The (HS⁻)₂-AFm and (HSe⁻)₂-AFm powder X-ray diffraction measurements were carried out on a BRUKER AXS D8 ADVANCE Bragg-Brentano diffractometer with CuK α radiation. An airtight holder was used to prevent oxidation during the measurement.

3 Results and discussion

3.1 Synthesis and characterization of solid solution series

The formation of binary AFm solid solutions between the pairs SeO₃²⁻-Xⁿ⁻ and I-Xⁿ⁻ (with Xⁿ⁻ = SO₄²⁻, SO₃²⁻, S₂O₃²⁻, CO₃²⁻, OH⁻, OH⁻CO₃²⁻) as the intercalating anions was examined.

3.1.1 XRD

On a series of XRD diagrams, a continuous solid solution can be identified by a gradual peak shift of the basal reflexion from one end member to the other. This is the case with the pair SeO₃-SO₄ at pH ~ 13, where a progressing exchange of the smaller SeO₃²⁻ anion (2.39 Å) for the larger SO₄²⁻ anion (2.58 Å) (Jenkins and Thakur, 1979) results in a gradual peak shift of the basal reflexion towards higher d-values (Figure 1). Both AFm phases, SeO₃-AFm and SO₄-AFm have a rhombohedral structure which favours anion exchange in the interlayer. At pH < 13, no solid solution is formed in mixtures with varying SeO₃-SO₄ mol fractions, and the synthesized solid consists of a mixture of the end members - SeO₃-AFm and SO₄-AFm. The reason for this seems to be the different hydration state of the SeO₃-AFm (no clear peak at ~21° 2 θ) at pH < 13. An AFm phase can exist in several hydration states depending on the relative humidity and exposure temperature; each hydrate is characterized by a specific interlayer distance caused by the different number of water molecules in the interlayer (Baquerizo et al., 2015). For the SO₄-AFm, for instance, the hydrates Ms9, Ms10.5, Ms12 and Ms14 (with the index number giving

the water content of the phase in moles) are known. Slight changes in the relative humidity during drying of the samples could have led to the different hydration state of the SeO_3 -AFm. To verify these results, the series is being repeated and the new samples are still to be analysed.

Solid solution formation was also observed between the pairs I_2 -OH and I_2 -OH- CO_3 both, at pH ~ 13 and pH < 13 , as OH-AFm and hemicarbonates (OH- CO_3 -AFm) have a rhombohedral structure. The increasing substitution of the larger I^- anion (2.10 Å) by the smaller OH^- anion (1.33 Å) is reflected by a gradual decrease of the interlayer distance from 8.83 Å in the I_2 -AFm phase down to 8.44 Å at a total iodide fraction of 0.1 ($x_{\text{I}_2} = 0.1$) (Figure 2). At this composition two phases exist – a mixed I_2 -OH-phase and a OH-AFm with $d = 7.92$ Å indicating the presence of a miscibility gap at very low I^- contents. Similar evolution of the interlayer distance was found in the I_2 -OH- CO_3 pair where the d value decreases to 8.20 Å moving towards the OH- CO_3 -AFm end member. In this case, the solid solution is complete as no miscibility gap is observed.

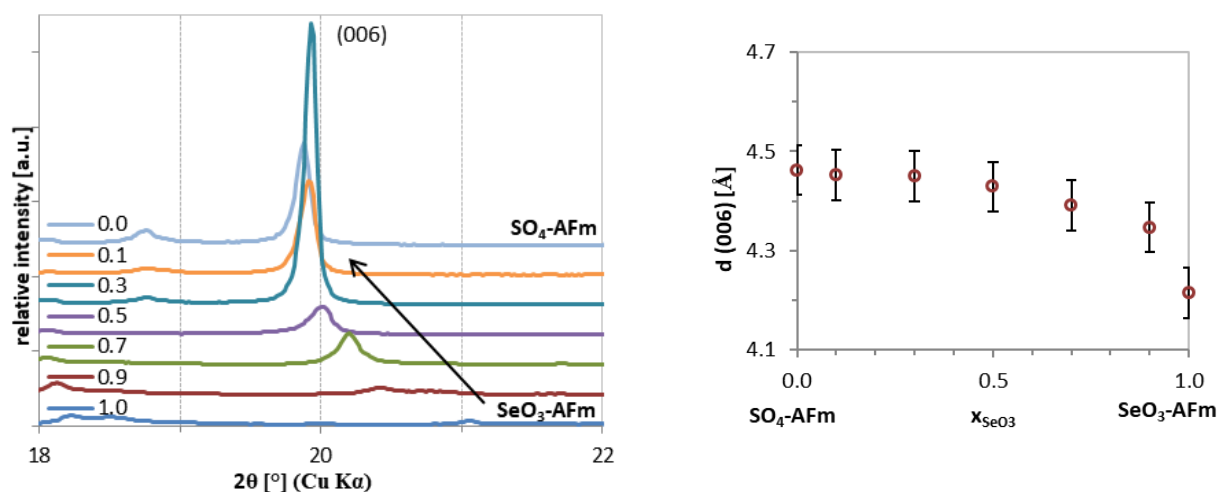


Figure 1: Evolution of the (hkl 006) reflexion (left) and the interlayer distance (right) in the $(\text{SeO}_3\text{-SO}_4)\text{-AFm}$ solid solution series (pH ~ 13) after 3 months equilibration time and drying over a saturated NaOH solution. The numbers 0.0, 0.1, 0.3, 0.5, 0.7, 0.9 and 1.0 indicate the mole fraction of the SeO_3 -end member (x_{SeO_3}).

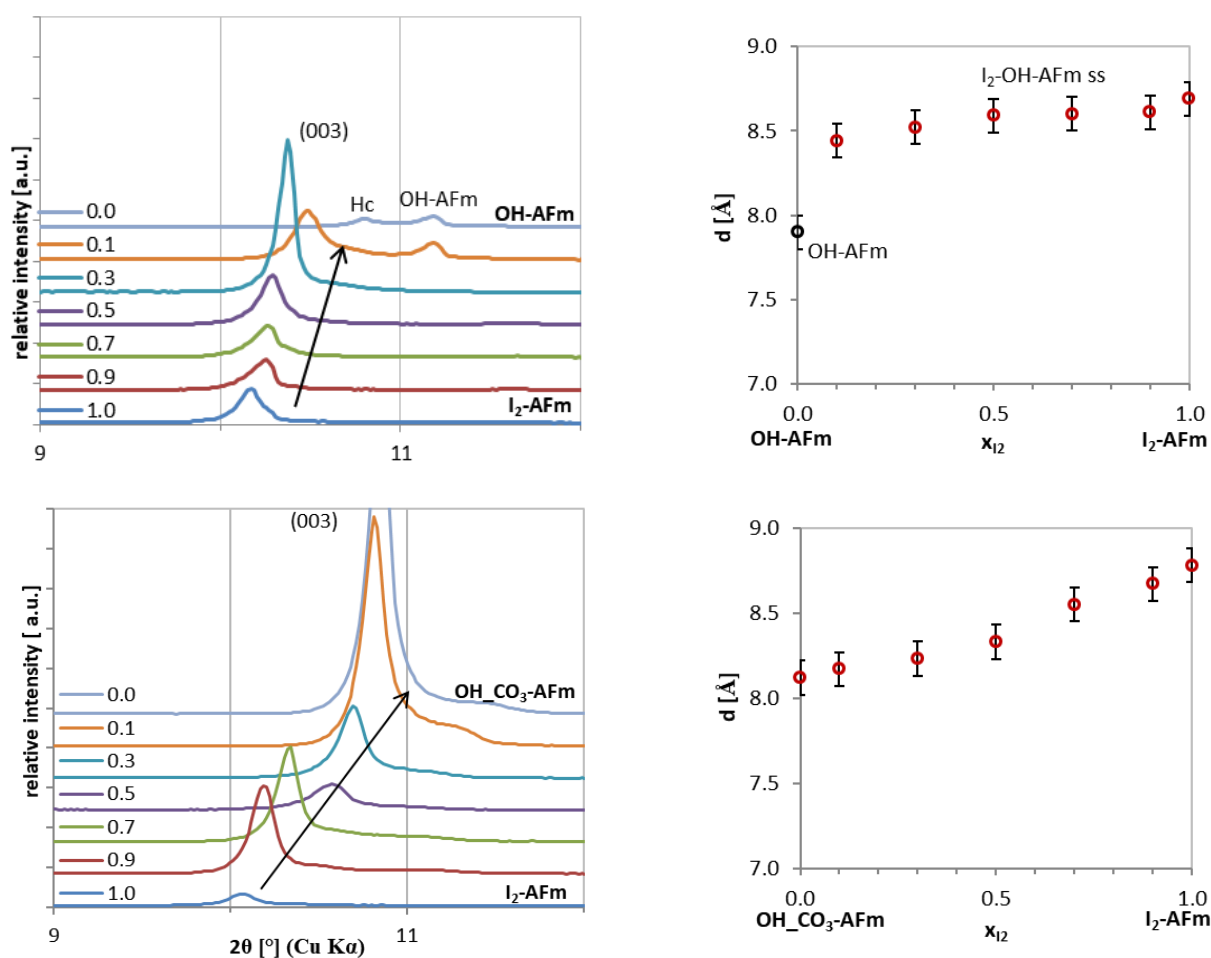


Figure 2: Evolution of the (hkl 003) reflexions and the interlayer distance in the (I₂-OH)-AFm (top) and the (I₂-OH₂CO₃)-AFm (bottom) solid solution series (pH ~13) after 3 months equilibration time and drying over a saturated NaOH solution. The numbers 0.0, 0.1, 0.3, 0.5, 0.7, 0.9 and 1.0 indicate the mole fraction of the I₂-AFm end member (x_{I_2}). Hc: hemicarbonate (= OH₂CO₃-AFm); ss: solid solution.

The solid solution formation between the I₂-AFm and the CO₃-AFm, on the other hand, is incomplete and a miscibility gap with the composition $0.5 \leq \text{CO}_3/(2\text{I}+\text{CO}_3)$ exists (Figure 3). An initial peak shift up to a composition of $0.3 \leq \text{CO}_3/(2\text{I}+\text{CO}_3)$ is observed, suggesting that small amounts of the CO₃²⁻ anion (ionic radius 1.78 Å; Jenkins and Thakur, 1979) can be well incorporated in the I₂-AFm structure to form a mixed I₂-CO₃-AFm phase. The solid solution is limited to compositions $0.5 \leq \text{CO}_3/(2\text{I}+\text{CO}_3)$, where two coexisting phases - an I₂-CO₃-AFm mixed phase and a CO₃-AFm, indicate the presence of a miscibility gap. This miscibility gap could be related to the difference in the structure as monocarbonate has a triclinic structure, and to the planar arrangement of carbonate in the CO₃-AFm interlayer which prevents the uptake of the larger I⁻ anion into the structure. A comparable behaviour has been observed for chloride uptake in monocarbonate (Mesbah et al., 2011).

Between all of the other attempted pairs, SeO₃-CO₃, SeO₃-OH₂CO₃, SeO₃-SO₃, and SeO₃-S₂O₃, no solid solutions could be detected (Table 1). Most surprising is the absence of a solid solution between the SeO₃-AFm and the SO₃-AFm, where despite the same crystal symmetry, the same anion charge and similar anion size the formation of a solid solution was not favoured. Possible limiting factor here could be a different local arrangement of the respective anion in the interlayer.

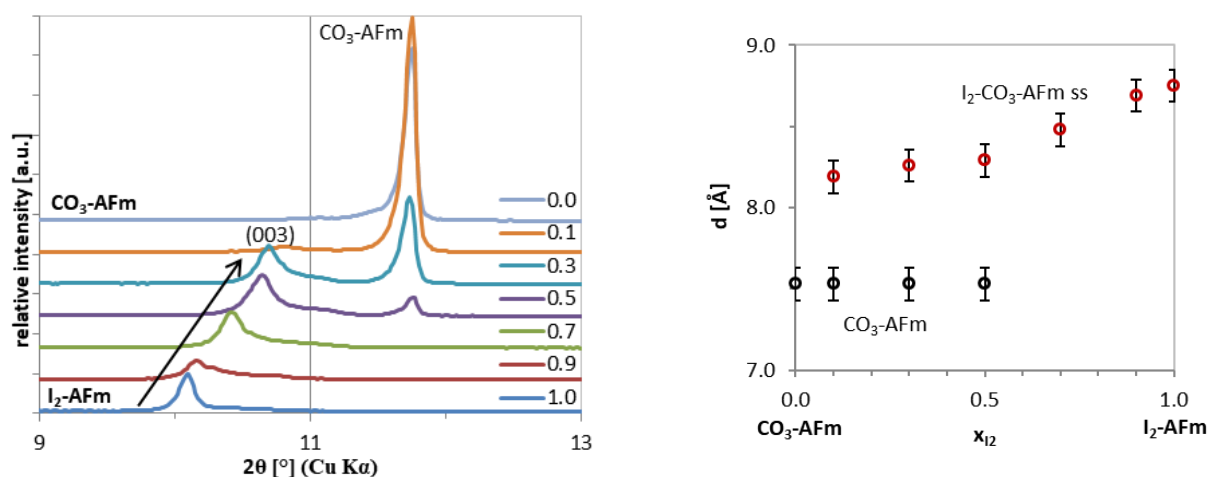


Figure 3: XRD patterns (left) and corresponding *d*-values (right) of the (I₂-CO₃)-AFm solid solution series showing a miscibility gap at compositions $0.5 \leq \text{CO}_3/(2\text{I} + \text{CO}_3)$ (pH ~13) after 3 months equilibration time and drying over a saturated NaOH solution. The numbers 0.0, 0.1, 0.3, 0.5, 0.7, 0.9 and 1.0 indicate the mole fraction of the I₂-AFm end member (x_{I_2}).

Table 1: Overview of all synthesized AFm solid solution series.

AFm end members	pH ~13	pH < 13
SeO ₃ -CO ₃	no ss	no ss
SeO ₃ -OH_CO ₃	no ss	no ss
SeO ₃ -SO ₃	no ss	no ss
SeO ₃ -S ₂ O ₃	no ss	no ss
SeO ₃ -SO ₄	ss	no ss?
I ₂ -CO ₃	ss for $x_{\text{I}_2} \geq 0.7$	ss for $x_{\text{I}_2} \geq 0.7$
I ₂ -OH_CO ₃	ss	ss
I ₂ -OH	ss $x_{\text{I}_2} \geq 0.1$	ss $x_{\text{I}_2} \geq 0.1$

ss: solid solution

3.1.2 FTIR

The observations on the solid solution series made in XRD were confirmed by FTIR analyses. The continuous solid solution between the I₂-AFm and OH_CO₃-AFm end members can also be seen in the FTIR spectra of the samples (Figure 4). The absorption band at ~775 cm⁻¹ in the I₂-AFm is caused by the Al-OH deformation vibration in the rhombohedral structure. With decreasing amount of x_{I_2} the band is gradually weakened and shifts continuously towards ~745 cm⁻¹. This shift could be attributed to the different environment Al encounters in the sample as the composition changes.

In the FTIR spectra of the I₂-CO₃ solid solution series the two coexisting phases can be clearly distinguished. For compositions $x_{\text{I}_2} \geq 0.7$ the Al-OH absorption band shows the same behaviour as observed before and only a single phase is present. At composition $x_{\text{I}_2} = 0.5$ additional absorption bands at ~948 cm⁻¹, ~875 cm⁻¹ and ~667 cm⁻¹ appear indicating in addition the presence of triclinic CO₃-AFm.

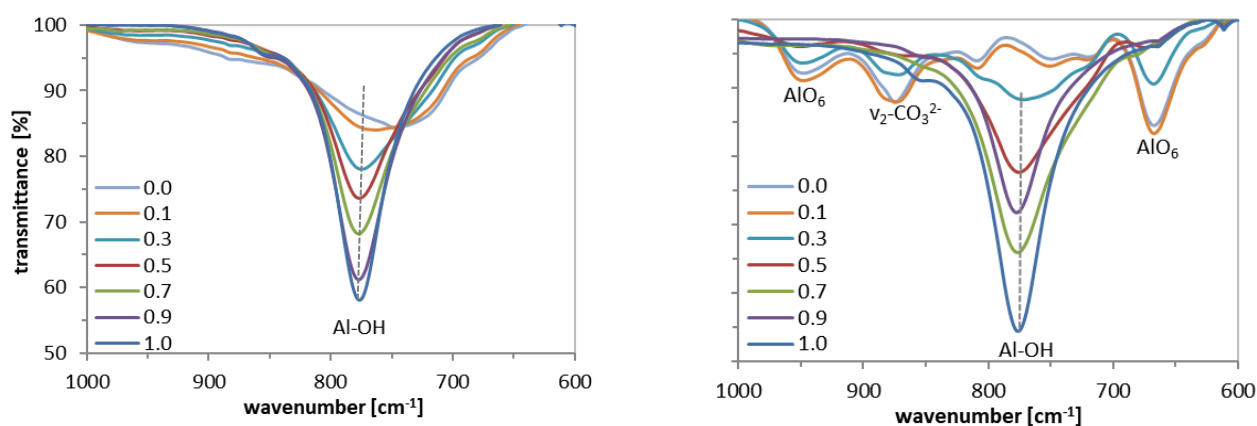


Figure 4: FTIR spectra of the $(I_2\text{-OH-CO}_3)\text{-AFm}$ (left) and the $(I_2\text{-CO}_3)\text{-AFm}$ (right) solid solution series showing the evolution of the Al-OH absorption band with changing x_{12} .

3.2 Synthesis and characterization of the $(HS^-)_2\text{-}$ and the $(HSe^-)_2\text{-AFm}$ phases

After a couple of days of aging, the $(HS^-)_2\text{-AFm}$ suspension obtained a bluish-green colour (Figure 5a) and this colour remained over the entire ageing period. After centrifugation a clear liquid phase and a bluish-green solid remained. The dry product was a greyish-white powder whose colour remained stable in the glovebox (Figure 5b).

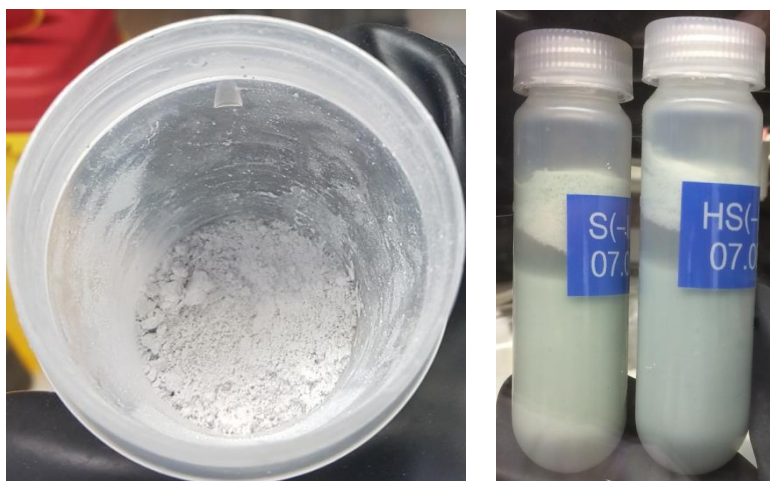


Figure 5: Synthesis of the $(HS^-)_2\text{-AFm}$ phase: a) the AFm-suspension before filtration; b) the solid after drying over a saturated NaOH solution.

The XRD spectra of both synthesized phases show the formation of an AFm phase with rhombohedral structure with its characteristic main layer peak (hkl 110) at about $31^\circ 2\theta$ (Figure 6). In addition, both phases display high-intensity basal reflections corresponding to an interlayer distance for the (hkl 003) reflection of 8.46 Å for the $(HS^-)_2\text{-AFm}$ and 8.27 Å for the $(HSe^-)_2\text{-AFm}$, respectively. These d-spacings are smaller than the d-spacings of the corresponding rhombohedral AFm phases with doubly charged interlayer anions $SO_4\text{-AFm}$ ($d = 8.93$ Å), $SO_3\text{-AFm}$ ($d = 8.51$ Å) and $SeO_3\text{-AFm}$ ($d = 9.75$ Å); consistent with the smaller size of the hydrated HSe^- and HS^- anions compared to the larger oxyanions. Minor impurities of portlandite and katoite were observed in both samples.

With the measured concentrations of calcium, sodium, aluminium and sulfur in the liquid phase in equilibrium with the $(\text{HS}^-)_2\text{-AFm}$ solid a solubility product of $\log K_s^0 = -28$ at 23°C was calculated. In the case of the $(\text{HSe}^-)_2\text{-AFm}$, partial oxidation of HSe^- in the liquid phase hindered the accurate determination of the solubility.

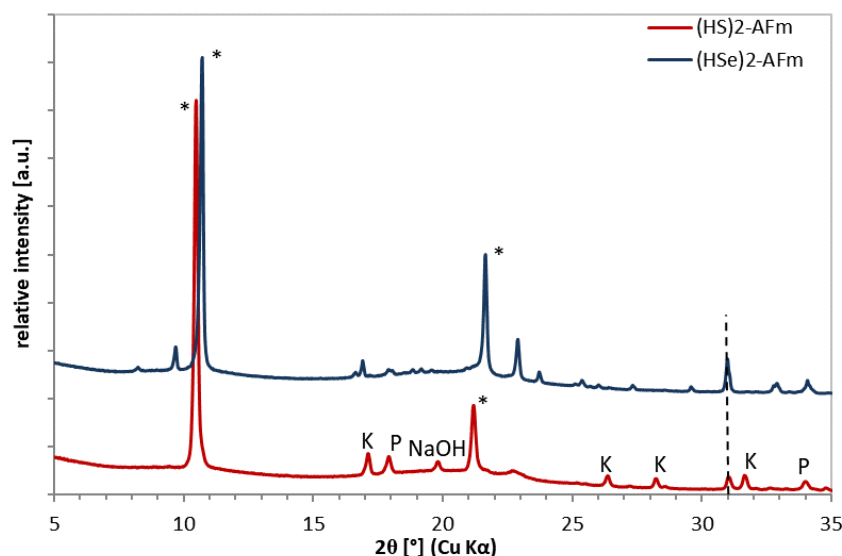


Figure 6: XRD-pattern of the synthesized $(\text{HS}^-)_2\text{-AFm}$ and $(\text{HSe}^-)_2\text{-AFm}$ phases after 1 month equilibration time and drying over a saturated NaOH solution. K: katoite; P: portlandite; *: basal reflexion.

4 Conclusions and Future work

In this study the potential of Se and I to form binary AFm solid solutions was investigated in several types of solid solution series. AFm containing the following anion pairs were found to form solid solutions: $\text{SeO}_3\text{-SO}_4$, $\text{I}_2\text{-CO}_3$, $\text{I}_2\text{-OH_CO}_3$ and $\text{I}_2\text{-OH}$. The limiting factors hereby seem to be the crystal symmetry, the size of the interlayer anion and the hydration state of the phase.

Furthermore, the formation of AFm phases with the strongly reduced sulfur and selenium species HS^- and HSe^- was observed. The synthesized phases show an AFm-like structure consistent with a rhombohedral symmetry and interlayer distances of 8.46 Å for the $(\text{HS}^-)_2\text{-AFm}$ and 8.27 Å for the $(\text{HSe}^-)_2\text{-AFm}$. These data suggest that the $(\text{HS}^-)_2\text{-AFm}$ and $(\text{HSe}^-)_2\text{-AFm}$ phases could be potentially stable under the reducing and alkaline conditions expected in a cement-based L/ILW repository after closure.

Future objectives are:

- Construction of solid solution thermodynamic models describing the above-mentioned solid solutions with the obtained XRD data, bulk chemical analysis of the liquid phases and pH measurements using GEMS modelling software.
- Sorption studies with Se(VI), Se(IV) and I(-I) onto $\text{CO}_3\text{-AFm}$, $\text{OH_CO}_3\text{-AFm}$ and $(\text{HS}^-)_2\text{-AFm}$; comparison of sorption data with experimental solid solution results.
- Thermodynamic modelling of sorption experiments with the solid solution thermodynamic model.

Acknowledgement

The research leading to these results has received funding from the European Union's Horizon 2020 Research and Training Programme of the European Atomic Energy Community (EURATOM) (H2020-NFRP-2014/2015) under grant agreement n° 662147 (CEBAMA).

References

- Aimoz, L., Wieland, E., Taviot-Gueho, C., Dähn, R., Vespa, M., Churakov, S.V. (2012a). Structural insight into iodide uptake by AFm phases. *Environmental Science & Technology*, 42, 3874-3881.
- Aimoz, L., Kulik, D.A., Wieland, E., Curti, E., Lothenbach, B., Mäder, U. (2012b). Thermodynamics of AFm-(I₂-SO₄) solid solution and of its end-members in aqueous media. *Applied Geochemistry*, 27, 2117-2129.
- Baquerizo, L.G., Matschei, T., Scrivener, K.L., Saeidpour, M., Wadsö, L. (2015). Hydration states of AFm cement phases. *Cement and Concrete Research*, 73, 143-157.
- Baur, I. and Johnson, C.A. (2003). Sorption of selenite and selenate to cement minerals. *Environmental Science & Technology*, 37, 3442-3447.
- Bonhoure, I., Baur, I., Wieland, E., Johnson, C.A., Scheidegger, A.M. (2006). Uptake of Se(IV/VI) oxyanions by hardened cement paste and cement minerals: An X-ray absorption spectroscopy study. *Cement and Concrete Research*, 36, 91-98.
- Jenkins, H.D.B. and Thakur, K.P. (1979). Reappraisal of thermochemical radii for complex ions. *Journal of Chemical Education*, 56, 576-577.
- Mace, N., Landesman, C., Pointeau, I., Grambow, B., Giffaut, E. (2007). Characterisation of thermally altered cement pastes. Influence on selenite sorption. *Advances in Cement Research*, 19, 157-165.
- Mesbah, A., Cau-dit-Coumes, C., Frizon, F., Leroux, F., Ravaux, J., Renaudin, G. (2011). A new investigation of the Cl⁻-CO₃²⁻ substitution in AFm phases. *Journal of the American Ceramic Society*, 94, 1901-1910.
- Motzet, H. and Pöllmann, H. (1999). Synthesis and characterization of sulfite-containing AFm phases in the system CaO-Al₂O₃-SO₂-H₂O. *Cement and Concrete Research*, 29, 1005-1011.
- Landesman, C., Bailly, C., Baty, V., Vandenborre, J., Grambow, B. (2012). Speciation of reduced selenium species in hyperalkaline solutions: attempt at developing a specific analytical protocol. *In: 4th Annual Workshop Proceedings, 7th EC FP – Recosy CP*.
- Le Cornec, D., Wang, Q., Galois, L., Renaudin, G., Izoret, L., Calas, G. (2017). Greening effect in slag cement materials. *Cement and Concrete Research*, 84, 93-98.
- Olin, Å., Nöläng, B., Osadchii, E.G., Öhman, L.-O., Rosén, E. (2005). *Chemical thermodynamics of Selenium*. Elsevier, Amsterdam.
- Rajo, H., Scheinost, A.C., Lothenbach, B., Laube, A., Wieland, E., Tits, J. (2018). Retention of selenium by calcium aluminate hydrate (AFm) phases under strongly-reducing radioactive waste repository conditions. *Dalton Transactions*, *in press*.
- Taylor, H.F.W. (1997). *Cement chemistry*. 2nd edition. Thomas Telford, London.
- Wersin, P., Johnson, L.H., Schwyn, B., Berner, U., Curti, E. (2003). Redox conditions in the near field of a repository for SF/HLW and ILW in Opalinus clay. *Nagra Technical Report*, 02-13.

Retention and mobility studies of safety relevant radionuclides in cementitious materials

Matthew Isaacs^{1,2*}, Emily Rastrick¹, Steve Lange², Guido Deissmann², Dirk Bosbach²,
David Read^{1,3}

¹ University of Surrey (UK)

² Forshungszentrum Jülich GmbH (DE)

³ National Physical Laboratory (UK)

* Corresponding author: m.isaacs@surrey.ac.uk

Abstract

This paper summarises the results to date, from the University of Surrey's contribution to the CEBAMA project under Work Package 2. The affinity of ¹²⁵I (in the form of I⁻, IO₃⁻) and ⁷⁵Se (SeO₃²⁻, SeO₄²⁻) for cementitious materials has been determined via a series of batch sorption tests. These experiments have utilised five different cement formulations (CEM I, GGBS:OPC, PFA:OPC, NRVB, CEBAMA reference mix), used for either conditioning and packaging of radioactive waste, construction or as a backfill material, as well as specific mineral phases present in the cements (C-S-H, AFm, AFt). Carbonated hardened cement pastes (HCP) have also been used to test the effect of the degradation of cementitious materials on the uptake of each radionuclide. The results of these batch sorption tests have shown typically fast kinetics; extending the equilibrium period beyond 14-28 days had no impact on the R_d values obtained. The R_d values acquired are highly contrasting across the systems, ranging from 0.5 - 7,000 L/kg, depending on the speciation of the aqueous analyte and the solid phase/cement used. Iodate in particular has been shown to have a strong affinity for the AFm-SO₄ phase, with a high R_d (6,800 L/kg) coupled with a distinct morphological change from planar hexagonal to acicular crystals. Microanalytical investigations of the analyte distribution in the solids have been performed by XRD, SEM-EDX and TEM.

The batch uptake studies are complemented by through-diffusion experiments using previously established protocols (Felipe-Sotelo et al., 2017). Diffusion occurs radially from blocks composed of the aforementioned cement formulations into a surrounding pre-equilibrated water. These experiments have used ³⁶Cl and ⁹⁹Tc has also been added as additional scope with comparisons made to tritiated water under identical experimental conditions. Further experiments are planned using ⁷⁵Se and ¹²⁵I, although availability of sufficient ⁷⁵Se for the experiments is proving to be a problem. The mobility of ³⁶Cl and ⁹⁹Tc is highly dependent on the type of HCP. Radioisotope breakthrough for the more permeable HCP (NRVB, PFA:OPC) occurred within the first 7 days, whereas in the less permeable HCP, no significant breakthrough has been noted up to 54 days. A constant concentration of ³⁶Cl in the surrounding solutions was not reached in any system, confirming the results of previous work (van Es et al., 2015) and pointing to mineralisation of chloride within the cement. In contrast, ⁹⁹Tc in the NRVB and PFA:OPC HCP reached steady state within 21 days, indicating higher mobility of the pertechnetate ion. Comparison of these data to those for the slag blend will shed light on the potential for Tc reduction.

1 Introduction

Cementitious materials are used widely in radioactive waste management, for example in the solidification of low and intermediate level wastes, or as construction and barrier materials in underground and surface repositories. The retention of radionuclides in cements is controlled by solubility phenomena, diffusion, adsorption and/or incorporation into solids, including the formation of solid solutions. Within the framework of CEBAMA WP2, we are studying the solubility of selected radionuclides in conditions relevant to a geological disposal facility (GDF). The uptake of long-lived fission and decay products (Ra, Tc, I, Se, Cl) in cementitious materials, the diffusion of radionuclides through hardened cement paste and the radionuclide distribution between and within various hydrated cement phases on the micro-scale are also being investigated, using micro-analytical and spectroscopic tools. The objective of these investigations is to enhance mechanistic understanding of their uptake and retention and to assess the relevance of chemical alteration processes, such as carbonation, in aged cement. In this context, a bottom-up approach is being pursued using synthesised cement phases (model phases) on the one hand and hardened cement pastes covering a range of compositions on the other.

Numerous studies have been carried out to investigate: 1) the solubility of the radionuclides in solution under alkaline conditions analogous to those expected in a GDF (Baston et al., 1997; Heath et al., 1998; Felipe-Sotelo et al., 2014), 2) batch sorption studies with cement admixtures (Glasser et al., 1985; Beaudoin et al., 1990; Solem-Tishmack et al., 1995; Bonhoure et al., 2006; Tits et al., 2006; Mace et al., 2007; Tanabe et al., 2010) and 3) diffusion studies in cement using different experimental protocols i.e. in-, out-, or through-diffusion, or non-equilibrium, i.e. leaching; (Atkinson and Nickerson, 1984; Tallent et al., 1987; Brodda and Mingxia, 1988; Gilliam et al., 1990; Sarott et al., 1992; Mattigod et al., 2001; Chida and Sugiyama, 2008; Felipe-Sotelo et al., 2014; van Es et al., 2015). A full review of these topics can be found in the CEBAMA WP2 state of the art report (Lange et al., 2016). Several of the radionuclides addressed in this study can exhibit a range of oxidation states under anticipated GDF conditions (Se, Tc, I). Selenium is being considered as both selenite and selenite and iodine as iodide and iodate; these are believed to be the dominant species likely under GDF conditions (Thoenen et al., 2014). Technetium, introduced as Tc(VII), has been added to the original scope in view of its perceived geochemical mobility.

2 Methodology

2.1 Materials

The solids of interest for this work fall into two categories: HCP and single mineral phases. The five cement blends are: CEM I, a ground granulated blast furnace slag: ordinary Portland cement blend (GGBS:OPC), a pulverised fuel ash blend (PFA:OPC), a bespoke backfill material (NRVB, Nirex Reference Vault Backfill) and a CEBAMA reference cement blend (Table 1). In each case, the constituent powders were weighed in accordance with the ratios in Table 1 and mixed in a powder mixer for 2 hours.

Table 1: Powder ratios of selected cement formulations.

Cement Blend	OPC	PFA	GGBS	Hydrated Lime	Lime Flour	Silica Fume	Quartz	Water/cement ratio
CEM I	1	-	-	-	-	-	-	0.45
PFA:OPC	1	3	-	-	-	-	-	0.45
GGBS:OPC	1	-	9	-	-	-	-	0.45

Cement Blend	OPC	PFA	GGBS	Hydrated Lime	Lime Flour	Silica Fume	Quartz	Water/cement ratio
NRVB	1	-	-	0.38	1.1	-	-	0.55
CEBAMA	1	-	0.62	-	-	0.87	1.1	0.45
Reference mix								

The bulk composition of the individual components above was assessed by X-ray fluorescence (Table 2).

Table 2: XRF data providing the bulk composition of the powders used to form the cement blends.

Cement Powder	CaO (%)	SiO ₂ (%)	Al ₂ O ₃ (%)	SO ₃ (%)	MgO (%)	Fe ₂ O ₃ (%)	K ₂ O (%)	P ₂ O ₅ (%)	TiO ₂ (%)	MnO (%)
CEM I	66.27	17.86	4.78	3.98	2.75	2.65	1.52	<LOD	0.2	
PFA	3.86	48.66	25.97	1.82	1.27	12.36	5.05	0.18	0.84	
GGBS	42.93	31.92	11.40	4.10	6.76	0.45	1.01	-	0.41	0.59
Hydrated Lime	97.75	1.37	0.35	-	0.20	-	0.33	-	-	-
Lime Flour	96.57	1.70	0.71	0.18	0.29	0.16	0.39	-	-	-
Silica Fume	1.46	93.10	1.44	0.47	0.88	0.91	1.73	-	-	-
CEM I (VTT)	67.72	17.60	3.42	3.81	0.6	5.17	1.3	-	0.17	0.21
GGBS (VTT)	43.13	32.3	9.85	3.68	7.40	0.74	1.20	-	1.36	0.34

The individual phases comprise: calcium silicate hydrate (C-S-H), ettringite and monosulphate. These phases were selected as they comprise the major components of a CEM I cement, excluding portlandite; no significant interaction of the latter with radionuclides is expected. C-S-H was produced by direct synthesis using the method of Atkins et al. (1992), performed by mixing CaO with either silicic acid or silica fume in distilled, degassed water. Ca/Si ratios of between 0.9 and 1.4 are obtained using this method, with the lower ratios being applicable to an aged cement. Ettringite was synthesised using the method of Atkins et al. (1991) in which a slurry of water containing CaO is prepared at 5°C (w/s ratio = 10) and added to a solution containing Al₂(SO₄)₃.16H₂O. This is stirred for 24 hours followed by aging at 25°C. Excess gypsum is removed by repeatedly re-dispersing in water. The ettringite formed was used to synthesise monosulphate via a reaction with tricalcium aluminate (C₃A) over a 2 week period. Phase purity was confirmed by X-ray diffraction (XRD).

2.2 Preparation of cement equilibrated water

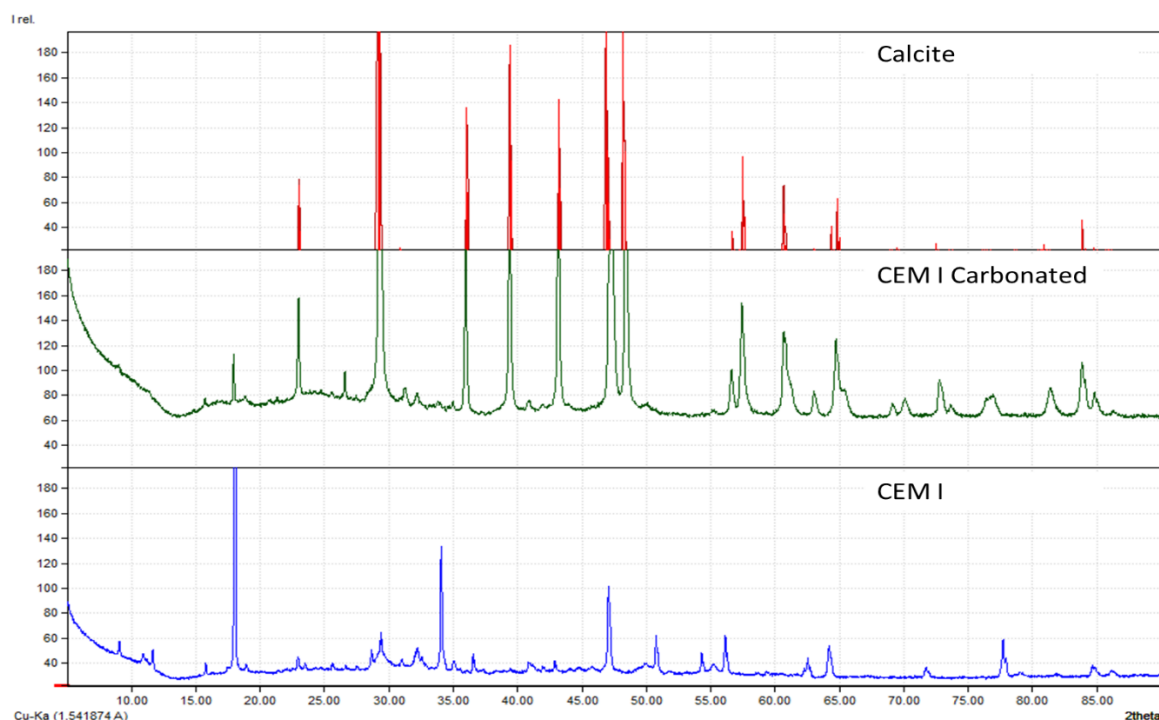
In order to prepare the cementitious equilibrated water for use in the solubility and batch sorption experiments, 50 g of the powders for each respective cement blend (Table 1) were weighed and deionised water (1 L) added under a N₂ atmosphere. The suspension was agitated daily to prevent sedimentation. After a 28 day period the solid was removed via filtration and the waters analysed by ion chromatography (Table 3).

Table 3: Compositional data for the equilibrated waters.

Cement Blend	Cl (ppm)	SO ₄ (ppm)	NO ₃ (ppm)	Na (ppm)	K (ppm)	Ca (ppm)	Mg (ppm)	pH	Eh (mV)
CEM I	18.0	36.9	18.1	267.6	453.3	1388.4	-	12.82	-14
PFA:OPC	14.4	31.0	16.3	129.8	195.2	675.8	39.0	12.29	-503
GGBS:OPC	16.9	34.7	17.6	68.6	70.2	299.6	-	12.80	-414
NRVB	16.0	33.6	17.2	172.5	224.7	1374.3	66.3	12.90	-129
CEBAMA	24.0	50.3	20.4	189.7	202.3	1046.6	137.0	12.69	-454
Reference mix									

2.3 Preparation of carbonated samples

HCP powders, hydrated for 3 months, were submerged in deionised water and placed inside a pressure vessel. The vessel was flushed with CO₂ before being pressurised with 100% CO₂ at 30 bar. The system was left at this pressure for a minimum of 24 hours. Carbonated cement equilibrated waters were prepared by bubbling CO₂ at 1 atm through the pre-equilibrated waters for 15 minutes. Figure 1 shows the results of degradation of the CEM I paste from a mixture of phases to calcite via carbonation.

Figure 1: XRD patterns of a 3 month hydrated CEM I, carbonated CEM I and calcite.

2.4 Sorption

Sample preparation was carried out in a glove box (N₂ or Ar atmosphere) to avoid carbonation. The element of interest was added from a stock solution to equilibrated water, to give an appropriate initial concentration of $5 \cdot 10^{-4}$ mol/dm³ for Se (Bonhoure et al., 2006) and $1 \cdot 10^{-3}$ mol/dm³ for Cl and I. A liquid to solid mass ratio of 10:1 was used in the batch studies and the tests run for a month with daily sampling in the first week followed by weekly sampling for the remainder of the experiment. The samples were allowed to reach equilibrium and aliquots of the supernatant taken and analysed by ICP-MS (Se, I, Cl). Residual solids were filtered and analysed by XRD and scanning electron microscopy. The results allow determination of the kinetics of uptake, as well as the steady state partitioning of the radionuclide between solid and solution, quantified in terms of the distribution ratio (R_d), defined as:

$$R_d = \frac{c_s}{c_{aq}} = \left(\frac{c_{tot} - c_{aq}}{c_{aq}} \right) \cdot \left(\frac{V}{m} \right) \quad (I)$$

2.5 Through-diffusion

Through-diffusion experiments were performed as described by Felipe-Sotelo et al. (2014, 2016, 2017); Hinchliff et al. (2016) and van Es et al. (2015). Cylindrical blocks of hardened cement paste (40 mm diameter and 45-50 mm height) were drilled longitudinally to create a central well (25-30 mm depth) for the addition of radioisotopes (Figure 2). 10 kBq of the radionuclide of interest (³H, ³⁶Cl, ⁹⁹Tc) was spiked into the central well with cement equilibrated water, which was then sealed, and the block placed in equilibrated water (120 mL). Movement of radionuclides through the block was monitored by taking 1 mL aliquots of the surrounding water and measuring activity using liquid scintillation counting (LSC). The experiments have been running for 4 months to date. After either the concentration of radionuclides becomes constant, or a specified maximum time (~1 year), the block is removed from the equilibrated water, sawn axially and the distribution of radionuclides measured by digital autoradiography.

Experiments using the shorter-lived isotopes ⁷⁵Se and ¹²⁵I are planned but due to their shorter half-life, 119 and 59 days respectively, the experimental run time is shortened in order to obtain useable autoradiography images at the conclusion of the experiment.

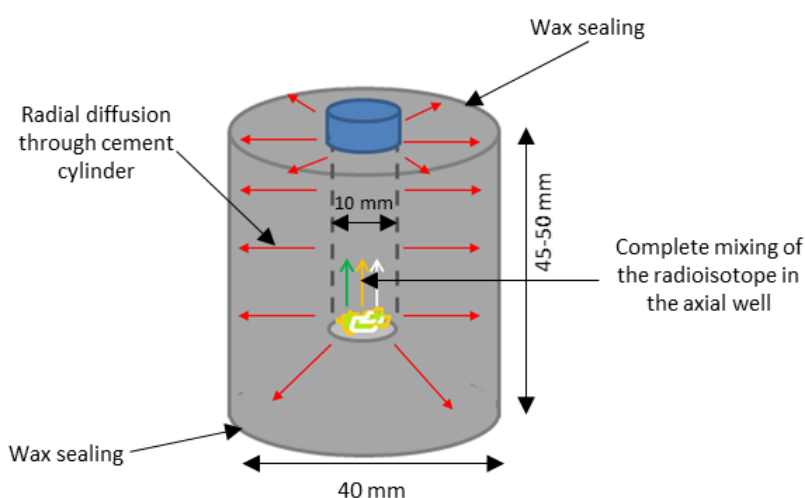


Figure 2: Schematic of the radial through-diffusion experiments.

3 Results

3.1 Kinetics of uptake

Selenium and iodine were taken up rapidly by both the single mineral phases and HCP, reaching a stable R_d value within 14-28 days. The fast kinetics of adsorption correspond to mineralogical changes in the solids. Figure 3 gives an example, showing IO_3^- in contact with the AFt phase reaching a stable concentration in solution after 14 days.

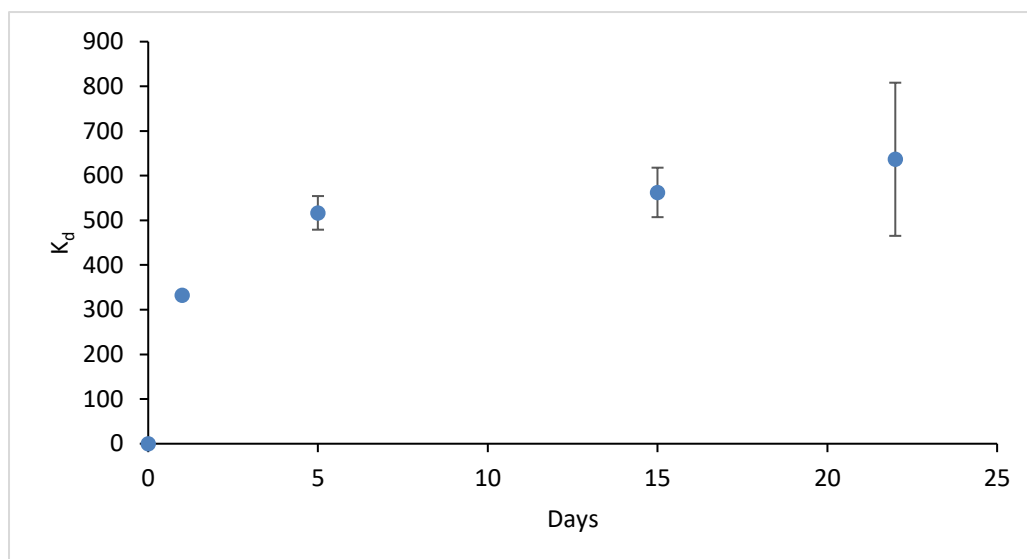


Figure 3: Distribution ratio of IO_3^- on AFt as a function of time.

When looking for phase transformation by SEM in the single phase batch tests the most obvious change was that, in the presence of all of the anions tested, the phase pure AFm appeared to degrade from a planar hexagonal structure to an ill-defined aggregate of acicular crystals (Figure 4). The mechanism of this transformation is unclear and more work is required to determine the reasons why this morphological change is occurring.

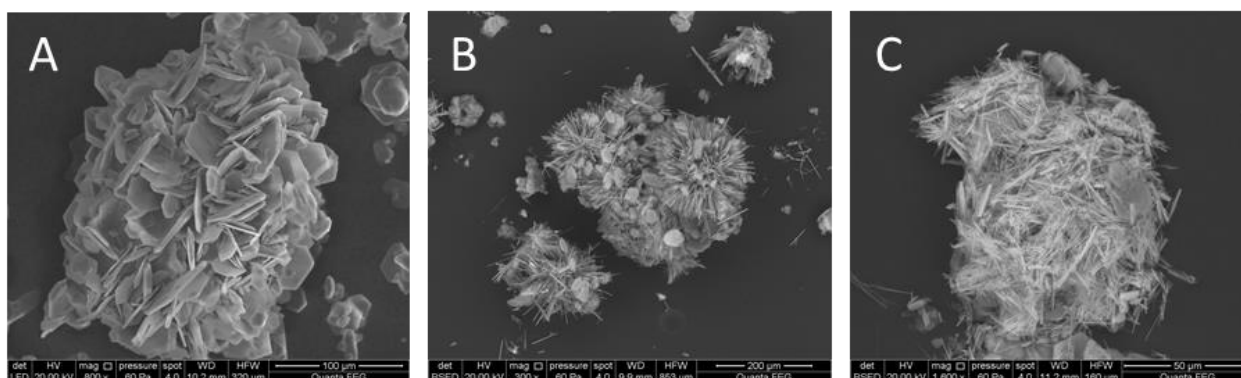


Figure 4: A: Phase pure AFm, B: AFm after co-precipitation with SeO_3^{2-} and C: AFm after batch sorption experiments with IO_3^- .

The batch experiments were also performed on hydrated cement pastes to give a more representative picture of a true system, albeit harder to interpret as far more interactions are present. An example iodate uptake by CEM I

paste gave an R_d value of 115 L/kg. SEM analysis revealed needle-like crystals similar in morphology to ettringite (Figure 5) with varying amounts of iodine associated with different regions along the axis. Corresponding EDX spot analysis data (Table 3) suggest the crystals incorporate iodine sporadically as it grows.

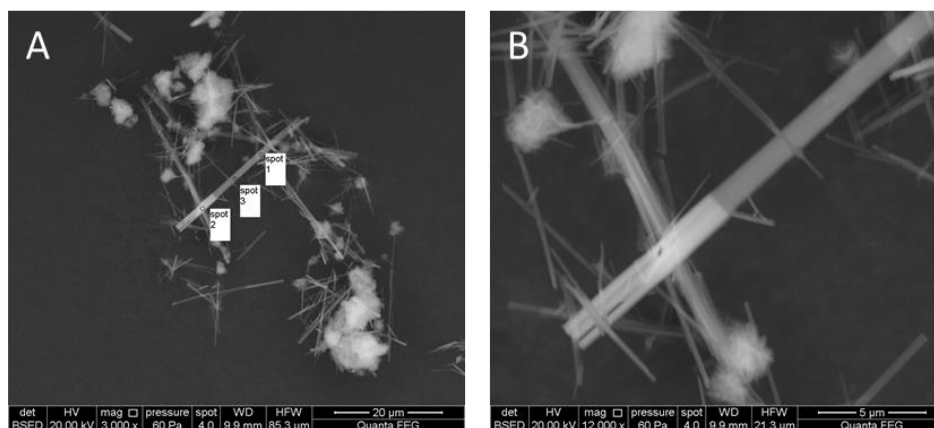


Figure 5: A: Location of EDX spot analyses and B: higher magnification image showing incorporation of I into needle-like phases found within CEM I paste.

Table 3: EDX spot analysis data along a single crystal from CEM I paste. Brighter regions correspond to higher iodine concentrations.

Element	Spot 1 wt%	Spot 2 wt%	Spot 3 wt%
O	59.83	55.56	66.74
Al	5.86	5.42	6
S	9.72	6.12	9.09
Ca	23.33	21.84	18.17
I	1.26	11.05	n.d.
Total	100	100	100

n.d. – not detected

3.2 Through-diffusion

Diffusion experiments were carried out with tritiated water (HTO) to provide a benchmark for the migration of anionic species. The results to date are summarised in Figure 6, which shows the activity concentration of ^3H in the water surrounding the block as a function of time. Each point represents the average of two replicates. Breakthrough of HTO was observed on day 1 of the experiments for all of the hardened cement pastes; however, the rate of HTO migration is slightly different for each formulation. The NRVB and PFA blend behave similarly and confirm previous results obtained with HTO in NRVB (Felipe-Sotelo et al., 2014). From day 14 the activity in the surrounding water fluctuates around a seemingly maximum value until the latest measured point at day 55, indicating that the radionuclide in the well has reached equilibrium in the system. The CEBAMA reference mix corresponds to a mid-value for the speed of HTO diffusion with the elution of HTO occurring more slowly before reaching a similar maximum to the NRVB and PFA mixes at approximately 30 days. The CEM I and GGBS hardened cement pastes demonstrate an even slower diffusion rate still not reaching a stable concentration within the current timeframe of the experiment. Variation in diffusivity is most likely attributable to differences in

porosity and permeability of the HCP. NRVB has a relatively high porosity at 38% (Vasconcelos et al., 2017), CEM I grouts show a lower porosity of ~12% (Espinosa et al., 2008), whereas slag blends tend to be lower still and dependent on micro-fractures (Isaacs et al., 2018).

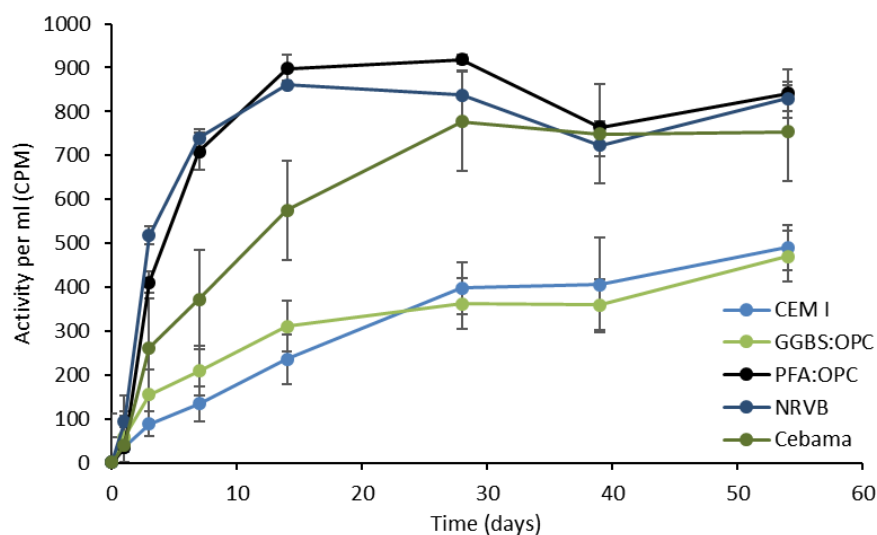


Figure 6: Diffusion of HTO through CEM I, GGBS, PFA, NRVB and CEBAMA reference HCP.

The movement of chlorine through the HCP samples (Figure 7) appears to follow a similar pattern to that of tritium, albeit with a slower rate of diffusion. The CEM I and GGBS show no breakthrough on the timescale of the experiments with the CEBAMA reference cement showing the slowest diffusion rate of those where breakthrough is seen. The PFA and NRVB cement pastes exhibit the fastest diffusion rates and the results for NRVB are in accordance with data previously obtained by van Es et al. (2015). The concentration has yet to reach steady state in any sample.

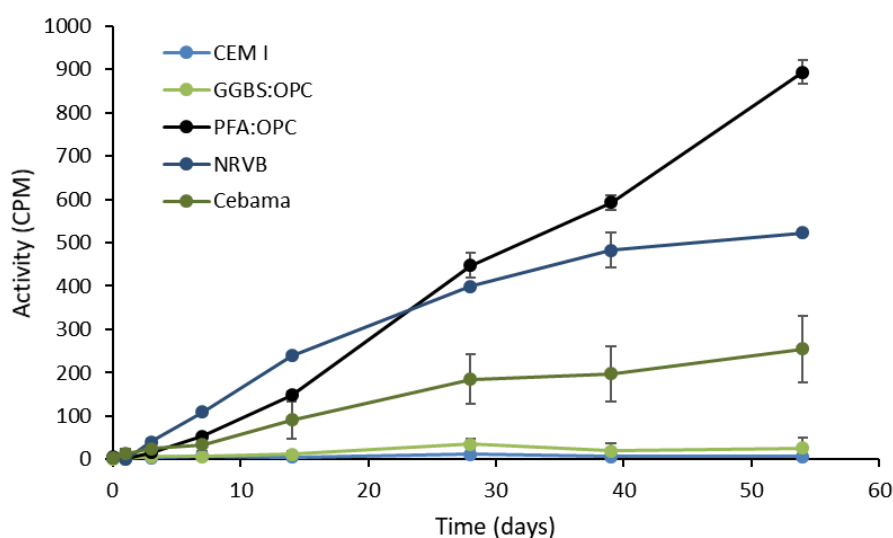


Figure 7: Diffusion of ³⁶Cl through CEM I, GGBS, PFA, NRVB and CEBAMA reference HCP.

The results for technetium diffusion can be placed in two very distinct categories. Technetium demonstrates either extremely fast diffusion, as in the case of the NRVB and the PFA cements, with breakthrough profiles comparable to that of HTO or, as in the case of the remaining HCP, shows little or no breakthrough through the block. Differences this pronounced cannot be explained solely by differences in permeability, when viewed in the light of the HTO results, and indicate changes in technetium speciation within the cement porewater. Technetium was added to the well in the form of pertechnetate which is known to be highly soluble and mobile in oxidising environments. If however, the pertechnetate is reduced from TcO_4^- to the Tc(IV) valence state it becomes much less mobile (Gilliam et al., 1990). Whether the reduction of TcO_4^- is responsible for the stark contrast in diffusion rate is not inherently obvious as the reduction potential values obtained from the equilibrated water analysis seem to contradict. The CEM I equilibrated water, which had the least apparent potential for reduction (-14 mV) exhibited extremely low technetium mobility. On the other hand, the PFA samples, which had a reduction potential of -414 mV and thus, could reasonably be expected to reduce the pertechnetate, displayed fast Tc migration. However, the Eh of the equilibrated water is unlikely to correspond to that of the intact monolith and so further work is required in this area to determine the speciation of Tc as it moves through the grout. The amount of technetium in solution surrounding the PFA samples does appear to be decreasing so reduction to Tc(IV) may be kinetically slow, which for the more permeable HCP, may allow the bulk of Tc added to diffuse through the block. The concentration of technetium will be continually monitored to determine if the reduction in solution is a continuing trend.

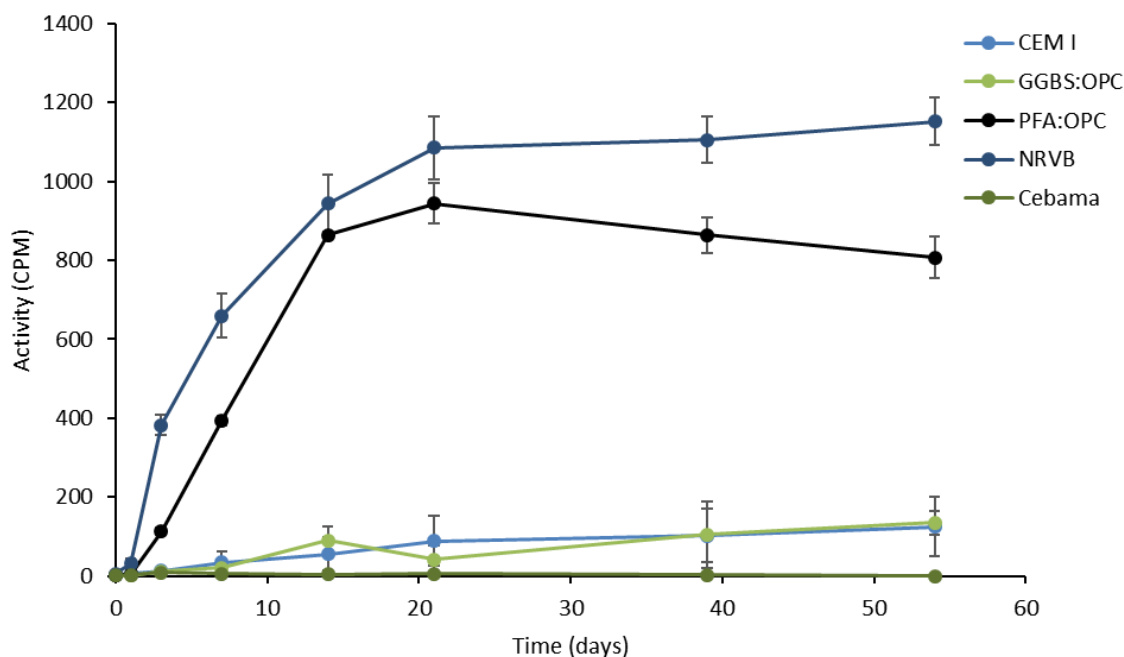


Figure 8: Diffusion of ^{99}Tc through CEM I, GGBS, PFA, NRVB and CEBAMA reference HCP.

4 Conclusions and future work

Characterisation of the solids from the batch sorption experiments is underway and has shown a number of mineral phases that have been formed as a result of being submerged in hyper-alkaline media. Batch sorption experiments for Cl and Tc will be completed to provide a full library of R_d values for the cement-based materials and individual phases for I^- , IO_3^- , SeO_3^{2-} , SeO_4^{2-} and Cl^- . Through-diffusion studies have given an indication of the rate of diffusion for HTO, Cl and Tc in each of the hardened cement paste blends. Further through-diffusion

experiments using ^{75}Se and ^{125}I will be undertaken to complete the set and more samples from the existing experiments will be taken to monitor the evolving systems over a longer period. It is intended to derive diffusion coefficients from the results obtained from these experiments. Once all through-diffusion experiments have been concluded, the blocks will be auto-radiographed to investigate the radionuclide distribution.

Acknowledgement

This research has received funding from the European Union's Horizon 2020 Research and Training Programme of the European Atomic Energy Community (EURATOM) (H2020-NFRP-2014/2015) under grant agreement n° 662147 (CEBAMA).

References

- Atkins, M., Macphee, D., Kindness, A., Glasser, F.P. (1991). Solubility properties of ternary and quaternary compounds in the $\text{CaO-Al}_2\text{O}_3\text{-SO}_3\text{-H}_2\text{O}$ system. *Cement and Concrete Research*, 21, 991-998.
- Atkins, M., Glasser, F.P., Kindness, A. (1992). Cement hydrate phase: Solubility at 25°C. *Cement and Concrete Research*, 22, 241-246.
- Atkinson, A. and Nickerson, A.K. (1984). The diffusion of ions through water-saturated cement. *Journal of Materials Science*, 19, 3068-3078.
- Baston, G.M.N., Brownsword, M., Smith, A.J., Smith-Briggs, J.L. (1997). Further Near-field Solubility Studies. Nirex Report, NSS/R257.
- Beaudoin, J.J., Ramachandran, V.S., Feldman, R.F. (1990). Interaction of chloride and C-S-H. *Cement and Concrete Research*, 20, 875-883.
- Bonhoure, I., Baur, I., Wieland, E., Johnson, C.A., Scheidegger, A.M. (2006). Uptake of Se(IV/VI) oxyanions by hardened cement paste and cement minerals: An X-ray absorption spectroscopy study. *Cement and Concrete Research*, 36, 91-98.
- Brodda, B.-G. and Mingxia, X. (1988). Leaching of chlorine, cesium, strontium and technetium from cement-fixed intermediate level liquid waste. *In: Symposium BERLIN – Scientific Basis for Nuclear Waste Management XII*, 127, 481-487.
- Chida, T. and Sugiyama, D. (2008). Diffusion behavior of organic carbon and iodine in low-heat Portland cement containing fly ash. *In: Symposium Q – Scientific Basis for Nuclear Waste Management XXXII*, 1124, 1124-Q10-15.
- Espinosa, E.S., Moragues, A., Massana, J., Fuentes, R.A. (2008). Strength and porosity evolution of two cement mortar submerged in pig slurry. *In: Proceedings of International Conference on Agricultural Engineering*.
- Felipe-Sotelo, M., Hinchliff, J., Drury, D., Evans, N.D.M., Williams, S., Read, D. (2014). Radial diffusion of radiocaesium and radioiodide through cementitious backfill. *Physics and Chemistry of the Earth, Parts A/B/C*, 70-71, 60-70.
- Felipe-Sotelo, M., Hinchliff, J., Field, L., Milodowski, A., Preedy, O. Read, D. (2017). Retardation of uranium and thorium by a cementitious backfill developed for nuclear waste disposal. *Chemosphere*, 179, 127-138.
- Gilliam, T.M., Spence, R.D., Bostick, W.D., Shoemaker, J.L. (1990). Solidification/stabilization of technetium in cement-based grouts. *Journal of Hazardous Materials*, 24, 189-197.
- Glasser, F.P., Rahman, A.A., Macphee, D., Angus, M.J., Atkins, M. (1985). Immobilization of radioactive waste in cement-based matrices. Department of the Environment, DOE-RW--85.063.
- Heath, T., Pilkington, N.J., Tweed, C., Williams, S. (1998). Radionuclide solubility at high pH. *In: S. Baker, T.G. Heath, R. McCrohon (Eds.) Proceedings of the Royal Society of Chemistry/Nirex Symposium: The chemistry of deep disposal of radioactive waste*. Nirex Report, S/98/008.

- Hinchliff, J., Felipe-Sotelo, M., Evans, N., Read, D. (2016). Solubility constraints affecting the migration of selenium through the cementitious backfill of a geological disposal facility. *Journal of Hazardous Materials*, 305, 21-29.
- Long, Q., Xia, Y., Liao, S., Li, Y., Wu, W., Huang, Y. (2014). Facile synthesis of hydrotalcite and its thermal decomposition kinetics mechanism study with masterplots method. *Thermochimica Acta*, 579, 50-55.
- Mace, N., Landesman, C., Pointeau, I., Grambow, B., Giffaut, E. (2007). Characterisation of thermally altered cement pastes. Influence on selenite sorption. *Advances in Cement Research*, 19, 157-165.
- Mattigod, S.V., Whyatt, G.A., Serne, R., Martin, P.F., Schwab, K.E., Wood, M.I. (2001). Diffusion and leaching of selected radionuclides (iodine-129, technetium-99 and uranium) through Category 3 waste encasement concrete and soil fill material. Pacific Northwest National Laboratory Report, PNNL-13639.
- Solem-Tishmack, J.K., McCarthy, G.J., Docktor, B., Eylands, K.E., Thompson, J.S., Hassett, D.J. (1995). High-calcium coal combustion by-products: Engineering properties, ettringite formation, and potential application in solidification and stabilization of selenium and boron. *Cement and Concrete Research*, 25, 658-670.
- Sarott, F.A., Bradbury, M.H., Pandolfo, P., Spieler, P. (1992). Diffusion and adsorption studies on hardened cement paste and the effect of carbonation on diffusion rates. *Cement and Concrete Research*, 22, 439-444.
- Tallent, O.K., McDaniel, E.W., Del Cul, G.D., Dodson, K.E., Trotter, D.R. (1987). Immobilization of technetium and nitrate in cement-based materials. *In: Symposium P – Scientific Basis for Nuclear Waste Management XI*, 112, 23-33.
- Tanabe, H., Sakuragi, T., Yamaguchi, K., Sato, T., Owada, H. (2010). Development of new waste forms to immobilize iodine-129 released from a spent fuel reprocessing plant. *Advances in Science and Technology*, 73, 158-170.
- Thoenen, T., Hummel, W., Berner, U., Curti, E. (2014). The PSI/Nagra Chemical Thermodynamic Database 12/07. PSI Bericht, 14-04.
- Tits, J., Kamei, G., Iijima, K., Wieland, E. (2006). The uptake of radium by calcium silicate hydrates and hardened cement paste. *Radiochimica Acta*, 38, 637-643.
- van Es, E., Hinchliff, J., Felipe-Sotelo, M., Milodowski, A.E., Field, L.P., Evans, N.D.M., Read, D. (2015). Retention of chlorine-36 by a cementitious backfill. *Mineralogical Magazine*, 79, 1297-1305.
- Vasconcelos, R.G.W., Beaudoin, N., Hamilton, A., Hyatt, N.C., Provis, J.L., Corkhill, C.L. (2018). Characterisation of a high pH cement backfill for the geological disposal of nuclear waste: The Nirex Reference Vault Backfill. *Applied Geochemistry*, 89, 180-189.

Reactive transport modelling of radionuclides migration in the low pH cement/clay interface

Vanessa Montoya^{1*}, Naila Ait Mouheb¹, Thorsten Schäfer^{1,2}, Horst Geckeis¹

¹ Karlsruhe Institute of Technology, Institute for Nuclear Waste Disposal. KIT-INE (DE)

² Friedrich-Schiller-Universität Jena, Institute of Geosciences (DE)

* Corresponding author: vanessa.montoya@kit.edu

Abstract

In this work, the predictive reactive transport model consisting of a one-dimensional (1D) fully water saturated isothermal (298.15 K) problem representing a laboratory through diffusion experiment of HTO, Be, $^{36}\text{Cl}^-$ and $^{129}\text{I}^-$ across the interface bentonite porewater/low-pH cement is presented. Porosity changes due to dissolution/precipitation reactions with feedback on transport properties is also assessed observing the formation of a degraded area in the cement phase of ~2 mm after one month of alteration. The alteration of the low-pH cement paste is mainly due to the partial kinetic dissolution of C-(A)-S-H phases resulting in an increase of the porosity. The carbonation of the cement is linked to the precipitation of calcite and thus the additional decalcification of the C-(A)-S-H phases.

The implementation of the different processes affecting HTO, Be, $^{36}\text{Cl}^-$ and $^{129}\text{I}^-$ (sorption/incorporation to cement) is on-going at this moment and all of them are considered as non-reactive tracers reaching steady-state diffusion after 5 days of interaction,

1 Introduction

Current deep geological repository concepts are based on the confinement of radioactive waste over a long period of time by multiple barriers. Many of the concepts developed internationally use concrete and clay as confinement barriers (ANDRA, 2005; ENRESA, 1995). Depending upon the design, cement could physically contact clay, or be sufficiently close to the point that porewater from both materials interact due to the large concentration gradients across this interface, thereby affecting in time and space their physico-chemical properties.

In the last 15 years, a substantial effort has been made in the development of predictive simulations of the long-term interactions between different clays and cementitious materials. Most of the studied systems have been mainly modelled as Thermo-Hydro-Chemical (THC) coupled processes at the continuum scale with various degrees of complexity. Most of these studies are related to the interaction of ordinary Portland cement type with clay (bentonite barrier or clay host rocks), but very few effort has been dedicated to study ‘low-pH’ cements/clay interactions. Low-pH cements were developed within the nuclear waste disposal context in the late 90’s (Gray and Shenton, 1998) the main feature of these cements is the less alkaline pore solution (pH ~11) compared to what is observed in “classical” cements and the absence of portlandite as hydrated solid phase. The Ca/Si ratio in the hydrated low-pH cement paste is less than 1.0 and C-(A)-S-H phases are the main solids present.

This work includes a predictive reactive transport model of the interface processes between a low-pH cement (50 wt.% CEM I 52.5N + 50 wt.% silica fume) and a MX-80 bentonite porewater and assesses the specific impact on HTO, ^{36}Cl , ^{129}I and Be migration. The modelling work supports the interpretation of the experimental results performed within CEBAMA and helps to identify possible missing parameters and to the process understanding.

2 Description of the system and conceptual model

The predictive reactive transport model consists of a one-dimensional (1D) fully water saturated isothermal (298 K) problem representing a laboratory through diffusion experiment of HTO, Be, ^{36}Cl , and ^{129}I across the interface bentonite porewater/low-pH cement (Ait Mouheb et al., 2018, *this document*). Porosity changes due to dissolution/precipitation reactions with feedback on the effective diffusion coefficient is also studied. A schematic representation of the diffusion experiments is presented in Figure 1. Diffusion of the selected tracers occurs across the interface between bentonite porewater and the low-pH cement MIX 3E (50 wt.% CEM I 52.5N + 50 wt.% silica fume) described in Ait Mouheb et al. (2017, 2018, *this document*).

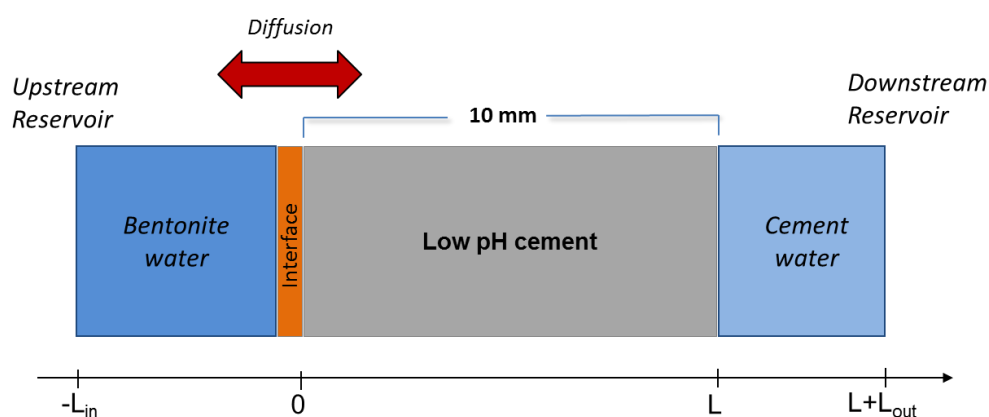


Figure 1: Schematic representation of the through diffusion experiments.

3 Model implementation

The system is implemented in the code PHREEQC v.3 (Parkhurst and Appelo, 2013) which can take into account geochemical and physical parameters variations due to mineralogical evolutions as a function of time.

3.1 Geometry, time and space discretization

Geometrical and transport parameters including the discretization of the system (water and solid domains) have been initially implemented. The studied periods correspond to 14 min, 5 days and 30 days. The mesh size and the time steps have been selected to ensure a satisfactory compromise between computation time and sufficient spatial resolution of the expected geochemical and transport processes, especially at the interface between the bentonite porewater and the hydrated low-pH cement. The proposed discretization is presented in Table 1. Note that the downstream reservoir is not discretized and it is included as boundary condition. A constant concentration and close flux condition has been imposed on the extremities of the upstream and the end of the low pH cement, respectively.

Table 1: Spatial discretization of the modelled system. Note: the downstream reservoir is not included in the model.

x (mm)	Mesh/grid size (mm)	Domain
0-18	1	Bentonite water
18-20	0.5	Bentonite water
20-30	0.5	Low pH cement

3.2 Physical properties (transport)

Mass transport in saturated porous medium can be numerically described by the “advection-dispersion-reaction” equation (Eq. 1), where C is the solute concentration in water (mol/kg_w), t is time (s), v is pore water flow velocity (m/s), x is distance (m), D_L is the hydrodynamic dispersion coefficient (m²/s, $D_L = D_e + \alpha_L v$), with D_e as effective diffusion coefficient and α_L the dispersivity (m), and q is concentration in the solid phase (expressed as mol/kg_w in the pores):

$$\frac{\partial C}{\partial t} = -v \frac{\partial C}{\partial x} + D_L \frac{\partial^2 C}{\partial x^2} - \frac{\partial q}{\partial t} \quad (1)$$

Considering no fractures in the sample and the very low permeability of cement, the advective transport term $\left(-v \frac{\partial C}{\partial x}\right)$ has been neglected and only diffusion-driven mass transport will be considered following Fick’s laws (Eq. 2) where the molar flux (J , [mol/m²·s]) is proportional to the concentration gradient $\frac{\partial C}{\partial x}$ (mol/m⁴):

$$J = -D_e \frac{\partial C}{\partial x} \quad (2)$$

An initial porosity of 35% has been determined experimentally by mercury intrusion porosimetry (MIP) in Ait Mouheb et al. (2017). Accordingly, the values for the transport parameters used in the numerical model have been tentatively selected as follows: total porosity $\phi = 0.35$ and pore diffusion coefficient, $D_p = 10^{-10}$ m²/s. The effective diffusion coefficient, was then related to the porosity according to Archie’s law assuming $n = 1$ (Eq. 3). However, the appropriate expression for calculating the effective diffusion coefficient will be updated in the model when it will be available during 2018 by through diffusion experiments of HTO (Ait Mouheb et al., 2018, *this document*).

$$D_e = D_p(\phi)^n \quad (3)$$

Additionally, porosity changes due to mineral precipitation/dissolution and feedback on the effective diffusion coefficient are also taken into account considering the molar volumes of the different solids formed or dissolved (Eq. 4).

$$\phi^{k+1} = 1 - \phi_{inert} - \sum_{i=1}^{N_m} V_{m,i} c_{m,i}^{k+1} \quad (4)$$

where:

ϕ = porosity

V_m = molar volume (m³/mol)

N_m = number of minerals

c = molality (mol/kg_w)

Electrostatic surface interactions are not included, although they may influence the transport of the anionic tracers $^{36}\text{Cl}^-$, $^{129}\text{I}^-$ and $\text{Be}(\text{OH})_3^-$ (Chagneau et al., 2015).

3.3 Thermodynamic database and chemical input parameters

Chemical reactions at equilibrium and kinetically controlled have been simulated using the thermodynamic database ThermoChimie v. 9b available in PHREEQC format (Giffaut et al., 2014) at the moment that this work was started. Update of the thermodynamic database according to new thermodynamic data available in 2018 is on-going (i.e. Roosz et al., 2018; Lothenbach et al., 2018). Additionally, thermodynamic data for the aqueous speciation of Be has been included according to Gaona et al. (2018, *this document*). Debye-Hückel equation, valid for the ionic strength of the studied system (< 0.3 M) is preferred to save computational time as it has been observed that calculations performed with SIT (Specific ion Interaction Theory) equation needs more computational effort. ThermoChimie v.9b includes hydrates commonly encountered in Portland cement systems in the temperature range 0-100 °C. Rate equations of precipitation/dissolution of secondary/primary phases are provided directly in the input files of PHREEQC by using the general equation given by Lasaga (2014) (Eq. 5).

$$r_n = \pm k_n S_n |1 - \Omega_n^\theta|^\eta \quad (5)$$

where:

r_n is the dissolution/precipitation rate of the mineral n (mol/(m³·s)),

S_n is the specific mineral surface area (m²/m³),

k_n is the kinetic dissolution /precipitation rate constant (mol/m²·s¹),

Ω_n is the saturation ratio.

The two parameters θ and η empirically describe the dependence of the reaction rate on the saturation ratio.

In Table 2, a summary of the selected kinetic parameters described in Marty et al. (2015) and Baur et al. (2004) is given.

Table 2: Selected parameters for the precipitation/dissolution reactions.

Minerals	Reactive surface area (m ² /g)	k_n (mol/(m ² ·s))	θ	η	Source
Ettringite	9.8	$1.2 \cdot 10^{-12}$	1	1	Baur et al. (2004)
CSH0.8	41	$k_n = f(\text{pH})$	1	1	Marty et al. (2015)
C-A-S-H	Set to C-S-H0.8		1	1	No data available
Calcite		Equilibrium assumed			

Additionally, the pH dependence of the dissolution/precipitation rate constant of the C-S-H phases is also implemented in the model by using the following equation (Eq. 6):

$$k_n = k_{25}^{nu} \exp \left[\frac{-E_a^{nu}}{R} \left(\frac{1}{T} - \frac{1}{298.15} \right) \right] + k_{25}^H \exp \left[\frac{-E_a^H}{R} \left(\frac{1}{T} - \frac{1}{298.15} \right) \right] (a_H)^{n_H} \quad (6)$$

where:

nu and H refer to a neutral and acidic environment, respectively,

k_{25} is the intrinsic kinetic constant at 298.15 K (25°C),

E_a is activation energy (J),

The term a_H^n is the activity of H^+ to the power of n,

R is the ideal gas constant (8.314 J/(mol K) and T is the reaction temperature (K).

Taking into account that variation of temperature is not studied in this work, the equation (Eq 6) can be simplified as follows (Eq 7):

$$k_n = k_{25}^{nu} + k_{25}^H (a_H)^{n_H} \quad (7)$$

where:

$$k_{25}^{nu} = 1.6 \cdot 10^{-18} \text{ mol}/(\text{m}^2 \cdot \text{s})$$

$$k_{25}^H = 5.9 \cdot 10^{-8} \text{ mol}/(\text{m}^2 \cdot \text{s})$$

$$n_H = 0.28$$

In the present status, sorption of the tracers in the cement matrix is not included. Sorption reactions of $^{36}\text{Cl}^-$, $^{129}\text{I}^-$ and Be tracers into the low-pH cement matrix will be considered as a thermodynamic mechanistic sorption model to be implemented in PHREEQC as a test case. Observations described in the recent review of Ochs et al. (2016) will be considered to select the most appropriate data, as well as data generated in the CEBAMA project, consisting of batch experiments of the studied radionuclides on the same solid materials (Ait Mouheb et al., 2017).

3.4 Initial mineralogy, porewater composition and geochemical modeling

The initial mineralogical composition of the cement hydrated phases has been determined experimentally in Ait Mouheb et al. (2017) and it is representative of a full hydrated low-pH cement (pH ~11.0) with a 93 wt.% being formed by C-(A)-S-H phases with a Ca/Si ratio of 0.8, as shown in Table 3. At this moment, it has not been possible to experimentally identify the solid phase containing iron and for this reason we have assumed that iron phases are in the form of Fe-ettringite. However, information of the iron speciation in the solid phase is expected to be obtained during 2018 (Vehmas et al., 2018, *this document*).

Table 3: Initial mineralogical composition in the low-pH cement paste determined experimentally and parameters used in the model.

Minerals	Mass fraction	Molar volume (cm ³ /mol)	Formula	Volume fraction	Process
C-S-H (am)	0.93	59.29	Ca _{0.8} SiO _{2.8} x 1.54H ₂ O	0.65	Kinetics $k_n = f(\text{pH})$
Ettringite	0.07	710.32	Ca ₆ Al ₂ (SO ₄) ₃ (OH) ₁₂ x 26H ₂ O	0.01	Kinetics
C-A-S-H	??	(72.0 - 59.29)	Ca _{0.8} (Si,Al _{1-x})O _{2.8+z} x YH ₂ O	-	-
Calcite	-	36.93	CaCO ₃	-	Equilibrium
Fe(OH) ₃	-	-	Fe(OH) ₃	-	-
Silica Fume	< 0.01	29.00	SiO ₂	-	-

Minerals	Mass fraction	Molar volume (cm ³ /mol)	Formula	Volume fraction	Process
Portlandite	-	33.06	Ca(OH) ₂	-	-
Porosity	-		-	0.34	-

Additionally, the hydration model (see Figure 2) of the low-pH cement, has also been performed using the code GEMS (Kulik et al., 2013) and the most updated CEMDATA18 database (Lothenbach et al., 2018) and it will be compared with the pore water composition, total porosity and the mineralogy composition obtained experimentally. The hydration model has not yet been used as input parameters of the initial conditions for the reactive transport model, in order to avoid inconsistencies with the use of different thermodynamic databases in the hydration model and the reactive transport model. This work will be done in the future when CEMDATA18 will be available in PHREEQC format.

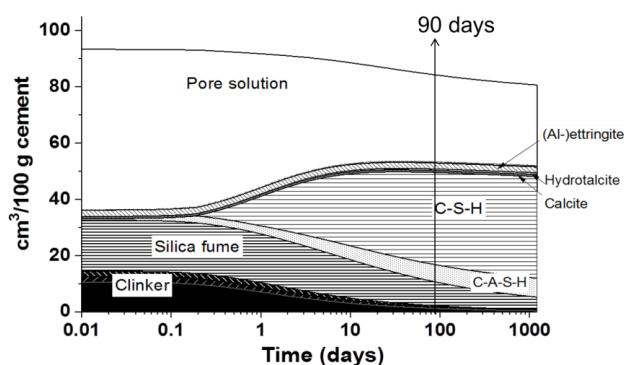


Figure 2. Hydration model of the low pH cement sample.

The initial porewater composition of the low-pH cement is defined as the experimental measured concentrations by ICP-MS and compares well with the calculated pH of a porewater in equilibrium with a C-S-H hydrated phase with low Ca:Si ratio present in the system. The porewater composition of the clay is representative of the MX-80 bentonite described in the literature (Wersin et al., 2003) and has been synthesized and measured in the laboratory (see Table 4).

Table 4: Initial pore water compositions used in the reactive transport model. Arrows represent the gradient of concentration to the bentonite water (blue) or to the cement (red).

	MX-80		Cement
pH	7.74	←	11.1
Ionic strength			
Solutes (mol/L)			
Na	0.31	→	5.70×10^{-3}
K	1.54×10^{-3}		7.50×10^{-3}
Ca	1.33×10^{-2}	←	6.70×10^{-3}
Cl	0.22	→	2.30×10^{-3}
SO ₄	6.86×10^{-2}		1.12×10^{-2}
Si	1.80×10^{-4}	←	1.22×10^{-3}
Al	2.11×10^{-8}	←	1.10×10^{-7}
Fe	5.00×10^{-5}	→	7.70×10^{-8}
Mg	9.63×10^{-3}	→	2.70×10^{-6}
CO ₃	9.20×10^{-4}	→	3.88×10^{-6}
³⁶ Cl	$4.55 \cdot 10^{-6}$		-
¹²⁹ I	$5.93 \cdot 10^{-5}$		-
HTO	$1.86 \cdot 10^{-9}$	→	-
Be	$>1 \cdot 10^{-8}$ (Be(OH) ₂ (s))		-

4 Results and discussion of the reactive transport simulations

The simulations were carried out for three different times of interaction (14 min, 5 days and 30 days) predicting that the low-pH cement in contact with the bentonite pore water will have a degraded area of ~2 mm after one month of alteration. No significant changes can be appreciated in the cement solid after 5 days (Figure 3). The alteration of the low-pH cement paste is mainly due to the partial dissolution of C-(A)-S-H phases (set as single C-S-H phases with low Ca:Si ratio) controlled by kinetic rates resulting in an increase of the porosity due to the difference of the molar volumes between the initial solids and the final products of the alteration process in the interface (Figure 3 and Figure 4). Carbonation is linked to the precipitation of calcite and thus the decalcification of C-(A)-S-H phases (Jenni et al., 2014). Magnesium enrichment in the decalcified area has been reported in the literature (Jenni et al., 2014; Dauzères et al., 2016). In our system, brucite is undersaturated, and attempts to model the magnesium perturbation using available thermodynamic data suggested the formation of hydrotalcite. However, the recent determination of solubility data for M-S-H phases will make it possible to account for the potential formation of M-S-H phases (Dauzères et al., 2016) and will be considered in the future. Finally, no attempts have been done to model the iron evolution.

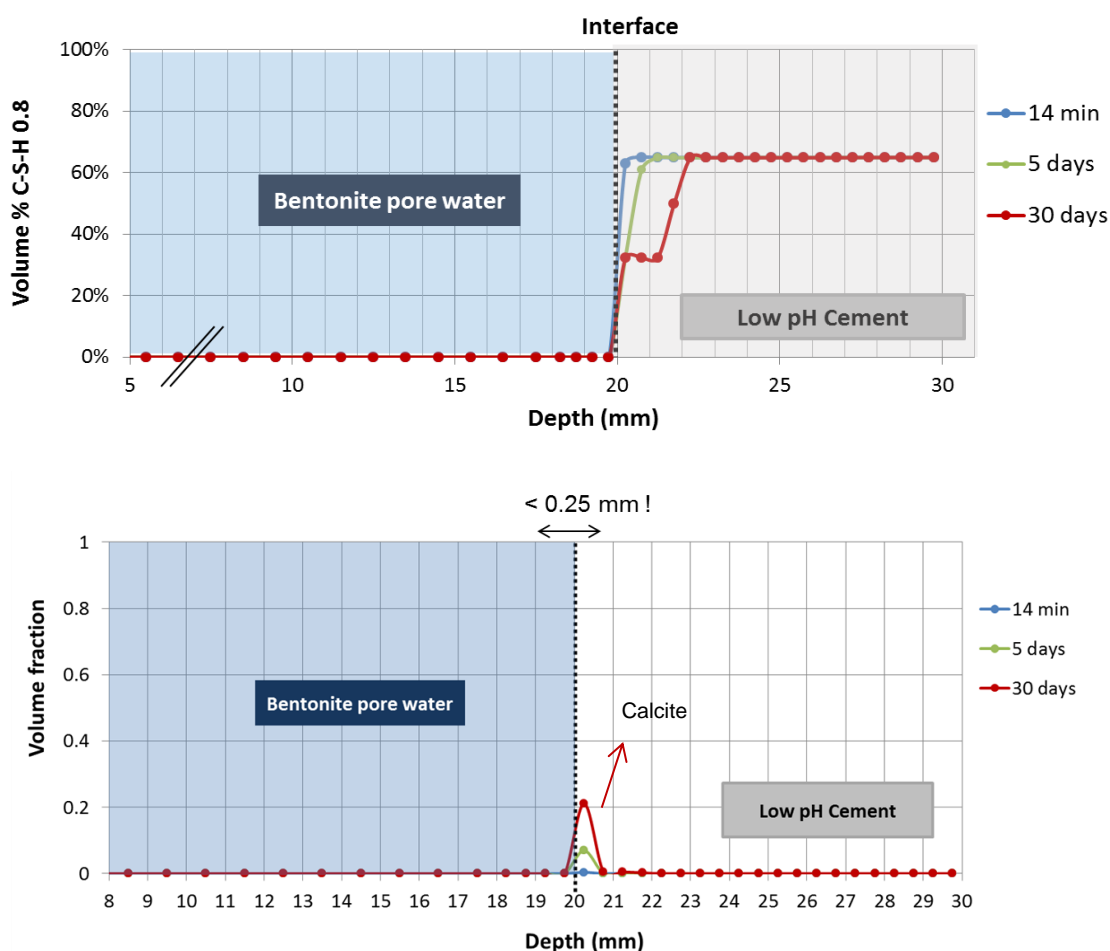


Figure 3: Simulation of the low-pH cement alteration at different periods of time represented as volume fraction of C-S-H phases dissolved vs. depth (top) and volume fraction of calcite precipitated vs. depth (down). The main process identified is the partial dissolution of C-S-H phases and carbonation.

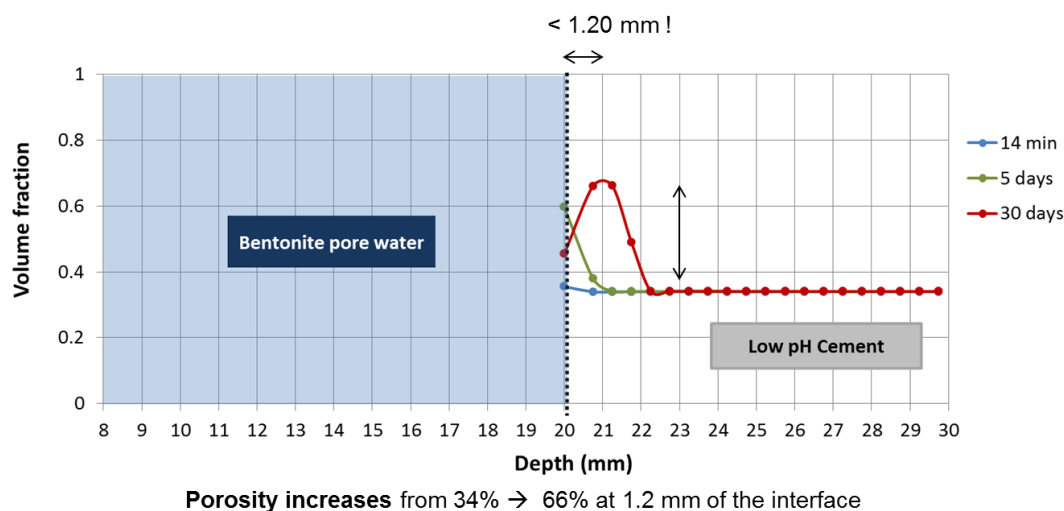


Figure 4: Simulation of the low pH cement alteration at different periods of time. The main process identified is the partial dissolution of C-S-H phases resulting in an increase of the porosity at few millimeters close to the interface bentonite/cement.

The diffusion of HTO at initial concentration of $1.86 \cdot 10^{-9}$ M in the system will reach steady-state after 5 days of interaction (Figure 5) which is similar to the results obtained for Be as at this moment as beryllium has been incorporated in the model as non-sorbing tracer as only the aqueous speciation of this metal is included in the model.

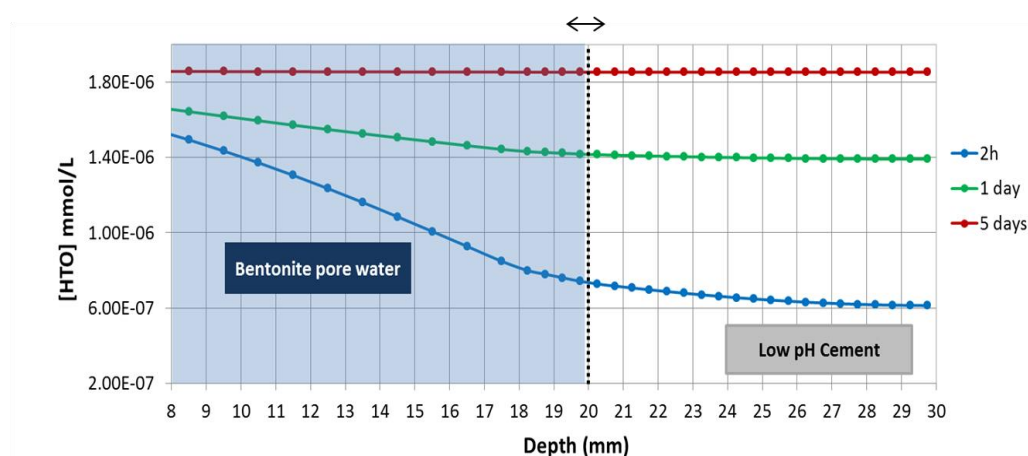


Figure 5: Simulation of the HTO diffusion in the low pH cement / bentonite interface.

5 Conclusion and Future work

We have developed and implemented a 1D model to simulate the interaction between a low-pH cement and bentonite porewater. The model considered a low-pH cement paste (pH ~11.0) synthesized in the CEBAMA project with a 93 wt.% of the initial mineralogy being C-(A)-S-H phases with a Ca:Si ratio of 0.8. The simulations predict the formation of a degraded area in the cement phase of ~2 mm after one month of alteration. The alteration of the low-pH cement paste is mainly due to the partial kinetic dissolution of C-(A)-S-H phases resulting in an increase of the porosity. The carbonation of the cement is linked to the precipitation of calcite and thus the additional decalcification of the C-S-H phases.

Finally, the diffusion of a not reactive and uncharged tracer (HTO) at initial concentration of $1.86 \cdot 10^{-9}$ M from the bentonite porewater to the low-pH cement in the present system would reach the steady state after 5 days of interaction. The implementation of all the processes (sorption/incorporation to the solid material) affecting the radionuclides or toxic elements studied ($^{36}\text{Cl}^-$, $^{129}\text{I}^-$ and Be) is on-going and it is still not implemented.

The model will be improved including the iron and M-S-H solid phases in the system. Additionally, the model will be implemented in the iCP interface (Nardi et al., 2014) and compared with the results obtained with PHREEQC and with the mentioned through-diffusion experiments which are on-going at this moment.

Acknowledgement

The research leading to these results has received funding from the European Union's Horizon 2020 Research and Training Programme of the European Atomic Energy Community (EURATOM) (H2020-NFRP-2014/2015) under grant agreement n° 662147 (CEBAMA). Additionally, the authors would like to express their appreciation to Andres Idiart for valuable comments.

References

- Ait Mouheb, N., Montoya, V., Borkel, C., Schäfer, T. (2017). Experimental studies on low pH cement/clay interface processes: Characterization of low pH cements. *In*: M. Altmaier, V. Montoya, L. Duro, A. Valls (Eds.) Proceedings of the 1st Annual Workshop of the CEBAMA Project. KIT Scientific Report, 7734.
- Ait Mouheb, N., Montoya, V., Joseph, C., Schäfer, T., Geckeis, H. (2018) Diffusion of tritiated water and chloride-36 through low pH cements. *In*: M. Altmaier, V. Montoya, L. Duro, A. Valls (Eds.) Proceedings of the 3rd Annual Workshop of the CEBAMA Project. *This document*.
- Ait Mouheb, N., Montoya, V., Schild, D., Soballa, E., Adam, C., Geyer, F., Schäfer, T. (2017). Characterization and sorption properties of low pH cements. *In*: M. Altmaier, V. Montoya, L. Duro, A. Valls (Eds.) Proceedings of the 2nd Annual Workshop of the CEBAMA Project. KIT Scientific Report, *in press*.
- ANDRA (2005). Andra research on the geological disposal of high-level long-lived radioactive waste—results and perspectives. June, 2005.
- Baur, I., Keller, P., Mavrocordatos, D., Wehrli, B., Johnson, Ca.A. (2004). Dissolution-precipitation behaviour of ettringite, monosulfate, and calcium silicate hydrate. *Cement and Concrete Research*, 34, 341-348.
- Chagneau, A., Tournassat, C., Steefel, C.I., Bour, I.C., Gaboreau, S., Esteve, I., Kupcik, T., Claret, F., Schäfer, T. (2015). Complete restriction of $^{36}\text{Cl}^-$ diffusion by celestite precipitation in Densely compacted illite. *Environmental Science & Technology Letters*, 2, 139-143.
- Dauzeres, A., Achiedo, G., Nied, D., Bernard, E., Alahrache, S., Lothenbach, B. (2016). Magnesium perturbation in low-pH concretes placed in clayey environment—solid characterizations and modelling. *Cement and Concrete Research*, 79, 137-150.
- ENRESA (1995). Almacenamiento Geológico Profundo de residuos radiactivos de alta actividad (AGP). Diseños conceptuales genéricos. Publicación Técnica, ENRESA 11/95.
- Gray, M.N. and Shenton, B.S. (1998). For better concrete, take out some of the cement. *In*: Proceedings of 6th ACI/CANMET Symposium on the Durability of Concrete, Bangkok, Thailand.
- Kulik, D.A., Wagner, T., Dmytrieva, S.V., Kosakowski, G., Hingerl, F.F., Chudnenko, K.V., Berner, U.R. (2013). GEM-Selektor geochemical modeling package: revised algorithm and GEMS3K numerical kernel for coupled simulation codes. *Computational Geosciences*, 17, 1-24.

- Gaona, X., Cevirim-Papaioannou, N., Böttle, M., Altmaier, M. (2018). Solubility and hydrolysis of Be(II) in dilute to concentrated NaCl and KCl solutions. *In*: M. Altmaier, V. Montoya, L. Duro, A. Valls (Eds.) Proceedings of the 3rd Annual Workshop of the CEBAMA Project. *This document*.
- Giffaut, E., Grivé, M., Blanc, P., Vieillard, P., Colàs, E., Gailhanou, H., Gaboreauc, S., Marty, N., Madé, B., Duro, L. (2014). Andra thermodynamic database for performance assessment: ThermoChimie. *Applied Geochemistry*, 49, 225-236.
- Jenni, A., Mäder, U., Lerouge, C., Gaboreau, S., Schwyn, B. (2014). In situ interaction between different concretes and Opalinus Clay. *Physics and Chemistry of the Earth, Parts A/B/C*, 70-71, 71-83.
- Lasaga, A.C. (2014). *Kinetic theory in the earth sciences*. Princeton University Press.
- Marty, N., Claret, F., Lassin, A., Tremosa, J., Blanc, P., Madé, B., Giffaut, E., Cochevin, B., Tournassat, C. (2015). A database of dissolution and precipitation rates for clay-rocks minerals. *Applied Geochemistry*, 55, 108-118.
- Nardi, A., Idiart, A., Trinchero, P., de Vries, L.M., Molinero, J. (2014). Interface COMSOL-PHREEQC (iCP), an efficient numerical framework for the solution of coupled multiphysics and geochemistry. *Computers & Geosciences*, 69, 10-21.
- Ochs, M., Mallants, D., Wang, L. (2016). *Radionuclide and metal sorption on cement and concrete*. Springer International Publishing Switzerland.
- Parkhurst, D.L. and Appelo, C.A.J. (2013). Description of input and examples for PHREEQC Version 3 — A computer program for speciation, batch-reaction, one-dimensional transport, and inverse geochemical calculations. *U.S. Geological Survey Techniques and Methods*, book 6, chapter A43, 6-43A.
- Roosz, C., Vieillard, P., Blanc, P., Gaboreau, S., Gailhanou, H., Braithwaite, D., Montouillout, V., Denoyel, R., Henocq, P., Madé, B. (2018). Thermodynamic properties of C-S-H, C-A-S-H and M-S-H phases: Results from direct measurements and predictive modelling. *Applied Geochemistry*, 92, 140-156.
- Vehmas, T., Leivo, M., Holt, E., Alonso, M.C., Fernández, A., García Calvo, J.L., Vašíček, V., Červinka, R., Večerník, P., Rosendorf, T., Svoboda, J., Finck, N., Montoya, V., Ait Mouheb, N., Dardenne, K., Rothe, J., Schäfer, T., Geckeis, H., Gaboreau, S. (2018). Cebama reference mix design for low pH concrete and paste, intermediate results. *In*: M. Altmaier, V. Montoya, L. Duro, A. Valls (Eds.) Proceedings of the 3rd Annual Workshop of the CEBAMA Project. *This document*.
- Wersin, P. (2003). Geochemical modelling of bentonite porewater in high-level waste repositories. *Journal of Contaminant Hydrology*, 61, 405-422.

Influence of internal relative humidity on the hydration of a low-pH cement. A modelling study.

Andrés Idiart^{1*}, Marcelo Laviña¹, Javier Olmeda¹

¹ Amphos 21 Consulting S.L. (ES)

* Corresponding author: andres.idiart@amphos21.com

Abstract

A low-pH cement mix is being used by USFD within CEBAMA for a set of chemical alteration experiments. During cement hydration, the mixing water is partially consumed to form hydrates. This cement mix contains a substantial amount of supplementary cementitious materials and a low water-to-binder ratio. If proper curing is not considered, self-desiccation may occur, leading to a decrease in the rate of hydration. The effect of curing can only be considered in a model if an open system is assumed. However, modelling of cement hydration using geochemical simulators have traditionally entailed the hydration process as a closed system, with no interaction with the environment. Hydration is simulated using thermodynamic modelling coupled with a set of dissolution kinetic reactions for the binder. The role of the internal relative humidity is studied here by coupling the hydration model with humidity-dependent dissolution rates of the binder. The model is used to assess the effect of internal moisture evolution on the degree of hydration and on the chemical composition of the system.

1 Introduction and objectives

The geological disposal of radioactive waste management in European countries relies to a relatively large extent, depending on the country, on the use of cementitious materials as one of the main engineered barriers. Besides their mechanical and structural properties, cement-based materials are preferred over other materials due to the low permeability and capacity to retain radionuclides via adsorption or exchange reactions, helping to prevent their potential migration. The assessment of the long-term performance of these barriers is of paramount importance to predict how will their safety functions will be affected. These barriers are typically designed to be used simultaneously with bentonite barriers and natural clay formations. In this context, the stability of clay minerals can be significantly affected in the long-term by the alkalinity of the concrete pore solution. To partly remedy this, low-pH cements have been developed in recent years. Low-pH cement mixes are being used in a set of chemical alteration experiments within CEBAMA (Vehmas et al., 2017). Typically, low-pH cement mixes are based on a significant substitution of cement by Supplementary Cementitious Materials (SCM). In combination with superplasticizers, the water-to-binder (w/b) ratio of these mixes is usually low. The hydration of these systems will therefore be affected by self-desiccation, a process by which the internal relative humidity (RH) decreases due to the consumption of water in the formation of cement hydrates. Consequently, it is well-known that the rate of hydration gradually decreases with moisture content and the hydration process is virtually stopped when reaching a threshold relative humidity (Jensen and Hansen, 2001). In the long term, however, moisture transfer from the surrounding environment may supply enough water to continue the hydration. Under these circumstances, the chemical composition and the resulting physical properties such as effective diffusion coefficient or permeability may be significantly affected. For instance, the apparent diffusion coefficient for

chloride ingress decreases as a function of time much more rapidly in mixes with high substitution of cement by SCM than in OPC (Riding et al., 2013). A deep understanding of the long-term evolution of the physical and chemical properties of low-pH cementitious systems is essential for their use in geological disposal of radioactive waste. Knowledge about the expected evolution of the transport properties with time of these barriers can have a crucial impact on the Safety Case of a repository.

Characterization and leaching experiments using two different cementitious systems are currently being conducted at the University of Sheffield within WP1 of CEBAMA: the NRVB high-pH cement (Vasconcelos et al., 2018a) and a low-pH cement paste mix cured for 28 days based on (Vehmas et al., 2017, Vasconcelos et al., 2018b). The goal of these experiments is to study the degradation by leaching of small samples when in contact with different synthetic groundwater compositions. However, given the short curing period and the low w/b ratio of the mix, it is expected that the impact of continued hydration of the binder during the leaching experiments will play an important role.

The ultimate goal of the present work is to increase our understanding about how the transport properties of low-pH cement and concrete designed with a low w/b ratio evolve with time as a result of continued long-term hydration and interaction with the surrounding materials. To this end, the above-mentioned leaching experiments on low-pH cement paste samples will be simulated by means of thermodynamic modelling of cement hydration, coupled to reactive transport modelling (Nardi et al., 2014) and moisture transfer (Idiart et al., 2011). The same mechanistic modelling strategy can be used to upscale in time and length to repository conditions. As a first step, in this contribution a model to simulate the hydration of these mixes is developed, coupling thermodynamic modelling (Lothenbach et al., 2008) with moisture-dependent dissolution kinetic rates of the binder components (Wyrzykowski and Lura, 2016). This approach is based on combining a set of humidity-dependent kinetic reactions of dissolution of the mix components with thermodynamic equilibrium calculations. The results of the hydration model are presented and its implications for the experimental leaching tests are discussed.

2 Description of experiments on cement paste

The composition of the mix used to cast 15 x 15 mm cylindrical specimens is given in Table 1. The oxide composition of the mix components considered in the model is listed in Table 2. The w/b ratio is 0.25. Samples were cured for 28 days at a temperature of 40°C with a relative humidity of $\geq 95\%$. The mineralogical composition of the hydrated cement paste after 28 days has been characterized using XRD, TGA-MS and SEM. The phases identified are the following: C-S-H, ettringite, a hydrotalcite-group phase, hydrogarnet and monocarboaluminate, clinker phases, silica fume (SF), and blast furnace slag (BFS). The total porosity, characterized by MIP, is 0.19, with a threshold pore entry radius below 0.2 μm . Micro tomography images of the hydrated cement paste have also been obtained on smaller samples.

Table 1: Composition of low-pH cement paste mix used in experiments.

Component	Amount (g/100g _{solid})	Density (kg/m ³)	Volume fraction (-)	Surface area (m ² /g)
CEM I 42.5 (C)	37.5	3,100	0.18	0.31
Silica fume (SF)	39.3	2,300	0.25	26.09
Blast furnace slag (BFS)	23.2	2,900	0.12	0.40
Superplasticizer (SP)	6.0	1,200	0.07	-
Water (W)	25	1,000	0.37	-
Total	131.0		1.00	1.00

Table 2: Oxide composition of mix components used in the model, as measured in CEBAMA.

Oxide	M _w (g/mol)	CEM I (wt.%)	SF (wt.%)	BFS (wt.%)
CaO	56.08	64	1.46	41.5
SiO ₂	60.08	21	93.1	32.8
Al ₂ O ₃	101.96	3.5	1.44	10.6
SO ₃	80.06	2.2	0.47	1.4
MgO	40.30	0.7	0.88	8.29
Fe ₂ O ₃	159.69	4.6	0.91	0.81
K ₂ O	94.20	0.62	1.73	0.62
Na ₂ O	61.98	0.07	-	0.62
CO ₂	44.01	2.2	-	-

3 Modelling the hydration of low-pH cement paste

The hydration model is implemented in Phreeqc version 3 (Parkhurst and Appelo, 2013) and is based on the work by Lothenbach et al. (2008). A set of kinetic reactions for the dissolution of the mix components is coupled to chemical equilibrium calculations of precipitation/dissolution of cement hydrates using the thermodynamic database Thermochemie version 9b (Giffaut et al., 2014). The result of the hydration model includes the porewater and mineralogical composition of the solid, and the total porosity. To this end, a closed system is typically considered, using the exact amounts of the mix (Table 1) in a batch calculation. Therefore, the effect of moisture transfer during the curing period is disregarded. Moreover, the dependence of the dissolution rates on the availability of water has usually not been given sufficient attention. These are important simplifications, especially in the studied system, due to the low water/solid ratio (0.25) and the small size of the samples (radius of 7.5 mm). In this case, water consumption (self-desiccation) is expected to be partly or even totally compensated by moisture transfer from the curing chamber.

The dissolution rates of the clinker phases (alite, belite, aluminate and ferrite) correspond to the empirical expressions proposed by Parrot and Killoh (1984). In turn, the (constant) dissolution rate of the BFS is taken from Schöler et al. (2017), while that of SF corresponds to the pH-dependent rate of quartz from Palandri and Kharaka (2004), based on transition state theory. The specific surface areas in Table 1 are either specified directly by the manufacturers or derived from their particle size distribution.

The rate of dissolution of each mix component decreases with the internal RH of the sample to account for the effect of limited water content during hydration. The humidity-dependent factor proposed by Wyrzykowski and Lura (2016), who studied low w/b mixes with high replacements of SF and BFS, is used in the present work (Eq. 1).

$$\beta_{RH} = \min[1; 3.7 \cdot RH^{25}] \quad (1)$$

In order to relate RH changes with the water content evolution calculated in the geochemical simulator, the sorption/desorption isotherms are used (Baroghel-Bouny, 2007). The model used in this study to relate RH and water content is based on experimental data for low w/b cementitious systems with SCM additions (Olsson et al., 2018). As a first approximation, the desorption isotherm used corresponds to a mortar sample with 70% of BFS

replacement and 0.38 w/b ratio at the age of 8 months (Figure 1). The evaporable water content is updated in the geochemical solver as a function of the consumption of water by precipitating minerals. Using the curve in Figure 1, the RH is calculated dynamically and the dissolution rates are decreased by multiplication with the factor given by Eq. 1.

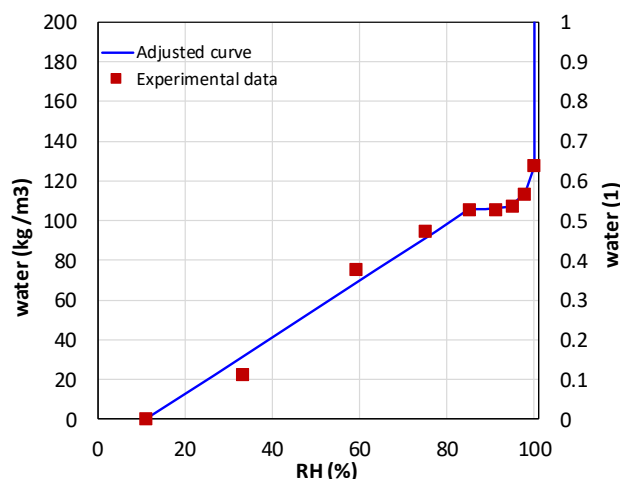


Figure 1: Water desorption curve as a function of RH, experimental results extracted from Olsson et al. (2018) (red dots) and adjusted curve implemented (blue).

The hydration simulation is performed at 40°C, correcting the kinetic rates of the clinker with activation energies from Lothenbach et al. (2008). The superplasticizer fraction is considered as chemically inert. The alkali uptake in C-S-H phases (Na and K) is considered using a cation exchange model based on Missana et al. (2017), with a cation exchange capacity that depends on the C-S-H concentration and its calcium-to-silica (C/S) ratio (Hong and Glasser, 1999). Aluminium uptake in C-S-H is however not considered in the simulations at this stage. To assess the influence of RH on dissolution rates of the binder components, two simulations are presented and compared. The first one (Model A) does not consider this dependency at all, while Model B includes the desorption isotherm and the humidity-dependent factor (β_{RH}) presented in Eq. 1.

4 Model results

Results from the two models are comparatively shown in terms of volume (cm³) per 100 g of solid to illustrate the implications of considering RH changes. The dissolution of the clinker and binder components as a function of time are shown in Figure 2. Both models show similar results during the first 10 days. Thereafter, dissolution of the clinker continues in Model A, while it is almost stopped in Model B due to the decrease in internal RH. The BFS and SF dissolution occurs between 1 day and some hundred days for Model A. At this point, BFS is completely dissolved, while SF stops dissolving due to the significant decrease in pH (Figure 2). Note that the dissolution of quartz is highly dependent on the pH of the pore solution. Similar to the clinker phases, SF and BFS dissolution in Model B is significantly slowed down after 10 days.

The evolution of the main phase assemblage of the cement hydrates is shown in Figure 3. Portlandite and C-S-H with C/S ratio 1.6 form rapidly. As hydration proceeds and more SiO₂ is released into the pore solution from dissolution of the binder (mainly from BFS and FA), portlandite dissolves and C/S ratio of C-S-H gradually decreases until reaching a value of 0.8 (Table 3). In Model A, C-S-H with higher C/S ratio is fully replaced by C-S-H of C/S ratio 0.8 after 100 days, while this process is much slower in Model B (a C-S-H of C/S ratio 1.2 is the main cement hydrate after 100 days, Figure 3). Other cement hydrates present after further hydration

(> 100 days) are ettringite, hydrotalcite, and strätlingite (although in smaller amounts for Model B than for Model A, due to self-desiccation).

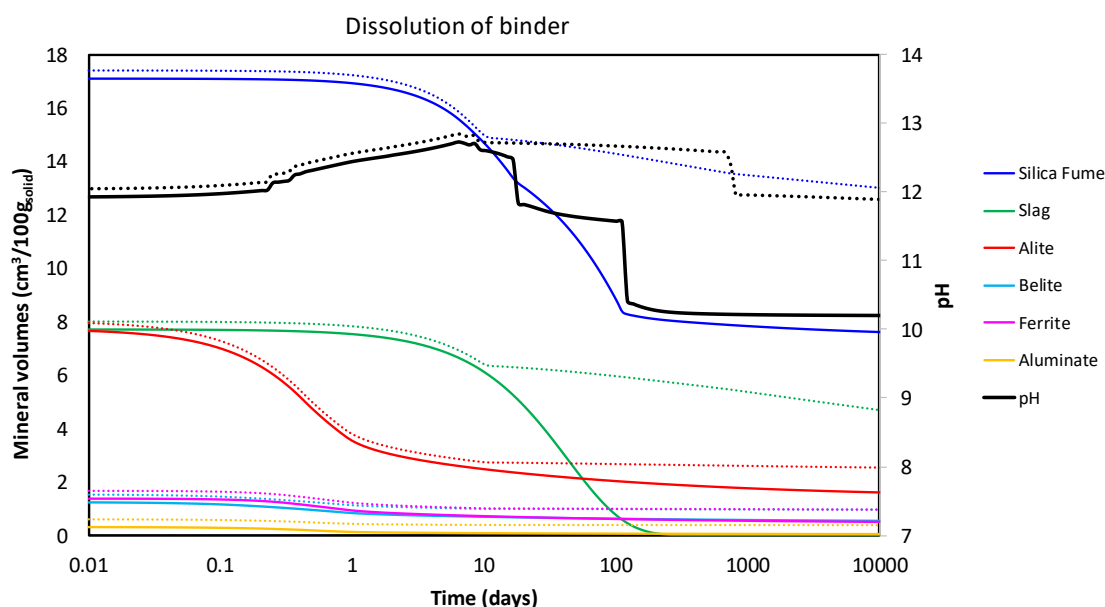


Figure 2: Dissolution of the binder: evolution of mineral volumes ($\text{cm}^3/100 \text{ g solid}$) and pH as a function of hydration time (days) for Model A (solid lines) and Model B (dotted lines).

The evolution of the pH is presented in Figure 2, showing a maximum value of 12.74 after ~7 days and then gradually decreasing upon portlandite redissolution and subsequent decalcification of the C-S-H (Figure 3). The pH reaches a plateau at around 10.2 after ~1 year of hydration for Model A, while pH only decreases to a value of 11.74 in Model B. This is due to the different C-S-H phase governing the system at this point. The largest pH drop is observed when C-S-H changes from C/S ratio 1.2 to 0.8 in Model A. At these values, the dissolution of SF is significantly slow, and the system reaches a situation close to equilibrium even though no effects of self desiccation on the dissolution rates are included in this model.

The mineralogical phase assemblage and porewater composition after both 28 and 365 days of hydration is shown in Table 3 and Table 4. It may be observed that portlandite formed at early ages has completely dissolved in both models after 28 days. The results also illustrate how the hydration is still significantly evolving between 1 month and 1 year of hydration, even if the amount of evaporable water is substantially reduced in the closed system setup assumed here. Hydration evolution between these two ages is not as noticeable for Model B, where self-desiccation significantly reduces the hydration rate after 10 days. The main differences between both models are again appreciable in C-S-H gels concentration and pH values.

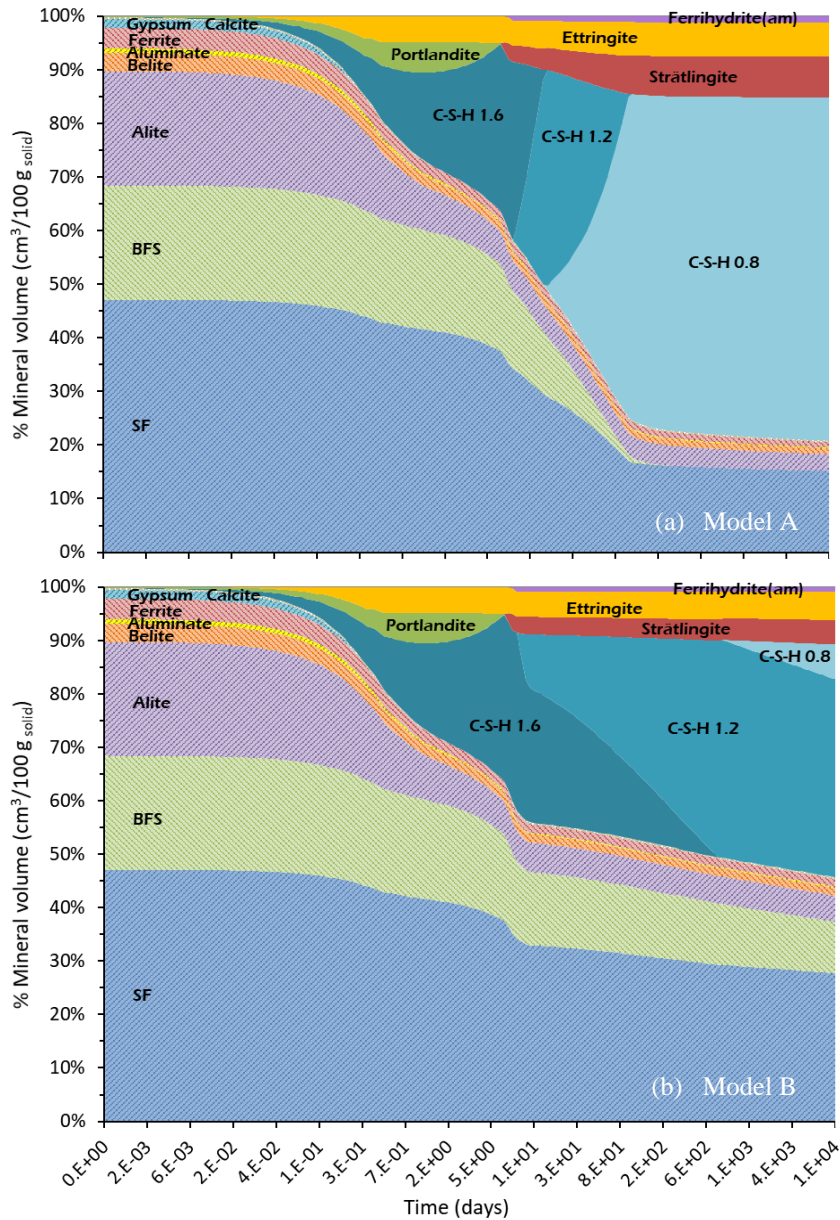


Figure 3: Evolution of main cement hydrates (in percentage $\text{cm}^3/100 \text{ g solid}$) as a function of hydration time (days) for (a) Model A and (b) Model B.

The total porosity (ϕ_{tot}) can be calculated from the hydration simulation if autogenous shrinkage is neglected. To this end, Eq. 2 can be used (Nardi et al., 2014). In this equation, ϕ stands for volume fraction (litre/litre medium), M_v for molar volume (litre/mol), c_m for mineral concentrations (mol/litre medium), and subscript inert for any chemically inert fraction. Total porosity evolution is shown in Figure 4 together with the evolution of the volume fraction of evaporable water (ϕ_w). The difference between these two quantities is the chemical shrinkage, ϵ_{ch} (litre/litre medium), which is the reduction in volume due to hydration. The values of total porosity after 28 days of hydration is 0.20 in Model A and 0.24 in Model B, while a slightly lower value (0.19) has been measured experimentally. The difference could be related to the effect of moisture transfer from the curing chamber in the experiment, leading to a higher volume of cement hydrates compared to the closed system considered in the model.

$$\phi_{tot} = 1 - \phi_{inert} - \sum_{i=1} c_{m,i} \cdot M_{v,i} \quad (2)$$

As a result of the hydration, the internal degree of saturation can be significantly reduced. From Figure 4, after 28 days, this reduction is from 1.0 to 0.7 (Model A) and 0.8 (Model B) litre water/litre pores. Therefore, even without considering the impact of moisture content on the dissolution rate, further hydration is hindered by this lack of water. This is a consequence of the assumption of a closed system (no moisture transfer from an external source). The evolution of the internal RH is shown in Figure 5, together with the humidity-dependent factor β_{RH} (Eq. 1). This factor drops sharply from a value of 1 to values below 0.05 when RH decreases from 0.95 to 0.84. This occurs at the age of 10 days, limiting further hydration of the system.

Table 3: Model results of the mineralogical phase assemblage after 28 days and 365 days of hydration for Models A and B.

Hydration time (days)	28	28	365	365
Model	Model A	Model B	Model A	Model B
Mineral	Concentration (mol/kg _{water})			
Portlandite	0.000	0.000	0.000	0.000
C-S-H 1.6	0.000	4.533	0.000	1.092
C-S-H 1.2	9.154	3.521	0.000	8.581
C-S-H 0.8	2.732	0.000	21.035	0.000
Ettringite	0.138	0.120	0.177	0.129
Calcite	0.135	0.135	0.135	0.135
Hydrotalcite	0.285	0.163	0.567	0.204
Strätlingite	0.403	0.278	0.694	0.319
Ferrihydrite (am)	0.527	0.458	0.684	0.485
Alite	1.227	1.332	1.013	1.289
Aluminate	0.036	0.039	0.029	0.038
Belite	0.511	0.533	0.460	0.524
Ferrite	0.212	0.225	0.182	0.220
SF	17.859	20.512	11.400	19.280
BFS	3.685	5.280	0.002	4.770

Table 4: Model results of porewater composition after 28 days and 365 days of hydration for Models A and B.

Hydration time (days)	28	28	365	365
	Model A	Model B	Model A	Model B
pH	11.75	12.60	10.24	12.50
Ionic strength (M)	0.101	0.255	0.145	0.181
Water mass (g)	0.393	0.518	0.105	0.472

Hydration time (days)	28	28	365	365
	Model A	Model B	Model A	Model B
Totals	Concentration (M)			
Al	$3.13 \cdot 10^{-4}$	$9.16 \cdot 10^{-4}$	$1.46 \cdot 10^{-4}$	$7.17 \cdot 10^{-4}$
Ca	$9.41 \cdot 10^{-4}$	$3.86 \cdot 10^{-4}$	$1.46 \cdot 10^{-2}$	$4.73 \cdot 10^{-4}$
Fe	$8.44 \cdot 10^{-7}$	$6.41 \cdot 10^{-6}$	$2.61 \cdot 10^{-8}$	$5.03 \cdot 10^{-6}$
C	$6.20 \cdot 10^{-5}$	$4.21 \cdot 10^{-4}$	$1.21 \cdot 10^{-5}$	$2.36 \cdot 10^{-4}$
K	$5.16 \cdot 10^{-2}$	$1.73 \cdot 10^{-1}$	$5.57 \cdot 10^{-2}$	$1.17 \cdot 10^{-1}$
Mg	$4.97 \cdot 10^{-9}$	$7.68 \cdot 10^{-10}$	$9.23 \cdot 10^{-7}$	$9.24 \cdot 10^{-10}$
Na	$2.92 \cdot 10^{-2}$	$7.48 \cdot 10^{-2}$	$3.43 \cdot 10^{-2}$	$5.74 \cdot 10^{-2}$
S	$2.93 \cdot 10^{-2}$	$3.70 \cdot 10^{-2}$	$5.84 \cdot 10^{-2}$	$2.01 \cdot 10^{-2}$
Si	$1.48 \cdot 10^{-3}$	$1.24 \cdot 10^{-3}$	$1.67 \cdot 10^{-3}$	$8.30 \cdot 10^{-4}$

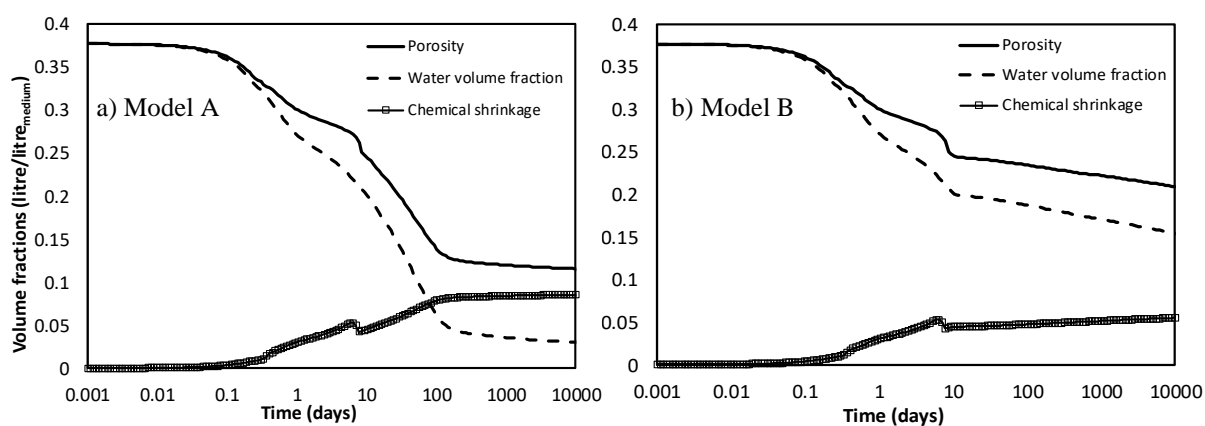


Figure 4: Evolution of evaporable water, total porosity and chemical shrinkage as a function of hydration time (days) for (a) Model A and (b) Model B.

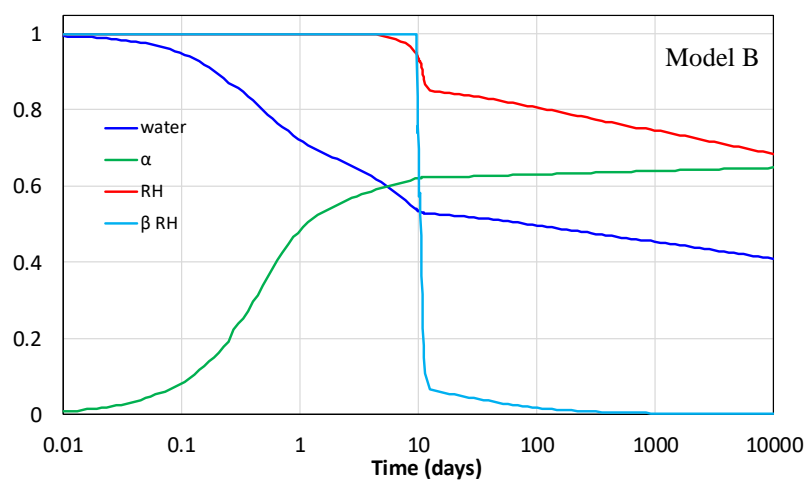


Figure 5: Evolution of water content, hydration degree (α), internal RH and the humidity-dependent factor (β_{RH}) in Model B.

5 Conclusions and Future work

The main conclusions of the present work may be summarized as follows:

- A hydration model for cement with addition of SCM has been developed and implemented in PhreeqC, based on coupling thermodynamic modelling and reaction kinetics for the clinker.
- So far, the model assumes a closed system during hydration, although the impact on the dissolution rates of the consumption of water during hydration is explicitly considered.
- The results illustrate the impact of a decrease in internal RH due to self-desiccation on the degree of hydration and resulting phase assemblage.

Explicit consideration of moisture transfer from an external source during hydration and curing would lead to different results, characterized by a higher degree of hydration and a larger volume of cement hydrates. On-going work aims at coupling the hydration model to moisture transfer and reactive transport processes during the curing period and beyond. To this end, moisture transport within the cementitious system will be modelled in iCP (Nardi et al., 2014) using the formulation presented in Idiart et al. (2011). This coupling may be especially relevant for the present study, given the small dimensions of the samples.

Acknowledgements

The research leading to these results has received funding from the European Union's Horizon 2020 Research and Training Programme of the European Atomic Energy Community (H2020-NFRP-2014/2015) under grant agreement n° 662147 (CEBAMA). Fruitful discussions with Barbara Lothenbach and Georg Kosakowski are gratefully acknowledged.

References

- Baroghel-Bouny, V. (2007). Water vapour sorption experiments on hardened cementitious materials. Part I: Essential tool for analysis of hygral behaviour and its relation to pore structure. *Cement and Concrete Research*, 37, 414-437.
- Giffaut, E., Grivé, M., Blanc, P., Vieillard, P., Colàs, E., Gailhanou, H., Gaboreau, S., Marty, N., Madé, B., Duro, L. (2014). Andra thermodynamic database for performance assessment: ThermoChimie. *Applied Geochemistry*, 49, 225-236.
- Hong, S.-Y. and Glasser, F.P. (1999). Alkali binding in cement pastes. Part I. The C-S-H phase. *Cement and Concrete Research*, 29, 1893-1903.
- Idiart, A., López, C.M., Carol, I. (2011). Modeling of drying shrinkage of concrete specimens at the meso-level. *Materials and Structures*, 44(2), 415-435.
- Jensen, O.M. and Hansen, P.F. (2001). Autogenous deformation and RH-change in perspective. *Cement and Concrete Research*, 31, 1859-1865.
- Lothenbach, B., Le Saout, G., Gallucci, E., Scrivener, K. (2008). Influence of limestone on the hydration of Portland cements. *Cement and Concrete Research*, 38, 848-860.
- Missana, T., García-Gutiérrez, M., Mingarro, M., Alonso, U. (2017). Analysis of barium retention mechanisms on calcium silicate hydrate phases. *Cement and Concrete Research*, 93, 8-16.
- Nardi, A., Idiart, A., Trinchero, P., de Vries, L.M., Molinero, J. (2014). Interface COMSOL-PHREEQC (iCP), an efficient numerical framework for the solution of coupled multiphysics and geochemistry. *Computers and Geosciences*, 69, 10-21.
- Olsson, N., Nilsson, L.-O., Ahs, M., Baroghel-Bouny, V. (2018). Moisture transport and sorption in cement based materials containing slag or silica fume. *Cement and Concrete Research*, 106, 23-32.

- Palandri, J.L. and Kharaka, Y.K. (2004). A compilation of rate parameters of water-mineral interactions kinetics for application to geochemical modeling. USGS Report 2004-1068, Calif., USA.
- Parkhurst, D.L. and Appelo, C.A.J. (2013). Description of input and examples for PHREEQC Version 3 — A computer program for speciation, batch-reaction, one-dimensional transport, and inverse geochemical calculations. U.S.G.S. Techn. and Meth., book 6, chapter A43, 6-43A.
- Parrot, L.J. and Killoh, D.C. (1984). Prediction of cement hydration. British Ceramic Proceedings, 35, 41-53.
- Riding, K.A., Thomas, M.D.A., Folliard, K.J. (2013). Apparent diffusivity model for concrete containing supplementary cementitious materials. ACI Materials Journal, 110(6), 705-713.
- Schöler, A., Winnefeld, F., Ben Haha, M., Lothenbach, B. (2017). The effect of glass composition on the reactivity of synthetic glasses. Journal of the American Ceramic Society, 100, 2553-2567.
- Vasconcelos, R.G.W., Idiart, A., Hyatt, N., Provis, J., Corkhill, C. (2018a). Leaching of Nirex reference vault backfill cement by clay, granite and saline groundwaters. MRS Advances, 3(21), 1175-1180.
- Vasconcelos, R.G.W., Walkley, B, Hyatt, N., Provis, J., Corkhill, C. (2018b). The physico-chemical evolution of a low-pH cement in contact with groundwater. In: M. Altmaier, V. Montoya, L. Duro, A. Valls (Eds.) Proceedings of the 3rd Annual Workshop of the CEBAMA Project. *This document*.
- Vehmas, T., Schnidler, A., Löija, M., Leivo, M., Holt, E. (2017). CEBAMA reference mix design for low-pH concrete and paste, preliminary characterisation. In: M. Altmaier, V. Montoya, L. Duro, A. Valls (Eds.) Proceedings of the 2nd Annual Workshop of the CEBAMA Project. KIT Scientific Report, *in press*.
- Wyrzykowski, M. and Lura, P. (2016). Effect of relative humidity decrease due to self-desiccation on the hydration kinetics of cement. Cement and Concrete Research, 85, 75-81.

Pore-scale reactive transport modelling of transport and leaching processes in cementitious materials

Stephan Rohmen^{1*}, Andrés Idiart², Guido Deissmann¹, Dirk Bosbach¹

¹ Forschungszentrum Jülich GmbH, Institute of Energy and Climate Research (IEK-6): Nuclear Waste Management and Reactor Safety (DE)

² Amphos21 Consulting (ES)

* Corresponding author: st.rohmen@fz-juelich.de

Abstract

Cementitious materials are used in a wide range of applications in nuclear waste management, for example for the solidification of waste or as construction and backfill material in underground and near surface repositories. In cementitious materials, chemical and microstructural heterogeneities exist on a wide range of length scales, from the nano- to the macro-scale. Reactive transport modelling at the pore-scale, i.e. at the micrometre scale, can be regarded as a promising tool to mechanistically describe the relation between transport processes and mineral reactions due to groundwater interaction and the associated microstructural changes in cementitious materials. In this context, we developed a modelling framework for the simulation of concrete degradation processes, based on the coupling of a flow and solute transport code utilising the Lattice-Boltzmann-Method with a geochemical solver based on the law of mass action. For improving scalability in terms of parallel computational performance, optimisations in the geochemical solver were implemented in order to allow fully coupled reactive transport simulations of larger systems. In this paper, we present first applications of the code to derive transport properties such as effective diffusion coefficients, and first results of the simulation of leaching experiments, using the CEBAMA reference low pH cement paste as an example. The microstructural input geometries were derived from μ X-ray computer tomography images combined with information on the phase assemblage from a simulation of cement hydration. Preliminary results indicate a rather isotropic effective diffusivity for the simulated geometry. The code was successfully applied to solve a 2D simulation of leaching of the hardened cement paste with pure water, using a simplified chemical system.

1 Introduction

Heterogeneities are present in cementitious systems on a wide range of lengths scales. It is known that microscopic heterogeneities may have rather huge effects on macroscopic transport properties such as permeability and effective diffusion coefficients. In this context, pore-scale reactive transport models can be regarded as an appealing approach to realistically describe the microscopic evolution of the pore structure and the heterogeneous distribution of hydrated phases and unhydrated binder components in cementitious materials and analyzing pore-scale processes in a mechanistic way. This approach can be used to address chemical degradation processes due to calcium leaching or carbonation of cementitious materials and their impact on physical and transport properties, such as porosity, pore-size distribution, permeability or diffusivity (Taylor, 1997).

In the frame of the CEBAMA project, a coupled code named iPP (interface **Palabos PhreeqC**) was developed. iPP is able to calculate reactive transport processes in porous media on the pore scale using the Lattice-Boltzmann method (Palabos; Flowkit, 2011) and utilizing a geochemical solver based on the law of mass action (PhreeqcRM; Parkhurst and Wissmeier, 2015). It exploits MPI parallelization and C++ template meta-programming techniques allowing usage of high performance computing (HPC) facilities (Rohmen et al., 2017a, *in press*). For improving scalability, in terms of parallel computational performance, optimizations in the PhreeqcRM code were implemented in order to allow fully coupled reactive transport simulations of larger models. As Lattice-Boltzmann scheme for diffusive solute transport a D2Q5 (2D) and D3Q7 (3D) scheme is used.

Recently, experimental data on the characterization of the CEBAMA low-pH reference cement paste prior to leaching were made available from the University of Sheffield (USFD) (Vasconcelos, 2018). These data encompass in particular imaging data from micro-X-ray computer tomography (μ XCT), which can be used as input data for reconstructing the microstructure of the hardened cement paste for pore-scale simulations using iPP. In this paper, we outline the current development status of iPP and its application to determine the effective diffusion coefficient of the cement paste, and preliminary results of simulations addressing the leaching of CEBAMA low-pH reference cement paste, using input geometries derived from microstructural analysis.

2 Setup of simulation models from μ XCT data

2.1 Geometry reconstruction from μ XCT data

USFD conducted μ XCT measurements on samples from the CEBAMA reference paste (casted at USFD, dimensions: 2 mm diameter, 5 mm height) and provided the raw volume image data to derive microstructural geometrical descriptions of the low-pH cement paste. The sample was cured for 28 days and measured by μ XCT with a resolution of 3 μ m per voxel, resulting into a grey value data set of $671 \times 742 \times 1449 = 721 \times 431 \times 018$ voxels. These image data resolve the grey values of unhydrated clinker (C2S/C3S and ferrite), blast furnace slag (BFS), silica fume, voids (air) and hydration products (mainly C-S-H). Different hydration products could not be further separated due to the similar X-ray attenuation effects (see Figure 1, left). For further information see also Rohmen et al. (2017b).

An artifact which is commonly known from CT measurements is the so-called partial volume effect, also known as volume averaging artifact. This artifact occurs when a single voxel contains more than one phase, leading to an intermediate X-ray attenuation value between all material fractions present in the voxel's volume (Ketcham and Carlson, 2001). As a consequence, separating the different phases by a simple grey value thresholding algorithm would eventually lead into false positive assignments for voxels corresponding to phase mixtures. In this work, a more sophisticated segmentation algorithm was developed to mitigate the partial volume effect (Rohmen et al., 2017b). Using this algorithm, a 3D phase distribution of the cement paste specimen could be derived, in which air, silica fume, calcium silicate clinker, blast furnace slag, ferrite clinker and hydration products could be distinguished. Unfortunately, further separating of different phases in the subset of hydrates was not possible.

2.2 Effective diffusion coefficient of cement paste

According to Fick's first law, at steady state the diffusion coefficient is calculated as the quotient of the diffusive flux and the concentration gradient in a through diffusion setup. To simulate this at the microscopic scale, the microstructure and transport properties of the different components need to be known. The three-dimensional model presented here consists of geometry of the microstructure and is used to determine the effective

diffusion coefficient in the x, y, and z directions to check for possible anisotropic diffusivity. To this end, closed (slip) boundary conditions are imposed on all boundaries, except the two faces perpendicular to the direction for which diffusivity is obtained. At both of these boundaries, a constant concentration (Dirichlet) boundary condition is imposed: 1 mol/L of an inert tracer at one boundary, while the concentration at the opposite boundary is set to 0 mol/L. Subsequently, the diffusive flux is tracked and the effective diffusion coefficient can be calculated as described above, when steady state is reached. In order to determine the effective diffusion coefficient of the cement paste sample, a representative cube with dimensions of $750 \times 750 \times 750 \mu\text{m}$ ($250 \times 250 \times 250$ voxels with a resolution of $3 \mu\text{m}$ per voxel) was extracted from the segmented μXCT data (Figure 1, right). It is assumed that the main diffusive phase in the sample is the hydration products phase, which has an intrinsic gel porosity of the C-S-H. Since the resolution of the μXCT imaging technique used cannot distinguish between different hydration products (i.e. C-S-H, portlandite and other hydrates), these are assumed to be homogeneously distributed in the hydration product phase.

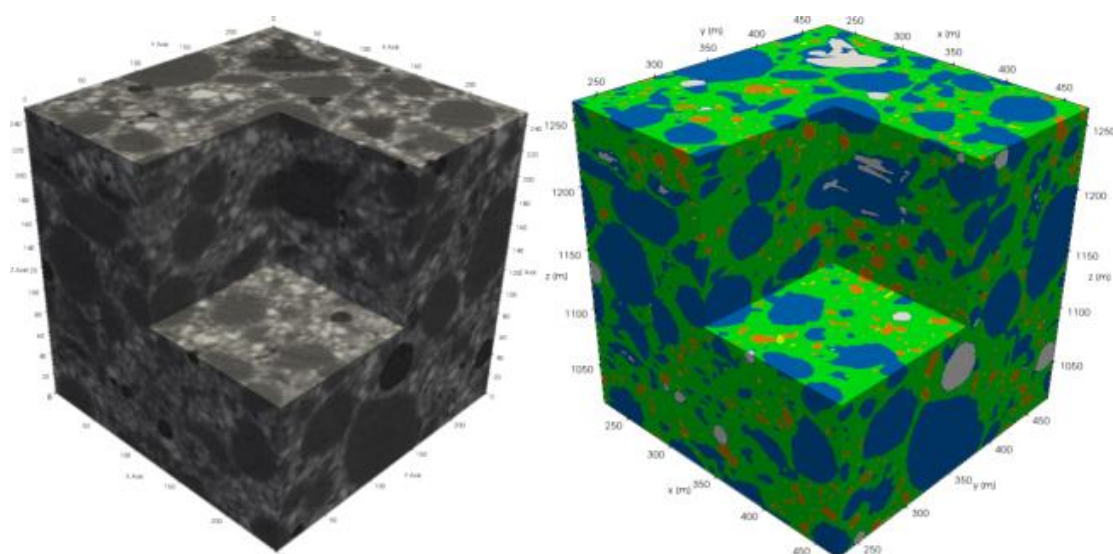


Figure 1: Plot of the original μXCT raw grey image data corresponding to the extracted cube (left) and microstructure of CEBAMA reference paste from segmented μXCT data used as input geometry for the calculation of effective diffusion coefficients (right). A box was clipped from the cube for illustrative purposes. Phases: Air (white), silica fume (blue), alite/belite (yellow), blast furnace slag (orange), ferrite (red) and hydration products (green). Total model size is $750 \times 750 \times 750 \mu\text{m}$ with a resolution of $3 \mu\text{m}$.

Table 1: Calculated amounts of hydration product phases and volume fractions of hydration products in the USFD cement paste after 28 days of hydration. The amounts were estimated by a kinetic hydration model using PhreeqC (Idiart et al., 2018).

Phase	C-S-H1.6	Ettringite	AFm	Hydrotalcite	Stratlingite	C3AH6	Inert	Hydrates porosity
amount (mol/L)	5.159	0.072	0.075	0.140	0.135	0.034	-	-
volume fraction	0.402	0.051	0.02	0.031	0.029	0.005	0.11	0.351

All other segmented phases such as silica fume, blast furnace slag and unreacted clinker were assumed as non-diffusive for the inert tracer. The effective diffusion coefficient and porosity of the hydration products phase

(green phase in Figure 1, right) depend on the volume fraction of C-S-H and other hydration products. To estimate the diffusion coefficient of the hydration products phase, a multiscale homogenization model (effective medium approach) was applied (Bary et al., 2014; Phan-Thien and Pham, 2000; Zheng and Du, 2001). This homogenization model requires information about the water-to-cement ratio (w/c), the degree of hydration to separate LD- and HD-C-S-H (Tennis and Jennings, 2000), and the volume fraction of C-S-H and other hydration products (Rohmen et al., 2017b). In order to estimate the amount of hydration products, a kinetic hydration model using PhreeqC was applied (Table 1). The resulting hydration products are qualitatively in agreement with XRD measurements from USFD (Vasconcelos et al., 2018). Moreover, the water-to-cement ratio was set to 0.25 and a degree of hydration of 0.6 was assumed, which was estimated by segmentation of μ XCT data. The resulting intrinsic diffusion coefficient for the hydration products is estimated as $4.1 \cdot 10^{-10} \text{ m}^2/\text{s}$ by this procedure, when assuming $1.0 \cdot 10^{-9} \text{ m}^2/\text{s}$ as free water diffusion coefficient. Although the estimated diffusion coefficient for the hydration products seems to be relatively high it was further used for the development of the methodology.

2.3 2D model of leaching of cement paste with pure water

The simulation of leaching of the CEBAMA low-pH reference paste by pure water was used as a test case for iPP. To this end, a rectangular 2D cross-section of the microstructure of the USFD cement paste derived from the μ XCT was extracted to generate a 2D input geometry. To simplify the chemical system, the hydration products were assumed to be comprised exclusively by an inextricable mixture of C-S-H 1.54 and portlandite, corresponding to an overall Ca-to-Si ratio of 1.67, consistent with the results of the hydration modelling for the 28 days old cement paste. By this means, the chemistry was reduced to Ca and Si only, which reduces also the possible phases in equilibrium to amorphous SiO_2 ($\text{SiO}_2(\text{am})$), portlandite and C-S-H. Furthermore, to avoid convergence issues within PhreeqC calculations when using the solid solution model of C-S-H implemented in the cemdata07 PhreeqC database (Jacques, 2009), a set of discrete C-S-H phases was used (cf. Lichtner and Carey, 2006). For this purpose, the C-S-H ideal solid solution model from Kulik (2011) and the corresponding data of C-S-H_{tob2} and C-S-H_{jen} end members were used. The C-S-H_{tob1}, C-S-H_{tob2} and C-S-H_{jen} end-member phases from cemdata07 were replaced by 19 distinct phases with interpolated log K values and molar volumes (V_m) (Table 2). Moreover, it was assumed that the hydration products domain has a total porosity of 50% (including C-S-H gel porosity), yielding to a corresponding initial amount of C-S-H 1.54 and portlandite.

The 2D cross section was setup as a closed system except for the left boundary, where a 10-voxel pure water reservoir and a zero-concentration boundary condition were imposed. All other phases except C-S-H, portlandite and $\text{SiO}_2(\text{am})$ were regarded as inert. In particular, for the unhydrated clinker phase, this is an over-simplification since the hydration reaction would proceed further at the same time as leaching occurs. However, to our knowledge no kinetic rate equations are available from experiments describing the rate of the hydration reaction at the microscopic scale.

Although PhreeqRM supports MPI parallelization during the PhreeqRM: runCells() function call, concentration update/requesting and retrieving of auxiliary information (e.g. solid phase compositions, pH values, etc.) are implemented with a global MPI reduction and collecting step. The implication of the reduction step is that all concentration couplings to transport codes are forced to be done via the main process and cannot perform on a local process basis. This reduction procedure causes high communication overhead and a major performance drawback when utilizing parallelization on a high amount of CPU nodes, leading eventually to negative scalability. In order to reduce that communication overhead, the PhreeqRM code was optimized, which led to a custom PhreeqRM version allowing local coupling to the Lattice-Boltzmann transport code. This optimization significantly improved the performance scalability behaviour.

Table 2: Interpolated equilibrium constants and molar volumes for emulating C-S-H ideal solid solution model with discrete phases.

C-S-H phase	log K	V _m
C-S-H_083	-8.00	59.0
C-S-H_092	-8.66	60.9
C-S-H_096	-8.96	61.9
C-S-H_100	-9.25	62.8
C-S-H_104	-9.54	63.8
C-S-H_108	-9.82	64.7
C-S-H_112	-10.09	65.7
C-S-H_117	-10.36	66.6
C-S-H_121	-10.62	67.6
C-S-H_125	-10.88	68.5
C-S-H_129	-11.14	69.5
C-S-H_133	-11.39	70.4
C-S-H_137	-11.64	71.4
C-S-H_142	-11.88	72.3
C-S-H_146	-12.12	73.3
C-S-H_150	-12.35	74.2
C-S-H_154	-12.57	75.2
C-S-H_158	-12.79	76.1
C-S-H_167	-13.17	78.0

3 Results and discussion

3.1 Effective diffusion coefficient of cement paste

In the simulations used to determine the effective diffusion coefficient of the low-pH reference paste, steady-state was reached after 550,000 iterations (equivalent to 27.5 minutes physical time) for each direction. The resulting concentration profile and flux streamlines for the z-direction are presented in Figure 2. From the outlet fluxes, the effective diffusion coefficients for each direction were estimated, as shown in Table 3. The values for x and y direction are quite similar, suggesting that the diffusivity is quasi-isotropic in these directions for the depicted sub-geometry of the USFD cement paste. Still, the value in the z-direction is slightly lower compared to the other two directions. A detailed analysis of the 3D geometry and streamlines revealed a flat and broad silica fume particle parallel to the xy-plane, obstructing the diffusive flux in the z-direction. Thus, it has to be emphasized that the selection of a representative geometry plays an important role for determining isotropic effective transport properties in these materials. However, the average diffusion coefficient estimated is comparable to the results obtained for a 2D simulation of the same sample (Rohmen et al., 2017b).

3.2 Leaching of cement paste with pure water

The 2D model was run for 3.6 mio. iterations, equivalent to a physical time of 3 hours. Results of the leaching simulation are shown in Figure 3 (right) and Figure 4. The Ca/Si plot (Figure 4) shows that the degradation front reached up to 350 μm , resulting in a decrease of the C/S in the C-S-H. Only a few microns (ca. 15 μm) of the C-S-H of the sample have dissolved completely at the dissolution front (compare green line to C/S values in Figure 4). Accordingly, Ca concentration in solution (Figure 3 right) is lowered in this domain, governed by equilibrium with the evolving C-S-H composition. Furthermore, the degradation of the sample reached a higher degree in the upper part of the system, caused by inert silica fume particles which are obstructing the access to the outlet on the left hand side.

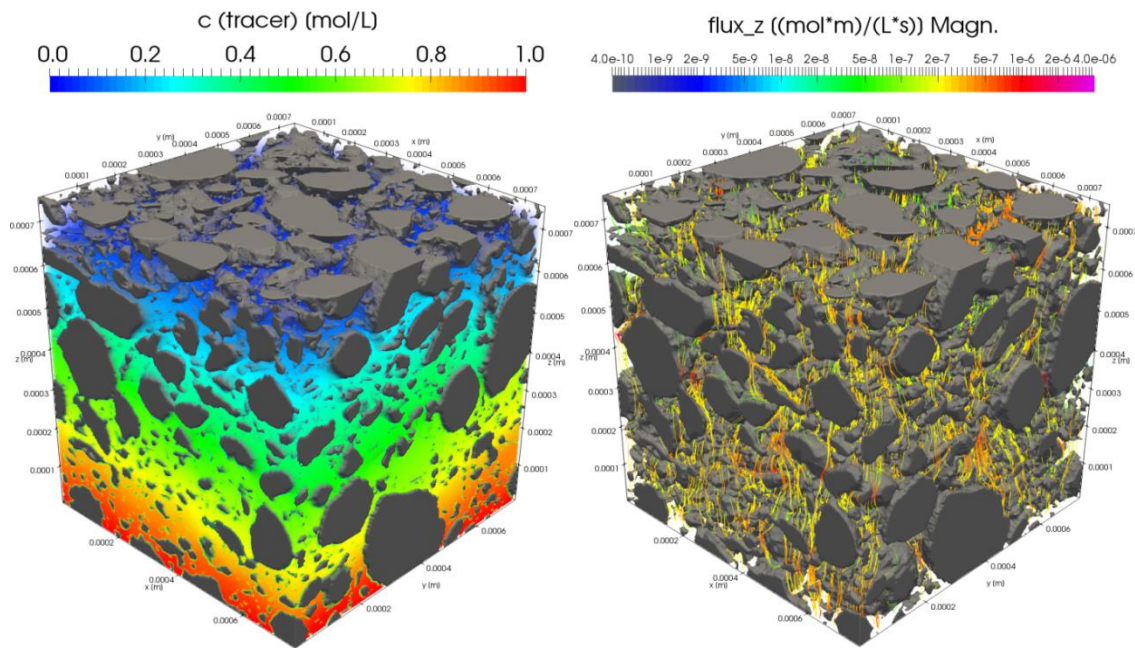


Figure 2: Concentration profile (left) and diffusive flux streamlines (right) of inert tracer after convergence of diffusion coefficient simulation in z direction. Non-permeable phases are indicated in grey while hydration products and voids are transparent.

Table 3: Results for the effective diffusion coefficient calculations for each spatial axis.

direction	D_e (m^2/s)
x	$8.5 \cdot 10^{-11}$
y	$8.5 \cdot 10^{-11}$
z	$7.1 \cdot 10^{-11}$
average	$8.0 \cdot 10^{-11}$

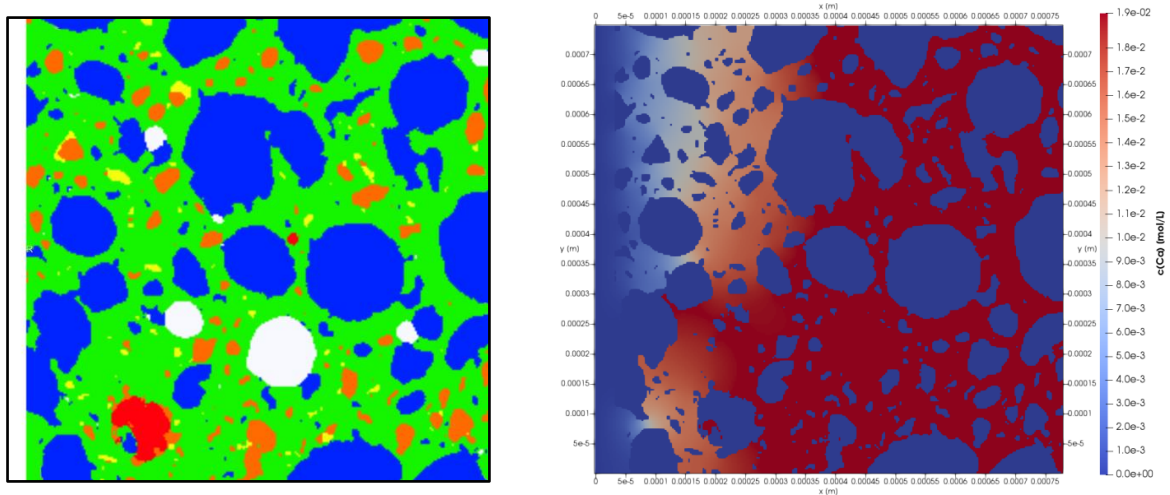


Figure 3: Left: Initial phase distribution data used as input geometry for the calculation of effective diffusion coefficients. Phases: Air (white), silica fume (blue), alite/belite (yellow), blast furnace slag (orange), ferrite (red) and hydration products (green). Total model size is $760 \times 750 \mu\text{m}$ with a resolution of $3 \mu\text{m}$. Right: Calcium concentration in the pore water after 3 hours of leaching of low pH cement paste with pure water entering from the left-hand side.

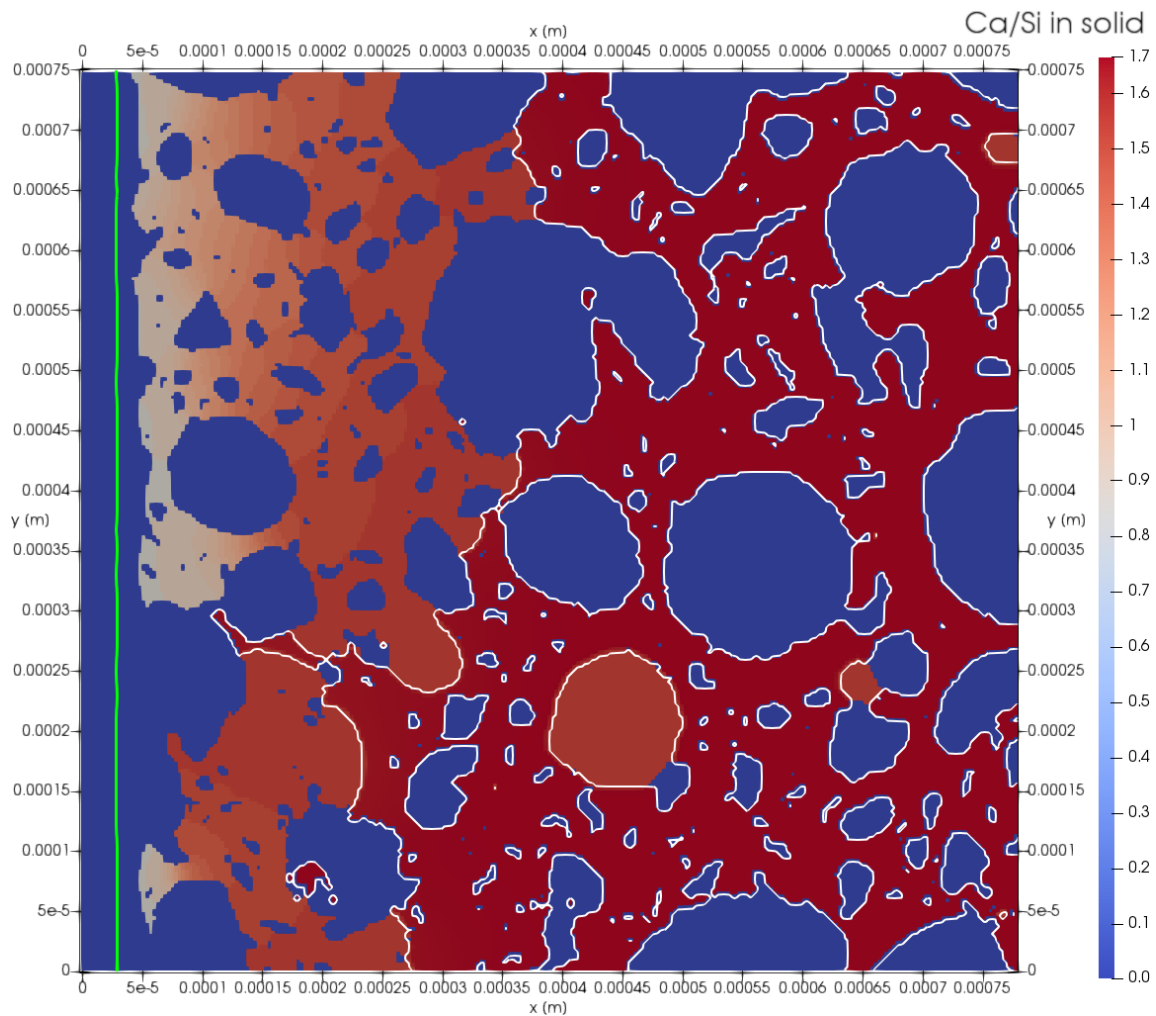


Figure 4: Ca-to-Si molar ratio of the residual solids after 3 hours of leaching of low-pH reference paste with pure water from the left-hand side. For guidance the initial cement boundary is indicated in green, while the residual portlandite boundary is shown as a white isoline.

4 Conclusions and Future work

Recently, first imaging data of the CEBAMA low-pH reference paste were provided by USFD, which is used as input data for reactive transport simulations at the pore-scale (i.e. micrometre scale). Several algorithms and approaches were developed and implemented to derive microstructural information in appropriate format from raw data from μ XCT volume images for subsequent usage in iPP. It could be shown that the developed framework iPP is capable of simulating solute transport in experimentally-derived data to predict effective diffusion coefficient and microstructural changes due to degradation of C-S-H.

With the current development status, results of 3D effective diffusion calculations and 2D calculations of a simplified chemical system (Ca and Si only) were obtained. Further refinements of the multiscale homogenization model for the diffusive phases (i.e. C-S-H gel) are under development. Applications with a more complex description of the chemical system including Al, Na, K, Cl, C, S, Mg, etc. are also in progress. A further step is to model the leaching processes using realistic groundwater compositions with complex chemistry in order to simulate the on-going leaching experiments of USFD (Vasconcelos et al., 2018). In those cases, additional processes may become more relevant, such as clogging effects due to precipitation of calcite (due to carbonate ingress) or ettringite (due to sulphate ingress), which can occur at the cement paste interface, due to relative high concentrations in the clay or granite water.

In addition, further optimizations are tested to improve the performance constraints, which are very computationally demanding, even with high performance cluster computing. Relaxing the performance limitations would enable reactive transport simulations using 3D microstructures.

Acknowledgement

The research leading to these results has received funding from the European Union's Horizon 2020 Research and Training Programme of the European Atomic Energy Community (EURATOM) (H2020-NFRP-2014/2015) under grant agreement n° 662147 (CEBAMA).

References

- Bary, B., Leterrier, N., Deville, E., Le Bescop, P. (2014). Coupled chemo-transport-mechanical modelling and numerical simulation of external sulfate attack in mortar. *Cement and Concrete Composites*, 49, 70-83.
- FlowKit (2011). Palabos user guide.
- Idiart, A., Laviña, M., Olmeda, J. (2018). Influence of internal relative humidity on the hydration of a low-pH cement. A modelling study. *In: M. Altmaier, V. Montoya, L. Duro, A. Valls (Eds.) Proceedings of the 3rd Annual Workshop of the CEBAMA Project. This document.*
- Jacques, D. (2009). Benchmarking of the cement model and detrimental chemical reactions including temperature dependent parameters. NIRON-TR Report, 2008–30 E.
- Ketcham, R.A. and Carlson, W.D. (2001). Acquisition, optimization and interpretation of X-ray computed tomographic imagery: Applications to the geosciences. *Computers and Geosciences*, 27(4), 381-400.
- Kulik, D.A. (2011). Improving the structural consistency of C-S-H solid solution thermodynamic models. *Cement and Concrete Research*, 41(5), 477-495.
- Lichtner, P.C. and Carey, J.W. (2006). Incorporating solid solutions in reactive transport equations using a kinetic discrete-composition approach. *Geochimica et Cosmochimica Acta*, 70(6), 1356-1378.

- Parkhurst, D.L. and Wissmeier, L. (2015). PhreeqcRM: A reaction module for transport simulators based on the geochemical model PHREEQC. *Advances in Water Resources*, 83, 176-189.
- Phan-Thien, N. and Pham, D.C. (2000). Differential multiphase models for polydispersed spheroidal inclusions: Thermal conductivity and effective viscosity. *International Journal of Engineering Science*, 38(1), 73-88.
- Rohmen, S., Idiart, A., Deissmann, G., Bosbach, D. (2017a). Implementation of crystallization and precipitation mechanism in pore-scale models based on the Lattice-Boltzmann method. *In*: M. Altmaier, V. Montoya, L. Duro, A. Valls (Eds.) *Proceedings of the 2nd Annual Workshop of the CEBAMA Project*. KIT Scientific Report, *in press*.
- Rohmen, S., Idiart, A., Deissmann, G., Bosbach, D. (2017b). *In*: A. Idiart (Ed.) D3.05: Preliminary results and interpretation of the modelling of WP1 & WP2 experiments. 22-30.
- Taylor, H.F.W. (1997). *Cement chemistry*. Thomas Telford.
- Tennis, P.D. and Jennings, H.M. (2000). A model for two types of calcium silicate hydrate in the microstructure of Portland cement pastes. *Cement and Concrete Research*, 30(6), 855-863.
- Vasconcelos, R., Walkley, B., Hyatt, N., Provis, J., Corkhill, C. (2018). The physico-chemical evolution of a low-pH cement in contact with groundwater. *In*: M. Altmaier, V. Montoya, L. Duro, A. Valls (Eds.) *Proceedings of the 3rd Annual Workshop of the CEBAMA Project*. *This document*.
- Zheng, Q.S. and Du, D.X. (2001). An explicit and universally applicable estimate for the effective properties of multiphase composites which accounts for inclusion distribution. *Journal of the Mechanics and Physics of Solids*, 49(11), 2765-2788.

Coupled THCM models of heating-hydration tests containing OPC concrete and compacted FEBEX bentonite

Javier Samper^{1*}, Alba Mon¹, Luis Montenegro¹, Acacia Naves¹, Jesús Fernández¹, Jaime Cuevas², Raúl Fernández², María Jesús Turrero³, Elena Torres³

¹ Centro de Investigaciones Científicas Avanzadas, Escuela de Caminos, Canales y Puertos, Universidade da Coruña (ES)

² Facultad de Ciencias, Universidad Autónoma de Madrid (ES)

³ Centro de Investigaciones Energéticas, Medio Ambientales y Tecnológicas (ES)

* Corresponding author: j.samper@udc.es

Abstract

We present coupled thermo-hydro-chemical-mechanical (THCM) models of a set of heating and hydration tests (HB1 to HB6) performed by Ciemat and UAM on columns containing OPC concrete samples in contact with compacted FEBEX bentonite. The tests lasted from 0.5 (HB1) to 11 (HB6) years. These tests provide unique data on the interactions of concrete and bentonite under repository conditions and potential changes in bentonite and concrete properties. These tests were performed on columns heated at 100°C at the bottom and hydrated at the top. The numerical models reproduce the general trends of the measured water content, porosity and temperature data and the experimental observations of mineral dissolution/precipitation. A sensitivity analysis of the model results for the HB4 column test has been performed to evaluate the relevance of the temperature gradient, the uncertainties in the mineral kinetic parameters and the finite element grid size.

1 Introduction

The main objectives of UDC contribution to the CEBAMA Project include: 1) Improving THCM codes and models for the interactions of concrete and bentonite; 2) Performing THCM models of the heating and hydration HB column tests (Turrero et al., 2011; Torres et al., 2013); 3) Performing long-term predictions of the interactions of bentonite, concrete and clay rock; and 4) Contributing to the analysis of time scaling issues. The geochemical evolution of the bentonite barrier during the initial of the hydration and heating stages of the repository depends on the thermal, hydrodynamic and mechanical processes. For this reason, coupled numerical THCM models are required. Samper et al. (2017) presented coupled THCM numerical models of heating and hydration experiments (HB1, 2, 3, and 4) performed by Ciemat on compacted FEBEX bentonite to study the interactions of concrete-bentonite under repository conditions and analyze how such interactions affect the bentonite and concrete properties. These experiments were performed at concrete and bentonite columns heated at 100°C at the bottom and hydrated at the top. They showed that the numerical model reproduces the general trends of the measured water content, porosity, and temperature data and the experimental mineral patterns. Here we present the coupled THCM models of the entire set of tests including HB1, HB2, HB3, HB4, HB5 and HB6 tests (Turrero et al., 2011; Torres et al., 2013). In addition, we also report a detailed sensitivity analysis of the model results of the HB4 column test. The sensitivity runs include: 1) Isothermal versus non-isothermal conditions; 2) Mineral kinetic

parameters and 3) Finite element grid size. The models were solved with the UDC code INVERSE-FADES-CORE. The first version of INVERSE-FADES-CORE was developed within the FEBEX I Project and was later improved within the FEBEX II, NFPRO, and PEBS Projects (Zheng et al., 2010; Samper et al., 2013; Mon, 2017).

2 Heating and hydration concrete/bentonite column tests

Several tests were performed to study the interactions of concrete and bentonite pore water at the conditions prevailing in the EBS during the early hydration stage (Turrero et al., 2011; Torres et al., 2013). The tests are denoted as HB (“*Hormigón-Bentonita*”). They were performed on medium-size cells containing a 7.15 cm thick bentonite sample in contact with a 3 cm thick concrete sample. The concrete was made of sulphate-resistant ordinary Portland cement (CEM I-SR) following the mix by CSIC-IETcc (Consejo Superior de Investigaciones Científicas- Instituto de Ciencias de la Construcción Eduardo Torroja): 400 kg of CEM I-SR cement, 911 kg of sand (0-5 mm), and 946 kg of aggregates (6-16 mm) with a w/c ratio of 0.45. The cells were hydrated at a constant pressure and at a temperature of 25°C at the top of the cell through the concrete, while the temperature was maintained constant at 100°C at the bottom of the cell (Figure 1). The HB column tests provide data on the concrete and bentonite interface at several times. They were dismantled after 6, 12, 18, 54 and 80 months for the HB1 to the HB5 tests and 104 months for the HB6 test, which was dismantled within the CEBAMA Project. However, the experimental data from HB5 and HB6 tests are not yet available for modelling. The initial porosity of the bentonite is 0.4 and the initial water content is 13.3%, which corresponds to a saturation of 57% and a suction of $1.27 \cdot 10^8$ Pa (Samper et al., 2018). There were experimental problems to maintain a constant water injection pressure during the experiment. The cells were hydrated with a synthetic Spanish reference clay porewater (Turrero et al., 2011; Torres et al., 2013).

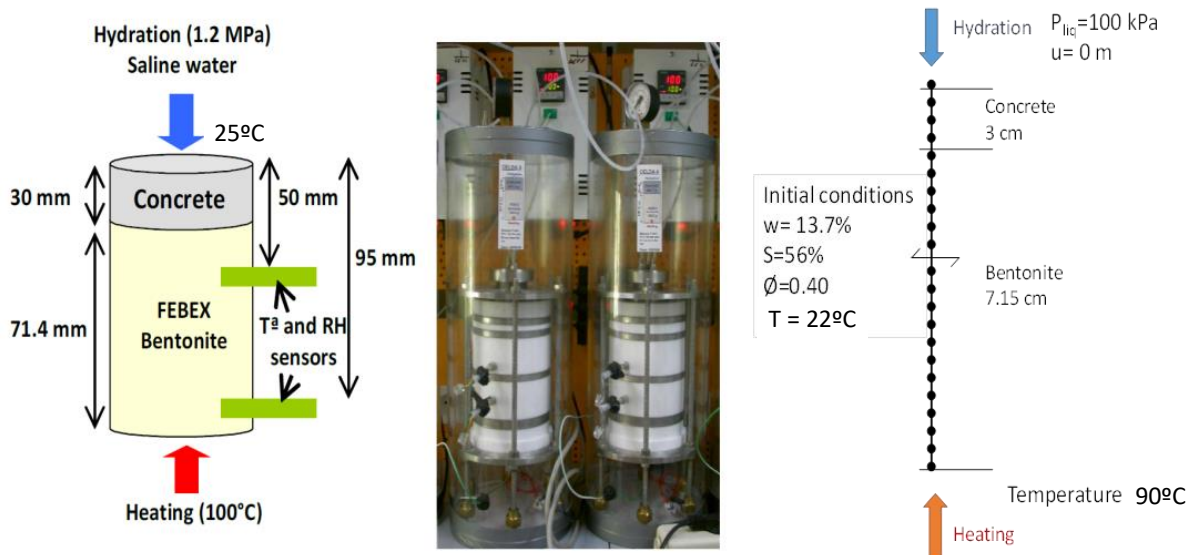


Figure 1: Setup of the concrete-bentonite HB column tests (left) and finite element mesh and boundary conditions for the numerical model (right).

3 Model description

HB1 to HB6 tests were modelled with a 1D grid (see Figure 1). Bentonite and concrete parameters were taken from the previous model of the HB4 test in Samper et al. (2013). The concrete has a porosity of 0.125 and a gravimetric water content of 2.2%. The initial temperature is 22°C along the cell. The prescribed temperature at

the bottom of the column, where the heater is located, is 90°C. Similar to previous THCM models of the FEBEX bentonite (Zheng et al., 2010), the initial total stress was assumed uniform, isotropic and equal to 250 kPa. Given the lack of reliable water injection pressure data, the injection liquid pressure was estimated from measured cumulative inflow data. Its value is equal to 100 kPa.

The initial composition of the OPC concrete porewater was derived from speciation runs performed with EQ3/6 (Wolery, 1992) by assuming that the concentration of dissolved Ca^{2+} is controlled by local chemical equilibrium with respect to portlandite, HCO_3^- concentration is at equilibrium with respect to calcite, Mg^{2+} concentration is derived from the equilibration with brucite, Al^{3+} is at equilibrium with ettringite and $\text{SiO}_2(\text{aq})$ is controlled by equilibrium with respect to C1.8SH. The initial mineral volume fractions in the concrete are: 7.4% for portlandite, 2.2% for ettringite, 14.6% for C1.8SH, 1% for brucite, 0.1% for calcite and 62.2% for quartz. Quartz is assumed to be nonreactive. The initial pore water composition of the FEBEX bentonite was taken from Fernández et al. (2004). The initial mineral volume fractions in the bentonite are: 0.36% for calcite, 0.08% for gypsum and 1.192% for cristobalite. The smectite was assumed to be not reactive. The model allows for the precipitation of the following secondary minerals: sepiolite, C0.8SH, anorthite and anhydrite. The dissolution/precipitation of portlandite, ettringite, C1.8SH, C0.8SH, quartz and cristobalite was simulated with the kinetic rate laws of Fernández et al. (2009). Cation exchange and proton surface complexation reactions are assumed to take place only in the bentonite. The current model accounts for the changes in porosity caused by solid deformation and swelling, but disregards the changes in porosity due to mineral dissolution/precipitation because the mechanical changes in porosity for bentonite are generally larger than the chemical changes in porosity. More details can be found in Mon (2017) and Samper et al. (2018).

4 Model results

4.1 THM results

The computed water content and porosity reproduce the general trends of the measured data at the end of the HB1 to HB 4 tests (see Figure 2). The concrete is fully saturated at 7 days and then, the bentonite hydrates at a very low rate through the concrete. Water content increases near the concrete and decreases near the heater due to the evaporation. The porosity increases in the bentonite near the concrete interface due to bentonite swelling. The model predictions of water content and porosity for the HB5 and HB6 column tests are similar to those of the rest of the HB column tests. The results of the HB1 to HB6 column tests are similar because the water intake is fast in the first months and slows down after 10 months.

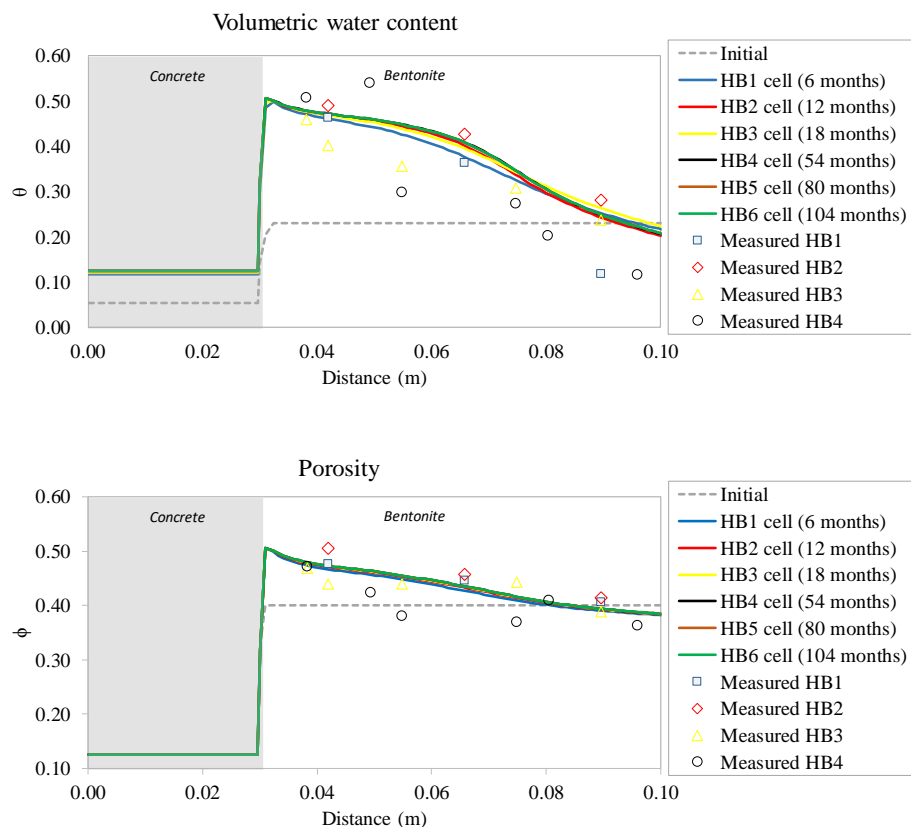


Figure 2: Computed (lines) volumetric water content (up) and porosity (down) and measured data (symbols) for the HB1, HB2, HB3, HB4, HB5 and HB6 tests.

4.2 Chemical results

Figure 3 shows the computed pH and the mineral volume fractions for the HB1 to HB6 tests. The main experimental observations on mineral phases at the end of the HB1, HB2, HB3 and HB4 tests are listed in Table 1. This table includes also a summary of the main trends of the computed mineral dissolution/precipitation for the HB1 to the HB6 tests.

A qualitative comparison of the computed values and the experimental mineral observations reveals that the numerical model captures the main trends of the experimental mineralogical observations. However, there are some discrepancies for ettringite and C-S-H precipitation. The numerical model predicts ettringite dissolution and a very small precipitation of C-S-H. Model discrepancies could be caused by uncertainties in: 1) The selection of the appropriate C-S-H, M-S-H and C-A-S-H phases; 2) The kinetic parameters (rate laws and specific surfaces); and 3) The selection of the appropriate secondary clay minerals. The porosity decreases in the bentonite/concrete interface and at the hydration boundary mainly due to brucite and calcite precipitation.

The computed mineral dissolution/precipitation concentrations in the HB5 and HB6 tests are similar to those of the rest of the HB column tests. The penetration of the pH front into the bentonite increases with time (see Figure 3). The high pH plume ($\text{pH} > 9$) penetrates 5.5 cm into the bentonite in the HB6 test. The diffusion of the alkaline plume is retarded by mineral precipitation in the bentonite near the concrete interface.

Table 1: Qualitative comparison of the laboratory observations and model results for mineral dissolution/precipitation.

	HB1		HB2		HB3		HB4		HB5	HB6
	Laboratory observations	Model results	Laboratory observations	Model results	Laboratory observations	Model results	Laboratory observations	Model results	Model results	Model results
CONCRETE (hydration)	Portlandite dissolution	✓	Portlandite dissolution	✓	Portlandite dissolution	✓			Portlandite dissolution	Portlandite dissolution
	Calcite precipitation	✓	Calcite precipitation	✓	Calcite precipitation	✓	Calcite precipitation	✓	Calcite precipitation	Calcite precipitation
	Brucite precipitation	✓	Brucite precipitation	✓	Brucite precipitation	✓	Brucite precipitation	✓	Brucite precipitation	Brucite precipitation
CONCRETE (30 mm)	Portlandite precipitation	✓	Portlandite precipitation	✓	Portlandite precipitation	✓	Portlandite dissolution	✓	Portlandite dissolution	Portlandite dissolution
		✓	Calcite precipitation in concrete	✓	Calcite precipitation in concrete	✓	Calcite precipitation in concrete	✓	Calcite precipitation in concrete	Calcite precipitation in concrete
	C-S-H gels precipitation	~	C-S-H gels precipitation	~	C-S-H gels precipitation	~	C-S-H gels precipitation	~	Some C-S-H precipitation	Some C-S-H precipitation
	Quartz precipitation	N	Quartz precipitation	N	Quartz precipitation	N				
	MSH precipitation	✓	MSH precipitation	✓	MSH precipitation	✓				
					Gypsum and thaumasite precipitation	✓				
	Zeolites precipitation	Not considered	Halite and K-feldspar precipitation	Not considered	Vaterite and aragonite precipitation	Not considered	Ettringite precipitation	N	No Ettringite precipitation	No Ettringite precipitation
CONCRETE/ BENTONITE INTERFACE (some mm)	Brucite precipitation	✓	Brucite precipitation	✓	Brucite precipitation	✓	MSH precipitation	✓	MSH precipitation	MSH precipitation
	Portlandite precipitation	N	Portlandite precipitation	N	Portlandite precipitation	N				
	Calcite precipitation	✓	Calcite precipitation	✓	Calcite precipitation	✓	Calcite precipitation	✓	Calcite precipitation	Calcite precipitation
	C-S-H gels (tobermorite and jennite type) precipitation	N	C-S-H gels (tobermorite and jennite type) precipitation	N	C-S-H gels (tobermorite and jennite type) precipitation	N	C-S-H gels (0.8) precipitation	N	No C-S-H precipitation	No C-S-H precipitation
			Ettringite precipitation	N	Ettringite precipitation	N	No Ettringite precipitation	✓	No Ettringite precipitation	No Ettringite precipitation
			Gypsum precipitation	✓	Gypsum precipitation	✓				
					Quartz dissolution	✓				
	Smectite alteration not observed	Not considered	Smectite alteration (brucite saponite-smectite mixed phase")	Not considered	Smectite alteration (brucite saponite-smectite mixed phase") Saponite formation	Not considered Not considered			Brucite precipitation	Brucite precipitation
BENTONITE	Unaltered bentonite mineralogy	~	Unaltered bentonite mineralogy	~	Unaltered bentonite mineralogy	~	Calcite dissolution Gypsum and chloride precipitation	✓ ✓		

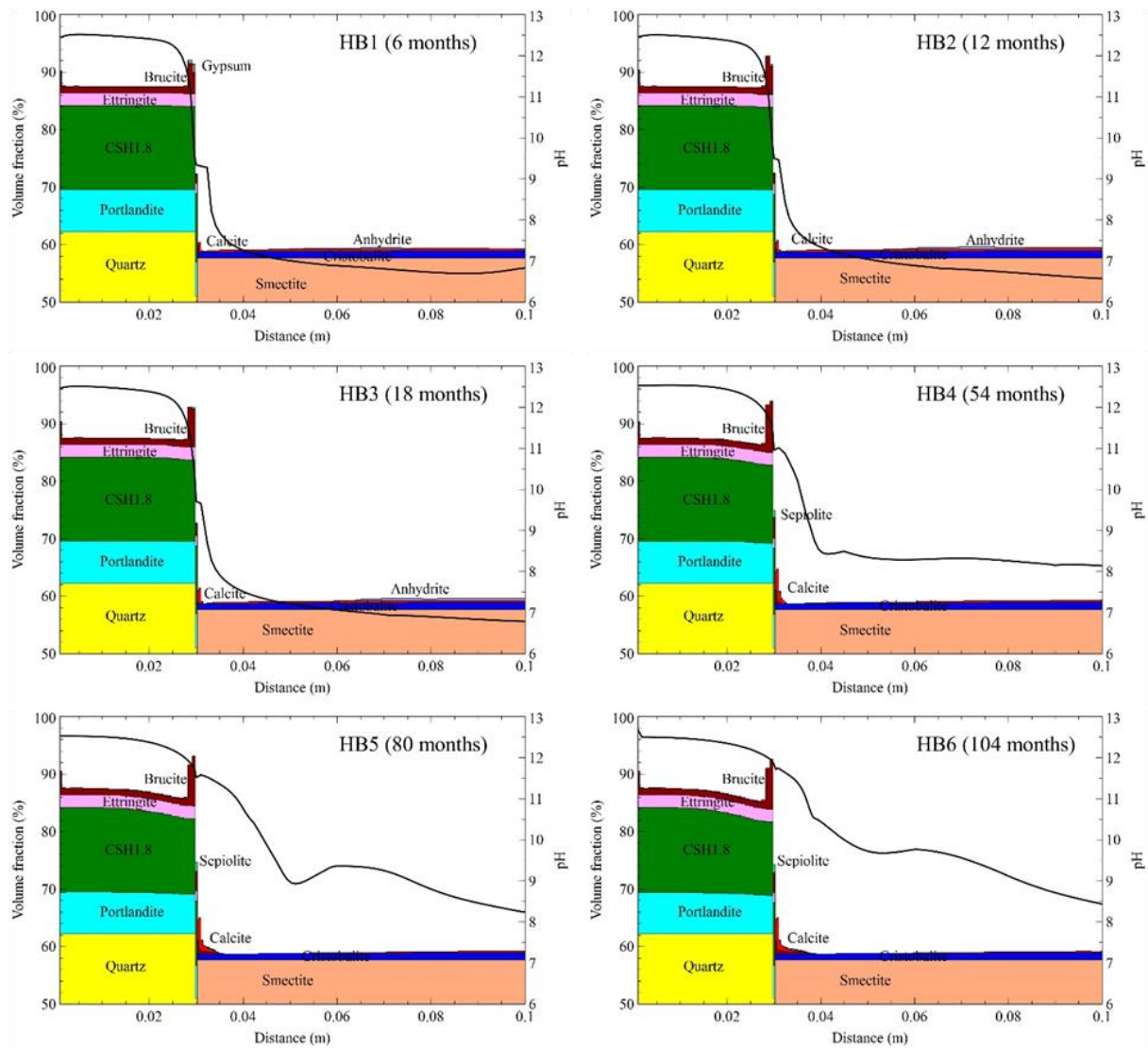


Figure 3: Computed pH and mineral volume fractions for the HB1, HB2, HB3, HB4, HB5 and HB6 tests.

5 Sensitivity analysis of the model of the HB4 column test

5.1 Sensitivity analysis to the thermal field

The base run of the HB4 column test is non-isothermal. The temperature of the hydration water is 25°C. The prescribed temperature at the bottom of the column, where the heater is located, is 90°C. This temperature is lower than the heater temperature due to lateral heat losses. A sensitivity run was performed at a constant and uniform temperature of 25°C. Figure 4 shows the computed cumulative precipitation of calcite and brucite for the base and sensitivity runs. The model results for constant temperature show significant differences in the precipitation of calcite and brucite. The peaks of brucite and calcite precipitation for constant temperature are smaller than those of the base run. Moreover, the thickness of the bentonite zone where calcite and brucite precipitate in the constant temperature run is larger than that of the base run. Brucite precipitates in the concrete and in the bentonite in the base run, while it only precipitates in the bentonite in the constant temperature run.

The reduction in porosity in the concrete near the bentonite interface and in the bentonite in the constant temperature run is smaller than that of the base run (Figure 5).

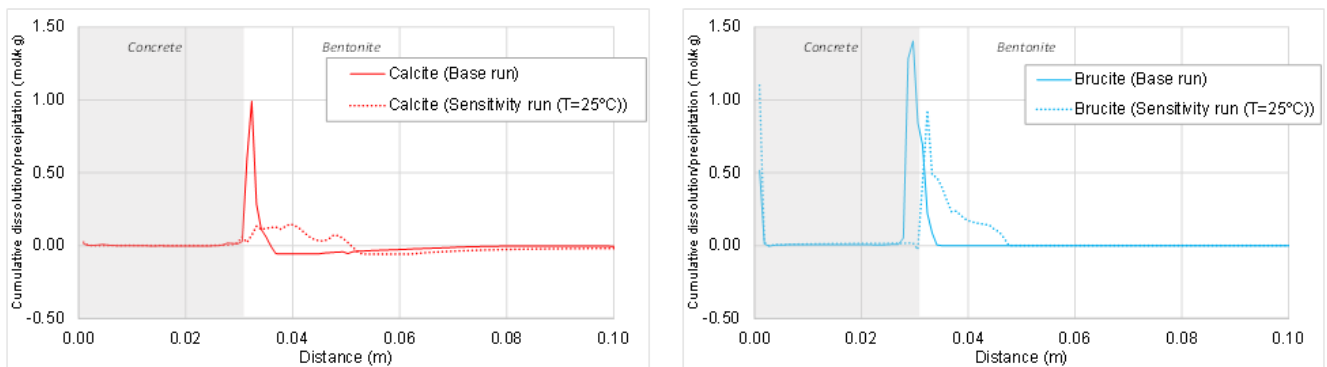


Figure 4: Computed calcite (left) and brucite (right) precipitation/dissolution for the base and sensitivity runs with a uniform temperature (25°C) for the model of the HB4 test.

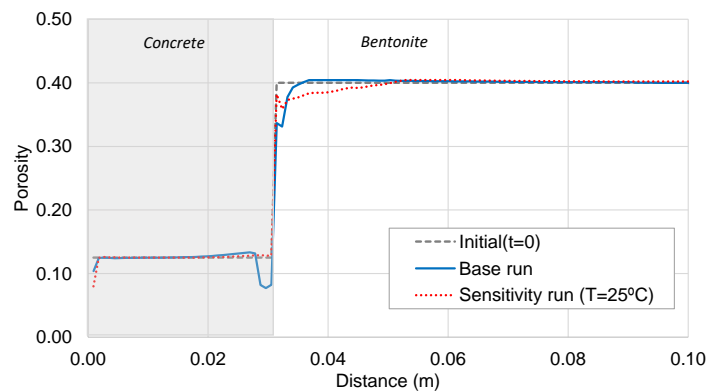


Figure 5: Computed porosity for the base and sensitivity runs with uniform 25°C temperature for the model of the HB4 test.

5.2 Sensitivity analysis to mineral phases

Sensitivity runs were performed to investigate the sensitivity of model results to changes in the specific surfaces of kinetically-controlled minerals (portlandite and ettringite). Model results are sensitive to an increase of the specific surface of portlandite by a factor of 2 and an increase of the specific surface of ettringite by a factor of 10 (see Figure 6). The increase in the specific surface of portlandite leads to larger portlandite dissolution rates, larger calcite precipitation and larger pH in the bentonite. The increase of the specific surface of ettringite leads to more precipitation of ettringite in the mid upstream part of the concrete, more ettringite dissolution in the concrete near the bentonite interface and larger pH in the bentonite. On the other hand, the model lacks sensitivity to the kinetic Mg-saponite precipitation (Figure 6) which was simulated with the kinetic law reported by Mon et al. (2017).

5.3 Sensitivity analysis to grid size

Grid size in the reference model is uniform and equal to 0.9 mm. Several sensitivity runs were performed in which the grid was refined in a 3 cm wide band around the concrete/bentonite interface. Grid sizes of 0.45 mm, 0.18 mm and 0.1 mm were considered in three simulation runs while the size of the rest of the elements was equal to 0.45 mm. Mineral precipitation increases at both sides of the concrete/bentonite interface when the grid size is

reduced (Figure 6). The calculated porosity in the concrete near the bentonite interface decreases drastically, reaching pore clogging for grid sizes smaller than 0.18 mm.

The numerical solution improves by decreasing the grid size because the discretization errors decrease when the grid size is decreased. Model results for the run with the smallest grid size should be considered the most realistic.

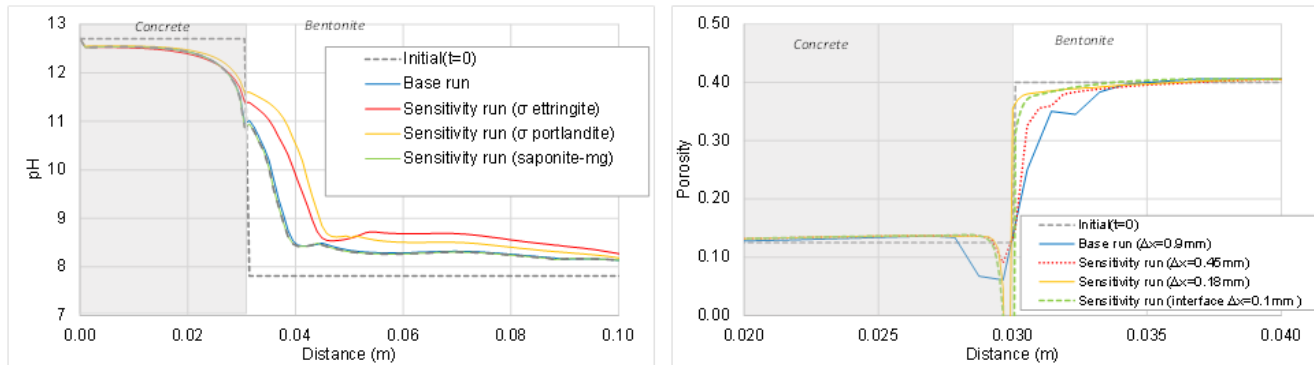


Figure 6: Model of the HB4 test: Sensitivity of the computed pH to changes in the mineral parameters (left) and sensitivity of the computed porosity to changes in the grid size (right).

6 Conclusions and future work

Coupled THCM models of the HB1, HB2, HB3, HB4, HB5 and HB6 tests have been presented. Model results reproduce the general trends of the measured water content, porosity, and temperature (not shown here) and the observed patterns of mineral phases for the HB1 to HB4 tests. The predictions of the HB5 and HB6 tests show similar trends to those of the rest of the tests. These predictions will be compared to measured data when they become available.

The thickness of the bentonite zone where calcite and brucite precipitate in the constant temperature run is larger than that of the base run. While brucite precipitates in the concrete and in the bentonite in the base run, this mineral precipitates only in the bentonite in the constant temperature run. The reduction in porosity in the concrete near the bentonite interface and in the bentonite in the constant temperature run is smaller than that of the base run. These results in the constant temperature run attest the conclusions of Lalan et al. (2016) who concluded that the temperature plays an important role in the degradation of C-S-H and the precipitation of mineral phases. The intricate interplays of thermal and chemical processes in this complex chemical system prevent a simple explanation for the results of the sensitivity run to temperature.

Model results are sensitive to the increase of the specific surfaces of portlandite and ettringite. On the other hand, model results are not sensitive to kinetic Mg-saponite precipitation. Mineral precipitation increases at both sides of the concrete/bentonite interface when the grid size is reduced. The calculated porosity in the concrete near the bentonite interface decreases drastically, reaching pore clogging for grid sizes smaller than 0.18 mm. It is planned to improve the THCM models of the HB column tests by: 1) Considering additional C-S-H and M-S-H phases; 2) Adjusting the kinetic parameters and 3) Accounting for the feedback effect of the changes in porosity caused by mineral dissolution/precipitation.

Acknowledgements

The research leading to these results has received funding from the European Union's Horizon 2020 Research and Training Programme of the European Atomic Energy Community (EURATOM) (H2020-NFRP-2014/2015) under grant agreement n° 662147 (CEBAMA).

References

- Fernández, A.M., Baeyens, B., Bradbury, M., Rivas, P. (2004). Analysis of pore water chemical composition of a Spanish compacted bentonite used in an engineered barrier. *Physics Chemistry of the Earth*, 29, 105-118.
- Fernández, R., Cuevas, J., Mäder, U.K. (2009). Modelling concrete interaction with a bentonite barrier. *European Journal of Mineralogy*, 21, 177-191.
- Lalan, P., Dauzères, A., DeWindt, L., Bartier, D., Sammaljärvi, J., Barnichon, J.D., Techer, I., Detilleux, V. (2016). Impact of a 70°C temperature on an ordinary Portland cement paste/claystone interface: An in-situ experiment. *Cement and Concrete Research*, 83, 164-178.
- Mon, A. (2017). Coupled thermo-hydro-chemical-mechanical models for the bentonite barrier in a radioactive waste repository. Ph. D. Dissertation. Universidad de A Coruña, Spain.
- Mon, A., Samper, J., Montenegro, L., Naves, A., Fernández, J. (2017). Long-term non-isothermal reactive transport model of compacted bentonite, concrete and corrosion products in a HLW repository in clay. *Journal of Contaminant Hydrology*, 197, 1-16.
- Samper, J., Mon, A., Montenegro, L., Pisani, B., Naves, A. (2013). Report on testing multiple-continua THCM models with laboratory and large-scale tests. Deliverable 3.4-1 of the PEBS Project.
- Samper, J., Mon, A., Montenegro, L., Naves, A., Fernández, J., Cuevas, J., Fernández, R., Turrero, M.J., Torres, E. (2017). Coupled THCM numerical models of heating and hydration tests to study the interactions of compacted FEBEX bentonite with OPC concrete. *In: M. Altmaier, V. Montoya, L. Duro, A. Valls (Eds.) Proceedings of the 1st Annual Workshop of the CEBAMA Project. KIT Scientific Report, 7734.*
- Samper, J., Mon, A., Montenegro, L., Cuevas, J., Turrero, M.J., Naves, A., Fernández, R., Torres, E. (2018). Coupled THCM model of a heating and hydration concrete-bentonite column test. *Applied Geochemistry*, 94, 67-81.
- Torres, E., Turrero, M.J., Escribano, A., Martín, P.L. (2013). Geochemical interactions at the concrete-bentonite interface of column experiments. Deliverable 2.3-6-1 of PEBS Project.
- Turrero, M.J., Villar, M.V., Torres, E., Escribano, A., Cuevas, J., Fernández, R., Ruiz, A.I., Vigil de la Villa, R., del Soto, I. (2011). Laboratory tests at the interfaces. Final results of the dismantling of the tests FB3 and HB4. Deliverable 2.3-3-1 of PEBS Project.
- Wollery, T.J. (1992). EQ3/3. A software package for geochemical modeling of aqueous system: package overview and installation guide version 7.0. Lawrence Livermore National Laboratory Report, UCRL-MA-110662-PT-I.
- Zheng, L., Samper, J., Montenegro, L., Fernández, A.M. (2010). A coupled model of heating and hydration laboratory experiment in unsaturated compacted FEBEX bentonite. *Journal of hydrology*, 386, 80-94.

Modelling and interpretation of diffusion experiments of selected radionuclides through cementitious samples

Dušan Vopálka^{1*}, Tomáš Rosendorf^{1,2}, Lucie Baborová¹, Jana Kittnerová¹

¹ Department of Nuclear Chemistry, Czech Technical University in Prague (CZ)

² Fuel Cycle Chemistry Department, ÚJV Řež (CZ)

* Corresponding author: dusan.vopalka@fjfi.cvut.cz

Abstract

A sophisticated tool for evaluation and modelling of diffusion experiments was implemented in the GoldSim environment. This model enables to evaluate through-diffusion experiments in steady and non-steady states and with variable concentration in the inlet and outlet containers. The three datasets describing each diffusion experiment could be evaluated simultaneously, i.e. break-through and depletion curves, and tracer concentration profile in the cementitious plug. This verified tool was applied to the evaluation of diffusion experiments performed either at our laboratory, or in cooperation with ÚJV and CTU CEG, within WP1 and WP2 of the CEBAMA Project. WP1: Through-diffusion experiments of HTO were performed on samples of hydrated cement paste (CEM II) that interacted with groundwater (GW Josef) or bentonite suspension for nine months under in-situ and high temperature (95°C) condition. The characteristic diffusion coefficients D_e and D_p of HTO, which was obtained also by a simple evaluation method based on the Fick's first law, were determined and discussed. WP2: Through-diffusion experiments with radium and strontium over 0.5 cm wide layers formed by pressed crushed hydrated cement paste (CEM II) were performed with portlandite equilibrated water and with synthetic cement pore water. Isotope ^{223}Ra was carrier-free, strontium ($C_0 = 3.5 \cdot 10^{-4} \text{ mol/L}$) was labelled by ^{85}Sr . In this case, only our original method of evaluation was used, as diffusion experiments with ^{223}Ra did not reach stationary state.

1 Introduction

For the evaluation and modelling of various types of diffusion experiments, a module being developed in the GoldSim environment (Vopálka et al., 2006; Vopálka et al., 2017; Baborová et al., 2016) is used in our laboratory. Among other applications, the current version of this tool enables to well describe through-diffusion experiments conducted in a static diffusion cell with variable concentration of studied species in the inlet and outlet containers, which is an advantageous laboratory method, since it is not necessary to keep constant concentrations in working containers by renewing inlet and outlet solutions, which might bring a systematic error into the system. The model enables further to determine effective diffusion coefficient, D_e , and apparent diffusion coefficient, D_a , without the need of having to wait until steady-state is reached. The possibility to evaluate through-diffusion experiments before the steady-state is reached enables to reduce the experiment duration significantly. The evaluation method mentioned needs to determine the total concentration profile in the studied layer after the experiment termination. This way, one diffusion experiment provides three experimental curves, i.e. break-through (downstream) and depletion (upstream) curves, and tracer concentration profile in the studied layer, which might be then fitted by

model curves. A simplified reactive transport modelling is considered by implementation of either linear or non-linear empirical (Freundlich or Langmuir) sorption isotherms, describing reversible uptake/release of observed species. The fitting of model curves to experimental data is possible by multi-parametric optimization using Box's method (Box, 1965). The model serves not only to the evaluation of experiments performed, but it also can be used to better understand the behaviour of the diffusion cell, which could facilitate the preparation of experiments.

2 Modelling

The evaluation of diffusion experiments should give parameters, i.e. effective diffusion coefficient, D_e , and apparent diffusion coefficient, D_a , necessary for the characterization of the studied material and for further modelling of radionuclide transport in barrier materials in the safety assessment of a repository. The determination of both diffusion coefficients from their definition equations, from the first Fick's law, is very simple if the experiment is in stationary state (e.g. Shackelford and Moore, 2013). In this state the diffused mass flows in the layer and from it are equal and the concentration drop in the liquid phase in the layer is linear, if the cross-section is constant along the length of a porous sample. This linearity will be valid also for the total concentration (sum of contributions corresponding to both liquid and solid phases) in the case of a linear sorption isotherm.

The modelling tool was used for the assessment of the time necessary to reach the stationary state for experiments by using similar conditions to those of diffusion experiments performed within WP1 in CEG CTU (see below). The results of the simulation study are presented in two figures. In Figure 1, it can be seen that for the conditions of the numerical experiment, which assumes linear sorption ($K_d = 10$ L/kg), the stationary state would be attained not sooner than in 50 days. The drop of total concentration on the beginning of the sample is also remarkable in this figure, which reflects the reversibility of sorption and the decrease of concentration in the relatively small volume of the input container ($V_1 = 60$ mL).

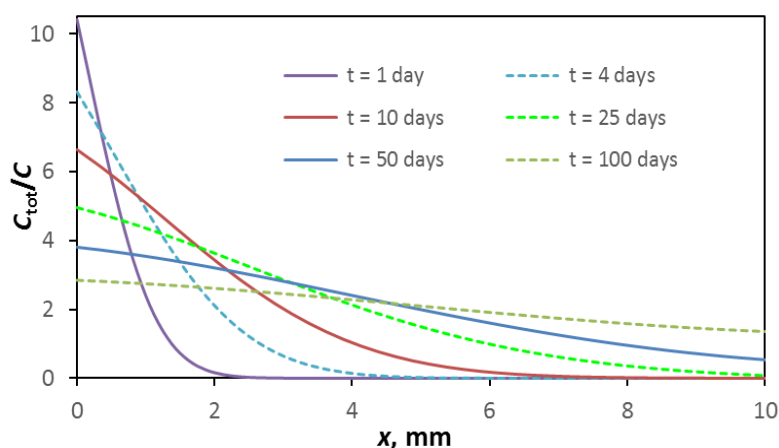


Figure 1: Modelled time evolution of total concentration profiles in diffuse layer for a sorbing species (characterized by $K_d = 10$ L/kg); volumes of working containers $V_1 = V_2 = 60$ mL; parameters of the layer: diameter 50 mm, width 10 mm, porosity 0.5, diffusivity in pores $D_p = 1 \cdot 10^{-10}$ m²/s).

The quasi-stationary state of the modelled type of through-diffusion experiment is attained when the downstream and upstream mass flows are same. In the case of same volumes of working reservoirs, the changes of concentration in both reservoirs should be then opposite, but numerically same. So, if concentration in output container is presented as a reminder to the unity (relative concentration in the input reservoir prior the diffusion

starts), the quasi-stationary state can be characterized by the constant distance between curves corresponding to concentrations in both working reservoirs. From results of modelling of through-diffusion experiments with variable concentration of studied species in the inlet and outlet containers presented in Figure 2 it is seen that the quasi-stationary state is reached, for the experiment, in which no sorption was assumed, after approximately 10 days. In turn 50 days are needed in the experiment with $K_d = 10$ L/kg, while the experiment with $K_d = 50$ L/kg does not reach steady-state conditions. In the latter, the diffusion coefficient cannot be determined by the simple method based on the first Fick's law.

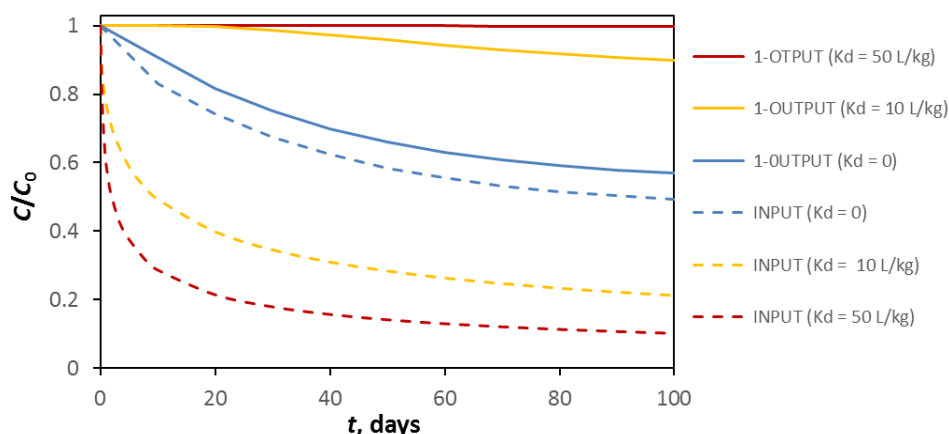


Figure 2: Modelled time dependences of concentrations in input and output containers ($V_1 = V_2 = 60$ mL; parameters of the layer: diameter 50 mm, width 10 mm, porosity 0.5, $D_p = 1 \cdot 10^{-10}$ m²/s) for three values of distribution coefficient K_d .

3 Evaluation of experiments

3.1 Diffusion of HTO through blocks of hydrated cement paste

One of the goals of Czech laboratory program within WP1 is the determination of changes in tritium diffusivities on samples of hydrated OPC that interacted with groundwater (GW Josef). The laboratory interaction experiments are designed for 9, 18 and 27 months under two different temperatures: 10°C (corresponding to in-situ conditions of Josef Underground Facility) and 95°C as an extreme temperature (Večerník et al., 2016). For the evaluation, we obtained results of the set of through-diffusion experiments on samples of hydrated OPC that interacted with GW Josef (Series I and Series II) and with bentonite B75 suspension (Series III and Series IV) for 9 months.

The experimental setup is schematically described as follows:

- WP1 Czech program – hydrated OPC mixture: CEM II A-S 42.5R + H₂O (w:c = 0.45), hydration 28 days.
- Hydrated OPC cylinders: ca. 50 mm of diameter, ca. 8.3 - 8.4 mm length.
- Diffusion cells identification, samples after 9 months of interaction:
 - Series I: hydrated OPC and GW Josef at 95°C, cells A, B, C
 - Series II: hydrated OPC and GW Josef at 10°C, cells D, E, F
 - Series III: hydrated OPC and B75 suspension at 95°C, cells J, K, L
 - Series IV: hydrated OPC and B75 suspension at 10°C, cells M, N, O

- Duration of diffusion experiments: 62-111 days.
- Volume of inlet and outlet containers: $V = 57\text{-}59\text{ mL}$.

The experiments were evaluated by two methods. The first one uses the model implemented in GoldSim assuming a transient state. In the second one, the simple method based on the first Fick's law was applied, as experiments seemed to be near the quasi-stationary state. As an example, the experimental and modelling results corresponding to Series I and obtained by the first method are presented in Figure 3. Differences among results corresponding to individual cells show a significant variability caused by the heterogeneity of the cement plugs of hardened cement paste. These differences lead to a significant uncertainty of the determined diffusion coefficients. In Table 1 the results obtained for all four series by the two methods are gathered, including the effective diffusion coefficients, D_e , and pore diffusion coefficients, D_p (for non-interacting species, D_p is equivalent to D_a). These results show that diffusion rate/flow is faster through samples that were under a high temperature load (95°C) for 9 months, with significant increase of D_p (approx. one order of magnitude) in the comparison with samples under ambient temperature (10°C). As the ratio D_e/D_p , which represents a porosity assessment, did not change significantly (the mean equals 0.50 ± 0.06), it can be concluded that chemical processes caused by long-term heating led to less tortuous diffusion pathway (larger values of geometrical factor G). No change of diffusion coefficient in free water, D_w , need be considered, as all diffusion experiments were performed by laboratory temperature. Ongoing ^{36}Cl through-diffusion experiments (where the sorption process is expected to be non-negligible) on the OPC affected by same thermal loads in UJV will outline how effective diffusion coefficient, D_e , develops for a non-conservative tracer.

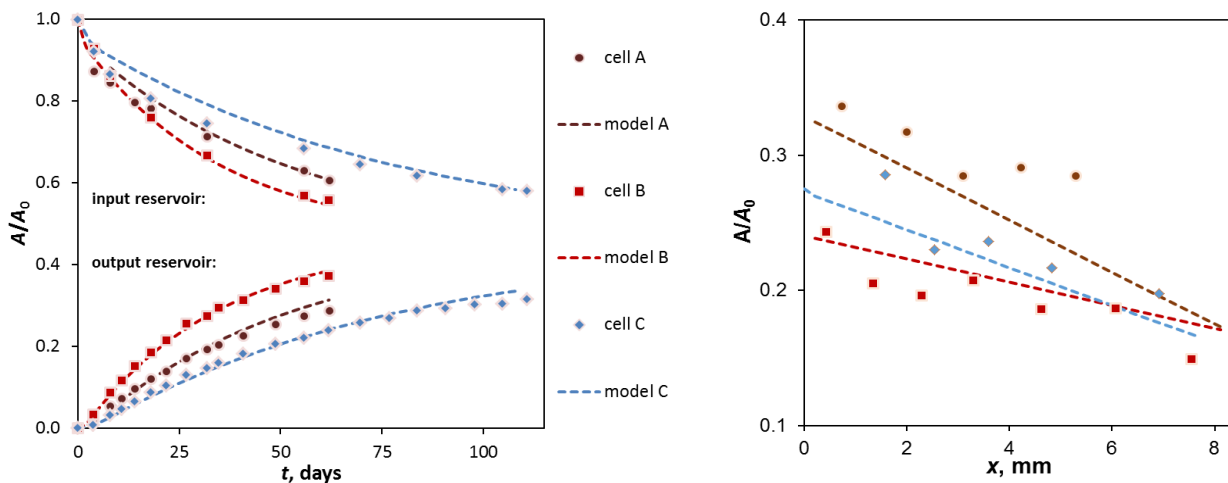


Figure 3: Measured and modelled relative HTO activities in three parallel diffusion experiments through the plugs of hydrated cement paste (Series I - hydrated OPC and GW Josef at 95°C) presented together with their model evaluations. $V_1 = V_2 = 57\text{-}59\text{ mL}$; parameters of the layer: diameter ca 50.3 mm, width ca 8.3 mm, porosity ca 0.5).

Table 1: Summary of determination of diffusion coefficients of HTO in cementitious plugs pre-treated in four different conditions. Two methods of evaluation were applied: “GoldSim” and “Fick”.

	D_e (GoldSim) m²/s	D_e (Fick) m²/s	D_p (GoldSim) m²/s	D_p (Fick) m²/s
Series I: hydrated OPC and GW Josef at 95°C	$(2.8 \pm 1.2) \cdot 10^{-11}$	$(1.9 \pm 0.8) \cdot 10^{-11}$	$(6.0 \pm 2.9) \cdot 10^{-11}$	$(3.9 \pm 2.2) \cdot 10^{-11}$
Series II: hydrated OPC and GW Josef at 10°C	$(0.3 \pm 0.1) \cdot 10^{-11}$	$(0.3 \pm 0.1) \cdot 10^{-11}$	$(0.6 \pm 0.3) \cdot 10^{-11}$	$(0.8 \pm 0.3) \cdot 10^{-11}$
Series III: hydrated OPC and B75 suspension at 95°C	$(2.0 \pm 0.8) \cdot 10^{-11}$	$(1.6 \pm 1.0) \cdot 10^{-11}$	$(3.6 \pm 1.2) \cdot 10^{-11}$	$(2.8 \pm 1.5) \cdot 10^{-11}$
Series IV: hydrated OPC and B75 suspension at 10°C	$(0.4 \pm 0.1) \cdot 10^{-11}$	$(0.5 \pm 0.2) \cdot 10^{-11}$	$(0.7 \pm 0.3) \cdot 10^{-11}$	$(1.1 \pm 1.0) \cdot 10^{-11}$

3.2 Diffusion of Sr and Ra through the pressed layer of crushed hydrated cement paste

A set of diffusion experiments was carried out in portlandite equilibrated water (saturated $\text{Ca}(\text{OH})_2$) or synthetic cement water (CPW) through the hydrated cement paste layers (CEM II A-S 42.5R), which were formed by pressing a crushed cementitious material. The aims of these experiments were the continuation in the study of the influence of phase ratio V/m on the value of distribution coefficient K_d and a comparison of results of diffusion experiments realized in compact and crushed (and pressed) samples. The solid material layer of 0.5 cm width was saturated with the appropriate solution prior to the addition of the migrating element. The volumes of the inlet and outlet containers were 50 mL, separating filters of 0.08 cm width was used for the separation of cementitious material from containers with working solutions. Strontium, with a concentration $C_0 = 3.5 \cdot 10^{-4}$ mol/L, was labelled by ^{85}Sr , and radium used for the diffusion study was the isotope ^{223}Ra , with a concentration in the range of 10^{-12} mol/L. The duration of experiments was 22 days.

In all four experiments performed it was necessary to use for evaluation the multicomponent fitting procedure in GoldSim environment, as in none of them the stationary state was reached. The model takes into account the presence of separating filters and eliminates their influence on the values of diffusion coefficient corresponding to the studied layer of pressed crushed cement paste. Figure 4 and Figure 5 show the experimental results of Ra and Sr diffusion in portlandite equilibrated water and model curves corresponding to the optimal fits. The quality of fits demonstrates that the model description assuming the linearity of the sorption model and reversibility of the sorption process might be valid for the retarded diffusion transport of both Sr and Ra. Determined values of diffusion coefficients and corresponding K_d values are gathered in Table 2.

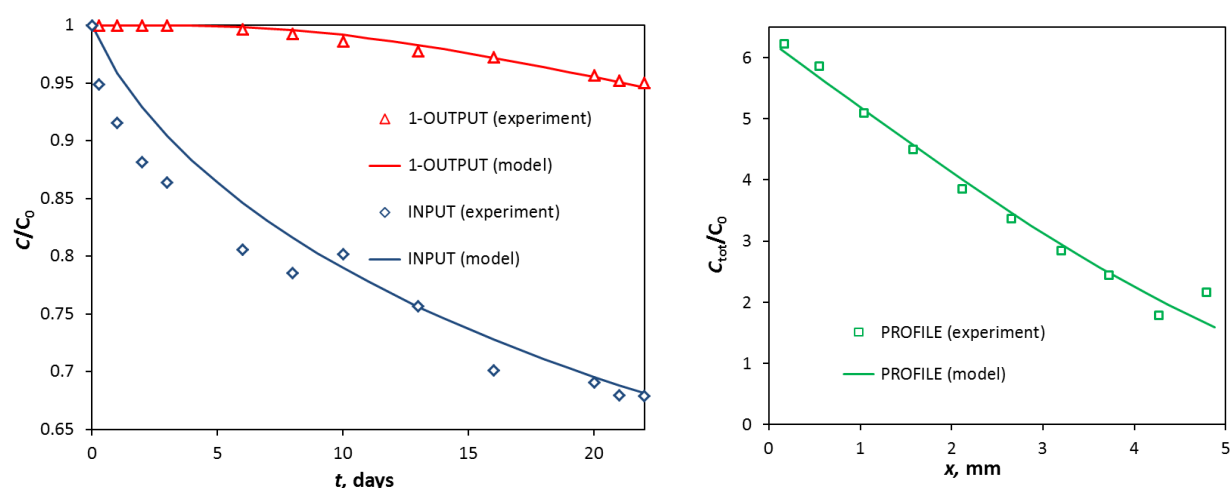


Figure 4: Results of Sr (labelled by ^{85}Sr) through-diffusion experiment, which lasted 22 days, in portlandite equilibrated water and its optimal fit.

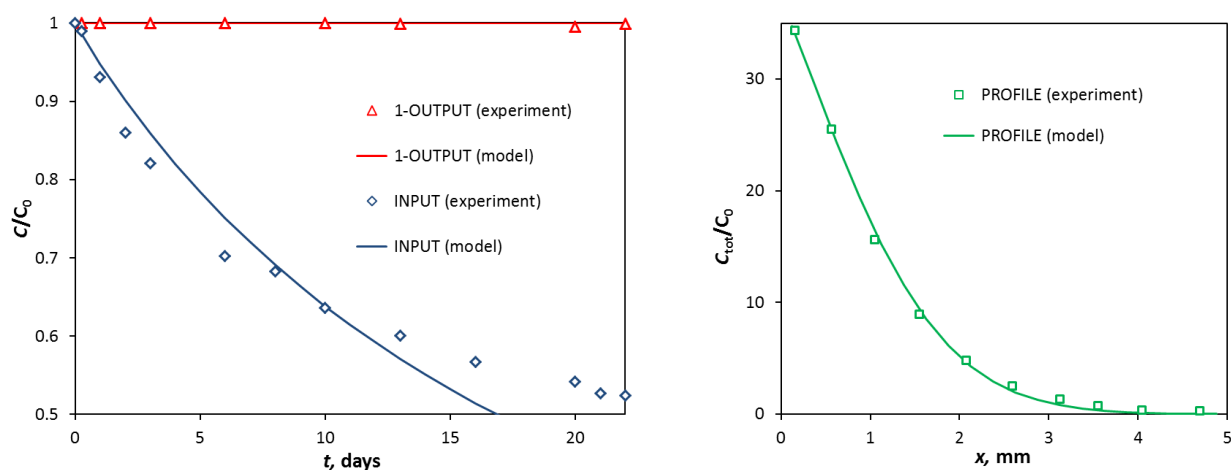


Figure 5: Results of ^{223}Ra through-diffusion experiment of, which lasted 22 days, in portlandite equilibrated water and its optimal fit.

The results of diffusion experiments are in agreement with results of batch experiments, in which similar K_d values were obtained for both tracers for lower values of phase ratio V/m . Further it is remarkable that the values of effective diffusion coefficients, which control the diffusion flux in stationary state, are for pressed blocks of crushed cementitious material significantly higher than that corresponding to samples of compact plugs of hydrated cement paste observed in the first part of our study, although determined total porosity of both materials are similar – about 0.5. It can be concluded that the diffusion pathway in crushed and pressed material is shorter than that in compact material. The diffusion experiments with compact plugs will be preferred in the further work.

Table 2: Determined diffusion coefficients of Sr and Ra in the layer of the crushed hydrated cement paste in two working solutions.

	D_e (Sr) m²/s	D_a (Sr) m²/s	K_d (Sr) L/kg	D_e (Ra) m²/s	D_a (Ra) m²/s	K_d (Ra) L/kg
Synthetic cement water	5.7·10 ⁻¹¹	5.5·10 ⁻¹²	8.5	5.1·10 ⁻¹¹	4.4·10 ⁻¹³	97
Portlandite water	6.0·10 ⁻¹¹	5.4·10 ⁻¹²	9.3	9.0·10 ⁻¹¹	4.9·10 ⁻¹³	153

4 Conclusions and Future work

Two methods of evaluation of diffusion coefficients using knowledge of total concentration profiles were practically implemented in a numerical model and successfully compared for the case of stationary state. A useful approach to the experimental determination of diffusion qualities of porous layers was presented, i.e. methods taking into account the concentration changes in working containers and presence of separating filters, for which the evaluation methods are available. This approach could help, in further studies, to discuss the suitability of application of simple interaction models for the description of diffusion transport of interacting species through cementitious layers. In the next period, special attention will be paid to the Cl⁻ and Ra²⁺ interaction models with cementitious materials and incorporation of them into diffusion transport codes.

Acknowledgement

The research leading to these results has received funding from the European Union's Horizon 2020 Research and Training Programme of the European Atomic Energy Community (EURATOM) (H2020-NFRP-2014/2015) under grant agreement n° 662147 (CEBAMA). This contribution is a partially result of SURAO project “Research Support for Safety Evaluation of Deep Geological Repository”.

References

- Baborová, L., Vopálka, D., Vetešník, A., Hofmanová, E. (2016). Migration behaviour of strontium in Czech bentonite clay. *Journal of Sustainable Development of Energy, Water and Environment Systems*, 4(3), 293-306.
- Box, M.J. (1965). A new method of constrained optimization and a comparison with other methods. *The Computer Journal*, 8(1), 42-52.
- Shackelford, C.D. and Moore, S.M. (2013). Fickian diffusion of radionuclides for engineered containment barriers: Diffusion coefficients, porosities and complicating issues. *Engineering Geology*, 152(1), 133-147.
- Večerník, P., Hausmannová, L., Červinka, R., Vašíček, R., Roll, M., Hloušek, J., Havlová, V. (2016). Interaction between cement and Czech bentonite under temperature load and in in-situ conditions: An overview of experimental program. *In: M. Altmaier, V. Montoya, L. Duro, A. Valls (Eds.) Proceedings of the 1st Annual Workshop of the CEBAMA Project. KIT Scientific Report, 7734.*
- Vopálka, D., Filipská, H., Vokál, A. (2006). Some methodological modifications of determination of diffusion coefficients in compacted bentonite. *MRS Proceedings*, 932, 983-989.
- Vopálka, D., Vetešník, A., Hofmanová, E. (2017). Methods of evaluation of through-diffusion experiments on sandwich bentonite cement layers in a simple experimental set-up. *In: M. Altmaier, V. Montoya, L. Duro, A. Valls (Eds.) Proceedings of the 1st Annual Workshop of the CEBAMA Project. KIT Scientific Report, 7734.*

Nernst-Planck Solver (NPS) applied to diffusion of ions through a constricted pore

Leonardo Hax Damiani^{1,2*}, Yuankai Yang³, Sergey V. Churakov^{1,2}, Georg Kosakowski^{1*}

¹ Paul Scherrer Institut (CH)

² Institute for Geological Sciences, University of Bern (CH)

³ Tsinghua University (CN)

* Corresponding author: leonardo.hax@psi.ch; georg.kosakowski@psi.ch;

Abstract

Cement-based and clay-based materials are important for radioactive waste disposal. Both material groups contain mineral phases with charged surfaces, e.g. calcium-silicate-hydrates, or swelling and non-swelling clay minerals. In this study, we simulate the diffusion of ions through a narrow pore to analyse the influence of mineral surface charge on ion transport in a constriction. We use the newly developed reactive transport code Nernst-Planck Solver (NPS), which couples electrochemical migrations of ions under the influence of electric fields with diffusive transport. The simulations reproduce anticipated enrichment of opposite-charge ions closer to the surfaces whereas same-charged ions are expelled from the constricted pore space due to the repulsive electric field exerted by the charged mineral surface. The presented NPS framework can be applied to a large variety of chemically reactive systems and at the same time provides full control of the use of numerical algorithms to solve the underlying differential equations.

1 Introduction

Cement and clay materials are used in various geo-engineering applications. Specifically, they constitute essential parts of the engineered barrier systems in radioactive waste repositories (Kosakowski and Berner, 2013). For materials like clay, reactive transport codes need to represent the transport of ions across various pore types confined by charged mineral surfaces, such as clay minerals or C-S-H phases in cementitious materials. For clay minerals which have strongly negatively charged surfaces, the porosity accessible for anions is influenced directly by the ionic strength due to the formation of an electric double layer (Van Loon et al., 2007). The pore space in non-swelling clays, in a simplified approach, can be partitioned into two compartments: free pore space and surface layers. The concentration of counter ions near the charged surface will be enriched to compensate the electrostatic potential due to the surface charge. Electrostatic interactions of ions with charged mineral surfaces strongly influence the transport of ions in a constricted pore space and the traditional Fickian diffusion approach does not apply in all situations. It is necessary to consider the effect of the charged mineral surfaces and species-dependent diffusion coefficients. One approach is based on the Gouy-Chapmann model (Bard and Faulkner, 2001). The region near the charged mineral surface where the electric field is influencing the mobility of ions is called electric double layer (EDL). The understanding of the EDL and its influence into the diffusive transport in clay minerals is relevant for describing the movement of charged species in the presence of charged surfaces.

The newly developed NPS reactive transport code (Hax Damiani et al., 2016) is applied to analyse the anion accessibility of ions diffusing through pores with charged surfaces. This study case is inspired in Wang et al. (2007). NPS considers the Poisson-Nernst-Planck (PNP) system of equations as in Samson and Marchand (1999) to model the transport of species and the chemical solver to account for chemical reactions and mineralogical changes.

2 Approach/Tools

NPS is developed with the primary goal to provide the flexibility needed to deal with a wide variety of reactive transport problems. NPS is based on the finite element framework FEniCS (Alnaes et al., 2015) and the chemical solver Reaktoro (Leal et al., 2017). Coupling between transport and chemical solvers is based on the sequential non-iterative approach (SNIA), presented in Figure 1.

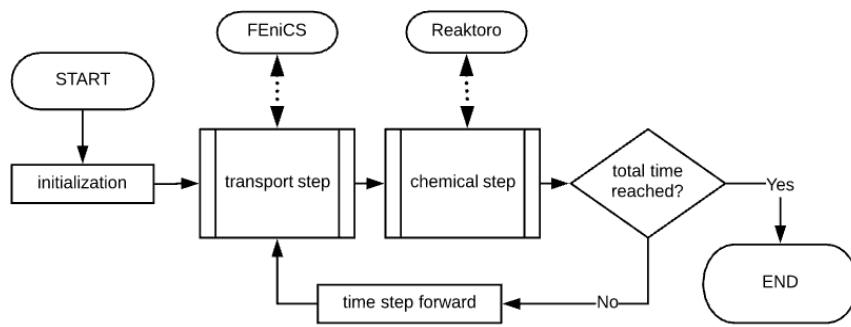


Figure 1: Sequential Non Iterative Approach adopted in NPS.

To couple the transport solver, FEniCS, and the chemical solver, Reaktoro, we use the Python scripting language (Python Software Foundation, <http://www.python.org>). NPS has been validated by simulating the benchmark problems like the one formulated by Lichter (1994) and described in Rasouli et al. (2015), as Case 1.

3 Diffusion Transport

To describe the influence of an electrostatic potential on the movement of charged species we have coupled the Nernst-Planck equations with the Poisson equation. The Poisson-Nernst-Planck (PNP) system of equations take into account the electric field originated from charged surfaces which favours attraction of charged counter-ions and repulsion of charged co-ions closer to this surface. It also considers the fact that the diffusive movement of charged particles generates electric field acting on the ions in the system.

The Nernst-Planck equations are composed of two flux terms, the Fickian flux and the electrochemical flux

$$J_{total} = J_{fickian} + J_{electrochemical} \quad (1)$$

where

$$J_{fickian} = -D_i \nabla c_i \quad (2)$$

and

$$J_{electrochemical} = -\frac{z_i D_i F c_i}{RT} \nabla \phi \quad (3)$$

D_i is the diffusion coefficient (m^2/s) for species i , c is the concentration (mol/m^3), z is the charge (C), F is the Faraday constant (C/mol), R is the gas constant ($(\text{kg}\cdot\text{m}^2)/(\text{mol}\cdot\text{K}\cdot\text{s}^2)$), T is the temperature (K) and ϕ is the electric field (V).

The simple Fickian diffusion approach is not sufficient for describing the transport of ions through charged porous media since it neglects the effect the electric field. The electric field is described by the Poisson equation:

$$\nabla^2 \phi + \frac{F}{\epsilon} (\sum_{i=1}^{N_s} z_i c_i) = 0 \quad (4)$$

where ϕ is the electric potential (V), ϵ is the dielectric constant (F/m) of the porous media and N_s is the number of species in the system. To comply with finite element (FE) methods the system of coupled Nernst-Planck-Poisson equations is transformed to its weak formulation for a sub set of test functions $\{V_i\}$:

$$\int_{\Omega} J_i \cdot V_i dx = \int_{\Omega} \left(-D_i \nabla c_i - \frac{z_i D_i F}{RT} \nabla \phi \right) \cdot \nabla V_i dx \quad (5)$$

$$\int_{\Omega} \nabla \Phi \cdot \nabla V_{\phi} dx - \frac{F}{\epsilon} \int_{\Omega} (\sum_{i=1}^{N_s} z_i c_i) \cdot V_{\phi} dx = 0 \quad (6)$$

With some algebraic manipulation, the final FE formulation of the problem solved in NPS is

$$\int_{\Omega} c_i \cdot V_i dx = \int_{\Omega} -D_i \left(\nabla c_i + \frac{z_i F}{RT} \nabla \phi \right) \cdot \nabla V_i dx \quad (7)$$

$$\int_{\Omega} \nabla \Phi \cdot \nabla V_{\phi} dx - \frac{F}{\epsilon} \int_{\Omega} (\sum_{i=1}^{N_s} z_i c_i) \cdot V_{\phi} dx = 0 \quad (8)$$

The equation system is solved with a Newton algorithm readily implemented in FENICS.

4 Constricted pore study case

We implemented a 2D model to analyze the diffusion of NaCl through a constricted pore space. The values of species-dependent diffusion coefficients were $\text{Na}^+ = 1.334 \cdot 10^{-9} \text{ m}^2/\text{s}$ and $\text{Cl}^- = 2.032 \cdot 10^{-9} \text{ m}^2/\text{s}$ (values from Flury and Gimmi (2002) for 25°C). Chemical reactions between species are not considered. Figure 2 presents the schematic setup of this study case. Figure 2 also shows the three cross-sections: (a) horizontal in the middle of the domain ($y = 7.5 \text{ nm}$); (b) horizontal next to the charged surface ($y = 5 \text{ nm}$) and (c) vertically in the middle of the domain ($x = 15 \text{ nm}$).

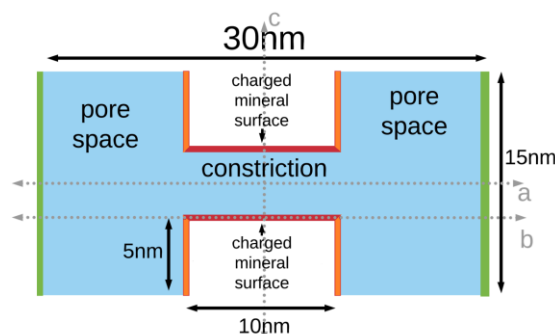


Figure 2: Schematic setup of the 2D model of the constricted pore and charged mineral surface.

We consider a 5 nm thin confinement, representing a typical size of mesopores in clay rocks that vary from 2 to 50 nm (Wigger and Van Loon, 2017). The boundary condition applied to the charged mineral surface (indicated in red in Figure 2) is

$$\nabla\phi = \frac{F}{\epsilon_R T} \sigma \vec{n} \quad (9)$$

where σ is the charge density of the clay mineral and \vec{n} denotes the outward unit normal vector. We impose the gradient of the electric potential to be related to the charge density of the mineral. In our case, we apply a charge density of $-1.0 \cdot 10^{-14}$ Q/m². Such value is in agreement to surface charge in clay rocks (Tournassat and Steefel, 2015). The reference electric potential of $\phi = 0$ is applied at the right boundary. To ensure zero charge flux (no current) in the system, we apply a no-flux condition to the electric potential ($\nabla\phi = 0$) at the left boundary (indicated in green in Figure 2). A Dirichlet boundary condition is applied to the left and right boundaries regarding the concentrations of Na⁺ and Cl⁻. We impose a concentration gradient by setting the concentrations on the left boundary to 100 mol/m³ and on the right boundary to 50 mmol/m³. The initial concentration of electrolyte in the model domain was set to 50 mol/m³.

Figure 3 shows the triangular numerical discretization of the domain. We adopt a higher discretization close to the charged surface to properly resolve steep gradients near the surface. The smallest nodes distance is 0.1 Å, and the biggest is 10 Å.

For the calculations we use standard Lagrange Finite Elements method with degree 1.

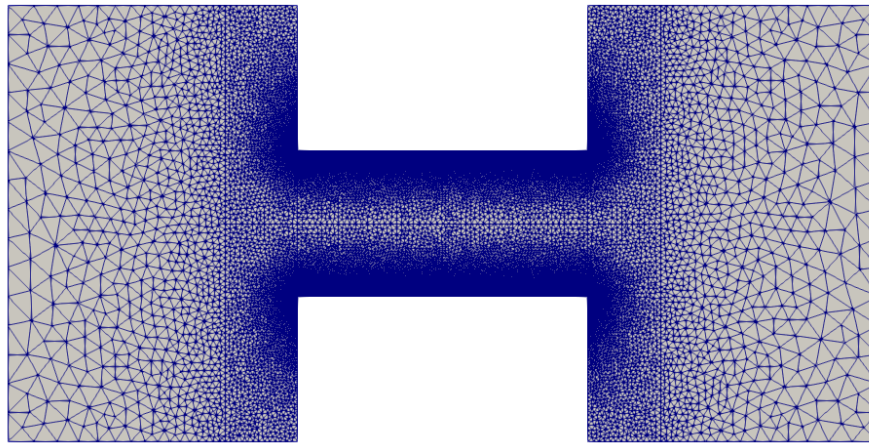


Figure 3: FE mesh discretization.

5 Results

Figure 4 (upper left) shows the profiles, at steady state, of ions Na⁺ and Cl⁻ and electric potential along the different cross sections marked in Figure 2. Along a line in the centre of the pore, cross-section a), we observe small differences between Cl⁻ and Na⁺ concentrations due to the influence of the overlapping electric potentials from the charged surfaces (upper right part of Figure 4). Please note that the charge of ions is compensated by the second derivative of the electric potential (Eq. 4) and not by the electric potential itself.

The spatial concentrations distribution, at steady state, of Na⁺ and Cl⁻ ions are presented in Figure 5. The steady state ion flux across the system imposed by the applied concentration gradient is $2.6 \cdot 10^{-6}$ mol/m²/s.

The cross section along the charged surface (middle left part of Figure 4) shows a significantly higher concentration for Na^+ at the surface while Cl^- concentrations are very low. The peaks in ion concentrations and in the electric potential (Figure 4 middle right) at distances of 10 nm and 20 nm are artefacts caused by the sharp tips of the constrictions (corners). Figure 6 presents the electric potential charges throughout the domain. Due to the boundaries conditions imposed at the charged mineral surface, very steep gradients are imposed at the corners. The utilized numerical method, linear Lagrange Finite Elements, cannot handle such situations very well which enforces small numerical artefacts into the electric potential and ion concentrations. It should be noted that this does not invalidate the correctness of the general numerical solution.

Problems regarding imposing the gradient and the electric potential are known, and the extended Poisson Boltzmann equation in combination with other high order FE methods has been used to smooth model more realistically ion concentrations near charged surfaces.

The ion concentration profiles perpendicular to the charged surfaces (Figure 4 lower left) show the enrichment of Na^+ near the surface and the expulsion of Cl^- . The magnitude and extent of enrichment and expulsion are influenced by the combination of ion concentrations (ionic strength of solution) and the surface charge. In this work we use the simplest approach in form of the classic PNP equations to describe the interaction between surface charge and ion fluxes. This method is known to give unrealistic results for ion concentrations under certain conditions. Several extensions of the PNP method are presented in literature (see e.g. Tournassat and Steefel, 2015).

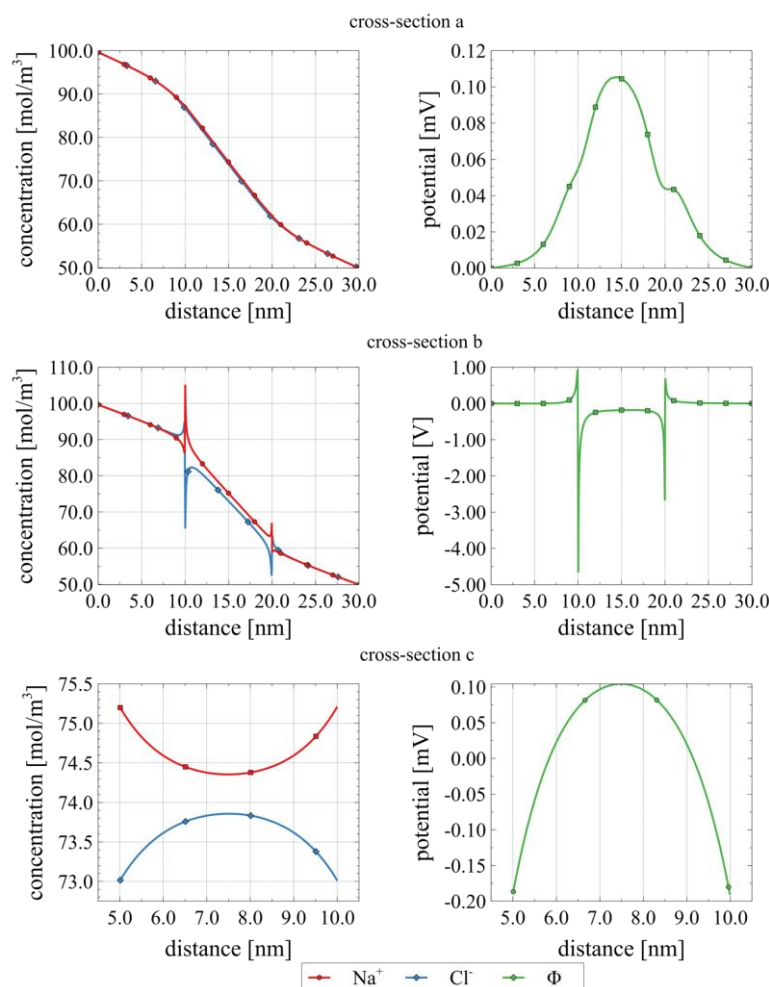


Figure 4: Concentrations profile through cross-sections.

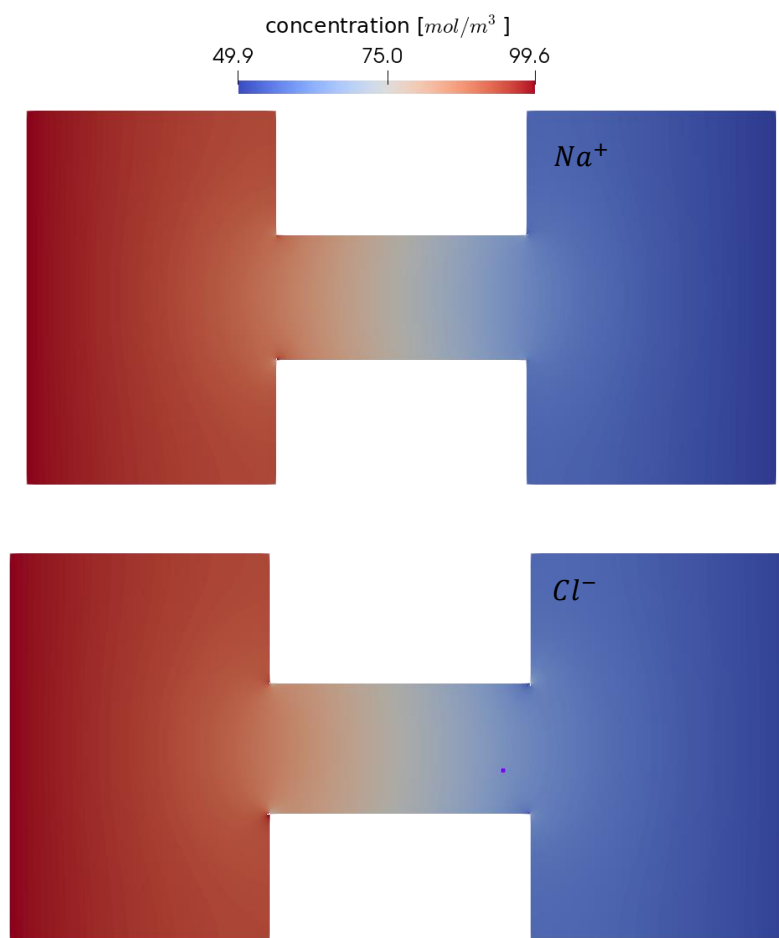


Figure 5: Na^+ and Cl^- concentration distribution throughout the domain.

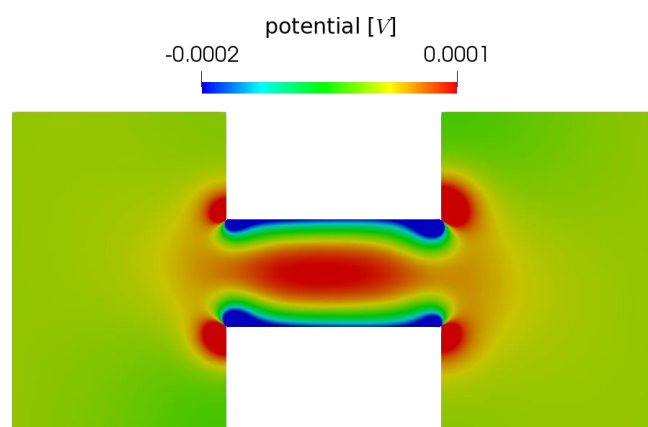


Figure 6: Electric potential charges throughout the domain.

6 Summary and Future work

With the newly developed reactive transport code NPS, we can solve a wide variety of (chemically reactive) problems and at the same time have full flexibility for the choice numerical methods to solve the underlying differential equations. NPS can be easily adapted to accommodate new processes, arbitrary domain geometry in 1D, 2D and 3D, boundary conditions, new source and sink terms or kinetic reactions.

NPS is also useful when applied for simulation of pore-scale problems such as diffusion of ions through a constricted pore. Such meso-scale simulations can be used to the analysis of the influence of charge mineral surface on diffusive transport in a porous medium.

The results of the study case show the coupled impact of the charged mineral surface on the diffusive transport of ions. Counter-charged ions are attracted by the surface charges, while the surface charges expel same-charged ions. In a highly compacted system, ions can be entirely excluded or strongly enriched in the pore space between charged mineral surfaces depending on their charge.

In the next step, we will extend the meso-scale model and consider the ion distribution in the EDL taking into account the chemical reactions, and work on the influence between the Poisson equation and the extend Poisson equation to describe the electric potential generated from the charged mineral surfaces. In addition, we will implement an electrostatic model in the form of a Donnan Approach (Overbeek, 1956) into Reaktoro to be able to consider the effects of charged surfaces also in continuum-scale simulations. The Donnan model partitions the pore space into two parts with different chemical composition and transport properties: surface charges do not influence one part, and the other has a different composition (specific ions cannot enter due to electrostatic repulsion). These phenomena are presented and discussed extensively in Appelo et al. (2010), Glaus et al. (2015) and Tournassat and Appelo (2015).

Acknowledgement

We would like to thank Dr. Luc Van Loon, Dr. Ravi Patel, Dr. Andrea Sabau and Dr. Denis Bykov for helpful discussions about the presented work.

This work was supported by the Swiss State Secretariat for Education, Research and Innovation (SERI) under contract number 15.0186-2. The opinions expressed and arguments employed herein do not necessarily reflect the official views of the Swiss Government. Authors receive partial financial support from Nagra. The research leading to these results has received partial funding from the European Union's Horizon 2020 Research and Training Programme of the European Atomic Energy Community (EURATOM) (H2020-NFRP-2014/2015) under grant agreement n° 662147 (CEBAMA).

References

- Alnaes, M.S., Blechta, J., Hake, J., Johansson, A., Kehlet, B., Logg, A., Richardson, C., Ring, J., Rognes, M.E., Wells, G.N. (2015). The FEniCS Project Version 1.5. *Archive of Numerical Software*, 3(100), 9-23.
- Appelo, C.A.J., Van Loon, L.R., Wersin, P. (2010). Multicomponent diffusion of a suite of tracers (HTO, Cl, Br, I, Na, Sr, Cs) in a single sample of Opalinus Clay. *Geochimica et Cosmochimica Acta*, 74(4), 1201-1219.
- Bard, A.J. and Faulkner, L.R. (2001). *Electrochemical Methods: Fundamentals and Applications*. New York: Wiley, 2001.
- Berner, U., Kulik, D.A., Kosakowski, G. (2013). Geochemical impact of a low-pH cement liner on the near field of a repository for spent fuel and high-level radioactive waste. *Physics and Chemistry of the Earth*, 64, 46-56.
- Bradbury, M.H. and Baeyens, B. (2009). Sorption modelling on illite Part I: Titration measurements and the sorption of Ni, Co, Eu and Sn. *Geochimica et Cosmochimica Acta*, 73(4), 990-1003.
- Churakov, S.V. and Gimmi, T. (2011). Up-scaling of molecular diffusion coefficients in clays: A two-step approach. *The Journal of Physical Chemistry*, 15(14), 6703-6714.
- Flury, M. and Gimmi, T. (2002). Solute diffusion. In: *Methods of soil analysis, Part 4, Physical Methods*, Soil Science Society of America Book Series 5.4.

- Glaus, M.A., Aertsens, M., Appelo, C.A.J., Kupcik, T., Maes, N., Van Laer, L., Van Loon, L.R. (2015). Enhanced mass transfer rates for Sr^{2+} , Co^{2+} and Zn^{2+} in compacted illite caused by cation diffusion in the electrical double layer. *Geochimica et Cosmochimica Acta*, 165, 376-388.
- Hax Damiani, L., Glaus, M., Churakov, S.V., Kosakowski, G. (2016). Rapid development of a reactive transport code with FEniCS and Reaktoro. CEBAMA Contract Number: 662147 Deliverable n°D3.04.
- Jenni, A., Mäder, U., Lerouge, C., Gaboreau, S., Schwyn, B. (2014). In-situ interaction between different concretes and Opalinus Clay. *Physics and Chemistry of the Earth*, 70-71, 71-83.
- Kosakowski, G. and Berner, U. (2013). The evolution of clay rock/cement interfaces in a cementitious repository for low- and intermediate level radioactive waste. *Physics and Chemistry of the Earth*, 64, 65-86.
- Kulik, D.A., Wagner, T., Dmytrieva, S.V., Kosakowski, G., Hingerl, F.F., Chudnenko, K.V., Berner, U.R. (2013). GEM-Selektor geochemical modeling package: Revised algorithm and GEMS3K numerical kernel for coupled simulation codes. *Computational Geosciences*, 17(1), 1-24.
- Leal, A.M.M., Kulik, D.A., Smith, W.R., Saar, M.O. (2017). An overview of computational methods for chemical equilibrium and kinetic calculations for geochemical and reactive transport modeling. *Pure and Applied Chemistry*, 89(5), 597-643.
- Lichtner, P.C. (1994). Principles and practice of reactive transport modeling. *MRS Proceedings*, 353, 117.
- Overbeek, J.T. (1956). The Donnan equilibrium. *Progress in Biophysics and Biophysical Chemistry*, 6, 57-84.
- Parkhurst, D.L. and Appelo, C.A.J. (2013). Description of Input and Examples for PHREEQC Version 3 — A Computer Program for Speciation, Batch-Reaction, One-Dimensional Transport, and Inverse Geochemical Calculations. U.S. Geological Survey Techniques and Methods, book 6, chapter A43, 497p. U.S. Geological Survey Techniques and Methods, Book 6, Chapter A43, 6-43A.
- Rasouli, P., Steefel, C.I., Mayer, K.U., Rolle, M. (2015). Benchmarks for multicomponent diffusion and electrochemical migration. *Computational Geosciences*, 19(3), 523-533.
- Samson, E. and Marchand, J. (1999). Numerical solution of the extended Nernst–Planck model. *Journal of Colloid and Interface Science*, 215(1), 1-8.
- Tournassat, C. and Appelo, C.A.J. (2011). Modelling approaches for anion-exclusion in compacted Na-bentonite. *Geochimica et Cosmochimica Acta*, 75(13), 3698-3710.
- Tournassat, C. and Steefel, C.I. (2015). Ionic transport in nano-porous clays with consideration of electrostatic effects. *Reviews in Mineralogy & Geochemistry*, 80(1), 287-329.
- Van Loon, L.R., Glaus, M.A., Müller, W. (2007). Anion exclusion effects in compacted bentonites: Towards a better understanding of anion diffusion. *Applied Geochemistry*, 22(11), 2536-2552.
- Wang, X., Xue, J., Wang, L., Guo, W., Zhang, W., Wang, Y., Ouyang, Q. (2007). How the geometric configuration and the surface charge distribution influence the ionic current rectification in nanopores. *Journal of Physics D: Applied Physics*, 40(40), 7077-7077.
- Wigger, C. and Van Loon, L.R. (2017). Importance of interlayer equivalent pores for anion diffusion in clay-rich sedimentary rocks. *Environmental Science and Technology*, 51(4), 1998-2006.

POSTERS

Table of Posters

Radionuclide migration at the low pH cement / clay interface: derivation of reactive transport parameters <i>N. Ait Mouheb, V. Montoya, T. Schäfer, H. Geckeis</i>	321
Mechanism of molybdenum uptake by hydrated calcium aluminate (AFm) <i>N.C.M. Marty, S. Grangeon, E. Elkaïm, C. Tournassat, C. Fauchet, F. Claret</i>	322
Experiments on interface processes at the cement/Callovo-Oxfordian claystone interface and the impact on physical properties; mechanical and flow properties of fresh interfaces <i>R. Cuss, A. Wiseall, M. Dobbs, D. Parkes, J. Harrington, J. Talandier, X. Bourbon</i>	323
Comparison of mass transfer in concrete-bentonite interface based on HB6 laboratory and full-scale FEBEX in-situ tests <i>M.J. Turrero, A. Garralón, P. Gómez, J. Peña, L. Sánchez, E. Torres</i>	324
Effects of porosity evolution on the evaluation of radionuclide diffusion coefficients in mortars and concrete <i>M. García-Gutiérrez, M. Mingarro, T. Missana</i>	325
Pore-scale reactive transport modelling of transport and leaching processes in cementitious materials <i>S. Rohmen, A. Idiart, G. Deissmann, D. Bosbach</i>	326
The physico-chemical evolution of UK high-pH backfill material <i>R.G.W. Vasconcelos, N.C. Hyatt, J.L. Provis, C.L. Corkhill</i>	327
Property of bonded planar interface between COx claystone and low-pH concrete <i>Z. Liu, J. Shao, S. Xie, X. Bourbon, G. Decamps</i>	328
Development of Surface Reactivity Interface Experiments (SERIE) for studying FEBEX bentonite-concrete interaction <i>D.E. González-Santamaría, M. Angulo, J. González-Yelamos, R. Fernández, A. Ortega, A.I. Ruiz, E. Rodríguez, J. Cuevas</i>	329
Clayey water interaction with high and low-pH concretes <i>Á. Fernández, M.C. Alonso, J.L. García Calvo</i>	330
FEniCS-Reaktoro coupling: constricted pores and cement/clay interfaces <i>L. Hax Damiani, Y. Yang, S.V. Churakov, G. Kosakowski</i>	331

Aged interface between Opalinus Clay and low-pH mortar: sample preparation, X-ray computed tomography and core infiltration experiment for hydraulic-chemical properties

E. Bernard, U. Mäder, A. Jenni

332

Changes in groundwater composition following interaction with cement

E. Rastrick, M. Isaacs, M. Felipe-Sotelo, D. Read

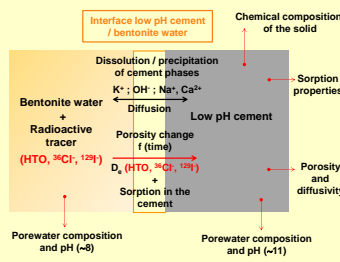
333

Radionuclide migration at the low pH cement / clay interface: derivation of reactive transport parameters

Naila Ait Mouheb*, Vanessa Montoya, Thorsten Schäfer, Horst Geckeis

Background / Objectives

- Repository evolution vs time and space:** Physical and Chemical processes taking place in the engineered barrier system will define the radionuclide mobility / retention.
- Concrete and clay** are used as confinement barriers → During the prolonged period of disposal, they will undergo alterations → In order to minimize the interaction, **low pH cements** were developed in the late 90's.
- Objectives:** Filling the gaps in the process understanding of the interactions occurring between **low pH cement** materials and clay and to assess the impact that these processes can have in radionuclide migration.



Materials

Composition (wt.%) of the solid mixtures

	MIX 1	MIX 2	MIX 3	Cebama paste
CEM I	39 ^a	40	50	25 ^b
Silica fume	39	40	50	27
Limestone filler	19	20	-	-
Superplasticizer	3 ^c	-	-	4 ^d
Blast furnace slag	-	-	-	16
Quartz filler	-	-	-	28
w/b	0.6			0.25

^a CEM I 52.5N SR, ^b CEM I 42.5 MH/SR/LA, ^c Inorganic superplasticizer (SiocX®), ^d Superplasticizer naphthalene-based Pantarhit LK (FM).

Bentonite pore water: MX-80 [1]: pH ~ 7.8, [HCO₃⁻] ~ 9 · 10⁻⁴ M

Tools / Methods

- Chemical / structural characterization:** XRF, XRD, TG-DTA, FTIR, ²⁹Si and ²⁷Al MAS NMR, SEM-EDX, XAS (Fe and Cl K-edge), N₂-BET and MIP.
- Pore solution characterization:** 1) Ex-situ leaching method [2] and 2) The steel die method [3] – B. Lothenbach (EMPA).

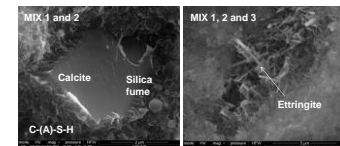
- Kinetic batch sorption experiments** (HTO, ³⁶Cl, ¹²⁹I and Be): Glovebox (Ar atmosphere). S/L ratio = 0.133 kg·L⁻¹. Background electrolyte → low pH cement porewater (pH ~11) → Radionuclide concentrations measured by LSC.
- Through diffusion experiments** (HTO and ³⁶Cl): → Construction of diffusion cell. – V. Krepper (INE).

- Geochemical modelling:** Code: GEMS [4] [5]. Database: CEMDATA18 [6]. Concept: ideal solid solutions for C-N-A-S-H phases [7].
- Predictive reactive transport modelling:** Code: PhreeQC 3.3 – (1D) [8]. Database: CEMDATA07 [9]. Concept: Precipitation / dissolution by kinetics & thermodynamic → Porosity change.

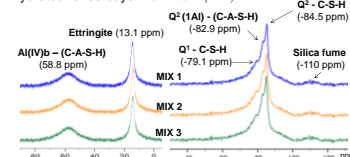
Selected results

Characterization of low pH cements

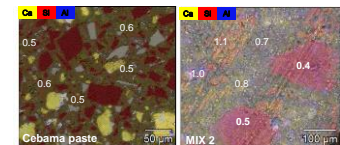
→ SEM images after 90 days of hydration



→ ²⁷Al and ²⁹Si MAS NMR spectra of low pH cements hydrated for 90 days – C. Adam (INE)



→ SEM-EDX mapping of Ca, Si, and Al + local Ca/Si ratios – D. Schild (INE).

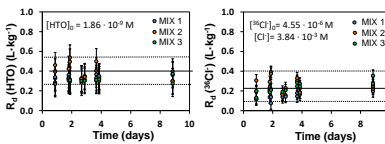


→ XRD and TG-DTA: Calcite identification.

Sorption parameters

→ R_d values as a function of time for HTO and ³⁶Cl.

→ R_d values for Be(II) in cement – N. Cevrim, X. Gaona (INE)



→ TG-DTA: bound water: 29.10 ± 1.70 wt.% → R_d for HTO = fraction of bound water → $R_d = 0.29 ± 0.02$ L·kg⁻¹ [10].

→ Zeta potential measurements – J. Lützenkirchen (INE)
→ ($\xi_{MIX1} = -17 ± 1$ mV, $\xi_{MIX2} = -16 ± 1$ mV, $\xi_{MIX3} = -13 ± 1$ mV).

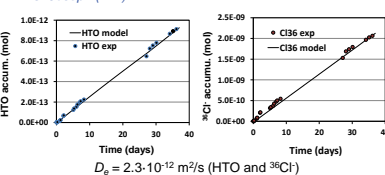
→ Cl K-edge: Cl: chemically bound / physically adsorbed

Transport parameters

→ Determination of the D_e and porosity (ϵ_{acc}) → Comsol Multiphysics 5.3 → Fick's law

$$Fick's \text{ first law: } J = -De \frac{\partial C}{\partial x} \quad \alpha = \epsilon_{acc} + \rho \cdot K_d$$

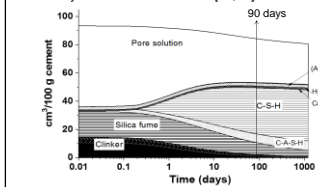
→ Accumulate HTO and ³⁶Cl vs time in the outlet reservoir – C. Joseph (INE)



$D_e = 2.3 \cdot 10^{-12}$ m²/s (HTO and ³⁶Cl)

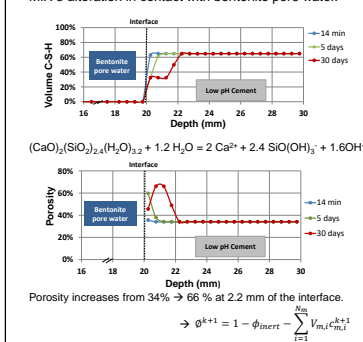
Geochemical modelling (hydration)

→ Hydration model of MIX 3 [11,12].



Reactive transport modelling

MIX 3 alteration in contact with bentonite pore water.



Conclusions

Characterization of low pH cements

- Main phases identified (> 80% wt) → C-S-H and C-A-S-H → Ca:Si = 0.8 - 1.0. Al:Si = 0.05.
- Minor phases: ettringite + silica fume. No portlandite.
- Porewater pH ~ 11.

Sorption parameters

- Very weak sorption of HTO and ³⁶Cl on low pH cement → $R_d < 0.40 ± 0.13$ L·kg⁻¹.

Transport parameters

- Effective diffusion coefficient of $2.3 \cdot 10^{-12}$ m²/s determined for HTO and ³⁶Cl on Cebama paste.

Hydration modelling

- The use of C-A-S-H solid solution is mandatory to simulated the solid phase assemblages after hydration
- Reactive transport modelling**
- Low pH cement in contact with bentonite pore water → degraded area ~ 2 mm after one month of alteration.

Contact person: *naila.ait-mouheb@kit.edu

Collaborators: 

References:
[1] Bradbury, M. H., and Baeyens, B. (2011). PSI report 11-05
[2] Alonso, M.C., et al. (2012). SKB report 12-02, Sweden.
[3] Lothenbach, B., et al. (2014). Phys. Chem. Earth 70-71, 3-16.
[4] Kulk, D.A., et al. (2013). Comput. Geosci. 17, 1-24.
[5] Wagner, T., et al. (2012). Can. Mineral. 50, 1173-1195.
[6] Lothenbach, B., et al. (2018). Cem. Concr. Res. in preparation.

[7] Myers, R.J., et al. (2014). Cem. Concr. Res. 66, 27-47.
[8] Parkhurst, D.L., et al. (2013). pubs.usgs.gov/of/2013/
[9] Lothenbach, B., et al. (2009). Cem. Concr. Res. 38, 848-860.
[10] Tits, J., et al. (2003). J. Contam. Hydrol. 61, 45-62.
[11] Pami, L.J., et al. (1984). Brit. Ceram. Proc. 35, 41-53.
[12] Lothenbach, B., et al. (2008). Cem. Concr. Res. 38, 1-18.



Mechanism of Molybdenum uptake by hydrated calcium aluminate (AFm)

Nicolas C.M. Marty^{1*}, Sylvain Grangeon¹, Erik Elkaïm², Christophe Tournassat¹, Clémence Fauchet¹, Francis Claret¹

¹ BRGM; ² Synchrotron SOLEIL

Marty et al. (accepted) Thermodynamic and crystallographic model for anion uptake by hydrated calcium aluminate (AFm): an example of molybdenum. *Scientific Reports*

Abstract

Amongst all cement phases, hydrated calcium aluminates (AFm) are foreseen to play a major role in the retention of anionic species (including radionuclides) that might enter in contact with cement-based materials. The Cl/MoO₄²⁻ exchange processes occurring on a AFm initially containing interlayer Cl were studied in alkaline conditions using flow-through experiments (Figure 1 and Table 1), and the evolution of the solid phase was characterized using electron probe microanalyzer and synchrotron high-energy X-ray scattering. For the latter technique, data were processed in both the reciprocal and real spaces. All data, together with their quantitative modelling, coherently indicated that Mo replaced Cl in AFm interlayer, with Mo being incorporated under the MoO₄²⁻ form by replacing 2 Cl⁻. In addition, modelling of several independent chemical experiments could prove that Cl/OH⁻ exchange processes occur together with Cl/MoO₄²⁻ exchange.

Table 1: Experimental conditions of flow-through experiments.

Exp. n°	Initial Mass (g)	Flow rates* (mL min ⁻¹)	Duration (h)
1	0.142	2.03–2.01	6.9
2	0.242	2.00–1.96	6.9
3	0.499	2.23–2.16	6.9

* monitored maximum and minimum flow rates

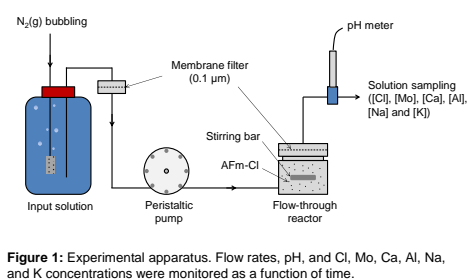


Figure 1: Experimental apparatus. Flow rates, pH, and Cl, Mo, Ca, Al, Na, and K concentrations were monitored as a function of time.

Modeling and determination of exchange parameters

- Exchange parameters (Table 3)
- Flow-through experiments (Figure 4)
- Evidence of Cl/OH exchange reactions (Figure 5)

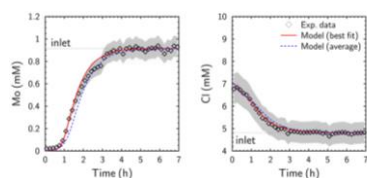


Figure 4: Evolutions of experimental and modeled Mo and Cl concentrations as a function of time (Exp. 1). “Best fit” models were obtained using different AEC (Table 3), while “average” models considered the same AEC_{site 1} (230 meq 100 g⁻¹) and AEC_{site 2} (126.3 meq 100 g⁻¹) for all experiments.

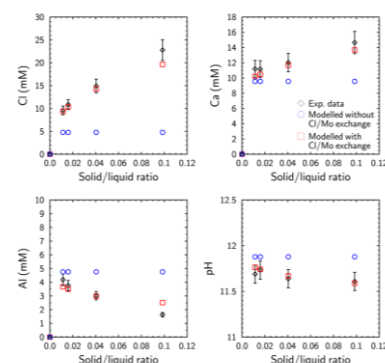


Figure 5: Evolution of experimental and modeled Cl, Ca, and Al concentrations and pH as a function of solid/liquid ratios (leaching experiment).

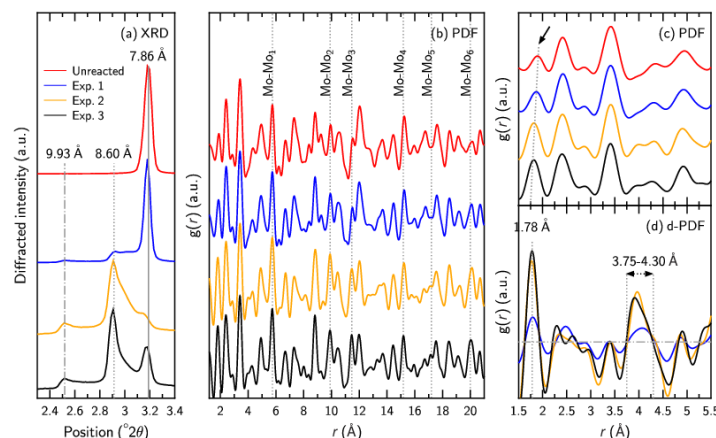


Figure 2: High-energy X-ray scattering data. (a): Detail of the 2.3–3.4 °2θ region of the data (b): PDF data of the same samples. (c): Detail of the 1.5–5.5 Å region of the PDF data. (d): d-PDF data obtained by subtracting the data obtained on the fresh sample from the data obtained on the samples that underwent contact with Mo.

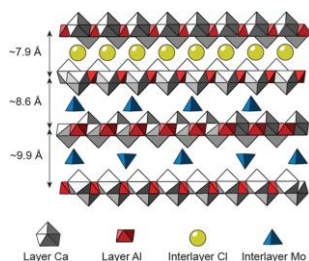


Figure 3: Proposed evolution of layer-to-layer distance as a function of interlayer anion nature and composition.

Mineralogical transformations

- Chemical composition of initial and reacted samples (Table 2)
- Crystal structure (Figures 2 & 3)

Table 2: Average initial and final AFm compositions (results reported in mole of element per mole of AFm).

Exp. n°	Ca	Al	Cl	Mo	OH*
AFm-Cl (initial)	4	1.8 ± 0.1	1.8 ± 0.2	0	0
1	4	1.9 ± 0.1	0.8 ± 0.5	0.4 ± 0.3	0.3
2	4	1.8 ± 0.1	0.2 ± 0.0	0.7 ± 0.1	0.2
3	4	1.9 ± 0.1	0.4 ± 0.1	0.6 ± 0.1	0.3

* Calculation: OH = Al - Cl - 2Mo

Table 3: Calculated final exchanger and AFm compositions. AFm compositions were established from exchanger compositions.

Exp. n°	AEC		log K _{Mo}	log K _{OH}	Exchanger composition		Anionic composition			
	(meq 100 g ⁻¹)				(equivalent fraction)		(mole of element per mole of AFm)			
	Site 1	Site 2			Site 1	Site 2	Mo	Cl	OH	
1	178.1	178.2	1.3	-0.8	Afm ₂ MoO ₄	0.92	--	0.5	0.6	0.5
					AfmCl	0.04	0.54	(0.4 ± 0.3)*	(0.8 ± 0.5)*	
					AfmOH	0.03	0.46			
	Afm ₂ MoO ₄	0.91	--	0.7	0.4					
2	260.3	96.0	1.3	-0.8	AfmCl	0.05	0.57	(0.7 ± 0.1)*	(0.2 ± 0.0)*	0.3
					AfmOH	0.04	0.43			
					Afm ₂ MoO ₄	0.91	--	0.6	0.5	
	3	235.8	120.5	1.3	-0.8	AfmCl	0.05	0.58	(0.6 ± 0.1)*	(0.4 ± 0.1)*
AfmOH						0.04	0.42			
Afm ₂ MoO ₄						0.91	--	0.6	0.5	

* Measured by EPMA (Table 2)

The research leading to these results has received funding from the European Union's European Atomic Energy Community's (Euratom) Horizon 2020 Programme (NFRP-2014/2015) under grant agreement, 662147 – Cebama

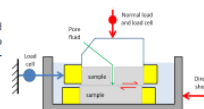
* Corresponding author. Tel.: +33-238-643-343; fax: +33-238-643-062
E-mail address: n.marty@brgm.fr

Robert Cuss^{1*}, Andrew Wiseall¹, Marcus Dobbs¹, Dan Parkes¹, Jon Harrington¹, Jean Talandier² and Xavier Bourbon²

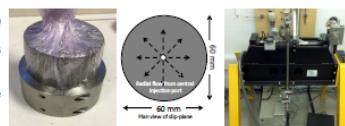
² Andra, 1-7, rue Jean Monnet, 92290 Chateaufort, France

2. Experimental apparatus

BGS have three bespoke shear rigs, 2 of which have been modified for the Cebama project. The Direct Shear Rig (DSR) has been used to investigate the flow characteristics of rock (Opalinus Clay, Callovo-Oxfordian Claystone). The apparatus has the following specifications:



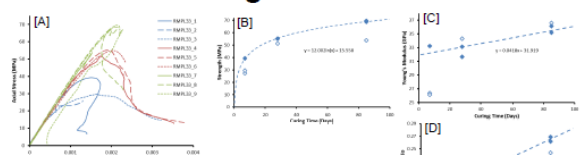
- Normal/vertical stress up to 20 MPa
- Variable shear rate of 1 mm per second to 3 month
- Vertical displacement accurate to < 60 nm
- Sample dimension 60 mm diameter, 53 mm height
- Pore pressure 0.5 - 25 MPa
- Central injection point ensuring pore fluid is delivered directly to the fracture



4. Concrete strength

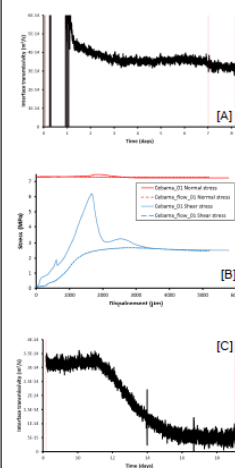


- Aggregate (4 – 12 mm), sand (0 – 4 mm) and binder were mixed with water and superplasticizer and thoroughly mixed as per instructions.
- A collar, sealed with Hylomar blue, was placed on top of the COx samples using a 60 mm inner diameter 3 mm diameter o-ring as a spacer [A].
- A small quantity of concrete was added and tamped using a piece of wood [B] and a modified vibrating toothbrush [C]. Up to 3 layers were added with the top surface finished flat with a trowel.
- The top surface was cleaned and a second collar [D] was added, sealed by means of an o-ring.
- Squares of lime-water saturated cloth were added to the collar in direct contact with the concrete in order to aid hydration of the concrete [E].
- The sample was vacuum packed at least three times and stored with the wet cloth at the bottom in the temperature controlled laboratory.

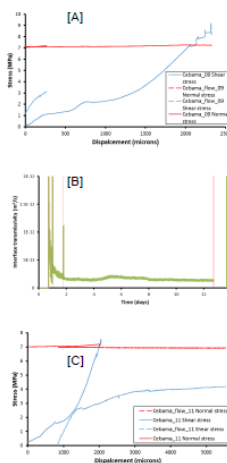


- Uniaxial tests have been conducted on cylindrical samples of 64.5 mm and 130 mm length
- At 7, 28 and 85 days following casting with 3 tests each.
- Uniaxial results are shown in [A], some tests resulted in premature failure attributed to the size of the sample.
- The strength of the concrete increased [B]. After 7 days the concrete had a strength of 39.3 MPa, increasing to 55.09 and 69.14 after 28 and 85 days. This is in line with expected strength.
- Young's modulus [C] and Poisson's ratio [D] also increased during curing.

6. Shear and flow of interface CO_x/USC



- The early stage of the flow experiment saw the rehydration of the interface [A].
- Flow reduced by one order of magnitude to 4×10^{-14} m²/s through hydration alone.
- The sample was sheared for a period of 14 days [B].
- The interface showed little strength during shearing [B] with a peak strength close to the residual strength of the virgin COx sample.
- The form of the stress-strain curve also changed with classic brittle behaviour during virgin deformation and elastoplastic behaviour, with a small degree of strain softening, for the interface [B].
- During the initial stages of shearing the flow remained constant [C].
- At the time of maximum slope of the shear stress (250 MPa shear modulus) the flow started to reduce [C].
- Flow reached a minimum of 2.8×10^{-15} m²/s, demonstrating a one-order of magnitude reduction in flow properties in response to shear.



- Flow testing in the USC variety of COx has been less successful.
- In test Cebama_09 a limited amount of shear was undertaken [A].
- During rehydration flow reduced from about 2×10^{-12} m²/s to 1.3×10^{-13} m²/s, more than a one order of magnitude reduction [B].
- Due to a logging error, flow was not recorded during the initial stage of shearing. However, at the end of shearing a pore pressure could not be sustained and flow was very large.
- Therefore the interface had opened significantly and had created an effective pathway.
- In test Cebama_11 the sample was sheared to its full extent [C].
- The shear modulus of the interface matches that of the virgin rock.
- The strength of the interface is considerably less than the virgin rock and shows classic elastoplastic behaviour.
- At all stages of this test a pore pressure could not be established suggesting that the interface had broken prior to shearing.

Column planning	Week 1	Week 2	Week 3	Week 4	Week 5	Week 6
Column 1						
Column 2						
Column 3						
Column 4						
Column 5						
Column 6						
Column 7						
Column 8						
Column 9						
Column 10						
Column 11						
Column 12						
Column 13						
Column 14						
Column 15						
Column 16						
Column 17						
Column 18						
Column 19						
Column 20						
Column 21						
Column 22						
Column 23						
Column 24						
Column 25						
Column 26						
Column 27						
Column 28						
Column 29						
Column 30						
Column 31						
Column 32						
Column 33						
Column 34						
Column 35						
Column 36						
Column 37						
Column 38						
Column 39						
Column 40						
Column 41						
Column 42						
Column 43						
Column 44						
Column 45						
Column 46						
Column 47						
Column 48						
Column 49						
Column 50						
Column 51						
Column 52						
Column 53						
Column 54						
Column 55						
Column 56						
Column 57						
Column 58						
Column 59						
Column 60						
Column 61						
Column 62						
Column 63						
Column 64						
Column 65						
Column 66						
Column 67						
Column 68						
Column 69						
Column 70						
Column 71						
Column 72						
Column 73						
Column 74						
Column 75						
Column 76						
Column 77						
Column 78						
Column 79						
Column 80						
Column 81						
Column 82						
Column 83						
Column 84						
Column 85						
Column 86						
Column 87						
Column 88						
Column 89						
Column 90						
Column 91						
Column 92						
Column 93						
Column 94						
Column 95						
Column 96						
Column 97						
Column 98						
Column 99						
Column 100						

Note: samples shown in red will be stored for future testing after Cebama has finished

- Fresh interface samples have been tested
- Repeat testing will occur over regular intervals
 - Determine changes in mechanical and flow properties as the interface ages
- SEM and fluorescence analysis to identify flow paths within the interface and to examine the chemical exchange across the interface
- Flow tests will be conducted in 'intact' COX, USC and TL concrete to determine baseline properties over a range of stresses.
- Continue uniaxial tests to observe changes in elastic properties as the concrete continues to cure.



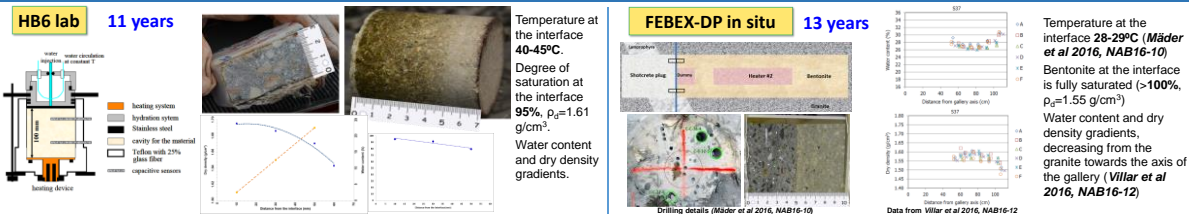
Comparison of mass transfer in concrete-bentonite interface based on HB6 laboratory and full-scale FEBEX in situ tests

Maria J. Turrera, Antonio Garralón, Paloma Gómez, Javier Peña, Lorenzo Sánchez, Elena Torres
CIEMAT, Unidad de Geología Ambiental Aplicada, Avda. Complutense, 40, 28040 Madrid, Spain

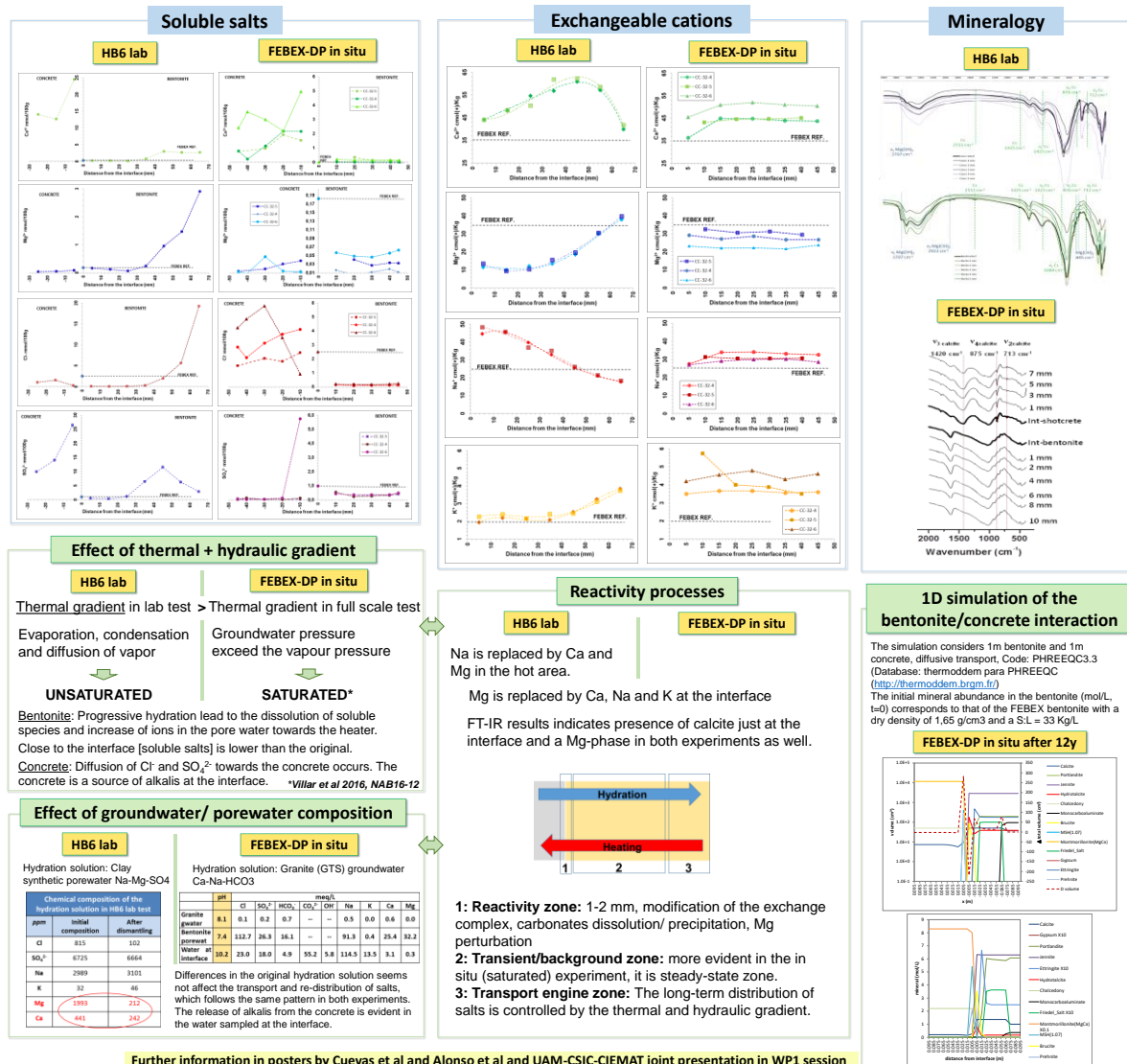
INTRODUCTION

This poster reports jointly the results of the analysis of the concrete/bentonite interface in the **full-scale FEBEX in situ test** and in the **HB6 laboratory test** that reproduces the thermal and hydraulic conditions of the in situ test (continuous hydration and heating - temperature 100°C - by opposite ends). The analyses were carried out at different distances from the interface in both the concrete and the bentonite samples. Heterogeneity of the real system is put in front of well controlled conditions of the lab test and the changes observed are used to compare geochemical processes in both. 1D geochemical modelling was made to simulate the concrete/bentonite interaction of the in situ test.

CONCRETE-BENTONITE INTERFACE SAMPLES



RESULTS AND DISCUSSION



CEBAMA 3rd Annual Workshop, Nantes, 17-18 April 2018

Acknowledgement The research leading to these results has received funding from the European Union's Horizon 2020 Programme of the EURATOM (H2020-NFRP-2014/2015) under grant agreement n° 662147 (CEBAMA). FEBEX-DP consortium (<http://www.grimseil.com/gts-phase-vi/febex-dp/febex-dp-introduction>) provided concrete and bentonite samples for this study and made possible groundwater sampling.



Effects of porosity evolution on the evaluation of radionuclide diffusion coefficients in mortars and concrete

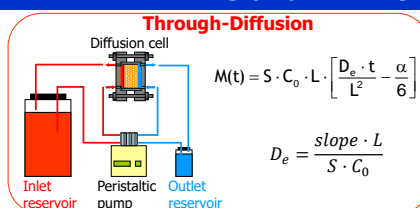
M. García-Gutiérrez, M. Mingarro, T. Missana

CIEMAT, Departamento de Medio Ambiente, Avenida Complutense, 40 - 28040 MADRID (SPAIN)

INTRODUCTION

Cement and concrete are widely used in repositories for low and medium radioactive waste. Cementitious materials have a good sorption capability for radionuclides (RNs) and generate an alkaline environment which produces a decrease in their solubility. The main transport process for RN in these materials is diffusion (retarded by sorption), which occurs within the networks of fissures and interconnected pores saturated by the porewater. Thus, the porosity of the system is one of the main important physical parameters for contaminant transport. The determination of reliable transport parameters in cements, mortars and concretes is much more complicated than in other materials of interest for isolating radioactive waste (as compacted or consolidated clays) and conventional experimental methods might not always provide accurate values of effective or apparent diffusion coefficients.

MATERIALS and METHODS



In-Diffusion

$$C = C_0 \cdot \operatorname{erfc} \left(\frac{x}{2\sqrt{D_a \cdot t}} \right)$$

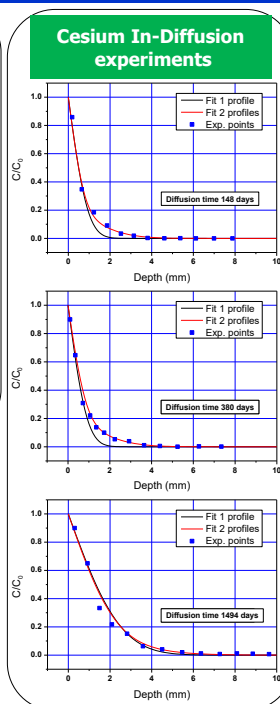
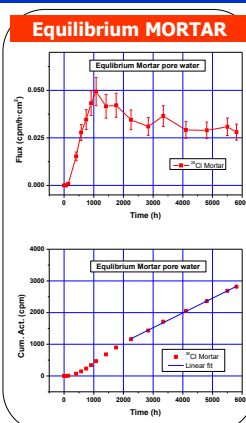
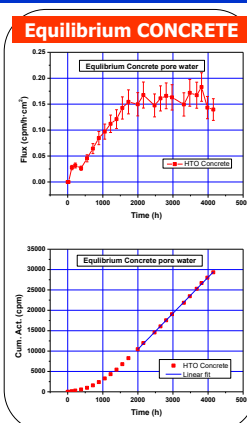
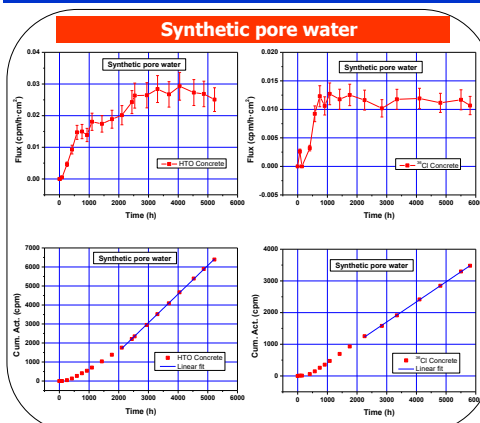
$$\alpha = \varepsilon + \rho_d K_d$$

D_e effective diffusion coeff.
 D_a apparent diffusion coeff.

Analytical solutions with:

M cumulative mass
 C_0 initial concentration
 S cross-sectional area
 L sample thickness
 α capacity factor
 ε porosity
 ρ_d dry density
 x depth
 t diffusion time

EXPERIMENTAL RESULTS



Cement pore waters composition (mol/L)

Element	Synthetic	Equilibrium Concrete	Equilibrium Mortar
Na ⁺	4.71·10 ⁻²	1.82·10 ⁻⁴	3.11·10 ⁻⁴
K ⁺	1.79·10 ⁻²	9.26·10 ⁻⁴	1.68·10 ⁻³
Ca ²⁺	8.00·10 ⁻³	1.20·10 ⁻²	7.24·10 ⁻³
Al ³⁺	1.00·10 ⁻⁵	1.22·10 ⁻⁵	1.16·10 ⁻⁵
Cl ⁻	1.97·10 ⁻³	3.86·10 ⁻⁴	3.07·10 ⁻⁴
SO ₄ ²⁻	3.12·10 ⁻⁴	1.46·10 ⁻⁴	8.86·10 ⁻⁵
SiO ₂	5.00·10 ⁻³	2.03·10 ⁻⁵	5.84·10 ⁻⁵
pH	12.8	12.8	12.7

Effective Diffusion Coefficients (m²/s)

Tracer & Material	Synthetic Porewater	Equilibrium Porewater
HTO Concrete	(1.1 – 1.9)·10 ⁻¹²	(3.3 – 3.7)·10 ⁻¹²
HTO Mortar	(1.4 – 1.6)·10 ⁻¹²	(1.1 – 1.3)·10 ⁻¹²
³⁶ Cl Concrete	(1.6 – 1.9)·10 ⁻¹³	(2.4 – 2.8)·10 ⁻¹³
³⁶ Cl Mortar	(2.2 – 2.6)·10 ⁻¹³	(3.4 – 3.9)·10 ⁻¹³

Apparent Diffusion Coefficients (m²/s)

	148 days	380 days	1494 days
¹³⁷ Cs D_a (m ² /s) Mortar	1.8·10 ⁻¹⁴	1.2·10 ⁻¹⁴	0.7·10 ⁻¹⁴

CONCLUSIONS

- The experimental constraint for diffusion experiments in cementitious materials must be checked with great accuracy. Cement is not an *inert* material with a fixed pore distribution, and when water or solute transport through the pore exist, alteration into its pore structure due to cementations process, can change the pore size and distribution. Chemical conditions and their evolution must be accounted for to understand the possible variations of transport parameters.
- Special care must be taken with kinetic processes that might influence the material structure. Diffusion tests with Cs showed that the determination of apparent diffusion coefficients is dependent on the experimental time. Furthermore, if the selected diffusion time is short, the simulation of concentration profiles could be obtained only by the superposition of two diffusion profiles, whereas this was not necessary to fit data obtained upon longer diffusion times (4 years), indicating that the material is evolving with time. This indicates that more appropriate results are obtained upon large experimental times, which cannot be always attainable for elements more strongly sorbing than Cs.

Acknowledgements: The research leading to these results has received funding from the European Union's Horizon 2020 Research and Training Programme of the European Atomic Energy Community (EURATOM) (H2020-NFRP-2014/2015) under grant agreement n° 662147 (CEBAMA).



Physical Chemistry of Actinides and Fission Products



GOBIERNO DE ESPAÑA
 MINISTERIO DE ECONOMÍA, INDUSTRIA Y COMPETITIVIDAD



CIEMAT
 Centro de Investigaciones Energéticas, Medioambientales y Tecnológicas

AMPHOS²¹



The
University
Of
Sheffield.



Pore-scale reactive transport modelling of transport and leaching processes in cementitious materials

S. Rohmen^{1*}, A. Idiat², G. Deissmann¹, D. Bosbach¹

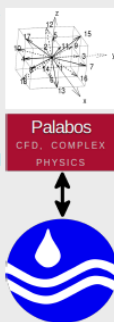
¹Institute of Energy and Climate Research (IEK-6): Nuclear Waste Management and Reactor Safety, Forschungszentrum Jülich GmbH, Jülich, Germany

²Amphos21 Consulting, Barcelona, Spain

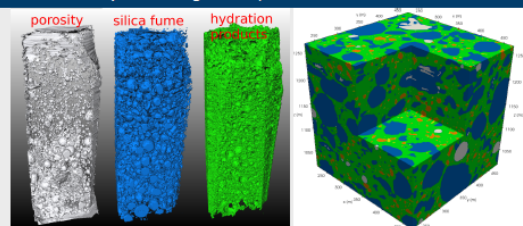
*e-mail: st.rohmen@fz-juelich.de

Motivation

- Application of reactive transport simulations on chemically complex systems like alteration/degradation of cement-based materials
- Geometric changes on microscopic scale can have significant effects on macroscopic hydrodynamic properties of porous media
- Pore-scale models provide an approach for a more accurate and mechanistic description of physical/chemical processes in heterogeneous porous media
- Coupling of transport code (Lattice-Boltzmann code **Palabos**) and geochemical code (**PhreeqcRM**)
- Sequential non-iterative approach (SNIA)
- Iterative synchronizing between codes
- Implemented with C++ template meta-programming techniques and MPI capabilities for HPC facilities

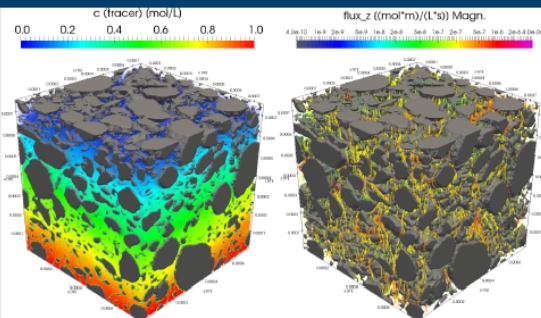


Microstructure input from segmented μ -XCT data



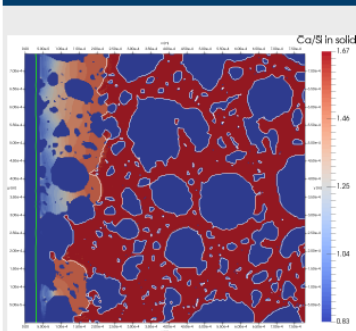
- Volume data of μ -XCT measurement of VTT reference cement paste provided by USFD
- Development of segmentation algorithm to derive microstructure and phase distribution
- Combining geometric description with information from a kinetic hydration model using Phreeqc

Estimation of effective diffusion coefficient



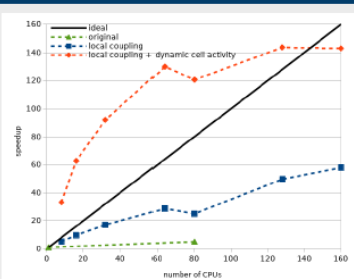
- Effective diffusion coefficient of VTT reference cement paste estimated from 3D steady state through diffusion simulations

2D simulation of cement paste leaching



- Leaching of VTT reference cement paste with pure water
- Constant concentration boundary condition applied on left hand side
- Simplified chemical system as test case
- Physical running time: 75 minutes
- Leaching depth of up to 200 μ m and decalcification of C-S-H
- Slight increase of porosity in the leached zone

Optimization of computing performance



- MPI communication overhead within PhreeqcRM leads to limitations in performance for complex systems
- Optimization of local process coupling and dynamic reaction cell activity results in significant improvement of performance

Outlook and future work

- Application to more complex chemical systems (i.e. leaching by granitic, saline and clay water) involving item additional processes such as clogging due to precipitation of solids like calcite and/or ettringite
- Reducing numerical limitations of the current Lattice-Boltzmann scheme (SRT-LBM) which can occur due to high contrasts in diffusion coefficients
- Further optimization in order to reduce computational demands to extend the reactive transport applications to larger 3D simulations
- Comparison of predicted effective diffusive coefficients to experimental data from CEBAMA project partners
- Comparison of simulations to results of leaching experiments performed in CEBAMA WP1

Acknowledgment

The research leading to these results has received funding from the European Union's Horizon 2020 Research and Training Programme of the European Atomic Energy Community (EURATOM) (H2020-NFRP-2014/2015) under grant agreement n° 662147 (CEBAMA).





The University
Of Sheffield.

NucleUS
Immobilisation Science Laboratory

midas

Radioactive Waste
Management

HORIZON 2020

Ce ba ma

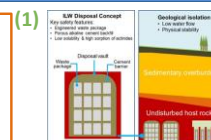
The Physico-Chemical Evolution of UK High-pH Backfill Material

Rita G. W. Vasconcelos^{*1}, Neil C. Hyatt¹, John L. Provis¹ and Claire L. Corkhill¹

NucleUS Immobilisation Science Laboratory, Department of Materials Science and Engineering, University of Sheffield, Sheffield, United Kingdom
*presenting author: rgwvasconcelos1@sheffield.ac.uk

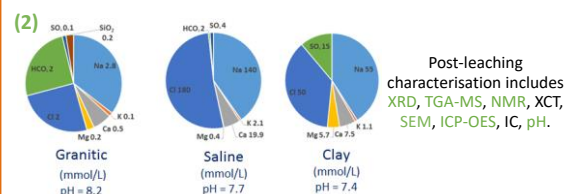
1. Introduction

Nirex Reference Vault Backfill (NRVB) is a high pH cementitious material considered for use as a backfill material in one of the conceptual scenarios for the UK geological disposal of intermediate level waste (Fig. 1). The aim of this project is to understand how the physico-chemical properties of NRVB will be affected by interactions with groundwater. We present the results of the first 6 months of NRVB in contact with 3 different types of groundwater (granitic, saline and clay) experiment.

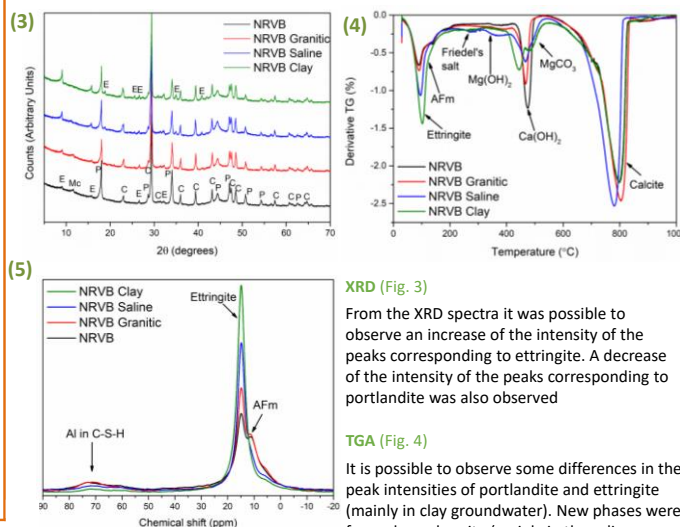


2. Experiment Methodology

- NRVB paste was prepared using the formulation previously outlined in the literature (1): 450 kg/m³ CEM I 52.5 N 170 kg/m³ hydrated lime and 495 kg/m³ limestone flour, with a water/solid ratio of 0.55.
- After 28 days of curing, cylindrical monoliths were prepared, each with 15 mm height x 15 mm diameter. The ends of the cylinders were sealed with epoxy resin.
- Semi-dynamic dissolution experiments were conducted in 60 mL vessels in contact with each of the 3 types of groundwater (Fig. 2), in an oven at 40 °C with controlled nitrogen environment. Sampling and replacement of the groundwater is taking place every 2 months.



3. Cement Characterisation



XRD (Fig. 3)

From the XRD spectra it was possible to observe an increase of the intensity of the peaks corresponding to ettringite. A decrease of the intensity of the peaks corresponding to portlandite was also observed

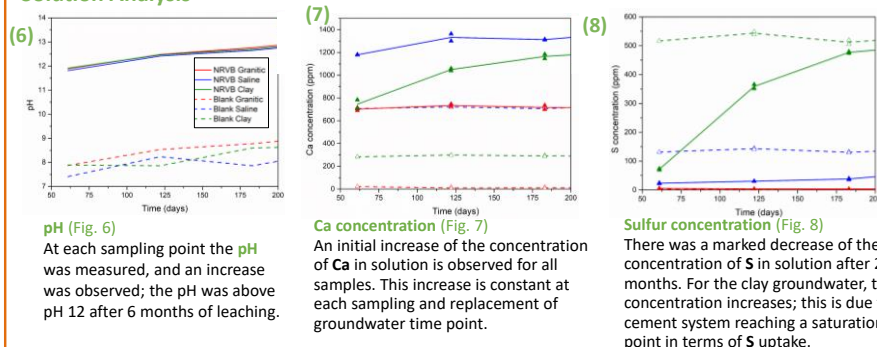
TGA (Fig. 4)

It is possible to observe some differences in the peak intensities of portlandite and ettringite (mainly in clay groundwater). New phases were formed, e.g. brucite (mainly in the saline groundwater) and possibly Friedel's salt.

AI MAS NMR (Fig. 5)

Formation of more ettringite, mainly in the samples in contact with clay and saline groundwater, was observed and there was a decrease in the chemical shift corresponding to the Al incorporated into the C-S-H.

Solution Analysis



pH (Fig. 6)

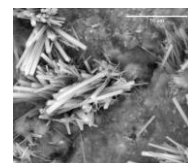
At each sampling point the pH was measured, and an increase was observed; the pH was above pH 12 after 6 months of leaching.

Ca concentration (Fig. 7)

An initial increase of the concentration of Ca in solution is observed for all samples. This increase is constant at each sampling and replacement of groundwater time point.

Sulfur concentration (Fig. 8)

There was a marked decrease of the concentration of S in solution after 2 months. For the clay groundwater, the S concentration increases; this is due to cement system reaching a saturation point in terms of S uptake.



(9)

SEM (Fig. 9)
Ettringite needles in a NRVB sample in contact for 4 months with clay groundwater

4. Conclusions

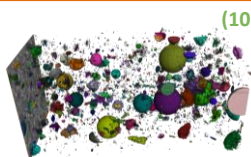
After 6 months of NRVB in contact with granitic, saline and clay groundwater, it was possible to observe differences:

- An increase of the pH was observed, which is consistent with the decrease of the concentration of portlandite observed in the XRD and TG data.
- The marked decrease of concentration of S in solution, correlates well with the increase of the formation of ettringite for all samples in contact with groundwater, but mainly in the samples in contact with clay groundwater.
- The formation of other phases was also observed, including the formation of brucite, magnesium hydroxide and possibly Friedel's salt.

The formation of different phases may have an effect in the buffering capacity of the NRVB and in the porosity.

5. Future Work

Ongoing sampling and replacement of the groundwater is being performed for over 1 year. This same experiment is also being performed in the Cebama reference cement paste. Post-leaching characterisation will include all the techniques shown here and also X-ray computed tomography (Fig. 10), scanning electron microscopy, ion chromatography and Rietveld refinement of the XRD data for quantification. A second long-duration experiment is currently being performed with the two cements. This is a static experiment, where cement samples were placed in a 2L vessel in contact with granitic, saline and clay groundwater. The cement samples will be only analysed at the end of the experiment.



(10)



@ISL_Sheffield
@cementsatshf

References

A.J. Francis et al (1997). NSARP Report no: S/97/014

Acknowledgements: The authors wish to acknowledge funding for this research from Radioactive Waste Management Limited and the European Commission Horizon 2020 Research and Training Programme of the European Atomic Energy Community (EURATOM) (H2020-NFRP-2014/2015) under grant agreement n° 662147 (CEBAMA). Amy Shelton (RWM) is thanked for her comments and input to this work.



Property of bonded planar interface between COx claystone and low-pH concrete

Zaobao Liu¹, Jianfu Shao¹, Shouyi Xie¹, Xaviers Bourbon^{2,3}, Guillaume Decamps^{2,3}

¹LaMcube, University of Lille, Villeneuve d'Ascq

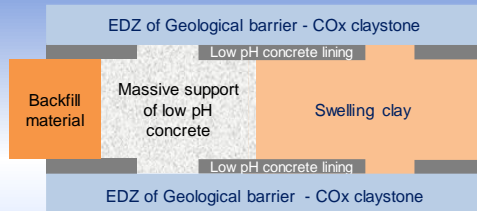
²RD, Andra, Laboratoire de Recherche Souterrain de Meuse/Haute-Marne, Bure

³Andra - French National Radioactive Waste Management Agency, Châtenay-Malabry, France

Author e-mail: zaobao.liu@polytech-lille.fr; jianfu.shao@polytech-lille.fr; shouyi.xie@polytech-lille.fr



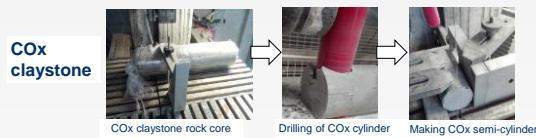
Background



- Repository sealing component consists of multiple materials
- Low-pH concrete will be poured on the surface of geological barriers, e.g. the Callovo-Oxfordian(COx) claystone
- Shear force comes from swelling clay - **Shear strength** and **permeability** of interface

Materials & Methods

Interface sample preparation

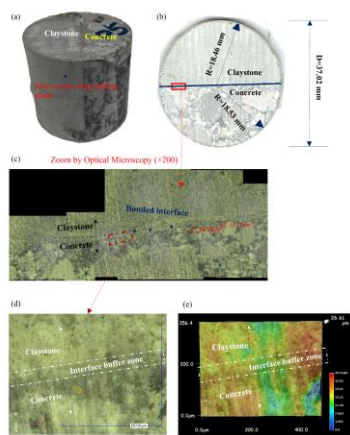


Low pH concrete	Type	Superplasticizer %	Binder	Cement	Silica fume	Flying ashes	Dairy	Sand	Gravels	Effective water	W/B	G/S
	T _L	1.5	380	76	123.5		180.5	855	949	152	0.4	1.1



- Water dissolution of COx claystone at contacting surface during concrete pouring and vibration
- Cementation occurs at interfaces due to concrete hardening
- Bonding force grows during concrete maturation

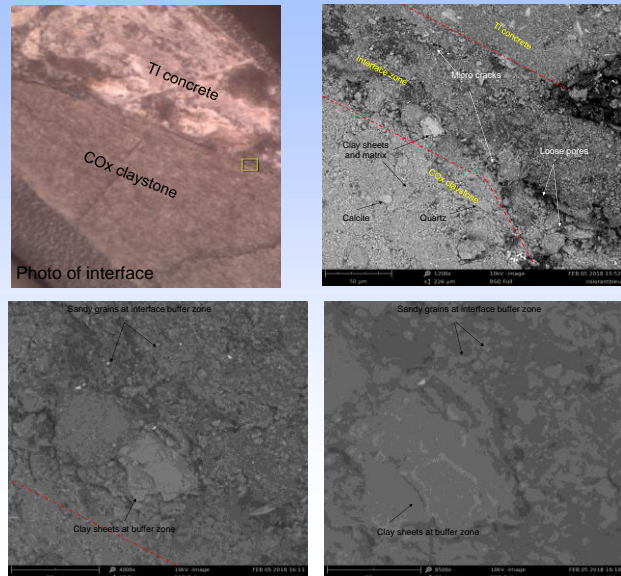
Interface bonding features under Optical Microscopy



- Micro cracks creates in COx claystone
- Interface cements well with pores in a few tens of micrometers
- A buffer zone creates at the interface
- Indication of strength growth during concrete maturation
- Indication of ultra-low permeability of well-bonded interface

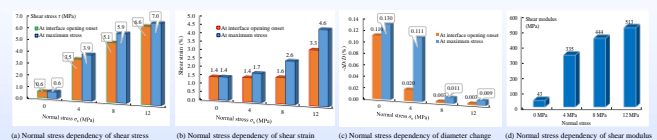
Results

Interface buffer zone under SEM

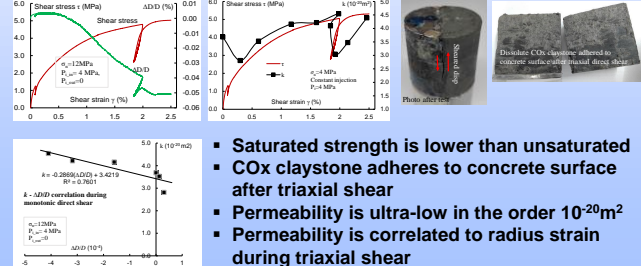


- A buffer zone of tens of micrometers creates at the interface
- Clay sheets appears at the interface buffer zone
- Interface buffer zone is more loose than the COx clay or TI concrete with larger pores included

Interface mechanical properties during triaxial direct shear



Interface hydro-mechanical properties



Conclusions

- COx claystone can be well-cemented with the T₁ low-pH concrete due to concrete hardening at the interface
- Shear strength depends on normal stress and there is bonding strength
- Permeability of bonded interface sample is ultra-low as the COx claystone and TI concrete under confined saturated conditions

Acknowledgments:

The research leading to these results has received funding from the European Union's Horizon 2020 Research and Training Programme of the European Atomic Energy Community (EURATOM) (H2020-NFRP-2014/2015) under grant agreement n° 662147 (CEBAMA).

More details in:

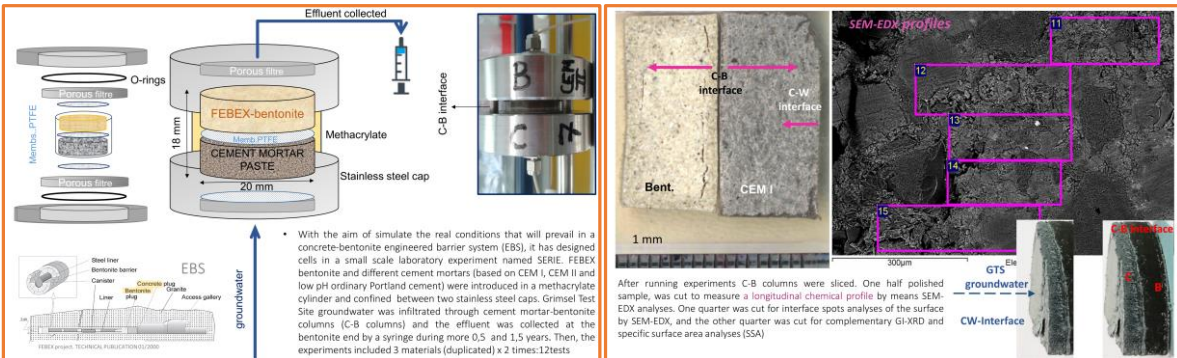
[1] Zaobao Liu, Jianfu Shao, Shouyi Xie, Guillaume Decamps, Xavier Bourbon, Claystone-concrete interface process and mechanical properties in argillaceous rock hosted underground repositories, Scientific Report, March 2018 revised.
[2] Zaobao Liu, Jianfu Shao, Shouyi Xie, Xaviers Bourbon, Guillaume Decamps, Bonding and hydro-mechanical properties of claystone/concrete interface, 3rd Annual Workshop of CEBAMA, submitted March 2018.



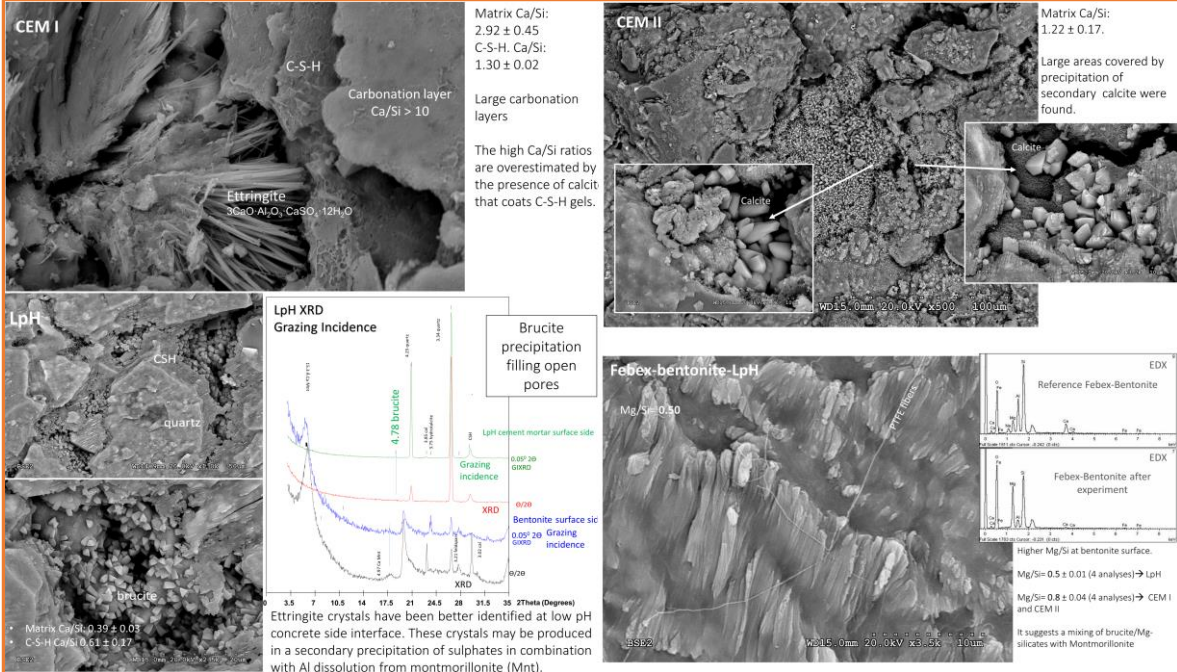
Development of Surface Reactivity Interface Experiments (SERIE) for studying FEBEX bentonite-concrete interaction

Daniel E. González-Santamaría¹, María Angulo¹, Javier González-Yelamos¹, Raúl Fernández², Almudena Ortega¹, Ana Isabel Ruiz¹, Enrique Rodríguez², Jaime Cuevas^{1*}
¹ Universidad Autónoma de Madrid (UAM) (SP)

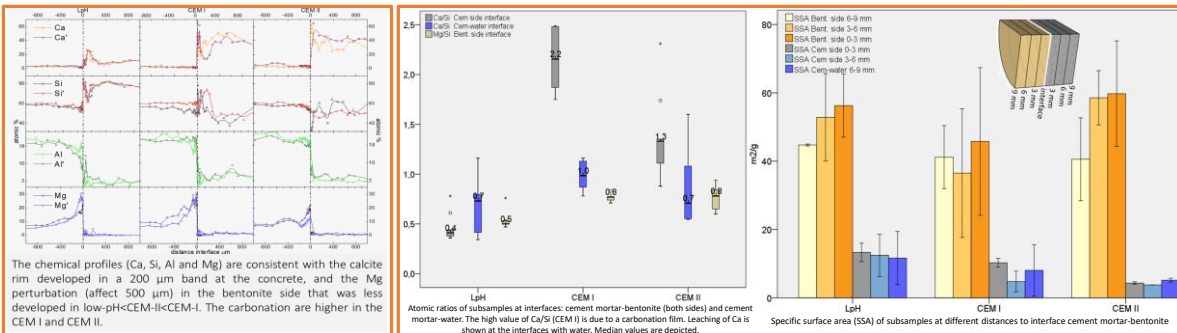
Introduction and methods



Results



Results



Conclusions and future work

The comparative study is able to help in the discrimination of the reaction processes for the 3 types of cementitious materials. The main observations were: (a) formation of protective calcite layers, relevant in CEM I and CEM II by means of secondary calcite precipitation, (b) high Mg/Si ratio at FEBEX-bentonite side where perturbations were less developed in low-pH <CEM-II <CEM-I in parallel with the intensity of carbonation in the cement mortar, (c) $1.3 > \text{Ca/Si} > 1$ characterizes C-S-H matrix of cement mortar in CEM I and CEM II, while LpH experiments shown $\text{Ca/Si} < 1$. It suggests tobermorite-like structures. Mg phases were observed in the bentonite, and were not observed in the cement mortar. C-(A)-S-H have presumably formed in the cement mortar interface. These processes reproduce at small scale the perturbation previously observed at larger scales. The analysis of the remaining 1.5 years SERIE experiments will give us a more concise view of the processes development. Some uncertainties as the evolution of C-(A)-S-H, Ca/Si ratios and the nature of Mg-silicate phases have to be solved to constrain the modelling exercises.

Acknowledgements

The research leading to these results has received funding from the European Union's Horizon 2020 Research and Training 302 Programme of the EURATOM (H2020-NFRP-2014/2015) under grant agreement n° 662147 (CEBAMA).

Cebama 3rd Annual Workshop, Nantes, 17-18 April 2018

Clayey water interaction with high and low-pH concretes

Á. Fernández, M.C. Alonso, J.L. García Calvo
CSIC- Institute of Construction Science Eduardo Torroja, SPAIN

Introduction

The modifications promoted in different concretes, high and low pH, by its interaction with simulated clayey groundwaters (GW) is evaluated. This interaction is studied through percolation tests. High pH concrete based on CEM I 42.5 R/SR binder (hpH-CEM I) and low pH concrete based on 60% OPC + 40% SF (lpH-OPC+SF) were studied. Also, the percolated liquids are periodically evaluated.

Simulated clayey water composition

Simulated clayey water (pH = 8.0)								
Component	Ca	Fe	Mg	K	Na	SO ₄	Si	HCO ₃
Content (ppm)	460	0.3	216	28	2933	7271	2.8	119
Cl	845							

Concretes composition

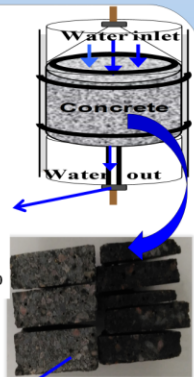
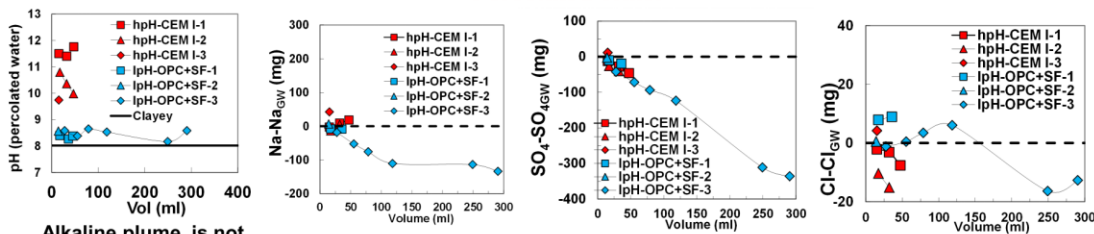
	Binder (kg/m ³)	Coarse agg (kg/m ³)	Sand (kg/m ³)	Water (kg/m ³)	Superplasticizer (kg/m ³)
hpH-CEM I	300	1017	816	165	-
lpH-OPC+SF	320	855	1033	160	3.2



Results

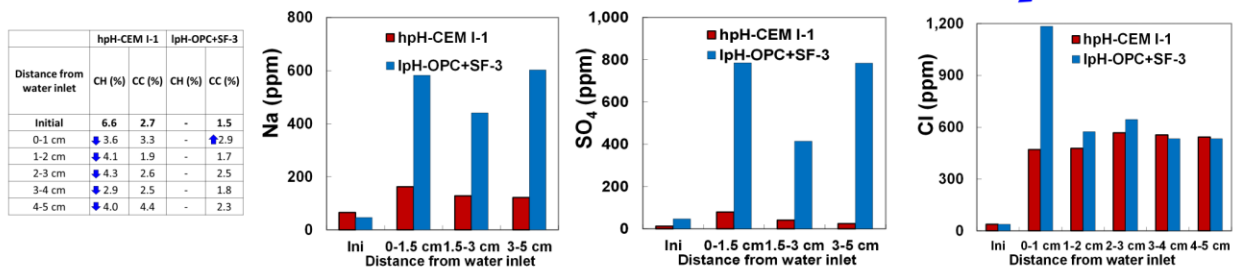
Interaction of hpH and lpH concretes with clayey water

Percolated Water



Microstructural Changes

hpH-CEM I (9 months, 50 ml water percolated) / lpH-OPC+SF (9m, 290ml)



The characterization of the concretes after percolation test confirms the retention of Na, SO₄ and Cl from the clayey water in the concretes

Conclusions

- The low hydraulic conductivity of the concretes does not cause significant changes in the microstructure of the concretes after 9 months tests.
- The alkaline plume is detected in the hpH concrete but it is not detected in lpH concrete.
- Na, SO₄ and Cl from clayey water are retained in the concretes.
- Portlandite is progressively depleted in hpH concrete due to the clayey water interaction.
- Calcite content increases in the lpH concrete, especially in the cm in contact with the water inlet. An external layer on the surface is not observed.

Acknowledgement

The research leading to these results has received funding from the European Union's European Atomic Energy Community's (Euratom) Horizon 2020 Programme (NFRP-2014/2015) under grant agreement, 662147 – Cebama.

PAUL SCHERRER INSTITUT

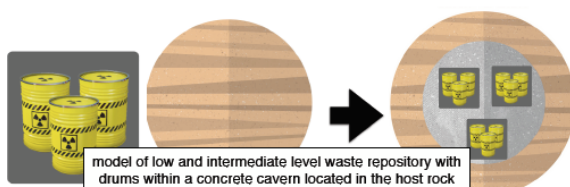
u^bUNIVERSITÄT
BERN

FEniCS-Reaktoro coupling: constricted pores and cement/clay interfaces

Leonardo Hax Damiani^{a,b}, Yuankai Yang^c, Sergey V. Churakov^{a,b} and Georg Kosakowski^a^aLES, Paul Scherrer Institut, CH-5232 Villigen PSI, Switzerland^bInstitute for Geological Sciences, University of Bern (CH), Switzerland^cDepartment of Engineering Mechanics, Tsinghua University, Beijing 100084, China

Motivation & description

- Cement and clay based materials are foreseen for engineering and natural barriers in deep geological repositories for radioactive waste.

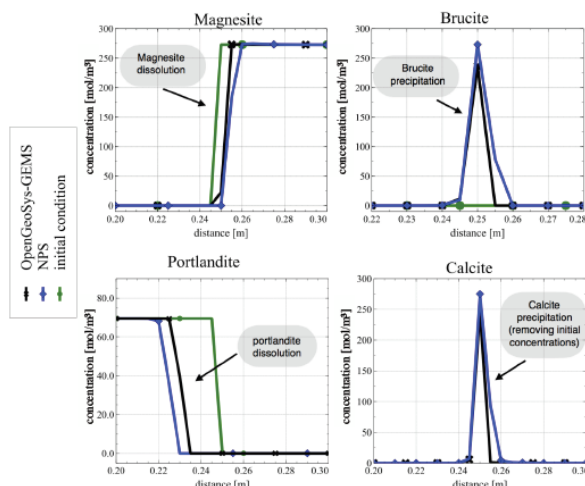


- Clay minerals and cement phases like C-S-H have charged surfaces.
- Consideration of charged surfaces and electrochemical migration of ions is important for quantification of diffusive transport in clay and cement media.

Approach

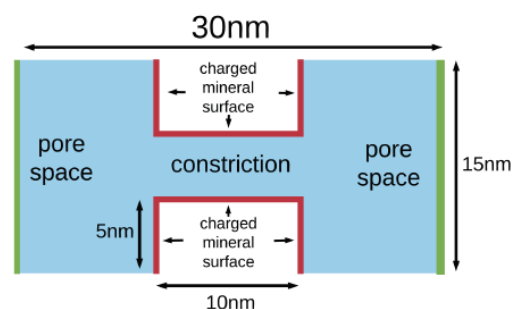
- We developed an open-source code for reactive transport simulations called *NPS*. *NPS* couples the finite element framework *FEniCS* [1] and the chemical solver *Reaktoro* [2] based on the operator splitting approach.
- NPS* uses the *Poisson-Nernst-Planck (PNP)* equation to describe the transport of ions and it has been tested and validated in different scenarios:
 - ✓ Experimental data for the flux of charged species through an uncharged porous membrane. This is done by imposing a concentration gradient with a constant background electrolyte [3].
 - ✓ Comparative benchmark study with *OpenGeoSys-GEMS* [4] of a simplified carbonation experiment.

→ Portlandite and magnesite dissolution causing calcite and brucite precipitation.



Application: diffusion in a constricted pore

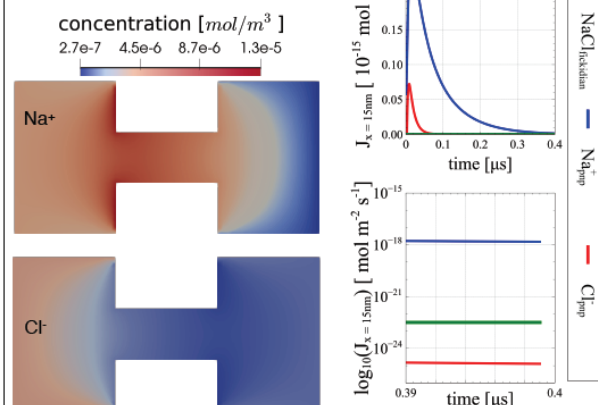
- Ions can be fully excluded or strongly enriched in the pore space because of the influence of charged mineral surfaces.
- We set up a 2D model of a compacted pore space with charged mineral surfaces (-0.033V). The initial distribution on the domain is $5 \mu\text{mol/m}^3$ NaCl on the left boundary and $1 \mu\text{mol/m}^3$ NaCl elsewhere. At the boundaries the concentration are fixed (Dirichlet BC).



- NaCl is fully dissociated into Na^+ and Cl^- (with different mobilities). Their mobilities is coupled via the PNP equation.

- At steady state, Na^+ concentration is increased and Cl^- is decreased closer to the charged mineral surface.

- At steady state, Na^+ flux is higher than that of Cl^- . Theoretical Fickian flux is between both.



Ongoing

- Benchmarking and modelling experiments from WP1 partner (UniBern).



ACKNOWLEDGMENTS

This project is part of CEBAMA and addresses key scientific questions related to the use of cement-based materials in nuclear waste repositories including interface processes between cement-based materials and host rocks, retention of high priority radionuclides, and the development of models predicting changes in transport properties of cement-based materials. This work was supported by the Swiss State Secretariat for Education, Research and Innovation (SERI) under contract number 15.0186-2. The opinions expressed and arguments employed herein do not necessarily reflect the official views of the Swiss Government. Authors receive partial financial support from Nagra.

REFERENCES

- [1] Amini, M. S., Bacht, J., Hahn, J., Johansson, A., Kahle, B., Lagg, A., ... Vella, G. N. (2016). The FEniCS Project Version 1.5. *Archive of Numerical Software*, 3(10), 1-10. <https://doi.org/10.1155/ans.2016.1002003>
- [2] Amini, M. S., Kulkarni, D. A., Smith, W. R., & Sauer, M. O. (2017). An overview of computational methods for chemical equilibrium and kinetic calculations for geochemical and reactive transport modeling. *Pure and Applied Chemistry*, 89(5), pp. 697-743.
- [3] Damiani, L. H., Gauss, M., Churakov, S. V., Kosakowski, G. (2018). Rapid development of a reactive transport code with FEniCS and Reaktoro. *CEBAMA Deliverable n° D3.04*
- [4] Kosakowski, G., & Watanabe, N. (2014). OpenGeoSys-GEMS: A numerical tool for calculating geochemical and porosity changes in saturated and partially saturated media. *Physics and Chemistry of the Earth*, 70-71, 138-146. <https://doi.org/10.1016/j.pce.2013.11.008>

Aged interface between Opalinus Clay and low-pH mortar: sample preparation, X-ray computed tomography and core infiltration experiment for hydraulic-chemical properties

Ellina Bernard, Urs Mäder, Andreas Jenni
University of Bern, Institute of Geological Sciences, RWI, 3012 Bern, Switzerland

Introduction

The interfaces between “low-pH” (Portland cement and silica fume binder) mortar and Opalinus Clay (OPA) collected after few years of interaction in field are studied in laboratory to get the reactive transport properties of the transitional zone at the interface and also, a better understanding of the chemical changes (mineralogy and porosity). Experimental devices under confining pressure with independent control of the hydraulic gradient are an excellent way to look at the reactive transport properties of the system. The analysis of the sample aliquots collected in syringes that percolated across the old interface gives the advective properties of water transport (D_2O) and anion transport (Cl), and the bulk hydraulic conductivity according to Darcy's law. In case of a compound sample including a mortar/claystone interface, a back analysis can be made knowing the individual properties of the undisturbed materials involved.

Material properties

The samples were recovered during the sampling campaigns of 2015 in the CI Experiment (Cement-Clay Interaction Experiment) at the Mont Terri rock laboratory (St. Ursanne, Switzerland, www.mont-terri.ch, e.g. [1]) after 3.2 years after mortar emplacement.

Parameters	Opalinus Clay (Mont Terri, shaly facies)	
	Range*	best estimate
Grain density (kg/dm^3)	2.40 - 2.53	2.45
Bulk dry density (kg/dm^3)		
Specific surface area (m^2/g)		
Porosity (vol%)	13-21	16
Water content (wt%)	5.0-8.9	6.6
Effective diffusivity (m^2/s)		
Tritium (HTO)	$7.1 \cdot 10^{-12}$ - $1.1 \cdot 10^{-11}$	$1 \cdot 10^{-11}$
	$5 \cdot 10^{-11}$ - $6.8 \cdot 10^{-11}$	$5.4 \cdot 10^{-11}$
I ⁻	$2.3 \cdot 10^{-12}$ - $4.2 \cdot 10^{-12}$	$3 \cdot 10^{-12}$
	$1 \cdot 10^{-11}$ - $3 \cdot 10^{-11}$	$2 \cdot 10^{-11}$
Hydraulic conductivity (m/s)	$2 \cdot 10^{-14}$ - $1 \cdot 10^{-12}$	$2 \cdot 10^{-13}$

*[1]

Parameters (Test after 3 years*)		ESDRED	stand. dev.
water permeability	$[10^{-17} m^2]$	23	36
water hydraulic conductivity	$[10^{-10} m/s]$	22	35
wet density	$[kg/m^3]$	1970	
Backfill density	$[kg/m^3]$	1860	
Porosity	$[%]$	31	

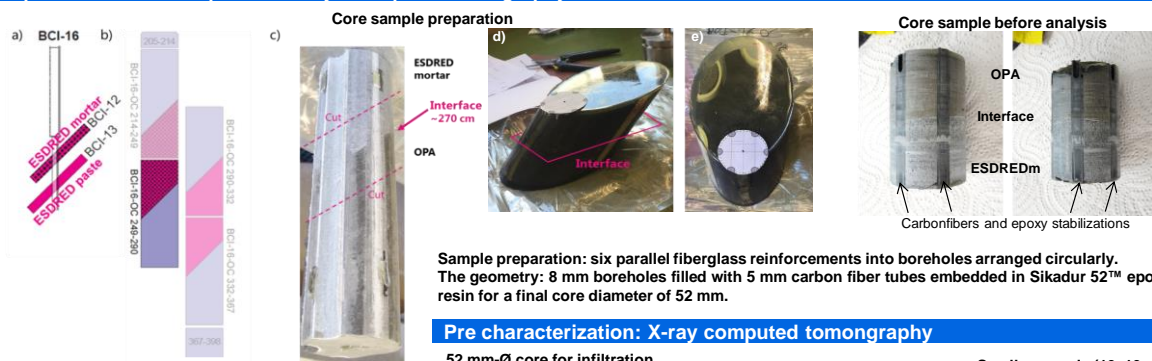
*[2]

Goals

- Preparation of an aged well-preserved interface in a core of 50 mm in diameter without dislocations to:
- Assess the physical and hydraulic properties of the interface via experiments using the core infiltration technique for hydraulic-chemical properties coupled with X-ray computed tomography for pre and post characterization.

Experiment

Preparation of the sample and X-rays computed tomography

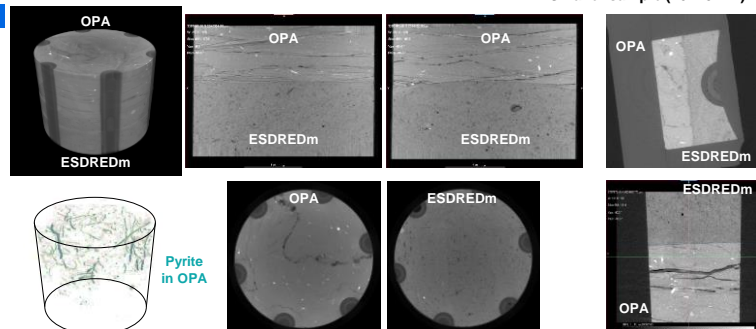


Sample preparation: six parallel fiberglass reinforcements into boreholes arranged circularly. The geometry: 8 mm boreholes filled with 5 mm carbon fiber tubes embedded in Sikadur 52™ epoxy resin for a final core diameter of 52 mm.

Pre characterization: X-ray computed tomography

52 mm-Ø core for infiltration

Smaller sample (10x19mm)



Infiltration and advective displacement

Core infiltration cell

Artificial OPA pore water

	g/L
NaCl	12.393
NaHCO ₃	0.044
CaCl ₂ ·2H ₂ O	2.134
KCl	0.108
MgCl ₂ ·6H ₂ O	3.337
Na ₂ SO ₄	2.018
SrCl ₂ ·6H ₂ O	0.131
D ₂ O	~ 0.035

The artificial pore water (APW) kept at equilibrium with the atmospheric CO₂ pressure and only composed of salts (Na⁺, K⁺, Sr⁺, Ca²⁺, Mg²⁺, Cl⁻, HCO₃⁻, SO₄²⁻) + D₂O.

Future work

- Collection of all data to give proper water transport properties
- Additional SEM/EDS analysis and autoradiography measurement for porosity quantification (Uni. of Helsinki)

Similar work will for the Portland concrete - OPA interface aged for 10 years + positron emission tomography (PET) (Uni. of Dresden)

After reconstruction (pixel/voxel size of 30 µm, 1920x1920 pixels)

OPA:

- Trace of a fracture subparallel to bedding (more or less horizontal) as a sinusoidal trace containing some macro-porosity
- Bright specks represent small inclusions of phases with very high X-ray attenuation, such as pyrite. The isolated pyrite in shown in green blue
- Cracks are the only porosity observable

ESDREDm:

- Uniform distribution of the biggest pores and supposedly of the hydrates
- Homogeneous overall fabric in the Ø-52 mm
- More details resolved on smaller samples at higher resolution (pixel/voxel size of 10 µm, 1920x1920 pixels) and the mineral grains can be detected

Contact: ellina.bernard@geo.unibe.ch [1] Bossart et al., Mont Terri rock laboratory, 20 years of research: introduction, site characteristics and overview of experiments, Swiss Journal of Geosciences, 110 (2017) 3-22. [2] F. Jacobs, CI-Experiment: Water permeability analysis of 2 year old samples, Mont Terri Technical Note TN 2015-101, Mont Terri Project (2015).

Changes in Groundwater Composition Following Interaction with Cement

E. Rastrick¹, M. Isaacs^{1,2}, M. Felipe-Sotelo¹ and D. Read^{1,3}

¹ University of Surrey (UK), ² Institute of Energy and Climate Research: Nuclear Waste Management and Reactor Safety (IEK-6) (DE)

³ National Physical Laboratory (UK)

Introduction

The disposal concept for low and intermediate level waste in the UK envisages the use of cementitious materials for structural purposes, waste grout and as backfill material. The high pH of the cement is intended to reduce the solubility and limit the migration of several safety critical radionuclides. An influx of groundwater upon closure of the repository will degrade and alter the cement, potentially compromising radionuclide containment during the service life. Degradation processes include changes in pH, leaching of alkali hydroxides and decalcification [1,2]. The extent of degradation will depend on the type of cement and the composition of the groundwater with which it is in contact. This research aims to understand the changes in groundwater composition following interaction with cementitious materials.

Methodology

The experimental protocol was employed to investigate the interaction of various groundwaters with cements. Three cement blends have been chosen to cover those being considered as part of different European repository concepts. These are a Portland cement (CEMI), a ground granulated blast furnace slag: ordinary Portland cement (GGBS:OPC) blend and Nirex Reference Vault Backfill (NRVB). The three synthetic groundwaters produced broadly emulate granitic, clay and saline host rock environments. The cement conditioning groundwater experiments use equal volumes of cement and groundwater, whereby changes in groundwater composition should be evident. The analysis methods used to analyse the groundwater solutions were ion chromatography and flame atomic spectroscopy techniques.

Results and Discussion

Changes in groundwater pH due to interaction between cement and groundwater

For the cement conditioning groundwater experiments (solid/solution ratio = 1) the pH of the groundwaters increased from pH 7-8 to pH 11.5-13.5 after 9 days. The three cement blends studied within this experiment were CEMI, GGBS:OPC and NRVB. The pH change for CEMI and NRVB is similar yet the GGBS:OPC blend leads to consistently lower groundwater pH compared with the other two cement blends. Figure 1 shows that the high pH, greater than 11.5, remained at this level for the duration of the experiment (116 days).

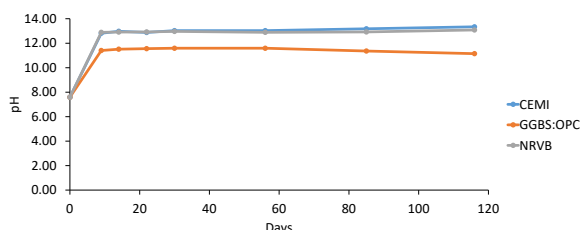


Figure 1: Changes in clay groundwater pH as a result of interaction with cementitious materials.

Changes in anion concentration of groundwaters following interaction with cement

Over 116 days, the chloride and sulphate concentrations in the groundwaters decreased following interaction with cementitious materials. The cement blends can be grouped, with CEMI and NRVB behaving similarly compared to GGBS:OPC. Figure 2 shows the chloride and sulphate concentrations, respectively, of clay groundwater following interaction with the cement blends as an example.

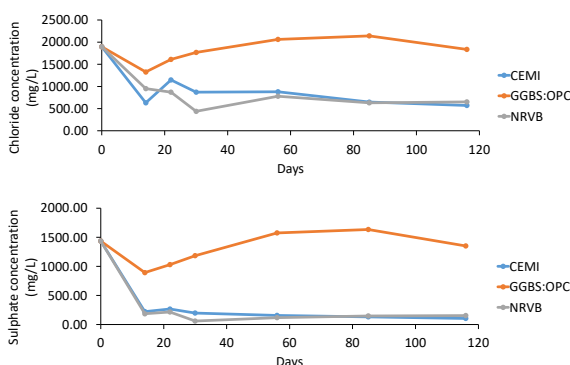


Figure 2: Changes in chloride and sulphate concentrations of clay groundwater after interaction with cement for 116 days. Anion concentrations were determined using ion chromatography.

Changes in concentration of alkali and alkaline earth metals following interaction with cement

Concentrations of sodium, potassium and calcium were determined from samples obtained over a period of 116 days. There is an increase in sodium and potassium in the groundwaters following interaction with cement, this correlates with the increase in pH which is measured. The sodium and potassium hydroxides in the cement are leaching out of the cement. For calcium, it is clear that decalcification is occurring to the cements as there is an increase in calcium concentration within each of the cement blends in each of the groundwaters. Figure 3 shows an example of the increase in sodium and potassium for clay groundwater.

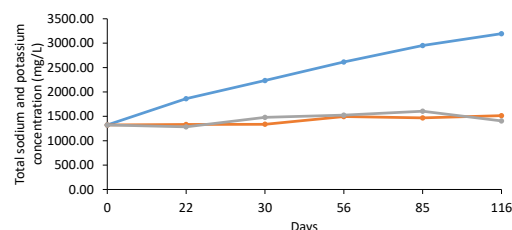


Figure 3: Changes to total sodium and potassium concentration of clay groundwater following interaction with cementitious materials for a period of 116 days.

Conclusions and Future Work

Changes to the groundwater composition has been observed following interaction with cement for a period of 116 days. There is an overall decrease in the concentration of chloride and sulphate yet an increase in the sodium and potassium due to leaching of alkali hydroxides. Future work will consist of completing the same experiments with the CEBAMA reference blend. Analysis of the solids is also required to determine the phases that the analytes have interacted with and potentially incorporated in. Techniques to be used for solid characterisation include X-ray computed tomography, scanning electron microscopy-energy dispersive spectroscopy and X-ray diffraction. Advective transport of groundwater will also be studied to determine how the composition changes compared to the diffusive transport currently studied.

Advection

The advection experiments, based on previous research completed by Felipe-Sotelo *et al.* [3], involve flowing groundwater through the cement blocks under pressure. The cement blocks contain a central well with a depth of 25 mm and a diameter of 10 mm. A pressurised vessel, using nitrogen, containing groundwater will be attached to the advection cell and the groundwater forced through the cement block. The groundwater will be collected via the outlet holes at the edges of the advection cell. The composition of the synthetic groundwater which has moved through the cement block will be analysed to observe any changes. Alterations could be due to ions that have originated from dissolution of cement. The groundwater flow through the cement block will be at a constant rate but the migration of groundwater accelerated compared to the diffusion experiments. The cement block can also be analysed to observe the changes in the phases which are within the cementitious material, the use of SEM-EDS and XRD will achieve this.



References and Acknowledgements

- [1] NDA (2010) Geological Disposal: Near-field evolution status report, NDA Report NDA/RWMD/033, 1-152.
- [2] Jacques, D., Perko, J., Seetharam, S.C. and Mallants, D. (2014) A cement degradation model for evaluating the evolution of retardation factors in radionuclide leaching models, *Applied Geochemistry*, **49**, 143-158.
- [3] Felipe-Sotelo, M., Hinchliff, J., Field, L. P., Milodowski, A. E., Holt, J. D., Taylor, S. E. and Read, D. (2016) The solubility of nickel and its migration through the cementitious backfill of a geological disposal facility for nuclear waste, *Journal of Hazardous Materials*, **314** 211-219

We would like to thank the National Physical Laboratory for assistance with the experimental programme. The research has received funding from the European Union's Horizon 2020 Research and Training Programme of the European Atomic Energy Community (EURATOM) (H2020-NRFP-2015/2016) under grant agreement n° 662147 (CEBAMA) and from Radioactive Waste Management (RWM), UK.